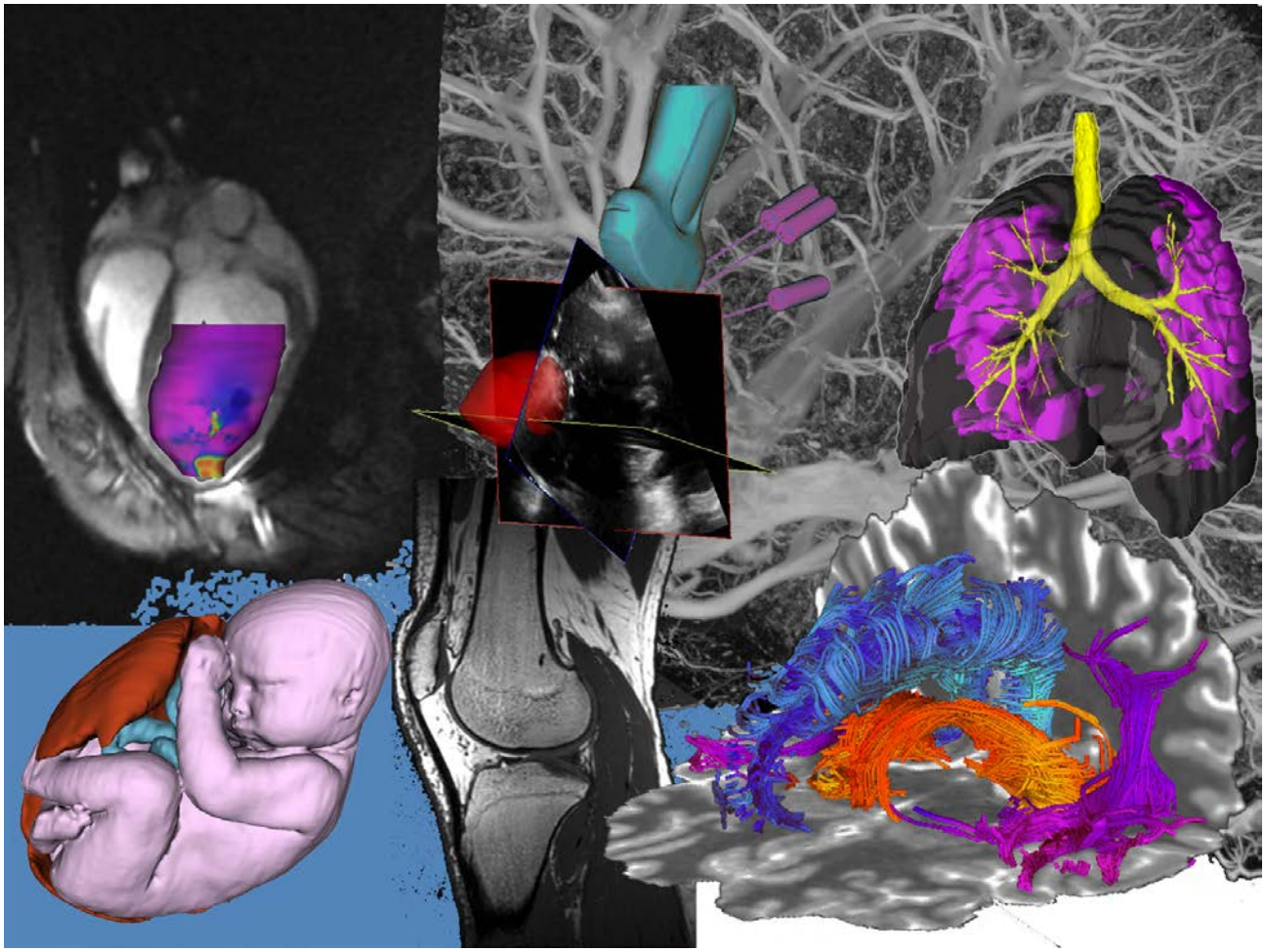

15th Annual Meeting

of

IMAGING NETWORK ONTARIO

LONDON, ON

MARCH 15 – 16, 2017

CORPORATE SPONSORS

GOLD SPONSORS

Synaptive is a medical device and technology company pursuing connections to transform the process of care in and beyond the operating room. In collaboration with leading clinicians and healthcare systems, Synaptive is revolutionizing products and services that cross traditional barriers to provide clinicians with the information they need to ensure the best possible outcomes for patients.

Western University's Bone and Joint Institute aims for lifelong mobility by engaging in high-impact transdisciplinary research that will enhance active living, mobility and movement; investigate causes, prevention, diagnosis, and treatment options; and improve support systems and palliation for a wide range of MSK conditions.

SILVER SPONSORS

As part of the federal government's Networks of Centres of Excellence (NCE) program, CANet is a multidisciplinary, multi-sectoral research and development network of over 100 investigators, well-positioned industry partners, patients and healthcare providers focused on arrhythmia research and commercialization activities. At the core of CANet's success are our connections with our researchers, our trainees, and our fully-engaged patients and partners.

FUJIFILM VisualSonics, Inc is the undisputed world leader in real-time, in vivo, high-resolution, micro-imaging systems, providing modalities specifically designed for preclinical and clinical research.

From radiotherapy and imaging QA phantoms to automated QA software, 3D dosimetry and optical CT scanners, Modus QA products are built to provide you with confidence that every patient is receiving the best possible treatment.

Philips is a leading health technology company focused on improving people's health and enabling better outcomes across the health continuum – from healthy living and prevention, to diagnosis, treatment and home care.

Shelley Medical Imaging Technologies. Realistic multimodality phantoms for radiation therapy & diagnostic imaging. Products include; physiological flow pumps, anatomical vascular & heart models, heart motion phantoms, MRI compatible motion phantoms, tissue mimicking Doppler phantoms & micro-CT phantoms.

15 March 2017

Dear ImNO 2017 Attendees:

Welcome to the Imaging Network Ontario (ImNO) 2017 Meeting. This year marks our 15th annual meeting.

ImNO is an initiative created in response to a request by the Ontario Research Development Challenge Fund – now the Ontario Research Fund – for assistance in harmonizing its investments in imaging research. The establishment of ImNO provides a means of harnessing and focusing the intellectual and innovative capabilities at Ontario universities in partnerships with emerging and established medical imaging companies to create a strong and sustainable internationally competitive imaging industry based on scientific excellence in Ontario.

Since its' inception in 2003, the annual ImNO meeting has welcomed invited presentation from world-class scientists and proffered presentations from Ontario and across the county. This year, I am pleased to welcome three new consortia to our conference: 1) NIH – Hyperpolarized 13C MRI of Placental Metabolic Abnormalities; 2) Canada First Research Excellence Fund (CFREF) – BrainsCAN; 3) Ontario Research Fund – Development & Translation of MRI Technology for Neuro-Interventional Applications.

For the 2017 meeting, we received a total of 175 submitted abstracts that were reviewed by an average of 3 reviewers. The ImNO 2017 Scientific Committee then assembled the final program: 5 keynote speakers, 62 oral presentations and 113 poster presentations

In closing, I would like to acknowledge the significant contributions made by the members of the Scientific and Organizing Committees. Together they have worked very hard to bring us this year's meeting. We hope you enjoy this year's program and world-renowned keynote speakers.

Sincerely,

David Holdsworth

Chair, Scientific Committee, 2017 ImNO Meeting

Sponsoring Consortia

The Annual Meeting of Imaging Network Ontario (ImNO) promotes Canada's role as a leader in medical imaging innovation by cultivating synergy among consortia and partnerships between Ontario and other Canadian imaging entities.

The following consortia and programs supported the 2017 ImNO Symposium financially:

Development of Novel Therapies for Bone and Joint Diseases

Director: Dr. David Holdsworth **Ontario Research Fund**

Musculoskeletal disorders are the most common cause of severe long-term pain and physical disability, affecting hundreds of millions of people around the world. The economic burden is high; joint diseases cost the Ontario economy more than $2 billion per year. To reduce this disease burden, this Ontario Research Fund Research Excellence program focuses on the "Development of Novel Therapies for Bone and Joint Diseases," including improved diagnostic imaging techniques and new approaches for image-guided therapy. A multidisciplinary team of imaging scientists, biomedical engineers, physical therapists, and orthopaedic surgeons work together on key research projects, including the development of new ways to post-process 3D MRI and CT data to guide surgery, dynamic imaging of moving joints (under load), and image-based design of "patient-specific" orthopaedic components.

Heart Failure: Prevention Through Early Detection Using New Imaging Methods

Director: Dr. Frank Prato **Ontario Research Fund**

Consortium partners: Lawson Health Research Institute, Sunnybrook Research Institute and University of Ottawa Heart Institute. Ten percent of Ontarians over 60 have heart failure. One quarter will die within one year of diagnosis and almost all in ten years. Our LHRI/SRI/UOHI consortium is developing combined PET and MRI imaging methods for early diagnosis when treatment is still possible. The imaging methods developed are being commercialized and will benefit Ontario by improving the health of its citizens and creating new jobs.

Imaging for Cardiovascular Device Intervention

Director: Dr. Graham Wright **Ontario Research Fund**

Cardiovascular diseases have evolved from an acute killer to a chronic disease challenge. In recent years, there have been major advances in less invasive treatments, placing an emphasis on the development of imaging and tracking technologies. Focusing on electropathophysiology, percutaneous procedures, and valve replacement, researchers at Sunnybrook and Robarts Research Institutes, working with local, national, and multinational diagnostic imaging and interventional device companies, are advancing the state-of-the-art in image acquisition and analysis with ultrasound, MRI, x-ray, and CT methods, including the design of visualization platforms and associated communication and control interfaces for interventional guidance, facilitating fusion and manipulation of prior and real-time imaging and device information. The ultimate goal is more effective utilization of imaging to improve outcomes for patients with chronic ischemia, complex arrhythmias, and heart failure related to structural heart diseases.

Development & Translation of MRI Technology for Neuro-Interventional Applications

Director: Dr. Blaine Chronik **Ontario Research Fund**

In partnership with Synaptive Medical Inc., researchers in the Department of Physics and Astronomy at Western University are working on the development of new MRI platforms customized for clinical point-of-care imaging. The objectives of the program are to design and

produce new high-strength, customized head gradient coils for use within new magnet systems for neuro-interventional and point-of-care applications; to develop delta-relaxation-enhanced MRI ("dreMR") for neuro-interventional applications; and to establish new procedures and facilities for the systematic evaluation and development of MR-compatible technology.

Ontario Institute for Cancer Research Imaging Translation Program

Directors: Dr. Aaron Fenster/Dr. Martin Yaffe **Ontario Institute for Cancer Research**

The OICR Imaging Translation Program (OICR ITP) accelerates the translation of research into the development of new imaging innovations for earlier cancer detection and diagnosis and treatment through four major projects: probe development and commercialization, medical imaging instrumentation and software, pathology validation, and imaging for clinical trials. We facilitate improved screening and treatment options for cancer patients by streamlining advances of medical imaging through the complex pipeline from discovery through clinical translation and ultimately to clinical use.

Ontario Institute for Cancer Research Smarter Imaging Program

Directors: Dr. Martin Yaffe/Dr. Aaron Fenster **Ontario Institute for Cancer Research**

The goal of the OICR Smarter Imaging Program (OICR SIP) is to increase both the sensitivity and specificity of cancer imaging and to use information from images to help optimize selection of therapy to avoid over- or under-treatment of disease. OICR SIP focuses on diagnosing and effectively treating cancer with imaging technology and probes that target biomarkers representing molecular, physical or functional changes associated with cancer. In conjunction with the Imaging Translation Program, OICR SIP develops and translates techniques for earlier detection and diagnosis of cancer into clinical practices by exploiting recent advances in molecular biology, chemistry and physics.

Canada First Research Excellence Fund – BrainsCAN

Directors: Dr. Adrian Owen and Dr. Lisa Saksida **Canada First Research Excellence Fund**

BrainsCAN is a multidisciplinary and cross-sectoral program supported at Western by Government of Canada's Canada First Research Excellence Fund (CFREF). BrainsCAN's goal is to reduce the burden of brain disorders, which affect nearly 3.6 million Canadians, diminishing quality of life and creating an enormous burden on society and on our health-care system. Brain impairments create deficits in memory, attention, knowledge, problem solving, and communication, affecting how those affected interact with everything and everyone around them. BrainsCAN researchers will transform our understanding of brain disorders and deliver effective solutions to the grand challenge of maintaining brain function across the lifespan.

NIH – NICHD Human Placenta Project - Hyperpolarized 13C MRI of Placental Metabolic Abnormalities Resulting from the Western Diet

Director: Dr. Charles McKenzie **NICHD**

Over 30% of all pregnancies in North America occur in women that are obese. Maternal obesity is often a result of lifelong consumption of an obesity-promoting Western Diet. Altered placental metabolism contributes to increased rates of adverse outcomes in these Western Diet exposed pregnancies, but there is currently no method available to non-invasively measure placental metabolism. The goal of this project is to develop and validate an MRI based method that can be used in human pregnancy to distinguish the placenta with normal metabolism from one where metabolic function is abnormal due to exposure to the Western Diet. Ultimately this will allow improved diagnosis and monitoring of metabolically compromised pregnancies and allow improved treatment that will reduce the rates of adverse outcomes.

Keynote Speakers

Gediminas Čepinskas, Lawson Health Research Institute, London, Ontario

Dr. Cepinskas, DVM/PhD is an Associate Professor at the Department of Medical Biophysics, Schulich School of Medicine & Dentistry, Western University, and a Director at the Centre for Critical Illness Research, LHRI, London. His research is focused on the initiating and regulatory mechanisms of severe inflammatory conditions and ischemia/reperfusion injury at organ/cell levels. The prime subjects of his research are diagnostic/prognostic markers of systemic inflammation, inflammatory activation of leukocytes and vascular endothelial cells, and leukocyte-endothelial cell inflammatory interaction in various organs.

Jörn Diedrichsen, Western University, London, Ontario, Canada

Dr. Diedrichsen, PhD is a Western Research Chair in the Brain and Mind Institute at Western University, and Professor for Statistics and Computer Science. His laboratory studies cerebellar function and motor control and motor learning in the human brain. He has also developed a number of novel multivariate analysis techniques for functional imaging data.

Ellen Grant, Boston Children's Hospital, Boston, MA, USA

Dr. Grant, MD is the Founding Director of the Fetal-Neonatal Neuroimaging and Developmental Science Center at Boston Children's Hospital. She holds MSc and MD degrees from the University of Toronto. Dr. Grant headed the Division of Pediatric Radiology at Massachusetts General Hospital for five years before moving to BCH where she was named the first incumbent of the Boston Children's Hospital Chair in Neonatology. The FNNDSC is focused on developing tools and analysis streams for better understanding normal and abnormal brain development with the goal of improving cognitive and neurological outcomes.

Brian Hargreaves, Stanford University, California, USA

Dr. Hargreaves, PhD is Associate Professor of Radiology at Stanford University, with a research focus on body magnetic resonance imaging (MRI). He completed his PhD at Stanford University in Electrical Engineering before moving to the Radiology Department in 2005. He directs the Body MRI research group, which develops and implements new MRI techniques for breast, abdominal, and musculoskeletal imaging, with the goal of improving patient care. Many of his group's methods are used clinically, both at Stanford and around the world.

David Hawkes, University College, London, United Kingdom

Dr. Hawkes, PhD is the Founding Director of UCL Centre for Medical Image Computing, which he led from 2005 – 2015, growing it from 30 researchers to over 100, with 14 academic staff. His main research interests encompass image reconstruction, image matching, data fusion, visualization, shape representation, surface geometry and modelling tissue deformation with applications in image guided interventions and using medical imaging as an accurate measurement tool and biomarker.

Scientific Committee

Jerry Battista
Maria Drangova
Aaron Fenster
Gabor Fichtinger
Richard Frayne
Fay Harrison
David Holdsworth
Charles McKenzie
Frank Prato
Giles Santyr
Aaron Ward
Graham Wright
Martin Yaffe

Organizing Committee

Johanne Langford (Chair)
Janette Wallace
Carol Richardson
Jean Rookwood
Yulia Yerofeyeva
John Stuart Haberl Baxter

Abstract Reviewers

Special thank you to the abstract reviewers:

Daniel Ansari
Timothy Burkhart
Catherine Coolens
Maria Drangova
Paula Foster
Stuart Gaede
Nilesh Ghugre
Kevin Jordan
Ali Khan
Emily Lalone
Ting Lee
Lisa Mielniczuk
Chris Macgowan
Mihaela Pop
Giles Santyr
Timothy Scholl
John G. Sled
Matthew Teeter

Judges – Oral & Poster

Thank you to Dr. Savita Danvantari and Dr. Richard Frayne for organizing the poster and oral judging and to our Judges:

Alireza Akbari
Jerry Battista
Yuri Boykov
Gediminas Cepinskas
Rachel Chan
Marcus Couch
Charles Cunningham
Mamadou Diop
Gabor Fichtinger
Nilesh Ghugre
Donna Goldhawk
Amanda Hamilton
Michael Hardisty
Brian Hargreaves
David Hawkes
Justin Hicks
Ali Khan
Andras Lasso
Anne Martel
Charles McKenzie
Gerald Moran
Grace Parraga
Terry Peters
Csaba Pinter
Giles Santyr
Keith St Lawrence
Jonathan Thiessen
Graham Wright
Alfred Yu

and all the last-minute volunteers.

DAY 1 - WEDNESDAY, MARCH 15, 2017

7:00	**REGISTRATION OPEN**	BALLROOM FOYER
8:00 – 8:40	**POSTER SET-UP & LIGHT BREAKFAST**	BALLROOM WEST
8:40 – 8:50	**OPENING REMARKS** *David Holdsworth, PhD* Western University, ImNO 2017 Scientific Committee Chair *Marlys Koschinsky, PhD* Robarts Research Institute, Scientific & Executive Director	BALLROOM EAST & CENTRE
	KEYNOTE SESSION *Chairs: Jerry Battista, Ali Khan*	BALLROOM EAST & CENTRE
8:50 - 9:35	***Inflammation: The Good, the Bad and the Ugly*** Gediminas Čepinskas, DVM/PhD Lawson Health Research Institute, London, Ontario, Canada	
9:35 - 10:20	***Studying structure and function of the human cerebellum using MRI*** Jörn Diedrichsen, PhD Western University, London, Ontario, Canada	
10:20 – 10:40	**POSTER SESSION & NUTRITION BREAK**	BALLROOM WEST
10:40 – 11:25	**KEYNOTE SESSION** *Chair: Charles McKenzie, PhD* ***Perinatal Imaging: MRI, Optical, MEG and Informatics Innovations*** Ellen Grant, MD Boston Children's Hospital, Boston, MA, USA	BALLROOM EAST & CENTRE

	BALLROOM EAST **BRAIN: PATIENT-CENTERED STUDIES** Chair: Keith St. Lawrence, PhD	BALLROOM CENTRE **TISSUE CHARACTERIZATION** Chair: Rebecca Thornhill, PhD
11:30 - 11:45	Bridging the gap between thoughts and actions: a functional near infrared spectroscopy study *Androu Abdalmalak*	Quantitative magnetic resonance characterization of calcified and lipid-laden blood clot in vitro at 3T *Spencer Christiansen*
11:45 - 12:00	Axonal damage and global hyperconnectivity persist 3-months after a concussion in young hockey players *Kathryn Manning*	Quantitative Cardiac B0, Fat Fraction, and R2* Mapping Using Pre-Channel-Combination Phase *Zahra Hosseini*
12:00 - 12:15	Reduced Brain Choline in Male Adolescent Hockey Players after Concussion *Amy Schranz*	Comparison of a dual-modality intravascular ultrasound and optical coherence tomography imaging catheter to each imaging modality alone using cadaveric coronary artery specimens *Jill Weyers*
12:15 - 12:30	Does Trancranial Direct Current Stimulation Modify Glutamate: A 7 Tesla 1H MR Spectroscopy Study *Kayla Ryan*	Quantitative CT assessment of myocardial edema in acute myocardial infarction: a validation study *Lisa Hur*
12:30 - 12:45	Assessing Reperfusion in Ischemic Stroke Patients using CT Perfusion after Successful Intra-Arterial Therapy *Eric Wright*	Relationship between cardiac fat and microvascular dysfunction in non-obstructive coronary artery disease *Stephanie Skanes*

12:45 – 13:45	**LUNCH**	

DAY 1 - WEDNESDAY, MARCH 15, 2017

	BALLROOM EAST	BALLROOM CENTRE
	PERINATAL AND LUNG IMAGING	**NEW IMAGING APPROACHES**
	Chair: Giles Santyr, PhD	Chair: Jonathan Thiessen, PhD
13:45 - 14:00	Measurement of placental T2* in a guinea pig model of intrauterine growth restriction *Kevin Sinclair*	Assessing the integrity of the blood-brain barrier using dynamic contrast-enhanced NIRS *Daniel Milej*
14:00 - 14:15	Comparison between 2-point Dixon and Quantitative IDEAL for Magnetic Resonance Imaging of Fetal Adipose Tissue *Stephanie Giza*	A novel multi-echo GRE protocol for simultaneous fat/water separation and multi-parameter mapping *Junmin Liu*
14:15 - 14:30	Asthma Ventilation Abnormalities Measured using Fourier-Decomposition Free-breathing Pulmonary Proton MRI *Dante Capaldi*	A PET/MR Approach to Non-Invasive Quantification of Cerebral Blood Flow *Tracy Ssali*
14:30 - 14:45	Pulmonary Magnetic Resonance Imaging Ventilation Defects in Asthma: Stochastic or Deterministic? *Rachel Eddy*	Motion and B0 correction in MRI using FID-SNAVs *Patricia Johnson*
14:45 - 15:00	Ultra-Short Echo Time MRI Quantification of Airspace Enlargement in Bronchopulmonary Dysplasia and Alpha-1 Antitrypsin Deficiency: Parenchyma Destruction, Air trapping or Both? *Heather Young*	Time-Resolved Mapping of Arterial Pulse Wave Dynamics with High Frame Rate Ultrasound (HiFRUS) *Adrian J.Y. Chee*

15:00 – 15:45 **POSTER SESSION & COFFEE BREAK** BALLROOM WEST

	BALLROOM EAST	BALLROOM CENTRE
	PRE-CLINICAL IMAGING STUDIES	**PERFUSION, METABOLISM, HYPOXIA**
	Chair: Paula Foster, PhD	Chair: Ting Lee, PhD
15:45 - 16:00	In Vivo Magnetic Resonance Imaging Investigating the Development of Experimental Brain Metastases due to Triple Negative Breast Cancer *Amanda Hamilton*	Ultrasound-triggered conversion of porphyrin microbubbles to nanobubbles: Extending cavitation activity beyond the vasculature *Carly Pellow*
16:00 - 16:15	A multimodality imaging model to study concomitant tumour resistance *Katie Parkins*	Preliminary study for personalization of renally excreted cancer drugs using pulse dye densitometry *Fiona Li*
16:15 - 16:30	Dual-Energy Micro-Computed Tomography on a Gantry-Based Micro-CT Scanner *Justin Tse*	Correcting PET images for tissue transport in order to accurately quantify hypoxia in tumours *Edward Taylor*
16:30 - 16:45	Lanthanide-based nanoparticles as vascular contrast agents in pre-clinical computed tomography *Charmainne Cruje*	Physics-based scatter correction for quantitative PET imaging of hypoxia *Jennifer Gottwald*
16:45 - 17:00	Patterns of Porcine Acute Myocardial Infarction: Dependence on Breed and Coronary Anatomy *Xiuling Qi*	Longitudinal Monitoring of Tumour pH Gradient with MRI *Patrick Lim*

17:00 – 19:00 **POSTER SESSION & CASH BAR RECEPTION** BALLROOM WEST

DAY 2 - THURSDAY, MARCH 16, 2017

7:00	**REGISTRATION**	BALLROOM FOYER
8:00 – 8:50	**POSTER SESSION AND LIGHT BREAKFAST**	BALLROOM WEST
	KEYNOTE SESSION	BALLROOM EAST & CENTRE
	Chairs: Terry Peters, PhD, David Holdsworth, PhD	
8:50 - 9:35	***Multi-scale Computational Anatomy for Image Guided Interventions*** David Hawkes, PhD University College, London, United Kingdom	
9:35 - 10:20	***Advances in Orthopedic MRI*** Brian Hargreaves, PhD Stanford University, Palo Alto, California, USA	
10:20 – 10:40	**POSTER SESSION & NUTRITION BREAK**	BALLROOM WEST

	BALLROOM EAST **HISTOLOGY: ANALYSIS AND VISUALIZATION**	BALLROOM CENTRE **MUSCULOSKELETAL: INSTRUMENTATION AND QUANTITATIVE IMAGING**
	Chair: Tamie Poepping, PhD	Chair: Emily Lalone, PhD
10:40 - 10:55	Automated vascular segmentation, reconstruction, classification and simulation on whole-slide histology *Yiwen Xu*	Knee joint motion measurement during the timed up and go test using low-cost wearable sensors *Riley Bloomfield*
10:55 - 11:10	3D Lung Histology Reconstruction and Registration to in vivo Imaging *Sean Pentinga*	Computational Evaluation of Glenoid Bone Loading using Micro-CT *Nikolas Knowles*
11:10 - 11:25	Automatic Prostate Cancer Detection and Contouring on Digital Histopathology Imaging *Wenchao Han*	Tomographic Analysis of Ectopic Mineralization in Diffuse Idiopathic Skeletal Hyperostosis *Dale Fournier*
11:25 - 11:40	Quantitative Dataset Similarity for Fusing Multi-Institutional Image Collections *Ryan Therrien*	Validation of a Micro-CT Compatible Load-Controlled Knee Motion Simulator *Alexandra Blokker*
11:40 - 11:55	Nuclei Detection and Proliferation Index Estimation on Ki-67 and Hematoxylin Stained Images *Peter Morreale*	T1rho and T2 Relaxation Changes in Tibiofemoral Articular Cartilage Following a Functional Loading Stimulus in Early Knee Osteoarthritis: Preliminary Findings *Hayden Atkinson*
11:55 - 12:10	A system for high-frequency vibration of live cells during real-time microscopy *Daniel Lorusso*	Evaluation of Wearable Sensors using a Robotic Knee Joint Phantom and 3D Motion Capture *Megan Fennema*

12:10 – 13:10	**LUNCH**

DAY 2 - THURSDAY, MARCH 16, 2017

	BALLROOM EAST	BALLROOM CENTRE
	VISUALIZATION AND IMAGE ANALYSIS	**IMAGING FOR THERAPY AND DEVICES**
	Chair: Graham Wright, PhD	Chair: Gabor Fichtinger, PhD
13:10 - 13:25	Novel integrative framework to augment real-time MR-guided EP studies with 3D predictive modelling *Mihaela Pop*	Evaluation of a mobile, real-time, tracked augmented reality display for surgical navigation *Zachary Baum*
13:25 - 13:40	Vurtigo: Updates to a Visualization Platform for Image-guided Procedures *Labonny Biswas*	Robotic Catheter Contact-Force Control for Cardiac Ablation Therapy: In Vivo Evaluation *Daniel Gelman*
13:40 - 13:55	Investigating the relationship of myelin and axonal white matter microstructure uing longitudinal relaxation mapping and restricted diffusion *Jason Kai*	Registration of preoperative images for navigated brain surgery using ultrasound-accessible skull regions *Grace Underwood*
13:55 - 14:10	Virtual views controlled by surgical tools for computer assisted interventions *Thomas Vaughan*	Towards intra-operative needle guidance in interstitial gynecologic brachytherapy using 360 degree 3D transvaginal ultrasound *Jessica Rodgers*
14:10 - 14:25	Spinal cord tracts labelling via diffusion tensor imaging in the cervical spine verified against T1 MRI *Michael Hardisty*	An application of redundant sensors for intraoperative electromagnetic tracking error monitoring *Vinyas Harish*
14:25 – 15:30	**POSTER SESSION & COFFEE BREAK**	BALLROOM WEST
	BALLROOM EAST	BALLROOM CENTRE
	COMPUTER ASSISTED DIAGNOSIS/ IMAGE QUALITY / DOSE	**NEW IMAGING APPROACHES IN CANCER RESEARCH**
	Chair: Aaron Ward, PhD	Chair: Timothy Scholl, PhD
15:30 - 15:45	Discovery Radiomics via a Mixture of Expert Sequencers using Layered Random Projections (LaRP) for Prostate Cancer Classification *Amir-Hossein Karimi*	Whole mouse body fluorine-19 based MRI for detection of metastasis associated macrophages in the lung, lymph nodes and brain *Ashley Makela*
15:45 - 16:00	Flipping the Computer Aided Diagnosis (CAD) Training Paradigm for Prostate Cancer: Using PI-RADS Reporting of Multi-Parametric MRI (mpMRI) to Train a CAD System and then Validating with Pathology *Farzad Khalvati*	19F-perfluorocarbon-labeled human peripheral blood mononuclear cells can be detected in vivo using clinical MRI parameters in a therapeutic cell setting *Corby Fink*
16:00 - 16:15	Computer-Assisted Characterization of Malignancy and Gleason Grade of Prostate Cancer on Multi-Parametric MRI *Derek Soetemans*	OATP1A1 as a novel clinical-field strength MRI reporter gene for cell tracking *Nivin Nystrom*
16:15 - 16:30	Improving Image Quality in X-Ray Images with the Apodized-Aperture Pixel (AAP) Design *Tomi Nano*	Optimization of Slow-Proton-Exchange (SPE) Magnetic Resonance pH Sensor and Application for Monitoring Enzyme Activity *Ryan Correa*
16:30 - 16:45	Evaluation of an iterative reconstruction algorithm for optical CT dosimetry of small radiation fields *Kurtis Dekker*	Characterizing an Orthotopic C6 Glioblastoma Rat Model with Multiparametric Magnetic Resonance Imaging and Bioluminescence Imaging. *Trung (Adam) Le*
16:45 – 17:00	**AWARDS AND CLOSING REMARKS**	BALLROOM EAST & CENTRE
17:00 – 17:30	**POSTER TAKE DOWN**	

POSTER BY AUTHORS LAST NAME

POSTER #	NAME	SUBMISSION TITLE
76	Abbas, Ahmed	Characterizing an 18F-Growth Hormone Secretagogue Probe for Positron Emission Tomography Imaging of Cardiac Growth Hormone Secretagogue Receptor
49	Adams, Conner	Long-term Cerebrovascular Dysfunction Following Repeated Mild Traumatic Brain Injury
8	Adams, John	Metabolic Abnormalities in Epileptic Patients with Malformations of Cortical Development
22	Ahmadian, Ghazaleh	Coherent Point Drift Algorithms for Breast Image Registration
53	Albatany, Mohammed	CEST MRI of Acute Intracellular Acidification in Glioblastoma Multiforme Following a Single Dose of Cariporide and Quercetin
73	Albatany, Mohammed	Comparing AACID CEST MRI Measurement of Brain pH using the 2 ppm and 2.75 ppm Amine Resonances at 9.4T
106	Alizadeh Pourbouyeh, Kobra	Transverse Relaxation Rate in Magnetic Resonance Imaging Is Altered by Hepcidin
16	Ameri, Golafsoun	Development of a high frequency single-element ultrasound needle transducer for anesthesia delivery
52	Bakhshmand, Saeed	Superimposed Structural and Functional Brain Networks on Grey and White Matter
4	Baronette, Rudy	Calibration of single-plane fluoroscopy using a 3D printed calibration object
39	Baxter, John	Shape Complexes: Combining Shape and Label Ordering Information in Segmentation
100	Ben Daya, Ibrahim	Compensated Row-Column Ultrasound Imaging System Using Conditional Random Fields
41	Bibic, Eden	Public Library for Ultrasound (PLUS) Model Catalog: A library of 3D-printable models
38	Blokker, Alexandra	Image based soft tissue strain measurement using embedded fiducial markers
60	Broeke, Nolan	Analysis of Endogenous Tissue Sodium Concentration as a Biomarker of Prostate Cancer Aggression
7	Cepek, Jeremy	A Method of Mechanically-Encoding Needle Shape for Image-Guided Interventions
27	Cesakov, Egor	Vascular tree estimation from micro CT images using GPU-accelerated centerline regularization
97	Chan, Rachel	Readout-Segmented and Reduced Field-of-View Diffusion-Weighted Sequences for Prostate MRI
59	Cheung, Alison	An immunofluorescence biomarker multiplexing approach to study breast cancer heterogeneity and tumour microenvironment
23	Chiang, Sylvester	Motion Corruption Detection in Breast DCE-MRI
37	Church, Ben	Scoliosis visualization using transverse process landmarks
46	Dona, Olga	Fractal analysis of the brain rs-BOLD signal and DTI analysis in cancer patients experiencing chemotherapy-related cognitive impairment
103	Dunmore-Buyze, Joy	Cardiovascular tissue contrast enhanced micro computed tomography: correlation with 2 dimensional histology
44	El-Baba, Mazen	Dynamic Functional Connectivity Analysis Reveals Temporal Differences Between Wake and Stage 2 Sleep
101	Enjilela, Esmaeil	Sparse-view image reconstruction with filtered backprojection in CT myocardial perfusion imaging

POSTER BY AUTHORS LAST NAME

POSTER #	NAME	SUBMISSION TITLE
92	Escartin, Terenz	Development of a robust tool to determine radiographic detector dose efficiency (DQE) in clinics
110	Frayne, Mark	A Method to Automatically Detect and Measure Erosions in the Metacarpal Joint
15	Gillies, Derek	A Comparison between User Initiated and Continuous Real-time Motion Compensation Techniques for 3D Ultrasound-guided Prostate Biopsy
25	Guo, Fumin	Ultra-short-echo-time MRI Lung Segmentation using High-Dimensional Features and Continuous Max-Flow
88	Harasym, Diana	Development of a Standardization Phantom for Measuring Brain gamma-aminobutyric acid (GABA)
62	Harris, Andrew	Automatic Image Registration and Stitching in 3D Ultrasound for Monitoring of Neonatal Post-Hemorrhagic Ventricle Dilation
45	Hiebert, Nole	Effect of Parkinson's disease and dopaminergic therapy on intra- and inter-connectivity of brain networks
66	Ho, Chung Kit	Design of Ultrasound-Compatible Anthropomorphic Flow Phantoms with Tortuous Vascular Geometries
63	Ho, Marjorie	Non-invasive Monitoring of Brain Temperature during Rapid Selective Brain Cooling by Zero- Heat-Flux Thermometry
17	Holden, Matthew	Assessing Technical Competence in Simulated Colonoscopy Using Joint Motion Analysis
6	Holdsworth, David	Intra-operative gamma probe using a 3D-printed focused collimator
89	Holdsworth, David	Calibration light source for optical molecular imaging systems
1	Hong, Gregory	Characterization of Metal Artifacts using a 3D-Printed Grid Phantom with an Embedded Hip Implant
90	Hosseini, Mahdi	Color calibration for Digital Pathology Scanners
50	Hosseini, Zahra	Multi-Parametric MRI at 7 T for Differentiation of MS and Age-Related White Matter Lesions
83	House, Rachael	Validation of breast volume measurement using 3D surface scanner
68	Huang, I-Lun	CT Perfusion versus SPECT MIBI for assessing myocardial ischemia in coronary artery disease
64	Hussain, Bushra	A Novel Vector Doppler Ultrasound Method for Improved Near-Wall 2D-Vector Blood Velocity Estimations: Aperture - Translation
51	Ikeda, Kristin	Network Connectivity after a Single Unprovoked Seizure using Resting-State fMRI
2	Ilina, Anna	Creating patient-specific anatomical models from highly elastic materials using 3D-printed molds
29	Inoue, Jiro	Computer-Aided Method of Left Atrial Wall Thickness Measurement
67	Ishii, Takuro	Non-Invasive Imaging of Urine Flow Dynamics Using High Frame Rate Ultrasound (HiFRUS)
28	Jayarathne, Uditha	Visualizing US In-situ in Laparoscopic Interventions
21	Johnson, Carol	Radiomics Made Easy: Translation of Image Analysis Tools to a Clinical Trial-Ready Platform
40	Johnson, Starr	Macroscopic Anatomy at Microscopic Scale: Registration of Serial Sections of Histopathology for 3D
24	Karami, Elham	Towards lung tissue stiffness imaging by using a micromechanical model of the alveolar sac

POSTER BY AUTHORS LAST NAME

POSTER #	NAME	SUBMISSION TITLE
26	Kashani, Hany	Optimization of CT coronary angiography for coronary vessel wall visualization and detection of non-calcified plaque
18	Kewin, Matthew	Evaluation of Recovery Coefficients applied to Image-derived Input Functions for Patlak analysis of FDG-PET MRI - A manifestation of Occam's Razor?
61	Kishimoto, Jessica	Three dimensional head ultrasound for the detection of shunt failure in infants with hydrocephalus: pilot study
9	Knull, Eric	Evaluation of MRI-Guided Focal Laser Ablation Therapy Procedures
81	Krahn, Philippa	Dynamic electrogram measurements after radiofrequency ablation relate to MRI-based lesion visualization
47	Kulaseharan, Sancgeetha	Identifying epileptogenic lesions using cortical thickness
43	Kumar, Devinder	Deep Medical Imaging Visualization for Clinical Decision Support
3	Laing, Justin	Patient Specific Atria Models for Training and Pre-Procedure Surgical Planning
86	Lau, Jonathan	Clinical integration of ultra-high field templates for target selection in deep brain stimulation surgery
78	Liu, Hanlin	Gadolinium-Free Blood Pool MRI Contrast Agents Based on Manganese(III) Porphyrin for High Clinical Field (3 T) MRA: Probing and Tuning the Serum Albumin Binding
91	MacFarlane, Michael	Patient-specific calibration of cone-beam computed tomography images for dose tracking and plan assessment
70	Marants, Raanan	Renal Perfusion Falls during Hemodialysis: An Explanation for the Loss of Residual Renal Function in Dialysis Patients
12	Martin, Peter	How should we target prostate tumours using fusion biopsy?
20	Martire, Daniel	Audio-frequency dB/dt Exposure System for MRI-Conditional Device Testing: A Design Study
34	McCooeye, Daniel	The Impact of Motion and Maternal Body Mass Index on Segmentation in Fetal Magnetic Resonance Imaging
107	McCunn, Patrick	Neurite Orientation and Dispersion Density Imaging of the Rat Brain at 9.4 Tesla
96	McNabb, Evan	Contrast and Conspicuity of Fiducial Localization using Undersampled co-RASOR MRI
13	Michael, Justin	3D Ultrasound and Mechatronic Template Tracking for Guidance of Permanent Seed Breast Brachytherapy
10	Mouawad, Matthew	Registration of DCE-MRI Images: Effects of Percent Sampling on Kinetic Analysis and Computation Time
74	Murrell, Emily	A Fluorine-Containing OBOC Peptide Library for the Discovery of Cancer Imaging Probes.
94	Nano, Tomi	Observer Study to Determine Minimal Detectable Improvement in DQE of X-Ray Detectors
105	Omidi, Parsa	Photoacoustic computed tomography 3D image reconstruction for detecting breast cancer
58	Ouriadov, Alexei	Accelerated Diffusion-weighted 129Xe MRI Morphometry of Emphysema
5	Paish, Adam	Rapid prototyping of a lightweight bone plate for complex fracture fixation in a peregrine falcon

POSTER BY AUTHORS LAST NAME

POSTER #	NAME	SUBMISSION TITLE
98	Polak, Paul	Evaluation of reduced sampling schemes with 3D radial projections for 23Na MRI
79	Pop, Mihaela	MR-based computer models of chronic infarct for prediction of cardiac electro-mechanical function
72	Qi, Qi	Multimodal in vivo imaging of perfusion and glycolysis in the C6 rat model of glioma
32	Rajaram, Ajay	Development of a hybrid broadband NIRS/diffusion correlation spectroscopy system for real-time monitoring of cerebral perfusion and oxygenation in preterm brain injury
75	Rajora, Maneesha	Porphyrin-lipid apoE3-lipoprotein nanoparticles as glioblastoma-targeting theranostic platforms
80	Rankin, Adam	Augmented Reality Cardiac Interventions using the Microsoft HoloLens
102	Rathod, Bhavini	Application of Iterative Reconstruction Techniques to Retrospectively Gated Cardiac Micro- CT Mouse Images
69	Renaud, Jennifer	Quantification of myocardial blood flow with C-11-hydroxyephedrine positron emission tomography imaging
33	Riberdy, Vlora	MRI of Pluripotent Stem Cell-Derived Alveolar-Like Macrophages for Treatment of Chronic Lung Diseases
93	Robinson, Alec	Open-source film dosimetry analysis application based on 3D Slicer
109	Rockel, Conrad	Intravoxel Incoherent Motion Analysis of the Guinea Pig Placenta: Preliminary Findings
99	Santos Diaz, Alejandro	Highly Accelerated Phosphorus Metabolic Imaging using Compressed Sensing
55	Shapira Zaltsberg, Gali	Apparent Diffusion Coefficient of the Placenta in Twins versus Singleton Pregnancies
56	Shapira Zaltsberg, Gali	Volumetry, ADC and T2-Weighted Values of the Placenta in Fetuses With and Without CNS Abnormalities
87	Simard, Nicholas	A Spinal Cord Phantom to Test and Standardize MEGA-PRESS gamma-aminobutyric acid (GABA) Measurements
57	Smith, Lauren	Optimizing Hyperpolarized Carbon-13 Magnetic Resonance Imaging in Pregnancy
42	Stanley, Olivia	Whole time course coil combination using singular value decomposition
77	Sullivan, Rebecca	Expression of the Growth Hormone Secretagogue Receptor and Ghrelin in Human Heart Failure
11	Suriyakumar, Vinith	Collision detection for external beam radiation therapy applications in SlicerRT
36	Tam, Clara	Boundary Regression Segmentation of Spinal Images
82	Tong, Olivia	Method for detection of breast cancer using 3D surface scanning
108	Umoh, Joseph	Characterization of Bone and Soft-Tissue Structure in Developing and Aging Mice Using Micro-Computed Tomography
113	Van de Kleut, Madeleine	Validation of radiostereometric analysis for use with reverse total shoulder arthroplasty
31	Vannelli, Claire	Image Fusion for Improved Ultrasound Mitral Valve Segmentation and Modelling
84	Vaughan, Thomas	Electromagnetically-generated catheter paths for breast brachytherapy

POSTER BY AUTHORS LAST NAME

POSTER #	NAME	SUBMISSION TITLE
95	Vickress, Jason	Dosimetric impact of Deformable image registration error in lung 4DCT images
104	Wang, Hui	A Developing Non-contact 3D Photoacoustic Computed Tomography Scanner for Detecting Early Response to Neoadjuvant Chemotherapy in Breast Cancer Patients
35	Wang, Qingguo	Evaluation of a new Nonrigid-registration method using Non-local Spatio-temporal Priors on liver perfusion CT in patients with hepatic cellular carcinoma
71	Wang, Xinying (Cindy)	Early Tumour Perfusion and Diffusion Evaluated in Multi-modal Imaging following Radiosurgery for Metastatic Brain Cancer
112	Webster, Jared	The relationship between soft tissue balancing performed during total knee arthroplasty and postoperative tibiofemoral contact kinematics
19	Whelan, Timothy	Implementation of a parallel processing pipeline of multi-channel phase data
111	Willmon, Renee	Assessing Health Through The Ages: Imaging and the Bioarchaeology of Tuberculosis
48	Wong, Dickson	Improved Glutamate Detection in the Brain at 7 Tesla Using Long Echo-Time Proton Magnetic Resonance Spectroscopy
65	Wu, Kai Yi	The Impact of Diabetes Mellitus on Global Myocardial Flow Reserve in the Presence of Epicardial Coronary Disease
30	Xia, Wenyao	A combinational 3D ultrasound image segmentation approach with spatial coherency constraint for patient specific dynamic mitral valve model
14	Yan, Christina	Quantification of tumor localization needle displacement prior to tumor excision in navigated lumpectomy
54	Yang, Dae-Myoung (Danny)	Comparison of Dynamic 18F-DCFPyL and 18F-FCH Positron Emission Tomography Imaging in Patients with Prostate Cancer
85	Yip, Lawrence	Intraoperative Breast Tumour Margin Assessment: A Photoacoustic Solution

Characterizing an ^{18}F-Growth Hormone Secretagogue Probe for Positron Emission Tomography Imaging of Cardiac Growth Hormone Secretagogue Receptor

Ahmed Abbas*, Tyler Lalonde, Lihai Yu, Leonard G. Luyt, Savita Dhanvantari
Heart Failure: Prevention Through Early Detection Using New Imaging Methods Consortium
Lawson Health Research Institute, London, Ontario, Canada

Introduction: Cardiovascular disease affects 1.6 million Canadians, of which one-third have heart failure (HF). Currently, HF is diagnosed using circulating biomarkers that are not cardiac-specific; thus, there is critical need for a biomarker that is endogenous to myocardial tissues. One potential biomarker is the growth hormone secretagogue receptor (GHSR), which binds the peptide hormone ghrelin. GHSR is expressed on the surface of cardiomyocytes and its activation plays a role in protection of cardiomyocytes. Cardiac GHSR expression is elevated in end-stage heart disease in humans. We are investigating Positron Emission Tomography (PET) imaging of GHSR expression using a novel molecular imaging probe, named ^{18}F-[1-Nal^4,Lys^5(4-fluorobenzoic acid)]G-7039 (^{18}F-G-7039), a small molecule that binds to GHSR with strong affinity *in vitro*. This work characterizes ^{18}F-G-7039 for *in vivo* imaging of cardiac GHSR expression as a biomarker for HF.

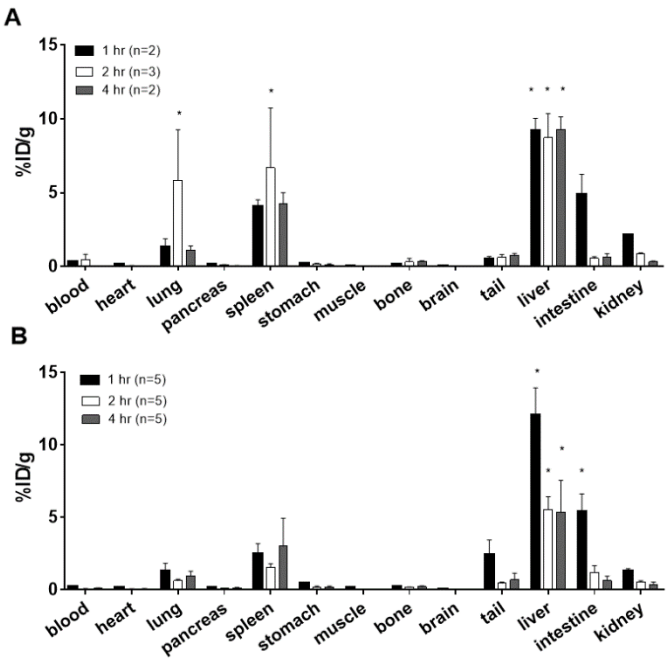

Figure 1. ^{18}F-G-7039 biodistribution in (**A**) fasted and (**B**) fed female C57BL/6 mice at 1h, 2h, and 4h post-injection.

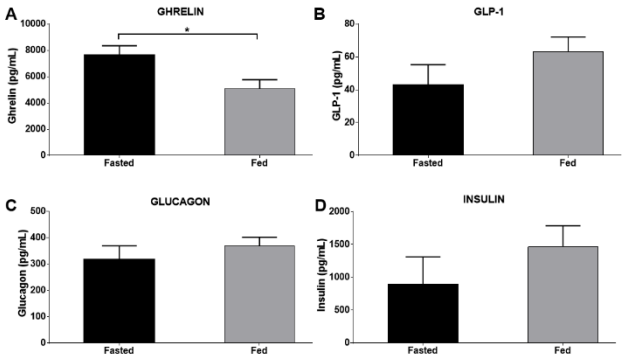

Figure 2. Blood plasma concentrations of (**A**) ghrelin, (**B**) glucagon-like peptide-1 (GLP-1), (**C**) glucagon, and (**D**) insulin in fasted and fed mice sacrificed 2h post-injection.

Methods: Whole body probe uptake was assessed by biodistribution in healthy female C57BL/6 mice, aged 8-18 weeks, fasted for 4h prior to injection or fed. The mice were injected i.v. via tail vein with 9-10 MBq of ^{18}F-G-7039 and sacrificed at 1h (n=2), 2h (n=3), and 4h (n=2) post-injection when fasted and 1h (n=5), 2h (n=5), and 4h (n=5) post-injection when fed. Radioactivity in organs was calculated as % injected dose per gram of tissue (%ID/g). Blood plasma samples, collected from fasted and fed mice sacrificed at 2h post-injection were assessed for ghrelin, glucagon-like peptide-1 (GLP-1), glucagon, and insulin concentrations by ELISA. Data analyses were performed using two-tailed t-test, two-way ANOVA and Tukey's test, where significance was set at $p<0.05$.

Results: In both fasted and fed mice, ^{18}F-G-7039 exhibits similar uptake profile, distributing primarily to the lung, spleen, liver, and intestine with similar uptake values. ^{18}F-G-7039 uptake in both groups was significantly ($p<0.05$) higher in the liver compared to all other tissues at all time points (except intestine at 1h in both groups and spleen at 1h and lung at 2h in fasted mice). No significant heart uptake was observed. Plasma ghrelin levels were significantly ($p<0.05$) elevated in fasted mice compared to fed mice. No other differences were observed in plasma protein concentrations.

Conclusions: Our PET probe, ^{18}F-G-7039, presented negligible cardiac uptake and high liver and intestinal uptake and negligible tissue distribution, possibly indicating hepatobiliary elimination. Probe uptake was independent of ghrelin plasma concentrations. Future experiments will investigate ^{18}F-G-7039 uptake specificity in GHSR null mice.

Bridging the gap between thoughts and actions: a functional near-infrared spectroscopy study

Androu Abdalmalak[1,2,*], Daniel Milej[1,2], Mamadou Diop[1,2], Mahsa Shokouhi[1,2], Lorina Naci[3], Adrian M. Owen[3], and Keith St. Lawrence[1,2]

[1]Department of Medical Biophysics, Western University, London, ON, Canada
[2]Imaging Program, Lawson Health Research Institute, London, ON, Canada
[3]Brain and Mind Institute, Western University, London, ON, Canada
*aabdalma@uwo.ca

Introduction: There has been an increasing interest in developing brain computer interfaces (BCI) for patients who are aware but lack the physical ability to follow commands. Owen and colleagues have previously shown using functional magnetic resonance imaging (fMRI) that some patients diagnosed as being in a vegetative state can communicate by performing a motor imagery task in response to commands[1]. Although promising, this study highlights the need to explore alternative techniques considering the cost and limited accessibility of MRI. An attractive alternate is functional near infrared spectroscopy (fNIRS) given the technology is inexpensive and portable, which enables studies to be conducted at the bedside. Furthermore, brain regions associated with motor imagery (the supplementary motor area (SMA) and the premotor cortex (PMC)) can be interrogated by NIRS. However, the reliability of fNIRS – which is critical to this application – is challenged by a number of factors, most notability signal contamination from the scalp that can potentially mask true activation. Time-resolved (TR) NIRS has been proposed as one approach for enhancing the sensitivity of fNIRS to brain activity since late-arriving photons have a higher likelihood of interrogating the brain. The objective of this study was to assess the reliability of TR-fNIRS in detecting brain activity associated with motor imagery. For validation, all participants performed the same task in a 3T MRI scanner.

Methods: Data were acquired with an in-housed developed TR-NIRS system consisting of one emission fiber ($\lambda = 830$ nm) and four detection channels. The detection fiber bundles were placed at a distance of 3 cm around the emission fiber, each in a separate quadrant, to interrogate the SMA and PMC. Fifteen healthy subjects were recruited (5 females, mean age 26, right handed) for the study. The experimental paradigm consisted of five 30-s cycles of rest and motor imagery. The order of fMRI and fNIRS were randomized to avoid possible training effects. Depth sensitivity was achieved by analyzing the TR-NIRS data in terms of statistical moments of the distribution of times of flight (DTOFs), since the higher moments are more sensitive to late-arriving photons that have a higher probability of reaching the brain.

Results: In 13 of the 15 subjects, significant activation ($p<0.05$) in the SMA and/or PMC was observed by both fMRI and fNIRS. Of the remaining 2 subjects, 1 showed activation with fNIRS only and 1 had detectable activation with fMRI only. The fNIRS group analysis revealed an increase in oxy-hemoglobin with a subsequent decrease in deoxyhemoglobin during the task as expected. The sensitivity of the of the zero, first and second moments were 64%, 93% and 86% respectively, while the precision of all three moments was greater than 90%. The excellent agreement between the two imaging modalities proves the usefulness of TR-NIRS as a portable brain-mapping tool.

Conclusion: This study demonstrates the robustness of fNIRS for detecting brain activity during motor imagery. The next aim is to apply the same fNIRS protocol to disorders-of-consciousness patients who are confirmed by fMRI to be responsive.

1. Owen, A. M. *et al.* Detecting awareness in the vegetative state. *Science* **313,** 1402 (2006).

Long-term Cerebrovascular Dysfunction Following Repeated Mild Traumatic Brain Injury

Conner Adams[1,2,*Primary], Margaret Koletar[1], Tina L. Beckett[1], Lindsay Cahill[3], Lydiane Hirschler[4,5,6], Jan M. Warnking[4,6], Emmanuel L. Barbier[4,6], JoAnne McLaurin[1,7], John G. Sled[2,3], Bojana Stefanovic[1,2,*Supervisor]

1. Sunnybrook Research Institute, Toronto, ON, Canada 2. Medical Biophysics, University of Toronto, Toronto, ON, Canada 3. Mouse Imaging Centre, The Hospital For Sick Children, Toronto, ON, Canada 4. Grenoble Institut des Neurosciences, Université Grenoble Alpes, Grenoble, France 5. Bruker Biospin MRI, Ettlingen, Germany, 6. Inserm, U1216, Grenoble, France 7. Laboratory Medicine & Pathobiology, University of Toronto, Toronto, ON, Canada

Introduction: Traumatic Brain Injury (TBI) damages brain tissue, both directly and indirectly, by inducing ischemia and hypoxia[1]. Rodent models of TBI have hitherto primarily employed single-impact TBI; in contrast, our model involves a series of impacts so as to more faithfully recapitulate the experience of some groups at high risk of suffering TBI - including athletes, and military personnel. In the present study, we used Pseudo-Continuous Arterial Spin Labelling (pCASL) to quantify both resting perfusion and CBF reactivity to vascular perturbation in injured mice following repeated cortical insults[2]. **Methods:** ***TBI:*** Serial TBI preparation involved three impacts performed at four week intervals. Mice underwent craniotomy over the mid-parietal region, and cortical impacts were conducted to depth of 0.5mm below dural surface[3]. ***MRI:*** Structural and functional MRI, two weeks following the final impact, was performed at 7T. Mice were anesthetized with isoflurane. T2 RARE data were collected (0.7mm thick coronal slices, 62.5µm nominal in-plane resolution, TR/TE of 2500/33ms). pCASL was used for assessment of resting perfusion (n=4) and functional response to 10% CO^2. RF Pulses were applied perpendicular to the common carotid artery. Single slice EPI images were then collected with TR/TE=3500/14ms, 1mm coronal slice thickness, 250µm nominal in-plane resolution. For multi-post label delay (PLD) experiments, pCASL pairs were acquired for eight PLDs. Resting CBF was computed in absolute units by modelling the pCASL signal vs. PLD using a single compartment model[4]. For assessment of cerebrovascular reactivity to 10% inspired CO_2, pCASL imaging was performed during one-minute hypercapnic challenges. **Results:** Structural images revealed severe tissue damage. Multi-PLD experiments allowed absolute quantification of CBF both peri- and contra-lesionally (Figure 1). Peri-lesional CBF (235±8 ml/min/100ml tissue) was reduced relative to that of healthy cortical tissue (303±24 ml/min/100ml tissue); $p<0.005$. Initial evidence suggests enhanced vascular reactivity in the lesion as the pCASL signal increased 13.01±0.02% from baseline in response to the 10% CO^2 challenges, while the signal of the healthy tissue increased by 10.96 ±0.02%. **Conclusions:** Following TBI, peri-lesional depression of resting CBF was observed, suggesting an increase in vessel tone. Concomitantly, hypercapnic challenge appears to yield a greater increase in peri- (vs. contra-) lesional CBF. Reduced resting CBF indicates newly added vessels of greater resting tone. Furthermore, enhanced vascular reactivity could result from functional recruitment of newly generated unperfused vessels.

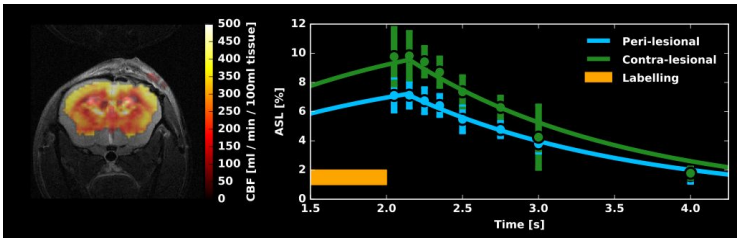

References: 1. Hayward NM, et. al., JCBFM 2011 **2.** Hirschler L, et. al., Proc 23rd ISMRM, #3168 **3.** Dixon CE, et. al., J Neurosci Meth 1991 **4.** Parkes LM, et. al., MRM 2002

Metabolic Abnormalities in Epileptic Patients with Malformations of Cortical Development

John Adams[1], Suzan Brown[2], Robert Bartha[1] Jorge Burneo[2]

[1] Robarts Research Institute, The University of Western Ontario, London, Ontario, Canada; [2] Epilepsy Program, Western University, London Health Sciences Centre, London, Ontario, Canada

Introduction. Malformations of Cortical Development (MCD's) are a major cause of epilepsy; they are broadly classified into 3 subtypes based on when the normal process of brain development is initially interrupted [1], with the most common subtypes being heterotopias, cortical dysplasias, and polymicrogyria. In epilepsy patients, the functional and metabolic changes caused by these malformations are poorly understood, yet critical to ensure good patient outcomes. The aim of this work is to evaluate the metabolic differences between these MCD subtypes using Magnetic Resonance Spectroscopy (MRS).

Methods. Patients were recruited from the epilepsy unit at the London Health Sciences Centre University Hospital, after being diagnosed with intractable epilepsy caused by some form of MCD following routine clinical procedures. Data collection is ongoing; to date, data has been acquired from 17 patients (9 heterotopias, 3 polymicrogyria, and 4 cortical dysplasias) and 13 age matched healthy controls. All patients were scanned on a 3T Siemens MRI system to acquire T_1-weighted anatomical brain images along with ^{1}H spectra from each preidentified lesion. Spectra were acquired using a point resolved spectroscopy sequence (PRESS, TR= 2000 ms, TE= 135 ms, number of averages= 192). Spectroscopic data was then processed using a custom analysis tool (fitMAN) that incorporated line shape correction due to eddy current distortion (QUECC). Each spectrum was fitted in the time domain using a Levenberg-Marquardt non-linear minimization routine [2]. The concentrations of *N*-acetylaspartic acid (NAA), choline (Cho), glutamate (Glu), glutamine (Gln), and myo-inositol were then evaluated as ratios of the fitted creatine (Cr) signal. A two-tailed t-test was used to compare our 3 patient populations with one another and our control group.

Results. Preliminary results show a significant increase in Cho/Cr in patients with heterotopias compared to the polymicrogyria group and healthy controls (Fig. 1A), a significant decrease in NAA/Cr in patients with polymicrogyria compared to both the heterotopia group and healthy controls (Fig. 1B), and significantly lower Gln/Cr in the heterotopia group compared to the polymicrogyria group (Fig. 1C).

Conclusions. Metabolite differences were observed between subtypes of MCD and healthy controls. This is consistent with prior work, which has shown that patients with MCD's have lower NAA/Cr, and increased Cho/Cr, compared to healthy controls [3,4]. However, prior work has not found significant changes in Gln between MCD subtypes. Moving forward, we will increase the sample sizes for all groups, and determine whether metabolic abnormalities are associated with altered brain function as measured by functional MRI.

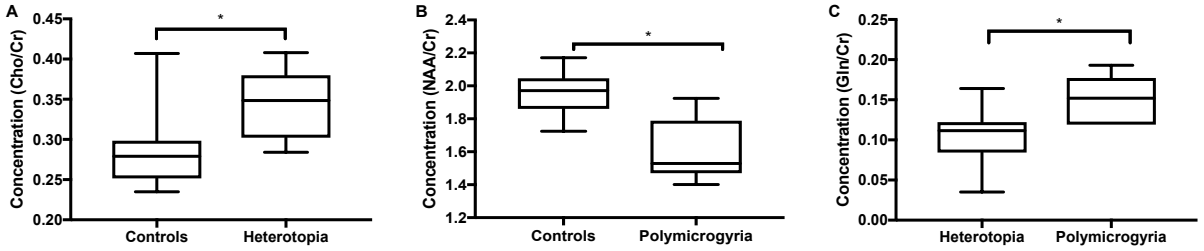

Figure 1: Comparison of significant differences in metabolite ratios for Cho (Left), NAA (Centre), and Glutamine (Right) between population groups

References.

[1] Cendes, F., Continuum; 19(3): 623-642 (2013)

[2] Bartha, R et Al., Magnetic Resonance in Medicine; 44: 641–645 (2000)

[3] Tschampa, H et Al, Seizure; 32: 23-29 (2015)

[4] Kuzniecky, R et Al, Neurology; 48: 1018-1024 (1997)

Coherent Point Drift Algorithms for Breast Image Registration

Ghazaleh Ahmadian, C. Sean Bohun, Mehran Ebrahimi
Faculty of Science, University of Ontario Institute of Technology (UOIT)
Oshawa, Ontario, Canada

Introduction: Breast Magnetic Resonance Imaging (MRI) is a reliable imaging tool for localization and evaluation of lesions prior to breast conserving surgery (BCS). MR images typically will be used to determine the size and location of the tumours before making the incision in order to minimize the amount of tissue excised. The arm position and configuration of the breast during and prior to surgery are different and one question is whether it would be possible to match the two configurations. This matching process can potentially be used in development of tools to guide surgeons in the incision process. Recently, a Thin-Plate-Spline (TPS) algorithm has been proposed to assess the feasibility of breast tissue matching using fiducial surface markers in two different arm positions. The registration algorithm uses the surface markers only and does not employ the image intensities. We apply and evaluate a coherent point drift (CPD) algorithm and registration of three-dimensional breast MR images of six patient volunteers [1, 2]. In particular, we evaluate the results of the previous TPS registration technique to the proposed rigid CPD, affine CPD, and deformable CPD registration algorithms on the same patient datasets. The preliminary results suggest that the CPD deformable registration algorithm is superior in correcting the motion of the breast compared to CPD rigid, affine, and TPS registration algorithms [1].

Materials: Table 1 presents the characteristics of patient datasets in [1]. Patient 5 was coughing throughout the scanning procedure leading to unacceptably poor quality images in which it was impossible to delineate the tumour; the data from this patient is therefore not included in the study.

Patient ID	Matrix size	Field of view (mm^3)	Tumor size arm down (cm^3)	Tumor size arm up (cm^3)
1	$256 \times 256 \times 66$	$180 \times 180 \times 79$	16.8 ± 0.4	18.0 ± 1.1
2	$256 \times 256 \times 56$	$180 \times 180 \times 84$	5.3 ± 0.7	6.9 ± 1.0
3	$256 \times 256 \times 66$	$180 \times 180 \times 79$	80.5 ± 4.1	73.8 ± 1.6
4	$256 \times 256 \times 72$	$180 \times 180 \times 86$	2.4 ± 0.1	2.4 ± 0.4
6	$256 \times 256 \times 46$	$180 \times 180 \times 55$	1.9 ± 0.2	1.5 ± 0.2

Table 1: Charateristics of patient datasets

Results: We computed the Centre of Mass (COM) of the tumours and evaluated the Euclidean distance between the tumours in the reference and arm up images; this is defined as the COM-displacement Table 2. Based on the results presented in Tables 2, it can be recognized that the deformable CPD point sets registration were generally superior than the CPD rigid and affine except in patient 4 in which an "irregular" motion was present.

Conclusion: The experimental results suggest that the deformable CPD registration of 3D breast MRI can perform more accurately compared to the rigid, affine, and TPS registration methods. In general, the motion of the breast is non-rigid so that rigid or affine transformations are not sufficient enough to describe the motion. These preliminary results also demonstrate that in general the experiments are affected by the tumour size, shape, and location. The CPD registration results reported in this paper took 0.2 to 0.4 seconds of CPU time on a standard PC running Matlab, which is significantly lower than the computation time using TPS (under a minute) reported in [1].

Patient ID	Unregistered	TPS registered	CPD-rigid registered	CPD-affine registered	CPD-deformable registered
1	(A) 17.5	(A) 2.7	(A) 6.5	(A) 3.2	(A) 2.5
	(B) 18.5	(B) 3.0	(B) 6.5	(B) 3.1	(B) 2.5
	(C) 19.5	(C) 4.0	(C) 7.4	(C) 4.1	(C) 3.6
2	(A) 33.0	(A) 0.9	(A) 6.2	(A) 2.8	(A) 3.1
	(B) 33.1	(B) 1.5	(B) 7.3	(B) 2.8	(B) 3.6
	(C) 32.0	(C) 2.2	(C) 7.3	(C) 2.4	(C) 2.5
3	(A) 31.6	(A) 9.0	(A) 4.7	(A) 9.8	(A) 4.0
	(B) 32.2	(B) 9.3	(B) 4.8	(B) 10.3	(B) 4.1
	(C) 30.3	(C) 7.9	(C) 4.5	(C) 9.0	(C) 4.2
4	(A) 46.8	(A) 8.5	(A) 21.0	(A) 10.6	(A) 17.6
	(B) 46.7	(B) 8.3	(B) 23.7	(B) 10.2	(B) 19.6
	(C) 46.1	(C) 8.5	(C) 21.0	(C) 10.0	(C) 17.7
6	(A) 11.0	(A) 3.9	(A) 1.2	(A) 2.8	(A) 2.5
	(B) 10.9	(B) 4.2	(B) 1.2	(B) 3.0	(B) 2.6
	(C) 11.2	(C) 5.2	(C) 3.4	(C) 2.3	(C) 2.4

Table 2: COM-displacement (mm)

Acknowledgements: The authors would like to thank Dr. Anne Martel (Sunnybrook Research Institute, Toronto, Ontario, Canada) for providing the volunteer patient datasets.

References:

[1] Mehran Ebrahimi, Peter Siegler, Amen Modhafar, Claire MB Holloway, Donald B Plewes, and Anne L Martel, *Using surface markers for MRI guided breast conserving surgery: a feasibility survey*, PMB, 59(7), pp. 1589, (2014)

[2] Andriy Myronenko and Xubo Song,*Point-Set Registration: Coherent Point Drift*, IEEE Trans. on Pattern Analysis and Machine Intelligence, 32(12), pp. 2262, (2010)

Comparing AACID CEST MRI Measurement of Brain pH using the 2 ppm and 2.75 ppm Amine Resonances at 9.4T

Mohammed Albatany[1,2] and Robert Bartha[1,2]
[1]*Department of Medical Biophysics,* [2] *Centre of Functional and Metabolic Mapping,*
Robarts Research Institute, The University of Western Ontario, London, Ontario, Canada

Introduction: Chemical exchange saturation transfer (CEST) can produce image contrast that is dependent on tissue pH. The CEST method called Amine and Amide Concentration Independent Detection (AACID)[1] shows acidification of the brain following stroke,[1] and increased pH in brain tumors.[2,3] The method can also detect acute tumor acidification using pharmacologic agents.[2,3] The 2.0 ppm amine CEST peak is better defined and shows a greater in-vivo pH response than the 2.75 ppm peak. Therefore, use of the 2.0 ppm rather than the 2.75 ppm amine peak could increase the sensitivity of the AACID radiometric measurement.[4] The purpose of this study was to compare the range and precision of AACID measurements made in the mouse brain using the 2.75 ppm and 2.0 ppm amine resonances.

Methods: AACID was calculated using the AACID Equation.[1] To validate the use of the 2 ppm amine resonance in the AACID equation, we verified that the AACID response was linear over the physiological pH range. A series of protamine (EMD Millipore, Canada) phantoms were created in 5 mm diameter tubes with pH: 6.12, 6.32, 6.56, 6.78, 7.12, 7.44, 7.71, and 8.03. Protamine produces a 2 ppm amine CEST peak.[5] The phantoms contained protamine at a concentration 12 mg/ml dissolved in phosphate buffered saline. CEST images of all phantoms were acquired at 37 °C on a 9.4T MRI. CEST images were also acquired in 24 mice with U87MG brain tumors and in a transgenic Alzheimer's model mouse (5XFAD).

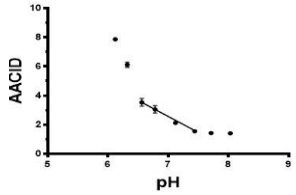

Figure 1.: AACID using the 2 ppm amine resonance as a function of pH in protamine samples. The relationship between AACID and pH is linear.

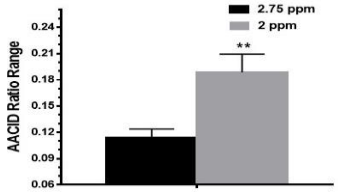

Figure 2. Average difference in AACID values between tumors and contralateral tissue in 24 mice.

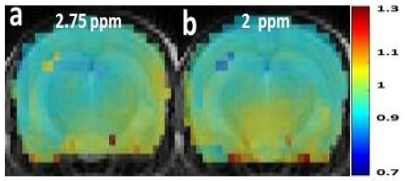

Figure 3. Normalized AACID maps obtained in a single mouse brain using the at 2.75 ppm (a) and 2 ppm (b) amine resonance.

Results: Figure 1 shows the relationship between the 2.0 ppm derived AACID value and pH, and verifies that there is a linear response in the range from pH 6.6-7.4. The AACID value is most sensitive to change at low pH (6.1-6.6) and does not change above pH 7.4. The difference in AACID values between tumor and normal tissue with the 2 ppm amine resonance was 39% greater than that obtained with the 2.75 ppm resonance (Figure 2). Normalized AACID maps obtained for a mouse brain show greater symmetry when using the 2 ppm amine resonance (Figure 3b) compared to the 2.75 ppm amine resonance (Figure 3a).

Discussion: AACID measurement made using the 2 ppm amine resonance showed a significantly greater absolute difference in values between tumor and normal tissue compared to the AACID measurement made with the 2.75 ppm amine resonance. This increase is likely because the 2 ppm amine resonance is more prominent in the in-vivo CEST spectrum compared to the 2.75 ppm amine resonance and is more sensitive to change as a function of pH.

Conclusion: AACID CEST measurements sensitive to tissue pH have greater range when using the 2 ppm amine CEST peak compared to the 2.75 ppm CEST peak. Therefore, use of the 2 ppm amine resonance could increase the precision of AACID based pH measurement in-vivo.

References: **1.** McVicar, N., Journal of Cerebral Blood Flow &Metabolism. **2.** McVicar, N., NMR in biomedicine. **3.** Marathe, K., Journal of Neuro-Oncology. **4.** Desmond K, Contrast Media. **5.** Bar-Shir, ACS chemical biology. **6.** Kim, M., Magnetic resonance in medicine.

CEST MRI of Acute Intracellular Acidification in Glioblastoma Multiforme Following a Single Dose of Cariporide and Quercetin

Mohammed Albatany[1], Alex Li[2], Susan Meakin[3], and Robert Bartha[1,2]
[1]Department of Medical Biophysics,[2] Centre of Functional and Metabolic Mapping,[3]Molecular Medicine Group, Robarts Research Institute, Western University, London, Ontario,Canada

Introduction: Glioblastoma Multiforme remains one of the most lethal cancers with a mean survival of 12-18 months. In this work, we explore the use of a physiological challenge to detect cancer cells. Specifically, the goal of this study is to determine whether chemical exchange saturation transfer (CEST) MRI measurement of tumour intracellular pH (pH_i) is sensitive to tumour acidification after cariporide or quercetin injection. Cariporide is a Na^+/H^+ exchange inhibitor, quercetin is MCTs inhibitor. We hypothesized that both cariporide and quercetin would selectively increase tumor acidity within 2 hours of injection.

Methods: CEST is a relatively novel MRI contrast mechanism that can be made to be dependent on intracellular pH (pH_i). Amine and amide concentration-independent detection (AACID)[1,2] is sensitive to pH_i. Using a 9.4T MRI scanner, full CEST spectra (2 averages) were acquired in 12 mice approximately 14 days after implanting 10^5 U87 human glioblastoma multiforme cells in the brain, before and after administration of cariporide (dose: 6 mg/kg)[3]or quercetin 200mg/kg. Cariporide and quercetin were dissolved in DMSO. The MR imaging protocol included standard anatomical imaging (T_1-, T_2-, diffusion-weighted imaging), and pre-injection B_0, B_1, and AACID-CEST images. AACID-CEST images were reacquired ~2 hours following cariporide or quercetin injection.

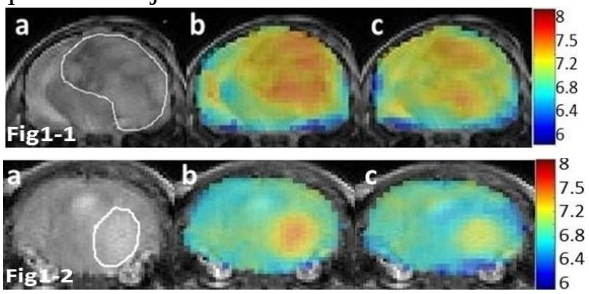

Figure1. Mouse brain with GBM tumor: a) T_2-weighted image b) pH map prior to drugs injection c) pH map ~2 hours after drugs injection. Fig1-1 is cariporide injection. Fig1-2 is quercetin injection.

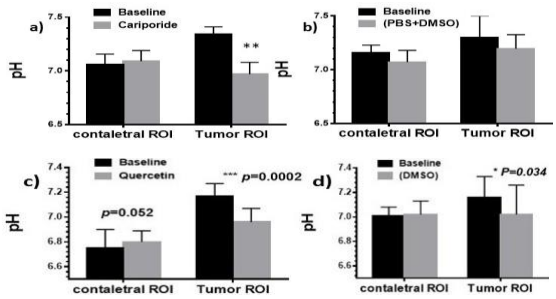

Figure2. Average pH_i in tumor and contralateral ROIs: a) pre and post cariporide 6mg/kg intraperitoneal injection (N=6), b) pre and post PBS+DMSO injection as control N=3. c) pre and post quercetin 200mg/kg intraperitoneal injection (N=6), b) pre and post DMSO injection as control N=3.

Results: Figure 1a shows a T_2-weighted image of the mouse brain tumour. Figures 1b and 1c show pH maps prior to and after drug injections respectively. Figure 2a shows the changes in pH_i for cariporide (N=6). In the tumour ROI the pH_i significantly decreased after cariporide injection by 0.37±0.05 ($p< 0.05$), but there was no change in pH_i within the contralateral ROI. There was no significant change in pH_i for three mice (N=3) injected with (PBS+DMSO) only (control, Figure 2b). Figure 2c shows the changes in pH_i for quercetin (N=6). In the tumour ROI the pH_i significantly decreased after quercetin injection by 0.21±0.07 ($p< 0.005$), but there was no change in pH_i within the contralateral ROI. There was a small decrease in pH_i and significant change in pH_i for three mice (N=3) injected with DMSO only (control, Figure 2d).

Discussion: In this experiment, the observed decrease in pH_i within the tumour may be due to the blockage of Na^+/H^+ exchange by cariporide or blockage of MCTs by quercetin in the cancer cells. The physiological change induced by cariporide or quercetin could help localize brain cancer and monitor tumour response to chemotherapy. This unique approach to cancer detection does not require injection of an imaging contrast agent.

References: **1.** McVicar, Nevin, NMR in Biomedicine (2015). **2**. Marathe, Kamini, Journal of Neuro-Oncology (2016). **3**. Harguindey, Salvador, Journal of translational medicine (2013). **4.** Sagiyama, Koji, Proceedings of the National Academy of Sciences (2014).

Transverse Relaxation Rate in Magnetic Resonance Imaging Is Altered by Hepcidin

[1,2,3*]Alizadeh, K; [1]McGuire, T; [1,2]Thompson, RT; [1,2,3]Prato, FS; [1,2] Gelman, N; [1,2,3]Goldhawk, DE
*Trainee, Supervisor
[1] Imaging Program, Lawson Health Research Institute; [2] Medical Biophysics & [3] Collaborative Graduate Program in Molecular Imaging, Western University, London, Canada

Introduction: Magnetic Resonance Imaging (MRI) is a non-invasive tool which can be used to track cellular activities in the body using iron based contrast agents [1, 2]. This suggests that a particular cell's iron handling mechanism may influence the detection of magnetic resonance (MR) contrast [3]. For instance, inflammation involves downregulation of iron export in monocytes and macrophages by the hormone hepcidin [4], due to degradation of the iron export protein ferroportin (FPN) [5].We therefore examined the effect of hepcidin on transverse relaxation rates in multipotent P19 cells, which provide a convenient model of molecular activities present during inflammation due to their high iron import and export activities, similar to macrophage [6].
Hypothesis: Pro-inflammatory signalling by hepcidin is detectable by MRI due to regulation of iron export.
Methods: Iron-exporting P19 cells were cultured in plain medium (-Fe) and iron-supplemented medium (+Fe) containing 25 µM ferric nitrate for 7 days prior to removal of extracellular supplement and culture for an additional 1 (1h – Fe), 2 (2h – Fe), 4 (4h – Fe) and 24 (24h – Fe) hours. To examine interruption in iron export, hepcidin (200 ng/ml) was added to the medium 1h after iron supplement removal. Cells were then harvested; mounted in a gelatin phantom; and scanned at 3 Tesla. Image-based measurements of total transverse relaxation rate (R_2*= $1/T_2$*) and the irreversible component ($R_2=1/T_2$) were performed [7]. The difference between R_2* and R_2 yields a reversible component ($R_2' = R_2^* - R_2$) that is closely correlated with cellular iron content in some cell types [3]. Therefore, changes in the MR signal of P19 cells can be related to total cellular iron content, which will be measured by inductively-coupled plasma mass spectrometry (ICP-MS). Changes in ferroportin protein expression were evaluated by Western blot using rabbit anti-FPN as the primary antibody. Analysis of covariance (ANCOVA) will identify further differences at different time points.

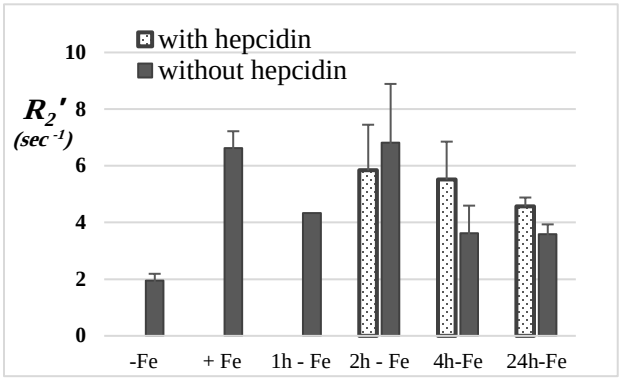

Figure 1. Comparison of R2' transverse relaxation rates in P19 cells +/-iron and hepcidin. Data are the mean ± standard error (SE) where n=3-8. For 1.h-Fe, n=1.

Results: Transverse relaxation rates in P19 cells decreased within an hour of withdrawal of iron supplement, consistent with high ferroportin expression and high iron export activity (Figure 1). When hepcidin was added, the expected decrease in iron export resulted in a stabilization of R_2', despite the absence of extracellular iron supplementation. Disruption of ferroportin expression in cells treated with hepcidin was related to changes in MR signal.
Discussion: We showed that hepcidin-related regulation of ferroportin is detectable by MRI in cells that exhibit high ferroportin expression and actively export iron. This finding provides a mechanism for monitoring inflammatory signalling in macrophages. We anticipate that an interruption in iron export, in combination with continued iron import, may transiently induce an iron retention phenotype, as described for macrophages responding to inflammatory signalling through hepcidin [4]. In the future, MRI may provide an effective non-invasive imaging modality for the diagnosis of inflammatory diseases by tracking changes in the cellular regulation of iron.

[1] Li *et al* (2013) Theranostics 3, 595
[2] Goldhawk *et al* (2012) Wiley Interdiscip Rev Nanomed Nanobiotechnol 4, 378
[3] Goldhawk *et al* (2015) Magnetic Resonance Insights 8, 9
[4] Theurl *et al* (2008) Blood 111, 2392
[5] Nemeth *et al* (2004) Science 306, 2090
[6] Liu (2015) MSc Thesis, Western Univeristy
[7] Sengupta *et al* (2014) Frontiers in Microbiology 5, 29

Development of a high frequency single-element ultrasound needle transducer for anesthesia delivery

Golafsoun Ameri[a,b], Jungik Son[c], F. Stuart Foster[c,d], Sugantha Ganapathy[b,e], and Terry M. Peters[a,b]

[a]Robarts Research Institute, London, ON, Canada; [b]Western University, London, ON, Canada; [c]Sunnybrook Health Sciences Centre, Toronto, ON, Canada; [d]University of Toronto, Toronto, ON, Canada; [e]London Health Science Centre, London, ON, Canada

Epidural anesthesia is one of the most commonly used and yet challenging techniques employed for pain management and anesthesia delivery. The major complications of this procedure are due to accidental dural puncture, with an incidence of 1-3%, which could lead to both temporary and irreversible permanent neurological complications. Needle placement under ultrasound (US) guidance has received increasing interest for improving accuracy. However, Poor needle visibility in US, difficulties in displaying relevant anatomical structure such as dura mater due to attenuation and bone shadowing, and image interpretation variability among users pose significant hurdles for any US guidance system. As a result, US guidance for epidural injections has not been widely adopted for everyday use in the performance of neuraxial blocks. The difficulties in localizing the ligamentum flavum and dura mater with respect to the needle tip can be addressed by integrating A-mode US, provided by a single element transducer at the needle tip, into the B-mode US guidance system. We have taken the first steps towards providing such a guidance system. Our goal is to improve the safety of this procedure with minimum changes to the clinical workflow. This work presents the design and development of a 20 MHz single-element transducer housed at the tip of a 19 G hypodermic tube, which can fit inside an introducer needle, Figure 1. Initial transducer characterization tests have been carried out and the performance of the transducer in a euthanized porcine model has been evaluated.

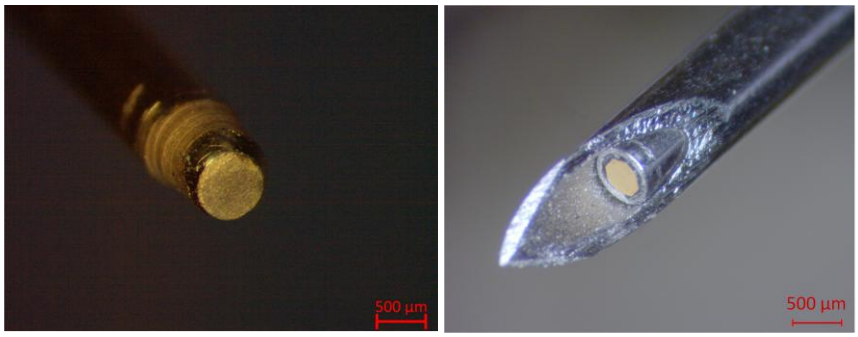

(Left) Cross-section of the needle transducer housed at the tip of a hypodermic tube. (Right) Needle transducer placed inside an introducer needle.

Title: T1rho and T2 relaxation changes in tibiofemoral articular cartilage following a functional loading stimulus in early knee osteoarthritis: Preliminary findings

Authors: **Hayden F. Atkinson**[1,3], Trevor B. Birmingham[1,3], Rebecca F. Moyer[1,3], Jaques S. Milner[2,3], David W. Holdsworth[1,2,3], J. Robert Giffin[1,3]
Hayden F. Atkinson's PhD supervisor is Dr. Trevor B. Birmingham.
[1]Wolf Orthopaedic Biomechanics Laboratory, Fowler Kennedy Sport Medicine Clinic, Western University, London, Canada
[2]Robarts Research Institute, Western University, London, Canada
[3]Bone and Joint Institute, Western University, London, Canada

Introduction: Healthy knee articular cartilage effectively transfers and disperses load during ambulation. Articular cartilage degeneration is the hallmark of osteoarthritis (OA), and induces aberrant knee joint loading, leading to the functional decline of the joint. Quantitative MRI measures such as T1rho and T2 relaxation are proposed to enable detection of early pathological changes in knee articular cartilage biochemical properties such as collagen and proteoglycan. T1rho and T2 are inversely correlated with proteoglycan, collagen integrity, and water content, which are essential for articular cartilage health. The purpose of this study is to explore the changes in T1rho and T2 relaxation immediately following a functional loading stimulus in early knee OA.

Methods: A programmable dual-belt treadmill capable of moving with six degrees of freedom provided a knee loading stimulus throughout a 20-minute walking test. The stimulus was intended to load the knee in multiple planes and challenge the participant. T1rho and T2 maps were obtained at baseline, and immediately after the loading stimulus, using a Siemens 3T Magnetom Tim Trio magnet with a dedicated 15-channel knee coil housed in the Centre for Functional and Metabolic Mapping at the Robarts Research Institute. T1rho-weighted images were acquired using an 8-shot gradient echo sequence, with spin locking times of 0, 10, 20, 30, and 40 ms, at a B1 field strength of 500 Hz. T1rho maps were generated via software developed in-house by fitting image intensities of the T1rho weighted images pixel-by-pixel to the equation $S(TSL) \propto \exp(-TSL/T1rho)$ using a Levenberg-Marquardt mono-exponential fitting algorithm implemented in ITK. T2-weighted images were acquired using a multi-echo spin echo sequence, echo train length of 7 with inter-echo spacing of 11.1 ms, and TR of 2700 ms. T2 maps were generated using Siemens MapIt software. Load-bearing regions of the medial tibia and medial femur articular cartilage were segmented manually and analysed using 3D Slicer software.

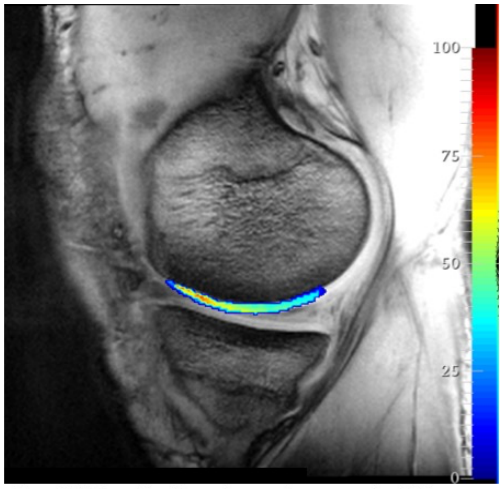

Figure 1. T1rho-weighted image demonstrating segmented and T1rho mapped cartilage of the medial femur. Values are in milliseconds.

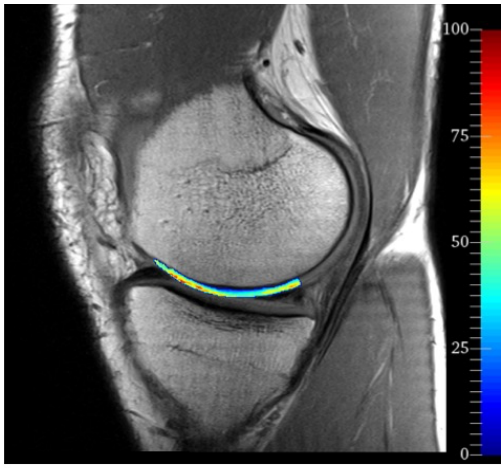

Figure 2. T2-weighted image demonstrating segmented and T2 mapped cartilage of the medial femur. Values are in milliseconds.

Results: One patient has been tested to date (48-year-old male with mild medial knee OA). Mean T1rho of the affected knee for the medial femoral and tibial cartilage at baseline was 45.47 and 49.72 ms, respectively. After the loading stimulus, T1rho increased to 53.01 ms and 60.75 ms, a change of 7.54 and 11.03 ms, respectively. Mean T2 of the affected knee for the medial femoral and tibial cartilage at baseline was 58.84 and 41.35 ms, respectively. After the loading stimulus, T2 decreased to 50.71 and increased to 42.82 ms, a change of -8.13 and 1.47 ms, respectively.

Conclusions: In this one patient with mild knee OA, an increase in T1rho in the medial femoral and tibial cartilage, and a decrease in T2 in the femoral cartilage, suggest changes in these parameters can be induced using a functional knee loading stimulus.

Superimposed Structural and Functional Brain Networks on Grey and White Matter

Saeed M. Bakhshmand*, Sandrine de Ribaupierre, Roy Eagleson
The University of Western Ontario, London, Ontario, Canada

Introduction. Representation of brain mapping relying on 3D anatomical structures can facilitate our understanding of the implications of connectivity, whether this is for neuroscience or for neurosurgery. In order to minimize damage to healthy tissue, one heuristic is to choose the path that minimizes the length of the access path – but when at the surgical coalface the pressing concern is to consider the "eloquence" of the tissue along any candidate pathway, in order "to spare eloquent areas". In general terms these are areas which, if damaged, would lead to a measurable loss of motor, sensory, or linguistic function; leading to a concern as to why neural function that does not lead to a deficit in low-level behavioural scores are somehow exempt. To address this, we are proposing an objective metric of the importance of a neural pathway, based on a number of connectivity metrics, including eloquence score for each Grey Matter (GM) atlas region and White Matter (WM) fiber to facilitate assessment of brain tissue eloquence.

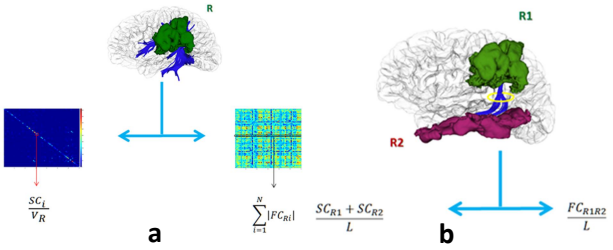

Figure1. a) Connectional importance for a GM area, SS on the left, FS on the right **b)** Connectional importance of the fiber pathways, SC on the left and FC on the right. N is total number of ROIs (N=70), SC_R is the number of fibers that intersects with region R, FC_{RS} is functional correlation score between regions R1 and R2, L is the number of fibers with similar origin and end point, V_R is the volume

Methods. The new metric consists of structural score (SS) and functional score (FS) for GM regions and WM fibers and is compatible to be visualized over relevant tissue type. Model driven FC yields graph matrices which are suitable for computing FS. SS is built from deterministic tractography and relevant SC matrix. According to Fig.1 (a) SC for GM is equal to the total number of fibers attached to a region of interest (ROI), divided by its volume. FS is the sum of all functional links that each atlas region holds with the rest of the brain. For WM pathways, FS is summation of existing correlation between ROIs at the end points of the fiber normalized by number of fibers in linkage bundle (L). SS of each fiber is represented by summing up SC score of relevant GM areas, followed by dividing to L. In order to demonstrate proposed technique we used a dataset (rs-fMRI, dMRI and T1) from an 8 years old healthy pediatric subject. FC is computed from Dynamic FC analysis [1] method correlation. Eigen connectivity matrix with largest eigenvalue has been considered for the rest of the pipeline.

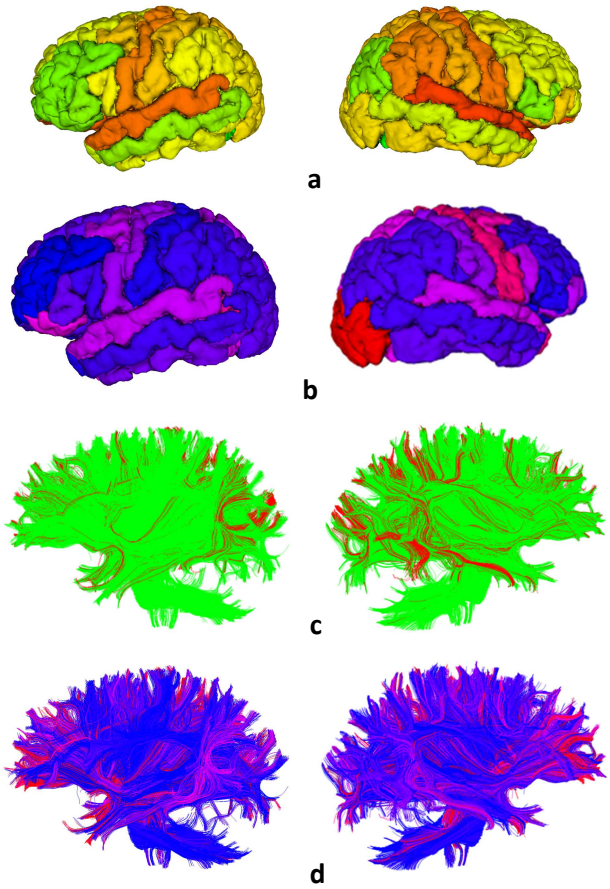

Figure2. a) FS colormap: [red,yellow,green], range:[0,1] b) SS, colormap:[blue,purple,red], range:[0,1] of the GM areas shown in lateral view of the cerebral cortex. c) FS of fiber pathways, majority of the fibers hold a zero FS, range:[0,600] d) SS of fiber pathways ,range: [0,4000]

Results. Fig. 2 shows overlay of SS and FS on GM areas and WM pathways. There exists a high amount of similarity between SS and especially FS scores in interhemispheric regions (e.g. superiortemporal or posteriorCG). Regarding the WM pathways, most of the high importance fiber tracts are situated inside CC or CST tract.

Conclusions. This novel method displays underlying connectivity data while jointly modelling connectional importance of WM and GM. In addition, this allows superimposing functional correlatives on fiber pathways or anatomical linkages on cortical hubs.

References.[1] N. Leonardi, et.al.*NeuroImage*, vol. 83, pp. 937–950, 2013.

Calibration of single-plane fluoroscopy using a 3D printed calibration object

Rudy Baronette[1,2,3], Xunhua Yuan[2], Matthew G Teeter[1,3,4,5], David W Holdsworth[1,2,3,4]
Development of Novel Therapies for Bone and Joint Diseases Consortium
[1]Western Bone and Joint Institute
[2]Imaging Research Laboratories, Robarts Research Institute
Depts. of Medical Biophysics[3] and Surgery,[4] Western University
[5]Lawson Health Research Institute, London ON, Canada

Introduction: Quantitative assessment of 3D dynamic motion in lower extremity joints under natural weight-bearing conditions allows for evaluation of joint diseases and their treatments. Fluoroscopic kinematic analyses of total knee arthroplasty (TKA) have characterized unique motions resulting from implant design that relate to function and wear performance.[1] To achieve accurate 2D/3D registration of a knee implant using single-plane fluoroscopy, it is essential to determine the focus position with respect to the imaging plane.[3] Recent advances in 3D printing have made it possible to accurately manufacture plastic structures in any shape, providing potential for novel calibration phantom designs. We describe a 3D printed cubic calibration phantom, comprised of tantalum marker beads at known locations.

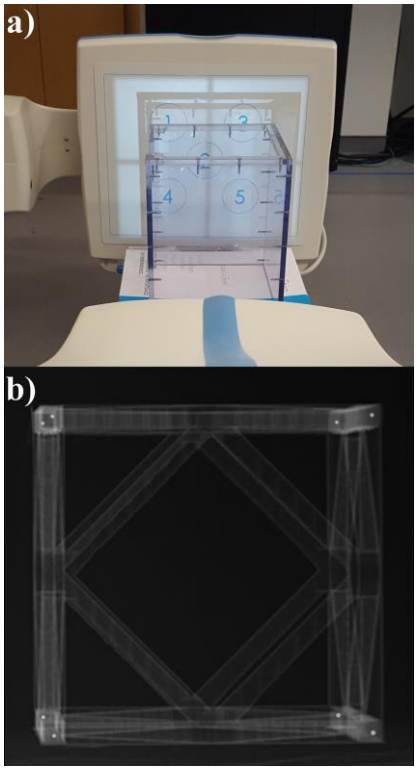

Fig. 1: (a) photo of RSA calibration cage positioned within the ceiling-mounted single-plane fluoroscopy; (b) x-ray of 3D printed cube, used to calibrate fluoroscopy system.

Methods: A calibration cube phantom was fabricated by fused-deposition printing in polylactic acid (PLA) plastic with a commercial 3D printer (Dremel® Idea Builder); this phantom was then used to calibrate the system. The phantom contains eight 1.0 mm diameter tantalum markers inserted into the vertices of the cube. Exact coordinates of the markers were determined using radiostereometric analysis (RSA) in a dedicated RSA lab. An RSA calibration cage containing eighteen 0.8 mm diameter tantalum markers (RSA Biomedical, Umea, Sweden) was also used to calculate the focus position. The acquisition of radiographs was conducted using a ceiling-mounted x-ray fluoroscopy system (Adora RF, Nordisk Røntgen Teknik A/S, Denmark) equipped with a flat-panel detector with a 35 x 43 cm field of view and 160 µm pixels (CXDI-50RF, Canon). The focus position was calculated using custom MATLAB code (MATLAB R2015a, USA) and measurements from UmRSA (RSA Biomedical, Umea, Sweden). Both calibration objects were imaged (n=10) at 70 kVp, 2 mAs using 1200 mm nominal source-to-image distance (SID) without repositioning the x-ray equipment between all exposures.

Results: The focus position was calculated using the 3D printed cube to be 213.33 mm ± 0.53 mm, 171.99 ± 0.59 mm, and 1220.64 ± 0.62 mm for the corresponding x, y and z planes. The source position angles were -93.23 ± 0.02°, -2.02 ± 0.03°, and 90.7 ± 0.004° for the respective x, y, and z planes. The focus location was calculated using the RSA calibration cage to be 195.11 ± 0.06 mm, 183.96 ± 0.04 mm, and 1234.41 ± 0.03 mm for the respective x, y, and z planes. The source position angles were -92.65 ± 0.004°, 2.35 ± 0.03°, and 90.75 ± 0.0002° for the respective x, y, and z planes. Statistically significant differences were observed between all respective angles and translations by one-way ANOVA ($p<.05$).

Conclusion: We have demonstrated that 3D printed objects have the potential to be a useful tool for calibrating single-plane fluoroscopy systems when studying joint kinematics after total knee arthroplasty. Previous studies[2] have shown that increasing the number of markers and size of the 3D printed cube will improve the standard deviation of the focus translations when calibrating using the 3D printed cube. The data demonstrated 3D printed calibration objects produce similar results for calculating SID and source angles, in comparison to a standard RSA calibration cage.

References: 1.Banks, S. A. and W. A. Hodge (2004). Clinical Orthopaedics and Related Research **426**: 187-193. 2. Yuan, X., et al. (1997). Journal of biomechanics **30**(9): 989-992. 3. Yuan, X., et al. (2002). The Journal of Bone and Joint Surgery **84**: 908-914.

Return to Program

Evaluation of a mobile, real-time, tracked augmented reality display for surgical navigation

Zachary Baum*, Tamas Ungi, Andras Lasso, Gabor Fichtinger
Laboratory for Percutaneous Surgery, Queen's University, Kingston, Canada

INTRODUCTION: Surgical navigation under Computerized Tomography (CT) and Magnetic Resonance (MR) image guidance is used in practice for various needle interventions. Images are typically acquired throughout the insertion process to track the needle path. This method leads to patient discomfort from procedure length, and the possibility of multiple needle insertions. Augmented reality (AR) image overlay systems have been proposed to limit required images, failed insertion attempts, and patient discomfort. Though they have not been translated to clinical settings due to a lack of portability and robustness; overlaying a single image slice on a patient renders it easier for clinicians to locate targets and insert needles correctly[1, 2]. Our goal was to create a portable, robust, and simple to operate system for intraoperative AR guidance.

METHODS: A mobile AR image overlay system allows users to wirelessly navigate scanned patient images using software built on the open-source 3D Slicer platform. The system can be handheld or mounted to a table at patient bed-side. Once set-up for image exploration and needle navigation, our software provides calibration of the system and other tools, and provides users with a method for registering patients to images. A passive optical tracking camera acquires real-time tracking data and transfers it to our software. With this system, we can provide clinicians with an augmented intraoperative view by overlaying medical images directly onto patients (Figure 1). Medical professionals were asked to navigate patient images while using the image overlay and plan needle insertions (Figure 2).

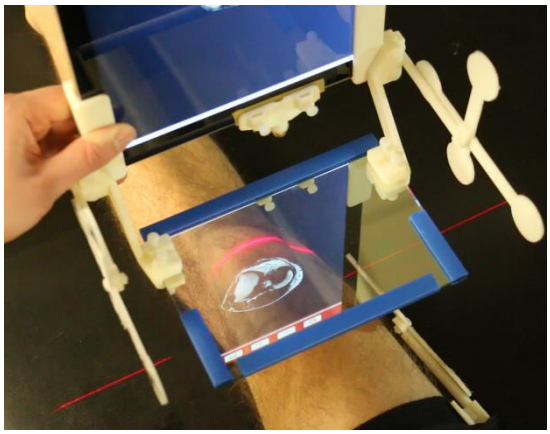

Figure 1: User's view of overlaid image on a patient's leg while using the image overlay system.

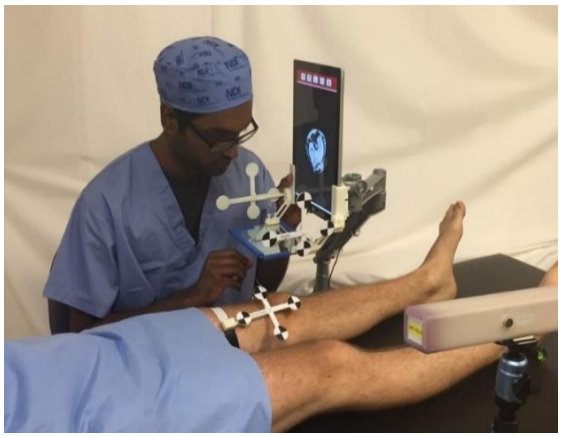

Figure 2: Participant using the system and adjustable table-mounted arm to plan a needle insertion path.

RESULTS: In our evaluation study, five physicians responded to a series of questions to assess handheld and table-mounted forms of the image overlay system by rating them on a Likert scale. Responses showed participants felt it was simple to learn how to use the image overlay system, and that it was simple to understand where the projected image was located on the patient. Participants indicated that there was a significant increase in how demanding the handheld version of the system was to use ($p = 0.002$, $n = 5$). Additionally, participants felt they could position themselves more comfortably and navigate images more easily using the table-mounted system.

CONCLUSION: The image overlay system was developed with the goal of bringing clinically usable AR guidance with CT and MR images to minimize radiation exposure and reduce the likelihood of failed insertions. In evaluating the system, participants identified it as being simple to use and understand. By offering real-time browsing of patient images for surgical navigation without pre-planning or image review before the intervention, the image overlay system may save valuable time in CT or MR suites. The system shows promise for use in clinical practice for surgical navigation and further assessment of the image overlay system in a real-world clinical setting is to follow.

REFERENCES: [1] Fichtinger *et al.*, "Image Overlay Guidance for Needle Insertion in CT Scanner," *Biomedical Engineering, IEEE Transactions on*, 52(8):1415-1424, 2005. [2] Fritz *et al.*, "Augmented reality visualization with use of image overlay technology for mr imaging-guided interventions: assessment of performance in cadaveric shoulder and hip arthrography at 1.5 t.," *Radiology*, 265(1): 254–259, 2012.

Shape Complexes: Combining Shape and Label Ordering Information in Segmentation

John SH Baxter*, Jiro Inoue, Maria Drangova, and Terry M Peters
Robarts Research Institute, The University of Western Ontario, London, Ontario, Canada

Introduction: Encoding shape information has always been of interest in medical image segmentation allowing for an a priori understanding of the anatomy's geometry to ameliorate difficulties with signal strength and homogeneity. This shape information has often been encoded in the form of statistical shape models [1] and atlas registration/propagation [2] which lack rigorous optimality guarantees. Global optimization based segmentation techniques have recently been expanded with notions of label ordering which allow them to include multiple interacting objects with defined sub-components. [3] In continuous max-flow segmentation, these label orderings structures have allowed for more complex intensity distributions and regularization requirements to be encoded without sacrificing optimality guarantees. By combining shape information in the form of *geodesic star convexity* with label orderings, shape information about complex objects can be encoded and addressed for in a globally optimal framework. These *shape complexes* bring together the optimality and intuitive structure of label orderings with the robustness of shape information.

Methods: Shape complexes use *directed acyclic graph max-flow* (DAGMF) [4] to address the optimization:

$$\min_{\theta(x)} \sum_{\forall L} \int_{\Omega} (D_L(x)u_L(x) + S_L(x)|\nabla u_L(x)|)dx$$

where the segmentation labeling functions, $u_L(x)$, are arranged in a directed acyclic graph representing the label ordering. A geodesic star convexity constraint, $e_L(x) \cdot \nabla u_L(x) \geq 0$, can be applied to each label. This constraint implies that the particular label cannot have a decreasing edge at location x with an orientation within 90^O of the direction $e_L(x)$. By applying these constraints to not only objects, but also their constituent parts, more complex shapes can be represented.

Results: As shown in Figure 1, adding shape information to DAGMF can significantly improve the segmentation accuracy in an ultrasound vessel segmentation example. In addition, Figure 2 shows that incorporating shape information vastly improves the robustness of the segmentation algorithm with respect to regularization, which would facilitate its use in various medical image segmentation scenarios.

Conclusions: We have successfully shown that a limited degree of shape information can be applied in tandem with label ordering information in image segmentation. Ultimately, this allows for more complex representations of anatomical knowledge to be expressed in a readily human- and computer-understandable manner.

References: [1] Lorenz et al. IEEE 3DDIM, 1999, 414-23. [2] Aljabar et al. NeuroImage, 2009, 726-38. [3] Rajchl et al, MedIA, 2016 45-56. [4] Baxter et al., MICCAI BAMBI, 2015.

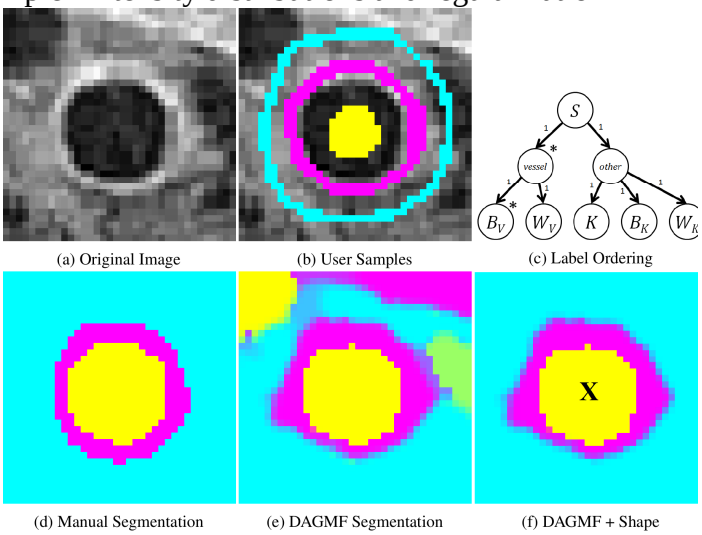

(a) Original Image (b) User Samples (c) Label Ordering

(d) Manual Segmentation (e) DAGMF Segmentation (f) DAGMF + Shape

Figure 1: Ultrasound vessel segmentation - qualitative results

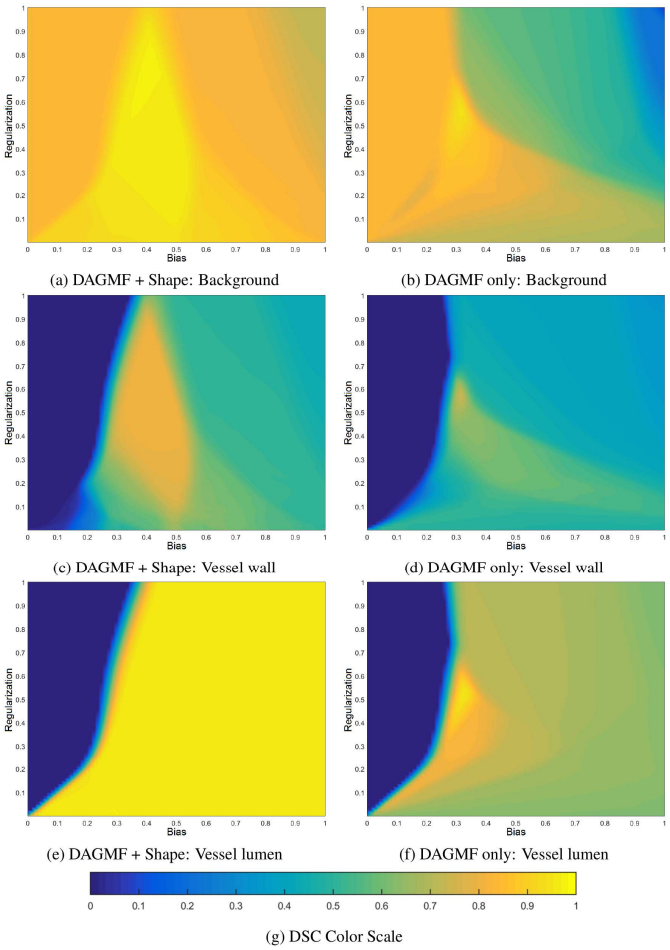

(a) DAGMF + Shape: Background (b) DAGMF only: Background

(c) DAGMF + Shape: Vessel wall (d) DAGMF only: Vessel wall

(e) DAGMF + Shape: Vessel lumen (f) DAGMF only: Vessel lumen

(g) DSC Color Scale

Figure 2: Ultrasound vessel segmentation - quantitative results

Compensated Row-Column Ultrasound Imaging System Using Conditional Random Fields

Ibrahim Ben Daya*, Albert I.H. Chen, Mohammad Javad Shafiee, Alexander Wong, John Yeow
Vision and Image Processing (VIP) Research Group & Advanced Micro- / Nano- Devices Research Group,
Department of Systems Design Engineering, University of Waterloo, Waterloo, Ontario, Canada

Introduction. Addressing 2-D arrays for 3-D imaging has been an active area in medical sonography. The row-column method is a simplification technique that reduces the complexity of a fully addressed 2-D array by using a pair of orthogonally positioned arrays of rows and columns. The row-column method for ultrasound suffers from a few intrinsic limitations: data sparsity, speckle noise, and spatially dependant point spread function (PSF) that suffers from edge artifacts. In this study, we take an existing row-column ultrasound imaging system and characterize it, and then use this characterization to compensate for the intrinsic limitations of the method through two conditional random field based models.

Method. First we characterize the baseline row-column system through an image formation model, a noise model and a point spread function model. The image formation model helps us understand sparsity in the image. Through empirical testing, it was found that noise is best modelled using the Fisher–Tippett distribution. The PSF was estimated using Field II, a MATLAB toolkit for ultrasound simulation. Field II uses the Tupholme-Stephanisshen model for the spatial impulse response to estimate the PSF at different depths based on a user defined transducer setup. Given these characterizations, we formulate an image reconstruction framework based on conditional random fields (CRF).

We define the image reconstruction problem as a Maximum A Posteriori (MAP) problem and use CRF to model the posterior probability. CRF allows us to directly model the posterior without specifying a prior model while relaxing the conditional assumption. Instead CRFs are based on unary potential functions, which incorporate information corresponding to the observation, and pairwise potential functions, which incorporate spatial information. The unary function was modeled after the Fisher-Tippet distribution to account for noise, while incorporating the estimated PSF. The pairwise function was modeled using penalty terms that attempts to give closer pixels and pixels with similar intensities the same label. The first proposed system (CRC-UIS) [1] is based on multilayered CRFs, it only employs local information into the model. The second system (EG-CRCUIS) uses edge-guided, stochastically fully connected random fields (EG-SFCRF) to employ more global information into the model. We will compare the output of both systems.

Results. A scan of the cross section of four 644 µm wires is shown in figure 1; in the baseline row-column system, only two wires are clearly visible. Both CRC-UIS and EG-CRCUIS have shown all four. Both proposed systems have shown great noise suppression, with CNR levels at 2.651, 1.5419, and 0.7703 dB for EG-CRCUIS, CRC-UIS, and baseline row-column respectively. CRC-UIS has noticeable ovesmoothing of the wire cross sections (particularly the bottom right), which is corrected in EG-CRCUIS. EG-CRCUIS also shows better noise suppression and clearer wire edges when compared with CRC-UIS.

Conclusion. The utility of using a physical model to better reconstruct ultrasound images has been shown here. A baseline row-column ultrasound imaging system has been characterized, and this characterization was the basis for two imaging systems: CRC-UIS, based on MCRF, which improved the image output seen in the baseline system, and EG-CRC, based on EG-SFCRF, which improved the images from CRC-UIS by employing more global information. Together with the simplification method, the reported methods takes a step further in understanding and demonstrating the potential of row-column imaging, thus providing a better 3-D visualization technique for medical diagnosis.

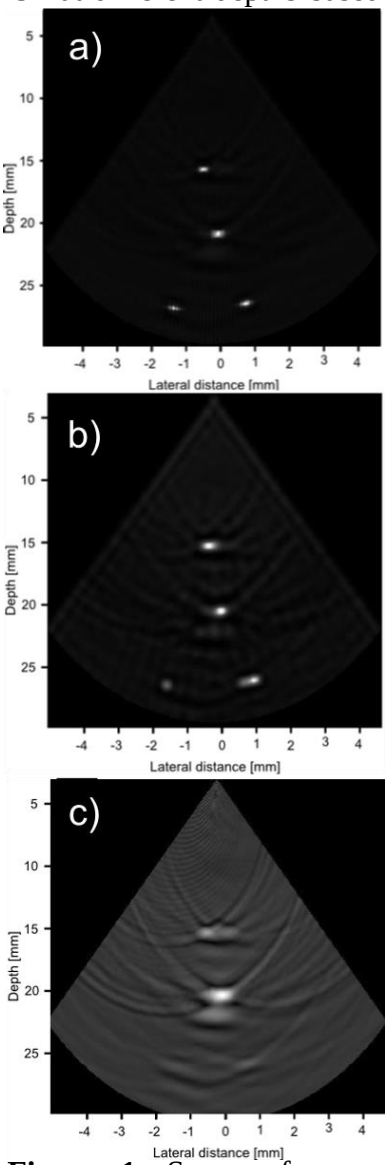

Figure 1. Scans of cross sections of four wires from (a) baseline RC, (b) CRC-UIS, and (c) EG-CRCUIS.

References. [1] Ben Daya *et al.* PLoS ONE 2015

PLUS Model Catalog: A library of 3D-printable models

Eden Bibic, Zachary Baum, Vinyas Harish, Tamas Ungi, Andras Lasso, Gabor Fichtinger

Laboratory for Percutaneous Surgery, Queen's University, Kingston, ON, Canada

Introduction: 3D-printable tools are ubiquitous in computer-assisted interventions; they are used in a variety of tasks, such as calibration, treatment planning, simulation, and instrument tracking. Previously, we have created the Public Library for Ultrasound (PLUS, www.PlusToolkit.org), a free open-source software platform to support the development of ultrasound-guided intervention application [1]. We enhanced the PLUS Toolkit with an online file library of 3D-printable models for public access and support, as presented in this paper.

Methods: Computer-Aided Design (CAD) software tools, SolidWorks (www.SolidWorks.com) and FreeCAD (www.FreeCADWeb.org), are used to create models of various tools and devices frequently used in computer-assisted intervention applications. Both the source files and STereoLithography (STL) files for the models are listed in a Model Catalog at the PLUS main distribution site (www.PlusToolkit.org). Images and descriptions accompanied the files for simplicity and ease of use. A static HTML page of the catalog automatically updates nightly with the most recent content, allowing the public to download and use the most recent versions of the models for free. The models, with their dimensions and properties, can also be directly imported into 3D Slicer (www.Slicer.org) using the PLUS Model Catalog browser module of the SlicerIGT (www.SlicerIGT.org) extension.

Results: The library currently contains 34 models, while more are being added on a regular basis and upon user request. The PLUS Toolkit has been downloaded approximately 1,500 times per year. It is emerging as a widely used platform in computer-assisted intervention research, and currently has been cited over 70 times, according to Google Scholar. Most PLUS users access the Model Catalog as a resource for tracking fixtures and other 3D-printable surgical tools. The majority of PLUS users have tracked ultrasound that they calibrate with a 3D-printed phantom in Model Catalog (Fig. 1). Other frequently used catalog items include fixtures to mount position-tracking sensors to surgical tools (Fig. 2). Items from the Model Catalog are conveniently inserted into 3D Slicer-based applications, as shown in the navigation scene below with a tracked ultrasound, needle, and spine, all of which are from the Model Catalog (Fig. 3).

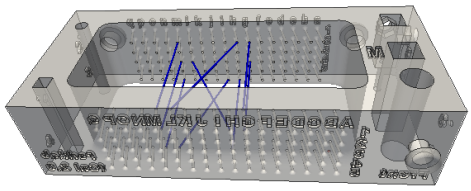

Fig. 1. Ultrasound calibration phantom [2].

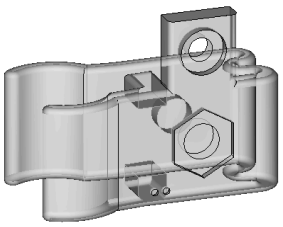

Fig. 2. Electromagnetic tracking sensor holder for electrosurgery cautery device [3].

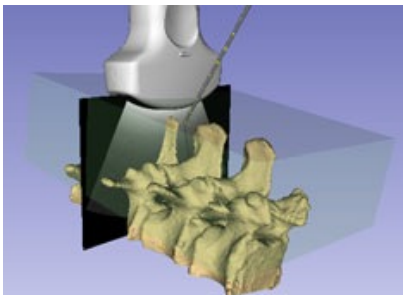

Fig. 3. 3D Slicer navigation scene with catalog models of tracked ultrasound, needle, and spine [1].

Conclusion: The PLUS Model Catalog contributes to the PLUS Toolkit (www.PlusToolkit.org) in promoting rapid development and clinical translation of computer-assisted intervention applications. The catalog is continuously expanded with new and revised models.

References:

[1] Lasso *et al.* "Plus: Open-source toolkit for ultrasound-guided intervention systems", IEEE TBME 2014

[2] Carbajal *et al.* "Improving N-wire phantom-based freehand ultrasound calibration", IJCARS 2013

[3] Ungi *et al*. "Navigated Breast Tumor Excision Using Electromagnetically Tracked Ultrasound and Surgical Instruments", IEEE TBME 2016

Vurtigo: Updates to a Visualization Platform for Image-guided Procedures

L. Biswas[1], S.N. Ferguson[1], P. Krahn[1,2], S. Jafarpour[1,3], S.O. Oduneye[1,2], M. Pop[1,2], G.A. Wright[1,2,3]
Image-guided device interventions for cardiovascular disease
[1]Physical Sciences, Sunnybrook Research Institute, Toronto, [2]Medical Biophysics and [3]IBBME University of Toronto

Introduction. Image-guided therapy for vascular diseases can improve procedures through intraoperative feedback and the incorporation of patient-specific data. Here we present recent updates to our visualization platform, Vurtigo [1], for integration in minimally invasive MR-guided and X-ray-guided interventions.

Methods. Vurtigo plays an important role in interventional procedures. Examples from several preclinical applications illustrate how Vurtigo fuses prior, processed and real-time information to provide the experimenter with a richer understanding of the procedure. Roadmap volumes, real-time scan planes, device coordinates, segmented surfaces and images, and electroanatomical maps can be visualized together in context. Vurtigo is written in C++ and built using open-source libraries. Plugins have been written to receive and send real-time data to applications using protocols such as OpenIGTLink and ZeroMQ.

Results. Using Vurtigo for visualization, MR electrophysiology catheters were guided into the left ventricle (LV) to map the arrhythmia substrate in porcine models of chronic infarct (Fig.1a). Further, post-processing was performed using Vurtigo to generate the LV shell (Fig.1b), electroanatomic voltage and isochronal maps. The latter can be compared to standard maps obtained using fluoroscopy [2] or computer simulations [3]. This framework has also been used to perform real-time MR-guided ablations in healthy porcine hearts (Fig.2) [4].

Real-time registration of a MR-derived 3D coronary sinus (CS) mesh to X-ray images was performed in Vurtigo and validated in simulation studies (Fig.3) to allow for optimal navigation and placement of cardiac leads [5].

Algorithms have been or are currently being developed to provide relevant and accurate views of target anatomies during procedures:

- A semi-automatic algorithm segments scar tissue in myocardium from delayed enhancement MRI [6].
- A respiratory motion model corrects catheter coordinates for accurate localization [7].
- Whole heart segmentation algorithms automatically extract heart chambers from MR images.

Conclusion. We have successfully integrated Vurtigo in image-guided interventions to support our ongoing preclinical MR and X-ray procedures. Current work includes navigation of catheters to ablate targets in the ventricles, intraoperative electroanatomic mapping, and fusion of X-ray and MR images to guide revascularization of preclinical peripheral chronic total occlusions.

References. [1] Radau PE, et al. LNCS 2012;7085:244–253. [2] Oduneye SO, et al. IEEE TBME 2013;60(9):2442–2449. [3] Pop M, et al. LNCS 2012;7746:364-374. [4] Krahn P, et al. Proc. ISMRM 2016;Singapore. [5] Choi J, et al. Med. Imag. Anal. 2016;31:98-107. [6] Lu Y, et al. Quant Imaging Med Surg.2012;2(2):81–6. [7] Xu R, et al. Comput. Methods Programs Biomed. 2016;136:31–43.

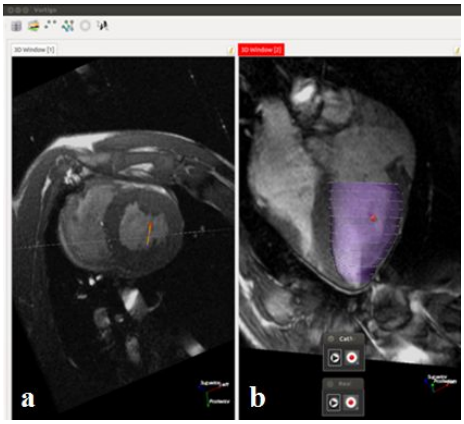

Figure 1. (a) An actively tracked catheter is shown against roadmap MR images of the heart and (b) a left ventricle shell.

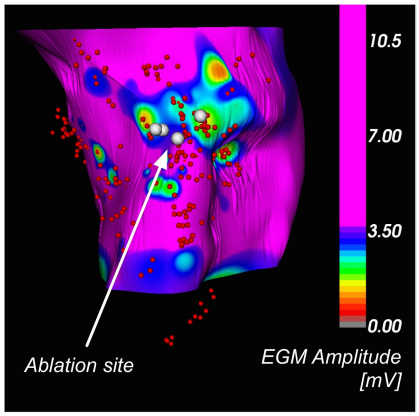

Figure 2.Electroanatomic voltage map with electrograms (EGMs) acquired at the red points under MR guidance after ablation.

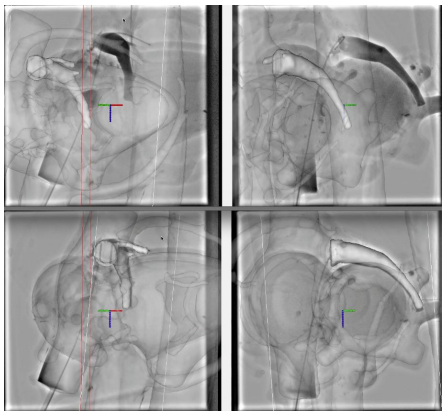

Figure 3. *Top*: Initial unregistered MR data (white) and two views of X-ray CS venogram (background). *Bottom*: Registered XMR data on two X-ray views.

Image based soft tissue strain measurement using embedded fiducial markers

Alexandra M. Blokker[a,b], Alan Getgood, MD[c,d], David W. Holdsworth, PhD[a,b,c], Timothy A. Burkhart, PhD[b,c,d]
Development of Novel Therapies for Bone and Joint Diseases Consortium
[a]Robarts Research Institute, [b]Department of Biomedical Engineering, [c]Department of Surgery and Medical Biophysics, [d]Fowler Kennedy Sports Medicine Clinic, all: Western University, London, ON, Canada

Introduction. Kinematic tracking is an essential tool for understanding the complex biomechanics of the human body. Knee joint biomechanics is a highly active area of research, given that upwards of 14% of anterior cruciate ligament reconstruction (ACLR) cases experience short term failure, and up to 60% of cases experience early onset osteoarthritis. These failure rates can partially be attributed to the lack of an accurate model of knee joint biomechanics, with little non-invasive information about the joint's soft tissue strains during physiological motions. Many kinematic tracking systems exist to track the knee's loading patterns and motions, achieving accuracy to within a few millimeters. However, these systems often require invasive tracking markers or instrumentation which can disrupt the native biomechanical environment, and fail to fully capture the important micro-strain in the joint's soft tissues. To date, there is no experimental method capable of non-invasively and accurately measuring the mechanical properties of the anterior cruciate ligament (ACL) in an *in vitro* environment. Computed tomography (CT) imaging is commonly used for non-invasively assessing musculoskeletal disorders due to its high resolution and excellent bone contrast. This makes it an ideal candidate for non-invasive kinematic tracking; however, a CT scan does not provide the necessary contrast to track the soft tissue in the joint directly. Therefore, the purpose of this work is to validate the use of micro-CT fiducial markers as method to non-invasively quantify soft tissue strains.

Methods. Ten 800 µm zirconium beads were rigidly fixed in a random pattern to the bed of a micro-CT scanner (GE eXplore speCZT). A bone calibrator was placed in the scanner FOV to demonstrate that the contrast between the two materials was sufficient to isolate the beads. These specific beads were selected based on CT compatibility and size. Bead material was selected through material analysis, with high contrast (material density dependent), hardness, and biocompatibility as the main considerations. Bead diameter was selected based on ease of implantation through arthroscopic tools without disturbing the native anatomy. Once secured to the bed, nine, five-minute anatomic scans (90 kVp, 40 mA) of the beads were performed without moving the beads between scans (Figure 1). The images were then all reconstructed with a 0.1 mm isotropic resolution. The coordinates of each bead in the scanner coordinate system were determined with a custom software which identifies areas of interest by thresholding using material radiodensity (in HU). The Euclidian displacements of each bead were determined with respect to one baseline bead to eliminate location error from scanner bed motion. The standard deviation of these distances was averaged to determine the error in measuring distances, providing purely systematic error for strain measurement with this system.

Results. Preliminary results suggest that 800 µm diameter zirconium dioxide beads can be used to track 3D displacements between beads to sub-voxel accuracy, within 82.6 (66.7) µm. Fiducial markers are easily visible in the image, with little material artefact. Markers are also clearly distinguishable from surrounding bone (Figure 1), and therefore surrounding soft tissue.

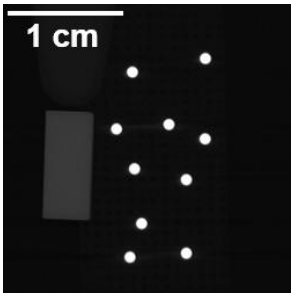

Figure 1. Maximum intensity projection (MIP) of ten 800 µm diameter zirconium dioxide fiducial markers, with bone calibrator for reference.

Conclusion. This tracking method is highly promising for applications in non-invasive soft tissue strain measurement. While the application in tracking the soft tissue of the knee joint was mentioned in this work, the tracking method is applicable to other bony joints with soft tissue as well. Future work will determine the optimal bead pattern placement to fully capture multi-axis soft tissue strain, as well as the bead's effects on soft tissue material strength. This method of kinematic tracking can be combined with an existing load controlled, knee joint motion simulator to investigate the properties of the ACL, reconstructed ACL, and surrounding bone as a function of graft fixation method. The outcomes of this research will facilitate interdisciplinary research aimed at improving the outcome of ACL injuries. This work has the potential to improve treatment of these injuries, reducing the costs associated with treatment and improving an individual's quality of life.

Validation of a Micro-CT Compatible Load-Controlled Knee Motion Simulator

Alexandra M. Blokker[a,b], Alan Getgood, MD[c,d], David W. Holdsworth, PhD[a,b,c], Timothy A. Burkhart, PhD[b,c,d]
Development of Novel Therapies for Bone and Joint Diseases Consortium
[a]Robarts Research Institute, [b]Department of Biomedical Engineering, [c]Department of Surgery and Medical Biophysics, [d]Fowler Kennedy Sports Medicine Clinic, all: Western University, London, ON, Canada

Introduction. More than 100,000 anterior cruciate ligament reconstructions (ACLR) are performed annually in the United States and despite significant advancements in ACLR methods, upwards of 14% fail. The primary causes of failure are non-anatomic graft placement, impingement, and failure of graft incorporation. To date, there is no experimental method capable of non-invasively measuring the mechanical properties of the ACL and graft under varying fixations and physiological loading protocols; this may be partially responsible for sub-optimal reconstruction methods. Therefore, the purpose of this research was to validate a novel, micro-CT compatible knee joint motion simulator that will be used to quantify the mechanical behaviour of the ACL and reconstruction grafts in response to physiologic loading.

Methods. A series of load patterns were used to assess the previously described knee joint motion simulator (Figure 1) system's accuracy and repeatability. A two-phase validation protocol was performed on two different structures: i) a structure with constant material properties (rubber tubing, 11.34 kg bending resistance); and ii) a cadaveric knee specimen. Both structures were loaded: i) independently along each axis (internal rotation, valgus rotation, anterior translation, axial compression); and ii) to a combined multi-axis state. Each loading pattern was repeated 5 times, at 0° and 30˚ of static knee flexion. Load-time curves from each loading protocol were assessed for overshoot, settling time, and steady state error (SSE), with an inter-trial coefficient of variation (CV) calculated across trials. The cadaveric specimen was used to validate the image-based kinematic tracking by acquiring a standard imaging protocol (16 s anatomical scan at 80 kVp, 50 mA) first at an unloaded state, then at a combined loaded state of 20˚ flexion, 100 N anterior translation, 10 Nm valgus rotation, 5 Nm internal rotation, and 100 N compression. All degrees of motion were frozen during the scanning protocol to prevent motion artefact, while the cadaver's stress relaxation was continuously tracked. Isosurfaces generated from the bone in the images (Figure 2) were used to identify 14 anatomical landmarks to create a joint coordinate system to determine relevant joint rotations and translations.

Results. The simulator accurately and repeatedly loaded the construct and cadaveric specimen to within a mean (SD) of 0.05 (0.02)% and 0.06 (0.02)% of the set point respectively. All images were qualitatively artefact free and captured the relevant structures within the joint capsule in 3D with isotropic resolution of 0.15 mm. The joint was determined to move a mean (SD) of 17.02 (2.43)° in internal rotation, -2.00 (1.29)° in valgus rotation, and 13.80 (0.96) mm in anterior translation.

Conclusions. The five degree-of-freedom knee motion simulator presented here loaded the cadaveric knee while high-resolution micro-CT images were acquired. Independent axis actuation facilitates a wide range of potential physiological loading patterns, while the 6 DOF load cell captures joint reaction loads along all axes. Placing high-contrast fiducial tracking beads into the tissues will allow for the accurate image-based quantification of mechanical properties of the ACL, reconstructed ACL, and surrounding bone as a function of graft fixation method. The outcomes of this research will facilitate interdisciplinary research aimed at improving the outcome of ACL injuries. This work has the potential to improve treatment of these injuries, reducing the costs associated with treatment and improving an individual's quality of life.

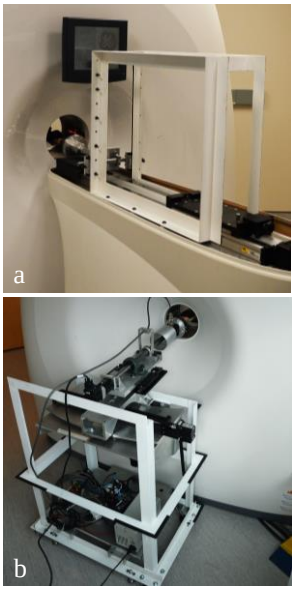

Figure 1. Knee motion simulator from the (a) table side, and (b) back side of micro-CT scanner.

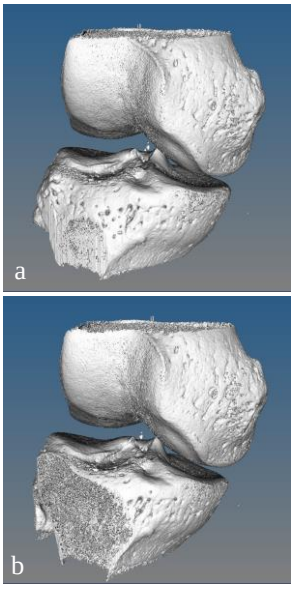

Figure 2. (a) Unloaded, and (b) combined load isosurfaces of a cadaveric knee joint mounted in the simulator.

Knee joint motion measurement during the timed up and go test using low-cost wearable sensors

Riley A Bloomfield[1,4,5], Megan C Fennema[2,4,5], Brent A Lanting[3], Kenneth A McIsaac[1], Matthew G Teeter[2-5]
Development of Novel Therapies for Bone and Joint Diseases Consortium
[1]Dept. Electrical & Computer Engineering, [2]Dept. Medical Biophysics, [3]Dept. Surgery,
[4]Robarts Research Institute, Western University; [5]Lawson Health Research Institute

Introduction: Despite extensive research concerning the satisfaction of patients after total knee replacement surgery, up to 20% of individuals are dissatisfied with their surgery. Observation of the knee during functional testing could identify underlying joint characteristics and provide quantitative analysis to complement qualitative post-surgery feedback. The timed-up-and-go (TUG) test has been identified as an effective, yet simple to execute functional test for prospective outcomes research and clinical assessment of patients.[1] Current instrumentation of the test is accomplished with a stopwatch. Recently, a single waist-mounted inertial measurement unit with the capacity to autonomously identify and time stages of the TUG test has been demonstrated.[2] By equipping a subject with multiple sensors on the lower limb, knee usage metrics such as range of motion, number of steps taken, and knee joint velocity can be found in addition to tracking the test time and performing stage segmentation autonomously.

Methods: A single Yost Labs YEI 3-Space inertial measurement sensor was attached to both the upper and lower leg of six healthy subjects. Rules of the TUG test were explained to each individual and five trials were registered per subject. The quaternion orientation of each sensor was streamed from the sensors and logged with a custom Matlab script. The TUG test was performed during a 30 second time range and all further analysis and classification was completed autonomously with an additional custom Matlab script following trial execution.

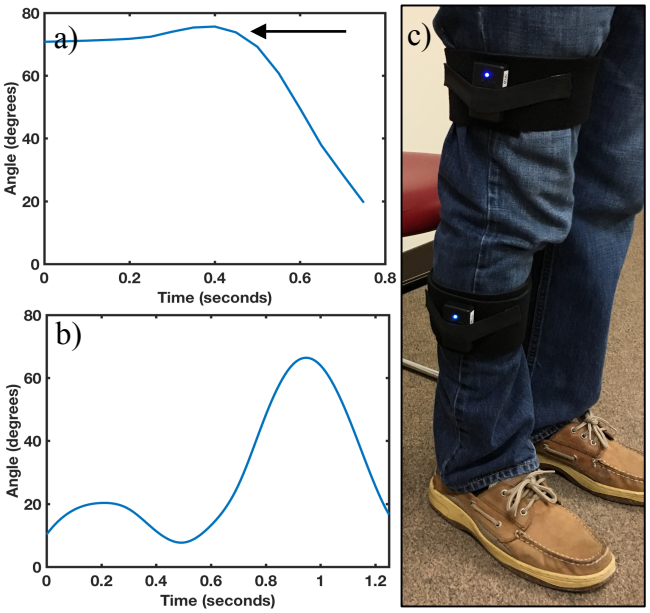

Fig. 1: (a) Flexion/Extension angle during an extracted sit to stand data segment including knee preload (arrow); (b) flexion/extension angle recorded during a step; and (c) the sensors attached to a subject during a trial.

Results: Time metrics of the TUG test were obtained by segmenting the test autonomously. Time taken during sit-to-stand activities was found to vary on average ±0.23 s per person and ±0.36 s between subjects. Time to rotate around the goal was found to be on average 1.2 s with ±0.3 s deviation between subjects. The average number of steps taken with the instrumented leg was found to be 5.8, varying ±0.4 steps between subjects. Maximum range of motion during walking stages was found to be 62.9° deviating on average ±4° per person and ±6° between subjects. On 5 of 6 subjects, an observable preloading effect was captured during initiation of the sit-to-stand stage with an average flexion angle increase of 2° ±1° between subjects with the observed effect.

Conclusions: Segmentation was successful in classifying all 6 stages of the TUG test on 28 trials, which suggests that the low-cost sensor configuration provides accurate data required to classify stages of the TUG test. Analysis of time taken during the sit-to-stand stage shows there was a 57% difference in deviation between test subjects over deviation between sequential trials from the same subject. This suggests measureable performance differences between subjects exist despite a healthy sample. Additionally, notable differences are present in range of motion between subjects indicating an individual difference in joint usage while walking. The presence (or lack of) the observed preloading feature could indicate a physiological characteristic or strategy for standing. Further work is required to assess these features across populations.

References: [1] Dobson et al. (2013), "OARSI recommended performance-based tests to assess physical function in people diagnosed with hip or knee osteoarthritis," Osteoarthritis and Cartilage, 21(8), pp. 1042-1052. [2] Vervoort et al. (2016), "Multivariate Analyses and Classification of Inertial Sensor Data to Identify Aging Effects on the Timed-Up-and-Go Test," PLoS ONE, 11(6), p. e0155984.

Analysis of Endogenous Tissue Sodium Concentration in Human Prostate Cancer as a Biomarker of Tumor Aggression

N.C. Broeke[1], J. Peterson[1], A. Farag[2], A. Ward[1], J. Chin[3], S. Pautler[3], G. Bauman[3], R. Bartha[1,4] and T.J. Scholl[1,4,5]
[1]*Medical Biophysics, Western University, London,* [2]*Ceresensa, London,* [3]*London Health Sciences Centre, London,* [4]*Robarts Research Institute, Western University, London,* [5]*Ontario Institute for Cancer Research, Toronto*

INTRODUCTION: Overtreatment of prostate cancer (PCa) is a persistent problem in men's healthcare [1,2]. It consumes limited healthcare resources and reduces the quality of life for patients [3,4] since most men will die with this disease rather than as a result of it. Reliable lesion detection and characterization is required to classify patients for immediate treatment or active surveillance. The goal of this study is to determine whether tissue sodium concentration (TSC) assessed by sodium MRI is related to tumour grade in patients with PCa.

METHODS: Imaging data were acquired from ten men with biopsy-proven PCa. This included *in vivo* multi-parametric MRI and sodium MRI obtained at 3 Tesla. Post surgery, fiducial markers were added to the prostates for *ex vivo* MRI and histology. *Ex* and *in vivo* images were manually co-registered prior to integration with histology data for analysis. Sodium images were acquired using a custom endorectal (ER) receive-only radio frequency (RF) coil and an asymmetric transmit-only birdcage RF coil. A normalization procedure developed by Axel *et al*. [5] was used to correct the receive sensitivity profile of the sodium ER coil. Absolute TSC was computed from the normalized sodium images using three vials containing known concentrations of saline solution, which were incorporated into the ER coil as reference standards. Prostate lesions were contoured by a pathologist on four histological sections and assigned a Gleason score. The corresponding average TSC was calculated for each lesion in the peripheral zone of the prostate and compared with TSC for healthy peripheral zone tissue.

RESULTS: Full data analysis has been completed for 3 of 10 subjects (see Figure 1). TSC measurements ranged from ~65 mM in healthy prostate to over 100 mM in Gleason 4 lesions. Percent changes in measured TSC were calculated as: $100 \times (TSC_{Lesion} - TSC_{Healthy}) / TSC_{Healthy}$. Percent changes have a positive correspondence with Gleason score for all subjects. A statistically significant difference in TSC measurements was observed between highly aggressive lesions (≥ Gleason 4+3) and moderately aggressive lesions (≤ Gleason 3+4).

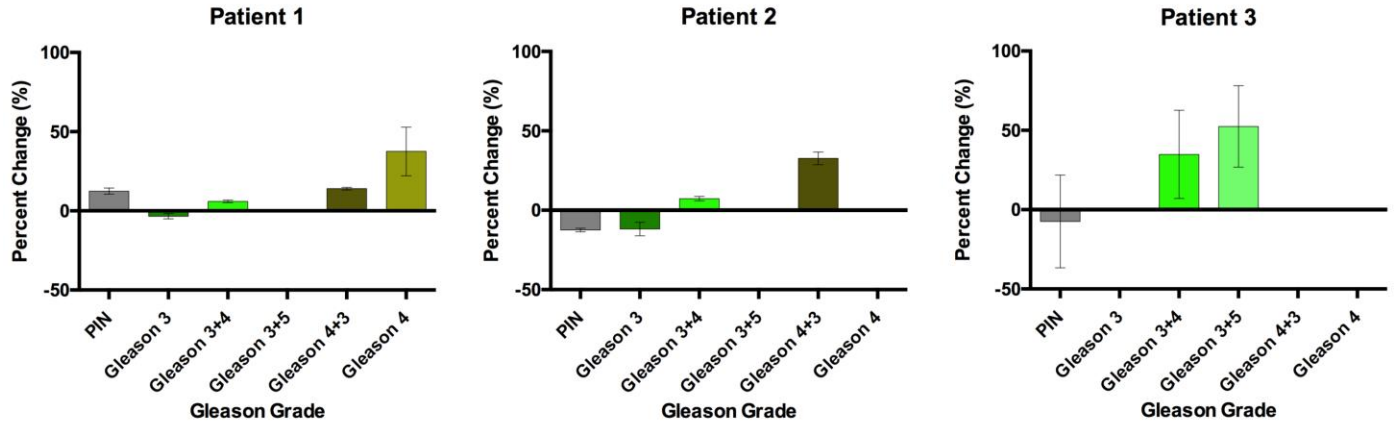

Figure 1: Comparison of TSC measured in peripheral zone (PZ) lesions to TSC in healthy PZ prostate tissue as a function of Gleason grade.

DISCUSION: These preliminary results suggest that TSC assessed by sodium MRI has utility for non-invasive characterization of prostate lesions. Improved detection and characterization of prostate lesions using new imaging methods such as sodium MRI could help increase the confidence of men with early-stage disease to choose active surveillance instead of radical treatment.

REFERENCES: [1] Rouse P. et al., Urologia Internationalis, 2011, 87(1), 49-53, [2] Djavan B. et al., Primary Care, 2010, 37(3), 441-459. [3] Dragomir A. et al., CMAJ Open, 2014, 2(2), E60-E68, [4] Eisemann N. et al., Qual Life Res, 2015, 24, 128-128. [5] Axel L. et al., Amer J Roentgenol, 1987, 148, 418-420.

Asthma Ventilation Abnormalities Measured using Fourier-Decomposition Free-breathing Pulmonary ^{1}H MRI

Dante PI Capaldi[1,2], Khadija Sheikh[1,2], Rachel L Eddy[1,2], Sarah Svenningsen[1,3], Miranda Kirby[4], David G McCormack[5], Grace Parraga[1,2] for the Canadian Respiratory Research Network

[1]Robarts Research Institute, [2]Department of Medical Biophysics, The University of Western Ontario, London, Canada; [3]Firestone Institute for Respiratory Research, St. Joseph's Healthcare, Hamilton, Canada; [4]Centre for Heart Lung Innovation, St. Paul's Hospital, Vancouver, Canada; [5]Division of Respirology, Department of Medicine, Western University, London, Canada

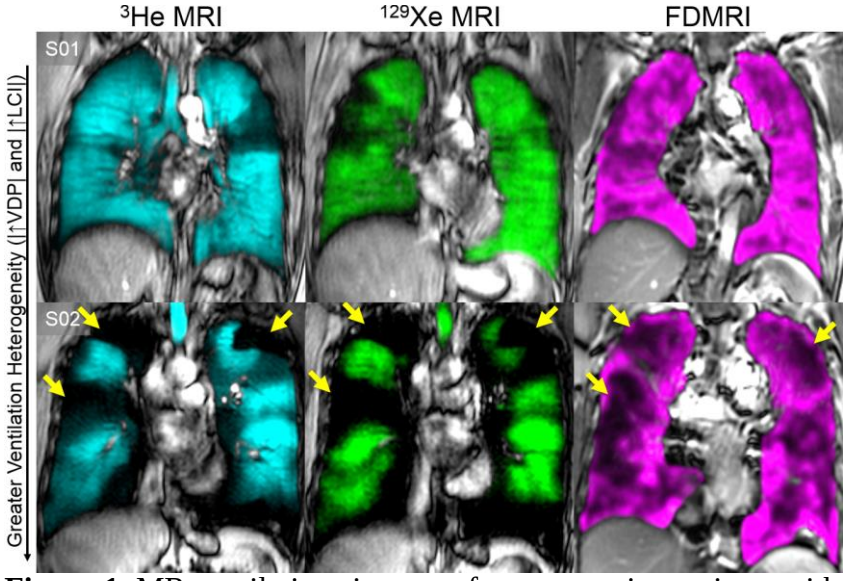

Figure 1. MR ventilations images of representative patients with asthma. Hyperpolarized ^{3}He MRI in blue co-registered to anatomical ^{1}H MRI in grey scale, hyperpolarized ^{129}Xe MRI in green co-registered to anatomical ^{1}H MRI in grey scale, and FDMRI in magenta co-registered to anatomical ^{1}H MRI in grey scale for two representative patients with asthma show there were a greater number and volume of MR ventilation abnormalities in patients with a greater LCI. Furthermore, ventilation abnormalities regionally corresponded between MR ventilation imaging methods.

Purpose: Recently, inhaled-gas MRI measurements of ventilation-heterogeneity were evaluated in severe-asthmatics and these were shown to explain asthma-severity and exacerbations/control.[1] These important and encouraging results are motivating the development of less complex ^{1}H MRI acquisition and analysis-methods for the measurement of pulmonary ventilation. In this regard, Fourier-decomposition of free-breathing ^{1}H MRI (FDMRI) has been proposed as a way to evaluate regional-ventilation by exploiting fast-pulmonary MRI acquisition and non-rigid-registration.[2] Here our objective was to measure ventilation-defects using FDMRI in asthma-patients for comparison with inhaled-noble-gas MRI. We hypothesized that ventilation-abnormalities would be qualitatively/quantitatively indistinguishable using both methods.

Methods: Twenty-participants with severe-asthma (49±11yrs) provided written-informed-consent to an ethics-board-approved and Health-Insurance-Portability-and-Accountability-Act-compliant protocol. Plethysmography/spirometry were performed (MedGraphics-Corporation).[3] Multiple-breath-nitrogen-washout (MBNW) was performed (ndd-Medical-Technologies) to measure the lung-clearance-index (LCI).[4] Hyperpolarized ^{3}He/^{129}Xe ventilation-images, ^{1}H anatomical-images, and free-breathing ^{1}H images were acquired as previously described[5,6] (3T-MR750 General-Electric-Health-Care). FDMR ventilation-image were generated as previously described.[5] Semi-automated-segmentation was used to generate ventilation-defect-percent (VDP) for both inhaled-gas and FDMR ventilation-images in order to identify ventilation-abnormalities[7] and their relationships with other clinical-measurements. Spearman-correlation-coefficients (ρ) were used to determine the relationship between MR ventilation-measurements and LCI. All statistics were performed using GraphPad-Prism V7.00 (GraphPad-Software-Inc).

Results: Figure 1 shows hyperpolarized ^{3}He, ^{129}Xe and FDMRI centre coronal-slice ventilation-maps for representative asthmatics. There was qualitative spatial agreement for ventilation-defects (ventilation-heterogeneity including size/number of defects) for the subject with abnormal LCI -an independent-measurement of ventilation-heterogeneity. FDMRI was correlated with ^{3}He (ρ=.61,p=.01) and ^{129}Xe VDP (ρ=.63,p=.04). Furthermore, LCI was significantly correlated with FDMRI (ρ=.54,p=.01), ^{3}He (ρ=.85,p<.01), but not ^{129}Xe VDP (ρ=.36,p=.4).

Conclusion: In this proof-of-concept demonstration, we generated FDMRI in 20 asthmatics to visualize and measure ventilation-abnormalities. FDMRI ventilation-defects abnormalities were spatially related to inhaled gas MRI ventilation defects and related to other clinical-measurements of ventilation-heterogeneity in severe-asthmatics. Importantly, there were spatial-differences and FDMRI ventilation-defects are smaller than inhaled-gas MRI ventilation-defects.

References:1.Svenningsen.-ERJ-(2016);2.Bauman.-MRM-(2009);3.Miller.-ERJ-(2005);4.Becklake.-Thorax-(1952);5.Capaldi.-*AcadRadiol*-(2015);6.Sheikh.-EJR*Open*-(2015);7.Kirby.-*AcadRadiol*-(2012).

A Method of Mechanically-Encoding Needle Shape for Image-Guided Interventions

Technical Development

Cepek, J.[1], Barker, K.[2], Ameri, G.[2,3], Fenster, A.[2,3]
[1]Schulich School of Medicine & Dentistry, Western University, London, Canada
[2]Robarts Research Institute, Western University, London, Canada
[3]Biomedical Engineering, Western University, London, Canada

Introduction

A variety of needle-based medical procedures are routinely performed for the diagnosis and treatment of disease. Many of these procedures are performed under direct image guidance, since medical imaging can be used to precisely locate target tissue. In an attempt to accurately deliver needles to targets identified using imaging, various methods of tracking the needle's trajectory are often used, including electromagnetic, optical, and mechanical tracking methods. Such methods allow the user to visualize the expected trajectory of the needle with respect to the target and, combined with a user interface, can guide the user to accurately align the needle's trajectory with its target. However, while this technique has been shown to increase the accuracy of needle placement, only the base of the needle is usually tracked, leading to uncertainty in needle placement and needle placement error if deflection occurs within the tissue. This work presents a method for estimating the shape of a deflected needle during insertion using mechanical sensors, providing a physician with a handheld needle whose deflection from its intended path is tracked in real-time. This method could be applied to needle-based biopsy or therapy procedures to improve diagnostic accuracy or treatment delivery quality, and has been developed with the goal of minimal disruption of clinical workflow in mind.

Methods

A method for estimating the shape of a needle deflecting within tissue has been developed. This method uses mechanical position sensors that measure the length of wires running along the length of the needle's internal diameter. Each measured length is proportional to the slope of the needle at its point of fixation, and is used as an input in a linear system to compute an estimated needle shape using Euler-Bernoulli beam theory and a parameterized model of tissue forces on the needle. A prototype 18 gauge needle of 145 cm length was constructed with a two degree-of-freedom sensor setup. The needle was deflected using a simple point load at its tip and the estimated position of its tip using the mechanical encoding method was compared to its true deflection measured using a digital caliper.

Results

The error in estimation of the needle tip deflection was less than 0.15 mm at a tip deflection of 15 mm. This demonstrates the potential of this technique to target some of the smallest clinically relevant tumours for biopsy or ablation. The estimated tip deflection was computed in near real-time, at approximately 10 samples per second.

Conclusions

A method of mechanically-encoding the shape of a deflecting needle was developed. A prototype 145 cm length, 18 gauge needle was constructed and demonstrated an error in estimated needle tip deflection of 0.15 mm at a deflection of 15 mm. This prototype and experiment helped direct a second iteration design of a handheld needle with a shape estimate that is transferred via a Bluetooth wireless interface to a PC for display of the needle shape and integration with image-guidance software.

Readout-Segmented and Reduced Field-of-View Diffusion-Weighted Sequences for Prostate MRI

Rachel W. Chan[1], Aaron Boyes[1], Ruby Endre[1], Vivekanandan Thayalasuthan[1], Mala Singh[1], Robert K. Nam[1], Masoom A. Haider[1,2]

1. Sunnybrook Health Sciences Centre, Toronto, Canada, 2. University of Toronto, Toronto, Canada

Introduction: Magnetic resonance imaging (MRI) holds promise in allowing for better detection, localization and characterization of prostate cancers. In multi-parametric MRI (mpMRI), anatomic T2-weighted imaging is combined with other MRI sequences, including diffusion-weighted imaging (DWI) sequences and/or dynamic contrast-enhanced (DCE)-MRI. DWI is an important component of prostate mpMRI. However, diagnostic quality in prostate DWI can be compromised by image distortion that is caused by susceptibility effects at the air-tissue interfaces near the colon. The focus of this work is to assess two DWI sequences that aim to reduce susceptibility-related image distortion.

Methods: Two DWI sequences, i) readout-segmented echo-planar imaging (EPI) [1] and ii) reduced-field-of-view (FOV) EPI [2], were investigated in phantom experiments. The phantom consisted of samples with different diffusion coefficients. As the diffusion coefficient is temperature-dependent, an ice-water bath was used to keep the samples at a constant temperature of 0°C throughout the experiment [3]. The accuracy of apparent diffusion coefficient (ADC) measurements, distortion levels and image quality were assessed. The chosen DWI protocol was applied in an ongoing clinical trial called the MRI Versus PSA in Prostate Cancer Screening or "MVP" study (PI: Dr. Robert Nam) at Sunnybrook Health Sciences Centre. The MVP study is a randomized controlled trial to determine if prostate cancer screening using mpMRI improves the detection rate of clinically significant prostate cancer compared with prostate cancer screening using prostate-specific antigen.

Results & Conclusions: Results from phantom experiments and selected images from the MVP study are presented. The figure below shows a set of images acquired with the chosen (6-min) readout-segmented EPI sequence. There was sufficient SNR to detect the presence of prostate cancer. The relatively short scan duration is expected to reduce the chances of subject motion during the scan. The MVP study is ongoing and full results from the study will become available in the future.

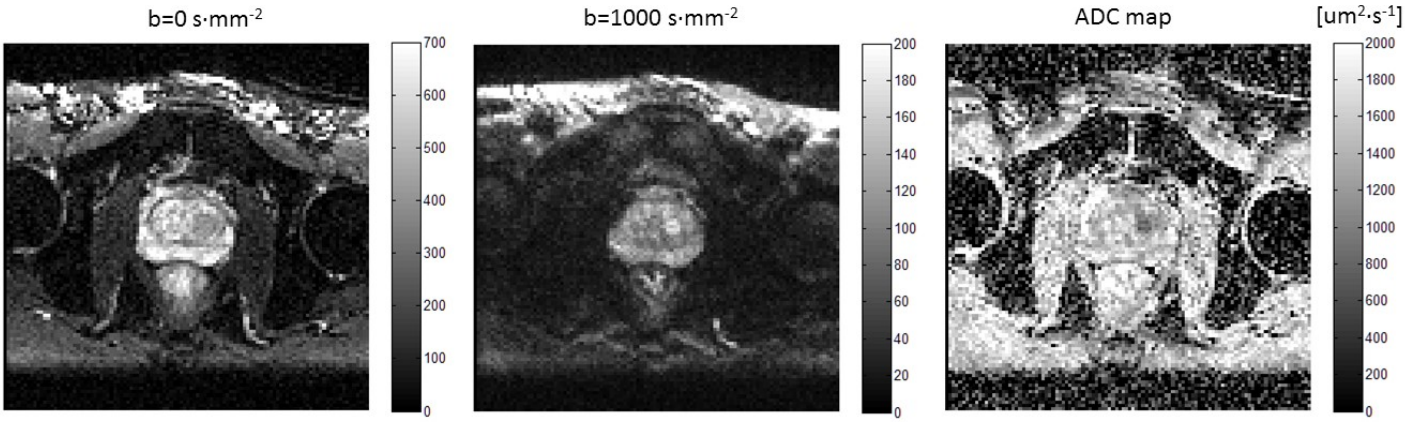

References:

[1] Holdsworth SJ et al. Readout-segmented EPI for rapid high resolution diffusion imaging at 3T. European Journal of Radiology. 2008 Jan 31;65(1):36-46. **[2]** Reischauer C et al. High-resolution diffusion tensor imaging of prostate cancer using a reduced FOV technique. European Journal of Radiology. 2011 Nov 30;80(2):e34-41. **[3]** Chenevert TL et al. Diffusion coefficient measurement using a temperature-controlled fluid for quality control in multicenter studies. Journal of Magnetic Resonance Imaging. 2011 Oct 1;34(4):983-7.

Acknowledgements: We would like to thank Bart Schraa from Siemens Healthcare for helpful advice on the sequences.

Time-Resolved Mapping of Arterial Pulse Wave Dynamics with High Frame Rate Ultrasound (HiFRUS)

Adrian J. Y. Chee, Billy Y. S. Yiu, and Alfred C. H. Yu
Schlegel-UW Research Institute for Aging, University of Waterloo, Waterloo, ON, Canada

Introduction. Mapping the pulse wave (PW) dynamics over an arterial segment can aid the detection of vascular diseases. For instance, an anomalous increase in PW propagation speed is recognized as a surrogate marker of arterial stiffening, which in turn is a predictor for future cardiovascular events and stroke. Also, a detected swift change in the local PW propagation speed can indicate the presence of arterial lesion, thereby facilitating early diagnosis of atherosclerosis. One emerging way of quantifying such changes is to use high frame rate ultrasound (HiFRUS) to capture and estimate the local PW speed over an arterial segment. However, this estimation task is not trivial because, when arterial structure changes locally, PW reflection is known to emerge and it would clutter the signals from the desired forward PW. In this work, we present a new framework for robust ultrasound-based PW tracking by applying eigen-processing to suppress the biasing impact of PW reflections.

Methods. Our framework involves: 1) HiFRUS data acquisition; 2) eigen-processing (for PW reflection suppression); 3) phase-based motion estimation (for PW velocity derivation). Pre-beamformed plane wave pulse echoes were first acquired using an L14-5W array on a SonixTouch scanner equipped with SonixDAQ (PRF: 10 kHz; freq: 5 MHz). After beamforming the raw echoes (using GPUs) [1], the slow-time ensemble at different lateral positions of the arterial wall were extracted, and they were stacked to form space-time data matrices. Then, singular value decomposition was applied to the space-time data matrix for each lateral position. Phase changes to the right singular vectors (spatial domain) were analyzed to identify the dominant forward wave and its corresponding left singular vector (temporal domain) is used to derive axial wall velocity through the Kasai method. To obtain the local PW velocity, pulse arrival time search and sliding-window regression were performed on the set of wall velocity estimates. Results were color-coded and were overlaid on top of the B-mode image. Also, to render PW propagation, positions of PW front were mapped and were trailed with its past positions.

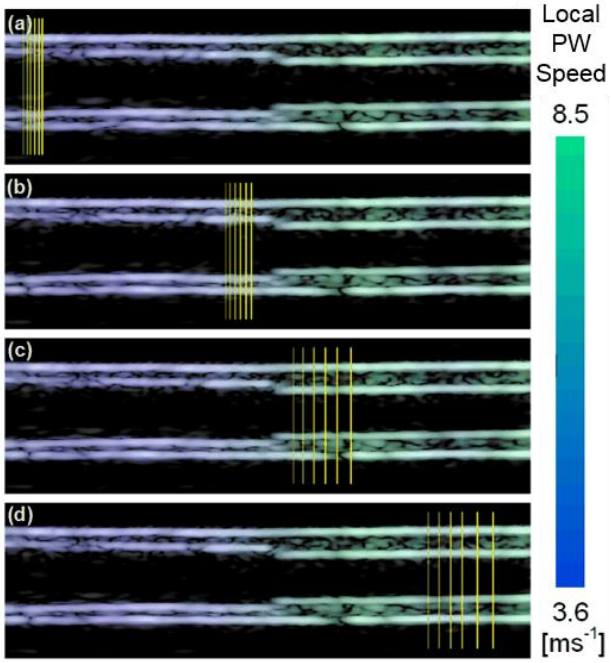

Fig. 1. Mapping of pulse wave speed
The estimated local PW speed was color-encoded onto the B-mode image with PW front mapped and trailed with its past positions. A faster PW speed is indicative of greater arterial stiffness, as observed at the thicker segment.

Results. Experiments were conducted on a PVA vessel phantom that was fabricated using a modified version of a walled phantom design protocol developed by our lab previously [2]. This phantom comprised two segments of different wall thicknesses (1.5 & 3mm) where PW reflection would emerge at the transition point. In the two segments, PW velocity was estimated to be 4.2 and 7.8 m/s respectively (see Fig. 1). The estimated PW velocity was close to theoretical values computed from Moens-Korteweg equation (<13%). Within each segment, the estimated PW velocity showed limited deviation (< 0.1 m/s), demonstrating our framework's robustness in the presence of PW reflections especially near the transition.

Conclusion. A robust framework for reliably mapping the arterial PW speed is devised using HiFRUS to capture arterial dynamics at fine spatial-temporal resolution. With this imaging innovation, new functional information on arterial physiology can be gained, such as dynamic mapping of vascular wall stiffness.

References.
[1] BYS Yiu, IKH Tsang, ACH Yu. *IEEE Trans Ultrason Ferroelec Freq Contr*, 2011; 58: 1698-1705.
[2] AJY Chee, CK Ho, BYS Yiu, ACH Yu. *IEEE Trans Ultrason Ferroelec Freq Contr*, 2016; 63: 1852-1864.

Return to Program

An immunofluorescence biomarker multiplexing approach to study breast cancer heterogeneity and tumour microenvironment

Alison Cheung[1], Dan Wang[1], Tyna Hope[1], Kela Liu[1], Yulia Yerofeyeva[1], Sharon Nofech-Mozes[2] & Martin Yaffe[1]

Ontario Institute for Cancer Research - Imaging Translation Program

[1]*Biomarker Imaging Research Lab (BIRL), Sunnybrook Research Institute, Toronto, ON*

[2]*Department of Anatomic Pathology, Sunnybrook Health Sciences Centre, Toronto, ON*

Introduction: There are multiple histopathological and molecular subtypes of breast cancer, each with different prognosis and clinical outcomes. Both inter-tumoural and intra-tumoural heterogeneity in breast cancer have been reported. Both tumour cells and those in their environment (tumour microenvironment, TME) play pivotal roles in promoting malignant progression and may affect the response to treatment. In an attempt to better understand these factors, we are using quantitative imaging of biomarker multiplexing to study molecules that are altered in these cell populations. **Methods:** We used the Immunofluorescence Multiplexer (MxIF) developed by General Electric Global Research Centre (GE GRC, Niskayuna, NY) which employs a sequential-stain-(image) bleach (SSB) approach (1-2). Single tissue sections of invasive breast cancer were labeled with a panel of antibodies of protein markers associated with breast cancer - Estrogen Receptor (ER), Progesterone Receptor (PgR) and Epidermal Growth Factor Receptor (HER2/neu), proliferative marker (Ki67), cell cycle regulators p53 and p21, and markers of tumour-infiltrating lymphocytes (CD3, CD4 and CD8). Each antibody on the panel was conjugated to fluorochome Cy3 or Cy5. Staining condition for each conjugated antibody was tested using appropriate tissue sections as controls. The signal intensity and staining patterns were compared to standard immunohistochemistry to optimize IF staining condition. Following individual optimization, each pair of conjugated antibodies (a Cy3- and a Cy5-labeled pair) was sequentially applied to single tissue sections of invasive breast cancer together. Regions of interests were selected for image acquisition and analysis. **Results:** Using the software tools provided by GE GRC and analysis tools developed at BIRL, the expression of each protein marker, or lack thereof, on individual cancer cell or lymphocyte was quantified and its spatial location recorded (Fig. 1). The percentages of cells expressing each biomarker or in combinations were quantified. The frequencies at which cellular subsets expressing different biomarker signatures are localized in close proximity to each other were quantified. These measurements will provide estimates of the levels of heterogeneities within the tumour lesion and the microenvironment. **Conclusions:** Our work demonstrates an example of the use of biomarker multiplexing in studying cancer heterogeneity and cancer-stroma relationship. Validation of this technique with clinical diagnostic markers is currently in progress. Future study with a large patient cohort using tissue microarrays will provide a more in depth investigation of cellular heterogeneity in different subtypes of breast cancers.

References:

1. Clarke G et al., *Histopathology* 64(2):242-55, 2015
2. Gerdes M et al., *PNAS* 110(29): 11982-7, 2013.

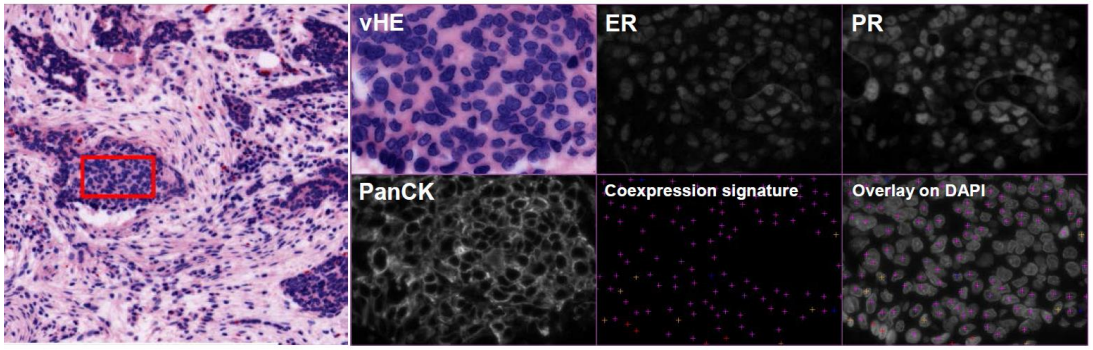

Figure 1. Single-cell biomarker expression analysis. A breast cancer tissue section was stained with antibodies against ER and PR, together with segmentation markers (PanCK and DAPI). Region of interest (ROI) was selected on H&E (red box). Staining of individual biomarker in ROI is displayed in grayscale using the MxIF analysis software. Biomarker co-expression on each cancer cell (PanCK-positive) was marked (RED – ER-positive, BLUE – PR-positive, MAGENTA – ER and PR-positive, ORANGE – ER and PR-negative).

Motion Corruption Detection in Breast DCE-MRI

Sylvester Chiang, Sharmila Balasingham, Lara Richmond, Belinda Curpen, Mia Skarpathiotakis, Anne Martel

Department of Medical Biophysics, University of Toronto, Sunnybrook Health Sciences Centre, Imaging Research, Toronto, ON, Canada

Abstract. Motion corruption can result in difficulty identifying lesions, and incorrect diagnoses by radiologists in cases of breast cancer screening using DCE-MRI. Although registration techniques can be used to correct for motion artifacts, their use has a computational cost and, in some cases can lead to a reduction in diagnostic quality rather than the desired improvement. In a clinical system it would be beneficial to identify automatically which studies have severe motion corruption and poor diagnostic quality and which studies have acceptable diagnostic quality. This information could then be used to restrict registration to only those cases where motion correction is needed, or it could be used to identify cases where motion correction fails. We have developed an automated method of estimating the degree of mis-registration present in a DCE-MRI study. We build and compare two predictive models, the first is based on a feature extraction method in which we calculate intensity and texture features and utilize traditional supervised learning methods to train a predictive model. A second one approach using a deep learning involves training a convolutional neural network (CNN). These models are trained using estimates of deformation generated from unlabeled clinical data which we generate by registering pre and post-contrast images using Elastix and finding the average pixel shift by calculating the sum of the deformation field. We validate the predictions on a labeled dataset from radiologists denoting cases suffering from motion artifacts that affected their ability to interpret the image. By calculating a binary threshold on our predictions, we have managed to identify motion corrupted cases on our clinical dataset with an accuracy of 86% based on the area under the ROC curve (Fig. 1). In our experiments we present a novel use of phase correlation as a pre-processing step to produce input data that is more robust to the presence of contrast enhancement. As well we explore a method of deformation estimation that is independent of physician subjectivity and did not require any manual creation of landmarks. This approach is a preliminary attempt at defining a clinically relevant level of motion corruption.

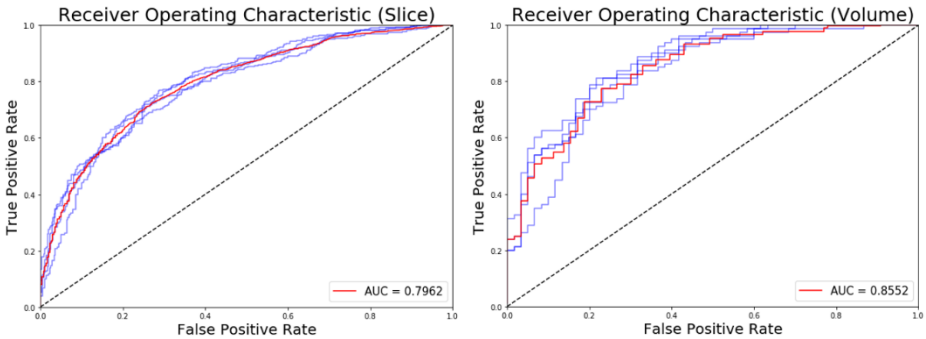

Figure 1The ROC curve calculated from the regression values predicted by the CNN. The left image shows the curve per slice while the right curve plots the metric aggregate over a volume

Quantitative MR characterization of calcified and lipid-laden blood clot in vitro at 3T

Spencer D. Christiansen, Junmin Liu, Michael B. Boffa, Luciano Sposato and Maria Drangova
Robarts Research Institute, The University of Western Ontario, London, Ontario, Canada
Consortium: Imaging for Cardiovascular Device Intervention, Supervisor: Dr. Maria Drangova

Introduction: Thrombotic occlusion is the underlying cause behind a number of common and devastating pathologies including heart attack and stroke. Knowledge of thrombus composition may provide highly useful clinical information towards the treatment of such conditions, including predicting the efficacy of thrombolytic agents[1] and mechanical thrombectomy procedures,[2] and possibly determination of etiology.[3] Current MR methods for inferring thrombus composition rely on a qualitative "susceptibility vessel sign" obtained from late-echo gradient echo (GRE), a metric sensitive only to red blood cell (RBC) concentration and capable only of global assessments of composition, rendering invisible other informative components that may be present such as calcium[4] and fat.[5] This work evaluates the ability of a tailored multi-echo GRE acquisition paired with recently developed novel post-processing algorithms to characterize relevant thrombus components in a cohort of *in vitro* blood clots of varying composition and throughout clot ageing over a biologically relevant timescale.

Methods: ***Imaging-*** Scans were performed at 3T with a 32-channel transmit/receive head-coil using a custom dual echo-train 3D GRE sequence ($TE_1/\Delta TE/TE_5$ = 3.20/1.46/9.04 ms, $TE_6/\Delta TE'/TE_{10}$ = 16.75/7.15/45.35 ms, TR: 47.6 ms, resolution: 0.94x0.94x1 mm^3, matrix: 192x192x42, BW: 142.86 kHz, flip angle: 10°). Total scan time for the acquisition was 6 minutes 28 seconds; no acceleration was performed.

Image post-processing- Individual channel phase data were saved and the inter-echo variance channel-combination algorithm[6] was used to create local frequency shift (LFS) maps for QS mapping,[7] and the non-iterative B0-NICE algorithm[8] was used to calculate fat fraction (FF), B0 field and R2* maps.

Phantom- Arterial porcine blood was used to create duplicate 1.5mL blood samples of 0, 20, 40 and 60% hematocrit. Samples were clotted inside 1cm diameter polystyrene tubes by the addition of calcium chloride and thromboplastin. To emulate clinically observed emboli with calcified or lipidic components,[9] 2.5mm length pieces of either calcium carbonate or lard were added to clots of each hematocrit. Platelet-poor plasma filled the remainder of each tube. Tubes were kept inside an agar phantom and at 37°C throughout the experiment except while scanning. The phantom was scanned at 2, 6 and 17 hours and daily thereafter up to 9 days post-clotting.

Results: Figure 1 shows **A.** magnitude images (representing clinical standard; TE = 31 ms), **B.** QS and **C.** FF maps of the 40% hematocrit clots throughout the experiment. Lard and calcium were easily detected in, and significantly different from, clot on FF and QS images, respectively, while widely undetectable in late-echo magnitude images, and indistinguishable otherwise. Clot R2* values are shown over time in Figure 2. Between days 2 to 6, R2* values of the 0, 20 and ≥40% hematocrit clots were each significantly different (denoted by *).

Figure 1:

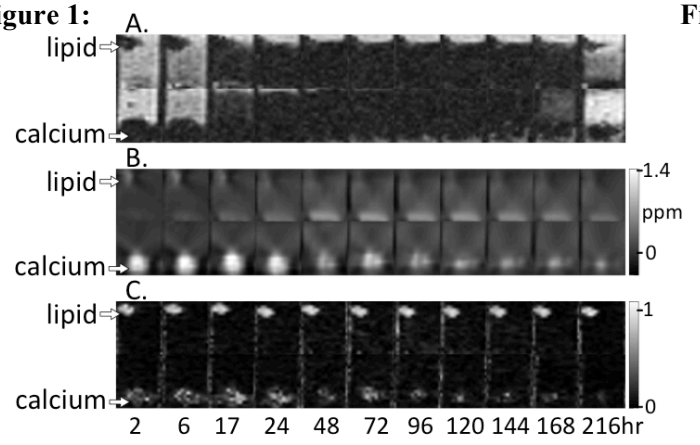

Figure 2:

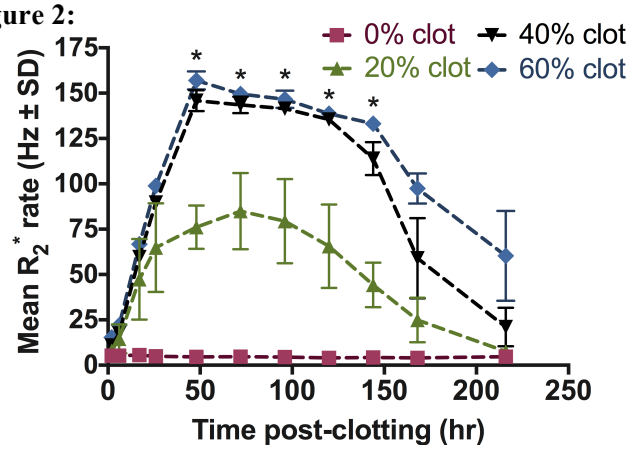

Conclusions: With the proposed protocol, clinically relevant sized pieces of lard and calcium carbonate were readily differentiated inside blood clot of up to 60% hematocrit aged up to 9 days. Blood clots of negligible (0%), low (20%) and medium to high (40-60%) hematocrit can be differentiated on the basis of R2* values, but only once the RBCs have become sufficiently aged/deoxygenated. This method shows promise for clinical discrimination of calcified and lipidic components within *in vivo* thrombi, and inferring an approximate clot hematocrit in thrombi that are not extremely fresh; neither task was possible using current clinical methods.

References: [1] Niessen, F., et al. Stroke, 2003. [2] Yuki, I., et al. Am J Neuroradiol, 2012. [3] Boeckh-Behrens, T., et al. Clin Neuroradiol, 2014. [4] Almekhlafi, M.A., et al. Ann Neurol, 2008. [5] Ezzeddine, M.A., et al. Neurology, 2000. [6] Liu, J., et al. Magnet Reson Med, 2015. [7] Bilgic, B., et al. J Magn Reson Im, 2014. [8] Liu, J. and M. Drangova. Magnet Reson Med, 2015. [9] Walker, B.S., et al. Am J Neuroradiol, 2014.

Scoliosis visualization using transverse process landmarks

Ben Church[1], Andras Lasso[1], Christopher Schlenger[2],
Daniel P. Borschneck[3], Parvin Mousavi[4], Gabor Fichtinger[1,3], Tamas Ungi[1,3]

1. Laboratory for Percutaneous Surgery, School of Computing, Queen's University, Kingston, ON, Canada
2. Premier Chiropractic, Stockton, CA, USA
3. Department of Surgery, Queen's University, Kingston, ON, Canada
4. Medical Informatics Laboratory, School of Computing, Queen's University, Kingston, ON, Canada

Introduction Scoliosis is a lateral curvature of the spine, typically diagnosed in adolescence and monitored by periodic X-ray imaging until skeletal maturity. Ultrasound has been investigated as a radiation-free imaging modality for spinal curvature measurement [1, 2]. The spinal curvature is computed from sparse skeletal landmarks, such as transverse processes (TrP), localised in ultrasound. This information, however, does not allow for intuitive visualization of the spine which practitioners or patients might easily comprehend.

Methods We propose a method for producing spinal visualizations by deforming an average model to the patient's anatomy based on TrP landmarks as they are localized in tracked ultrasound. Each landmark was supplemented with an anchor point, at an offset determined from local landmark geometry. A vector, pointing to the landmark being supplemented from its neighbor below, was averaged with a vector pointing to the landmark above. This vector was cross-produced with the vector from the landmark to its symmetric neighbor. Anchor points placed in the direction of this cross product ensured that the subsequent landmark registration encode vertebral orientation transformations in an anatomically realistic way. The offset size was determined from anatomic scale. Thin-plate spline registration yielded deformation fields, which, applied over the continuity of the average spine, warped it to the patient's anatomy. To validate our method, we marked the TrP on five (n=5) CT scoliosis patient scans. We computed the deformation field according to our method, applied it to the average spine model, and compared it to the surfaces obtained from CT.

Results Figure 1 shows the visualization resulting from a typical registration: The patient's CT with TrP landmarks, registered model, and the registered model with color code indicating the surface distances. Larger registration errors occur at the dorsal processes of the highest and lowest vertebrae, due to lack of constraints. Moderate registration errors occur at protruding structures in the AP plane, where landmarks provide less constraint for registration. In all cases, larger and moderate errors are constrained to the AP plane, irrelevant to scoliosis assessment. The average of all patients' average and maximum Hausdorff distances were 2.7mm and 20.7mm, respectively. The average is favorably low. The maxima occur only in the dorsal process of the highest and lowest vertebrae, not affecting scoliosis assessment.

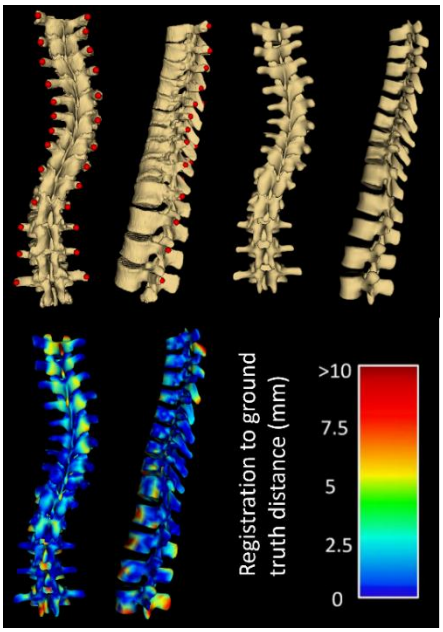

Figure 1 - Top row: Patient #5 ground truth (left), resulting visualization (right). Bottom: Visualization with color code showing error

Conclusions Larger registration error occurs mainly at the highest and lowest vertebrae, due to a lack of constraints. Fortunately, the error is constrained to the dorsal processes and vertebral bodies, which are irrelevant to the assessment of scoliosis; our method produces visualization that is both perceptually and quantitatively accurate for assessing scoliosis.

References [1] Ungi et al. Ultrasound in Medicine and Biology 2014; 40(2):447-54. [2] Chueng et al. Journal of Orthopaedic Translation 2015; 3:123-33.

Optimization of Slow-Proton-Exchange (SPE) Magnetic Resonance pH Sensor and Application for Monitoring Enzyme Activity

Ontario Institute for Cancer Research Smarter Imaging Program: An Ontario Imaging Consortium
Ryan Correa[a,b], Loise Perruchoud [a b], and Xiao-An Zhang[a,b,c *]
[a]Department of Chemistry, University of Toronto. [b]Department of Physical and Environmental Sciences,
[c]Department of Biological Sciences, University of Toronto Scarborough.

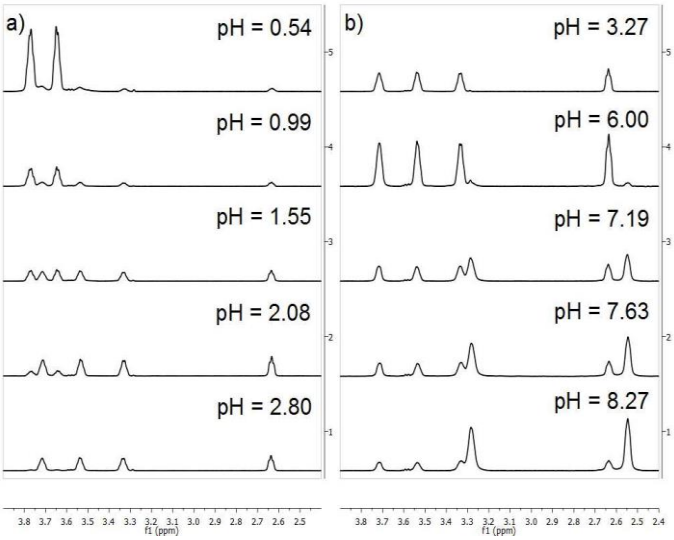

Figure 1: Selected ^{1}H NMR spectra for the titration of **SPE2**. a) at pH values near pK_{a1} (1.35). b) at pH values near pK_{a2} (7.45).

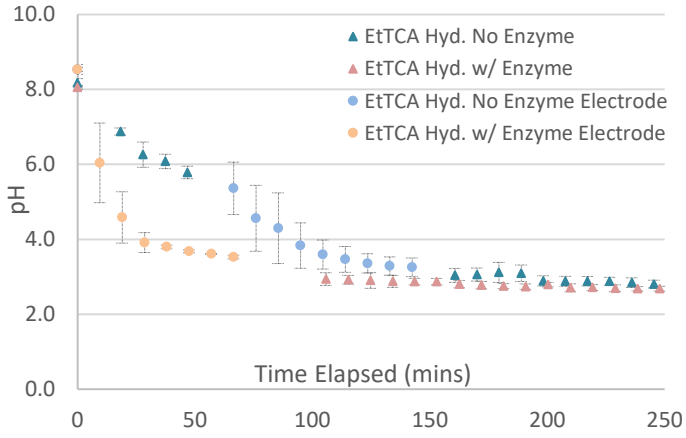

Figure 2: Monitoring the hydrolysis of ethyl trichloroacetate (+/- esterase) by pH change, using **SPE2**. A pH electrode was used to complement data in the pH windows not covered by **SPE2**.

Introduction: Noninvasively monitoring pH change with deep penetration and high accuracy holds great promise for precise detection of various diseases, including cancer. Magnetic resonance based techniques, such as NMR and MRI, are preferred choices. However, classic MR-based methods for pH measurement are compromised by low sensitivity and accuracy, partially due to rapid proton transfer beyond NMR time scale. We developed a novel Slow Proton Exchange (SPE) strategy for measuring pH using a ratiometric NMR pH sensor, **SPE1**.[1] With this method, unprecedented accuracy of NMR pH measurement (ΔpH = 0.02) was achieved. **SPE1** is biocompatible and can be used for real-time monitoring of pH dynamic of live cells, but its pK_a (~7.72) is sub-optimal above common physiological pH. In this study, a second-generation pH sensor, **SPE2**, is developed and applied for monitoring enzymatic reactions in real-time.

Methods: Through rational structural modification, **SPE2** was designed with a lower pK_a than **SPE1**, thus better suited for biological applications. Unlike **SPE1**, which exhibits an apparent single pK_a due to positively cooperative protonation, **SPE2** is expected to have separate two step protonation and consequently a broader operating pH window. **SPE2** was chemically synthesized and structurally characterized. The protonation behaviour and pK_a values were determined by NMR titration. **SPE2** was incubated with an esterase to monitor the enzymatic ester hydrolysis by NMR.

Results: **SPE2** was prepared through two steps of chemical reactions, with total yield of 45%, and was structurally characterized by NMR, IR and mass spectroscopies. Similar to **SPE1**, it exhibits proton exchange rate slower than NMR timescale. The NMR pH titration revealed two well-separated protonation steps, with apparent pK_a values of 7.45 and 1.35 respectively (Figure 1). Therefore, **SPE2** can measure pH over a much wider range, in contrast to **SPE1**, including biologically relevant pH windows. For example, the enzyme-catalyzed ester hydrolysis could be monitored by **SPE2** in real time (see Figure 2). The obtained kinetics data of different substrates fit well with the expectation and can be verified with other methods.

Conclusions: **SPE2** is a second generation slow-proton-exchange NMR sensor, with high accuracy and optimized pK_a and wider operating pH windows. We have demonstrated the effectiveness and potential for future biomedical applications.

1. Perruchoud, L. H., *Chem. Sci.*, **2015**, *6*, 6305.

Lanthanide nanoparticles as vascular contrast agents in pre-clinical computed tomography

Charmainne Cruje,[1,2] David W. Holdsworth,[1,2] Elizabeth R. Gillies,[3,4] and Maria Drangova[1,2]
[1]Robarts Research Institute, [2]Department of Medical Biophysics, [3]Department of Chemistry, [4]Department of Chemical and Biochemical Engineering, The University of Western Ontario, London, Ontario, Canada
Supervisors: *M. Drangova and E. Gillies*

Introduction. Recent advances in nanotechnology have led to the development of blood pool contrast agents in pre-clinical computed tomography (CT). The advantage of using nanoparticles is the ability to achieve prolonged residence times that are suitable for pre-clinical CT, which can take tens of minutes; this is attained by polymer-coated nanoparticles exceeding 10 nm in size. Although long-circulating nanoparticle-based agents exist for pre-clinical CT, they are predominantly based on iodine, which has a low atomic number. Superior CT contrast can be achieved using elements with higher atomic numbers, such as lanthanides, particularly at higher energies. While lanthanide-based contrast agents are used clinically in MRI, they are composed of small molecules (< 1 nm) that exit the bloodstream of small animals within seconds. Thus, the purpose of this work was to develop polymer-encapsulated lanthanide nanoparticles exceeding 10 nm in size as a vascular contrast agent in pre-clinical CT.

Methods. Lanthanide nanoparticles were synthesized by following a method reported by Zhao et al.[1] The Pluronic® F-68 polymer (Sigma-Aldrich, Oakville ON) was used to encapsulate the synthesized nanoparticles. Dynamic light scattering (DLS) with a Zetasizer Nano ZS instrument (Malvern Instruments Ltd, Malvern Worcs), transmission electron microscopy (TEM) with the Philips CM10 (Philips, Amsterdam), and micro-CT with the eXplore speCZT (GE Healthcare, London ON) acquired at 90 kVp, 40 mA (900 views, 16 ms per view) were used to characterize the nanoparticles *in vitro*. The reconstructed micro-CT images were rebinned at 2×2 for a voxel size of 100×100×100 µm and analyzed in MicroView (GE Healthcare, London ON). Linear regression was used to determine the relationship between Hounsfield Units (HU) and mg/mL of lanthanide by scanning solutions of known lanthanide content. The nanoparticles were added to a mouse serum mimic (Mouse Primary Antibody Isotype Control, Invitrogen Corporation, Camarillo CA) to monitor stability by DLS.

Results and Discussion. TEM images of the nanoparticles are shown in Figure 1a and b. As shown in Figure 1c, the average size of the unmodified nanoparticles was 28.4 ± 0.4 nm with a low size dispersity of 0.08, while for encapsulated nanoparticles, it was an average of 120.0 ± 3.2 nm with a moderate size dispersity of 0.18. The CT contrast of the agent in the reconstructed image (Figure 2a) was 2282 HU, which corresponds to 33 mg/mL of lanthanide as per the HU calibration curve (Figure 2b). DLS measurements showed no change in nanoparticle size when added to a mouse serum mimic for up to 30 minutes, suggesting contrast agent stability in the blood pool for this duration. The *in vitro* results show that the synthesized contrast agent has potential to improve contrast in pre-clinical CT. There is ongoing development to increase loading using other polymers.

References. [1] Zhao, G., et al. Langmuir 2014; 30(23): 6980-6989.

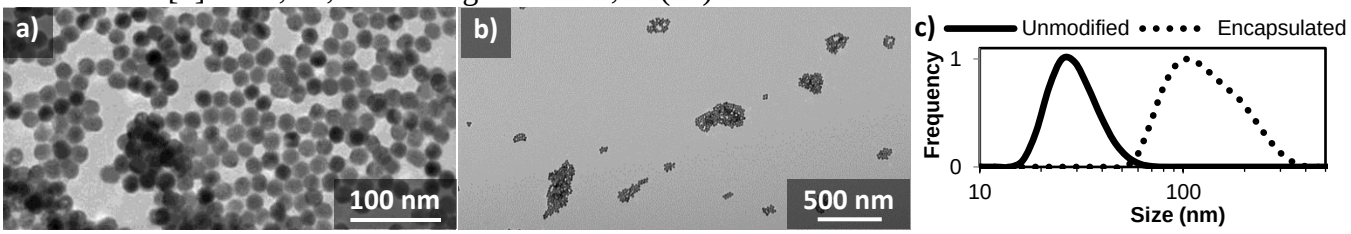

Figure 1. TEM of lanthanide nanoparticles when unmodified (A), and polymer-encapsulated (B), and their size distributions (C).

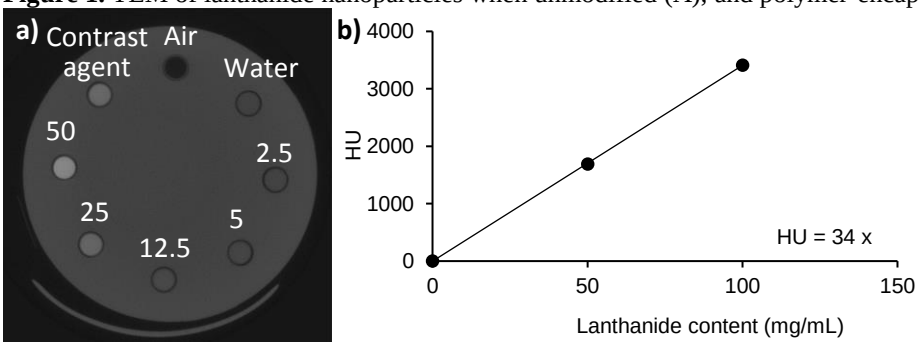

Figure 2. Micro-CT of the contrast agent and solutions of known lanthanide content, in mg/mL (A) and the HU calibration curve (B).

Evaluation of an iterative reconstruction algorithm for optical CT dosimetry of small radiation fields

Kurtis H. Dekker[1]*, Kevin J. Jordan[1,2], Jerry J. Battista[1,2]
[1]Department of Medical Biophysics, Western University, London, Ontario, Canada
[2]London Regional Cancer Program, London Health Sciences Centre, London, Ontario, Canada

Introduction: Iterative CT reconstruction algorithms are gaining popularity in x-ray CT, and have been proposed for optical CT-based gel dosimetry [1],[2] due to the noise reduction achievable compared to filtered backprojection (FBP). One promising algorithm makes use of ordered subsets method with total variation minimization based regularization (OSC-TV) [2]. In this study, we evaluate OSC-TV for optical CT gel dosimetry. We examine the effect of varying the empirical regularization constant "*c*" built into the algorithm, in order to achieve accurate dosimetry of small radiation fields.

Methods: A 15cm diameter radiochromic gel dosimeter was irradiated from the top with jaw-defined 3x3, 2x2, 1x1 and 0.6x0.6 cm square fields (Figure 1) on a Varian 21X linear accelerator (6 MV). Optical CT scans were acquired using an in-house scanning laser system. Reconstructions were performed with in-house GPU-accelerated code using either filtered backprojection (ramp or hamming filter) or OSC-TV with values of *c* between 0.05 and 2.0. Reconstruction voxel size was 0.33 mm, isotropic. The mean and standard deviation at the center of each field (at an axial plane corresponding to max dose) was measured, as well as the mean and standard deviation in the background region, to calculate the contrast-to-noise ratio (CNR). Additionally, field profiles were examined to ensure that spatial information was preserved in the dose gradients. This was quantified using the distance between the 80% and 20% points of the beam penumbra (80-20 distance).

Results: The 80-20 distances varied by sub-voxel amounts for all reconstructions, indicating that OSC-TV preserved gradient sharpness. OSC-TV also substantially reduced reconstruction noise, resulting in up to 5x improvement in CNR compared to filtered backprojection (Figure 2). For fields larger than 1x1 cm, a wide range of regularization constants are acceptable. However, for the small 0.6x0.6 cm field, setting this value too high results in a drop in the mean attenuation value at field center (figure not shown). For *c = 0.25*, the effect was less than 0.5%, while CNR remained 3x higher than that seen in the FBP reconstructions. Most 3D dosimetry problems will not have isolated fields smaller than 1x1 cm, so this effect should be a minor concern except when performing tasks such as small field commissioning for radiosurgery or grid therapy. Our recommendation for quality assurance is to reconstruct dosimetry datasets with both OSC-TV and FBP, and ensure that the mean value within the smallest structure is preserved.

Conclusions: OSC-TV can greatly improve image quality in optical CT dosimetry. Reducing noise in measurements will improve dosimetric evaluation of treatment plans using methods such as Gamma analysis [3], whose validity is negatively affected by noise [4].

References:

[1] Du et al. *Med. Biol.*, vol. 61, no. 24, p. 8425, Nov. 2016.
[2] Matenine et al, *Med. Phys.*, vol. 42, no. 11, pp. 6376–6386, Nov. 2015.
[3] Low et al, *Med. Phys.*, vol. 25, no. 5, pp. 656–661, May 1998.
[4] Low and Dempsey, *Med. Phys.*, vol. 30, no. 9, p. 2455, 2003.

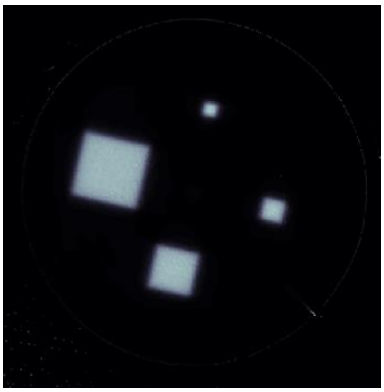

Figure 1. Reconstruction slice (FBP, hamming filter)

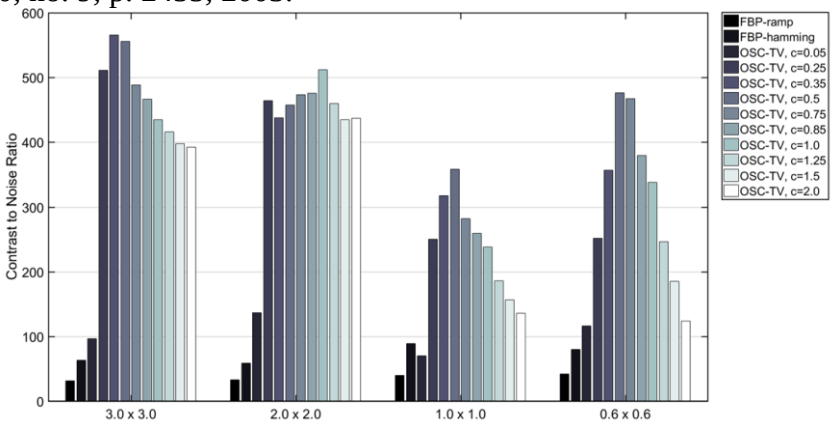

Figure 2. Contrast to noise ratios for small-field reconstructions for each field size and regularization constant (*c*) value.

Fractal analysis of the brain rs-BOLD signal and DTI analysis in cancer patients experiencing chemotherapy-related cognitive impairment.

Olga Dona[1,2], Mitchell Doughty[1,2], Geoffrey B. Hall[2,5], Raimond Wong[6], and Michael D. Noseworthy[1,2,3,4*]

[1] McMaster School of Biomedical Engineering, McMaster University, Hamilton, ON, Canada.
[2] Imaging Research Centre, St. Josephs Healthcare, Hamilton, ON, Canada.
[3] Department of Electrical and Computer Engineering, McMaster University, Hamilton, ON, Canada.
[4] Department of Radiology, McMaster University, Hamilton, ON, Canada.
[5] Department of Psychology, Neuroscience & Behaviour, McMaster University, Hamilton, ON, Canada.
[6] Department of Medicine, Division of Oncology, McMaster University, Hamilton, ON, Canada.
* Corresponding Author: Dr. Michael D. Noseworthy, Ph.D., P.Eng.
Email:nosewor@mcmaster.ca

Introduction: Chemotherapy-related cognitive impairment, also known as chemo-brain or chemo-fog, is a long lasting and disturbing side effect of chemotherapy. The rapidly increasing number of patients, who have survived cancer, yet now live with the side effects of treatment, has lead to an increase of chemo-brain related studies. However, there is yet to be a definitive answer describing the etiology of chemo-brain, the affected brain regions and how to manage the symptoms. The purpose of this study was to assess the viability of using a complexity analysis of the rs-BOLD signal in combination with DTI to detect brain abnormalities in chemo-brain patients.
Methods: Five patients were scanned using a GE Discovery MR750 3T MRI and 32-channel RF-coil. Axial FSPGR-3D images were used to prescribe rs-BOLD (TE/TR=35/2000ms) and DTI (60 directions, TR/TE = 8800/87ms). Complexity analysis, performed on grey matter, was done by estimating the voxel-wise Hurst exponent using de-trended fluctuation analysis and signal summation conversion methods. Voxel-wise analysis of the DTI data was performed obtaining FA, MD, AD and RD. All the results were normalized with a database of 180 healthy controls using a Z-score analysis.
Results: Although no significant differences were found on the fractal dimension of the rs-BOLD signal when compared to controls, we were able to detect significant ($p<0.05$) changes in FA specifically in the corpus callosum, inferior fronto-occipital fasciculus and right inferior longitudinal fasciculus. These regions also correlated with neuropsychological scores of visuospacial constructional ability and visuospacial memory.
Conclusions: This study demonstrates that white matter and gray matter integrity can be explored on patients experiencing chemo-brain with a single subject approach based on FD and DTI. The combination of these techniques provides a deeper, multifocal understanding of chemo-brain and will hopefully lead to design of improved drugs and treatments to prevent or lessen the cognitive collateral effects.

Cardiovascular tissue contrast enhanced micro CT: correlation with 2D-histology

Joy Dunmore-Buyze,[a] Zengxuan Nong,[a] John A Kiernan,[e] J. Geoffrey Pickering,[a,c,d] and Maria Drangova[a,b]
[a]Robarts Research Institute, [b]Department of Medical Biophysics, [c]Departments of Medicine and Biochemistry, [d]Department of Physiology and Pharmacology, [e]Department of Anatomy and Cell Biology, University of Western Ontario, London ON, Canada

Introduction: Tissue contrast enhanced micro computed tomography (TCE micro CT) using highly attenuating tissue "stains" has allowed for visualization of various soft tissue structures of experimental animals ex vivo. While most work in this area has been done using the immersion of the fixed tissue in potassium iodide (I_2KI) solution [1] or phosphotungstic acid (PTA) [2] for periods of many days or weeks, our group has developed a method for staining tissue using whole-body vascular perfusion of the same stains in under 30 minutes [3]. The aims of this study were to automate the perfusion method in order to yield more reproducible staining and to identify – by correlation to optical histology – which tissues are preferentially stained by the different agents.

Methods: C57Bl/6 mice were perfused with 3.75% potassium iodide in iodine (I_2KI) and 5% phosphotungstic acid (PTA). The whole body was perfused using a modified ValveBank perfusion system (Automate Scientific, Berkeley CA) via retrograde perfusion of the abdominal aorta at physiological pressure (110 mm Hg). The same protocol was followed for both stains: first, the vasculature was flushed with 0.9 % saline; stain was delivered for 15 (I_2KI) or 30 (PTA) minutes; finally the vasculature was flushed with saline for 5 minutes. Immediately following perfusion, whole animal micro CT scans were obtained using an eXplore specCZT scanner (5 minute acquisition, 90 kVp, reconstructed to 50 or 100 µm isotropic voxels). Following this scan, tissue samples were harvested for histology or the entire mouse was scanned using the higher resolution GE eXplore Locus scanner (40 µm isotropic voxels, 2.75 hour scans). The I_2KI tissue were embedded in OCT and frozen sections were taken. The PTA samples were fixed in formalin and paraffin-embedded samples were sectioned at 10 µm. Sections were viewed (Olympus BX51) without additional histological processing, or – in the case of the colourless PTA, the sections were first counter-stained with toluidine blue (which is known to bind to the PTA) and compared to the TCE micro CT images.

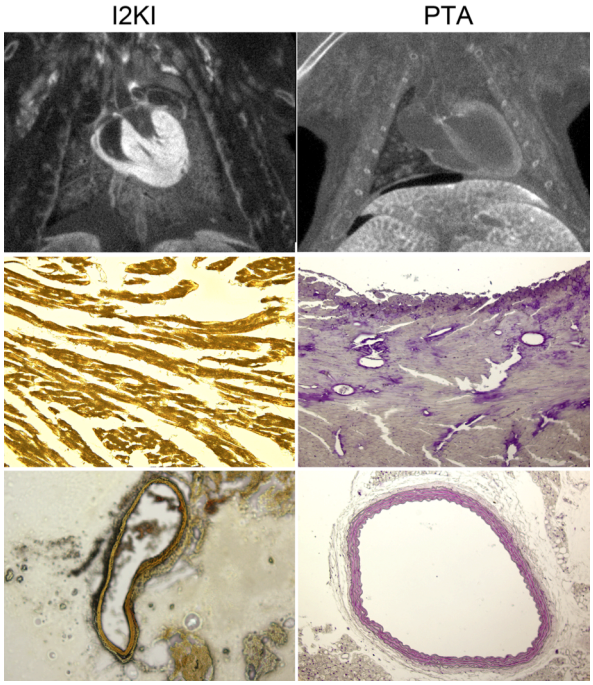

Example CT images (top, 50 µm reconstructions) of stained thoracic region: I_2KI and PTA. Histological sections through the myocardium (middle) and aorta (bottom) showing location of stain used.

Results: Both stains enhanced the soft tissue components of the heart and vascular wall. As previously reported I_2KI and PTA demonstrated tissue enhancement of the myocardial tissue and histology showed that the I_2KI preferentially adheres to the myocardial fibers but also diffuses through the aortic wall. PTA diffuses through the heart to a lower extent than I_2KI and appears to adhere to the cellular matrix in blood vessels.

Conclusion: An automated system can be used to perfuse mouse vasculature with highly attenuating "stains". I_2KI strongly adheres to the myocardial fibers while PTA selectively adheres to more strongly to vessel wall. Enhancement of non-vascular tissues is also apparent and is being evaluated.

References: [1] Gignac *et al.* J Anat. 2016; 228: 889-909. [2] Nierenberger *et al.* C.R. Biologies 2015; 338:425-33. [3] Dunmore-Buyze *et al.* Contrast Media and Mol. Imaging 2014; 5:383-90.

Pulmonary MRI Ventilation Defects in Asthma: Stochastic or Deterministic?

Rachel L Eddy[1,2],* Dante PI Capaldi[1,2], Khadija Sheikh[1,2], Sarah Svenningsen[1], David G McCormack[3] and Grace Parraga[1,2]

[1]Robarts Research Institute, [2]Department of Medical Biophysics, [3]Division of Respirology, Department of Medicine, The University of Western Ontario, London, Canada

INTRODUCTION: Pulmonary MRI provides strong evidence that lung ventilation abnormalities are temporally and spatially persistent; this has generated a paradigm shift in our understanding of asthma as a spatially and temporally heterogeneous, non-stochastic disease. With the development of pulmonary functional MRI, the exact location of functional abnormalities within the asthmatic lung may be determined and evaluated. MRI-derived ventilation defects are now recognized as a hallmark characteristic of asthma[1] and these respond to treatment[2] and persist over time.[3] We hypothesized that ventilation abnormalities are deterministic and that their spatial distribution will vary depending on disease severity and in response to treatment. Therefore, our objective here was to describe the spatial probability distribution of MRI-derived ventilation defects as a first step towards generating functional atlases of the asthmatic lung.

METHODS: We evaluated hyperpolarized ^{3}He static-ventilation MRI in 12 patients with mild-moderate asthma and 19 patients with severe-poorly-controlled asthma who provided written informed consent to an ethics-board approved protocol (NCT02351141). MRI was performed as previously described[4] and images were segmented for the ventilation-defect-percent (VDP).[5] All segmented images were co-registered using a deformable-registration by way of the modality-independent-neighbourhood-descriptor (MIND) method. Once co-registered, the final atlased image was evaluated for superior-inferior and anterior-posterior ventilation defects and airway-connectivities to non-random ventilation-heterogeneity.

RESULTS: Figure 1 shows ventilation defect probability maps for mild-moderate and severe asthma at baseline and post-methacholine. The spatial distribution of ventilation was qualitatively more heterogeneous following methacholine in both mild-moderate and severe asthma. In both cases, there was a visually obvious superior-inferior gradient, such that superior regions were more likely to be ventilated. This gradient was lessened post-methacholine. There was a visually obvious posterior-anterior ventilation gradient post-methacholine, such that posterior regions were more likely influenced post-methacholine (larger number and greater size of ventilation defect). The pattern of ventilation was more heterogeneous in severe asthma as compared to mild-moderate asthma and this difference was enhanced post-methacholine.

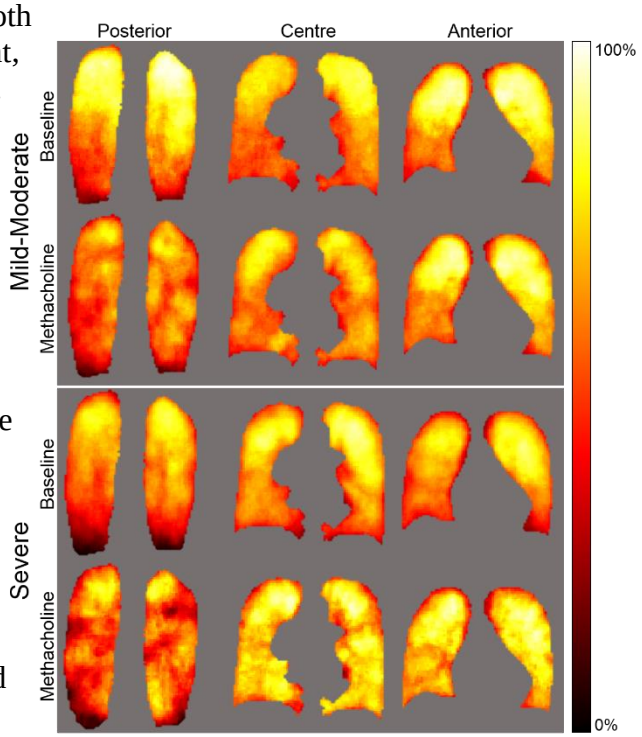

Figure 1. Posterior, centre and anterior slices of the ventilation defect probability maps for mild-moderate and severe asthma at baseline and after methacholine.

CONCLUSIONS: In this proof-of-concept study, we generated and evaluated functional MRI-derived ventilation atlases showing qualitatively obvious differences in ventilation patterns between mild-moderate and severe asthma as well as the changes in these patterns induced by methacholine. This suggests a deterministic nature of the location of ventilation defects and the abnormally remodelled airways that are hyper-responsive and worsened or constricted post-methacholine.

REFERENCES:

1 Teague, W. G. *et al. J Asthma*, (2014).
2 Samee, S. *et al. J Allergy Clin Immunol*, (2003).
3 de Lange, E. E. *et al. Radiology*, (2009).
4 Parraga, G. *et al. Acad Radiol*, (2008).
5 Kirby, M. *et al. Acad Radiol*, (2012).

Dynamic Functional Connectivity Analysis Reveals Differences between Wake and Stage 2 Sleep

Mazen El-Baba[1,2], Daniel J. Lewis[3], Zuo Fang[2], Adrian M. Owen[1,2], Stuart M. Fogel[4], J Bruce Morton[1,2,3]

[1]Program in Neuroscience, Schulich School of Medicine, Western University, London, ON
[2]Brain and Mind Institute, Western University, London, ON
[3]Department of Psychology, Western University, London, ON
[4] School of Psychology, University of Ottawa, Ottawa, ON

Introduction: The transition from wakefulness to sleep is marked by profound changes in neurophysiology, suggesting that changes in awareness might be accompanied by changes in functional network organization. Evidence in support of this association however is mixed, with many studies reporting few differences in inter- or intra-network connectivity across wakefulness and sleep (Horovitz et al., 2008; Kaufmann et al., 2006; Larson-Prior et al., 2009). One possibility is that standard methods that assume a static connectivity architecture obscure dynamic connectivity differences that are observable on shorter timescales (Allen et al., 2014; Hutchison et al., 2013).

Methods: To investigate this possibility, brain activity of 38 healthy adult participants (16 males, mean age, 21.7 years) was measured via simultaneous functional magnetic resonance imaging (fMRI; Siemens Prisma 3T scanner; TR = 2.1s, 36 slices, matrix size 64 x 64) and electroencephalography (EEG; Brain Vision, 64-channels) as participants transitioned from being fully awake to deeply asleep. EEG data were used to classify sleep stages. 21 of 38 participants had sufficient fMRI volumes to compare functional connectivity across Wake and Stage 2 sleep (S2S). Markedly fewer participants had sufficient data for comparing additional sleep stages. Therefore, in the interest of maximizing statistical power, the present analysis focused on comparing Wake and S2S. All fMRI volumes were pre-processed using SPM12 and ICA-decomposed (model order 65) using GIFT software (http://icatb.sourceforge.net/, Calhoun et al., 2001), yielding 42 neurophysiologically plausible sources. Independent component (IC) time courses were used to estimate static (or mean) FC (via Pearson correlation) and dynamic FC using a sliding window technique (Allen et al., 2014; window width = 15TR, time step = 1TR). Windowed correlation matrices were then submitted to K-means clustering analysis (k = 7, L2 norm) resulting in 7 connectivity states (CSs). Windowed correlation matrices were classified under one of the resultant CSs yielding a state label vector for each participant in Wake and S2S. Of interest was to explore dynamic features of the data, including number of transitions, inter-transition interval, mean dwell time, and CS frequency difference across Wake and S2S. To test for statistical significance, paired t-tests and repeated-measures ANOVA were performed. Greenhouse-Geisser degrees of freedom were used to correct for violation of sphericity assumptions, and Bonferroni's method was used to correct for multiple pair-wise post-hoc comparisons.

Results: Mean FC in Wake and S2S were highly comparable and were marked by strong intra-network connectivity and weaker inter-network connectivity. Dynamic analysis revealed differences in temporal features of the data. Namely, participants transitioned more between different CSs in wake than in S2S; consistently, the average time spent across all CSs was longer in S2S than in wake (i.e., significantly higher inter-transition interval in S2S than in wake). Furthermore, four of the seven dynamic CSs significantly differed in the frequency of their expression across Wake and S2S.

Conclusions: Consistent with previous findings, there were minimal differences between mean FC across Wake and S2S (Larson-Prior et al., 2009). The current analysis suggests traditional FC analyses that assume static connectivity architecture obscure differences in FC that are observable on a finer temporal scale.

Sparse-view image reconstruction with filtered backprojection in CT myocardial perfusion imaging

[1]Esmaeil Enjilela, [1,2]Ting-Yim Lee, [3]Jiang Hsieh and [1,2]Aaron So
[1]Robarts Research Institute, London, Ontario, Canada, [2]Lawson Health Research Institute, London, Ontario, Canada, [3]CT Engineering, GE Healthcare, Waukesha, Wisconsin, United States

Introduction: In this study, we investigated a view-interpolation method for minimizing aliasing artifacts in dynamic contrast-enhanced (DCE) heart images reconstructed from undersampled x-ray projections with the standard filtered backprojecton (FBP) algorithm. This method may facilitate the implementation of sparse-view dynamic acquisition for ultra-low dose CT myocardial perfusion imaging.

Methods: DCE heart images of five Landrace pigs (40-60 kg) were acquired after contrast injection with a 64-row GE Healthcare HD750 CT scanner using a prospective ECG gating protocol: 22 axial scans at every other mid-diastole, tube voltage 140 kV, tube current 80 mA, gantry speed 350 ms. DCE heart images were reconstructed with FBP from all measured projections (984, full-view) and 1/4 of projections (246, sparse-view) evenly distributed over 360^{o}. The same set of sparse-view projections were also interpolated to full-view using a cubic spline routine method to reconstruct DCE images (synthesized full-view). The three sets of DCE heart images were then anlayzed with the CT Perfusion software (GE Healthcare) from which MP maps were generated. Mean MP values in the lateral, apical and septal wall of the myocardium over eight consecutive 5-mm slices of the heart were compared among the three protocols using Bland-Altman analysis.

Results: Compared to full-view DCE images (Fig. 1A), sparse-view DCE images (1B) were markedly affected by streak artifacts arising from undersampling which led to degradation of the MP map (1E). By contrast, DCE images generated from the synthesized full-view approach had reduced streaks (1C) and the quality of MP map (1F) was comparable to that of the reference full-view method (1D). Relative to full-view, mean bias in MP measurement associated with the synthesized full-view protocol was 3.3 ml/min/100g (95% CI – 6.7 to 13.2), which was over 3 times lower than that of the sparse-view protocol (10.0 ml/min/100g, 95% CI -8.9 to 28.9).

Conclusion: The view-interpolation method effectively minimized aliasing artifacts in DCE heart images reconstructed from ¼ of views of a full-view acquisition and preserved the accuracy of MP measurement. This method can be applied to conventional FBP which is computationally efficient, and facilitates up to 4 times reduction in radiation dose for quantitative CT MP measurement (≤ 2 mSv for whole-heart coverage).

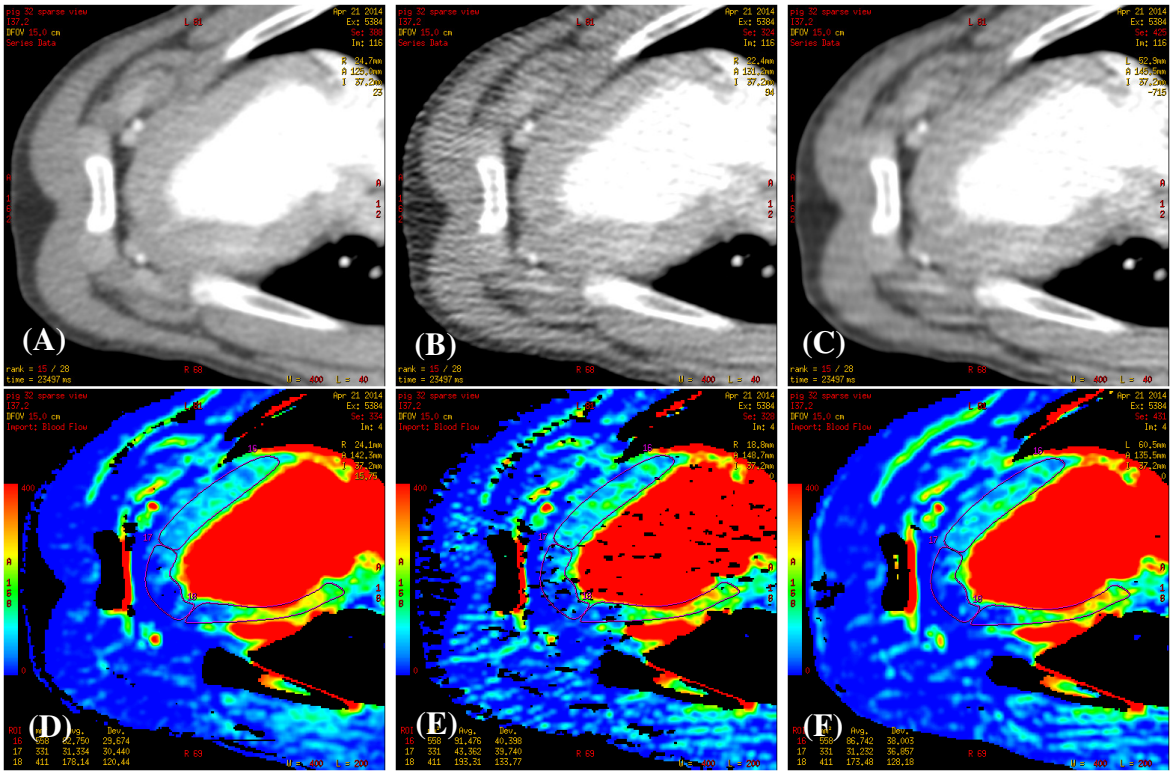

Figure 1. DCE heart images acquired with the (A) full-view, (B) sparse-view, (C) synthesized full-view protocols. The corresponding MP maps are shown in (D) to (F) respectively.

Development of a robust tool to determine radiographic detector dose efficiency (DQE) in clinics

Terenz Escartin*, Tomi Nano, Ian Cunningham
OICR Imaging Translation Program, Robarts Research Institute, Western University

Introduction: In x-ray imaging, exposure to radiation carries a small risk of creating new cancers. However, it is also true that higher exposures improve image quality. Hence, there is always a delicate balance between the radiation exposure used and the quality of images acquired. The ability to acquire high quality images using low patient exposures is quantitatively described by the detective quantum efficiency (DQE). While the DQE is widely used in scientific research and large manufacturer settings, little to no attention is directed to measure the DQE in clinics where DQE-expertise and instrumentation is limited. The challenges in measuring the DQE in clinics include: i) adaptive image modifications ii) non-linear edge contrast image enhancements iii) consistently determining correct image plane exposure. Our objective is to develop an intuitive and robust prototype that is well-suited for measuring the DQE in a clinical environment.

Methods: The prototype was designed to conduct the analysis with no moving parts, and to contain all components required to measure the DQE. This ensures consistent processing of all images acquired by the system. Non-linear edge contrast enhancements negates the ability to conduct an analysis because the DQE follows linear systems theory. By using a semi-transparent edge to determine the MTF, we minimize the effects of proprietary edge enhancement algorithms that negate the ability to conduct a DQE test. Calibrating the solid state sensor to always provide correct image plane (IP) exposure readings was performed (Fig 1). An RQA-5 spectrum with a HVL of 7.1mm Al was used. A standardized ion chamber was used to acquire and average 5 free air exposure readings 21 cm from the IP with a lead sheet covering the front surface of the detector to eliminate the effects of back scattered radiation (Fig. 1b). This process was repeated by replacing the ion chamber with the back surface of the prototype at the same location (Fig. 1c). A calibration factor was determined and implemented in the prototype's IP exposure calculation while considering inverse square law corrections. IP and sensor exposure readings were acquired at varying distances from the IP.

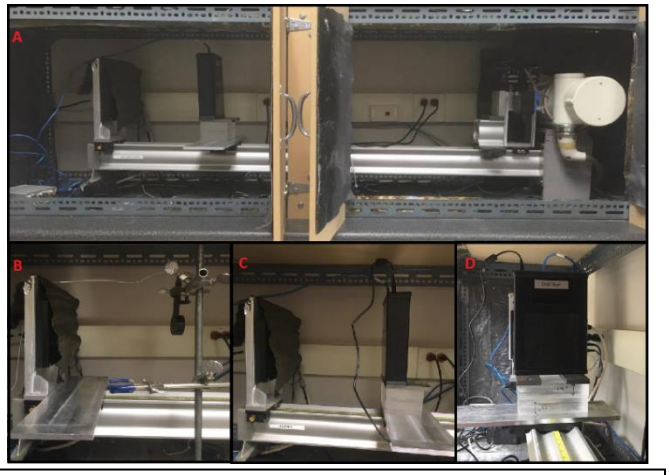

Figure 1: A) X-ray Detector (far left), prototype (middle), X-ray tube (far right). B) X-ray Detector (left), Ion Chamber (right). C) X-ray Detector (left), prototype (right). D) Frontal view of the clinical prototype.

Results: IP exposure readings (o) calculated by the prototype remained consistent across all distances (Fig. 2a). As expected, sensor exposure (*) readings increased as the prototype was moved closer to the x-ray source (Fig. 2a). To determine if an inverse square relationship truly existed between IP and sensor exposure readings, the linearized form of the inverse square law represented as a natural logarithm, suggests a theoretical slope of m = -2. A First order polynomial was fitted that revealed a slope m = -1.981.

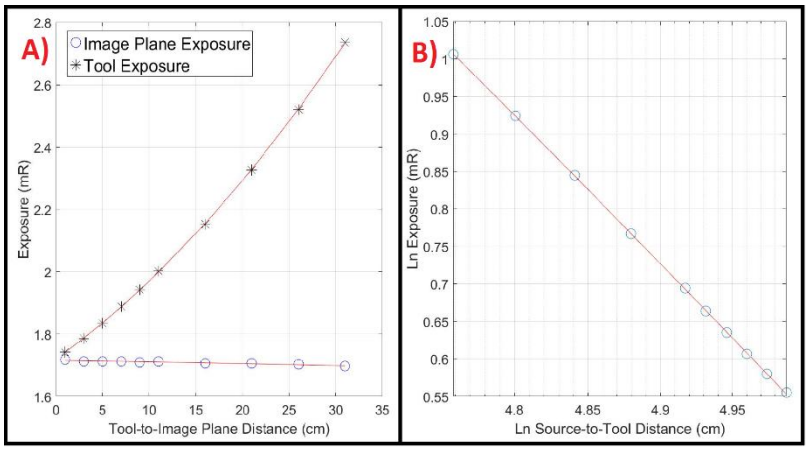

Figure 2: A) Exposure (mR) as a function of distance (cm) from the image plane is shown. B) First order polynomial fit on the logged datasets to confirm an inverse square relationship (m = -1.981).

Conclusion: Strategic prototypical designs have been implemented to ensure the robustness of the prototype. It was verified that the correct image plane exposure was determined over a range of 0 to 31 cm from the detector. The ability to consistently determine correct IP exposures independent of the relative distance of the prototype from the IP is important because the exact IP location is typically unknown and varies across manufacturers. The robustness of this prototype will ensure accurate clinical DQE results while suppressing experimental burden on non-experts.

Evaluation of Wearable Sensors using a Robotic Knee Joint Phantom and 3D Motion Capture

Megan C Fennema[1,2,3,7], Riley Bloomfield[1,2,4], Trevor Birmingham[6,7], Brent Lanting[2,5], Matthew G Teeter[1,2,3,5,7]

[1]Robarts Research Institute; [2]Lawson Health Research Institute; Depts. of [3]Medical Biophysics, [4]Engineering, and [5]Surgery, Western University; [6]Wolf Orthopaedic Biomechanics Laboratory; [7]Collaborative Training Program in Musculoskeletal Health, Western University, London ON, Canada

Development of Novel Therapies for Bone and Joint Diseases

Introduction: Wearable sensor technology has become an exciting platform for more intelligent assessment of patient function. These novel sensors have the potential to be used alongside current functional tests to provide more quantitative metrics that are relevant to patient important outcomes in total knee arthroplasty (TKA). Goniometric and inertial wearable sensors are a few of the technologies available to study joint kinematics. While these sensors have been previously used to assess knee joint kinematics (1,2), limited research is available on pre- and post-TKA sensor measures and correlations to patient satisfaction. The purpose of this preliminary experiment is to report on the precision and accuracy of goniometric and inertial sensors in comparison with 3D motion cameras in order to determine suitability for use with TKA patients.

Methods: Motion of the knee joint was simulated using a six degree-of-freedom robot controller and a skin-enclosed, anthropomorphic leg model (Figure). 3D motion capture markers for motion sensing cameras, inertial sensors, and an electro-goniometer were attached to the leg phantom to measure knee joint flexion. The goniometer was attached to the lateral side of the leg phantom across a fully extended knee joint. Two inertial sensors were attached in line with the goniometric sensor, at proximal and distal positions. Three motion capture markers were placed on the phantom, on the upper thigh, knee, and heel. Sensors were tared in a straight leg position immediately prior to data recording, and sensor data were acquired concurrently. The robot was programmed to simulate knee flexion, and each motion pathway consisted of ten cycles of approximately 120° flexion. The path was repeated at three different speeds, approximately 15, 30, and 50 °/s. Data were processed using GraphPad Prism 7.00, using one-way ANOVA, Tukey's multiple comparisons correction, as well as Bland-Altman's method comparison.

Figure 1: *Robotic limb phantom and sensor setup*

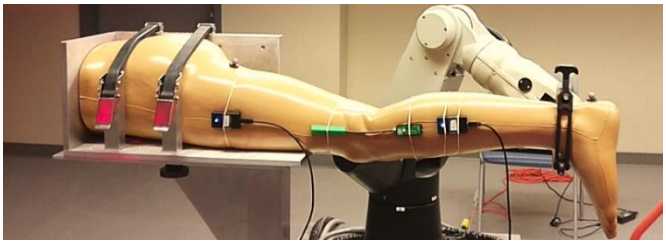

Table 1: *Mean and standard deviation of max. flexion*

	3D Motion	Goniometer	Inertial Sensors
Speed 1	116.4±0.06°	112.1±0.13°	118.7±0.16°
Speed 2	115.8±0.03°	112.3±0.10°	117.5±0.80°
Speed 3	116.0±0.02°	112.4±0.10°	115.9±0.44°

Figure 2: *Motion capture and sensor flexion angles vs. time*

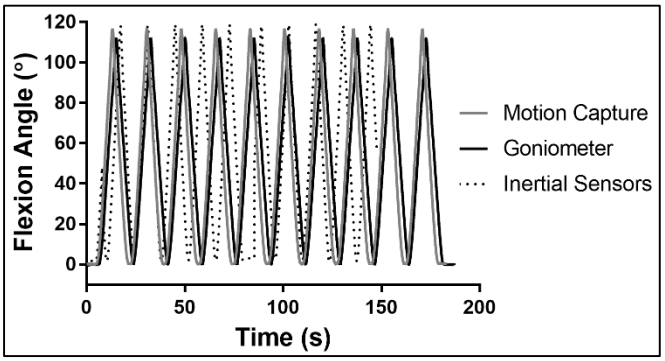

Results: The 3D motion sensing, goniometric sensor, and inertial sensors all demonstrated sub-degree standard deviation in maximum flexion angle within trials (Table 1). The motion capture technique had significantly reduced flexion peaks at the medium speed compared to the low speed ($p=0.0025$). The inertial sensors demonstrated significant differences in peak flexion between all three speeds ($p<0.0001$ for all cases). No significant differences in peak flexion angles were observed between speeds for the goniometer. Bland-Altman's comparison revealed sub-degree widths of the 95% limits of agreement between all methods. Average discrepancies of 2.3° between the inertial sensors and motion capture, 4.3° between the motion capture and goniometer, and 6.6° between the inertial sensors and the goniometer were observed. Both the goniometric and inertial-based sensors had discrepancies from the expected flexion angle. Instances of missed data, incorrectly recorded data, and timing inconsistencies were also observed for the inertial sensors (Figure 2).

Conclusions: Both the goniometer and the inertial sensors were deemed to be acceptably precise with their sub-degree standard deviation within tests. While the variation of the two sensor types was under 5° from the motion capture camera data, the accuracy of the sensors have room for improvement. The goniometric sensor was found to be much more reliable than the inertial sensors in its data collection, although its flexion angles were further from the expected values than the inertial sensors. Moving forward, efforts to improve accuracy will include creating custom calibration motion sets for the sensors. The wearable sensors demonstrated great potential for precise data collection in further human tests and for future use in TKA studies.

References: [1] Amaratunga *et al*. Ceylon Med J 2014;59:45-8. [2] Bolink *et al*. Physiol Meas 2012;33:1947-58.

^{19}F-perfluorocarbon-labeled human peripheral blood mononuclear cells can be detected *in vivo* using clinical MRI parameters in a therapeutic cell setting

Corby Fink[1,3], Jeffrey M. Gaudet[2,4], Matthew S. Fox[2,4], Shashank Bhatt[5], Sowmya Viswanathan[5], Michael Smith[1,3], Joseph Chin[6], Paula J. Foster[2,4], Gregory A. Dekaban[1,3]

[1]Molecular Medicine and [2]Imaging Research Laboratories, Robarts Research Institute, [3]Departments of Microbiology & Immunology and [4]Medical Biophysics, University of Western Ontario, [5]Krembil Research Institute, University Health Network, Toronto, Ontario and [6]London Health Sciences Centre, London, Ontario

Introduction: With respect to antigen presenting cell-based (APC) cancer vaccines, the quantity of tumor antigen-specific APC reaching a secondary lymphoid organ post-injection is directly proportional to the magnitude of the ensuing anti-cancer immune response. We performed a pre-clinical validation study in order to progress towards a clinical trial. The main purpose, as a proof of principle study, was to determine if we could label human peripheral blood mononuclear cells (PBMC) under GMP conditions with a ^{19}F labeling agent and detect these cells *in vivo* at an immunotherapeutic-relevant depth using a clinical MR scanner.

Methods: For manufacturing validation studies, human PBMC were obtained from 5 subjects and labeled with ^{19}F (5mg/mL) overnight under GMP conditions. Phenotyping and viability assessment (using 7-AAD) took place both pre- and post-transport to Robarts Research Institute. Prior to *in vivo* imaging studies, NMR was performed to determine ^{19}F uptake per cell. Nude mice were then injected with ^{19}F-PBMC and subjected to MR imaging.

Pre-clinical mouse MRI was conducted at 9.4T using a balanced steady state free precession (bSSFP) sequence with a resolution of 1x1x1mm^3 for ^{19}F scans and 200x200x200μm^3 for ^{1}H scans. ^{19}F-human PBMC detection was quantified by using the *in vivo* ^{19}F signal and comparing it to a ^{19}F reference tube concentration.

Clinical *in vivo* MRI was performed on a 3T system using a dual-tuned surface coil (4.3cmx4.3cm) approved for human use. Intradermal mock injections of ^{19}F-human PBMC ranging from 1x10^6 to 20x10^6 were performed in a ham shank as well as a subcutaneous injection of 4.5x10^6 cells 1.2 cm below the surface. A resolution of 0.5x0.5x1cm^3 and scan time of 15min was used to acquire ^{19}F-bSSFP images.

During this pre-clinical study, the question arose as to which main cell lineages (B cells, T cells and monocytes) within the PBMC formulation were producing *in vivo* signal in the lymph node. To address this, PBMC were negatively selected to purify out T cells, B cells and monocytes. Each lineage was then doubly labeled with ^{19}F and a unique intracellular fluorophore. Prior to footpad injection of 3x10^6 PBMC in mice, lineages were recombined at physiologic proportions. Two days later, draining popliteal lymph nodes were removed and sectioned for fluorescence microscopy to determine the degree of migration by each lineage.

Results: Our laboratory demonstrated near 100% ^{19}F labeling of human PBMC and NMR revealed loading at 6.17x10^{10}±1.80x10^{10} ^{19}F/cell. GMP-labeling and transport of human PBMC had no significant effect on viability and all sterility and quality assurance requirements were met. The functionality of APC within the PBMC mixture, as assessed by a mixed lymphocyte reaction, is unaffected by ^{19}F-labeling. Together, this indicated that the current manufacturing process is suitable for an upcoming clinical trial. Human ^{19}F-PBMC were detected and quantified *in vivo* in mice at both the subcutaneous flank injection site and draining lymph node.

Clinical 3T imaging was first optimized using cell pellets in which as little as 4x10^{17} ^{19}F/spin were detected (data not shown). This is to date is highest sensitivity reported using clinical 3T parameters, despite human PBMC labeling with low ^{19}F spins per cell (6.17x10^{10}). Next, MRI of a ham shank after surface intradermal and deeper subcutaneous (1.2cm, a depth similar to inguinal lymph nodes) injections ranging from 1-20x10^6 ^{19}F-PBMC permitted a minimum detection of 4.11x10^6 and 3.76x10^6 ^{19}F-labeled PBMC, respectively.

Immunofluorescent microscopy confirmed that the originally injected PBMC were producing ^{19}F lymph node signal and that all 3 of the main lineages within PBMC are present at physiologic proportions.

Conclusions: This proof of principle pre-clinical study provides a GMP-labeling procedure and experimental layout that yields near 100% ^{19}F human PBMC labeling without affecting viability or compromising sterility and other quality assurance criteria that must be met for injection into humans. We outline a clinical 3T MR protocol approved for human that is capable of producing the lowest sensitivity for ^{19}F detection reported thus far in the literature and the detection of an ^{19}F signal deeper *in vivo* than what has ever been reported using a surface coil. Further optimization is being performed prior to clinical trial approval to image ^{19}F-labeled PBMC in humans.

Tomographic Analysis of Ectopic Mineralization in Diffuse Idiopathic Skeletal Hyperostosis (DISH)

Dale E. Fournier[1], Katherine E. Willmore[1], S. Jeffrey Dixon[2], Christopher S. Bailey[3], David W. Holdsworth[3,4], and Cheryle A. Séguin[2]

[1]Anatomy and Cell Biology, [2]Physiology and Pharmacology, [3]Surgery, [4]Medical Biophysics, Schulich School of Medicine & Dentistry, Bone and Joint Institute, The University of Western Ontario, London, Ontario, Canada

Introduction: Diffuse idiopathic skeletal hyperostosis (DISH) is a non-inflammatory spondyloarthropathy characterized by calcification of the spinal ligaments of the vertebral column. Current diagnosis of DISH is based on radiographic criteria initially proposed by Resnick and Niwayama in 1976: i) flowing calcifications along the anterolateral aspect of at least 4 contiguous vertebral bodies, with or without osteophytes; ii) preservation of intervertebral disc height (*vs* degenerative disc disease); and iii) absence of bony ankyloses of facet joints, sacroiliac erosion, sclerosis or fusion (*vs* ankylosing spondylitis) [1]. The estimated prevalence of DISH in North America is 15-25%, with a higher occurrence in men (2:1) over the age of 50 years [2]. Despite its prevalence, the pathology of DISH has been poorly characterized and its aetiology remains unknown. We postulate the current diagnostic criteria for DISH captures a heterogeneous pool of disorders, from which key features of pathological calcification can be further defined.

Methods: This study involved 20 embalmed human cadavers (14 males, 6 females; mean age = 81 years; range 65-95 years) from the HEART (Haase Education in Anatomy & Research Technologies) Lab at Western University, ON. Intact vertebral columns (cervical-thoracic) were dissected and scanned by high resolution µ-CT (150 µm isotropic resolution, eXplore Ultra, GE Medical). From these scans, a series of imaging outputs were generated, including: maximum-intensity projections, 3D isosurface renderings, and images converted to radiographic and clinical CT equivalents (Figure 1). This bank of images will be used to i) diagnose DISH based on the current clinical standard; ii) identify specific pathological features of ectopic calcification in DISH; and iii) assess the ability of different imaging modalities to detect these features.

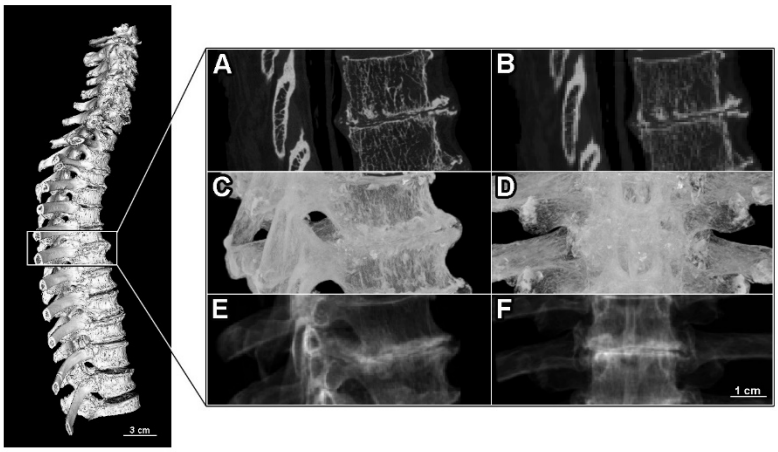

Figure 1: 3D isosurface rendering of intact vertebral column (C1-T12) of an 83 year old female. Panels A-F: the various image modalities of isolated T6-7 segment. A – 154µm resolution CT; B – 616µm clinical CT; C – lateral MIP; D – anterior MIP; E – medial-lateral radiographic reprojection; F – anterior-posterior radiographic reprojection. CT, computed tomography; MIP, maximum intensity projection.

Results: Analysis of the 20 vertebral columns, via µ-CT images and MIPs, identified 10 specimens that fulfilled Resnick's criteria for DISH (7 males, 3 females). Preliminary analysis of these specimens identified immense heterogeneity in the presentation of ectopic mineralization (i.e., mineral density and physical appearance – size, shape, location, abundance). Within the pool of DISH samples, we noted pathological features falling within two broad categories: i) continuous thin bands of ectopic calcification along the anterolateral aspect of the spine, and ii) ectopic calcifications forming overt osteophyte-like structures associated with the intervertebral discs.

Conclusions: The current diagnostic criteria for DISH captures a heterogeneous population of features that may be further categorized and defined. Importantly, the high-resolution tomographic scans allow for the detection of features currently unreported through current clinical imaging techniques. Conversion to current imaging standards allows for the confirmation or refutation of these features for future diagnosis of DISH. Thereby, results from this investigation serve to further define classifications associated with DISH diagnosis, with an emphasis on identifying the early stages of the disease and, in the long term, enabling the development of targeted interventions.

References: [1] Resnick D, Niwayama G. Radiology. 1976;119(3):559-68. [2] Weinfeld, Robert M., *et al*. Skeletal radiology. 1997;26(4):222-225.

A Method to Automatically Detect and Measure Erosions in the Metacarpal Joint

Mark CH Frayne*; Steven K Boyd, PhD; Cheryl Barnabe, MD; Sarah L Manske, PhD
McCaig Institute for Bone and Joint Health, University of Calgary

Introduction

In joints affected by rheumatoid arthritis (RA) bone damage leading to erosions is common and one of the more severe effects of the condition. Currently, the method for detecting these erosions uses planar hand radiographs. As these images are two dimensional (2D), it is difficult to accurately measure the size of erosions, therefore, a semi-qualitative scoring method is employed.[1] With the developments in high-resolution peripheral quantitative computed tomography (HR-pQCT), three dimensional (3D) volumetric measurements of erosions can be performed, however, the only published method still requires manual identification and segmentation of the erosions[2] and only approximates the erosion volume. The goal of this project was to develop an automated method of erosion segmentation for true volumetric measurement.

Methods

Participants ($N = 61$) undergoing treatment for RA were scanned 3 months into their treatment with a HR-pQCT scanner (XtremeCTII, Scanco Medical AG, Brüttisellen, Switzerland). The scans were acquired using standard acquisition parameters[3] at a nominal isotropic resolution of 61 µm. The second and third metacarpal joints (n=122) were analyzed with the proposed method. The metacarpal and phalanx were each individually segmented from the surrounding tissue and cortical and trabecular regions identified through a custom script developed in Image Processing Language (5.42, Scanco Medical AG). The segmentation was done automatically with manual correction if the bones were connected due to either patient motion during the scan, or joint space loss. The trabecular mask was used to fill the interior of the segmented bone in order to avoid having segmented volumes leak into the trabecular bone. The segmented bone volume was sequentially dilated and eroded to fill in all of the erosions present. The image with the filled in erosions then had the original bone image subtracted so that only the filled in (*i.e.*, eroded bone) volume remain. Eroded volumes greater than 4.5 mm^3 were identified, analyzed individually, and displayed superimposed on the original bone image (see Figure 1). The eroded volumes were manually verified to confirm that they were the results of erosion[2] and not false positive findings caused by a semi-erosion resulting from osteophyte growth (*i.e.*, a concave area of bone surface) or the results of a motion artifact. The volume and surface area of the volumes were obtained from a surface generated with the marching cubes algorithm.

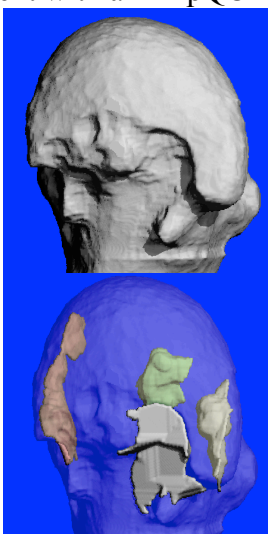

Figure 1: 3D model of a metacarpal bone both alone (top) and with the erosions overlaid (bottom).

Results

Of the 122 joints analyzed, erosion was detected on 43 (35.2%) joints on at least one of the metacarpal bones. A total of 85 different erosions were identified. Manual checking of these erosion volumes confirmed that 50 (58.8%) contained one or more erosions. For the other 35 volumes, 19 (22.3%) were semi-erosions, 6 (17.1%) were due concavity in the bone shape, while the remaining 10 (28.6%) were due to motion artifacts. Of the 85 detected erosion volumes 81.2% had the correct shape by visual inspection. The average erosion volume and surface area were 44.9 $mm^3$and 111.4 mm^2 , respectively.

Conclusions

The development of a novel method for automated erosion detection and volume measurement was presented and demonstrated to be effective at detecting large erosions. While more work is needed to prevent detection of concave volumes and distinguishing erosions from semi erosions (where it remains a challenge due to similarities in shape). The average measured erosion volume and surface area were larger than what is reported in literature[4] but this may be because the studied erosions were more developed in our patient population. Additional investigation is needed to reduce the false positive rate of the method. The proposed method, nonetheless, has proven to be a viable method for detection of erosion and is considerably faster than the current method even with manual verification.

References

1 van der Heijde *J Rheumatology* 1999; **26**: 743-5.
2 Barnabe *et al*. *J Rheumatology* 2016; **43**: 1935-40.
3 Manske *et al*. *Bone* 2015; **79**: 213-21.
4 Töpfer *et al*. *Rheumatology* 2014; **53**: 65-71.

Robotic Catheter Contact-Force Control for Cardiac Ablation Therapy: *In Vivo* Evaluation

D. Gelman,[1] A. C. Skanes,[2] D. L. Jones,[3] M. Timofeyev,[4] T. Bar-on,[4] M. Drangova[1,5]

[1]Robarts Research Institute and the Biomedical Engineering Graduate Program, Western University, Canada;
[2]Dept. of Medicine, Schulich School of Medicine & Dentistry, Western University, Canada;
[3]Dept. of Physiology & Pharmacology, Schulich School of Medicine & Dentistry, Western University, Canada;
[4]Biosense Webster Ltd., Yokneam, Israel;
[5]Dept. of Medical Biophysics, Schulich School of Medicine & Dentistry, Western University, Canada

Consortium: Image-guided Device Interventions for Cardiovascular Disease **Supervisor:** M. Drangova

Introduction. To treat cardiac arrhythmia – an irregular heart rhythm – ablation catheters are introduced into the heart and manipulated until the distal tip contacts the targeted myocardium. Radiofrequency (RF) energy is delivered to form ablation lesions that isolate the heart from electrical pathways responsible for the arrhythmia. Controlling the size of the lesion is vital for good patient outcome. RF power, delivery time, and catheter-tissue contact force (CF) are metrics that are used to estimate lesion size. However, fluctuations in CF due to inherent cardiorespiratory motion make it difficult to assess lesion size during treatment. The solution to this problem would be to maintain a desired level of CF throughout RF delivery, enabling the interventionalist to deliver a lesion under predetermined ablation parameters. To facilitate CF regulation, we developed a catheter contact force controller (CFC) and the objective of this work is to evaluate its performance in a swine model. The CFC is a hand-held, electromechanical device that monitors changes in CF and compensates by autonomously adjusting the position of a force-sensing ablation catheter within a steerable sheath in real-time [1].

Methods. Two male farm pigs were prepared for catheterization. A research-based CARTO® 3 catheter mapping system, C-arm fluoroscopy, and intracardiac echocardiography (ICE) were used to facilitate in catheter navigation, as illustrated in Figure 1. A SMARTTOUCH™ (ST) force-sensing ablation catheter and a steerable sheath were introduced into the heart. Several target locations in the left and right atria were evaluated. An interventionalist manipulated the ST catheter tip to a target and attempted to maintain 20 g for 30-60 seconds; following this, the CFC was engaged and programmed to deliver a force of 20 g; manual and CFC profiles were recorded. For consistency, the catheter tip was not repositioned between manual and CFC-controlled profiles. The catheter-tissue incident angle was kept < 30 degrees. After the force experiments were performed, several CFC-assisted ablations were delivered.

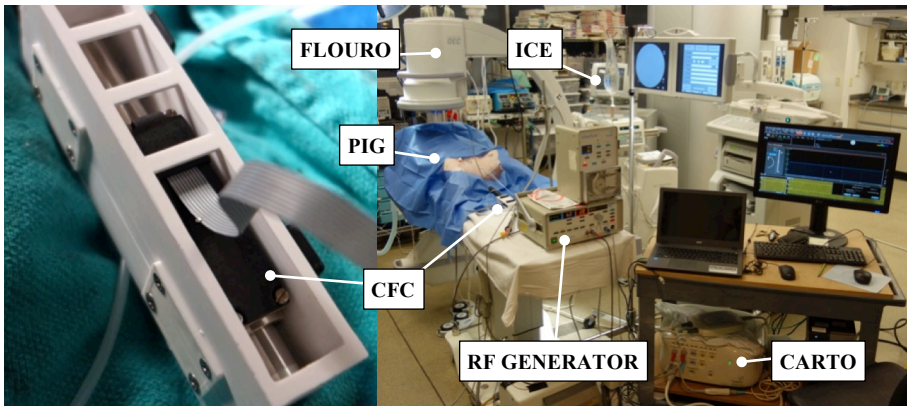

Figure 1. Photograph of the CFC (left) and the *in vivo* setup (right).

Results. During CFC-controlled profiles, the average force was within 0.5 g of the desired level; the root mean squared errors (with respect to 20 g) reduced by a factor of 2-4 when comparison to the manual intervention. With apnea the error improved by a factor of 8, illustrated in Figure 2.

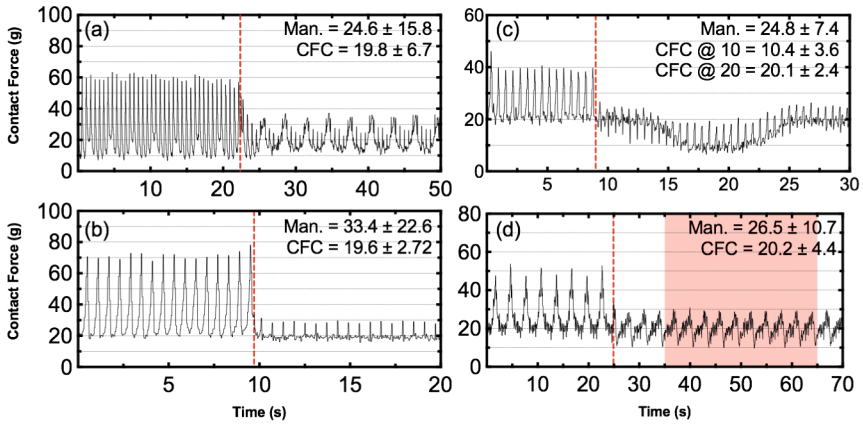

Figure 2. Four example experiments performed in various locations in the left and right atrium (LA and RA, respectively). Each CF profile begins with manual intervention, prior to CFC engagement (red line). LA anterior appendage without (a) and with apnea (b), high RA with apnea (c) while changing the desired level of force, ablation (red area) of the RA septum (d). A significantly improved CF profile was observed while the CFC was engaged.

Conclusion. The CFC is the first robotic catheter device to demonstrate catheter-tissue CF control *in vivo* for cardiac ablation therapy, with force variation of less than 2.5 g over periods of over 30 seconds.

[1] D. Gelman *et al.*, "Design and Evaluation of a Catheter Contact-Force Controller for Cardiac Ablation Therapy," IEEE Trans. Biomed. Eng., vol. 63, no. 11, pp. 2301-2307, 2016.

A Comparison between User Initiated and Continuous Real-time Motion Compensation Techniques for 3D Ultrasound-guided Prostate Biopsy

Derek J Gillies*, BSc[1,2], Lori Gardi, BSc[1,2], Shuang-ren Zhao, PhD[3], Aaron Fenster, PhD[1,2,3]

[1]*Department of Medical Biophysics, Western University, London, Ontario, Canada;*
[2]*Robarts Research Institute, Western University, London, Ontario, Canada;*
[3]*Centre for Imaging Technology Commercialization, London, Ontario, Canada;*
Consortia: Ontario Institute for Cancer Research - Imaging Translation Program

Introduction: Biopsy is the current clinical standard for definitive diagnosis of prostate cancer and is conventionally guided by two-dimensional transrectal ultrasound (2D TRUS). This procedure suffers from undesirable false negative rates, which has led to the use of three-dimensional (3D) TRUS and magnetic resonance (MR) fusion images for targeted biopsies. Fusion images have offered an improvement for needle guidance accuracy and diagnoses by augmenting the conventional 2D TRUS guidance; however, prostate motion can cause misalignment of the anatomical and planned targets identified using the 3D TRUS/MR fused images. Misalignment has led to missed cancer diagnoses and an increase in repeat patient biopsies, but a single user initiated correction can be performed to temporarily compensate for prostate motion. Since this must be repeated multiple times throughout a biopsy, and with the overall goal of improving biopsy outcomes, we are developing a real-time registration technique to continuously align 2D and 3D TRUS images.

Methods: Rigid registration between 2D and 3D TRUS images was performed using an intensity based normalized cross-correlation similarity metric optimized with the Powell method. The algorithm was tested on a tissue-mimicking prostate phantom made from agar. 2D and 3D TRUS images were acquired and the algorithm was tested for in-plane (IP) and out-of-plane (OP) motion compensation up to 12 mm in 1 mm increments. The difference between the known displacement and corrected registration distance was used to determine error. Rotational (R) compensation around the long axis of the TRUS transducer in 1° increments up to 15° was also tested. The difference between encoder displayed rotations and corrected rotation matrices were used to determine error. These procedures were experimented with user initiated and continuous image registration techniques.

Results: Computation time results are shown in Figure 1 for IP and OP motions. The user initiated correction performed with observed computation times of 108 ± 38 ms, 60 ± 23 ms, and 89 ± 27 ms for IP, OP, and R motions, respectively, corresponding to errors of 0.4 ± 0.3 mm, 0.2 ± 0.4 mm, and 0.8 ± 0.5°. The continuous correction performed significantly faster ($p < 0.01$) than the user initiated method, with observed computation times of 35 ± 8 ms, 43 ± 16 ms, and 27 ± 5 ms for IP, OP, and R motions, respectively, corresponding to errors of 0.2 ± 0.3 mm, 0.7 ± 0.4 mm, and 0.8 ± 1.0°.

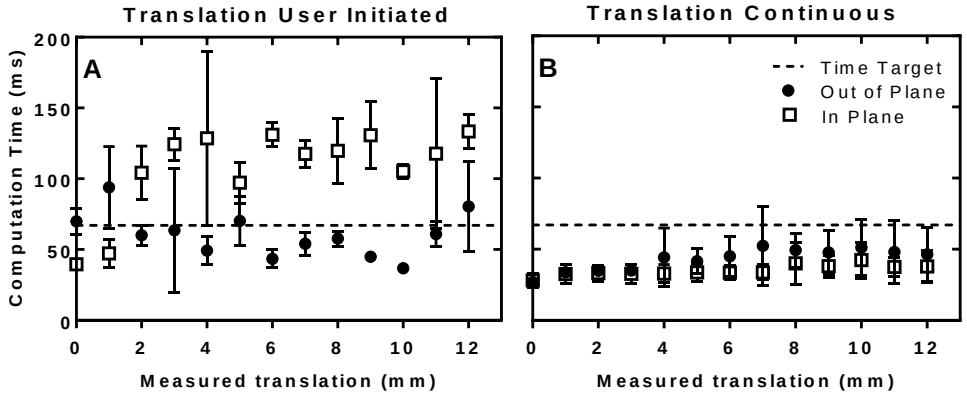

Figure 1. Comparison of registration times when testing IP and OP motion compensation for the user initiated (A) and continuous procedures (B). The dashed line represents the real-time target computation time of 67 ms.

Conclusions: Continuous motion compensation was significantly faster than a user initiated correction, with similar error, when investigated on a rigid phantom. Future work will involve validating the continuous motion compensation algorithm on patients undergoing biopsy procedures.

Comparison between 2-point Dixon and Quantitative IDEAL for Magnetic Resonance Imaging of Fetal Adipose Tissue

Stephanie Giza*[1], Barbra de Vrijer[2,3], Charles McKenzie[1,2]
[1]Medical Biophysics, Western University, [2]Division of Maternal, Fetal and Newborn Health, Children's Health Research Institute, [3]Obstetrics and Gynaecology, Western University, London, Ontario

Introduction. Fetal adipose tissue development is reflective of the energy balance within the fetus, and may be altered due to maternal health (e.g. gestational diabetes) or pregnancy complications (e.g. fetal growth restriction or macrosomia). Imaging techniques such as ultrasound (US) and magnetic resonance imaging (MRI) provide valuable information on the development of fetal adipose tissue volume *in utero*, but have failed to measure the lipid content of these tissues. We are investigating the lipid content of fetal adipose tissue using two water-fat MRI techniques that are sensitive to lipid within tissues: 2-point Dixon and Quantitative IDEAL. 2-point Dixon uses 2 echoes and B_0 field mapping to model water and fat (1,2), but does not account for the complex fat spectrum and T2* effects (1,2). Quantitative IDEAL uses 6 echoes and corrects for a variety of sources of bias, including T2* and the complex fat spectrum; however, it has a lower signal to noise ratio (SNR) per unit time [3-5]. Both sequences can produce fat fraction images (fat/(water+fat); FF), but the FF of the 2-point Dixon method will be biased due to limitations in signal modelling. We have previously shown that 2-point Dixon water-fat imaging can be used to assess the lipid content of fetal adipose tissue *in utero*. Here we compare lipid volume and FF of fetal adipose tissue between 2-point Dixon and Quantitative IDEAL.

Methods. Volunteers with singleton pregnancies were recruited from low-risk and high body mass index (BMI) obstetric clinics and imaged in a wide-bore (70cm diameter) MRI (GE MR450w). During an approximately 30 min MRI exam, 3D 2-point Dixon (TR 6.1-6.5 ms, flip angle 5°, receiver Bandwidth (rBW) +/-62.5 kHz, FOV 50 cm, frequency encodes 160, phase encodes 128-160, slice thickness 4-6 mm, 42-64 slices) and 3D Quantitative IDEAL (TR 9.8-11.8 ms, flip angle 6-7°, rBW +/-83.3 kHz, FOV 50 cm, frequency encodes 128-160, phase encodes 128-160, slice thickness 4-6 mm, 42-64 slices) were used during maternal breath hold to image fetal fat. The fetal total adipose tissue was segmented on both the 2-point Dixon and Quantitative IDEAL FF images using 3D Slicer (v4.7.0-2016-12-06), and segmented volume, FF, and lipid volume were compared using intraclass correlation coefficient (ICC) (SPSS v.24) and Bland-Altman plots (GraphPad Prism v.7.01).

Results. Five women (gestational age: 33+4 to 37 wk, BMI 16.6 to 40.6 kg/m^2) were recruited and imaged. The FF of the adipose tissue from 2-point Dixon and Quantitative IDEAL (Figure 1) had an ICC of 0.95 (P=0.002). A Bland-Altman plot of FF agreement is shown in Figure 2. The fat fractions agree between the two imaging methods, with the largest difference being 6% in an image set with motion artefact. Both the segmented volumes and the lipid volumes had an ICC of 0.97 (P=0.001). Bland-Altman plots of both segmented volume and lipid volume show some disagreement, which is likely due to differences in segmentation caused by different SNR. Investigation into methods to minimize these segmentation differences needs to occur with a larger sample size.

Conclusion. It appears the FF measured using the 2-point Dixon and Quantitative IDEAL methods are in good agreement, however this is a small sample size and further investigation is required.

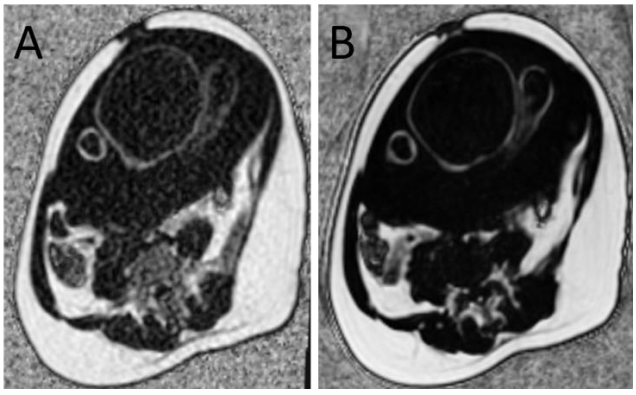

Figure 1. FF images of A. Quantitative IDEAL and B. 2-point Dixon techniques.

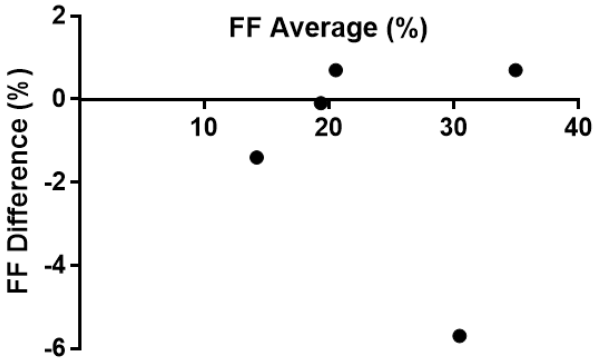

Figure 2. Bland-Altman plot of FF between Quantitative IDEAL and 2-point Dixon techniques.

References. (1) Ma. Magn Reson Med 2004;52: 415-419. (2) Ma. J Magn Reson Imaging 2008;28: 543-558. (3) Hines *et al.* J Magn Reson Imaging 2011;33: 873-881. (4) Meisamy *et al.* Radiology 2011;258: 767-775. (5) Yu *et al.* Magn Reson Med 2011;66:199-206.

Physics-based scatter correction for quantitative PET imaging of hypoxia

Jennifer Gottwald[1,2], Gregory Bootsma[1,2], Ivan Yeung[1,4], Harald Keller[1,4], Michael F. Milosevic[1,4], Brandon Driscoll[1,2],

Edward Taylor[1,2] and David A. Jaffray[1,2,3,4,5,6]

1. Princess Margaret Cancer Centre, University Health Network, Toronto, Canada
2. Techna Institute, University Health Network, Toronto, Canada
3. Department of Medical Biophysics, University of Toronto, Toronto, Canada
4. Department of Radiation Oncology, University of Toronto, Toronto, Canada
5. Institute for Biomaterials and Biomedical Engineering, University of Toronto, Toronto, Canada
6. Research Supervisor

Introduction: Photon scattering contributes significantly to the imaging degrading effects in 3D PET imaging. It results in a loss of contrast and overall image quality which makes accurate tracer quantification challenging. These scatter effects are particularly important in regions where two adjacent tissues have vastly different tracer concentrations. Scattered events from photons originating from the intense uptake region contaminate the low uptake region. This "cross talk" changes the linearity, the noise level and the reconstruction accuracy of PET. The objective of this study is to develop a Monte Carlo (MC) based model to validate the calculated scatter distributions with measured scatter estimates as well as to investigate the shape and magnitude of the scatter distribution in relationship with different imaging parameters (the activity concentration, different distances for the occurrence of the scatter contamination and changes in object size).

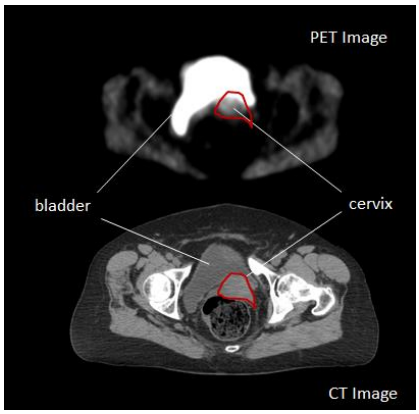

Figure 1 Clinical observation in cervix cancer show a scatter contamination effect in the tumor, originating from the bladder which makes the quantification of hypoxia challenging. UHN REB#: 14-8648-C

Methods: To investigate scatter effects in PET imaging the MC simulation tool GATE 7.2 has been used [1]. The geometry of the MC model is a pre-defined GE Discovery 610 PET/CT detector model and the following technical details were implemented, equivalent to our clinical scanner - an Energy Resolution of 425-650 keV, a Dead Time of 650 ns and a Coincidence Window of 4.875 ns. To generate and implement a voxelized material phantom and source in GATE, regions of interest (ROIs) are defined based on CTAC images. Based on the containing range of image pixel values, CT numbers are transferred into a voxelized material density map by using pre-defined look up tables in GATE. A similar approach is used to assign individual activity values in the voxelized source. The calculated scatter distribution is validated against the measured scatter estimates with the help of the NEMA NU 2- 2012 standard [2]. The NEMA IEC Body phantom will be used to investigate the influence of the imaging parameters, such as the activity concentration (1 : 5 up to 1 : 10) of F^{18} on the scatter distribution

Results: Results have shown that the MC model simulates the isolated scatter distribution accurately and that the influence of different imaging parameters on the scatter distribution can be studied.

Conclusion: The MC model is a useful tool to simulate the isolated scatter distribution accurately as well as to investigate different imaging parameters to propose a further Fourier analysis of the scatter distribution to guide the research work towards a MC based scatter correction model.

Reference:

[1] Jan S et al.: GATE: a simulation toolkit for PET and SPECT. Phys. Med. Biol. 49 (2004) 4543-4561
[2] National Electric Manufactures Association NEMA standards publication NEMA NU 2-2012: Performance Measurements of Positron Emission Tomographs

Return to Program

Ultra-short-echo-time MRI Lung Segmentation using High-Dimensional Features and Continuous Max-Flow

Fumin Guo[1], Khadija Sheikh[1], Aaron Fenster[1] and Grace Parraga[1]
[1]Robarts Research Institute, The University of Western Ontario, London, CANADA

Introduction: Ultra-short-echo-time (UTE) MRI is ideally suited for serial and longitudinal evaluation of pediatric patients and young adults as it does not require ionizing radiation or exogenous contrast.[1] Previous studies[1-3] have demonstrated the potential of UTE MRI biomarkers to phenotype lung structural-functional abnormalities and perhaps facilitate the development of novel lung disease treatments. To generate these imaging biomarkers and enable the widespread clinical application of UTE MRI, optimal lung segmentation methods are required. Therefore, here we aim to develop an improved UTE MRI lung segmentation approach.

Methods: Ten asthma patients underwent UTE MRI under breath-hold conditions, as previously described.[2] One observer seeded the lung and background three times on three days. We employed a K-nearest neighbour kernel K-means approach[4] combining lung signal intensities and neighbourhood location information for improved data term construction. The high-order data term was relaxed to a point-wise formulation by deriving its upper bound[4] and the segmentation was regularized using image edge information. The data and regularization terms were entered into a continuous max-flow segmentation approach,[5] which was implemented iteratively to update the data term. Algorithm segmentation accuracy was evaluated by comparing algorithm and manual lung masks using Dice-similarity-coefficient (DSC), root-mean-squared-error (RMSE) of lung surface distances and absolute-percent-volume-error ($|\delta V_p|$). The reproducibility was measured using Coefficient-of-Variation (CoV) and Intraclass-Correlation-Coefficient (ICC).

Results: Subject demographics are provided in Table 1 and representative UTE MRI voxel labelling probability and segmentation results are shown in Figure 1. We achieved a DSC of 92.8±2.5%, RMSE of 2.9±0.6mm and $|\delta V_p|$ of 7.2±3.6% in ~2min for each subject. CoV(ICC) were 0.4%(0.98) and 1.6%(0.97) for DSC and RMSE, respectively.

Conclusions: The proposed approach compensates for UTE signal intensity inhomogeneity and preserves lung segmentation continuity with simpler user interaction. Our segmentation approach provides the accuracy, reproducibility and computational efficiency needed for widespread clinical application of UTE MRI.

References: [1] Ma *et al. J. Magn. Reson. Imaging*, (2015). [2] Sheikh *et al. J. Magn. Reson. Imaging*, (2016). [3] Walkup *et al. Am. J. Respir. Crit. Care Med.*, (2015). [4] Tang *et al.* in *IEEE International Conference on Computer Vision (2015).* [5] Yuan *et al.* in *IEEE International Conference on Computer Vision and Pattern Recognition (2010).*

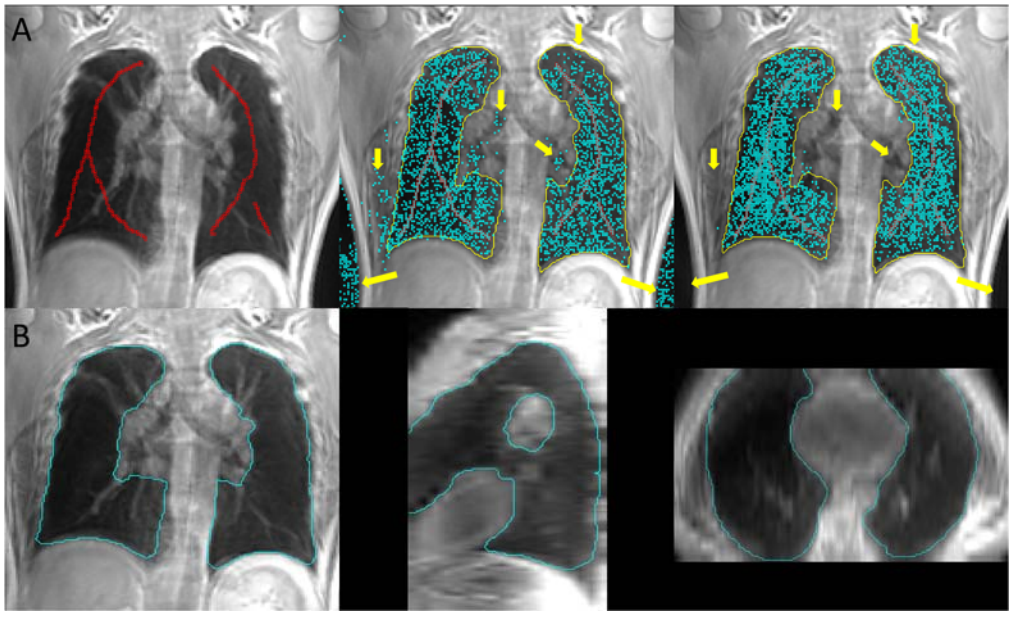

Figure 1. Representative UTE MRI voxel labelling probability map using the adaptive kernel K-mean approach and lung segmentation results. A) UTE MRI lung signal intensity inhomogeneity and example user seeds (red), probability map (cyan) using signal intensity only, and probability map (cyan) combining signal intensity and neighbourhood location information are shown from left to right. Yellow contours represent manual segmentation and the arrows indicate improvements by incorporating neighbourhood location information. B) Representative lung segmentation results are shown in coronal, sagittal and axial views from left to right.

In Vivo Magnetic Resonance Imaging Investigating the Development of Experimental Brain Metastases due to Triple Negative Breast Cancer

Amanda M Hamilton* and Paula J Foster
Smarter Imaging Program, Ontario Institute for Cancer Research Consortium
Robarts Research Institute, The University of Western Ontario, London, Ontario, Canada

Introduction. Triple negative breast cancer (TNBC) is consistently aggressive in nature with a high incidence of brain metastasis and the shortest median overall patient survival after brain metastasis development compared to all other breast cancer subtypes.[1,2] As therapies that control the primary cancer site improve, the incidence of brain metastases is increasing and the management of patients with breast cancer brain metastases continues to be a significant clinical challenge.[3] Mouse models have been developed to permit in depth evaluation of breast cancer metastasis to the brain.[4] In this study, we used longitudinal MRI analysis and end point histology to assess the efficiency and metastatic potential of two experimental mouse models of TNBC over time. **Methods.** Murine 4T1-BR5 and human MDA-MB-231BR (231-BR) mammary carcinoma cells were iron labeled with MPIO beads (IO) and delivered by intracardiac injection into anesthetized mice. All MRI examinations were performed on a 3T GE Discovery MR750 whole-body clinical MR scanner using a custom-built high-performance gradient and a custom solenoid radiofrequency mouse head coil. All mice were imaged with a bSSFP sequence within 24 h post-cell injection to determine successful cell delivery. Mice were imaged at two additional time points (days 10 and 15 for the 4T1-BR5 model and days 23 and 30 for the 231BR model) to assess tumour progression over time. At end point, fixed mouse brain sections stained with either Hematoxylin and Eosin (H&E) to examine tumour morphology or immunohistochemistry was performed with Ki67 to examine the proliferative status. All data was summarized for each individual mouse and summary data was compared across models using GraphPad Prism software. **Results.** Significant differences were evident in the appearance of brain tumours between the two tumour models by *in vivo* MRI and *ex vivo* histological analysis. By quantifying the initial cell arrest and the number and volume of metastases that developed in the brain over time, we showed significant differences in MRI appearance, tumor progression and model efficiency between the syngeneic 4T1-BR5 model and the xenogeneic 231-BR model. Both cell lines exhibited high percent positive expression of the proliferation marker, which is indicative of poor prognosis (>20%).[5] The 4T1-BR5 model was clearly the more aggressive as an equivalent tumour burden was established within the first 10 days of growth compared to what was detected in the 231-BR model after 3 weeks. By end point the 4T1-BR5 model grew a greater tumour burden within approximately half of the timeline of the 231-BR model despite 7.5 fold less cells being injected upon initiation of the model. **Conclusions.** As TNBC does not respond to many standard breast cancer treatments and TNBC brain metastases lack effective targeted therapies, these preclinical TNBC models represent invaluable tools for the assessment of novel systemic therapeutic approaches. Further pursuits of therapeutics designed to bypass the blood tumor barrier and permit access to the brain parenchyma and metastatic cells within the brain will be paramount in the fight to control and treat lethal metastatic cancer. **References.** [1] Niikura N et al (2014) Jpn J Clin Oncol 44(12):1133-40. [2] Arvold ND et al (2012) Breast Cancer Res Treat 136(1):153-60. [3] Lin NU et al (2013) Clin Cancer Res 19(23):6404-18. [4] Daphu I et al (2013) Clin Exp Metastasis 30(5):695-710. [5] Stuart-Harris R et al (2008) Breast 17(4):323-34

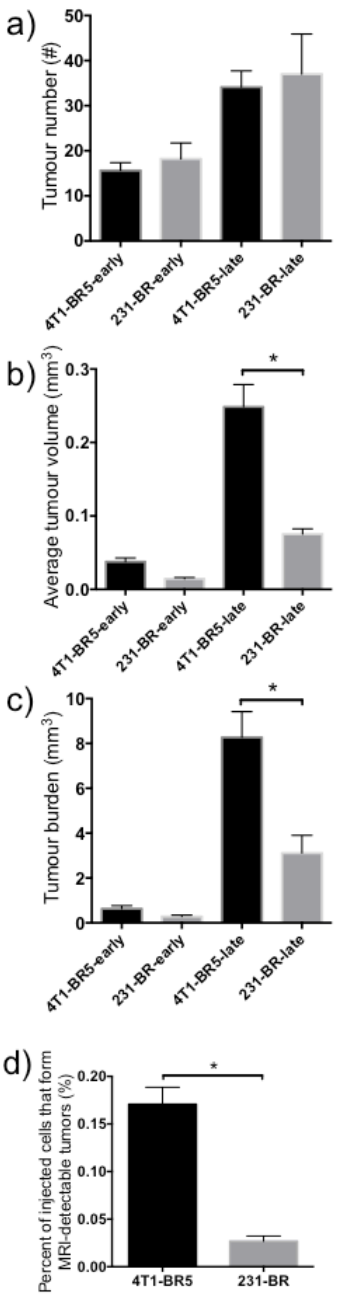

Comparison of 231-BR and 4T1-BR5 tumor progression overtime. No significant difference was seen in the number of MR detectable tumors (a) at both early and late time points. By endpoint (late time point), however, the average tumor volume (b) and total tumor burden (c) in the 4T1-BR5 tumor model was significantly greater than that of the 231-BR model. (d) The 4T1-BR5 model exhibited spastically greater efficiency as a greater percentage of injected cells successfully arrested in the brain and formed MR detectable tumors.

Automatic Prostate Cancer Detection and Contouring on Digital Histopathology Imaging

Wenchao Han[1,2,6], E. Gibson[7], M. Gaed[5], J. A. Gomez[5], M. Moussa[5], J. L. Chin[4,5], S.E. Pautler[4,5], G. Bauman[2,5], A. D. Ward[1,2,5,6] (research supervisor)

[1]Baines Imaging Research Laboratory, London Regional Cancer Program, Depts. of [2]Medical Biophysics, [3]Pathology, [4]Surgery, [5]Oncology, Western University, [6]Lawson Health Research Institute, London, Ontario, Canada; [7]Centre for Medical Image Computing, University College London, London, UK

Introduction: The prognosis of a prostate cancer patient is known to be related to the volume and Gleason grades of tumours observed in the specimen.[1] The volumes, spatial locations, and extents of tumours are particularly challenging to report quantitatively and are subject to inter-observer variability; this complicates the decision to undertake adjuvant therapy post-prostatectomy.[2] Our goal is to enable quantitative pathology reporting via development of a machine learning-based software system for automatic detection and contouring of cancerous lesions on whole-slide digital histology images obtained from prostatectomy specimens.

Methods: Our experiments were conducted on hæmatoxylin and eosin (H&E)-stained digital histology images scanned at 0.5 µm/pixel from 20 mid-gland tissue sections obtained from 17 patients. From these scans, 4406 sub-images of size $480\mu m \times 480\mu m$ were sampled from all cancerous foci; a further 4406 non-cancerous regions of the same size were randomly sampled. Computation proceeded in two stages: (1) tissue component labeling as nucleus, lumen, and stroma/other tissue, shown in Fig. 1 in black, white, and gray, repsectively; and (2) cancer/non-cancer classification. In stage (1), we used colour deconvolution to isolate the hematoxylin channel. To compensate for staining variability, we used adaptive thresholding to label nuclei, with the threshold optimized according to the number of connected components in the segmentation. Luminal areas were labeled by thresholding in the red-green-blue colour space to find the (near-white) clear slide areas within the prostate boundary. All remaining tissue was labeled as stroma/other. In stage (2), we calculated the proportion of each tissue component, as well as a set of first- and second-order gray level co-occurrence matrix-based texture features from the tissue component label map, as a description of distribution the density and spatial arrangement of different tissue components in each sub-image. We used supervised machine learning (fisher classifier, logistic linear classifier, nearest mean classifier [NMC], uncorrelated quadratic classifier [UDC]) to classify each unit as cancerous or non-cancerous. We measured performance using 5-split randomized cross-validation with 20 repetitions.

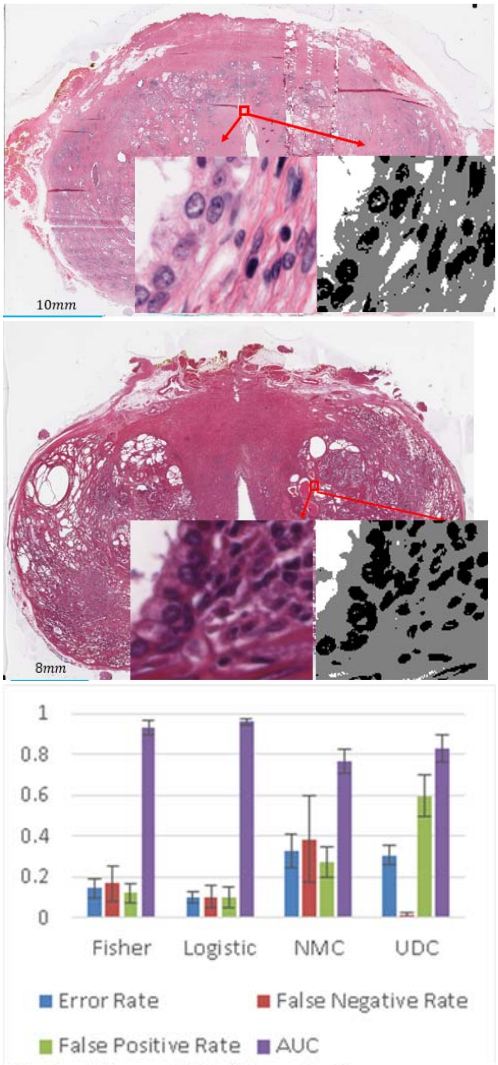

Fig. 1: (Top, middle) Sample tissue component maps from samples with different staining intensities. **(Bottom)** Classification performance metrics.

Results: Our system demonstrated robustness to staining variability in generating tissue component maps (Fig. 1 top, middle). For cancer vs. non-cancer tissue classification, the logistic classifier gave the best results, with an error rate of $11.1\% \pm 0.3\%$, false negative rate of $15.0\% \pm 6.4\%$, false positive rate of $7.26\% \pm 2.4\%$, and area under the receiver operating characteristic curve (AUC) of 0.95 ± 0.02 in randomized cross-validation.

Conclusion: Our adaptive thresholding method yielded tissue component maps that were robust to staining variability. This enabled our system to classify cancerous vs. non-cancerous regions on prostate digital histology imaging with 89% accuracy and 0.95 AUC. Ongoing work includes automatic Gleason grading.

References: [1]L. Egevad et al, Modern Pathology 24(1), 1–5, 2011; [2]T. H. van der Kwast et al, Modern Pathology 24(1), 16–25, 2011.

Development of a Standardization Phantom for Measuring Brain γ-aminobutyric acid (GABA)

Diana Harasym[1], Nicholas Simard[1], Alejandro Santos-Diaz[1], Aimee Nelson[1,2], Michael D. Noseworthy[1,3]
[1]McMaster School of Biomedical Engineering, McMaster University, Hamilton ON. Canada
[2]Department of Kinesiology, McMaster University, Hamilton ON. Canada
[3]Electrical and Computer Engineering, McMaster University, Hamilton ON. Canada

Introduction

γ-aminobutyric acid (GABA) is the most prevalent inhibitory neurotransmitter in the brain. Due to its importance in both normal brain function and in disease, there is considerable interest in reliable measurements. The concentration of GABA is significantly lower than other dominating metabolites, and there are brain regions with concentrations below the 3T detection limit. Thus a standardized quality assurance (QA) measurement protocol is needed. The purpose of this study was to develop a proton magnetic resonance spectroscopy (^{1}H-MRS) phantom for the standardization of GABA with the goal of long term QA measures.

Methods

A 20cm diameter spherical container (polyethylene terephthalate) was used as the housing for five 5cm diameter metabolite-containing spheres (polypropylene) that were fixed in a coplanar fashion in 3% agarose (**Figure 1**). One of the metabolite spheres was used as a reference based on the "Braino" phantom (GE Healthcare, Milwaukee WI). The other four spheres included Braino + 1mM GABA; 1mM of GABA dissolved in H_2O; Braino + 2mM GABA; and 2mM of GABA in H_2O. Two concentrations of GABA were chosen based on the average concentration in the human brain (1mmol) [1], and 2mmol to improve the resolvability of the GABA signals from the rest of the spectra. Single voxel spectroscopy was then acquired for each metabolite sphere, with 5 repetitions, during two sessions. PRESS (TE/TR=35/2000ms, NEX=64, 3x3x3cm voxel, 2048 points) was used for the reference sphere and MEGA-PRESS (TE/TR=68/2000ms NEX=360, 3x3x3cm voxel, 2048 points) for spheres with GABA. Each spectrum was fitted using Tarquin to provide measures of metabolite concentrations.

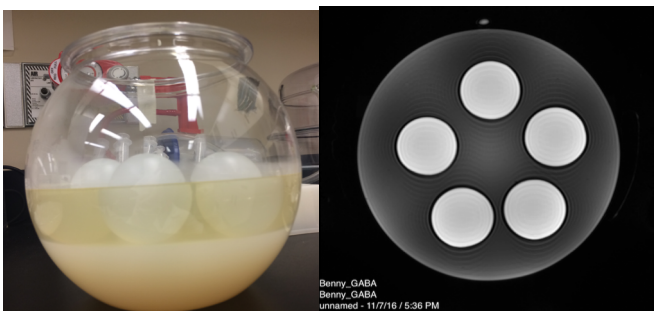

Figure 1: The metabolite spheres embedded coplanar in the center of the phantom (left). MR image of phantom (right).

Results

Spectral analysis showed that concentration ratios between NAA and GABA were far from the expected ratios (**Table 1**). The average ratio between 2mM and 1mM of GABA (with and without Braino) was 1.823, while the expected ratio is 2. There were also differences in the measured concentration between two spheres of the same concentration of GABA, suggesting the fitting algorithm is highly sensitive to B_0 and/or B_1 inhomogeneities. A 2-way ANOVA was performed to check the variability of GABA concentration within a session and between sessions and showed statistically significant differences.

	Average GABA/NAA	Expected GABA/NAA
Braino + 1mM GABA	0.052	0.08
Braino + 2mM GABA	0.088	0.16

Table 1: Average and expected GABA/NAA ratios

Conclusion

The results indicate that there is a difference in concentration within a session, as well as between sessions. This can be caused by B0 and B1 inhomogeneity. Temperature was assumed not to be a factor, as the phantom was kept in the scanner room. GABA concentrations are calculated by the fitting algorithms and should be compared between different fitting programs, such as LCModel and jMRUI. The phantom has promise as an option for long term QA but still needs to be improved further by choosing materials that are magnetic susceptibility matched [2] to reduce B0 inhomogeneity. It is important to have a QA protocol for the detection of GABA to allow for performing multi-centre patient studies, and longitudinal studies. Future work will assess both B0 and B1 differences over time and how these affect GABA consistency in a QA phantom.

References

[1] Keu Y., et al. (2000). Psychiatry Research: Neuroimaging Section, 1000, 169-178.
[2] Wapler S., et al. (2014). Journal of Magnetic Resonance, 242, 233–242.

Spinal cord tracts labelling via diffusion tensor imaging in the cervical spine verified against T1 MRI

Michael Hardisty PhD, Cari Whyne PhD, Stewart McLachlin PhD
Orthopaedic Biomechanics Laboratory, Sunnybrook Research Institute, Toronto, Ontario, Canada

Introduction: Neuronavigation may provide great utility in complex spinal surgeries, particularly when anatomy is distorted by pathology (tumour, degeneration, etc.). Spinal cord tractography generated via diffusion tensor imaging (DTI) can be used to generate streamlines; however, correspondence with white matter tract locations is unclear. The goal of this work was to evaluate the spatial correspondence of DTI tractography with anatomical MRI in healthy anatomy (when anatomical locations can be well defined in T1-weighted images).

Hypothesis: Atlas-based, patient-specific segmentation of the anatomical white matter tracts imaged with T1-weighted imaging will spatially correspond with DTI tractography streamlines.

Methods: A healthy volunteer subject was scanned with a 3T MRI system (Prisma Fit, Siemens Healthcare, Erlangen, Germany). T1-weighted (1x1x1 mm) and diffusion-weighted images (2x2x2 mm, 30 gradient directions) were processed and deformably registered (Spinal Cord Toolbox (SCT)) [1].

Anatomical Processing: Label maps of the left and right lateral corticospinal tracts were generated using an atlas-based approach. Specifically, an existing atlas including white matter tract location probabilities was deformably registered to the T1 volume (SCT) [2, 3]. A probability of 30% was used to define inclusion in the tract label maps. Tract label maps were then transformed to the diffusion space using the vector field determined above.

Diffusion Processing: Tensors were estimated using a weighted least squares algorithm (3D Slicer, Teem Library). Deterministic DTI tractography streamlines (3D Slicer 4.6, SlicerDMRI, seed spacing = 0.5 mm, stopping fractional anisotropy threshold = 0.15, minimum streamline length = 40 mm), were seeded with a single slice of the tract label map at the C3-C4 disc [4]. The generated streamlines were then used to create a new label map volumes (3D Slicer 4.6, Tractography to Mask Image).

The anatomical and diffusion based label maps of the corticospinal tracts were then compared within each vertebral level. Dice's similarity coefficient (DSC) was used to quantify agreement between the streamlines and anatomical white-matter tracts (3D Slicer 4.6, DiceComputation).

Results: The atlas-based lateral corticospinal tract label maps were 2-8 voxels per slice in the anatomic space. Approximately 8 streamlines in both left and right lateral corticospinal tract locations were identified.

There was fair to good agreement at both vertebral levels adjacent to seeding, C3 (DSC = 0.481 & 0.624) and C4 (DSC = 0.588 & 0.543) between the streamlines and atlas-based labels for the left and right corticospinal tracts respectively. At the adjacent segments (C2 & C5), the agreement decreased between the two label maps (C2: DSC = 0.336 & 0.383; C5: DSC = 0.438 & 0.420). Agreement further declined at C6 (DSC = 0.384 & 0.296).

Conclusion: Correspondence between DTI derived streamlines and anatomically segmented label maps of the lateral corticospinal cord tracts were similar to previously reported correspondence for multiple manual tract segmentations on anatomical volumes (DSC ~ 0.5) [2]. As such, this study supports further development of DTI tractography for spine neuronavigation, particularly in surgical applications where the pathology is isolated to small regions and the streamlines required extend only 1 or 2 vertebral levels. This is the first study to explore the use of a white matter atlas to seed deterministic tractography algorithms in the spinal cord. Future work will continue to explore rigorous validation of tractography prior to clinical application, thereby ensuring surgeon confidence and successful adoption.

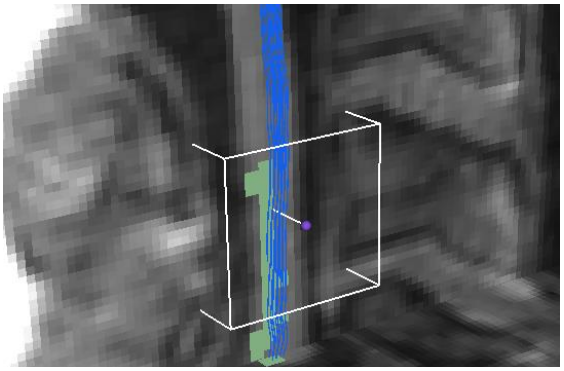

Fig 1. 3D visualization of the right lateral corticospinal streamlines (blue) generated via diffusion tensor imaging compared to the anatomic label map (green) determined from the white matter atlas-based segmentation of T1-weighted imaging.

Acknowledgements: FedDev Ontario and Mitacs.

References: [1] De Leener B et al. NeuroImage (online). [2] Levy S et al. Neuroimage 119: 262-271. [3] Fedorov A et al. Magn Reson Imaging. 30(9):1323-41. [4] Lundell H et al. 69(1): 144-149.

An application of redundant sensors for intraoperative electromagnetic tracking error monitoring

Vinyas Harish*, Eden Bibic, Andras Lasso, Matthew S. Holden, Thomas Vaughan, Zachary Baum, Tamas Ungi, Gabor Fichtinger

Laboratory for Percutaneous Surgery, Queen's University, Kingston, ON, Canada

Introduction. Intraoperative monitoring of electromagnetic (EM) tracking error is a necessary aspect of quality assurance for electromagnetically-navigated interventions. To maximize their effectiveness, intraoperative solutions must be easy to set up and use, readily interpretable, and unobtrusive to the procedure at hand. Jain *et al.* have described a method of characterizing EM tracking error that uses a constellation of redundant EM sensors that are rigidly fixed to a tool in the workspace[1]. Our goal was to develop a practical means of intraoperative error monitoring using redundant sensors. Additionally, we aimed to ensure reproducibility by building on an open-source medical image computing platform.

Methods. For testing purposes, a setup like Ungi *et al.*'s navigated breast cancer surgery setup was used[2]. EM sensors were affixed onto a rigid, rapid-prototyped frame placed around the workspace as well as onto surgical tools such as a needle and cautery (Figure 1). As an indicator of real-time tracking error, we compared the inter-sensor distances and angles to baseline measurements (Figure 2). EM tracking data was relayed to the 3D Slicer platform using the PLUS software toolkit[3]. A 3D Slicer software module was developed to calculate the difference between real-time measurements of the inter-sensor translations and rotations, compared to their respective baseline measurements. These differences were used as indicators of EM tracking error. Two linear support vector machine-based classifiers were developed to use these readings as an indicator for EM tracking error. One classifier was developed using readings from the four sensors on the frame (Classifier A) and another classifier was developed using readings from the two sensors on the cautery (Classifier B).

Results. It was determined that measuring discrepancies in inter-sensor geometry between baseline and real-time measurements was a valid indicator for tracking error. Classifier B outperformed Classifier A as shown in Table 1. The main concern with classifier performance was sensitivity—or ability to warn surgeons of legitimate tracking errors that could compromise surgical outcomes.

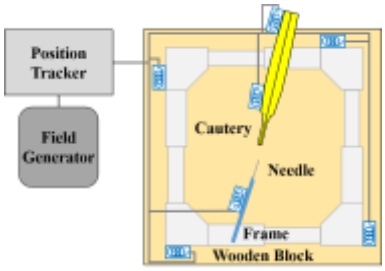

Figure 1. Hardware configuration diagram of a mock breast cancer surgery setup where redundant EM sensors are used to characterize tracking accuracy.

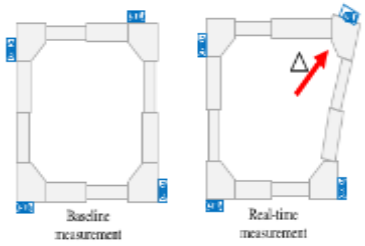

Figure 2. A diagrammatic representation of how measuring the geometry of a constellation of redundant sensors could indicate tracking error (Δ).

Table 1. Classifier Performance Measures

Classifier A		Classifier B	
Specificity	85 %	Specificity	93 %
Sensitivity	42 %	Sensitivity	82 %
Accuracy	63 %	Accuracy	86 %

Conclusion. It was found that tracking errors were better detected by affixing an additional sensor on the tool of interest than placing extra sensors around the tool workspace. While more data is needed to improve classifier sensitivity, the results above demonstrate a proof-of-concept for practical monitoring of EM tracking error using redundant EM sensors. With further improvements, this method may be feasible for clinical use.

References. [1] Jain *et al.*, Patent WO 2011110966 A2, 2011.

[2] Ungi *et al.*, *IJCARS*, 2015.

[3] Lasso *et al.*, *IEEE Trans Biomed Eng.*, 2014.

Automatic Image Registration and Stitching in 3D Ultrasound for Monitoring of Neonatal Post-Hemorrhagic Ventricle Dilation

Andrew Harris, BSc.[1,2], Jessica Kishimoto, BSc.[1,2], Lori Gardi, BSc.[1], Sandrine de Ribaupierre, MD, FRCSC[2], and (Supervisor) Aaron Fenster, PhD., FCCPM [1,2]

[1] *Robarts Research Institute*
[2] *Western University*

Introduction Neonatal post-hemorrhagic ventricle dilation (PHVD) occurs in pre-term babies when the ventricles become obstructed and cerebrospinal fluid (CSF) cannot circulate once produced causing increases in intracranial pressure (ICP). Regular monitoring is necessary to determine the necessity of surgical intervention to treat ICP-related symptoms. Three-dimensional (3D) imaging modalities provide clinicians with important anatomic detail not available when a medical image is confined to 2D. 3D ultrasound (3DUS) is an ideal imaging modality for neonates as no ionizing radiation is used, and the infant can remain in the incubator. For large ventricles, a single 3DUS image often cannot capture the entire ventricular system in a single scan. We hypothesize that if multiple overlapping images are obtained, a 3D panoramic view of a neonate's brain can be automatically created with no user input to provide similar advantages to other 3D scanning modalities, allowing cost effective and accurate monitoring of the infants while still in the incubator.

Methods Our lab previously developed both the technology to create 3DUS images using standard ultrasound equipment, a motorized housing, and a software product which captures 2D ultrasound images and location information for the motor system to generate a 3DUS volume, and this project builds on that work. We have established a registration pipeline including a Powell optimizer, Normalized Cross Correlation metric, and Rigid 3D transform along with a Nearest Neighbour interpolator. A rigid transform was applied as the brain should not deformon scans taken minutes apart. The images were cropped and masked to exclude extraneous or non-image data from the metric calculation. Additionally, the images were subsampled by a factor of 8 to reduce computation time. A large initial step-length was set to ensure the overlap region was traversed in every dimension prior to step-length reduction. The resulting registered moving-image data was blended pixel-by-pixel by a simple averaging filter with the fixed-image data.

Results Results from the working pipeline were obtained in the past week. As shown in Figure 1 the preliminary images tested look qualitatively well aligned and stitched. The NCC value for this particular pair of images was measured at 0.598 after optimization. Additionally, subsampling reduced the regisration time from 120 seconds to 22 seconds, with stitching taking 8 seconds in both cases. This result required no user input other than selecting images that overlap.

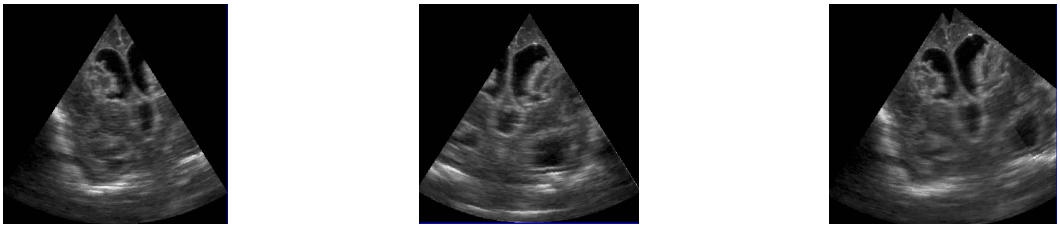

(a) (b) (c)

Figure 1: *Screenshot showing the two images to be registered and combined (a, b) and a stitched image (c) after registration*

Conclusions We are confident that our method for registration and stitching will be validated upon further study. To this end we plan to validate the technique through registered pairs of MRI and 3DUS scans taken within 24 hours from the same patients. The measured volumes will be compared using a linear regression and determined to be correlated if $R^2 > 0.95$. Given previous work comparing 3DUS to MRI in other organs, we would expect some significant differences in the registered surfaces, specifically in the lateral most margins of the images, but this has yet to be proven in the neonatal head.

Effect of Parkinson's disease and dopaminergic therapy on intra- and inter-connectivity of brain networks

Nole Hiebert, Lorina Naci, Adrian Owen, and Penny A. MacDonald
University of Western Ontario
Supervisors: Drs. Penny A. MacDonald and Adrian Owen

Introduction
Parkinson's disease (PD) is an extremely complex, heterogeneous neurodegenerative illness with a broad range of possible motor and non-motor symptoms. The neural changes underlying most PD symptoms and signalling disease progression, however, remain poorly understood. Further, PD biomarkers are nonexistent and there is no cure or disease-modifying therapies (DMTs) for this progressive illness. Though dopamine replacement medications treat many motor signs, dopamine-independent motor and non-motor symptoms, especially cognition, lack effective therapies, becoming more incapacitating with advancing disease. Availability of validated and consistent biomarkers, which are sensitive at the individual level, is imperative to the development of cures or DMTs. The overarching aim of this project is to examine changes in functional networks using 3T functional magnetic resonance imaging using patients with PD and healthy controls tested on and off dopaminergic therapy. The pattern of functional network changes between patients at different stages of disease and compared to healthy controls may provide a biomarker of PD and PD disease progression sensitive on an individual level.

Hypothesis
It is expected that patients with PD will have lower functional connectivity within and between the default mode (DMN), fronto-parietal (FP) and dorsal attentional networks (DAN), compared to healthy controls. we expect that dopaminergic therapy will remediate functional connectivity differences and as PD progresses, there will be a larger difference in connectivity between patients tested on and off dopaminergic therapy.

Materials and Methods
Patients with PD were tested on two consecutive days, once on their prescribed dose of dopaminergic therapy and once off. Healthy controls were also tested on two consecutive days, once on 100/25 mg of levocarbidopa and once on an equal volume of placebo. During each testing day, participants were exposed to a naturalistic paradigm that involved viewing a segment of a movie, followed by a resting state scan. On the second day, a different movie was shown and was also followed by a resting state protocol. The order of protocols was counterbalanced across participants. Data analysis involved examining the correlation between activation in regions of interest (ROIs) within and between DMN, FP, DAN, as well as auditory (AUD) and visual (VIS) sensory networks.

Results
PD patients were found to have a significantly lower connectivity ($p<0.05$) within DMN and FP functional networks and trending in DAN and AUD networks compared to controls, whether patients were watching the film clip or resting. Between-network functional connectivity was also significantly reduced in FP, DAN, and AUD networks in patients with PD compared to controls. Dopaminergic therapy remediated these differences in patients with PD. Lastly, duration of PD positively correlated with ON-OFF medication differences in functional connectivity.

Discussion and Conclusions
Functional connectivity within and between key networks (DMN, FP, DAN) are significantly reduced in patients with PD compared to controls. In addition, differences in PD progression can be elucidated based on the ON-OFF connectivity differences in functional connectivity. These results shed light on a possible PD biomarker for disease presence and severity, providing a necessary step toward improved diagnosis and management of PD.

Design of Ultrasound-Compatible Vascular Flow Phantoms with Tortuous Vessel Geometries

Chung Kit Ho, Adrian J. Y. Chee, Billy Y. S. Yiu, and Alfred C. H. Yu
Schlegel-UW Research Institute for Aging, University of Waterloo, Waterloo, ON, Canada

Introduction. It remains challenging to develop tortuous flow phantoms that are acoustically compatible with ultrasound imaging. There is a critical need for these tortuous phantoms because their corresponding flow patterns are more realistic than those of idealized straight-tube vessel models. Indeed, these phantoms can serve well as investigative tools for 3-D flow imaging developments. To address this methodological need, we have devised a new engineering protocol that is based on the integrative use of rapid prototyping and investment casting principles. A patient-specific intracranial aneurysm model is leveraged as an exemplar demonstration of our new tortuous phantom design framework.

Methods. Our framework develops tortuous flow phantoms according to the following steps. First, a computer-aided design (CAD) model of the tortuous vasculature is created based on an arbitrary vascular geometry or a medical imaging dataset (such as a computed tomography data volume) obtained from a patient. Second, supporting components such as flow connectors are added to the CAD model. After that, a 3D printer is used to create a physical replicate of the developed CAD model. Subsequently, the vascular replicate is mounted onto a phantom box, and polyvinyl alcohol (PVA) cryogel is casted around the replicate to mimic surrounding tissues. Subsequently, the PVA cryogel is allowed to congeal through multiple freeze and thaw cycles. At last, chloroform is used to remove the embedded replicate to create a void that resembles the lumen. The phantom was put into operation with a supporting flow circuit, and ultrasound imaging experiments were performed.

We tested the use of our developed phantoms by performing color-encoded speckle imaging (CESI) experiments to visualize the complex flow dynamics within the cerebral aneurysm. Developed by our lab earlier [1], CESI is a duplex visualization technique that renders complementary information on flow speed and flow trajectory, the latter of which is useful for determining flow direction in cases with Doppler aliasing. CESI frames were acquired and beamformed at high frame rates of 3,333 fps over multiple time-synchronized scan planes.

Results. As illustrated by B-mode images from two orthogonal planes (see Fig. 1), ultrasound-compatible cerebral aneurysm phantoms with geometry specific to an actual patient can be fabricated for the first time. Lumen dimensions were found to be consistent with the CAD model. The spatiotemporal evolution of flow patterns inside our aneurysm phantom was rendered using CESI (corresponding cineloops will be presented at the meeting). Results confirmed that the intra-aneurysm flow dynamics are 3-D in nature. Persistent recirculation was observed, and the vortex center was found to shift in position over a cardiac cycle, indicating 3-D flow recirculation inside an aneurysm.

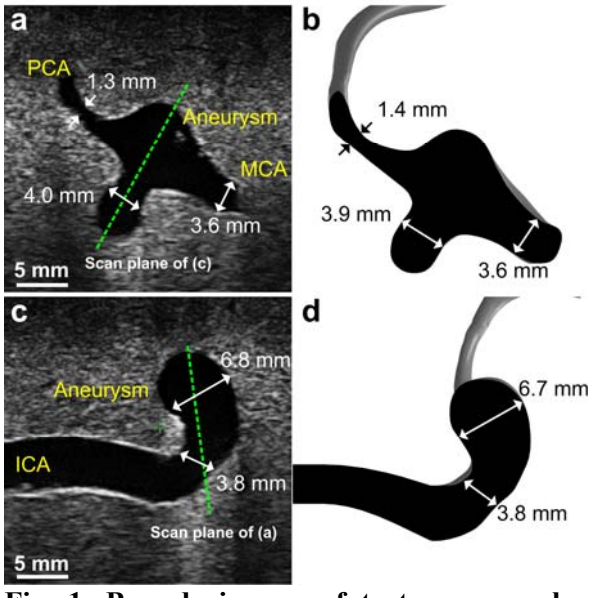

Fig. 1. B-mode images of tortuous vascular phantom acquired at orthogonal scan planes. *Left: Images taken from the flow phantom using clinical scanner. Right: The same scan-planes segmented from the CAD model.*

Conclusion. The tortuous flow phantoms developed using our reported protocol are applicable to performance investigations of new vascular imaging methods such as CESI. This new design protocol may be readily applied to develop phantoms for different vascular geometries, and in turn, enable investigations to pursue innovations in ultrasound flow imaging paradigms that track complex hemodynamics, especially in cases with significant flow disturbance due to its tortuous geometry. Other application development efforts in vascular ultrasound may also leverage these tortuous phantoms as calibration and training tools.

Reference. [1] BYS Yiu, ACH Yu. *Ultrasound Med Biol*, 2013; 39: 1015-1025.

Non-invasive Monitoring of Brain Temperature during Rapid Selective Brain Cooling by Zero-Heat-Flux Thermometry

Marjorie Ho, MD[1, 2*], Mohammad Fazel Bakhsheshi, PhD[1, 2*], Lynn Keenliside[1], Ting-Yim Lee, PhD[1, 2, 3]
[1] Imaging Program, Lawson Health Research Institute, London, ON, Canada. [2] Imaging Research Laboratories, Robarts Research Institute, London, ON, Canada.
[3] Department of Medical Imaging and Biophysics, The University of Western Ontario, London, ON, Canada. *These authors contributed equally to this work.

INTRODUCTION: Selective brain cooling (SBC) can minimize systemic complications associated with whole body cooling but maximize neuroprotection. Recently, we developed a non-invasive, portable and inexpensive system for selectively cooling the brain rapidly and demonstrated its safety and efficacy in porcine models. However, the widespread application of this technique in the clinical setting requires a reliable, non-invasive and accurate method for measuring local brain temperature so that cooling and rewarming rates can be controlled during targeted temperature management. In this study, we evaluate the ability of a zero-heat-flux SpotOn™ sensor (3M™ St Paul, Minnesota), mounted on three different locations, to measure brain temperature during selective brain cooling in a pig model. Computed Tomography (CT) was used to determine the position of the SpotOn™ patches relative to the brain at different placement locations.

METHODS: Experiments were conducted on two juvenile pigs. Body temperature was measured using a rectal temperature probe while brain temperature with an intraparenchymal thermocouple probe. A SpotOn™ sensor patch was placed on the pig's head at three different locations (Fig. 1): 1-2 cm posterior (Location #1, n=1), central (Location #2, n=1); and 1-2 cm anterior and lateral to the bregma i.e., supraorbitally on the forehead (Location #3, n=1).

RESULTS: The SBC system was able to rapidly cool the brain temperature to 33.7 ± 0.2°C within 15 minutes, and maintain the brain temperature within 33-34°C for 4-6 hours before slowly rewarming to 34.8 ± 1.1°C from 33.7 ± 0.2°C in 3 to 5 hours while keeping the core body temperature (as per rectal temperature probe) above 36°C (Fig. 3). We measured a mean bias of -1.1°C, -0.2°C and 0.7°C during rapid cooling in induction phase, maintenance and rewarming phase, respectively. Amongst the three locations, location #2 had the highest correlation (R^2 = 0.77) between the SpotOn™ sensor and the thermocouple probe (Fig. 2)

CONCLUSIONS: This non-invasive method of measuring intracranial temperature using the SpotOn™ sensor placed on the center of the head provides a good measurement of brain temperature in comparison to the invasive needle probe in our SBC experiments on pigs. This location has the highest correlation with an R^2 value of 0.77.

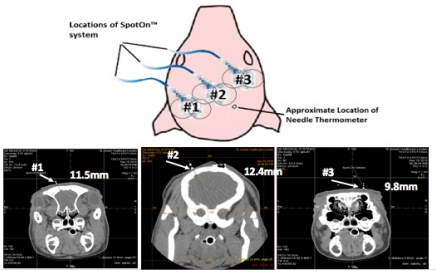

Fig 1.

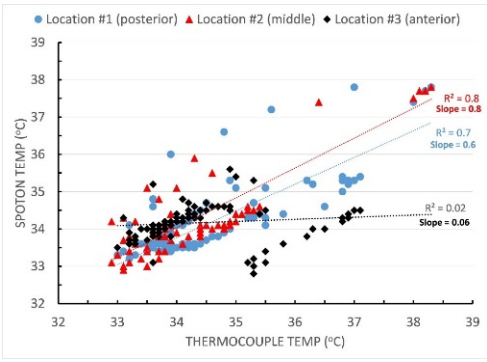

Fig 2.

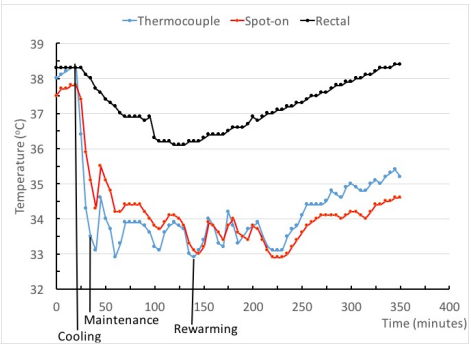

Fig 3.

Fig 1. Locations (#1-3) of the SpotOn™ sensor and of thermocouple probe to measure brain temperature.
Fig 2. Correlation plot comparing temperature readings using thermocouple probe and SpotOn™ sensor at three different locations on the pig's head. Each symbol represents data from one of three locations.
Fig 3. Measured brain, rectal and esophageal temperature over time during baseline, cooling and rewarming phase under control by the SBC system. Temperature data were obtained from thermocouple probe implanted in the brain and inserted into the rectum, and SpotOn™ sensor located centrally on the head (location #2 in Fig. 2).

Assessing Technical Competence in Simulated Colonoscopy Using Joint Motion Analysis

Matthew S. Holden[1], Chang Nancy Wang[2], Kyle MacNeil[1], Ben Church[1], Lawrence Hookey[2], Gabor Fichtinger[1], Tamas Ungi[1]

[1]School of Computing, Queen's University, Kingston, ON, Canada
[2]Department of Medicine, Queen's University, Kingston, ON, Canada

Category: Cancer; Theme: Technical Development; Research Supervisor: Gabor Fichtinger

INTRODUCTION: Colonoscopy is a commonly used image-guided therapy to treat many different types of disease in the colon. Because of the spatial awareness required to perform colonoscopy, it is critical that trainees master basic colonoscope manipulation techniques at an early stage of training [1]. Training on low-fidelity simulators allows trainees to master manipulation technique prior to more complex training scenarios. What remains a challenge, however, is assessing how well a trainee has mastered the manipulation techniques. In this work, we evaluate how well joint motion analysis can be used to determine whether an operator has mastered basic colonoscope manipulation techniques.

METHODS: Twenty-eight novice medical students and nine expert gastroenterologists navigated a previously validated, low-fidelity colon model [2] using a standard colonoscope (Figure 1). Participants' hands, forearms, and upper arms were tracked using position and orientation sensors (Ascension TrakStar, Northern Digital Inc.). Using the trackers and a series of calibration exercises, the angles of each wrist and elbow could be determined. We evaluated whether these angle times series could be used to discriminate colonoscope manipulation skill between novices and experts. Analysis was performed using the Perk Tutor software (www.perktutor.org).

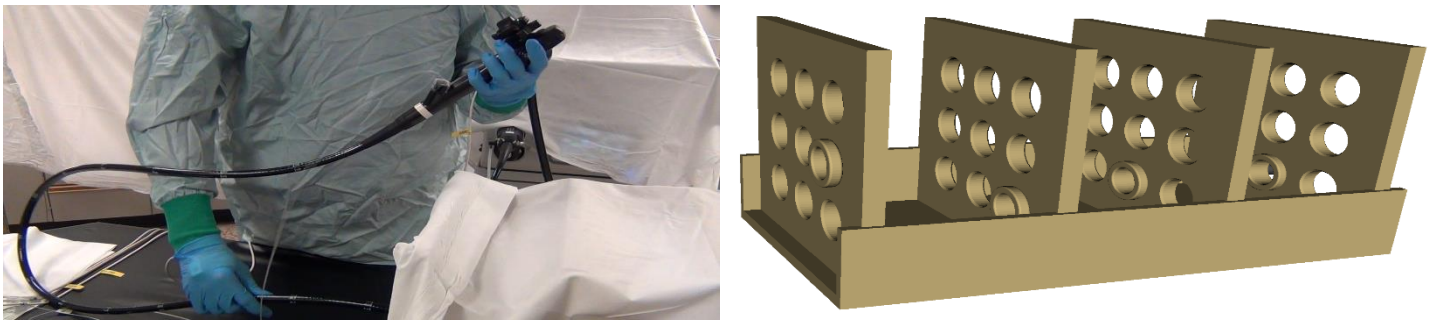

Figure 1: Photograph of operator performing simulated colonoscopy (left), and visualization of the low-fidelity colon model (right).

RESULTS: Novices spent significantly more time than experts performing the navigation tasks. Joint motion analysis revealed, however, that novices spent a significantly lesser proportion of time in extreme ranges of motion for the majority of joints. On the other hand, novices entered into extreme ranges of motion significantly more times than experts for the majority of joints.

CONCLUSION: Joint motion analysis demonstrates promise as a way of quantitatively measuring colonoscope manipulation skill, showing differences between novice and expert groups. More analysis is required, however, to fully analyze these patterns in join motion and to show whether this analysis can be used as an indicator of overall colonoscope manipulation competence.

ACKNOWLEDGEMENTS: This work was in part funded by Cancer Care Ontario through Applied Cancer Research Unit and Research Chair in Cancer Imaging grants.

[1] J. B. Marshall, "Technical proficiency of trainees performing colonoscopy: A learning curve," Gastrointestinal Endoscopy, vol. 42, no. 4, pp. 287-291, 1995.
[2] C. M. Walsh, *et al.*, "Gastrointestinal Endoscopy Competency Assessment Tool: development of a procedure-specific assessment tool for colonoscopy," Gastrointest. Endosc., vol. 79, no. 5, pp. 798-807, May 2014.

Calibration light source for optical molecular imaging systems

David W Holdsworth,[1,2,3]
Development of Novel Therapies for Bone and Joint Diseases Consortium
[1]Department of Surgery, Western University, [2]Robarts Research Institute, [3]Department of Medical Biophysics, Western University, London, Ontario, Canada

Introduction: The widespread availability of bench-top optical imaging systems for use with small animals and cell cultures has resulted in the rapid growth of research involving bioluminescent and fluorescent labels.[1,2] While these systems often provide values in quantitative units of radiance or intensity, there is typically no means for routine quality assurance. This makes it difficult to compare values between different units, or to maintain confidence in reported values following maintenance or system upgrades. It can also be challenging to ensure that light intensity values are being reported accurately over different fields of view or acquisition parameters. Specialized calibration and monitoring devices have been previously described,[3,4] but no routine solution is available for monitoring the performance of optical imaging systems. We describe the first implementation of an LED-backlit thin-film transistor (TFT) display for use as an optical imaging calibration device. The light intensity is controlled by pulse-width modulation of the LED backlight, providing several orders of magnitude of control over display radiance. This device can provide routine quality assurance for laboratory fluorescence and bioluminescence optical imaging systems.

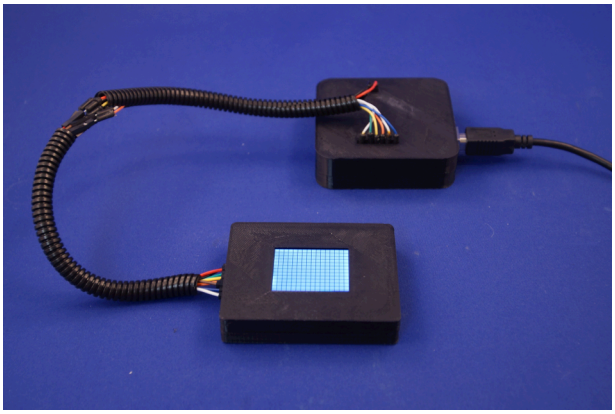

Fig. 1: Low-intensity optical calibration device with controller.

Methods: The calibration device is based on a 1.8" diagonal LCD TFT display (ST7735R) with 128x160 pixel resolution and an 18-bit (262,144) colour display (Fig. 1). The display is controlled by a dedicated microcontroller system (Arduino Uno), which uploads image data and controls the pulse-width and duty cycle for the transistor-controlled LED backlight display. The display unit is housed in a 1.5 cm thick plastic case, which allows it to be positioned face-up or inverted, depending on the imaging geometry of the system being tested. Custom software allows the operator to select either a uniform image, or a prescribed pattern (such as a regularly spaced grid). Illumination is controlled by selecting an interval for the backlight to be illuminated (i.e. the ON interval) and a period during which the backlight is off (i.e. the OFF interval). The ON interval can be selected from between 10 μs and 10,000 μs, while the OFF interval can be selected from between 1 ms and 300,000 ms. This approach provide a very wide range of effective optical intensities during time exposure imaging of up to 5 minutes in duration. Light output is calibrated with a photometer (J16, Tektronix) in units of irradiance (μW cm^{-2}; J6502 probe) and luminance (candelas cm^{-2}; J6503 probe). Testing was carried out in a commercially available optical imaging system (FX-Pro, Carestream) using standard image acquisition settings.

Results: Images of both geometric patterns and uniform intensity distributions were acquired and analyzed. The optical imaging system exhibited a high degree of uniformity over four orders of magnitude (slope 9.835 nW^{-1} cm^2 SR), $p < 0.0001$). The optical calibration system was stable and easy to use, providing the option of routine weekly quality assurance within a small-animal imaging facility.

Conclusions: An optical calibration system, based on a conventional backlit TFT display has been developed and implemented for calibration of laboratory optical imaging systems. The device that was tested (Kodak Carestream FX-Pro) exhibited excellent linearity over nearly four orders of magnitude.

References: **1.** Graves et al. "Fluorescence molecular imaging of small animal tumor models," *Curr Mol Med*. 2004; 4:419-430; **2.** Klose et al. " Bioluminescence tomography with CT/MRI co-registration," *Conf Proc IEEE Eng Med Biol Soc*. 2009; 2009:6327-6330; **3.** Bentz et al. "Fabrication and application of heterogeneous printed mouse phantoms for whole animal optical imaging," *Appl Opt*. 2016; 55:280-287; **4.** Diep et al. "Three-dimensional printed optical phantoms with customized absorption and scattering properties," *Biomed Opt Express*. 2015; 6:4212-4220.

Intra-operative gamma probe using a 3D-printed focused collimator

David W Holdsworth,[1,2,3] Hristo N Nikolov,[2] and Steven I Pollmann[2]
Development of Novel Therapies for Bone and Joint Diseases Consortium
[1]Department of Surgery, Western University, [2]Robarts Research Institute, [3]Department of Medical Biophysics, Western University, London, Ontario, Canada

Introduction: It is important during cancer surgery to identify and remove cancer cells that may have metastasized to the lymphatic system,[1] as well as cells near the margin of the tumour.[2] Recent developments in radiochemistry and nuclear imaging have resulted in the possibility of intra-operative gamma imaging of radiolabeled tissue.[3] In these procedures, radiation can be detected either by a small gamma probe (close to the tissue surface) or by an intra-operative gamma camera (which requires a longer exposure time). We have developed a real-time gamma probe that can detect radiation from a small region of interest, located several cm away from the probe face, through the use of a highly focused collimator. This approach offers the potential to improve the identification and localization of cancerous cells, facilitating more accurate biopsy data and more complete surgical resection.

Methods: Recent advances in 3D metal printing have made it possible to produce devices with very small feature size (i.e. <200 µm) in solid metal,[4] including dense metals such as tungsten. We take advantage of this new fabrication technology to produce a highly convergent collimator, with high spatial discrimination and high efficiency. This collimator can be coupled to any conventional gamma ray probe to provide real-time "spot" detection of radioactive tracers during intraoperative surgery and biopsy. The collimator design of Fig. 1 was fabricated in solid stainless steel (316L) using a commercial additive manufacturing system for selective laser melting (Renishaw AM125). Fabrication of the septa produced structures as thin as 250 µm. The collimator was designed to be attached to a conventional gamma probe (Ludlum Model 44) consisting of a 2.5 cm diameter, 2.5 cm thick NaI crystal coupled to a 2.5 cm diameter photomultiplier tube. A dedicated pulse counting circuit was designed, based on a programmable microcontroller (ATMEGA 2560).

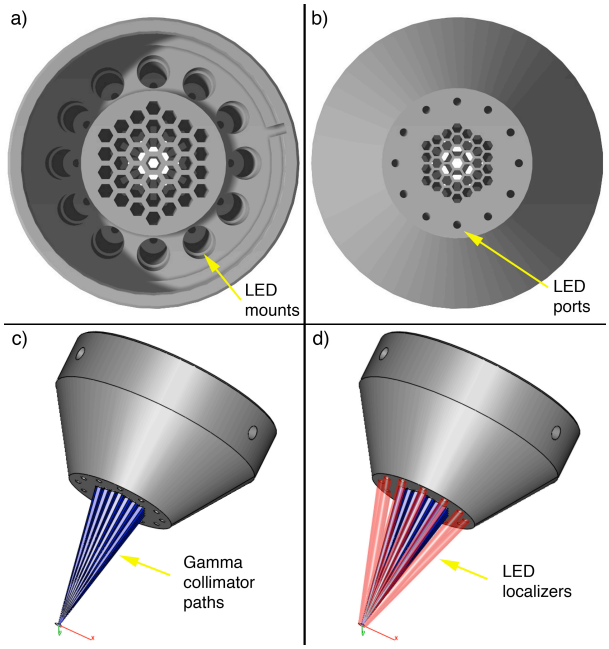

Fig. 1: 3D-printed gamma collimator design, illustrating co-axial optical localizers and close-packed collimator paths.

Results: Results of spatial resolution mapping show that the prototype collimator is capable of high sensitivity detection of 59 kev gamma rays (> 3000 CPM μCi^{-1}), while maintaining excellent spatial resolution (FWHM < 5.5 mm). Modifying the collimator hole design from simple cylinder to tapered hexagonal channels increased the efficiency of collection by over 70%, resulting in an overall geometric efficiency of 48% (with no increase in FWHM).

Conclusions: We have used 3D design and additive manufacturing to create a prototype gamma spot probe, which demonstrates excellent sensitivity and spatial resolution. The probe that we have developed has many applications during cancer surgery and biopsy, where it can be used to provide real-time localization and quantification of radiopharmaceutical tracers.

References: **1.** D. Hellingman et al, "Detecting near-the-injection-site sentinel nodes in head and neck melanomas with a high-resolution portable gamma camera," Clin Nuc Med **40**, e11-16 (2015); **2.** P. DeJean et al. "An intraoperative 3D ultrasound system for tumor margin determination in breast cancer surgery," Med Phys **37**, 564-570 (2010); **3.** S. P. Povoski et al., "A comprehensive overview of radioguided surgery using gamma detection probe technology," World Journal of Surgical Oncology **7**, 11 (2009); **4.** M. G. Teeter et al., "Metrology test object for dimensional verification in additive manufacturing of metals for biomedical applications," Journal of Engineering in Medicine **229**, 20-27 (2015).

Characterization of Metal Artifacts using a 3D-Printed Grid Phantom with an Embedded Hip Implant

Gregory Hong,[1,2] Matthew G Teeter,[1,2,3] Jaques S Milner,[1] Steven I Pollmann,[1]
Maria Drangova[1,2] David W Holdsworth,[1,2,3]
Development of Novel Therapies for Bone and Joint Diseases Consortium
[1]Robarts Research Institute, [2]Department of Medical Biophysics, [3]Department of Surgery,
Western University, London, Ontario, Canada

MRI is commonly used to detect soft-tissue damage associated with orthopedic implants; however, the difference in magnetic susceptibility between metals and tissue gives rise to substantial magnetic field inhomogeneity, leading to image artifacts. Phantom analysis of metal artifacts with geometric markers has been limited to planar phantoms, which allows for characterization of only a single slice.[1] Our group has previously developed a 3D-printed phantom for volume characterization of inherent field inhomogeneity using 3-dimensional grids of fiducial markers, which we now adopt to address the need for evaluation of metal artifact reduction (MAR) techniques. We present a phantom that provides fiducial markers completely surrounding an embedded object, facilitating volumetric characterization of in-plane and through-plane artifacts. We demonstrate the phantom design with an embedded hip implant, comprised of a titanium stem (χ=182[2]) and cobalt-chrome head (χ=1300[2]).

Methods: This design is based on our previous work in creating a geometric calibration phantom for MRI and CT[3]. The phantom was created using computer-aided design with a rectangular pattern of repeating cells consisting of a single 4.5 mm spherical marker and 0.8 mm supporting walls. To enable an implant to be embedded into the 3D phantom, the grid phantom must be fabricated from several interlocking conformal modules. Tight fitting "clips" were designed and integrated into the interfaces of the separate modules, with three modules used for the hip implant evaluated. The geometry of the implant was derived from a micro-CT image (eXplore Ultra, GE Medical) at 120 kVp with 300 µm voxels. This implant geometry was then subtracted from the modules to create a conformal cavity. The assembled phantom was then inserted into a cylinder containing CuSO4 solution and evacuated of air. Axial images were acquired with 3 mm slices separated by 3.5 mm, bisecting the planes of spherical markers and the midpoints between them, using a FSE-STIR (3T, knee coil, TE=50 ms, matrix=320x192, 40 slices, NEX=2, BW=41.67). In-plane distortions were analyzed by comparing the spacing of the centroids in the image with the known spacing of the markers and through-plane distortions were observed through the presence or absence of markers, depending on the slice location.

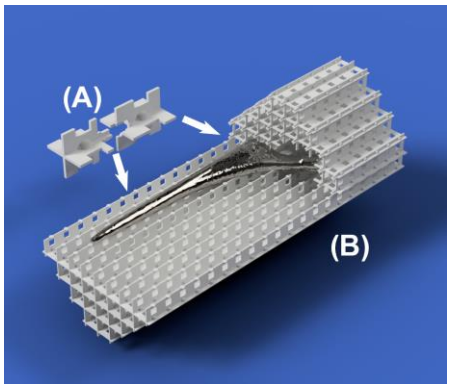

Figure 1: Rendering of clip design (A) and hip embedded grid phantom (B)

Results: Image analysis of the spherical markers shows in-plane deviation from their expected spacing throughout the axial slices, with minor deviations surrounding the titanium stem and severe in-plane and through-plane distortions surrounding the cobalt-chrome head.

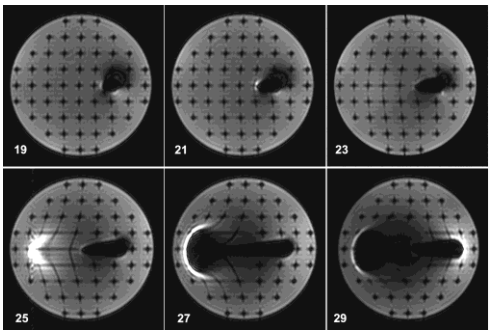

Figure 2: Axial images showing the distortions of the phantom grid near implant

Conclusions: The ability to characterize and evaluate metal artifacts is crucial for the validation and advancement of novel MAR techniques. We present a cost-effective, customizable solution that provides quantitative geometric measurements across a three-dimensional volume. The regular 3D array of markers allows for in-plane and through-plane distortions to be easily observed in image slices. In-plane marker deviation can be analyzed to characterize distortion, including regions of the image in close proximity to the metal object. The design flexibility granted by fabricating the grid in parts allows for a wide array of embedded test subjects, with minimal loss of fiducial markers. Future research in metal artifact reduction can make use of this phantom design to robustly and inexpensively test and validate novel techniques, which will improve development in the field.

References: **1.** Koff, M. F. *et al.* Quantifying image distortion of orthopedic materials in magnetic resonance imaging. *JMRI* **38**, 610-618, doi:10.1002/jmri.23991 (2013). **2.** Smith, M *et al.* Characterizing the limits of MRI near metallic prostheses. *Magnetic resonance in medicine* **74**, 1564-1573, doi:10.1002/mrm.25540 (2015). **3.** Holdsworth, D. W. *et al.* Geometric Calibration Phantom for MRI and CT. *In: Proceedings of the 2016 Imaging Network Ontario Symposium; 2016* **P43**.

Color calibration for Digital Pathology Scanners

Mahdi S. Hosseini[a,b*], Dohyoung Lee[a], Konstantino N. Plataniotis[a], Alfonso Ribes[b], Savvas Damaskinos[b], Jasper A.Z. Brawley-Hayes, Andy Myles, Frank Yang, and Patrick Myles

aThe Edward S. Rogers Sr. Department of ECE, University of Toronto, Toronto, ON M5S 3G4, Canada

bHuron Digital Pathology, 550 Parkside Drive, Waterloo, Canada, N2L 5V4

*Mahdi S. Hosseini, E-mail: mahdi.hosseini@mail.utoronto.ca

Introduction. Whole slide imaging (WSI) scanners in digital pathology (DP) use high resolution imaging optics to acquire submicron resolution images of organ tissues on glass-slides. Accurate color representation of DP images is critical for clinical decisions to distinguish the color features in stained glass slide. Unfortunately many scanners do not provide "true" color representation of the tissue due to spectral content of illumination and sensor setup. The objective of this abstract is to address the color calibration in DP scanners for accrate color transformation solutionin digital pathology.

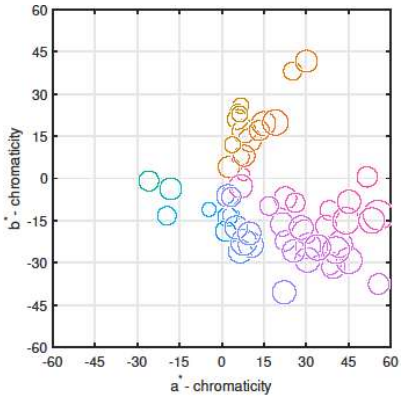

(a)

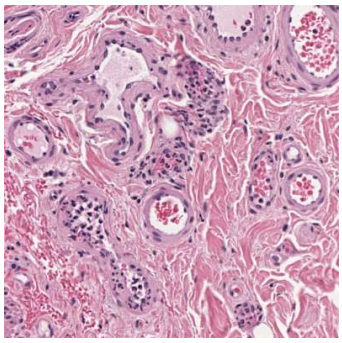

(b)

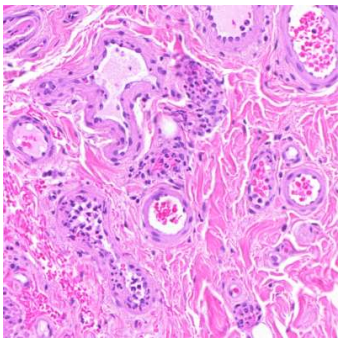

(c)

Figure.1. (a) color chromaticity distribution of 60 color stained slides, (b) sample color image acquired from DP scanner, (c) calibrated color

Methods. Data were is acquired with Huron's TissueScope LE120 Slide Scanner in super-resolution image mode. The brightfield scanner contains a well calibrated sensor that supports up to 0.25µm/pixel at 40X optical magnification. We selected 60 diverse tissue slides (mostly H&E) from in-house repository which contains a wide variation of tissue types, stain colors, sizes, and distribution density. The distribution of colors of selected tissues is shown in Figure.1(a) in chromaticity plane. Two coordinates a* and b* are correlates for the two opponent red-green and yellow-blue chroma axes, respectively [1]. The color distribution indicates the collected data mostly dominate in the blue-purple and pink-red tissue color districution. This distribution complies with the H&E color appearance found in pathology laboratories based on color staining protocols. We use the aforementioned colorspace distribution for calibration purpose. The is selected from An IT8.7/1 master target calibration slide [2] was mounted on a glass slide and scanned. A calibration method is then performed in RGB colorspace using a least square minimization [3] to build a color map from the source image to target image. The linear mapping is used after for color correction of the tissue scans.

Results and Concluding Remarks. We test the color mapping on a generic 2D camera

integrated within the scanner for 40X imaging. An image example is shown in Figure.1(b) of an H&E slide where the color values deviate from the ground-truth values. The corrected color image is shown in Figure.1(c) where the projected colors are much closer to the H&E representation.

References.[1] Konstantinos Plataniotis and Anastasios N Venetsanopoulos, Color image processing and applications, Springer Science & Business Media, 2013. [2] Wolf Faust IT8.7/1 Ektachrome, Type 3, L* a* b* (light D50, viewing angle 2) http://www.coloraid.de [3] Nguyen Ho Man Rang, Color mapping from camera-absed color calibration and color transfer, PhD dissertation, National University of Singapore, 2016.

Multi-Parametric MRI at 7 T for Differentiation of MS and Age-Related White Matter Lesions

Zahra Hosseini,[1,2] David Rudko,[3] Jacob Matusinec,[4] Marcello Kremenchutzky,[5] Ravi Menon,[2,6] Maria Drangova[1,2,6]

[1]Biomedical Engineering Graduate Program, UWO, [2]Imaging Research Laboratories, Robarts Research Institute, [3]Brain Imaging Center Montreal Neurological Hospital and Institute, McGill University, Quebec, Canada, [4] Medicine, Schulich School of Medicine & Dentistry, UWO, [5]Department of Clinical Neurological Sciences, Schulich School of Medicine and Dentistry, UWO [6]Department of Medical Biophysics, Schulich School of Medicine and Dentistry, UWO.

Introduction: MRI is conventionally applied for identifying multiple sclerosis (MS) white matter lesions (MSLs) based on T_2-weighted and FLAIR images. However, the number and volume of MSLs have shown only mild correlation with clinical symptoms. This may be due to the fact that the number of white hyperintensities increases normally with age. Normal age-related lesions (ARLs) can confound a diagnosis of MS when using the McDonald criteria.[1,2] Recently, multi-parametric MR images have shown promise for allowing improved visualization of active lesion substructure.[3-8] In this work we analyzed multiparametric 7 T MRI data at baseline and follow-up visits for patients and matched controls with ARLs to extract information on lesion sub-type.

Methods: ***Imaging:*** Five female relapsing-remitting MS patients and five gender and age-matched, healthy controls with ARLs were scanned at two separate time points four months apart using 7 T MRI and were retrospectively enrolled in our study. The MR imaging protocol included a six-echo GRE sequence (0.5 x 0.5 x 1.25 mm^3, TR/TE/ESP (ms): 40/3.77/4.01; FA=13°; GRAPPA R=2), a MP-FLAIR sequence and a T_1-weighted MPRAGE sequence. The MPRAGE and FLAIR acquisitions used a 1.0 mm isotropic resolution. ***Multi-Contrast Semi-Quantitative Image Processing:*** Using a non-linear least squares fitting algorithm, R_2^* maps were then calculated based on the multi-echo GRE magnitude data. In parallel, multi-echo GRE phase images were unwrapped, frequency shift maps were calculated, and a preconditioned conjugate gradient algorithm was applied to calculate quantitative susceptibility (QS) maps. All images were then registered[9] to MPRAGE data at the baseline for each participant. All images were also normalized to baseline. ***Data Analyses:*** 7 T FLAIR images were used for manual segmentation of ARLs and MS white matter lesions. The masks derived form this segmentation were then applied to calculate the mean R_2^* and QS value of each lesion at each time points. Additionally, appearance of the lesions on each contrast and their sizes were assessed. ***Statistical analyses:*** Lesion count and size was compared using an unpaired t-test. The difference between the normalized inter-visit lesion intensity changes was analyzed using multiple t-test (p-value <0.05 significant).

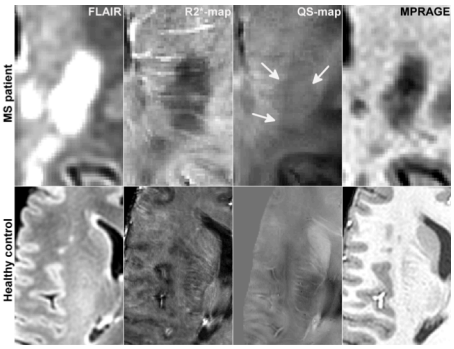

Fig. 1: Representative examples of MSL and ARL on multi-parametric MRI data. R2*- and QS-maps show noticeable differences, while the lesion signal on the MPRAGE and FLAIR data also varies.

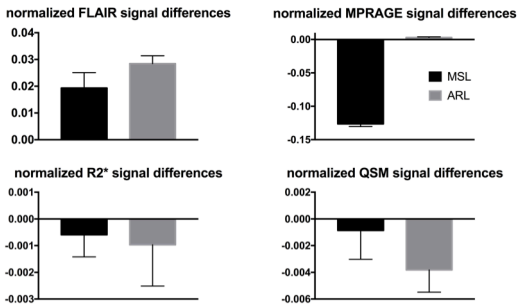

Fig. 2: Changes in mean lesion signal for MSL and ARL. MPRAGE signal change over two visits is opposite for MSL compared to ARL ($p<0.0001$).

Results: 181 ARLs and 420 MSLs were analyzed in our subject cohort. The average size of the ARLs was 51 mm^2 while the average size of the MSLs was 69 mm^2 ($p=0.2738$). Figure 1 illustrates examples of MSL and ARL appearance on the four 7 T MRI contrasts. MSLs and ARLs have the same general appearance on both FLAIR and MPRAGE contrasts, but have quite different contrast on the R_2* and QS maps. This may be due to the benign nature of ARLs. Figure 2 shows the normalized inter-visit signal change for MSLs and ARLs. Inter-visit variation on MPRAGE was significantly higher in MSLs compared to ARLs. The inter-visit signal change in the other contrasts (QSM, R2* and FLAIR) was not significant.

Discussion and Conclusion: In this work, we present an analysis of multi-contrast, 7 T MR images of MS patients and controls with ARLs. We report qualitative and quantitative differences between MSLs and ARLs. Characterization of MSLs using different MR image contrasts has previously been presented.[5,10] Our findings add to the prior literature to gain better understanding of the MR imaging biomarkers of MSLs and ARLs.

References: [1] Polman et al., DOI:10.1002/ana.20703[2] Polman et al., DOI: 10.1002/ana.22366. [3] Sinnecker et al., DOI:10.1212/NXI.0000000000000259. [4] Rudko et al., DOI: 10.1148/radiol.14132475. [5] Absinta et al., DOI:10.1002/ana.23959. [6] Tan et al., PMID: 10871010. [7] Grabner et al., DOI: 10.1002/jmri.22452. [8] Kau et al., DOI: 10.1007/s00330-013-2791-4. [9] Jenkinson et al., PMID. 12377157. [10] Chen et al., DOI: 10.1148/radiol.13130353.

Quantitative Cardiac B0, Fat Fraction, and R2* Mapping Using Pre-Channel-Combination Phase Processing

Zahra Hosseini,[1,2] Junmin Liu,[2] Maria Drangova[1,2,3]

[1]Biomedical Engineering Graduate Program, University of Western Ontario

[2]Imaging Research Laboratories, Robarts Research Institute

[3]Department of Medical Biophysics, University of Western Ontario

Consortium: Image-guided device interventions for cardiovascular disease

INTRODUCTION: Multi-echo gradient echo (GRE) imaging allows for calculation of quantitative maps (e.g. field map (B0), fat fraction (FF),[1] R2*,[2] local frequency shift and quantitative susceptibility maps). Quantitative GRE imaging requires accurate phase data and its application to cardiac imaging faces challenges due to cardiac and respiratory motion. Additional corruption of the phase signal is caused by the large phase gradients at the interface of the heart and lungs. Recent work has shown that channel-by-channel processing of MR phase data prior to channel combination results in the preservation of detailed information about underlying tissue.[3] We present a novel processing pipeline, based on this idea, for processing multi-echo GRE cardiac phase images in order to generate quantitative B0, FF, and R2* maps.

METHODS: ***Imaging*:** Image acquisition was performed in accordance with our institute's Research Ethics Board. Three male volunteers were scanned with a dark blood multi-slice four-echo GRE sequence using a 34-channel tx/rx coil on a 3T scanner. Fifteen breath-held short axis stack (SAX) and a single 2-chamber long axis stack (LAX) were acquired with the following imaging parameters: TE1/ESP/TR: 2.33/1.27/940 ms; resolution: 1.2x1.2x6.0 mm^3; R=2; 9 segments; BW 1150 Hz/px. ***Image processing*:** Channel data, were saved for offline post-processing. Channel images were corrected for bipolar acquisition.[4] The corrected images were processed with a non-iterative B0-mapping technique, which simultaneously calculates B0-, FF-, and R2*-maps.[5] The individual channel maps were combined using the channel magnitude for weighting. For comparison, adaptive channel combination[5] was also performed and the same B0-mapping algorithm was applied to the channel combined phase data.

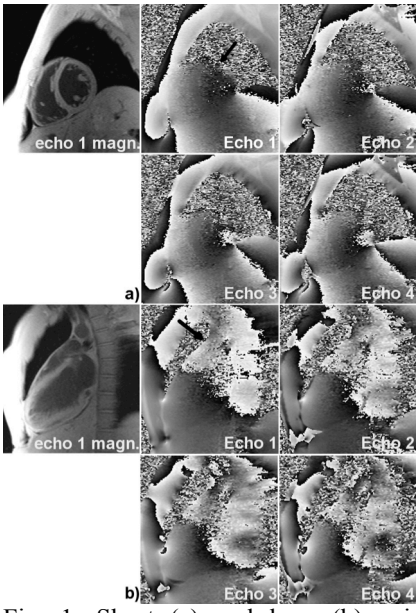

Fig. 1. Short (a) and long (b) axis magnitude images shown with the phase images at echoes 1 through 4. Arrows point to representative areas of high susceptibility.

RESULTS: Accurate quantitative maps were generated using the proposed processing pipeline (only B0-maps are shown). In contrast, B0-maps calculated from the channel-combined phase images were consistently corrupted due to susceptibility artifacts present in the original combined phase images. Figure 1 demonstrates this problem in the phase images at four echo times (the magnitude is shown as reference). A comparison between the B0-maps resulting from the pre-combined phase data and from the channel-by-channel processing pipeline are shown in Fig. 2. The myocardium signal near the heart/lung interface is clearly spared when B0-maps are calculated for prior to combination.

DISCUSSION/SIGNIFICANCE: This work represents a novel method of processing cardiac MR phase images to extract B0, FF, and R2* maps. Cardiac MRI is often performed at 1.5T to avoid field inhomogeneity-related artifacts.[6,7] This work demonstrate the ability to obtain high quality B0-, FF- and R2*-maps from a readily available multi-echo imaging sequence at 3T using a post-processing technique optimized for cardiac imaging and applied on a channel-by-channel basis. The increased time required for processing data from multiple channels can be compensated for by using parallel computing using non-iterative algorithms such as that used here. Future work will evaluate the efficacy of the presented methods for myocardial tissue characterization in a cohort of patients.

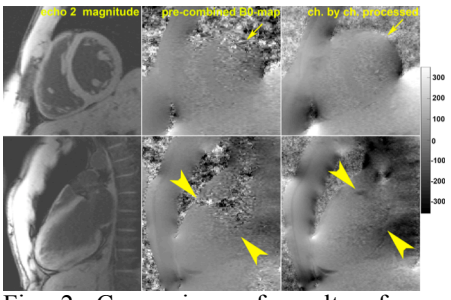

Fig. 2. Comparison of results of pre-combined and channel-by-channel processed field maps clearly shows the advantage of processing channel data prior to combining the information.

References: [1] Reeder et al., DOI:10.1002/jmri20831. [2] Yu et al., DOI: 10.1002/jmri21090. [3] Hosseini et al., DOI: 10.1002/jmri25409. [4] Peterson & Mansson, DOI: 10.1002/mrm24657. [5] Liu & Drangova, DOI: 10.1002/mrm25497. [6] Atakay et al., PMID: 11180442. [7] Storey et al., DOI: 10.1002/jmri20816.

Validation of breast volume measurement using 3D surface scanner

Rachael House[1], Andras Lasso[1], Glykeria Martou[2], John Rudan[2], Gabor Fichtinger[1]
[1]Laboratory for Percutaneous Surgery, Queen's University, Kingston, Canada
[2]Department of Surgery, Queen's University, Kingston, Canada

INTRODUCTION: Breast Cancer is the most frequently occurring cancer in Canadian women, with 5-year survival rate of 88 percent [1]. The standard of care for treating breast cancer normally involves breast conserving surgery and radiation therapy followed by breast reconstruction surgery. For successful breast reconstruction, the total volume loss must be accounted for. Unfortunately, the volume excised during surgery generally does not reflect total breast volume loss, for example, radiation therapy is known to cause volume loss of the breast [2]. To compensate for difference in volume the breast volume can be calculated following radiation treatment and compared against the baseline volume. Many techniques have been proposed to calculate the breast volume but most are invasive, require expensive scans, or produce an underestimation of the breast volume [3]. Our goal is to provide the software and workflow necessary to calculate the breast volume using a non-invasive technique. By calculating and comparing the breast volume of the patient before undergoing reconstruction surgery to the baseline volume will help surgeon's better estimate how much tissue needs to replace in procedures like fat grafting.

METHODS: A 3D surface scan of the patient's chest (Fig. 1-A) is obtained using the Artec Eva Scanner (www.artec3d.com). The scanning process (Fig. 2-B) allows for full visualization of the chest, the scanner is placed on a rolling dolly (Fig 1.-C) under the patient. The scan is then imported into 3D Slicer (www.slicer.org) where modules are used to isolate the target breast and calculate the volume. A model of the patient's chest wall is created by segmenting the chest wall from a chest computed tomography (CT) scan and used to isolate the target breast by subtracting it from the 3D scan. In order to have a ground truth in this study a mannequin was used, the ground truth breast volume was calculated using water displacement. A flat plane was used in place of the segmented chest wall because when using water displacement to calculate the volume a flat cut plane is assumed.

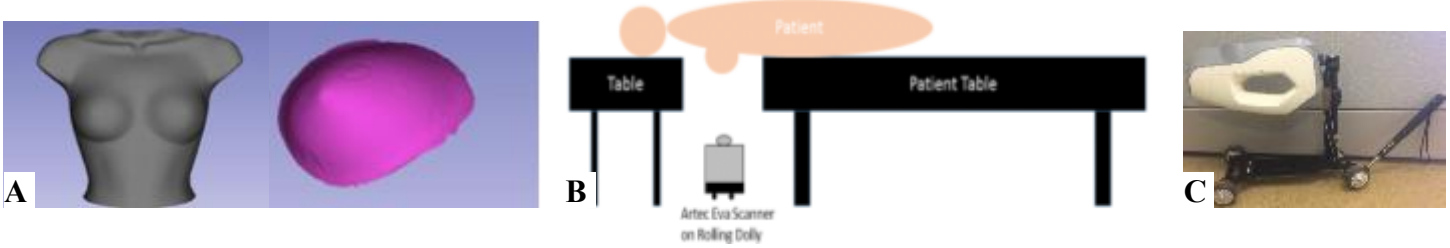

Figure 1. **A)** 3D surface scan of chest using Eva scanner, viewed as a model in 3D Slicer and isolated breast. **B)** Scanning position diagram. **C)** Artec Eva scanner mounted on rolling dolly.

RESULTS: The method provided to calculate breast volume is feasible using 3D Slicer and only requires one surface scan from the patient. The ground truth breast volume of the mannequin was 164mL with a standard deviation of 4.1ml (*n = 5)*. The volume of the mannequin's breast was calculated using the workflow provided, the mean calculated volume was 160.8mL and the standard deviation was 4.7ml (*n = 4)*. In this study the cut plane was manually placed in 3D Slicer, differences between placement of the plane could contribute to the difference in mean values of the calculated breast volume.

CONCLUSION: Using a 3D surface scanner provides a non-invasive and quick way to calculate breast volume. This initial validation suggests this system may be accurate enough to aid the surgeon in the reconstruction process. Further studies will be conducted to assess the accuracy of the system when using the segmented chest wall to isolate the breast opposed to the flat plane.

REFERENCES: [1] Canadian Breast Cancer Society. (2015). *Breast Cancer in Canada, 2015.* Retrieved from https://www.cbcf.org/ontario/AboutBreastCancerMain/FactsStats/Pages/Breast-Cancer-Canada.asp [2] Haykal, Siba, Colin P. White, and Nicolas A. Guay. "An estimation of volume loss after radiation therapy on free flap breast reconstruction." *Plastic and reconstructive surgery* 131.6 (2013): 937e-939e. [3] Kovacs, Laszlo, et al. "Comparison between breast volume measurement using 3D surface imaging and classical techniques." *The Breast* 16.2 (2007): 137-145.

CT Perfusion versus SPECT MIBI for assessing myocardial ischemia in coronary artery disease

[1]I-Lun Huang, [1]Ming-Ting Wu, [2,3]Ting-Yim Lee and [3]Aaron So
[1]Radiology, Kaohsiung Veteran General Hospital, Kaohsiung, Taiwan, [2]Imaging, Robarts Research Institute, [3]Imaging, Lawson Health Research Institute, London, Ontario, Canada.

Introduction Single photon emission computed tomography (SPECT) with radiotracer technetium-99m sestimibi (MIBI) is the most frequently used modality for assessing myocardial perfusion (MP) in patients with coronary artery disease (CAD), but the assessment is usually qualitative which requires normally perfused myocardium for reference. Hence, the true extent of balanced ischemia arising from left main/multi-vessel stenoses and microvascular disease can be underestimated. In this pilot study, we compared quantitative CT Perfusion (CTP) against SPECT MIBI for evaluating myocardial ischemia in patients with advanced CAD.

Methods Six CAD patients with persistent symptoms and/or previous myocardial infarction were enrolled. Data acquisition Each patient had the following tests within 6 weeks: SPECT MIBI and CTP for imaging MP at rest and maximal vasodilatory stress, coronary CT angiography (CCTA) or catheter-based coronary angiography (CA) for evaluating the degree of luminal narrowing in coronary arteries. The SPECT MIBI, CCTA and CA studies were acquired using routine clinical protocols. For each CTP study, iodinated contrast (Visipique 320 mgI/ml at 0.7 ml/kg dosage) was injected at 5 mL/s followed by dynamic scanning of the heart using a prospective ECG gated acquisition protocol run on a GE Revolution CT scanner: 20 axial scans with breath-hold at every 1-2 mid-diastoles, 100 kV tube voltage, 100 mA tube current and 280 ms gantry period. Upon the completion of rest CTP study, adenosine was administrated at 140 µg/min/kg and the CTP study was repeated at 3 minutes into adenosine infusion. DCE heart images from each CTP study were registered using a three-dimensional non-rigid algorithm, reformatted into short-axis and analyzed using CT Perfusion (GE) from which MP maps were generated using a model-based deconvolution algorithm. Myocardial perfusion reserve (MPR) in each short-axis myocardial segment was calculated as the ratio of MP at stress to that at rest. Data analysis The six patients were divided into two groups according to the anatomical assessment with either CCTA or CA: single-vessel disease (SVD), where only one coronary artery had >50% stenosis; non SVD, where 2 or 3 coronary arteries were >50% stenosed or no epicardial coronary stenosis was observed. Myocardial ischemia in each coronary territory was evaluated using a 3-point scoring system, according to the MIBI uptake and MPR assessed by SPECT and CT respectively. For MIBI uptake: 0 – normal, 1 – reversible defect, 2 – irreversible (fixed) defect; For MPR: 0 – normal (≥1.9), 1 – moderate reduction (1.50-1.89); 2 – severe reduction (<=1.49). The ischemia scores in each group were compared using Wilcoxon signed rank tests.

Results For the SVD group, the summed ischemia scores of 9 coronary territories assessed by SPECT and CTP were 4 and 6 respectively. The corresponding average scores were 0.44±0.88 and 0.67±0.87 (p=0.157). All the coronary territories that showed a fixed MIBI defect had severe reduction in MPR, and the corresponding supply arteries were >50% stenosed. For the non SVD group, there was a larger difference between the summed ischemia scores assessed by SPECT and CTP, 2 and 13 respectively, and the corresponding average scores were 0.22±0.67 and 1.44±0.73 (p=0.015). The largest differences between the SPECT and CTP assessment were observed in a patient where all the three coronary arteries were >50% stenosed, and in a patient who had no epicardial coronary stenosis but with suspected microvascular disease according to the clinical symptoms including arrhythmia. In both cases, the MIBI uptake was normal but MPR was moderately to severely reduced in all the coronary territories.

Conclusion CTP was not inferior to SPECT MIBI for assessing myocardial ischemia associated with single-vessel CAD. A larger discordance between CTP and SPECT MIBI was observed in non single-vessel CAD which could be attributed to balanced ischemia. These findings suggested that quantitative CTP could provide a more reliable assessment of the functional significance of left main and multi-vessel coronary artery stenoses and microvascular disease compared to the qualitative SPECT method.

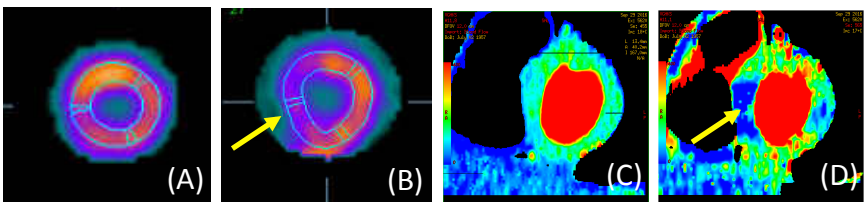

Figure 1. Comparison of SPECT MIBI maps at rest (A) and stress (B) to CT MP maps at rest (C) and stress (D) in the basal short-axis slice of a patient with SVD. Reversible ischemia in septum (yellow arrows) was identified by both modalities.

Quantitative CT assessment of myocardial edema in acute myocardial infarction: a validation study

[1]Lisa Hur, [2]Gerald Wisenberg, [2]Patrick Teefy, [1,3,4]Ting-Yim Lee and [1,4]Aaron So
IMAGE-GUIDED DEVICE INTERVENTIONS FOR CARDIOVASCULAR DISEASE
[1]Medical Biophysics, Western University, [2]Cardiology, London Health Sciences Centre, [3]Imaging, Robarts Research Institute, [4]Imaging, Lawson Health Research Institute, London, Ontario, Canada

Introduction Acute myocardial infarction (AMI) leads to accumulation of fluid in the interstitium as a result of enhanced cellular and vascular leakiness. Hence, myocardial edema is a hallmark of acute ischemic injury and can be used to delineate the extent of myocardium at risk, from which clinical decision on revascularization can be informed. Edema is not commonly assessed by cardiac CT due to the similar enhancement (x-ray attenuation) between myocardium and water. We developed a functional CT technique for imaging myocardial edema. This method relies on tracer kinetic modeling of the retention of x-ray contrast in myocardium following a small bolus injection (BI). We validated this method in a pig model of reperfused AMI against a model-independent constant infusion (CI) method and cardiac magnetic resonance (CMR) T2-weighted imaging.

Methods Animal model: AMI was induced in five Landrace pigs (40-60 kg) using a catheter-based approach, where a balloon catheter was advanced to the distal left anterior descending artery (LAD) and inflated to obstruct the downstream blood flow for one hour followed by reperfusion. Data acquisition: CT and CMR studies were performed on day 12±3 post ischemic insult. In each CT study, dynamic contrast-enhanced (DCE) heart images were acquired with a 64-row GE CT750 HD scanner after bolus injection of contrast (0.7 $mL \cdot kg^{-1}$ at 3 $mL \cdot s^{-1}$) using a 3-phase prospective ECG gating protocol: 1st phase: 22 axial scans at every 1-2 s, 2nd phase: 6 axial scans at every 14 s, 3rd phase: 4 axial scans at every 30 s. Next, the same dose of contrast was constantly infused intravenously for one hour. The heart was scanned five times both before and after contrast infusion. CMR T2W images of the heart were acquired on the same day with a Siemens Biograph PET/MR scanner using a routine clinical protocol. Data analysis: DCE CT heart images were analyzed using a modified Johnson-Wilson-Lee model that accounted for contrast exchanges among vascular, interstitial and cellular spaces in injured myocardium to estimate extravascular contrast distribution volume (ECDV, in units of ml/g) as a surrogate measure of edema (Fig 1A). The five pre- and post- infusion CT heart images were averaged and registered to each other using a three-dimensional non-rigid algorithm. The difference image (Fig 1B), generated by subtracting the average pre-infusion image from the average post-infusion image, was normalized to the arterial blood enhancement to derive partition coefficient (PC) as a surrogate measure of distribution volume in myocardium. Myocardial signal intensities in the CMR T2W images (Fig 1C) were recorded using Osirix (Pixmeo). Mean ECDV and PC values and T2W signal intensities in the apical-septal (LAD territory) and mid-lateral (non-LAD territory) wall of left ventricle were compared using one-way ANOVA.

Results ECDV in the infarcted apical-septal wall was 0.46±0.18 ml/g, which was higher than that in the normal mid-lateral wall (0.22±0.10 ml/g, $p<0.05$). Similarly, PC in the apical-septal wall was statistically higher than that in the mid-lateral wall (0.59±0.15 vs. 0.29±0.05, $p<0.05$). CMR T2W images confirmed the same apical segment with higher ECDV and PC than normal was edematous. The corresponding signal intensities in infarcted and normal myocardium were 65.6±55.7 and 34.0±39.0 ($p<0.05$ from infarcted) arbitrary units.

Conclusion Intercellular and interstitial edema coupled with enhanced leakiness in cardiomyocytes provide additional spaces for CT contrast to distribute. Thus, ECDV is a useful marker of edema in acutely injured myocardium. ECDV measured with the proposed model-based BI technique agreed with the reference CI method and CMR T2W imaging. Compared to CMR, CT has a higher accessibility and throughput and lower operating cost, and could be an alternative modality to assess edema and at-risk myocardium in the acute infarction setting. The proposed technique does not require prolonged contrast infusion which will increase patient throughput.

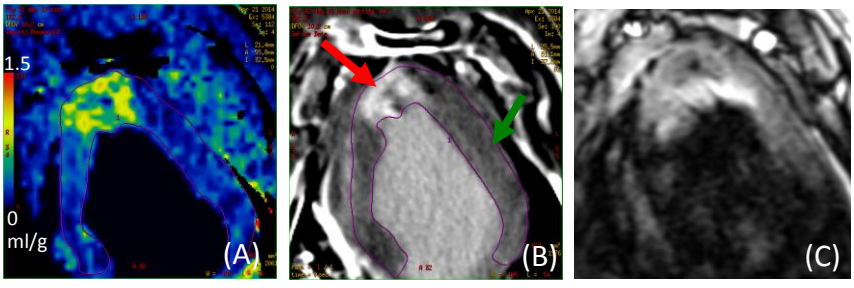

Figure 1. (A) ECDV map, (B) difference image, and (C) CMR T2W image of a porcine heart at 12 days after acute myocardial infarction. Apical-septal and mid-lateral wall of left ventricle were pointed by red and green arrows respectively.

A Novel Vector Doppler Ultrasound Method for Improved Near-Wall 2D-Vector Blood Velocity Estimations: Aperture – Translation

*Bushra Hussain[1], B. Y. S. Yiu[4], A. C. H. Yu[5], J. C. Lacefield[2,3], T. L. Poepping[1]

Departments of Physics &Astronomy[1], Medical Biophysics[2], Electrical &Computer Engineering[3], Western University, London, Canada; Department of Biophysics[4], Hong Kong University, Hong Kong; Department of Electrical and Computer Engineering[5], University of Waterloo, Canada.

Introduction: Accurate estimation of low blood velocities that lie near the vessel wall is important for improved measurement of low wall shear stress, which plays an important role in initiation and progression of atherosclerosis – a thickening or hardening of blood vessels – in large arteries [1]. Doppler ultrasound (DUS) is the first-line clinical tool for non-invasive diagnosis of vascular disease. Besides angle-dependence of DUS in which only single component of the blood velocity along the beam direction is measured, requiring a-priori knowledge of the direction of the velocity, it is also limited in the estimation of low blood velocities due to a high-pass/wall filter. This filter is applied to the received signal to remove the high-intensity, low-frequency signal of stationary or slowly moving tissue. It also attenuates the low frequency blood signal, which lies in the transition region of the filter, leading to an overestimation and incorrect measure of these velocities. Vector Doppler Ultrasound (VDUS) overcomes the angle-dependence by measuring 2 or 3 velocity components in 2D/3D space only if the signal is in the pass-band of the wall filter. Previously, it was suggested to increase the number of receiver orientations [2] to improve the chance of retaining at least two or more velocity components. Here we introduce a novel 2D vector Doppler ultrasound (VDUS) technique, 'Aperture-Translation', which aims to increase the strength of the signal of each velocity component, preserving the low velocity signal.

Methods: An in-vitro study was performed to demonstrate the proof-of-concept of the technique using simple Poiseuille flow in a straight wall-less phantom with matching diameter of an average common carotid artery (0.8 cm), generating a range of low velocities of up to 3 cm/s. The flow phantom was made of tissue-mimicking material (10% Polyvinyl alcohol gel) with the blood mimicking fluid through the vessel to match the attenuation and acoustic properties of tissue and blood, respectively. Data were acquired using a linear array with central transmit and two surrounding receiver apertures translated (swept) opposite to the flow with various sweep velocities of up to 5 cm/s. The translation of the apertures was performed both mechanically and electronically. The equivalence and potential of the two versions was studied varying the sweep velocities and the ensemble size (i.e. number of samples to obtain the mean Doppler frequency) and compared with the conventional 2D VDUS method with a suitable inter-beam angle.

Results: Both the mechanical and electronic version of the aperture-translation technique performed similarly with electronic version showing better accuracy and reliability when within the aliasing limit. At flow velocity of 1 cm/s, the relative error and standard deviation was within 14% ± 43% for the electronic aperture-translation method compared to >70% ± >100% for the conventional 2D VDUS method for all sweep velocities (3.5 cm/s – 5 cm/s).

Conclusion: The out-performance of the aperture-translation technique over the conventional 2D VDUS technique showed promise for future development, especially for its electronic version, which is more suitable for clinical implementation for improved diagnosis of vascular disease.

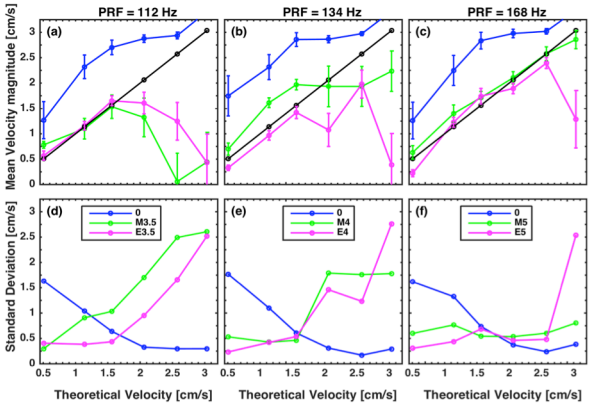

Fig.1 Velocity magnitude (a-c) comparing mechanical (in green) and electronic-sweep (in pink) methods with conventional method (in blue) for theoretical velocities ranging from 0.5 to 3 cm/s (in black) for three matching sweep velocities (3.5, 4, and 5 cm/s) with corresponding pulse repetition frequencies (as labeled) for an ensemble of 12 at inter-beam angle of 15°. Error bars represent standard error over 20 measurements. Standard deviations (d-e) comparing the three methods for the same velocities.

[1] Shaaban and Duerinckx, (2000) Am J Roentgenol,174:1657-1665.
[2] Hussain et al. (2016) *IEEE Transactions on UFFC,* 63:1786-1798.

Network connectivity following a single unprovoked seizure using 7 Tesla resting-state fMRI

Ikeda KM[1,2], Mirsattari SM[1,2], Khan AR[3,4], Peters TM[3,4], Burneo JG[1,2], Johnsrude I[5]

1. Schulich School of Medicine and Dentistry, Western University
2. Department of Clinical Neurological Sciences, London Health Sciences Centre
3. Robarts Research Institute
4. Department of Medical Biophysics, Western University
5. School of Communication Sciences and Disorders, Department of Psychology, Western University

Supervisors: SM Mirsattari and AR Khan.

Introduction:
Epilepsy is a common neurological disorder usually diagnosed after two unprovoked seizures. However, up to 10% of the general population has a single unprovoked seizure, whereas only 1% of the population has epilepsy. Currently we are unable to accurately predict who will develop epilepsy following a first seizure. Many network abnormalities have been detected in patients with epilepsy using resting-state functional MRI (rs-fMRI), and abnormalities generally worsen with duration of epilepsy. This study uses graph theory measures derived from rs-fMRI to determine if there are network abnormalities in patients after a first seizure that can be used as a biomarker for the later development of epilepsy.

Methods:
Patients who have experienced a single, unprovoked, generalized tonic-clonic seizure between the ages of 16 and 65 will be recruited, and age and sex matched with healthy controls. Participants will undergo MRI neuroimaging at 7 Tesla, acquiring structural and resting-state functional images. Data will be preprocessed, thresholded, then analyzed using the graph theory measures of global and local efficiency, average path length, clustering coefficient and betweenness centrality. Seizure patients will be followed for development of epilepsy.

Results:
Nine patients and nine control subjects have been recruited and analyzed. No differences in baseline characteristics were detected. No patients have developed epilepsy, with an average follow-up duration of 3 months (range 1-6). On a whole-brain network level, no differences were detected between groups at thresholds of 15-75%. At a 20% threshold, significant differences were seen in the default mode network. Patients demonstrated an increase in local efficiency ($p=0.02$), and clustering coefficient ($p=0.04$), and decrease in average path length ($p=0.02$) and betweenness centrality ($p=0.02$).

Conclusions:
No differences between were seen on a whole-brain level, suggesting that at this level, there are not network abnormalities occurring after a single unprovoked seizure. None of these patients have developed epilepsy, with a follow-up duration of one to six months. This indicates that patients who have not developed epilepsy do not have any network alterations after a single seizure. However, no patients who have developed epilepsy have been acquired to-date, and follow-up duration is currently insufficient to accurately detect development of epilepsy. In the default mode network, alterations were noted in local efficiency, path length and betweenness centrality, indicating specific alterations in this network reflecting increased segregation of network function.

Creating patient-specific anatomical models from highly elastic materials using 3D-printed molds

Anna Ilina*[a], Andras Lasso[a], Matthew A. Jolley[b], Brittany Wohler[b], Alex Nguyen[b],
Adam Scanlan[b], Zachary Baum[a], Frank McGowan[b], Gabor Fichtinger[a]
[a]Laboratory for Percutaneous Surgery, Queen's University, Kingston, Canada;
[b]The Children's Hospital of Philadelphia, Philadelphia, USA

Introduction. Realistic physical models of anatomical structures are useful for surgical simulations and other medical procedures. These physical models or 'phantoms' should mimic the functional, mechanical and acoustical properties of the structure being modeled. The shape of structures can be accurately modeled using direct 3D printing, but currently available soft printing materials may still be too rigid to imitate human tissue. We propose a method for designing 3D-printable molds, which can be filled with a highly elastic material to create flexible and tear-resistant phantoms. We demonstrated this method by creating heart valve phantoms.

Methods. 3D Slicer software is used for designing the 3D-printable mold[1]. **Step 1: Segmentation.** Segment the object of interest from a 3D image using Segment Editor module. **Step 2: Mold design.** Create a rectangular prism segment surrounding the object using Scissors effect. Separate the rectangular prism into two segments to create the top and bottom mold pieces, following the shape of the structure being modeled. Add air tunnels in the top mold segment to allow air bubbles to escape when filling the mold. Export the top and bottom mold segments as models and save as STL files. **Step 3: Mold printing.** 3D print the mold models using standard ABS printing plastic. **Step 4: Physical model creation.** Fill the mold with a highly elastic material such as silicone or PVC and allow to set. Remove the phantom from the mold and trim any excess material.

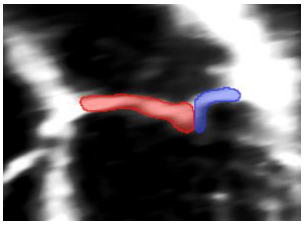

Figure 1. Segmentation of a mitral heart valve based on ultrasound image (step 1).

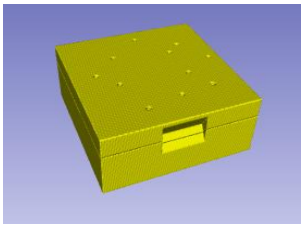

Figure 2. 3D mold box model for a mitral valve (step 2).

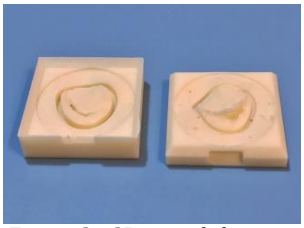

Figure 3. 3D-printed bottom mold (left) and top mold (right) for a mitral valve (step 3).

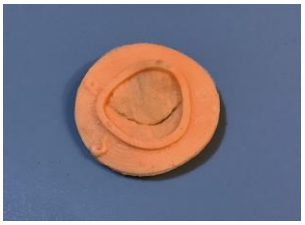

Figure 4. Silicone mitral valve created from mold (step 4).

Results. For simulating heart valve tissue, we created a silicone mixture of 2 parts Dragon Skin® Part A, 2 parts Dragon Skin® Part B, 1 part Slacker® tactile mutator and 1 drop Silc Pig® flesh tone silicone pigment (Smooth On, Inc., Macungie, PA, USA). This silicone is suitable for creating ultrasound phantoms[2] and its flexibility can be manipulated by altering the levels of tactile mutator added. Six cardiac surgeons evaluated the heart valve models and practiced suturing on them. They found the silicone material has a good flexibility, and cuts and holds sutures well without tearing[3]. For very thin or detailed structures such as heart valve leaflets, manually separating the mold into two pieces took 2-5 hours. To speed up the process, we wrote a module in 3D Slicer to automate mold creation for heart valves. This method can be used to create phantoms of various structures such as heart valves, livers, and brain tumours, and can be automated for a specific structure.

Conclusion. Custom molds can be designed in the open source 3D Slicer software to create patient-specific models of anatomical structures. We illustrated this method by creating heart valves for surgical simulation. Dragon Skin® silicone is well suited to mimicking tissue due to its flexibility and resistance to tearing.

References. [1] Fedorov et al., "3D slicer as an image computing platform for the quantitative imaging network," Magnetic Resonance Imaging 30(9), 1323-41 (2012). [2] Pacioni et al., "Patient-specific ultrasound liver phantom: materials and fabrication method," Int J Cars 10(7), 1065-75 (2015). [3] Ilina et al., "Patient-specific pediatric silicone heart valve models based on 3D ultrasound," SPIE Medical Imaging 2017.

Return to Program

Computer-Aided Method of Left Atrial Wall Thickness Measurement

J. Inoue,[1] Allan C. Skanes,[2] Lorne J. Gula[2] and M. Drangova[1]
[1]Robarts Research Institute, Western University, London, Ontario, Canada
[2]Arrhythmia Service, London Health Sciences Center, London, Ontario, Canada
Consortium: Image-guided Device Interventions for Cardiovascular Disease, Supervisor: M. Drangova

Introduction. Atrial fibrillation (AF) is often treated by radiofrequency catheter ablation in the left atrium (LA). However, areas of increased LA wall thickness (LAWT) are more likely to fail the initial ablation treatment, requiring repeated interventions. Pre-operative knowledge of LAWT may allow more precise ablation dosing and improve outcomes. Creation of a fully automated LAWT measure is hampered by the difficulty of segmenting the LA wall in cardiac CT images. In contrast, manual measurement is time consuming, imprecise, and is difficult to duplicate. In this work we describe a hybrid computer-assisted direct LAWT measurement method that does not require segmentation. Human expertise in interpreting the anatomy and image quality is combined with the speed, precision, and repeatability of computational methods.

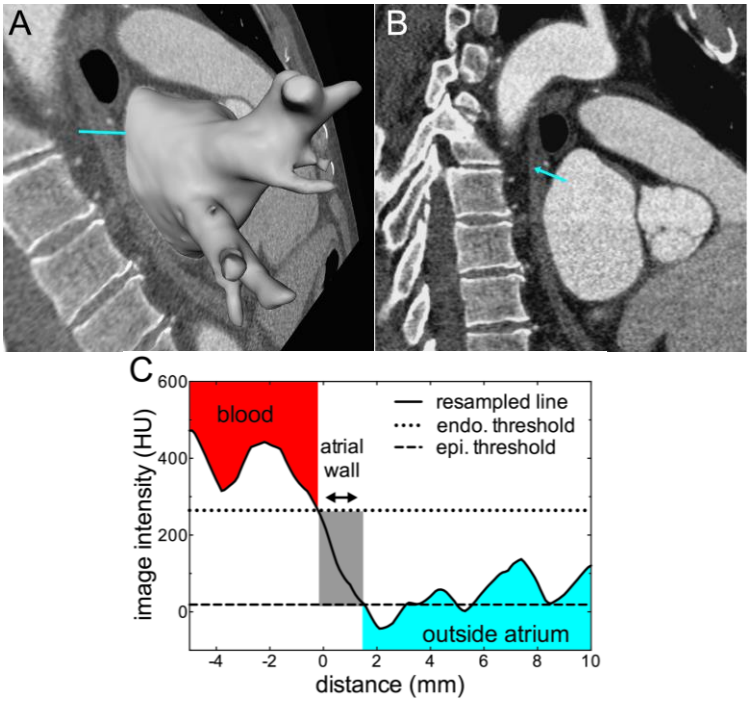

Figure 1. A: A 3D model of the patient's left atrial blood pool is illustrated along with a line perpendicular to the LA surface (cyan); a 2D CT image re-sliced in the direction of the selected line is also shown. **B:** The CT image was resampled along the selected ray from inside the atrium toward the epicardium. Actual calculations were made in 3D. **C:** The atrial wall was identified from the CT image intensities of the resampled line using endo- and epicardial thresholds derived from a patient-specific image-intensity model.

Methods. A software package was developed using MeVisLab and C++. This software allows an expert operator to select a location on a 3D rendering, and automatically measure LAWT at that location based on a patient-specific image-intensity model. Poor measurements can be rejected by the operator, who then selects a different nearby location that is easier to measure. This can be repeated any number of times. For each image, patient-specific endocardial and epicardial thresholds are calculated from the CT intensities of the patient's tissues. Automatic measurement is performed in 3D by resampling the image at 0.1 mm increments along a projection line and applying the endocardial and epicardial thresholds to isolate the atrial wall tissue. This process is illustrated in Figure 1. Retrospective analysis was performed on 86 contrast-enhanced CT images of patients who had undergone ablation for AF. Of these, 33 patients had experienced recurrence of AF within one year of initial treatment and 29 had returned for a repeat ablation. For each patient, LAWT was measured at 12 anatomical regions using the software. Analysis of variance (ANOVA) was used to compare the LAWT of patients who experienced recurrence to those who did not, and a Mann-Whitney U test was used to compare the LAWT at gaps (ablated regions that subsequently showed no lesion, identified intraoperatively in a repeat procedure), to non-gap regions.

Results. Patients with recurrent AF had greater LAWT (1.57 ± 0.58 mm, $p < 0.01$) compared to successfully treated patients (1.46 ± 0.49 mm) and gaps were found to be at regions of thicker tissue (1.63 ± 0.57 mm, $p = 0.04$) compared to non-gap regions (1.49 ± 0.53 mm).

Conclusions. Using this method, LAWT was measurable with sufficient accuracy to find expected differences in clinically-sourced data. Many manual-equivalent measurements could be made quickly with acceptability as determined by an expert operator.

Non-Invasive Imaging of Urine Flow Dynamics Using High Frame Rate Ultrasound (HiFRUS)

Takuro Ishii, Billy Y. S. Yiu, and Alfred C. H. Yu
Schlegel-UW Research Institute for Aging, University of Waterloo, Waterloo, ON, Canada

Introduction. Urethral voiding dysfunction is mainly attributed to mechanical and physiological aging of the vesico-urethral system. Visualization of flow behavior is anticipated to unveil a causal relationship between the mechanical obstruction and flow dynamics and quantify the symptom severity and therapeutic effects. Here, we report the first application of a high-frame-rate ultrasound (HiFRUS) vector flow visualization technique called Vector Projectile Imaging (VPI) to facilitate analysis of urinary flow dynamics.

Methods. The HiFRUS-based VPI technique is an ultrasound imaging innovation established by our lab recently [1]. In brief, it is based on the use of plane-wave excitation principles to achieve high imaging frame rates (>1,000 fps) that are well beyond the video display range. It derives local flow vector information (with axial and lateral velocity components) at every pixel position in the entire imaging view through a multi-angle, least-squares vector Doppler estimation approach [2]. These flow vectors are then visualized through a dynamic rendering algorithm that depicts the trajectory of individual vector projectiles.

To test the efficacy of VPI in visualizing urinary flow, we designed a new anatomically realistic urinary tract phantom that can reconstruct urine passage under controlled conditions (Fig. 1). Both healthy and diseased urinary tract models were devised. The diseased model was in the form of bladder outlet obstruction (BOO): a well-recognized anatomical characteristic in urinary tracts with voiding dysfunction symptoms. The flow system provided urine mimicking liquid at constant water head pressure to assume uniform detrusor function for both models.

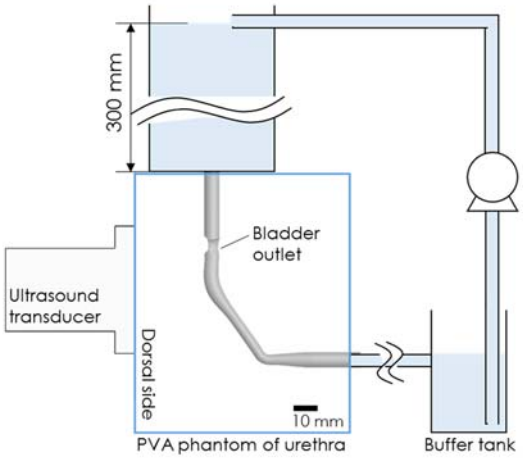

Fig. 1. Experimental setup
Static flow at constant water head pressure was fed into the urinary tract phantom. Ultrasound transducer was placed at dorsal side of the urethra.

Results. VPI cineloops were derived from these urinary flow phantoms (Fig. 2). Spatial- and temporal-resolution were, respectively, 0.1 mm and 400 μs/frame. Results show that VPI is capable of depicting differences in the flow dynamics of normal and diseased urinary tracts. In the case with BOO, VPI depicted the presence of BO flow jet and vortices in the prostatic urethra. The corresponding spatial-maximum flow velocity magnitude was estimated to be 2.43 m/s. It is significantly faster than that for the normal model (1.52 m/s), and is in line with values derived from computational fluid dynamics simulations.

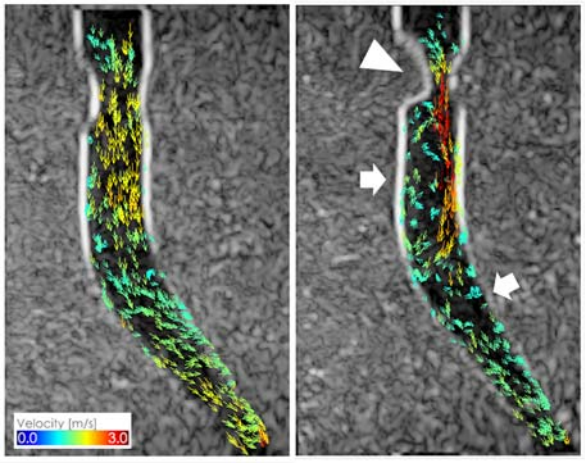

Fig. 2. Urine flow visualization in normal model (left) and obstructed model (right).
Triangle and arrows respectively indicate the location of BOO lesion and chaotic flow in the diseased model.

Conclusion. The work has demonstrated the feasibility of using HiFRUS (in the form of vector flow visualization) to examine internal flow characteristics related to voiding dysfunction. This new HiFRUS application shows promise in locating positions within the urinary tract where disturbed urine passage is evident.

References. [1] BYS Yiu, SSM Lai, ACH Yu. *Ultrasound Med Biol*, 2014; 40: 2295-309.
[2] BYS Yiu, ACH Yu. *IEEE Trans Ultrason Ferroelec Freq Contr*, 2016; 63: 1733-44.

Visualizing US In-situ in Laparoscopic Interventions

Uditha L. Jayarathne[1,2], Elvis C.S Chen[1,2], John Moore[2], and Terry M. Peters[1,2]
[1]Biomedical Engineering Graduate Program, Western University, London, Canada
[2]Robarts Research Institute, London, Canada

Introduction: During laparoscopic interventions, intra-corporeal ultrasound (US) is often used to visualize deep-seated, hidden surgical targets. The US image data is conventionally visualized in a display separate to the laparoscopic video, thus requiring additional cognitive efforts to infer location and geometry of the hidden targets. The mental processes involved in the fusion of information from the two displays are known to cause excessive cognitive load[1]. Because the US image is displayed separate from the surgical site, actions involving deep-seated targets rely heavily on an internal(mental) spatial representation of the target. Such a representation can be erroneous[2] and result in erroneous action. To alleviate issues due to perception-action decoupling, overlaying of ultrasound information in laparoscopic video has shown to be an effective[3] solution. This requires efficient algorithms to estimate the pose of the probe with respect to the camera and to render ultrasound data in the context of laparoscopic video resulting in accurate spatial perception.

Methods: To estimate the pose of the laparoscopic US probe in six degrees of freedom (6DoF), a fiducial pattern is attached to the curved back surface of the flexible tip of the probe. An efficient algorithm is employed to detect the fiducial pattern in the monocular laparoscopic video and to estimate the pose maintaining robustness to fiducial occlusion and clutter[4]. With the US calibration transformation determined with a method that cast the problem as a point-to-line registration problem[5], ultrasound pixel locations are accurately determined with respect to a coordinate system defined on the camera center. Captured US images with their poses determined by the above method are incrementally stitched into a 3D volume at isotropic voxel resolution of 0.5mm using a method that combines voxel-based and pixel-based reconstruction techniques. The incrementally reconstructed US volume is then rendered in-situ employing a direct volume rendering scheme with a one-dimensional transfer function[6]. Finally, the US volume is alpha-blended with the original and high pass filtered version of the laparoscopic video through a circular opacity mask to enhance depth perception (Figure 1). The entire visualization pipeline was implemented in C++ and is based on VTK[1]. 3D ultrasound reconstruction and direct volume rendering methods were GPU-accelerated to achieve real-time performance.

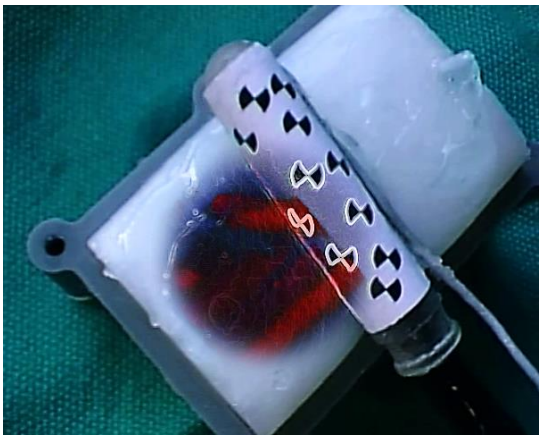

Figure 1: Overlay of 3D US volume in-situ with circular opacity mask

Results and Conclusions: The pose estimation algorithm was evaluated to have an RMS error of 1.98 ± 1.4 mm compared to an optical tracking-based reference. The average time taken by 3D US reconstruction algorithm to compound a single US image is 5.2miliseconds, while the entire visualization pipeline runs in 20 frames per second. The pipeline does not add overhead to current operating room workflow, and can easily be adapted to any laparoscopic application involving intracorporal US.

References:

1. Shepard, R. N. et. al., " Mental Rotation of Three-Dimensional Objects". *Science ,* 1971.
2. Klatzky, R. L. et. al., "Spatial Representations From Perception and Cognitive Mediation: The Case of Ultrasound", *Curr. Dir. Psychol. Sci.,* 2008.
3. Hughes-Hallett, A. *et al.* "Intraoperative ultrasound overlay in robot-assisted partial nephrectomy: first clinical experience", *Eur. Urol.***,** 2014.
4. Jayarathne, U. L. et. al., "Robust intraoperative US probe tracking using a monocular endoscopic camera", *Med. Image Comput. Comput. Assist. Interv.* **,** 2013.
5. Ameri, G. et. al., "Line fiducial material and thickness considerations for ultrasound calibration", *SPIE Med. Imag.*, 2015
6. Baxter, J. S. H. et. al., "A unified framework for voxel classification and triangulation", *SPIE Med. Imag.*, 2011

[1] www.vtk.org

Radiomics Made Easy: Translation of Image Analysis Tools to a Clinical Trial-Ready Platform

Carol A. Johnson[1], Sarah A. Mattonen[1,2], David A. Palma[1-3], Aaron D. Ward* [1-3]
Ontario Institute for Cancer Research – Imaging Translation Program *Supervisor
[1]Baines Imaging Research Laboratory, London Regional Cancer Program, London, Canada;
Departments of [2]Medical Biophysics, [3]Oncology, The University of Western Ontario, London, Canada

Introduction: As part of the Ontario Institute for Cancer Research (OICR) strategy to translate current cancer image analysis research to clinical trial, we are motivated to integrate cutting edge software tools developed in the laboratory into a robust, clinician-friendly, interactive platform accessible for use in clinical trials anywhere in the world via the Quantitative Imaging for Personalized Cancer Medicine (QIPCM) initiative. Although radiomics (the extraction and analysis of morphological and textural image characteristics for machine learning-based assessment of disease state) – is showing promise for cancer assessment on imaging[1,2], implementation of such techniques requires highly specialized skills. Our aim is to make radiomics studies possible for any clinician scientist using a familiar graphical user interface from any site in the world at low cost.

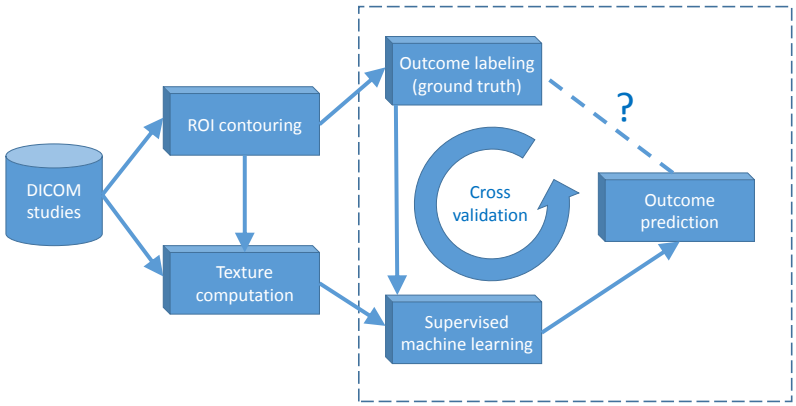

Fig. 1: Flow diagram illustrating steps executed by the platform.

Methods: We are developing a plugin in ClearCanvas Workstation, which provides a clinician-friendly graphical interface and full DICOM functionality for study retrieval. Fig. 1 illustrates the different steps in the workflow. The tool imports DICOM studies and contoured regions of interest (ROI) in binary image format and automatically computes an array of imaging texture features (e.g. second-order texture features computed from gray-level co-occurrence matrices, such as energy, entropy, and inertia) within the ROIs using the Insight Toolkit (www.itk.org). The tool provides the physician with an easy-to-use interface for labeling each study with a ground truth outcome (for instance, histologically verified post-radiation cancer recurrence, as in our previous work[2]). Supervised machine learning is then performed (our tool currently implements normal Bayes, k-nearest neighbors, support vector machine and random forest classifiers). The tool provides for multiple modes of automated validation, including leave-one-patient-out, folded, and randomized cross validation; in each validation fold training and testing sets are fully separated. Output metrics include error rate, false-positive rate, false-negative rate, and area under the receiver operating characteristic curve.

Results and conclusions: The development of the feature analysis tool in ClearCanvas Workstation provides a clinician-friendly interface to advanced image analysis techniques. Initial testing of our nearly-complete prototype reveals that the conducting of radiomics-based outcome prediction studies is feasible using our point-and-click interface without any specialized software development knowledge. Texture features and machine learning outputs from this platform were successfully validated against those of our Matlab-based radiomics platform. Formal user studies are planned to measure the usability and efficiency of the platform. Translation of this tool into a clinical trial setting may assist physicians in developing personalized treatment plans for patients and evaluating their effectiveness.

[1]Lambin et al, Eur J Cancer 48(4) 441-6 2012, [2]Mattonen et al, Int J Radiat Oncol Biol Phys 94(5) 1121-8 2016

Motion and B_0 correction in MRI using FID-SNAVS

PM Johnson[1], J Liu[1], M Drangova[1]
[1]Imaging Research Laboratories, Robarts Research Institute, Western University, London, Ontario, Canada
Supervisor: Dr. Maria Drangova

Introduction: Global shifts in B_0, caused by both motion and scanner heating[1] result in phase inconsistency in the MR data, which may cause ghosting and blurring of the image. The errors caused by shifts in B_0 (ΔB_0) become especially problematic in image sequences with long echo times (TE). It has been shown that correcting k-space data for the phase error introduced by ΔB_0 improves image quality.[2] Measuring ΔB_0 throughout image acquisition would allow for correction of the resulting phase errors and could be especially beneficial to image quality if paired with motion measurement and correction. Free induction decay (FID) acquisitions, inserted within a pulse sequence have been previously used to measure the change in precession frequency[1,3] but never in combination with motion measurement. The combination of an FID with an MR navigator would allow for simultaneous frequency shift (Δf) and motion monitoring, and ultimately Δf and motion correction. Spherical navigator echoes (SNAVs)[4] – k-space navigators used to measure 3D rigid motion – have previously been used to retrospectively correct brain images.[5] In this work we introduce an FID readout prior to the application of the SNAV gradient waveforms (FID-SNAV). We demonstrate simultaneous Δf and motion measurement in a controlled phantom experiment, and demonstrate improvement of motion measurement and image quality following Δf correction.

Methods: ***FID-SNAV:*** The FID readout, added prior to the SNAV, is made up of 64 sample points. The SNAV has a radius of 0.4cm^{-1} and 2508 sample points. The FID-SNAV is interleaved in a spoiled gradient echo (SPGR) sequence with TE/TR=3ms/15ms.

Motion experiment: A pineapple was placed on an MRI compatible linear motion stage and a motion profile with ±1.5cm excursions was delivered while FID-SNAVs were acquired every 120ms for 6.4mins.

Δf and Motion Measurement and Correction: FID-SNAVs and image data were processed in Matlab. Phase shifts between SNAVs were used to calculate translations, while phase shifts between FID sample points were used to calculate Δf. The measured Δf was used to correct the SNAVs by applying the appropriate phase ramp, and translations calculated using the Δf-corrected SNAVs were compared to the original translation estimates and known motion profile. Lastly, two corrected images were generated: the first was motion corrected using the SNAV translation estimates, and the second was Δf corrected and motion corrected using the Δf corrected SNAVs.

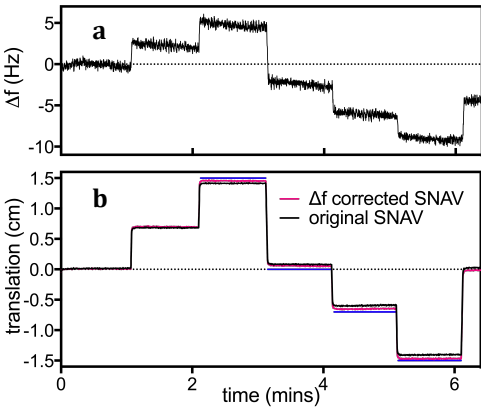

Fig. 1. The measured Δf (a) correspond to the measured translations (b). The blue lines in (b) indicate the prescribed stage locations. Following frequency shift correction of the SNAVs, the SNAV motion measurements are closer to the prescribed motion.

Results: ***Motion and Δf measurement:*** SNAVs measured the prescribed motion profile within a maximum error of 0.9 mm. Frequency shifts, measured using the FIDs (Fig 1a) correspond to the measured motion (Fig 1b). Following Δf correction of the SNAVs, accuracy of translation estimates improved and the maximum error was reduced to 0.5 mm.

Simultaneous Motion and Δf Correction: Figure 2 demonstrates that motion artifacts in the uncorrected image (a) are greatly reduced following motion correction (b) and further reduced following correction for motion and Δf (c).

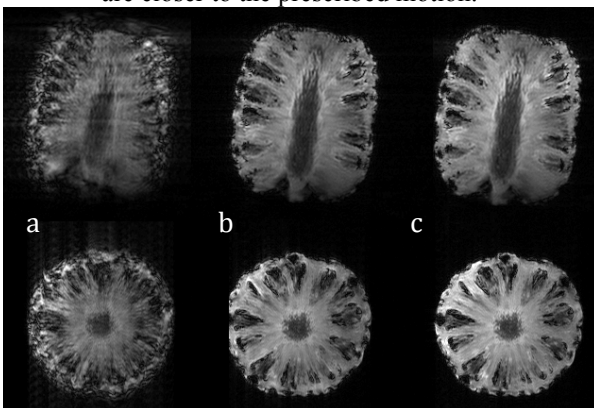

Fig. 2 Axial and sagittal slices from the uncorrected image (8-channel head coil): motion corrected image (b) and motion + Δf corrected image (c).

Discussion/ Conclusions: In this work, FIDs were added to SNAV acquisitions, thereby allowing monitoring of the Δf associated with motion and scanner heating. In controlled phantom experiments, we demonstrated that FID-SNAVS measure Δf and motion simultaneously and that Δf correction improves motion estimation and image quality. In this proof of concept work, FID-SNAVs are interleaved in an SPGR sequence, and dramatic image quality improvement was observed following correction for Δf, despite the short TE of the sequence (3ms). Greater phase errors accumulate in sequences with longer TE's, which are often associated with a longer acquisition time, rendering them more sensitive to field drift and motion. Incorporation of the presented FID-SNAV technique into long TE sequences and evaluation of FID-SNAVs in-vivo will be the focus of future work.

References: [1]Tal, et al., MRM70:895-904, 2013. [2]Loktyushin et al., ISMRM 2016. [3] Kramer, et al., Med Phys 24:164-73. [4]Liu, et al., MRM65:506-514, 2011. [5]Johnson, et al., Magn Reson Imaging 34:1274-82, 2016

Macroscopic Anatomy at Microscopic Scale: Registration of Serial Sections of Histopathology for 3D Analysis of Biological Structures

Starr Johnson[1], Tova Ablove[2], Scott Doyle[1]
[1]Department of Pathology and Anatomical Sciences, University at Buffalo SUNY, NY
[2]Obstetrics and Gynecology, University at Buffalo SUNY, NY

Introduction: In this research, we investigate the problem of reconstructing 3D models of anatomical structure using 2D serial cross sections of histopathology (**Figure 1**). Biological structures are inherently 3D, and analysis of 3D morphology yields valuable insight into both normal and diseased states. However, native 3D microscopy (e.g. confocal, multi-photon) is expensive and high-resolution images are only possible at a limited specimen depth. High resolution visualization is routinely done using 2D microscopic sections, which lose inherent 3D structure. To overcome these limitations, we aim to combine the *resolution* of 2D microscopy with the *structure* of 3D biology by registering stacks of serial histological sections to reconstruct the true architecture. We apply our methodology to the problem of modeling microvessels located between the vagina and bladder at the trigone region. Our goal is to understand the microvessel architecture to assist in developing treatments for recurrent urinary tract infections (UTIs).

Methods: *Image Acquisition:* Tissue samples of the trigone region were harvested from a fresh cadaver (12h post-mortem), fixed, and serially sectioned at a thickness of 6 µm. Tissue slides were stained with CD31 to visualize endothelial cells; these slides were subsequently scanned at 20x optical magnification (0.5 µm per pixel). Overall, 32 serial sections were obtained. For this study, a region of interest containing a vessel structure (**Figure 1**) was manually extracted for registration.

Registration: Unregistered images were imported into the TrakEM2 plugin from Fiji [1]. Registration was performed using the "Elastic Align and Montage" method, which has been shown to work well for datasets of 800+ sections and slide images measuring 6000 by 4600 pixels [2].

Segmentation: Structures of interest were manually annotated to identify tissue structures including smooth muscle and endothelial cells (**Figure 2**). Manual segmentation provides a true ground truth that can be used to validate the registration. Future work will include an automated tissue segmentation routine.

3D Model: The registered aligned and segmented objects were exported as STL files for visualization. **Figure 3** shows an example of the reconstructed 3D model.

Results: The reconstructed model surface displays some local discontinuities. A perfect registration would be expected to have a smooth surface, indicating that the current registration model is not yet optimized. Additionally, image noise (e.g. tissue artifact, tearing, debris, **Figure 4**) contribute to a poor registration result.

Conclusions: Our work illustrates the challenges of registering serial slice stacks to visualize 3D objects. These challenges include: (1) Multi-slice registration (stacks of 20+ slides); (2) Large image registration (500+ MB); and (3) Handling missing or corrupted data in the slice stack (image artifact, lost sections, etc.). Our future work will include increasing stack depth, ROI area, and slice separation to provide a robust solution for building 3D models for a wide variety of anatomical structures at microscopic resolution.

[1] Cardona, A.; Saalfeld, S. & Schindelin, J. et al. (2012), "TrakEM2 software for neural circuit reconstruction.", *PloS one* 7(6): e38011
[2] S. Saalfeld, R. Fetter, A. Cardona and P. Tomancak (2012) "Elastic volume reconstruction from series of ultra-thin microscopy sections", *Nature Methods*, 9(7), 717-720

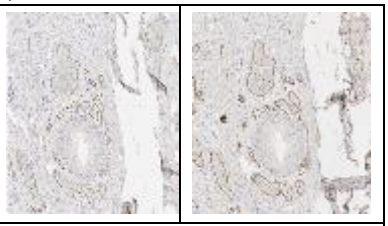

Figure 1: Two images of un-registered microvessel slices.

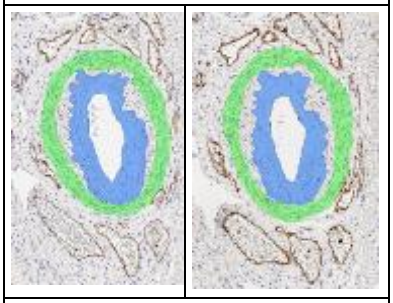

Figure 2: Two images of adjacent, segmented tissue slices. Colors represent smooth muscle (blue) and endothelial cells (green).

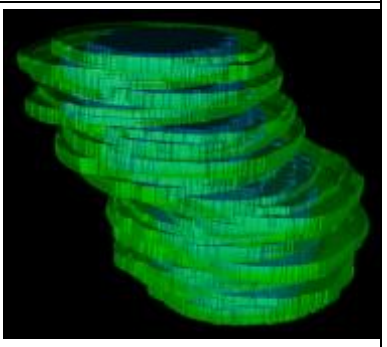

Figure 3: Virtual 3D model of a microvessels in the trigone.

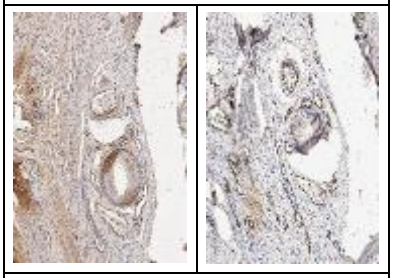

Figure 4: Examples of noisy tissue. Poor staining (left) and tissue folding / tearing (right) both lead to suboptimal registration between these slices and their adjacent slices.

Investigating the relationship of myelin and axonal white matter microstructure using longitudinal relaxation mapping and restricted diffusion

Jason Kai[a,b], BEng, Loxlan Kasa[a,c], MEng, and Ali R. Khan[a-c], PhD (Research Supervisor)
[a]*Robarts Research Institute,* [b]*Dept. of Medical Biophysics, and* [c]*Dept. of Biomedical Engineering, Western University, London, Ontario, Canada*

Introduction: Quantifying and characterizing white matter tracts and microstructure in the brain can aid in diagnosis and treatment of many neurological disorders, such as epilepsy and schizophrenia. Quantitative multi-parametric MRI with accelerated relaxometry mapping and multi-shell diffusion imaging provide the ability to interrogate myelin and axonal architecture respectively. We hypothesize that using these techniques in a unified framework will provide complementary information to allow for more accurate white matter tract segmentation and more sensitive biomarkers of abnormal architecture. To investigate the added benefit of a combined multi-shell diffusion and relaxometry framework, we first sought to explore the correlations between these quantitative parameters in white matter regions, such as those where differences in axonal packing and myelination are known to exist. We also compare these quantitative parameters to those reported in literature with conventional techniques, such as myelin water fraction (MWF) maps[1].

Methods: Ten healthy human subjects were scanned using the Siemens Prisma 3T MRI. T1-weighted (T1w) MPRAGE images were acquired for atlas mapping, and a 1mm MP2RAGE sequence was used to obtain high-resolution T1 maps, inverted to produce R1 maps. A multi-shell diffusion imaging protocol with 2mm resolution, b-values of 0, 1300, and 1600 s/mm^2, 140 gradient directions was acquired twice with L-R and R-L phase encoding directions. Diffusion images were corrected for EPI and eddy current distortions using topup and eddy (FSL), and diffusion kurtosis maps were generated (DKE toolbox) to characterize restricted diffusion (mean kurtosis). Furthermore, reported MWF values were used to investigate the relation with relaxivity rates.

The MNI152 atlas was registered to both the R1 and diffusion maps via the T1w volume. The JHU white matter atlas and Harvard-Oxford cortical and subcortical atlases were propagated to these maps (see figure 1) to compute mean values for each subject in each region.. Furthermore, the correlation of R1 and kurtosis is also calculated for each white matter structure.

Results: Different microstructures are shown to have varying relationships between mean R1 and mean MWF (see figure 2). Variance in the R1 between different subjects are seen. Further investigation show no similar correlation in R1 and kurtosis for different microstructures (see table 1).

Conclusion: The distinct values of each microstructure could improve accuracy of white matter tract segmentations. While R1 and kurtosis show no distinct correlation, further investigation is required due to the limited sample size. Analysis of these relations can advance our knowledge of the brain and aid in the development of the parcellation objective.

References: [1] Meyers *et al*. Magn. Reson. Imaging (2009);27:1096-03.

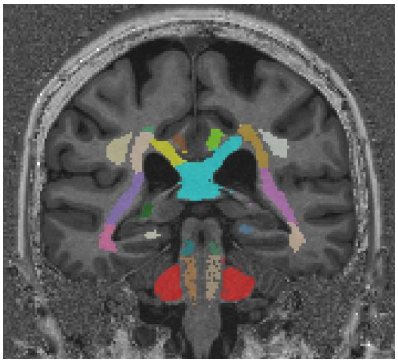

Figure 1. Registered white matter atlas to R1-map.

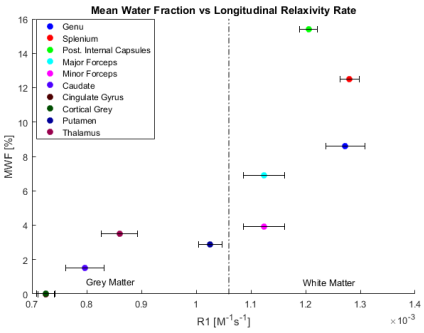

Figure 2. Myelin water content vs mean R1 with standard error

Structure	Correlation	p-value
Genu	0.8090	0.0046
Splenium	0.5565	0.0947
Post. Internal Capsule	-0.0411	0.9101
Major Forceps	0.3750	0.2856
Minor Forceps	0.7739	0.0157

Table 1. Correlation between R1 and kurtosis. Differences are expected due to underlying differences in microstructure (ie. myelination)

Towards lung tissue stiffness imaging by using a micromechanical model of the alveolar sac

Elham Karami[1,2], Behzad Seify[3], Hadi Moghadas[4], Masoomeh Sabsalinejad[5], Ting-Yim Lee[1,2,6,7], Abbas Samani[1,2,8,9]

[1]Department of Medical Biophysics, Western University; [2]Imaging Research Laboratories, Robarts Research Institute;[3]Department of Biomedical Engineering, Amirkabir University of Technology, Iran; [4] Department of Electrical and Computer Engineering, Isfahan University of Technology, Iran;[5] National Institute of Genetic Engineering and Biotechnology, Iran;[6]Imaging Program, Lawson Health Research Institute;[7]Department of Medical Imaging, Western University;[8]Department of Electrical and Computer Engineering, Western University;[9]Graduate Program in Biomedical Engineering, Western University, London, Ontario, Canada

Supervisors: Abbas Samani, Ting-Yim Lee

Introduction. Lung disease is the third leading killer in the United States, responsible for one in seven deaths, and is the leading cause of death among infants under the age of one. Biomechanical modeling is an effective tool for gaining insight into the nature of some lung diseases (e.g. COPD and lung cancer) and developing diagnostic and computer assisted treatment methods. Among various applications of lung biomechanical modeling are elastography and motion correction which are used for diagnosis and therapeutic procedures, respectively. The mechanical properties of the tissue are an essential component of lung biomechanical modeling. As such, we have developed a detailed microscopic model of lung tissue which can be utilized in the aforementioned applications. The main application of the proposed microscopic lung tissue model involves creating stiffness parameters maps of the lung using an inverse optimization framework and the macro-scale tissue mechanical properties obtained through experimentation. To model the alveolar sac, we used similar geometry to that of Denny and Schroter (2006)[1] where each alveolus is modeled with a truncated octahedron. In this study, we modelled two alveolar sacs which share one air way. Next, breathing was modeled as a fluid-structure interaction in ABAQUS software package where the air was modeled as fluid and the alveolar sacs as structure. Finally, the experimental data published by Zeng et al.[2] was used in an inverse optimization framework to calculate the alveoli wall stiffness value.

Results. The model geometry and its mesh are shown in Fig. 1. The results indicate that the average stiffness for the alveoli wall is 5.2 kP which agrees well with data reported in the literature.

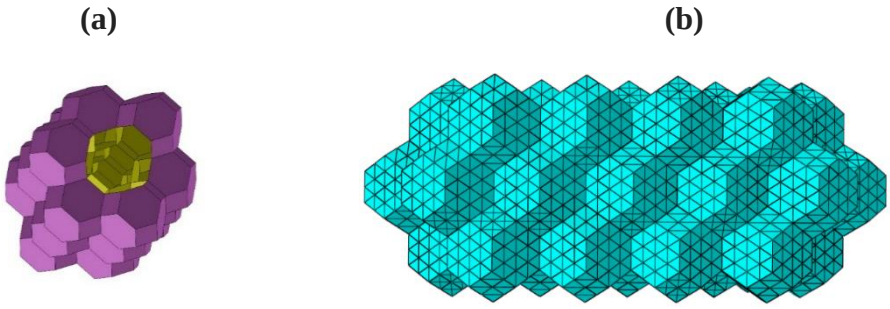

Fig. 1. (a) The proposed geometry for one alveolar sac. (b) The created mesh for two connected alveolar sacs.

Conclusions. A micromechanical model was proposed for lung parenchyma tissue. Calculated alveoli wall stiffness values obtained from optimization agree well with values reported in the literature. Although the preliminary results are encouraging, the model has to be further validated by applying it to various pathological conditions.

1. E. Denny and R. C. Schroter, “The mechanical behavior of a mammalian lung alveolar duct model.,” J. Biomech. Eng. **117**, 254–261 (1995)

2. Zeng et al., “Measurement of the mechanical properties of the human lung tissue.,” J. Biomech. Eng. **109**(2), 169–174 (1987)

Discovery Radiomics via a Mixture of Expert Sequencers using Layered Random Projections (LaRP) for Prostate Cancer Classification

Amir-Hossein Karimi[1], Audrey G. Chung[1], Mohammad Javad Shafiee[1], Farzad Khalvati[2], Masoom A. Haider[2], Ali Ghodsi[3], and Alexander Wong[1]

[1] Vision and Image Processing Research Group, University of Waterloo, Waterloo, ON, Canada
[2] Medical Imaging, University of Toronto and Sunnybrook Research Institute, Toronto, ON, Canada
[3] Statistics and Actuarial Science, University of Waterloo, Waterloo, ON, Canada

Introduction: Prostate cancer is the most diagnosed form of cancer in Canadian men, and is the third leading cause of cancer death. Magnetic resonance imaging (MRI) is a non-invasive imaging-based prostate cancer screening method, and automatic computer-aided prostate cancer classification or *radiomics*-driven methods based on MR images have been developed to help streamline the diagnostic process. Current radiomics-driven tumor gradings for prostate cancer screening use hand-crafted quantitative radiomic features extracted from multi-parametric MRI (mpMRI), making their performance highly dependent on the features used. This study extends the use of discovery radiomics for prostate cancer classification [1] to a mixture of expert sequencers, each a LaRP radiomic sequencer that discovers unique features, for more accurate prostate cancer classification.

Methods: We propose a novel framework via a mixture of LaRP sequencers (mLaRP), each individually trained to uncover and classify different abstract imaging-based features that capture highly unique tumour traits and characteristics. The weighted vote (based on feature expertise) of the individual expert sequencers was then leveraged to generate the mixture prediction for prostate cancer classification. A total of 8 LaRP sequencers were consulted in the weighted vote, each discovering distinct features using mpMRI data from 20 patients, i.e., T2w, ADC (using 0, 100, 400, 1000s/mm^2), high-b DWI (2000s/mm^2), and correlated diffusion imaging. Given the limited amount of available data, data augmentation was performed via the rotation of each tumour candidate at 45˚ intervals, resulting in 640 cancerous regions and 714 healthy regions that can be used as tumour candidates for training the individual LaRP sequencers.

Results: The mixture of discovered LaRP radiomic sequencers was evaluated against two state-of-the-art hand-crafted radiomic sequencers proposed by Peng et al. [2] and Khalvati et al. [3] for classifying tumour candidates as either healthy or cancerous using a feedforward neural network classifier with a single hidden layer of 100 nodes. Sensitivity, specificity, and accuracy were calculated via leave-one-patient-out cross-validation with the collected dataset. Despite dropping the T2w modality and using only 64 hidden nodes in the classifier, mLaRP produced comparatively improved sensitivity (0.46), specificity (0.91), and accuracy (0.85).

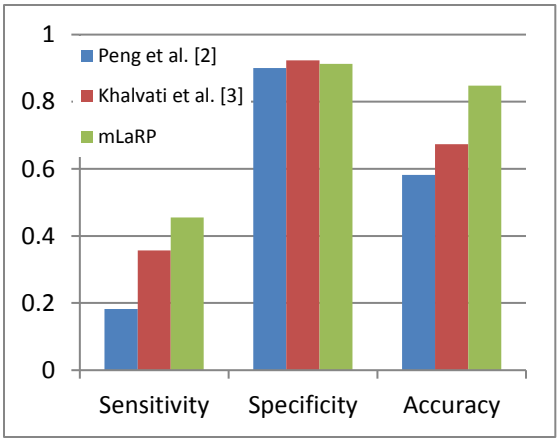

Fig. 1. Sensitivity, specificity, and accuracy metrics for mLaRP, Peng *et al.* [2], and Khalvati *et al.* [3].

Conclusion: Using a mixture of LaRP radiomic sequencers, each acting as an expert at discovering unique features from mpMRI data, we were able to generate radiomic sequences that are specifically tailored for quantifying and differentiating healthy and cancerous prostate tissue. This further demonstrates the potential of discovery radiomics, compared to conventional hand-crafted radiomic features, for building custom radiomic sequences for cancer classification.

Acknowledgements: This research has been supported by the Ontario Institute of Cancer Research (OICR), Canada Research Chairs programs, Natural Sciences and Engineering Research Council of Canada (NSERC), and the Ministry of Research and Innovation of Ontario. The authors also thank Nvidia for the GPU hardware used in this study through the Nvidia Hardware Grant Program.

References

[1] A. Chung et al., IEEE International Conference on Image Processing (ICIP), p. 246-250, 2016.
[2] Y. Peng *et al.*, *SPIE Medical Imaging*, pp. 86 701H–86 701H, 2013.
[3] F. Khalvati *et al.*, *BMC medical imaging*, vol. 15, no. 1, p. 27, 2015.

Optimization of CT coronary angiography for improved plaque detection

Hany Kashani [1], Graham Wright [2], Ali Ursani [3], Garry Liu [2], Narinder S Paul [3,4]

[1] Institute of Medical Science, University of Toronto, Toronto, ON
[2] Department of Medical biophysics, University of Toronto, Toronto, ON
[3] Department of Medical Imaging, University of Toronto, Toronto, ON
[4] Department of Biomedical Engineering, University of Toronto, Toronto, ON

Introduction

The study aims to determine the optimal X-ray exposure parameters that maximize spatial and contrast resolution during CT coronary angiography (CTCA) for detection of early non-calcified plaque (NCP).

Methods

An anthropomorphic coronary plaque phantom (CPP), was scanned on a second generation wide volume 320MDCT (VISION, TMS, Japan) using 320x0.5mm, 500ms, sFOV (180mm), 80-135kVp and 100-600mA; resulting in CTDIvol of 0.8-23 mGy. The CPP is a 10 cm cylinder (40HU @ 120kV) that contains 7 synthetic coronary vessels 3-5mm diameter and 10mm in depth. Each vessel contains variable thickness of synthetic cholesterol (40HU), muscle (60HU) and triglyceride (-100HU) with normal (1-1.5 mm) and abnormal (2-3 mm) wall thickness. The vessel lumen was opacified to 250 - 350 HU. The CPP was inserted into an anthropomorphic chest phantom (QRM, Germany).

Spatial resolution, contrast resolution and vessel wall thickness were measured at all exposures. Spatial resolution was measured using the modulation transfer function. Contrast resolution was quantified using the contrast to noise ratio (CNR). The vessel wall thickness was measured using a pixel intensity profile technique.

Results

The CTCA measured spatial resolution was 0.495 $\pm$ 0.058mm (range 0.385-0.625mm). The 1.5 mm vessel wall measured 1.82 $\pm$ 0.36mm (range 1.4-2.8 mm) and the 3 mm vessel wall measured 3.39 $\pm$ 0.46mm (range 2.45-4.9mm). Repeated measures ANOVA demonstrated a threshold of tube current for a significant decrease in spatial resolution as follows: 80kVp-500mA (4.2mGy), 100kVp-500mA (9.1mGy); 120kVp-400mA (11.6mGy); 135kVp-400mA (15.3mGy). CNR increased significantly with higher tube current for all tube potentials.

Conclusions

Focal spot size is a key determinant of spatial resolution and enlarges at a tube current threshold of 500mA for 80 and 100kV, and 400mA for 120 and 135kVp. Tube current has a more dominant effect on spatial and contrast resolution than tube potential in the exposure range used in clinical CTCA. Spatial resolution was optimized at a tube current of 300 mA at tube potential settings resulting in more precise vessel wall measurements.

Evaluation of Recovery Coefficients applied to Image-derived Input Functions for Patlak analysis of FDG-PET MRI - A manifestation of Occam's Razor?

Matt Kewin[1,2], Udunna C Anazodo[1,2], Jonathan D Thiessen[1,2], John Butler[1], Jennifer Hadaway[1], Laura Morrison[1], Keith S St. Lawrence[1,2]

[1]Lawson Health Research Institute, London, Ontario, Canada. [2]Medical Biophysics, Western University, London, Ontario, Canada.

Introduction: Hybrid PET and MRI provides a unique means of quantifying PET imaging without the need for serial arterial sampling by using MRI to define the feeding arteries from which the time-activity (i.e., the arterial input function, AIF) can be measured. Image guidance is necessary to minimize partial volume errors (PVE) and spill-in effects caused by the limited spatial resolution of PET. In this study, we evaluate four techniques for extracting image-derived input functions (IDIFs) for kinetic modelling of PET 18F-flourodexoyglucose (FDG) with and without recovery coefficients to account for PVE and spill-in. Three previously applied methods to extract PET activity were adapted to hybrid PET-MRI and the fourth is a novel method introduced in this study.

Methods: PET and MRI brain images from eight pigs were acquired on the Biograph MMR system (Siemens). 60 minutes of FDG data were acquired after an IV injection (71.36 ± 12.2 MBq) and the data was reconstructed to 51 time bins. AIFs were measured by a MR-compatible blood sampling system (Swisstrace GmbH) and analyzed using PMOD (PMOD Technologies). Anatomical TOF images were acquired during PET imaging and used to mask the carotid arteries accurately. The co-registered carotid mask was applied to the 60-min PET time series, and the IDIFs were extracted from volumes of interest using: 1) maximum pixel value, 2) average of four maximum pixels, 3) average pixel intensity, and 4) a novel technique that used the median pixel values. IDIFs were corrected for PVE and spill-in using a phantom study to determine the appropriate correction factors for arteries as a function of their diameter. IDIFs with and without the two recovery coefficients were used for Patlak kinetic modelling of FDG to determine the combined kinetic rate constant (K_i) which is proportional to the cerebral metabolic rate of glucose (CMR_{glc}).

Results: The mean carotid diameter across all animals was 4.3 ± 0.2 mm. All extraction methods had a strong correlation of Ki to the AIF, with Pearson correlation values over 0.94. The table below shows resulting Ki values for the AIF and the different IDIF methods with and without recovery coefficients. The graph displays an exemplary subject's IDIFs and AIF showing lack of influence of the spill in correction factor for the promising median method and the accurate correspondence of the maximum method to the AIF. These curves yielded K_i's of 0.003 min^{-1} for the AIF, 0.001 min^{-1} for the median PVE corrected IDIF, 0.001 min^{-1} with additional spill-in correction and 0.004 min^{-1} for the maximum IDIF.

Discussion and Conclusion: The strong correlation between all of the IDIF techniques and arterial blood sampling is supported by prior evidence and shows promise in the extraction methods. It is interesting to observe the consistency in the methods shown in the correlations, however, the corrected methods lack the accuracy and precision of the simple method using the uncorrected maximum intensity. Further investigation is required into these recovery techniques, yet kinetic modelling of PET-FDG using an MRI-derived IF can provide a valuable tool, and when combined with multi-parametric MRI techniques (perfusion, diffusion, spectroscopy, etc.) can improve the diagnostic accuracy of neuroimaging tools used in neuro-psychiatric or degenerative diseases.

Method	*Mean K_i ± std. dev. [min^{-1}]*
AIF	0.0096 +/- 0.013
[1] max	0.0133 ± 0.016
max PVE	0.0023 ± 0.003
max both RC	0.0031 ± 0.004
[2] four max both RC	0.0139 ± 0.018
four Max PVE	0.0024 ± 0.003
four max both RC	0.0033 ± 0.005
[3] mean	0.0222 ± 0.037
mean PVE	0.0048 ± 0.008
mean both RC	0.0048 ± 0.008
[4] median	0.0238 ± 0.039
med PVE	0.0042 ± 0.007
median both RC	0.005 ± 0.008

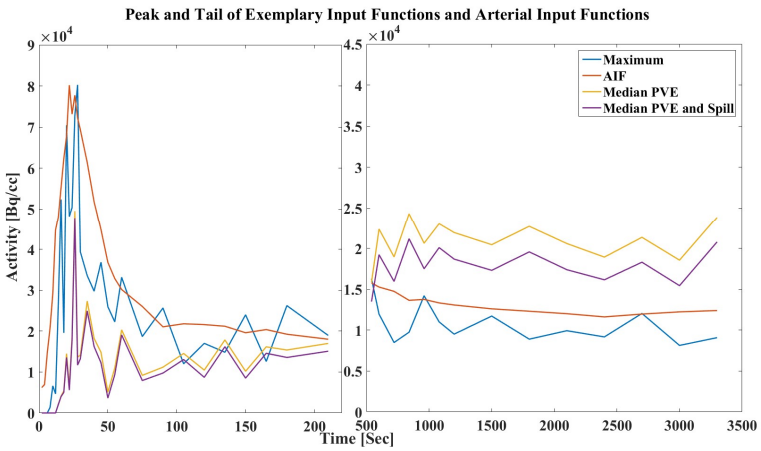

Flipping the Computer Aided Diagnosis (CAD) Training Paradigm for Prostate Cancer: Using PI-RADS Reporting of Multi-Parametric MRI (mpMRI) to Train a CAD System and then Validating with Pathology

Farzad Khalvati[1], Junjie Zhang[1], Sameer Baig[1], Alexander Wong[2], Masoom A Haider[1]
[1]Medical Imaging, Sunnybrook Research Institute, University of Toronto, Toronto, ON, Canada
[2]Systems Design Engineering, University of Waterloo, Waterloo, ON, Canada

Introduction: Most CAD systems for detection of prostate cancer are trained using wholemount sections from prostatectomy or biopsy results to identify cancerous regions [1]. This is becoming increasingly difficult as prostatectomies decline and biopsies are both harmful and painful to patients. The purpose of this study was to design a CAD system which uses PI-RADS v2 reports [2] from mpMRI to train a classifier via a radiomics feature model to detect clinically significant prostate cancer and examine whether this correctly identifies tumour sites by validating on a set of wholemount specimens.

Methods: PI-RADS reports were completed for 99 patients (age 66±8) with 43 patients having PI-RADS scores of 4 and 5. The prostate gland and transitional zone (TZ) were manually contoured and fed to a segmentation algorithm developed to automatically generate PI-RADS zone map. Each PI-RADS zone was segmented to smaller clusters of pixels (i.e., superpixels) and each superpixel was labelled using the PI-RADS score of the zone [3]. Using an mpMRI radiomics feature model [4], a comprehensive set of radiomics features (450 features) was constructed to train a support vector machine classifier and the best subset of features was selected using a feature selection algorithm. The trained classifier was first applied to the 99 patients' data via a leave-one-patient-out cross-validation to verify the CAD performance compared to PI-RADS scores. It was then applied to a separate dataset of 6 wholemount cases with Gleason score 7 and above to evaluate the performance compared to histology results.

Results: CAD performance compared to PI-RADS scores was calculated for TZ and peripheral zone (PZ) separately both per PI-RADS zone and per patient. PI-RADS zones results for TZ/PZ are: Sensitivity: 0.86/0.92, Specificity: 0.92/0.93, Accuracy: 0.92/0.93. Patients' results for TZ/PZ are: Sensitivity: 0.87/0.73, Specificity: 0.73/0.81, Accuracy: 0.75/0.79. The CAD performance compared to wholemount histology results was calculated for PI-RADS zones only since all 6 cases had clinically significant prostate cancer, which yielded (TZ/PZ): Sensitivity: 0.85/1.00, Specificity: 0.94/0.83, Accuracy: 0.93/0.84 (Table 1).

Table 1. Classification results for prostate cancer using CAD trained by PI-RADS scores

	Ground Truth	Sensitivity (TZ/PZ)	Specificity (TZ/PZ)	Accuracy (TZ/PZ)
Per PI-RADS zone	PI-RADS Scores	0.86/0.92	0.92/0.93	0.92/0.93
Per Patient	PI-RADS Scores	0.87/0.73	0.73/0.81	0.75/0.79
Per PI-RADS zone	Wholemount Histology	0.85/1.00	0.94/0.83	0.93/0.84

Conclusion: This paradigm enables training of CAD systems for prostate cancer using PI-RADS scores given by radiologists which enables detection of clinically significant prostate cancer compared to histology data. The ability to train a CAD system capable of detecting prostate cancer using PI-RADS scores only without using histology data for training can reduce the need for biopsy which is invasive and harmful.

References: [1] G. J. S. Litjens et al. "Computer-extracted features can distinguish noncancerous confounding disease from prostatic adenocarcinoma at multiparametric MR imaging," Radiology, vol. 278, no. 1, pp. 135–145, 2016. [2] J. O. Barentsz et al. "ESUR prostate MR guidelines 2012", European radiology, vol. 22, no. 4, pp. 746–757, 2012. [3] J. Zhang, F. Khalvati, et al. "Superpixel-based prostate cancer detection from diffusion magnetic resonance imaging," J. Comput. Vis. Imaging Syst., 2015. [4] F. Khalvati, et al. "Automated prostate cancer detection via comprehensive multi-parametric magnetic resonance imaging texture feature models," BMC Med. Imaging, 2015.

Three dimensional head ultrasound for the detection of shunt failure in infants with hydrocephalus: pilot study

J Kishimoto[1,2], A Fenster[1,] D.S.C Lee[3], [2], S. de Ribaupierre[1,4]

[1]Department of Medical Biophysics, University of Western Ontario; [2]Robarts Imaging, University, Western Ontario; [3]Department of Neonatology, University of Western Ontario, London Health Sciences Centre; [4]Department of Clinical Neurological Sciences, University of Western Ontario, London Health Sciences Centre: London, Ontario, Canada

Research Supervisors: Sandrine de Ribaupierre and Aaron Fenster

Introduction Infantile hydrocephalus, the abnormal accumulation of cerebral spinal fluid (CSF) within the brain ventricles, is a serious, potentially life threatening condition that occurs in about 1.1 in 1000 infants. Hydrocephalus is a highly variable disease with numerous causes that can be congenital, such as from spina bifida, or genetic abnormalities, but also can be acquired such as after meningitis or cerebral hemorrhage. For many of these patients, neurosurgical insertion of a ventriculoperitoneal (VP) shunt that constantly drains CSF into the abdomen is the treatment course to prevent further brain damage. Generally, VP shunts are usually valve-regulated in order to maintain a constant flow and/or pressure regardless of patient's position (i.e. lying down vs. standing). Despite the widespread use of VP shunts, 31% of shunts will fail within the first year and require revision surgery. Shunts can fail by either becoming blocked and no longer drain enough CSF, or through overdrainage of CSF leading to slit ventricle syndrome. Often shunt failure only becomes apparent when clinical symptoms occur, such as when an infant is overly irritable, lethargic, nauseous, ataxic, and is failing to thrive. Detecting shunt failure prior to clinical symptoms could decrease brain injury, and increase the quality of life for the infant and their caregivers.

3D ultrasound (US) can be performed in a neurosurgical clinic both before VP shunt insertion and at follow up for much less than the cost of other 3D medical images, and in fractions of the time. Changes in the ventricle volume measured from these images could inform clinicians as to whether or not the shunt is working appropriately, and whether this can be detected prior to clinical symptoms of shunt failure.

Methods Following parental informed consent, 3D US images were taken before and after VP shunt insertion to measure ventricle volume. Images were acquired post-VP shunt surgery at follow up neurosurgical appointments until the fontanelle had closed. This 3D US system has been previously validated in preterm neonatal brain ventricle volume imaging.[4] Ventricles increasing in volume could indicate underdrainage or a blockage. Overdrainage is likely to result in ongoing large decreases in ventricle volume even after symptoms of increased intracranial pressure has improved.

Results Five near term and term born neonates were involved in this study with hydrocephalus resulting from spina bifida revision surgery (N=2), meningitis (N=1), and intraventricular hemorrhage (N=2). All patients showed a decrease in ventricle volume and no patients had revision surgery due to underdrainage in the study period. One patient had a valveless shunt replaced with a valved VP shunt due to overdrainage risks. This patient's images and ventricle volumes can be seen in Fig. 1.

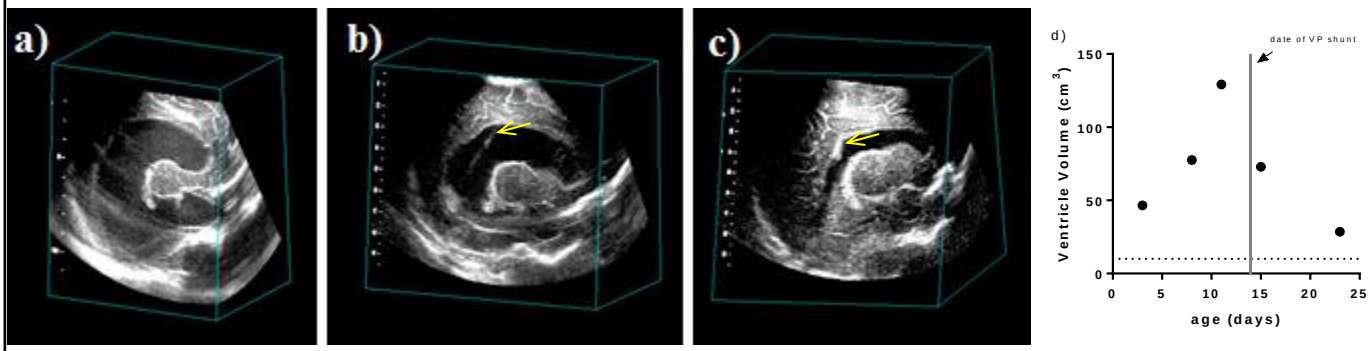

Fig 1 – 3D US images and ventricle volumes from a term born (39 weeks gestational age) neonate with hydrocephalus following a suspected *in utero* intraventricular hemorrhage. a) 11 days of life b) 15 days of life c) 23 days of life. Dramatic reduction in ventricle size can be seen and parents mentioned considerably less fussiness and increased ease of feeding after initial shunt surgery at 15 days of life. Arrows indicate where the shunt is placed. Patient had revision surgery to convert initially inserted valveless VP shunt to valved VP shunt around 60 days of life due to the infant's increased mobility.

Conclusions Through this initial study, we have shown collection of 3D US image based ventricle volumes is feasible in a neurosurgery clinic setting and that these images are able to provide acute shunt failure information at least in a single case of overdrainage. More study is required in patients as a blockage of the shunt causing underdrainage was not seen in the initial 5 patients.

Computational Evaluation of Glenoid Bone Loading using Micro-CT

Nikolas K Knowles[a,b,*], Andrew Nelson[b,c], Louis M Ferreira[a,b]
[a]Biomedical Engineering Graduate Program, The University of Western Ontario
[b]Collaborative Training Program in Musculoskeletal Health Research, and Bone and Joint Institute, The University of Western Ontario
[c]Department of Anthropology, The University of Western Ontario

Introduction: Accurate computational modelling of bone is essential to improve our understanding of bone quality and the mechanisms that compromise joint replacement components, and surgical procedures. Although significant advancements have been made in lower limb models, few studies have adapted these techniques to the upper limb. Furthermore, pre-processing and analysis of micro-level models involve extensive time and computational requirements, limiting their effectiveness for iterative model evaluation. The purpose of this work was to i) develop a CT-compatible compressive loading device, ii) develop a micro-bead tracking method to validate computational models of the glenoid using pre- and post-loaded micro-CT scan data, and iii) compare traditional finite element (FE) simulation software (Abaqus) to new geometrical-based simulation software (Simsolid).

Methods: The CT-compatible compressive loading device (Fig. 1) was manufactured and pilot testing was performed by acquiring pre- and post-loaded scans of a porcine glenoid (31 µm isotropic voxels, 200 kVp, 130 µA, 1 mm Cu filter) implanted with stainless steel micro-beads (~500 µm) (Fig. 2). A scan of a human scapula was also acquired (64 µm, 95 kVp, 64 µA) and used to create a micro-level computational model from the glenoid (Fig. 3). A 1 x 1 x 0.5 cm section of the glenoid vault was reconstructed as a stereolithography (STL) file. The raw STL was input into Simsolid and a 250 N compressive load was applied. The same STL model was meshed using tetrahedral elements with a maximum 60 µm edge length. The Abaqus finite element (FE) model was loaded with the same 250 N compressive load. All simulations were performed on 8 CPU cores and 128 GB RAM.

Results: No movement was detected during scan acquisition, indicating that the loading device is able to maintain constant load. The stainless steel micro-beads show high contrast with the surrounding bone/cartilage with no metal artifact and are easily reconstructed. Loading scans using the same method are currently being completed in cadaveric human glenoids (n=14).

Simsolid simulation time was 3 min 11 sec with no pre-processing steps required. Meshing of the Abaqus FE model required ~4 hours to mesh and ~12 hours to simulate. The strain results (Fig. 3) are comparable between both the Simsolid model and the Abaqus FE model.

Conclusions: This study evaluated a CT-compatible loading device for use with cadaveric glenoids. The micro-bead tracking method showed excellent contrast and will be used for computational model validation. Preliminary studies using Simsolid have shown comparable results to traditional FE simulation software, with a 100 fold decreased time requirement. The resultant output files were 250 MB and 38 GB for Simsolid and Abaqus, respectively. This significant time and computational savings may improve micro-CT studies, which are impaired by computational requirements.

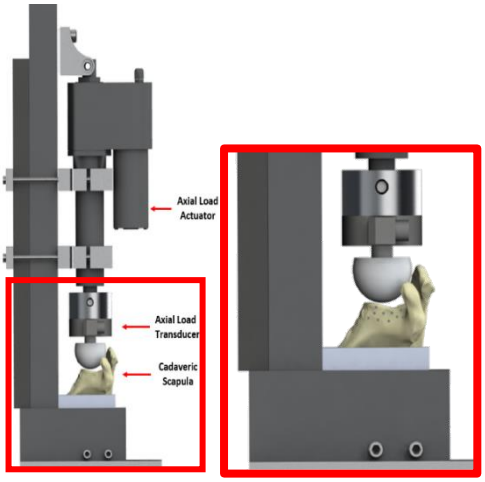

Figure 1: Micro-CT compatible uni-axial load application device designed for loading bone within the Nikon XT H 225 ST Micro-CT.

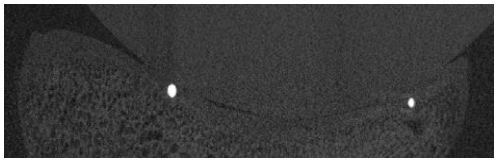

Figure 2: Micro-CT image (31 µm isotropic voxels, 200 kVp, 130 µA, 1 mm Cu filter) of porcine bone loaded in the uni-axial loading device during a fast acquisition scan.

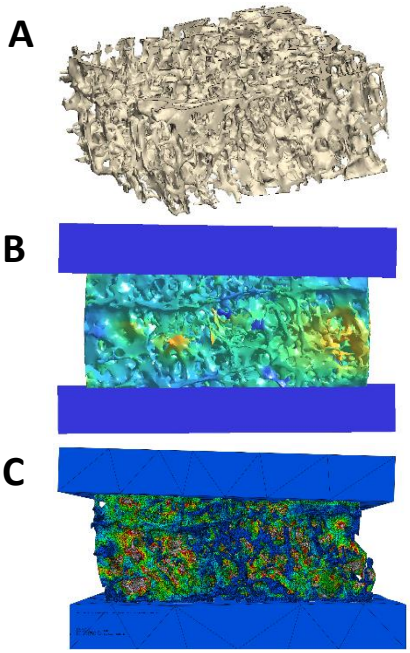

Figure 3: 1 x 1 x 0.5 cm section removed from glenoid vault (A). Strain results from Simsolid (B). Strain results from Abaqus (C). Note variations occur in colourmap rendering, but probed values between models are comparable.

Evaluation of MRI-Guided Focal Laser Ablation Therapy Procedures

Eric Knull[a], Aytekin Oto[b], David Tessier[a], Aaron Fenster[a]
OICR Imaging Translation Program
[a]Robarts Research Institute, Western University, London, Ontario, Canada; [b]University of Chicago Medicine, Chicago, Illinois
Under the supervision of Dr. Aaron Fenster

Introduction. Prostate cancer is the most common cancer among Canadian men with an estimated 21,600 diagnoses in 2016 (1). As an alternative to radical treatments such as resection of the prostate, focal laser ablation (FLA) therapy aims to eliminate small, low-risk lesions while preserving healthy tissue. This minimally invasive procedure has the potential to reduce patient morbidity and maintain urinary and erectile function by leaving delicate structures such as the neurovascular bundles and urethral sphincters intact. During FLA, the physician inserts ablation needles to identified targets within the prostate. It is important that needles are guided accurately to ensure complete ablation of malignant tissues while avoiding the critical structures. Multi-parametric magnetic resonance images (MPMRI) are acquired before, during, and following procedures to assist in identifying targets, guiding needles, and assessing treatment outcomes.

Methods. In this study, we evaluated the location of ablation zones relative to targeted lesions in 27 patients who underwent FLA therapy, with a total of 34 identified tumours. MPMRI were acquired for each patient several months preceding the procedure and during the procedure. Prostates (diagnostic and intra-operative), lesions (diagnostic), and ablation regions (intra-operative) were contoured on diagnostic 3T T2-weighted axial MRI scans and on intra-operative 1.5T T1-weighted contrast-enhanced axial MRI scans by a trained operator under the supervision of a clinician. The lesion surface was non-linearly registered to the intra-operative scan using an initial affine registration followed by thin-plate spline registration of the prostate surfaces. The margins between the registered lesion and ablation zone were measured using a uniform spherical distribution of rays, and the volume of intersection was also measured. Each prostate was contoured 5 times (with at least 2 days of separation) to determine the variability of segmentation and its effect on assessment of treatment outcome.

Results. Of the 34 identified lesions, 3 were poorly visible under MRI and thus were removed from the study. Of the remaining 31 lesions, 14 were completely ablated and 5 were completely unablated; the rest were partially ablated. The mean percentage of unablated tumour volume across all tumours was 24.3±36.5%. The mean furthest distance tumours extended beyond the ablation zone was 1.83±4.93mm, with the furthest tumour extending 21.97mm beyond the nearest ablation zone. In one patient, we found segmentation variability caused a change in prostate volume of up to 13.6% and lowered the treatment margin by up to 1.5mm with no effect on unablated tumour volume.

Conclusions. These results suggest a strong possibility that some patients were left with untreated malignant tissue, and that better needle guidance is required to ensure accurate ablation. Analysis of segmentation variability thus far did not find a significant impact on assessment of treatment outcome.

References. [1] Canadian Cancer Society, “Prostate Cancer Statistics” http://www.cancer.ca/en/cancer-information/cancer-type/prostate/statistics/?region=on (17 January 2017).

Dynamic electrogram changes after radiofrequency ablation relate to MR-based lesion visualization

Philippa Krahn[1,2], Jennifer Barry[2], Mihaela Pop[1,2], & Graham A Wright[1,2]
[1]Dept. of Medical Biophysics, University of Toronto, [2]Sunnybrook Research Institute
Consortium: Image-Guided Device Interventions for Cardiovascular Disease

Introduction: Many radiofrequency (RF) ablation procedures for patients with scar-related ventricular tachycardia (VT) result in late VT recurrence, often due to recovery of tissue excitability between discontinuous lesions. RF ablation causes a combination of reversible and irreversible injury, and of particular interest is the development of transient edema. Acute edema may reduce myocardial excitability, leading to overestimation of lesion extent by functional excitability-based measures. The objective of the current study is to relate excitability to MRI-based tissue characteristics.

Methods: Epicardial RF lesions were created via open-chest catheter ablation in 3 swine (1 lesion/animal). Electrograms (EGMs), which reflect myocardial excitability, were repeatedly recorded by probing the lesion core, rim, and remote tissue after ablation. After explanting the heart, the *ex vivo* MRI study included T2 mapping and T1-weighted imaging (inversion-recovery prepared steady-state free-precession, IR-SSFP) to visualize edema and necrosis respectively.

Results: The lowest EGM amplitudes were consistently observed at the lesion core (Fig 1A-B). The amplitude at the rim (9±4mm away) decreased over time, which may reflect the impact of spreading edema on excitability within the catheter's sensitive depth, at least 5mm. The MRI-derived edema and lesion core had maximum radii of 15±4mm (Fig 1C) and 6±1mm (Fig 1D) respectively. This suggests that edema contributes substantially to the broad region of altered excitability surrounding the lesion, likely not attributed to the lesion core alone. Our prior imaging studies have shown growth in edematous areas within 3h after endocardial ablation, by up to 2.6-fold the area at the first imaging time point.

Conclusions: The effect of edema on local excitability could confound detection of continuous lesions. This knowledge and the use of MRI in future ablation procedures may be used to guide in-procedure corrections and improve long-term success rates for VT ablation therapy.

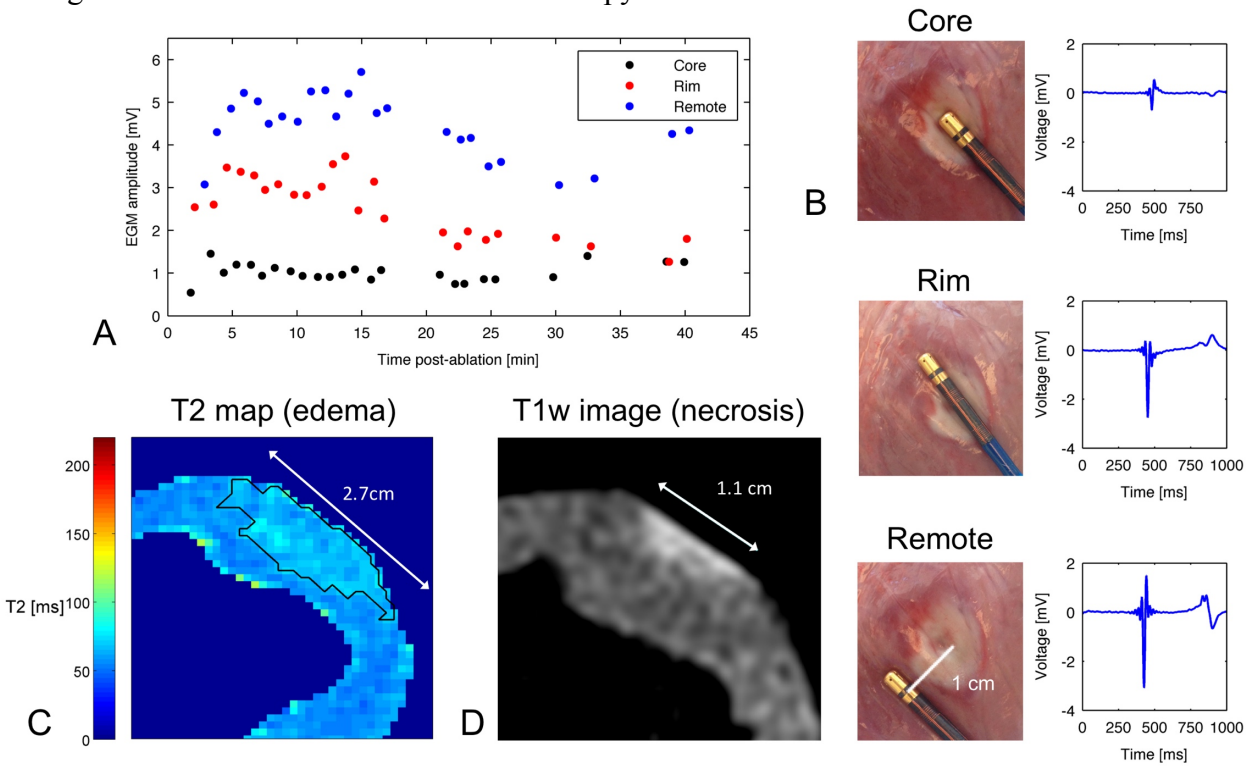

Figure 1: (A) EGM amplitudes measured at 3 key locations with time after ablation. (B) Catheter position with respect to the RF lesion and corresponding EGM waveforms. (C) T2 map and (D) T1-weighted IR-SSFP image demonstrating edema and necrotic lesion core respectively at the epicardial ablation lesion.

Identifying epileptogenic lesions using cortical thickness

Sancgeetha Kulaseharan(*), Mehran Ebrahimi(*), and Elysa Widjaja(**)
(*) Faculty of Science, University of Ontario Institute of Technology, 2000 Simcoe Street North, Oshawa, ON, Canada, L1H 7K4
(**) Diagnostic Imaging, The Hospital for Sick Children (SickKids), 555 University Avenue, Toronto, ON, Canada, M5G 1X8

Introduction: Focal cortical dysplasia (FCD) is a brain malformation that is frequently responsible for epilepsy in children. FCD is one of the most challenging lesions to detect on Magnetic Resonance Imaging (MRI) as the imaging features may be subtle and not infrequently missed. Abnormal cortical thickness is one of the features of FCD [2]. The aim of this study was to determine if using objective measure of cortical thickness could assist with identifying subtle FCD on MRI.

Methods: The volumetric T1-weighted imaging was acquired on 3T MRI in 32 children with focal epilepsy having subtle lesion that was suspected to be FCD. Five patients had focal cortical thickening that was visible on visual inspection of the MRI by a neuroradiologist. All patients underwent epilepsy surgery resection and had post-operative CT or MRI. Cortical thickness measurements were acquired using the Freesurfer software. The shortest distance from the pial surface to the gray-white matter junction is computed. The same is done from the gray-white matter junction to the pial surface. The average of these two values is taken to be the cortical thickness [1]. Cortical thickness measures were saved as a vector of values. These thickness values were sampled into a volume that could be read in MATLAB.

In MATLAB, for each case a 3D-Gaussian smoothing filter was applied followed by a gamma correction. Vertex points were selected that fell in the 95% confidence level. These vertexes were matched to their structure name and hemisphere using annotation files from Freesurfer. A threshold of 5 mm was applied to the cortical thickness values. The clusters of abnormal cortical thickness were classified into 8 possible locations: right and left frontal, temporal, parietal, and occipital. The location of clusters was compared to surgical resection site on post-operative CT or MRI.

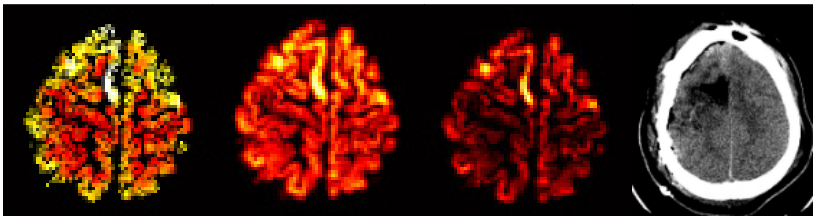

Figure 1 [a, b, c, d] - Case NL036 Processing of volumetric T1 MRI: (a) Showing raw non-filtered cortical thickness measurements, followed by the application of (b) Gaussian Smoothing (c) Gamma filtering. The cluster of abnormal signal corresponded to (d) surgical resection site on post-operative CT scan. Scan indicating location of lesion was removed.

Results: The mean age of the patients was 11.73 years. Of the 32 patients, clusters of abnormal cortical thickness were identified in all 32 patients and in 23 patients these corresponded to surgical resections sites. The overall sensitivity of cortical thickness measures to identify FCD was 70% and the specificity was 56%. Of the 5 patients that had focal cortical thickening by visuals inspection, objective measures of cortical thickness showed that the sensitivity and specificity were 100% and 74% respectively.

Conclusions: Objective measures of cortical thickness can be used to identify subtle FCD that may have been missed by visual inspection. Further research is need to reduce the false negative findings.

References: [1] Hong *et al.,* Automated detection of cortical dysplasia type II in MRI-negative epilepsy, Neurology 2014;83(1):48-55. [2] Lüsebrink *et al.*, Cortical thickness determination of the human brain using high resolution 3 T and 7 T MRI data, NeuroImage 2013;70: 122-131.

Deep Medical Imaging Visualization for Clinical Decision Support

D. Kumar[1], V. Menkovski[2], F. Khalvati[3], M.A. Haider[3], and A. Wong[1]
[1]Department of Systems Design Engineering, University of Waterloo, Waterloo, ON, Canada
[2]Department of Mathematics and Computer Science, TU Eindhoven, Netherlands
[3]Department of Medical Imaging, Sunnybrook Research Institute, University of Toronto, ON

Introduction: Deep Neural Networks (DNN) have shown great promise in recent years as a potential tool for clinical decision support. Much to the success of these networks is attributed to their ability to create and learn a hierarchy of robust features directly from the data, allowing them to capture nuances that handcrafted features based on clinical intuition may miss. One of the main drawbacks with current DNN approaches to clinical decision support systems is that it is very difficult to gain insight or rationale as to how DNNs makes decisions, thus limiting their utility to clinicians. While quantitative metrics such as accuracy or AUC can be used to evaluate their decision-making abilities, they do not convey any information about how a network makes decisions. Therefore, there is a vital need for tools that can help and aid clinicians in understanding the decision-making process of DNNs. Such tools can help the clinicians to: 1) understand the internal decision making process of DNNs instead of using them as "black boxes", which is pivotal for adoption into clinical decision support, 2) identify the regions of interest in a medical image that lead to the decisions. Both will lead to improved confidence of clinicians on the decision-making process of these networks. Motivated from this, in this study we present a deep medical imaging visualization tool that fulfills these goals by creating heat maps of the *regions of interest* in a medical image used for the decisions made by a DNN**.**

Method: The proposed deep visualization tool extends upon the approach first proposed by Zeiler & Fergus [1], where feature activities in the intermediate layers of a Convolutional Neural Network (ConvNet) are mapped back to the input pixel space using a Deconvolutional Neural Network (DeConvNet) attached to each layer of the network. To examine a given activation in the ConvNet, all the other activations are set to zero in the layer and the feature maps are passed as input to the attached DeConvNet layer. The single activation here resembles a small piece of the original input medical image, with structures weighted according to their contributions toward to the feature activation. Thus, the output image obtained from the DeConvNet gives an intuition of the most important pixels in the input medical image that trigger the activation functions, hence providing a heat map of the regions of interest in the medical image that is involved in the decisions of network.

Experiments and Results: We evaluate the efficacy of the proposed deep visualization tool via a ConvNET trained for human anatomy classification task [2]. The various output from the tool are shown in figure below:

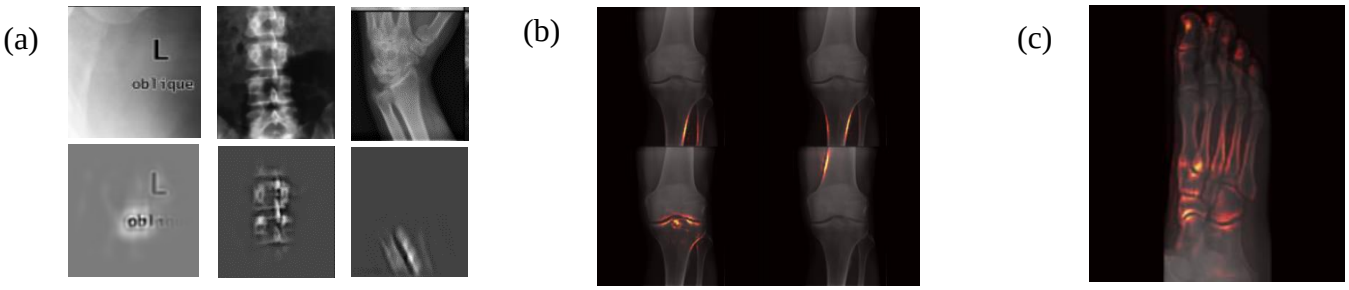

Fig.1 (a) Original anatomy X-ray images (above) and output from one random filter (below) in the last convolution layer of anatomy classification network. (b) Top 4 most activated filter from the last convolutional layer from the same network. (c) Top 25 filters from the last convolutional layer. In (b) and (c) the heat maps are produced by overlaying the deconvoluted outputs from the proposed tool on the original X-ray images. The heat maps show where in the images the network focuses to recognize anatomy in humans.

Conclusion: The proposed deep visualization tool aids clinicians in understanding the decision-making processes of deep neural networks, thus improving the confidence of clinicians on the output produced by such networks. The tool provides heat maps overlaid on the input image, showcasing the regions of interest responsible for the decisions made by the network. Thus, the proposed tool has great potential to speed up the screening and diagnosis process while improving consistency and accuracy.

Reference: [1] Zeiler, Matthew D., and Fergus, Rob. "Visualizing and understanding convolutional networks." European Conference on Computer Vision. Springer International Publishing, 2014
[2] Kumar, Devinder, and Menkovski, Vlado. "Understanding Anatomy Classification Through Visualization." 30th NIPS machine learning for health (MLH) workshop, 2016

Patient Specific Atria Models for Training and Pre-Procedure Surgical Planning

Justin Laing[a], John Moore[b], Daniel Bainbridge[c], Maria Drangova[ab], Terry Peters[ab]
[a]Department of Biomedical Engineering, Western University, 1151 Richmond St, London, ON Canada, N6A 3K7; [b]Robarts Research Institute, 1151 Richmond Street North, London, ON Canada, N6A 5B7; [c]Department of Anesthesiology, Western University, 1151 Richmond St, London, ON Canada, N6A 3K7

Introduction

Minimally invasive cardiac procedures requiring a trans-septal puncture such as atrial ablation and MitraClip© mitral valve repair are becoming increasingly common. These procedures are performed on the beating heart, and require surgeons to rely on image-guided techniques. For cases of complex or diseased anatomy, in which the image guidance can be difficult to interpret, surgical teams may benefit from patient-specific atrial models that can be used for training and surgical planning.

Methods

A patient specific atrial model was generated from computed tomography (CT) images of a patient's heart that were segmented and used to generate geometric models. Using rapid prototyping, the geometric models were converted into physical representations and used to build a mold. The atria were then molded using tissue-mimicking materials and imaged using CT. The resulting images were segmented, and used to generate a point cloud data set that could be registered to the original patient data. The absolute distance of the two point clouds was compared and evaluated to determine the model's accuracy.

Results

The two-point cloud models were compared using Euclidean offset distance. For this trial which only includes 1 patient data set, when comparing the point cloud of the physical model to the original data set, the results have a maximum distance of 4.5 mm, an average of 0.5 mm and a standard deviation of 0.6 mm.

Conclusions

Using our workflow for creating atrial models, potential complications, particularly for complex repairs, may be accounted for in pre-operative planning. The information gained by the clinicians involved in planning and performing the surgery should lead to shorter surgical times and better outcomes for patients.

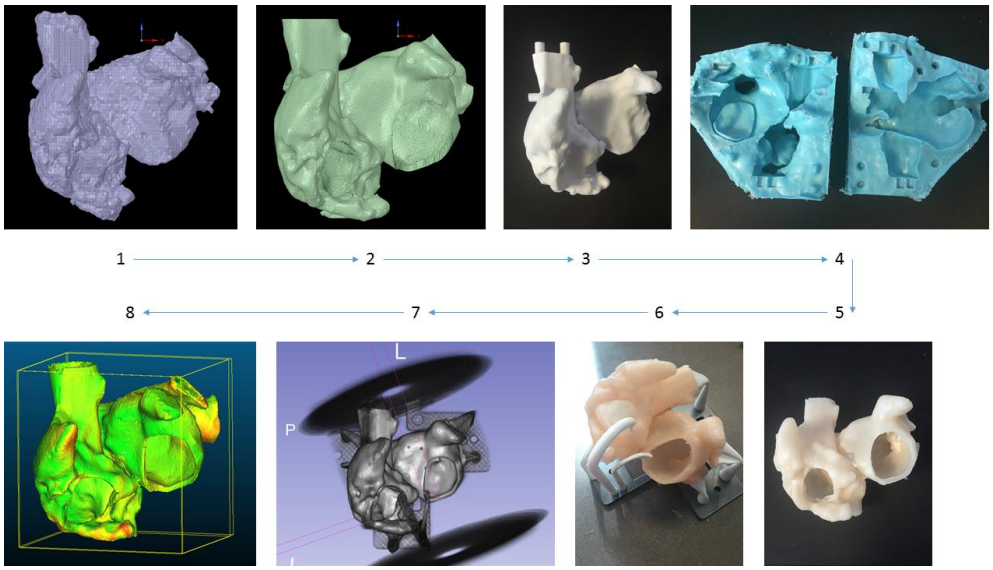

Figure 1: Workflow showing the progression from segmentation of patient CT data to silicone model

Clinical integration of ultra-high field templates for target selection in deep brain stimulation surgery

Jonathan C. Lau[1,2,3], Andrew G. Parrent[3], Keith W. MacDougall[3], Terry M. Peters[1,2,4], Ali R. Khan[1,2,4]

1. Imaging Research Laboratories, Robarts Research Institute
2. Biomedical Engineering Graduate Program, Western University
3. Department of Clinical Neurological Sciences, Western University and London Health Sciences Centre
4. Department of Medical Biophysics, Western University

London, Ontario, Canada

Introduction: Template and atlas-guidance are fundamental aspects of stereotactic neurosurgery. The recent availability of ultra-high field (7 Tesla) magnetic resonance imagers (MRI) has enabled *in vivo* visualization at the sub-millimeter scale. Here we describe our experiences with integrating ultra-high field templates into the clinical workflow to assist with target selection in deep brain stimulation (DBS) surgical planning.

Methods: The creation of 7T templates, derived from group data at our centre, has previously been described. A computational workflow is described for spatially aligning the 7T template with standard clinical data and furthermore, integrating the aligned templates into the surgical planning workstation.

Results: We demonstrate that our methodology can be effective for assisting with target selection in two cases: unilateral internal pallidum DBS for painful dystonia and bilateral subthalamic nucleus DBS for Parkinson's disease. The example for unilateral internal pallidum is shown.

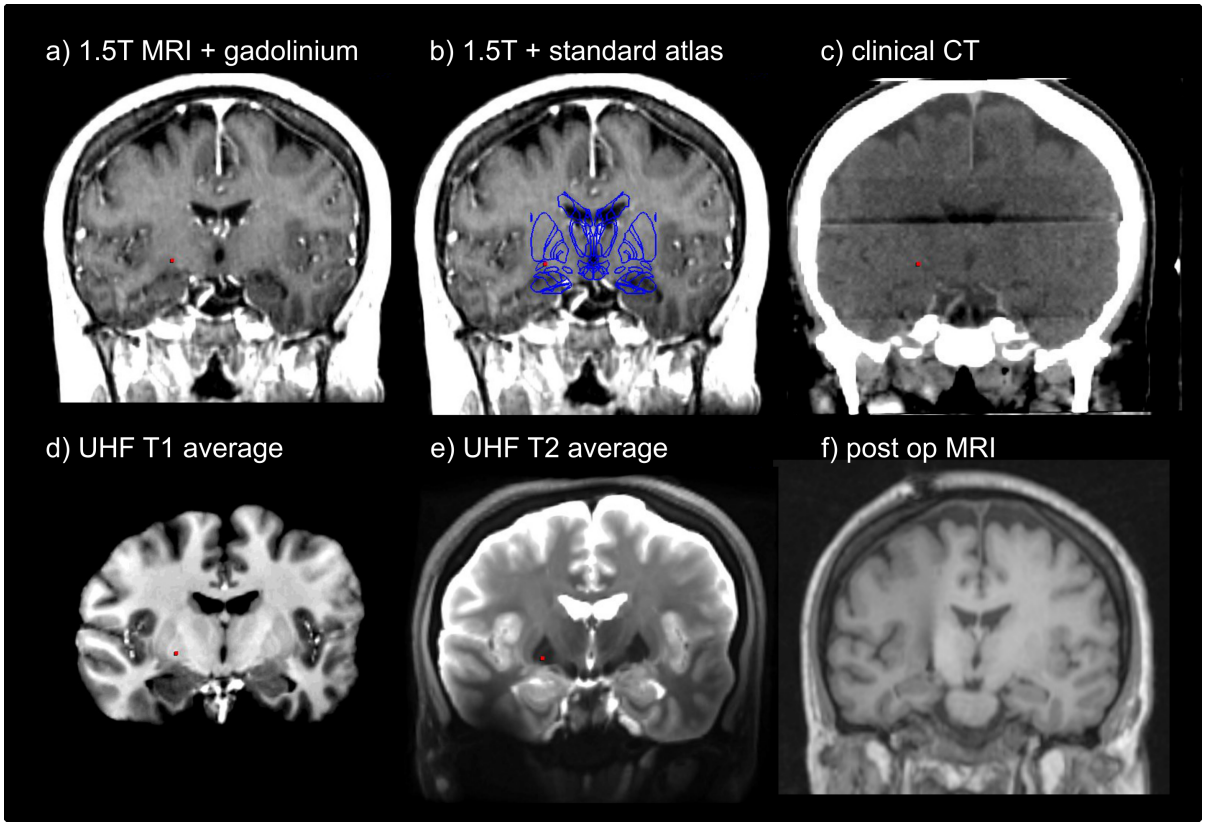

Conclusions: We have described a workflow for the integration of high-resolution *in vivo* ultra-high field templates into the surgical navigation system as a means to assist with DBS planning. Future work will include prospectively evaluating different templates and their impact on target selection quantitatively.

Title: Characterizing an Orthotopic C6 Glioblastoma Rat Model with Multiparametric Magnetic Resonance Imaging and Bioluminescence Imaging.

Authors: Trung N.T. Le[1], Heeseung Lim[1], Amanda Hamilton[2], Katie Parkins[1], Francisco M. Martínez[2], Timothy J. Scholl[1,2,3], John A. Ronald[1,2]

Affiliations: 1. Medical Biophysics, Western University, London, ON, Canada.
2. Robarts Research Institute, Western University, London, ON, Canada
3. Ontario Institute for Cancer Research, Toronto, ON, Canada

Introduction. Glioblastoma multiforme (GBM) is the most aggressive and invasive type of glioma and accounts for approximately 50% of all brain tumours. Despite various aggressive therapeutics, patients rarely survive past 18 months after diagnosis. Due to the unpredictable and complex nature of this disease, a more thorough understanding of GBM tumorigenesis is required to improve treatment of this disease. The C6 orthotopic rat model is a GBM model that shares many characteristics of human GBM tumour progression and reflects the highly invasive nature of the disease. The purpose of this study was to investigate the biological behaviour of the C6 GBM model during tumorigenesis and to identify key characteristics of the disease using bioluminescence imaging (BLI) and multiparametric magnetic resonance imaging (mpMRI).

Methods. Rat C6 glioma cells were transduced to express Firefly luciferase (Luc). 1×10^6 C6-Luc cells were stereotactically implanted into the right hemisphere of Wistar rat brains (n=6). All rats were imaged with BLI, and mpMRI on days 4, 8, 11, 15 and 18, post-implantation. BLI was performed on an IVIS Lumina XRMS in the lateral position following an i.p. injection of 300mg Luciferin/kg body weight. A 500-mT/m insertable gradient system was used for high-resolution mpMRI on a 3 Tesla scanner (GE Healthcare Discovery MR750). Anatomical images were obtained using a 3D T_2-weighted and 3D T_1-weighted post contrast (Magnevist) imaging sequence. Functional imaging included diffusion tensor imaging and dynamic susceptibility contrast imaging to assess perfusion. At end point, frozen sections of the rat brain were prepared for histology and compared with imaging data.

Results

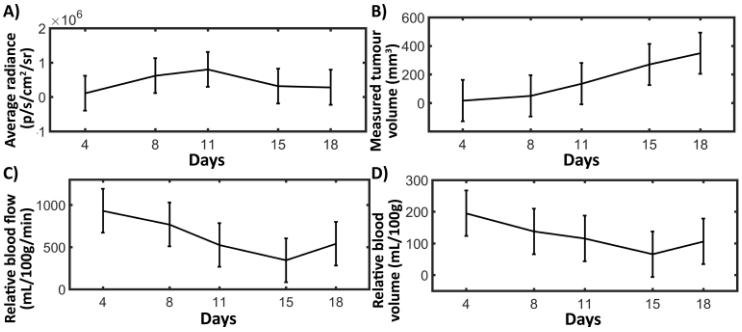

Fig 1. A) Average BLI signal from six animals is shown for five imaging time points along with the corresponding tumour volume based on T_2-weighted images (B), and relative blood flow (C) and volume (D). BLI signal peaks on day 11 and declines towards day 15 and 18, despite an increasing tumour volume. Relative blood flow and volume decrease over time as the tumour develops.

Additional functional parameters such as apparent diffusion coefficient (ADC), mean transit time (MTT) and fractional anisotropy (FA) were also obtained. ADC was increased compared to the contralateral hemisphere and appeared to decrease over time while FA and MTT increased over time.

Conclusion. This study has demonstrated the importance of characterizing the C6-Luc rat model during tumorigenesis using multi-modality imaging. Contrary to our initial hypothesis that BLI signal should increase with tumour size, this model showed an unexpected development in terms of BLI signal, tumour burden and functional information, as seen in Fig. 1. An expanded analysis is being performed to obtain evidence to explain the decrease in BLI signal despite increasing tumour volume. One potential hypothesis is limited perfusion of larger tumours leading to reduced D-luciferin delivery and/or increased necrotic regions in larger tumours that do not contribute to BLI signal but do to tumour volume. Functional information such as ADC, FA and MTT may provide further information to better understand this disease model. A deeper understanding of this model will help with future studies that examine treatment response or novel imaging modalities.

Preliminary study for personalization of renally excreted cancer drugs using pulse dye densitometry

Fiona Li[1], Alexandra Hauser-Kawaguchi[2], Leonard G Luyt[2], Christopher McIntyre[1], James Koropatnick[3] and Ting-Yim Lee[1]

Ontario Institute of Cancer Research (OICR) - Smarter Imaging Program

Department of [1]Medical Biophysics, [2]Chemistry, [3]Oncology, Western University
Supervisors: Ting – Yim Lee and James Koropatnick

Introduction: Over-dosing of cancer drugs can lead to complications ranging from fatigue to death. The therapeutic effectiveness and complications of these drugs are related to their plasma concentration over time. The optimal dose can be determined from the area underneath the plasma concentration vs time curve using Calvert's formula as long as the glomerular filtration rate (GFR) is known. Accurate measurement of GFR is therefore required for personalized drug dosing. GFR is a measure of kidney function. Clinically it is assessed by measuring creatinine content in a blood sample or in urine collected over 24-hr. However, the assessment is inaccurate in persons with either high or low muscle mass, as creatinine is also produced by muscle turn-over. Therefore, the goal of the project is to develop an optical method for accurate GFR measurement without the requirement of blood sampling or urine collections.

Method: To measure GFR, an optical dye, Cy7.5, was conjugated to a GFR reference agent, inulin. Transcutaneous pulse dye densitometry (TPDD) was used to measure the plasma clearance of Cy7.5-inulin following intravenous injection. TPDD developed for measurement of another dye, ICG, was calibrated for measurement of Cy7.5 instead by taking the ratio of absorption peak of the two dyes. This calibration was validated using CT contrast agent (CTCA), also a GFR agent. An open 2-compartment model (fig 1) was developed to simulate the measured plasma clearance curve. Curves with normal (120mL/min), mild (60 mL/min) and impaired (30mL/min) GFR were simulated for 30, 20 and 15 min of data acquisition and also the expected level of noise. The simulated curves were fitted using the open 2-compartment model.

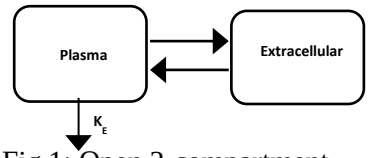

Fig 1: Open 2-compartment model. K_E is GFR

Result: The calibration factor for the TPDD determined as the ratio of GFR estimated by the TPDD and CTCA was similar to that estimated by the ratio of peak absorbance of ICG and Cy 7.5 (~1.7). Simulation studies estimated the reproducibility and accuracy of GFR estimation for 30, 20 and 15 min of data acquisition as 0.13± .56, -0.05±2.0 and -0.97±4.62 mL/min respectively (fig 2). This suggests that the difference in the GFR of 2.2, 7.9 and 18.1 mL/min can be measured with 95% confidence when the plasma clearance curve is acquired for 30, 20 and 15 min respectively.

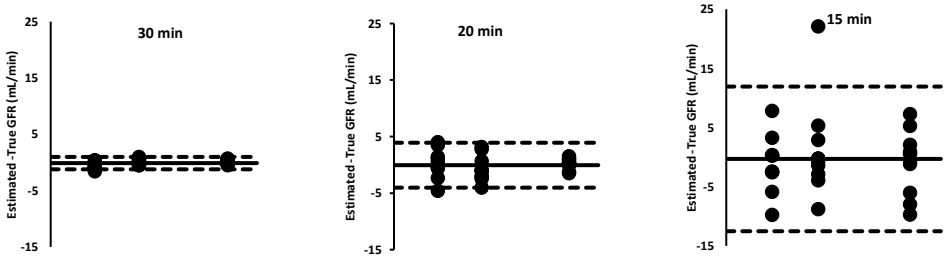

Fig 2: Bland-Altman plot for simulation studies to estimate reproducibility and accuracy of GFR estimation

Conclusion: TPDD can be used to non-invasively measure GFR directly without the need for blood sampling or urine collection and subsequent laboratory measurements of these biologic fluids. The TPDD acquisition time can be as short as 30 min making the technique clinically feasible for personalized drug dosing based on GFR leading to more efficient treatment without the risk of drug toxicity.

Longitudinal Monitoring of Tumour pH Gradient with MRI

Heeseung Lim[1], Mohammed Albatany[1], Francisco M. Martínez[1,2], Robert Bartha[1,2], Timothy J. Scholl[1,2,3]

[1] Medical Biophysics, Western University, London, ON, Canada; [2] Robarts Research Institute, Western University, London, ON, Canada; [3] Ontario Institute for Cancer Research

Introduction: The acid-base balance in the brain is tightly controlled by endogenous buffers such as bicarbonate and phosphate. Tumours often express a positive pH gradient (intracellular pH – extracellular pH) in contrast to a negative gradient in normal tissue. An alkaline intracellular pH (pH_i) in tumour increases the activity of several metabolic enzymes that drive cellular proliferation. In contrast, an acidic extracellular pH (pH_e) is established due to increased lactic acid production and the subsequent active transport of protons out of the cell. Given the pharmacokinetics of chemotherapeutic drugs are highly depended on tumour pH, the ability to non-invasively quantify tumour pH is an important aspect of cancer treatment. This study used two magnetic resonance imaging (MRI) techniques to map the intracellular/extracellular pH gradient longitudinally in a rodent glioma model. The pH_i was mapped with chemical exchange saturation transfer (CEST) and hyperpolarized ^{13}C bicarbonate magnetic resonance spectroscopic imaging (MRSI) was used to determine regional pH_e.

Methods: 7 Wistar rats were surgically implanted with one million C6 glioma cells in the right caudate nucleus of the brain. pH_i and pH_e were mapped in the tumour tissue and contralateral brain tissue at 8, 12 and 15 days post implantation. pH_i maps were measured using CEST MRI on a 9.4T small animal MRI scanner (Agilent, Santa Clara, CA). CEST spectra were acquired using a standard fast spin echo (FSE) pulse sequence. Immediately following CEST, pH_e was measured using hyperpolarized ^{13}C bicarbonate MRSI on a Discovery MR750 3.0T scanner (GE Healthcare, Waukesha, WI). The animal received a single bolus injection of 150-mM hyperpolarized ^{13}C sodium bicarbonate solution through the tail vein and ^{13}C spectra of the rat brain were acquired using an optimized 2D FID-CSI.

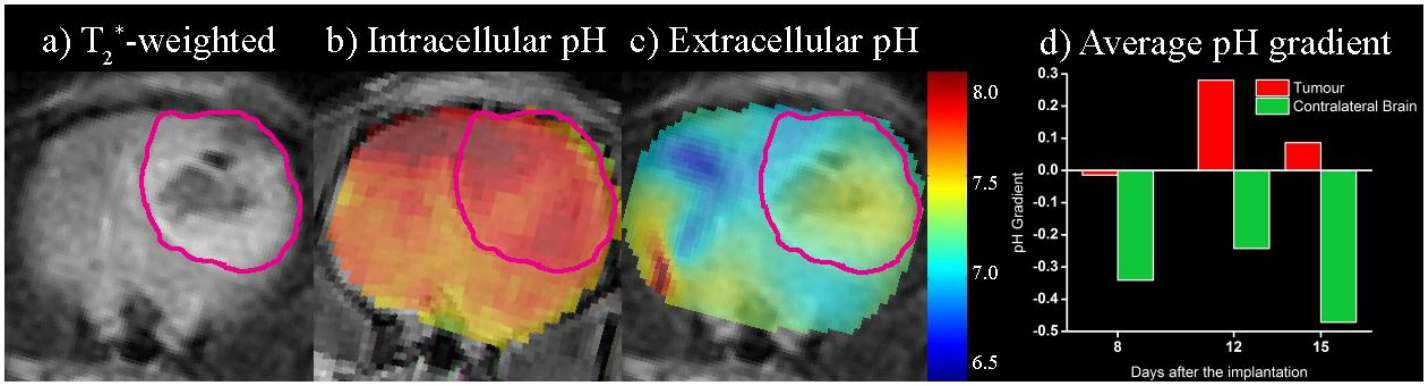

Figure 1: a) T_2^*-weighted proton anatomical image of rat glioma model. b) and c) pH_i and pH_e maps of a rat glioma model. The tumour is outlined with magenta lines. c) average pH gradient over 7 rodents are shown.

Results: Exemplary pHi and pHe maps of a representative rodent glioma model are shown in Figure 1 a) & b). The pH_e within the tumour was more acidic, whereas the pH_i was more alkaline leading to an increase in the pH gradient compare to contralateral. Longitudinal measurements of the average pH gradient for all rodents is shown in Figure 1 c). Overall, the averaged pH gradient in the tumour changed from -0.01 to 0.28 then 0.09. Conversely the pH gradient of contralateral brain tissue changed from -0.34 to -0.24 then -0.47.

Conclusions: Our results showed a consistent increase in tumour pH gradient compared with contralateral tissue. Furthermore, as demonstrated in Figure 1, the pH gradient of tumours increased during tumour growth and also the heterogeneity of tumour pH began to increase at later time point. These regional measurements may be useful to assess therapeutic response and predict local areas of treatment resistance. Overall, the intracellular/extracellular pH gradients in this rodent glioma model were non-invasively measured to a precision of ~0.1 pH units at three time points. Since most therapeutic agents are weak acids or bases, *a priori* knowledge of the pH gradient may help guide choice of therapeutic agent. In future work, tumour heterogeneity will be validated using histology.

Gadolinium-Free Blood Pool MRI Contrast Agents Based on Manganese(III) Porphyrin for High Clinical Field (3 T) MRA: Probing and Tuning the Serum Albumin Binding

Ontario Institute for Cancer Research Smarter Imaging Program: An Ontario Imaging Consortium
Hanlin Liu[a,b], Piryanka Sasidharan[b], Vladimir Constantinescu[b], and Xiao-An Zhang[a,b,c] *
[a]Department of Chemistry, University of Toronto. [b]Department of Physical and Environmental Sciences, [c]Department of Biological Sciences, University of Toronto Scarborough.

Introduction: Current clinical MRI contrast agents (CAs) are mainly gadolinium (Gd) based. Although relatively safe and sensitive (sensitivity measured as T_1 relaxivity or r_1), the r_1 decreases sharply as the magnetic field is increased to the clinic field strengths of 1-3 T. Worse yet, once the Gd ion dissociates from its chelator, the safety is compromised in the form of nephrogenic systemic fibrosis (NSF), a rare but life-threatening side effect pronounced in patients with renal dysfunction. In addition, cases of Gd-deposit in the brain have been increasingly reported. The issue could be amplified for blood pool agents (BPAs) used in MR angiography (MRA), as they require prolonged vascular contrast retention and exposure. To address both issues caused by the Gd based CAs (GBCAs), we focused on the manganese(III) porphyrin (MnP) platform as an attractive alternative, due to abnormally high r_1 at high clinic fields and Mn biocompatibility. We recently developed **MnP2**, the first MnP-based BPA that exhibits exceptionally high r_1 at 1-3 T as well as high affinity for human serum albumin (HSA) which prolongs vascular contrast enhancement.[1-3] The r_1 slightly decreases upon binding to HSA, which may be caused by the hydrophobic protein restriction on water accessibility, and opens room for improvement. This study aimed to understand where and how **MnP2** bound to HSA, which has multiple drug binding sites, and further to tune the binding through porphyrin structural modification to optimize r_1 and to modify HSA affinity and thus to control vascular retention.

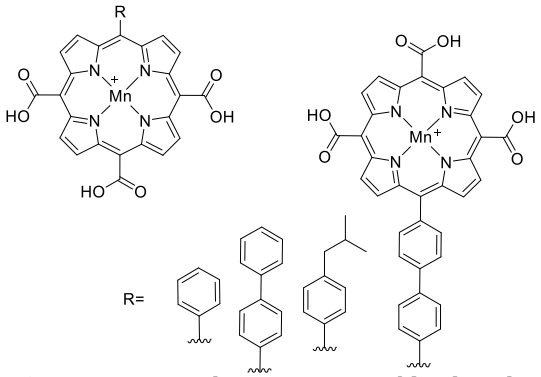

Figure 1. Proposed new generation blood pool agents, all containing hydrophobic HSA-binding moieties. All four MnPs will utilize COO^- groups for water solubility and to prevent hindrance to water accessibility.

Methods: The binding of **MnP2** and its fluorescent analog, **P2**, with HSA were monitored by optical methods, including UV-vis, circular dichroism (CD) and fluorescence spectroscopies, as well as by relaxometry, where applicable. Drugs with known binding sites on HSA were used for competing studies. Based on the results, four new MnPs were designed (Fig. 1), synthesized, and structurally characterized using ^{1}H-NMR, UV-Vis and mass spectroscopies, where applicable. The field-dependent r_1 (NMRD) profiles are obtained with a variable field NMR relaxometer covering magnetic fields from 0 to 3 tesla.

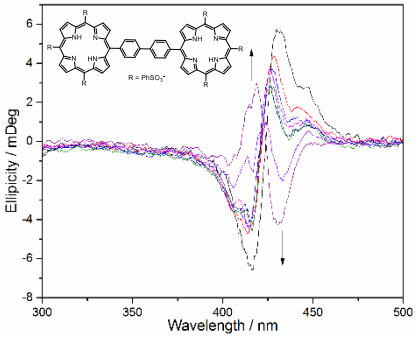

Figure 2. CD monitoring of P2 upon addition to HSA in the dark at 37 ˚C over 48 hours in 25 mM pH 7.4 HEPES. The induced chiral signal flip-flops over the time period.

Results and Discussion: Although most methods used were unable to detect the presence of multiple binding sites, CD monitoring showed that **P2** binds to HSA through two separate steps, possibly involving two binding sites. Subsequent studies pointed to subdomain IIIA as the first binding site based on competitive binding experiments using ibuprofen, followed by a slow transfer into subdomain IB. The new MnPs shown in Fig.1 were thus designed to incorporate structural features mimicking drugs known to bind in subdomain IIIA. Through increasing the affinity to subdomain IIIA, which is a more water-accessible site, and decreasing the affinity to subdomain IB, which is more hydrophobic, the new MnPs are expected to have higher r_1 upon HSA binding. Among them, one monomeric porphyrin has been successfully synthesized and characterized, where R = phenyl. Future work will be focused on its affinity for HSA as well as its r_1 change upon protein binding.

Conclusions: The HSA binding sites and a two-step binding model for **MnP2** was identified. Based on the molecular mechanism, next generation MnP-based BPAs with higher sensitivity and tunable pharmacokinetics are designed. We demonstrate the potential and versatility of MnPs as superior alternatives to the commonly used GBCAs, based on their lowered toxicity, high sensitivity at high clinic fields and tunable structural diversity.

References: [1] *J. Med. Chem.* **2014**, *57*, 516-520. [2] *J. Biol. Inorg. Chem.* **2014**, *19*, 229-235. [3] *J. Magn. Reson. Imaging* **2014**, *40*, 1474-1480.

A novel multi-echo GRE protocol for simultaneous fat/water separation and multi-parameter mapping

Junmin Liu[1] and Maria Drangova[1,2]
[1]Imaging Research Laboratories, Robarts Research Institute and [2]Department of Medical Biophysics
Schulich School of Medicine & Dentistry, Western University, London, Ontario, Canada

Introduction: T2*-based multi-echo GRE (T2*-mGRE) techniques[1] have been used to quantitatively map R2*, local frequency shift (LFS) and quantitative susceptibility (QSM). To match the tissue T2* and optimize susceptibility effects, most T2*-mGRE protocols prescribe long echo times (TE) with large echo spacing (ΔTE). Some clinical cases require fat suppression of the T2*-mGRE-based images. In principle, chemical-shift (CS) based fat/water separation techniques[2] could be used for this purpose, but the TEs have to be optimized differently from the T2*-mGRE, therefore requiring a separate scan. In this work we present a novel protocol (CS-T2*-mGRE) with two echo trains that enables simultaneous quantitative mapping and fat/water separation from a single mGRE scan.

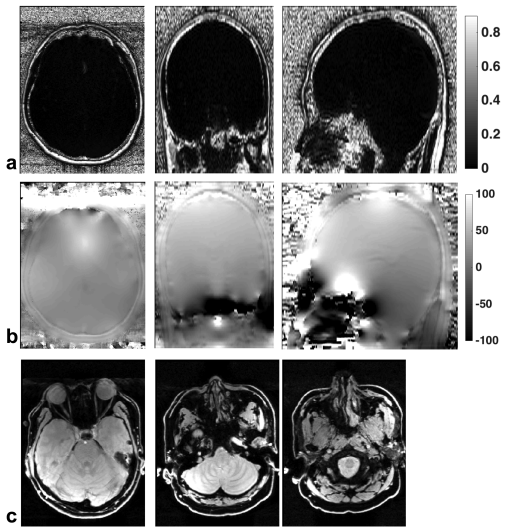

Fig. 1. Results from the first five echoes: corresponding axial, coronal and sagittal fat-fraction (a) and Δf_{B0} maps (b). Example axial fat-suppressed T1-weignted images (c).

Method: ***Protocol and data acquisition:*** The CS-T2*-mGRE protocol (~ 5 mins) was developed on a 3 T scanner: the first five echoes were selected with TEs optimized for fat/water separation (3.3, 4.7, 6.2, 7.7 and 9.5 ms); the late five echoes were designed with TEs optimized for susceptibility mapping (16.8, 23.9, 31.1, 38.2, and 45.4 ms) while keeping fat and water approximately in-phase. To ensure optimal TEs for the first five echoes, bipolar readout gradients were used.

Fat/water separation, B0 mapping and generating T1 weighted image using the first set of echoes: First, we corrected the phase errors associated with the bipolar acquisition. Second, we used B0-NICE[3] to generate a field (Δf_{B0}) map and fat-fraction (FF) map. Lastly, we generated fat-suppressed T1-weighted images by multiplying the T1-weighted images (obtained by averaging the set of magnitude images) by (1-FF).

QS mapping using the second set of echoes: LFS maps were calculated at each echo by first unwrapping the phase images,[4] applying a Gaussian filter and performing background correction.[5] Brain masks were then generated by thresholding the inter-echo-variance of the LFSs.[6] QS maps were calculated from the five-echo-averaged LFS maps.[7]

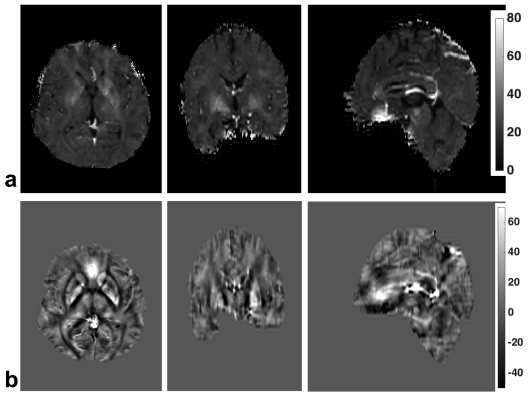

Fig. 2. Results from the late five echoes (a) R2* maps (units are 1/s) and (b) QSM maps (units are ppb).

Results and Discussion: Successful FF (Fig. 1a) and Δf_{B0} (Fig. 1b) maps were generated, as demonstrated by the lack of fat-water swaps in the whole brain and the uniform suppression of fat signal in the T1-weighted images (Fig. 1c). The R2* maps estimated from the first five echoes (detail no shown) using B0-NICE are very noisy because the TEs (< 10 ms) are very short compared to the tissue T2* values. As expected, the quality of R2* maps (Fig. 2a) improved significantly when all echoes were included for processing. Figure 2b demonstrates that QSM with bipolar acquisition is achievable with phase unwrapping, followed by applying Gaussian filter and RESHARP.[5] The data processing could be further improved, such as implementing the voxel spread function[8] to remove B0-effects from R2* and performing B1 correction to correct intensity inhomogeneity.

Conclusion: With a whole-brain acquisition time of ~ 5 mins, the proposed protocol that yields 1.0 ×1.0 ×2.0 mm^3 co-registered multi-parametric maps, promises to be an effective and rapid tool in clinical practice.

References: 1. Haacke et al., MRI 2015; 33(1):1-25. 2. Reeder et al., JMRI 2007; 25(3):644-652. 3. Liu and Drangova, MRM 2015;74:1177-1188. 4. Liu and Drangova, MRM 2012; 68(4):1303-1316. 5. Sun and Wilman, MRM 2014; 71:1151-1157. 6. Liu et al., MRM 2015; 73:1654-1661. 7. Bilgic et al., JMRI 2014; 40:181-131. 8. Yablonskiy et al., MRM 2013; 70:1283-1292.

A system for high-frequency vibration of live cells during real-time microscopy

Lorusso, D. †‡¶, Nikolov, H.N. †, Beach, R.J. ¶‡, Sims, S.M. ¶ ‡, Dixon, S. J. ¶‡, Holdsworth, D.W. ¶†§⊥

† Imaging Research Laboratories; Robarts Research Institute; ‡ Department of Physiology and Pharmacology; ¶ Bone and Joint Institute;§ Department of Medical Biophysics; ⊥Department of Surgery
Schulich School of Medicine & Dentistry
The University of Western Ontario, London, ON, Canada

Primary Author: Lorusso, D. **Research Supervisor**: Drs. S.J Dixon and D.W. Holdsworth

Introduction: Mechanotransduction is the process by which cells sense – and respond to – the local mechanical environment. This ability to react to external loads and forces is a critical component of mammalian physiology and is essential for normal functioning of our bones, lungs, and blood vessels; yet, the underlying mechanisms are not fully understood. A form of mechanical stimulation that is commonly implicated in mechanotransduction is acceleration due to vibration. Our goal is to observe the immediate responses of cells to high-frequency oscillatory vibrations. Here, we describe the development and validation of an integrated motion-control system for vibrating live cell cultures at frequencies up to 500 Hz and accelerations up to 1 *g*, and is compatible with real-time optical microscopy and photometry.

Methods: The motion-control system was mounted on an inverted microscope (Nikon Diaphot) and the moving parts were suspended on a linear air bushing system (NewWay) which was actuated by a voice-coil. Accelerations were measured *via* an on-board calibrated accelerometer (Dytran 7521A1). To ensure vibrations were transferred effectively to the cell culture dish, motion waveforms were imaged with a high-speed camera (Casio Exilim Ex-F1) at 1200 frames per second. MC3T3-E1 osteoblast-like cells were then seeded onto compatible glass-bottom dishes and imaged. In addition, cells were treated with fluorescent calcium dye fura-2 and exposed to vibration during photometry.

Results: During operation between 20 – 500 Hz and 0.1 – 1 *g*, sinusoidal motion of waveforms were observed from both optical and accelerometer-derived measurements, with displacements ranging from the nanometer to millimeter range. Cultured osteoblast-like cells were vibrated 0.3 *g* at 45 Hz during photometry and remained adherent and viable.

Conclusions: We have developed, fabricated, and tested a motion-control system capable of – for the first time – delivering physiologically relevant vibrations to live-cells during real-time microscopy and photometry.

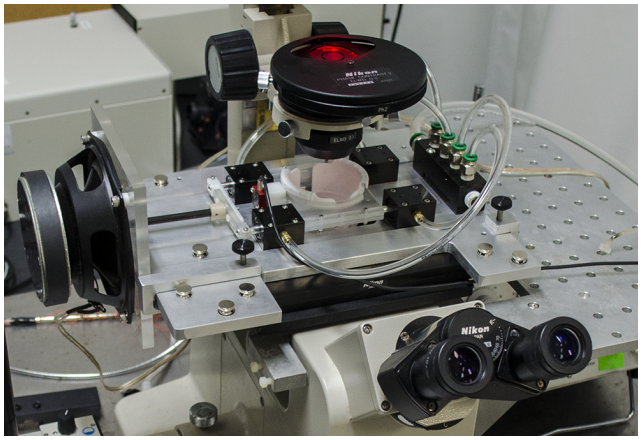

Fig. 1 The dynamic mechanostimulation platform mounted on an inverted Nikon microscope. Visible are key components of the device, including the voice coil actuator on the left, and the push rod connecting the actuator to the mobile carriage. The four black air bushing pillow blocks in the center suspend two aluminum tubes that couple the movement of the voice coil and the mobile carriage. The microscope is also equipped with a photometer for measuring fluorescent probes.

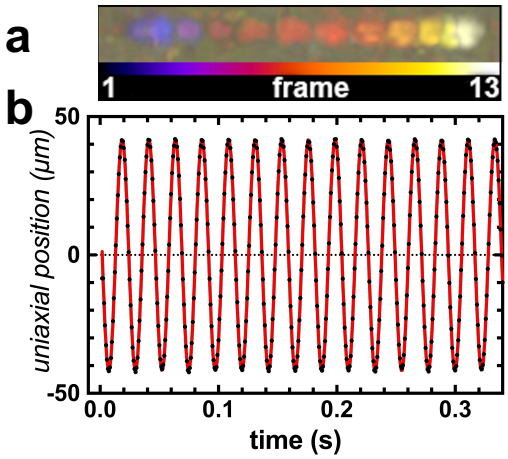

Fig. 2 (**a**) Maximum intensity projection of 1/2 cycle (13 frames) of a 6 μm marker bead vibrated at 0.3 *g* and 45 Hz and imaged on an inverted microscope with a high-speed camera (1200 FPS). Average displacement of the particle was found to be 83.5 ± 0.06 μm. (**b**) Position over time of the particle from Fig. 3. The red curve indicates the result of non-linear regression performed to fit a sine curve to the data.

Patient-specific calibration of cone-beam computed tomography images for radiotherapy dose tracking

Michael MacFarlane*, Douglas Hoover, Eugene Wong, Jerry Battista, Jeff Chen
Department of Medical Biophysics, Western University, London ON, Canada

Introduction: The direct use of cone-beam computed tomography (CBCT) images for radiation therapy dose calculation and plan assessment is desirable, since these image sets are regularly acquired just prior to treatment for patient setup and monitoring of anatomical changes. In order to use CBCT data for dose calculations, corrections need to be made to the CBCT so that accurate tissue density information can be inferred. A popular trend is to use deformable image registration (DIR) to map (voxel-by-voxel) the original planning CT onto the CBCT. This method, however, could yield dosimetric errors and incorrect organ delineation due to DIR mapping limitations. In this work, a patient-specific method of calibrating CBCTs (PSC) for dose calculation is proposed that is less sensitive to these DIR errors.

Methods: Rather than using DIR to map individual voxels, DIR is used to generate a linear relationship between the voxel pairs of the CBCT and the planning CT. This relationship is then applied to the CBCT voxels, thereby making the CBCT numerically-equivalent to a planning CT while preserving the patient's anatomy at the time of treatment. Conventional fan-beam CT tissue density calibration curves can then be implemented on the CBCT during dose calculations. The calibrated CBCT is then also merged with the original planning CT to extend the CBCT's limited field of view. This procedure is illustrated in Figure 1.

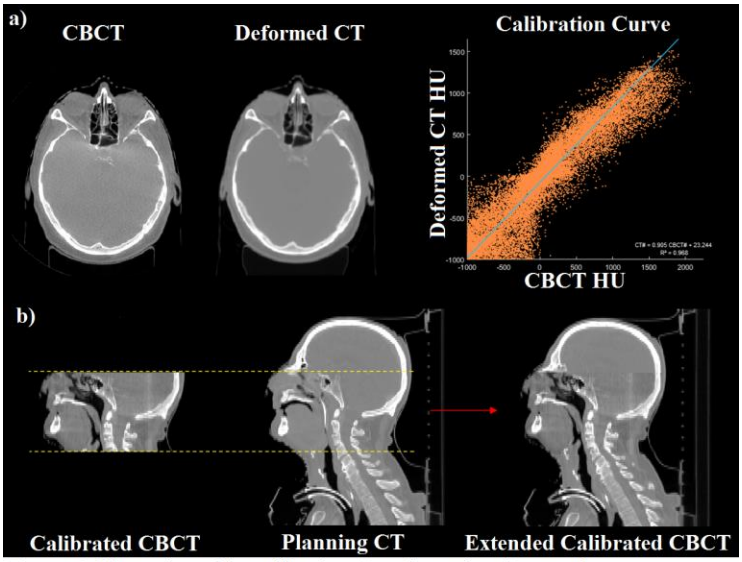

Figure 1: Illustration of the calibration (a) and merging (b) procedure

A retrospective study was performed on 15 head-and-neck patients to test the dosimetric accuracy of this patient-specific calibration (PSC) technique against a second fan-beam planning CT (serving as gold standard) and other calibration methods proposed in literature, viz. DIR and bulk density assignment. Dose metrics evaluating tumor volume coverage and organ-at-risk (OAR) doses were tabulated and compared to the gold standard technique, along with 3D gamma analysis of the dose distributions (3% / 4mm) using SlicerRT software package in 3DSlicer. MANOVA statistical testing was performed along with post-hoc testing when suitable. A 5% threshold for significance was used.

Results: On average, the differences in dose metrics were ≤ 1% compared with the gold standard for all three methods with slightly better average agreement for PSC (0.6%) *versus* DIR (0.8%) and density assignment (1.0%). Gamma analysis results were similar across the three techniques ($p = 0.27$), with average (standard deviation) pass rates of 97.6% (2.0%), 97.5% (2.4%), and 96.9% (2.6%) for the PSC, DIR, and density-override methods, respectively.

Conclusion: The results show that a slightly higher dosimetric agreement can be obtained using the patient-specific calibration (PSC) method, although each method may be sufficient for plan assessment. Unlike the DIR and density-override techniques, the PSC method does not require manual or automatic volume delineation and is less susceptible to DIR errors, providing a particular advantage in sites such as prostate or lung where large deformation errors are common. The techniques used in the PSC calibration method may also be used to conveniently identify regions of DIR error on a deformed CT, as illustrated in Figure 2.

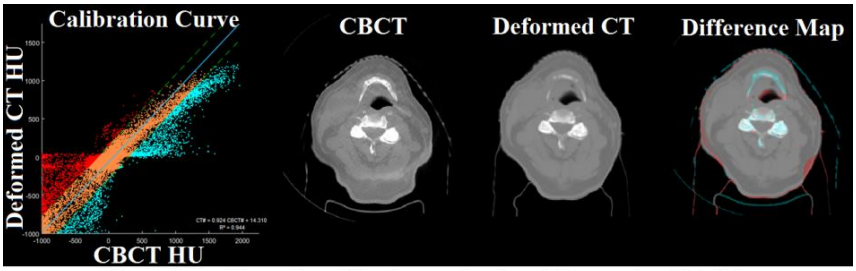

Figure 2: Illustration of how the calibration method could be used to highlight DIR errors by highlighting voxels outside of the calibration curve's 95% confidence interval.

Whole mouse body fluorine-19 based MRI for detection of metastasis associated macrophages in the lung, lymph nodes and brain.

AV Makela[1,2] and PJ Foster[1,2] [1]Department of Medical Biophysics, Western University, London, ON [2]Robarts Research Institute, London, ON

Introduction: Accumulating evidence shows that tumour associated macrophages (TAMs) play a pivotal role in breast cancer growth and metastasis. Metastases from breast cancer occur in the lung, liver, lymph nodes, bone and brain. Several studies have shown that macrophages are recruited to distant sites to support the growth of metastases, participating in the "premetastatic niche". Recently, Kitamura *et al.* demonstrated macrophage retention in breast cancer lung metastases.[1] Macrophages within metastases have a distinct phenotype and are known as metastasis associated macrophages (MAMs). Here we present the first evidence that ^{19}F-based MRI cell tracking can detect MAMs in breast cancer metastases within the lung, lymph nodes and brain. **Methods:** 4T1 murine breast cancer cells (300,000) were injected into the mammary fat pad in female BALB/c mice. 4T1 tumours generate spontaneous metastases in the lungs and lymph nodes. A brain-seeking version of the 4T1 cell line (4T1BR5) was used to generate brain metastases by injection of 20,000 cells via intracardiac injection. ^{1}H and ^{19}F images were acquired on a 9.4T small animal MRI scanner. A dual-tuned ^{1}H/^{19}F birdcage coil was constructed to allow head to toe mouse imaging, essential to visualize metastases in the whole body. Images were acquired 24 hours post intravenous injection of a red fluorescent PFC agent at 4 weeks post cell injection for 4T1 and 2 weeks post cell injection for 4T1BR5. Spatial resolution was 0.5x0.5x1.0 mm^3 (^{19}F) and 200x200x200 micron^3 (^{1}H). Mice were euthanized immediately following MRI and lungs, brains and lymph nodes with ^{19}F signal were excised. Tissues were examined using fluorescence microscopy to detect the red fluorescence of the PFC and green F4/80-FITC antibody to identify macrophages. In mice with primary 4T1 tumours we observed ^{19}F signal in lymph nodes and the lungs. Figure 1 shows images of ^{19}F signal in ipsilateral axillary (A), renal (B) and lumbar (C) lymph nodes. These nodes appeared enlarged in ^{1}H images. ^{19}F signal was not detected within lymph nodes on the contralateral side of the mouse. Figure 2 displays ^{19}F signal detected in lung metastases (2A - circled in yellow). ^{1}H images show hyperintense tumours within the lungs (2B). Figure 3 represents data collected from mice that received 4T1BR5 cells. ^{19}F signal was observed in brain images acquired at 9.4T (3A) and this signal corresponded to brain metastases detected in ^{1}H images obtained at 3T using a dedicated mouse head RF coil (3B). Brains were sectioned, stained with H&E and whole sections scanned to confirm metastases (3C&D). 3E (fluorescence microscopy) & 3F show metastases at higher magnification. Lymph node and lung metastases were also stained with F4/80 to detect macrophages. Whole body cryoimaging will be performed to detect areas with F4/80+ cells and the red PFC agent. **Conclusion**: This work represents the first time MAMs have been visualized by ^{19}F MRI. MAMs were detected within breast cancer metastases in the lymph nodes, lungs and brain. The ability to detect, quantify and track MAMs *in vivo* will allow for study of important, unanswered questions about MAMs and the tumour microenvironment, including how MAMs influence metastasis and when during cancer progression do MAMs infiltrate the metastatic site.

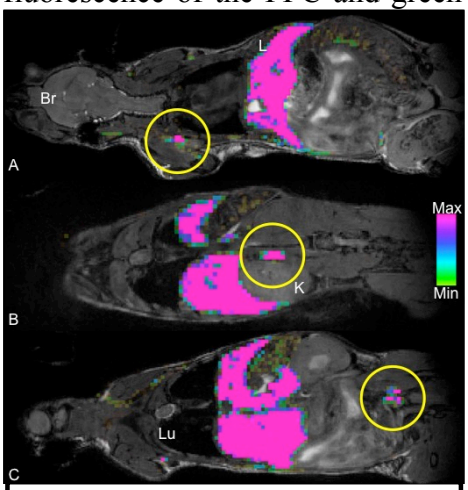

Figure 1: Lymph node metastases detected in a murine 4T1 model at 4 weeks post cancer cell implantation (Right mammary fat pad). Ipsilateral lumbar (A), axillary (B) and renal (C) lymph nodes are demonstrated by yellow circle. (Lu-Lung, L-Liver, Br-Brain, K-Kidney).

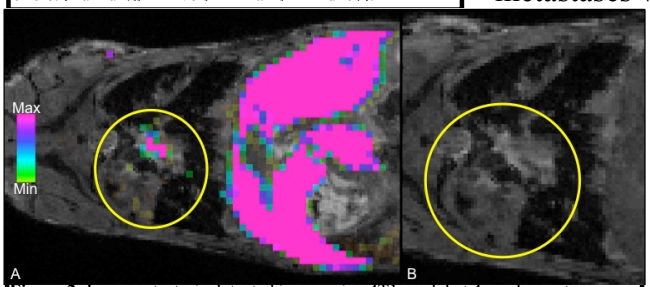

Figure 2: Lung metastasis detected in a murine 4T1 model at 4 weeks post cancer cell implantation. ^{1}H/^{19}F overlay confirms accumulation of PFC agent within hyperintense lung tumours (A), verified by ^{1}H MRI (B).

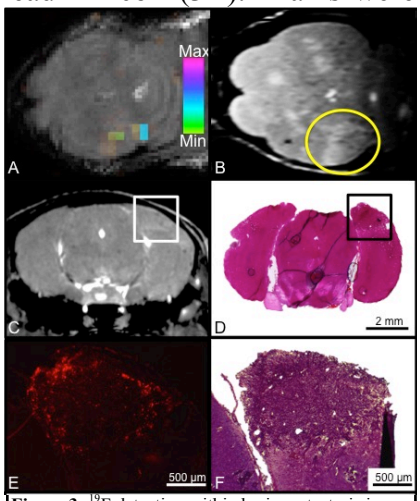

Figure 3: ^{19}F detection within brain metastasis in a 4T1BR5 murine model. (A) ^{1}H/^{19}F overlay demonstrates PFC accumulation within a brain metastasis. This is confirmed with 3T high resolution MRI of the brain (B). An MRI slice (C) correlates well with whole section scan of H&E brain (D). High magnification views of the tumour in box in D shows the red PFC in the tumour periphery (E&F).

1. Kitamura, T. *et al.* CCL2-induced chemokine cascade promotes breast cancer metastasis by enhancing retention of metastasis-associated macrophages, 2015.

Axonal damage and global hyperconnectivity persist 3-months after concussion in young hockey players

Kathryn Y. Manning[1,2], Amy Schranz[1], Gregory A. Dekaban[3], Arthur Brown[4], Lisa Fischer[5], Tim Doherty[6], Christy Barreira[3], Douglas Fraser[7], Robert Bartha[1,2], and Ravi S. Menon (Research Supervisor)[1,2]

[1]Medical Biophysics, University of Western Ontario, [2]Centre for Functional and Metabolic Mapping, Robarts Research Institute, [3]Molecular Medicine, Robarts Research Institute, Department of Microbiology and Immunology, University of Western Ontario, [4]Molecular Medicine, Robarts Research Institute, Department of Anatomy and Cell Biology, University of Western Ontario, [5]Primary Care Sport Medicine, Family Medicine, Fowler Kennedy Sport Medicine, [6]Physical Medicine and Rehabilitation, University of Western Ontario, [7]Paediatrics Critical Care Medicine, London Health Sciences Centre, London, Ontario, Canada. **BrainsCAN.**

Introduction: MRI-detectable changes due to concussion can remain well after athletes have been cleared to return to play. Ongoing developmental changes in white matter make it particularly vulnerable to injury in young children and may require extended recovery periods. Here we examined young concussed athletes using resting state functional MRI (RS-fMRI) and diffusion tensor imaging (DTI). This study had two specific aims: (a) to examine acute MRI changes post-concussion (PC) to further understand the neurobiological mechanisms underlying concussion, and (b) investigate the nature of any long-lasting structural and functional imaging changes. **Methods:** Male hockey players were recruited for this study (ages 11-14) including an independent age-matched control group (n=18), and players within 24-72 hours (n=15) and 3-months (n=13) after a diagnosed concussion. The 3T MRI session involved a DTI spin echo sequence with 64 gradient directions and a ten-minute RS-fMRI sequence. A diffusion tensor was fit at each voxel and used to create fractional anisotropy (FA), mean (MD), radial (RD) and axial diffusivity (AD) maps and were extracted for atlas-based major white matter tracts. Tract-specific spatial statistics were used to localize where the greatest changes occurred along these tracts, while regressing for age. Probabilistic tractography was used to explore the structural connections between relevant regions from the RS-fMRI functional connectivity (FC) analysis. RS-fMRI data was preprocessed using standard steps, and the CONN toolbox was used to examine group-level regional connectivity changes. **Results:** There was a significant main effect for DTI group differences in the corticospinal tract (CST), cingulum, and superior longitudinal fasciculus (SLF). Masks were created over spatially localized hotspots of compromised neuronal integrity. Within the SLF mask, MD and RD were significantly decreased acutely and 3-months PC compared to controls ($p<0.01$), and furthermore there were decreases in AD at both time points ($p=0.06$ and $p=0.003$). There were significant increases in FC in the occipital visual, cerebellar and sensorimotor RSNs as well as diffuse region-to-region hyperconnectivity at 3-months compared to the control and acute PC groups (Fig 1a) and within-subject MR changes were highly correlated (Fig 1b). There were striking changes in FC with the anterior supramarginal gyrus seed acutely PC (Fig 2a). Probabilistic tractography revealed that tracts connecting this seed with the frontal pole intersected directly with the SLF maximum diffusion changes (Fig 2b), and the probability of this structural connection was decreased in both PC groups compared to controls. Furthermore, the FC between these compromised regions was significantly correlated with symptom severity ($r=-0.44$, $p=0.003$). **Conclusion:** There were diffuse structural and functional changes 3-months PC, well after player's clinical scores had returned to normal and they had been cleared to return to play. Axonal damage may persist long after symptomatic recovery from concussion in young players, who are still undergoing critical brain development.

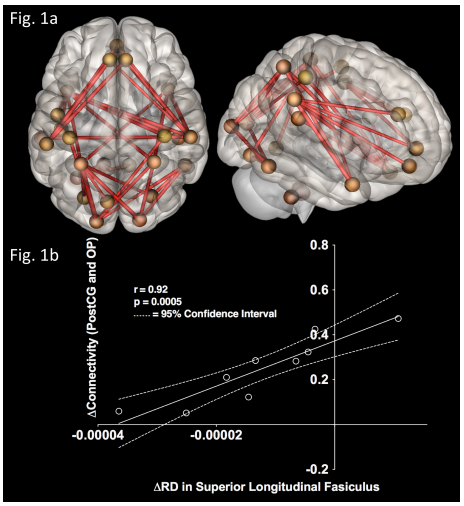

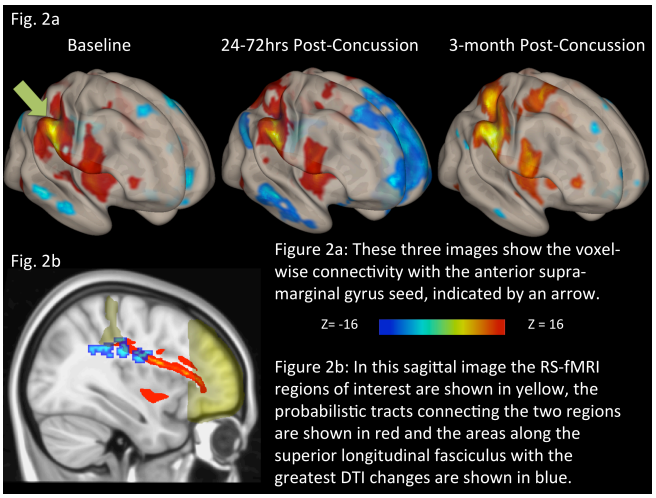

Renal Perfusion Falls during Hemodialysis: An Explanation for the Loss of Residual Renal Function in Dialysis Patients

Raanan Marants MSc[1], **Claire J Grant** MD[2], **Nanchuan Jiang** MD[3], **I-Lun Huang** MD[3], **Qingguo Wang** MD[3], **Ting-Yim Lee** PhD[1,3,4] and **Christopher W McIntyre** MD[1,2,4]
Consortium Affiliation: Medical Imaging Trial Network of Canada
[1]Department of Medical Biophysics, Western University, London, Canada
[2]Kidney Clinical Research Unit, Western University, London, Canada
[3]Robarts Research Institute, Western University, London, Canada
[4]Lawson Health Research Institute, London, Canada
Supervisors: Ting-Yim Lee, Christopher W McIntyre

Introduction: Residual renal function (RRF) maintenance has been shown to confer survival benefit in hemodialysis patients. However, preservation strategies are few, largely due to an inadequate understanding of the pathophysiology behind the characteristic rapid decline in RRF. The aim of this study was to directly examine the hypothesis that intradialytic circulatory stress results in ischemic challenge to the remnant kidney.

Figure 1: Flowchart illustrating the progression from end-stage renal disease to a decrease in residual renal function. The mechanism by which residual renal function declines following initiation of hemodialysis therapy is unknown.

Methods: 14 patients with urine output <100mL/24hrs underwent renal imaging before, 1 and 3 hours into, and after hemodialysis. Renal perfusion was measured using CT perfusion imaging with a 256-slice Revolution CT scanner (GE Healthcare). Following acquisition and offline non-rigid registration, images were analyzed to create functional maps for perfusion across the entire kidney. The heart was used as a reference organ system for ischemic response to dialysis-induced circulatory stress by detecting myocardial stunning with echocardiography.

Results: Baseline renal perfusion was markedly reduced (31.8±20.0mL/min/100g), compared to normal control values (>100mL/min/100g), and was related to dialysis vintage ($r=-0.68$, $p<0.001$). Hemodialysis resulted in significant reduction in renal perfusion to 26.4±16.5mL/min/100g ($p<0.05$) at peak stress (3hrs) and 8/11 patients in whom there was myocardial stunning exhibited a drop in renal perfusion [$X^2(1,N=11)=2.3$, $p=0.132$].

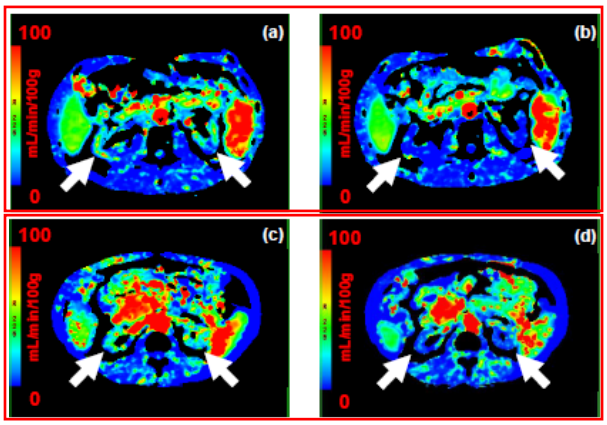

Figure 2: Parametric maps of renal blood flow at (a,c) baseline and (b,d) 3 hours into dialysis for two patients (top and bottom rows). A significant drop in kidney perfusion can be seen (white arrows).

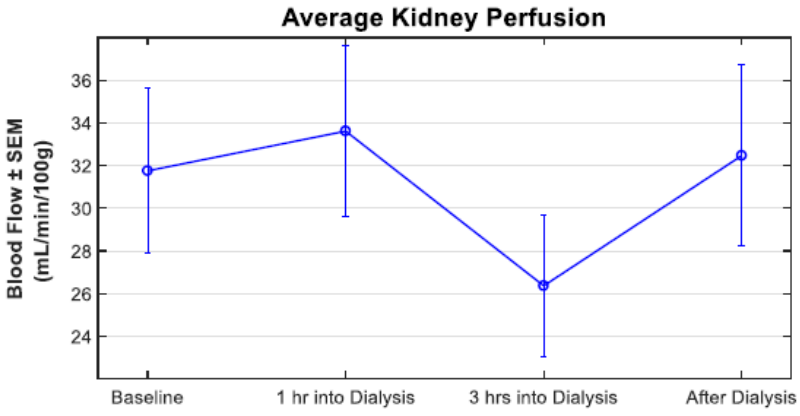

Figure 3: Kidney blood flow ± SEM averaged over 14 patients performed before, 1 and 3 hours into, and after dialysis.

Conclusions: Renal perfusion dropped acutely during hemodialysis and was related to demonstrable organ injury in another vulnerable vascular bed. Cumulative exposure to circulatory stress may be a key pathophysiological factor in declining RRF observed in hemodialysis patients. Longitudinal studies are needed to examine whether circulatory stress amelioration during hemodialysis helps preserve RRF.

How should we target prostate tumours using fusion biopsy?

Peter R. Martin[1,2], Derek W. Cool[3,5], Aaron Fenster[2,3,5] and Aaron D. Ward[1,2,4]
[1]Baines Imaging Research Laboratory, London Regional Cancer Program;
Departments of [2]Medical Biophysics, [3]Medical Imaging, [4]Oncology; [5]Robarts Research Institute;
The University of Western Ontario, London, Ontario, Canada
Ontario Institute for Cancer Research – Smarter Imaging Program, Research supervisor: Aaron D. Ward

Introduction: Magnetic resonance imaging (MRI)-targeted, 3D transrectal ultrasound (TRUS)-guided prostate biopsy aims to reduce the 21–47% false negative rate[1] of clinical 2D TRUS biopsy, but continues to yield false negative results. This may be improved via needle target optimization, accounting for guidance system errors, image registration errors, and irregular tumour shapes. As an initial step toward the goal of optimized prostate biopsy targeting, we investigated how needle delivery error impacts tumour sampling probability for two targeting strategies.

Methods: We obtained MRI and 3D TRUS images from 49 patients. A radiologist and radiology resident assessed these MR images, and contoured 81 suspicious regions, yielding tumour surfaces that were registered to 3D TRUS. The biopsy system's root mean squared needle delivery error (RMSE) and systematic error were modeled using an isotropic 3D Gaussian distribution. We investigated two different targeting strategies. First, we modeled the tumour's centroid as the target. Secondly, we modeled the target locations on a ring in the lateral-elevational plane. The ring was centred on the tumour centroid, and its radius was equal to the magnitude of systematic error in the lateral-elevational plane. For each simulation, targets were spaced at equal arc lengths on the ring. 1000 biopsy simulations of two, three and four attempts were conducted for each tumour, with RMSE and systematic error magnitudes ranging from 1 to 6 mm. The difference in mean sampling probability across all tumours was determined for the ring versus centroid targeting strategy.

Results: Fig. 1 (red boxes) indicates that ring targeting only outperforms centroid targeting when systematic error > RMSE. Asterisks show statistically significant differences, showing 4%–29% improvement in sampling probability due to ring targeting. For 2 biopsy attempts, ring targeting shows a significant increase in sampling probability from centroid targeting only when systematic error = 6 mm and RMSE $\leq$ 2 mm.

Conclusions: Our simulations suggest that optimal targeting for prostate biopsy depends on the relative levels of systematic and random errors in the system. Where systematic error dominates, ring targeting may yield improved probability of tumour sampling.

[1]Rabbani, F., J Urol 159(4), 1998

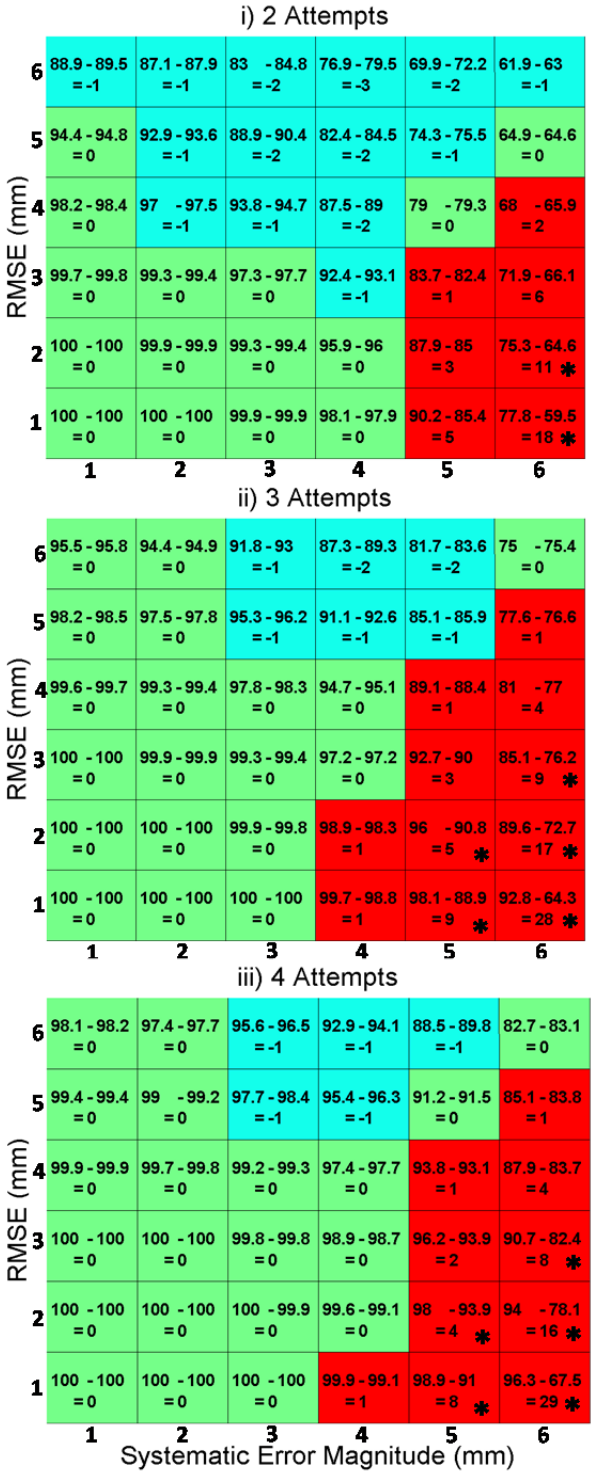

Fig. 1: Differences (rounded to integers) between the mean tumour sampling probabilities (%) for ring targeting minus the probabilities for centroid targeting, given RMSE and systematic error magnitude of the biopsy system in mm. Red boxes indicate a higher probability achieved through ring targeting, blue boxes indicate a higher probability achieved through centroid targeting, and green boxes indicate no difference. Asterisks indicate significant differences ($p<0.05$).

Audio-frequency dB/dt Exposure System for MRI-Conditional Device Testing: A Design Study

Daniel J. Martire, Justin C. Peterson, Colin M. McCurdy, William B. Handler, Blaine A. Chronik.
Physics and Astronomy, Western University, London, Ontario, Canada

Introduction: Magnetic resonance imaging of patients with implanted medical devices faces complication due to rapidly switched gradient fields. The induced eddy-currents on conductive materials can cause heating, vibration, image distortion, and interference of device function from induced voltages.[1] Devices require testing before they can be deemed MR conditional, but testing on MR scanners can be expensive and impractical. In this project, we present a design method for development of a separate gradient field exposure test platform. We use the Fabry notation[2] to describe the relationship between the field at the centre of a thick solenoid of uniform current density and the resistive power of the coil. The ratio of outer radius to inner radius of the coil is α, and the ratio of the half length to the inner radius is β. A third parameter, γ, is introduced here and is defined as the ratio of the half gap to the inner radius. This axial gap can improve homogeneity, similar to the concept of a Helmholtz coil.

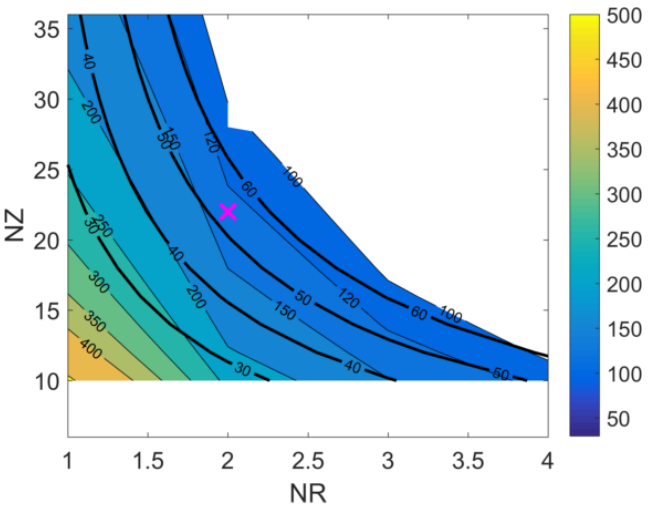

Figure 1: The slew rate [T/s] of the allowable parameter space is shown as a function of axial windings (NZ) and radial layers (NR), with field shift [mT] contour lines in thick black. The pink marker indicates the chosen coil.

Methods: Coils were numerically modeled with discrete windings and an array of wire elements, using the Biot-Savart law to calculate magnetic field. A grid search of parameter space (α, β, γ) was performed to provide understanding of the interactions between performance metrics such as the Fabry factor, homogeneity, slew rate, and maximum field shift. To reduce potential design choices, gamma was optimized to achieve the best field uniformity possible over a 6 cm DSV, for a coil of 13.75 cm radius. Further constraints included a minimum field shift of 40 mT and minimum slew rate of 120 T/s. Performance calculations were based upon an available power supply of 350V and 430A peak values and copper wires of 5 mm by 5 mm. The coil design selected from the final set had the optimal field uniformity with a field shift close to the lower bound, such that slew rate could be maximized.

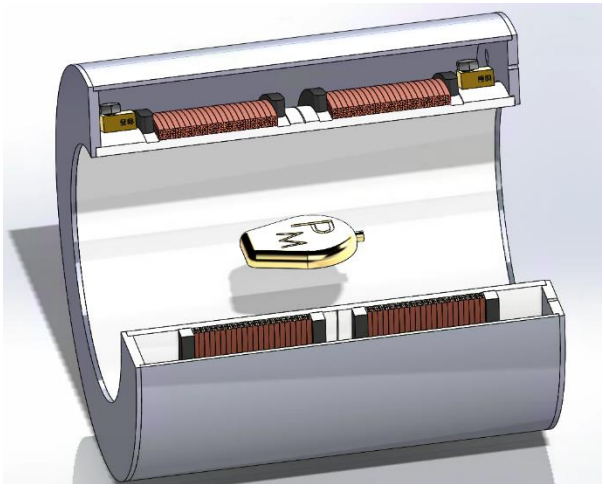

Figure 2: Drawing of optimized coil design for gradient field exposure system.

Results: By applying the constraints to parameter space only a small allowable region remained, from which a specific design was chosen due to its high field uniformity as well as slew rate and field shift values that satisfy ISO/TS 10974.[3] The coil properties are IR = 13.75 cm, OR = 14.81 cm, length = 28.74 cm, gap = 5.42 cm, axial windings = 22 pairs of wires in parallel, and radial layers = 2. Inhomogeneity is 1% over a sphere 10.5 cm in diameter, with a peak slew rate of 122 T/s, and a peak field shift of 53 mT. Figure 2 shows a drawing this coil, with a sample pacemaker device in the testing region.

Conclusions: An effective design tool for dB/dt systems for the purpose of medical device testing has been demonstrated. Typical MRI gradient systems produce peak field shifts of less than ±40 mT within the bore of the scanner. It is therefore not generally necessary to produce a dB/dt test platform of more than approximately 50% above this value. The coil presented is capable of gradient field exposure above that which is typically present in an MRI scan, and that also satisfies the requirements of ISO/TS 10974.

Acknowledgements: Ontario Research Fund, Canadian Foundation for Innovation, NSERC.

References: [1] Nyenhuis, J.A. et al. IEEE 5.3 (2005): 467-480. [2] Montgomery DB. *Solenoid Magnet Design.* 1969. [3] ISO/TS 10974. www.ISO.org 2016.

Impact of Motion and Maternal BMI on Segmentation in Fetal MRI

Daniel McCooeye[1], Stephanie Giza[1], Craig Olmstead[2], Barbra de Vrijer[3,4], Charles McKenzie[1,3]
[1]Department of Medical Biophysics, Western University, [2]Schulich School of Medicine and Dentistry, [3]Division of Maternal, Fetal and Newborn Health, Children's Health Research Institute, [4]Department of Obstetrics and Gynaecology, Western University. London, Ontario

Introduction: Fetal size and fetal adipose tissue volume are important indicators of fetal growth and metabolic development and are measured by segmentation of the relevant anatomy from images acquired through ultrasound (US) or Magnetic Resonance Imaging (MRI). US is routinely used in fetal imaging, but attenuation of the US beam by maternal subcutaneous adipose tissue results in reduced image quality in patients with a high body mass index (BMI) (1). MRI has the advantage of being relatively unaffected by subcutaneous fat, however, MRI image quality can be degraded by fetal and maternal motion (2). The severity of these motion artefacts may be affected by maternal BMI and gestational age (GA). Our objective was to assess how maternal BMI and GA interacts with motion artefacts to affect the segmentability of fetal MRI.

Figure 1. Motion artefacts in FIESTA

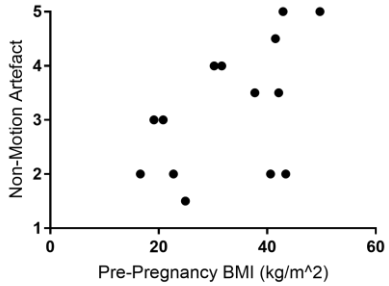

Figure 2. Non-Motion Artefacts vs Pre-Pregnancy Body Mass Index

Methods: Two readers viewed images in 3D Slicer 4.7.0 (www.slicer.org) and rated FIESTA 3D MRI images in 14 3D volumes (from 14 patients) for the impact of motion and other artefacts on the ability to segment structures. A 5-point Likert scale was used to rate the severity of image quality degradation and segmentability. No motion or artefacts in the image is denoted by 1 and 5 indicates a total loss of segmentability. Scores above 2 represent impaired segmentation of the fetus and placenta. Spearman correlations were determined for combinations of BMI, or Gestational Age (GA) vs Fetal Motion (FM), Maternal Motion (MM), or Non-Motion Artefacts (NMA). Prism 7.02 (GraphPad Inc, USA) was used to calculate the Spearman correlations and inter-reader reliability was calculated using the Intra-Class Correlation (ICC) coefficient available in SPSS (IBM, USA).

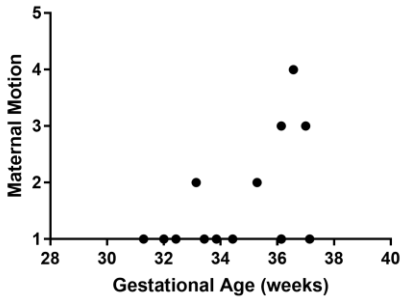

Figure 3. Maternal Motion vs Gestational Age

Results: Readers rated that image quality in 10 of the 14 3D volumes had a negative impact on their ability to segment the fetus or placenta; in 8 3D volumes this was attributed to motion. No statistically significant ($P>0.05$) correlations were produced via the mean data from both readers. NMA scores increased with increasing BMI and MM increased with GA. Inter-reader reliability had an ICC of 0.82 denoting a strong inter-reader reliability. Figures 2 and 3 display the mean data from both readers for the two strongest correlations with Spearman coefficients of 0.51 and 0.43 respectively.

Conclusion: 3D FIESTA fetal MRI produced images corrupted by artefacts due to motion and NMA. MM was affected by increased GA due to incomplete breath-holds and discomfort due to increased fetal size. Retrospective motion correction could be used to reduce motion artefacts. We postulate that the incidence of NMA in fetal MRI was affected by maternal BMI, as the consequence of chemical shift and B_0 inhomogeneity artefacts increase with BMI. Further investigation will help determine the prevalence and magnitude of artefacts as a function of maternal BMI in fetal MRI.

References: [1] Dashe, J. S., et al. (2009). "Effect of maternal obesity on the ultrasound detection of anomalous fetuses." Obstet Gynecology 113(5): 1001-1007. [2] Malamateniou, C., et al. (2013). "Motion-compensation techniques in neonatal and fetal MR imaging." AJNR Am J Neuroradiology 34(6): 1124-1136.

Neurite Orientation Dispersion and Density Imaging of the Rat Brain at 9.4 Tesla.

Patrick McCunn[1,2], and Robert Bartha[1,2]

1.Department of Medical Biophysics, The University of Western Ontario, London, ON, Canada, 2.The Center for Functional and Metabolic Imaging, Robarts Research Institute, The University of Western Ontario, London, ON, Canada

Introduction: Neurite Orientation Dispersion and Density Imaging (NODDI) is a novel diffusion MRI method that may increase the specificity of Diffusion Tensor Imaging (DTI) by probing unique diffusion patterns within three separate microstructural environments: intra-neurite, extra-neurite, and cerebral spinal fluid (CSF) compartments. Such detailed reconstruction of *in*-vivo neurite morphology may offer unique information regarding neural health. The bulk of previous research into the use of NODDI has focused largely on the feasibility of clinical applications in humans (Zhang et al. 2012). Due to the common use of rat models in pre-clinical imaging, the purpose of this work was to determine the feasibility of NODDI in a rat model at 9.4 Tesla.

Methods: One healthy male Sprague Dawley rat (age 8 week, weight 247 grams) was scanned on an Agilent (Santa Clara, CA) 9.4 Tesla small-bore animal scanner (maximum gradient 400 mT/m). We chose a NODDI diffusion encoding scheme utilizing a multi-shot Echo Planar Imaging (EPI) acquisition pulse sequence (slice thickness = 500 μm, 250 x 250 μm in plane resolution, 31 total slices, TE = 36 ms, TR=5.0s, 2 shot EPI acquisition, 4 averages). As we intended to acquire standard DTI metrics (FA and MD) in addition to the NODDI specific metrics (Orientation Dispersion Index [ODI], Neurite Density Index [NDI], and Isotropic Volume Fraction [IsoVF]), we chose a *b*-value of 1000 s/mm^2 for our inner shell. Following the work of Zhang et. al (2012) we used a second *b*-value of 2000 s/mm.^{2} These two choices of *b*-values have been show to produce reliable and reproducible values of NODDI specific metrics, and allow standard DTI measures to be obtained. For q-space sampling, we chose a scheme totaling 108 directions varying as q^1, optimized according to Caruyer et. al. (2013). Therefore, we used the following protocol:

A two-shell diffusion protocol

Shell one: 72 directions, four *b*-value = 0 and *b*-value = 2000 s/mm^2 with parameters: G = 298 mT/m, Δ = 17 ms, δ = 4.5 ms, TR = 5.0s.

Shell two: 36 directions, four *b*-value = 0 and *b*-value = 1000 s/mm^2 with parameters: G = 149 mT/m, Δ = 17 ms, δ = 4.5 ms, TR = 5.0s.

Analyses: Images were pre-processed using fMRI Software Library (FSL, v.5.0.10, Oxford, UK). EDDY was used to correct for eddy current induced distortions as well as susceptibility-induced distortions. The NODDI Matlab toolbox (available from the UCL Microstructure Imaging Group) was then used to produce maps of ODI, NDI, and IsoVF.

Results: NODDI specific images were obtained quantifying ODI, NDI, IsoVF, along with quantitative maps of our standard diffusion metrics (FA and MD). While these values fall in the expected range (ie values between 0-1 for ODI, NDI etc.) we have no previous measurements in by which to compare our absolute values, highlighting the need for validation within a rat model.

Conclusions: In the current study, we successfully produced high angular resolution NODDI image maps of the rat brain at 9.4 Tesla. Future work will focus on improving image quality (SNR and resolution) and will determine the inter and intra-subject reproducibility of each of these metrics.

Contrast and Conspicuity of Fiducial Localization using Undersampled co-RASOR MRI

Evan McNabb[1], Raimond Wong[2], Michael D Noseworthy[1,3]

[1]School of Biomedical Engineering, McMaster University, Hamilton ON; [2]Juravinski Cancer Centre, Hamilton ON; Department of [3]Electrical and Computer Engineering, McMaster University.

Introduction: Computed Tomography (CT) remains the clinical standard in radiation therapy using bony landmarks or metallic fiducial markers in pretreatment images for co-registration to online image guidance [1]. Both methods suffer from poor contrast using Magnetic Resonance (MR) imaging, limiting its inclusion in planning. Positive contrast of implanted interventional devices has demonstrated using centre-out radial sampling with off-resonance reception (co-RASOR) [2] which causes the mis-registration of signal intensities to be placed at similar spatial locations according to the field inhomogeneity pattern which can be identified around the device. Undersampling without prior calibration scans is possible as each radial readout acquires data through the centre of kspace. Multichannel coil data can be reconstructed using non-uniform FFT (NUFFT) [3] or iterative methods that apply penalty functions such as Total Generalized Variation (TGV) [4].

Methods: A cylindrical platinum seed fiducial marker (ISI Medical Products) with a long axis of 3 mm and diameter of 1 mm was placed in agarose gel phantom parallel to the main B0-field. MR imaging was performed using a GE Discovery MR750 (General Electric Healthcare, Milwaukee WI) and a 32-channel head coil. A 2D in-house sequence was developed acquiring centre-out radial readouts of kspace [2]. Fully sampled coronal and axial data sets were acquired (TE = 3.2 ms; TR = 100 ms; FOV = 20.0 cm; thickness= 3.0 mm; acquisition matrix = 256 x 804, transmit bandwidth = 4.5 kHz). Undersampled data sets (R=8) were also acquired. Contrast-to-noise (CNR) measurements were taken as the signal of the region enclosing the fiducial subtracted by a 3 mm shell of its surrounding area.

Results & Discussion: co-RASOR images, undersampled by a factor of 8 are shown in Fig. 1 highlighting the fiducial marker. Images off-resonance by 1 kHz show hyper-intensities at the geometric centre of the fiducial. CNR values of retrospectively undersampled co-RASOR images are shown in Fig. 2 with two different reconstruction methods. NUFFT reconstruction had higher contrast at all reduction factors and CNR decreases with the undersampling, however enough CNR remains even at R=8 to localize a fiducial at its centre. Beyond this limit, contrast diminishes towards zero and the hyper-intensities are no longer at the exact centre location. This work showed acceptable contrast in fiducial localization in accelerated imaging, as acquisition speed improved from 80.4 s to 10.1 s.

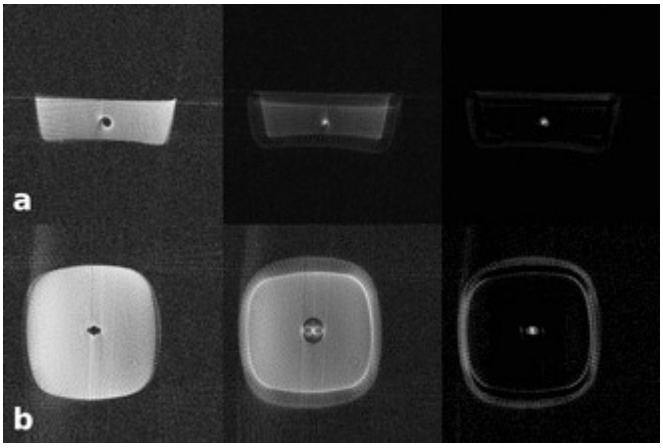

Figure 1: Undersampled co-RASOR images by R=8 showing on-resonance, off-resonance, and subtraction images for (a) axial and (b) coronal acquisitions of a platinum fiducial marker.

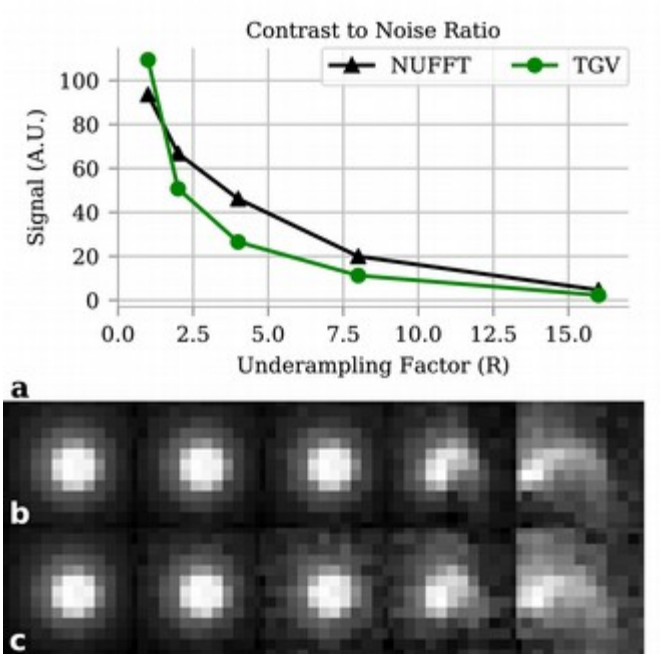

Figure 2: (a) CNR measurements versus undersampling for axial images of a fiducial marker using two different reconstruction techniques; zoomed images of the conspicuity for (b) NUFFT reconstructions and (c) TGV reconstructions.

References: [1]: De Los Santos et al. (2013) Int. J. Radiat. Oncol. Bio. Phys. 87(1): 33-45 **[2]:** Seevinck et al. (2011) MRM; 65: 146 **[3]:** Fessler et al. (2003) IEEE Trans 51(2): 560-574 **[4]:** Knoll et al. (2011) MRM; 67: 34

3D Ultrasound and Mechatronic Template Tracking for Guidance of Permanent Seed Breast Brachytherapy

Michael, Justin[1, 2]; Morton, Dan[3]; Batchelar, Deidre[3]; Hilts, Michelle[3]; Fenster, Aaron[1, 2, 4]

[1]Imaging Research Laboratories, Robarts Research Institute; [2]Biomedical Engineering Graduate Program, Western University, London ON; [3]Department of Medical Physics, British Columbia Cancer Agency, Cancer Center for the Southern Interior, Kelowna, BC, Canada; [4]Departments of Medical Biophysics and Medical Imaging, Western University, London ON

Consortia: Ontario Institute for Cancer Research - Imaging Translation Program

Research Supervisor: Aaron Fenster

Introduction Low dose-rate breast brachytherapy, known as permanent breast seed implantation (PBSI) is an emerging option for radiation therapy following lumpectomy for early stage breast cancer. PBSI is advantageous in reducing radiation treatment time to a single visit by permanently implanting 'seeds' of radioactive Pd-103 using needles inserted through a template under 2D ultrasound guidance. Operator dependence has been highlighted as a limitation of the procedure and reported seed placement accuracy (9±5mm) compares unfavorably to permanent seed implants in the prostate [1]. We propose a guidance system using 3D ultrasound (3D US) and an instrumented mechanical arm for localizing the needle template.

Methods A 3D US image is formed by the reconstruction of 150 2D images captured from a commercial transducer moved and tracked using a motors and encoder. A thin plate of sonulucent TPX plastic is used to prevent tissue motion during the scan. Additionally, a mechanical arm is mounted to the scanner with an additional encoder at each joint facilitating tracking of the arm's spherical tip. The spherical tip seats into conical divots at known positions on the needle template, allowing the templates position to be registered to a common coordinate system with the 3D image. 3D reconstruction was validated, 1) geometrically, using distance measurements of strings placed 10mm apart in each direction (N=40, each of 6 depth settings), and 2) volumetrically, using segmentations of two agar phantoms and compared to volume displacement measurements (N=4 for each phantom). 95% confidence intervals of distance and volume measurements were generated using a Wilcoxon signed rank test and an unpaired Student's T-test, respectively. Point measurement accuracy of the encoded arm was calibrated and validated using a test jig with machined divots at 180 known locations, each measured three times. 1/3 of test points were used to calibrate the 0° position ('offsets') of encoders and the transform between arm and scanner coordinate systems by optimizing a rigid point cloud registration as a function of the offsets. The remaining 2/3 of test points were used to validate accuracy.

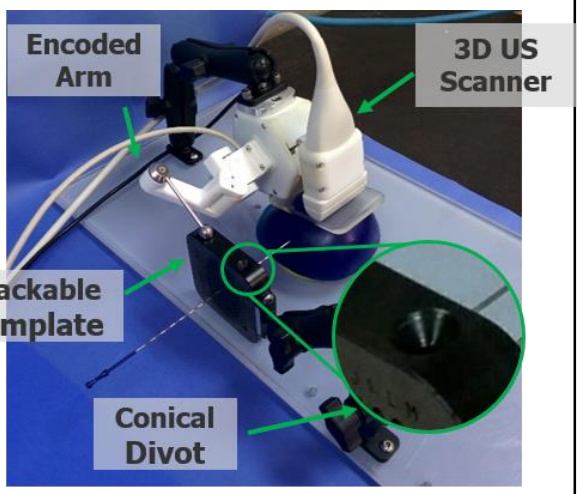

Figure 1 3D US scanner, encoded arm & trackable template. Breast phantom visible beneath scanner.

Results Geometric validation showed 95% confidence intervals within ± 2% (±0.2mm). Volumetric validation showed differences of ≤ 4.1% (≤0.16cm^3) with 95% confidence within ±10%**.** Point measurements showed median (interquartile range) error of 0.475mm (0.2717mm).

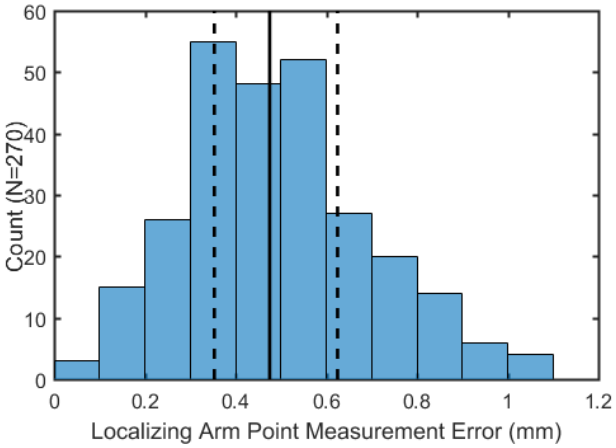

Figure 2 Histogram of point measurement errors. Solid line indicates median, dashed lines indicate 1st and 3rd quartiles.

Conclusions A 3D US scanner and encoded arm for PBSI have been constructed and validated. Future work includes evaluating needle placement accuracy under 3D US guidance in a liquid medium and conducting a phantom procedure with the integrated system.

[1] D. Morton, M. Hilts, D. Batchelar, and J. Crook, "Seed Placement in Permanent Breast Seed Implant Brachytherapy: Are Concerns Over Accuracy Valid?," *Int. J. Radiat. Oncol. Biol. Phys.*, Feb. 2016.

Assessing the integrity of the blood-brain barrier using dynamic contrast-enhanced NIRS

Daniel Milej[1,2,*], Androu Abdalmalak[1,2], Lise Desjardins[2], Hassaan Ahmed[1,2,3], Ting-Yim Lee[1,2,3], Mamadou Diop[1,2] and Keith St. Lawrence[1,2]

[1]Department of Medical Biophysics, Western University, London, ON, Canada
[2]Imaging Program, Lawson Health Research Institute, London, ON, Canada
[3]Imaging Program, Robarts Research Institute, London, ON, Canada

*dmilej@uwo.ca

Introduction: The blood-brain barrier (BBB), consisting of tight junctions between adjacent endothelial cells in cerebral capillaries, is essential for maintaining a microenvironment that enables neurons to function properly. However, neurological emergencies requiring intensive care, such as traumatic brain injury and stroke, can cause BBB disruptions, leading to extravasation of immune cells and impaired regulation of ionic and molecular fluxes. These complications can exacerbate existing injury, contributing to further brain damage. Therefore, determining the degree of BBB disruption could help guide patient management.
In this study we present a dynamic contrast enhanced (DCE) near-infrared spectroscopy (NIRS) method of measuring the permeability surface-area (PS) product based on a kinetic modelling approach used previously to characterize vascular leakage in tumors. To investigate the sensitivity of DCE NIRS to changes in BBB permeability, experiments were conducted in rats in which the BBB was opened by image-guided focused ultrasound (FUS). This approach enabled the location of BBB opening to be positioned in the sensitivity volume of the NIRS probes and the degree of permeability to be varied by adjusting the FUS power. To further assess the sensitivity of the method, experiments were conducted using two optical contrast agents of different molecular weights since permeability is inversely related to the size of the agent. Experiments were conducted using Indocyanie green ICG (Sigma-Aldrich, Saint Louis, MO, US), which has a molecular weight of 67 kDa due to binding with albumin, and IRDye 800 carboxylate (LI-COR Biosciences, Lincoln, NE, US), which weighs 1166 Da. For validation, the PS product was measured independently by DCE CT.

Methods: Data were obtained from eight rats (weight = 480 ± 120 g), which there divided into two equal groups based on the optical contrast agent used. Two sets of DCE NIRS data were collected per rat: one before (intact BBB) and one after sonication (opened BBB). BBB was opened by image-guided focused ultrasound. The procedure requires the intravenous injection of microbubbles, followed by 2 min of sonication. The selected power was changed between animals (0.5 – 2 W) to vary the degree of BBB opening. Optical contrasts were injected intravenously (0.1 mg/kg), followed by continuous recording of NIRS data from optical probes placed on the rat's head, to monitor the wash in and clearance of the dye from the brain. The DCE data were analyzed with a mathematical model to characterize BBB permeability (referred to as the permeability surface-area project, PS). Opening of the barrier was independently verified by acquiring CT permeability maps.

Results: The results indicate that change of the outflow rate of the contrast agent, based on the analysis of the time course of NIRS signal can be used to assess the degree of optical contrast accumulation in the brain caused by opening the BBB. The permeability parameter PS obtained for ICG reflects the extravasation of the dye due to opening of the BBB. This difference was evident in the change in the PS product measured before (~0 ml/100g/min) and after sonication (2.93 ml/100g/min). Due to its small molecular weight, evidence of extravasation was evident for IRDye even at baseline (PS = 2 ml/100g/min); however, permeability still increased after sonication (PS = 15 ml/100g/min). A relationship between sonication power and leakage of the optical dyes was also observed.

Conclusion: The results show the potential of NIRS as a simple method for evaluating BBB integrity, which could be used to monitor critical care patients at risk of BBB disruptions. The advantages of the proposed DCE NIRS is applicability at the bedside, its non-invasiveness, and the low toxicity of the optical contrast agent.

Nuclei Detection and Proliferation Index Estimation on Ki-67 and Hematoxylin Stained Images

Peter Morreale*, Emily Brouwer**, Geoffrey Wood**, April Khademi*
*Image Analysis in Medicine Laboratory (IAMLAB), School of Engineering, University of Guelph,
**Department of Pathobiology, Ontario Veterinary College, University of Guelph

Introduction: Clinical procedures for determining a breast cancer prognosis using a Ki67 proliferation index (PI) with hematoxylin counter stain are performed by a pathologist through a combination of manual counting and application of standardized scoring and grading systems. Despite these standardization systems there is still significant inter and intra observer variability among pathologists performing manual counting, which limits prognostic reproducibility [1]. Automatic image analysis algorithms have been proposed as a solution to these inherently subjective and time consuming counting procedures. However, many algorithms that involve nuclei seed detection can only process one stain type and require user defined parameters for optimal performance causing subjectivity to enter the model. This paper proposes a novel colour image processing framework that performs nuclei detection of hematoxylin and Ki67 positive stained nuclei separately and uses it to objectively estimate the proliferation index, which is the score used by pathologists for prognostication.

Methods: The proposed framework consists of: vector median filtering to smooth stain variation, background subtraction to isolate nuclei, stain separation to generate two separate stain images (Hematoxylin and Ki67), and the automatic seed detection proposed in [2] which requires accurate user cell radius estimation. Validation metrics were performed for each stain type through a sensitivity and precision analysis to calculate an overall F score for each stain in a single image. The F score was calculated using the formula: $F = \frac{2*S*P}{S+P}$, where S is sensitivity and P is precision. The PI was calculated for each image as a percentage using the formula: $PI = \frac{Total\ \#of\ Counted\ Positive\ Nuclei}{Total\ \#\ of\ Counted\ Nuclei} * 100$. Validation counts were calculated by isolating a circular window with a diameter of 4.5µm around each automatically detected seed. Coincident seed points within the circular window were counted as true positive, however if no labelled seed was located within the validation window the automatic seed was counted as a false positive. False negatives were labelled nuclei unaccounted for after automatic detection.

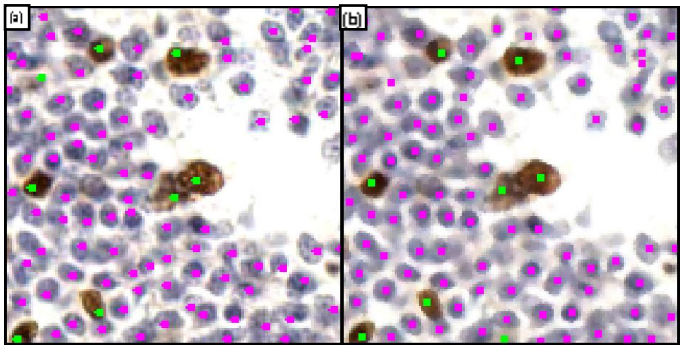

Figure 1 (a) Manually Labelled Nuclei. (b) Automatically Detected Nuclei

Results: The colour processing framework was applied to 27 canine mammary tumour tissue microarrays (TMAs) with an approximate image size of 1450x1450 pixels. Figure 1 shows the results of the proposed method compared to the manually labelled nuclei for a small TMA region. After separating the Hematoxylin and Ki67 stains, it was possible to choose separate cell radius estimates for healthy and tumour cells allowing for optimal detection. Figure 2 shows various cell diameter estimations that were implemented with ideal estimates of 1.5µm for hematoxylin and 2.5µm for Ki67 with F scores of 0.70 and 0.67 respectively. The mean PI for the this dataset was 19.0% +/- 23% for the manually labelled images and 19.7% +/- 25% using the proposed automatic method. The average difference between the PI estimation for the labelled and automatic images was 4% +/- 7%. These minimal differences suggest the proposed method obtains a reliable stain separation and a robust PI estimation for data with large variation between images.

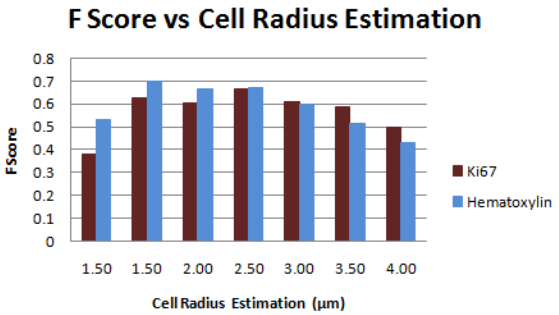

Figure 2 Cell Radii Estimates and Associated F Score.

Conclusions: This work shows that choosing different nuclei estimates for each stain type obtain better results than a single user estimate for multiple stain types, which can reduce subjectivity and variability among users of nuclei detection methods. This method also obtains a reliable and reproducible proliferation index estimate which is a strong prognostic tool for assisting pathologists in their everyday workflow.

References: [1] E. Gudlaugsson, I. Skaland, E. A. M. Janssen, R. Smaaland, Z. Shao, A. Malpica, F. Voorhorst, and J. P. A. Baak, "Comparison of the effect of different techniques for measurement of Ki67 proliferation on reproducibility and prognosis prediction accuracy in breast cancer," *Histopathology*, vol. 61, no. 6, pp. 1134–1144, 2012. [2] X. Qi, F. Xing, D. Foran, and L. Yang, "Robust Segmentation of Overlapping Cells in Histopathology Specimens Using Parallel Seed Detection and Repulsive Level Set," *IEEE Trans. Biomed. Eng.*, vol. 59, no. 3, pp. 1–28, 2012.

DCE-MRI Breast Image Registration: Effect of Percent Sampling on Kinetic Analysis and Computation Time

Matthew Mouawad*, Heather Biernaski, Muriel Brackstone, Michael Lock, Anat Kornecki, Olga Shmuilovich, Ilanit Ben Nachum, Frank S Prato, R. Terry Thompson, Stewart Gaede, and Neil Gelman
Ontario Institute for Cancer Research
Western University, Lawson Health Research Institute, London Health Sciences Center

Introduction: Dynamic contrast enhanced (DCE) MRI can provide information to aid diagnosis and treatment monitoring of breast cancer. However, patient movement can introduce artificial variation in the signal enhancement curves. Non-rigid image registration can improve signal enhancement curves, but computation time can be long. Reducing the percent of voxels sampled (PS) for estimating the cost function could reduce computation time, but affect the quality of the registration as well as the analysis of the signal enhancement curves. This work investigates the influence of PS on kinetic model parameter values and goodness-of-fit.

Methods: DCE-MRI breast images were acquired on a 3T-PET/MRI (Siemens Biograph mMR) in 8 patients with early stage breast cancer. Three-dimensional fat suppressed fast low angle shot (FLASH) images (spatial/time resolution =1.0x1.1x2.0mm/18s) were acquired from patients prior to and at 28 time points following Gadovist (0.1 mMol/kg) injection. Post-contrast images were registered to the pre-contrast using deformable registration of the affected breast with a 2cm isotropic grid spacing and PS values of 0.5%, 1%, 5%, 20%, and 100% (3DSlicer, 16GB ram, intel i7-4790 CPU). Tumours were segmented using Otsu's method. The Toft's model was fit voxel-by-voxel using a population derived AIF (Parker *et al.* 2007)**.** The root-mean-square-error (RMSE) about the fitted curve and best-fit values (K^{trans}, k_{ep}) were extracted. Absolute difference maps (ΔK^{trans}, Δk_{ep}) were created by taking the absolute value of voxel-by-voxel differences between 100PS and other PS cases (including unregistered data) to assess changes in the spatial distribution of parameter values. Pair-wise Wilcoxon rank sum tests were performed to compare the median and 90th percentile values for each parameter map (K^{trans}, k_{ep}, RMSE) within each patient image to corresponding values for 100PS, except for ΔK^{trans} and Δk_{ep} which were compared to 20PS since they were subtracted from 100PS.

Computation Time	Percent Sampling (PS)				
	0.5	1	5	20	100
Median (Hours)	0.88	0.88	0.98	1.3	3.2
Range (Hours)	0.77 - 0.88	0.78 – 0.92	0.93 – 1.2	1.2 – 2.2	2.7 – 7.7

Table 1 – Median and range of computation time in hours for the entire DCE data set (28 images) across all patients.

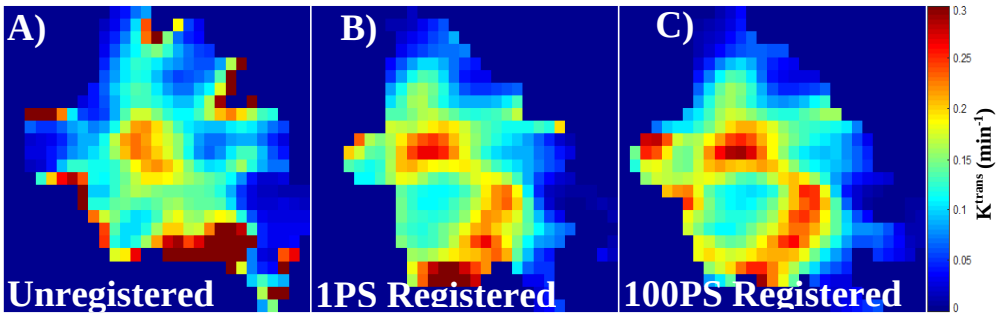

Figure 1 – K^{trans} maps for unregistered (A) and registered images at 1PS (B) and 100PS (C) from a representative patient. Compared to 100PS, both unregistered and 1PS registered images have different spatial distribution with similar median K^{trans}.

Results: Computation times (table 1) varied only slightly with PS between 0.5PS and 5PS. For median and 90th percentile of parameters K^{trans} and k_{ep}, no significant differences were found in comparison between 100PS and lower PS, although 90 percentile values obtained from unregistered images were significantly different than 100PS. However, there were large differences in the spatial distribution of these parameters as reflected statistically by significant differences in the median and 90th percentile of ΔK^{trans} and Δk_{ep} at 20PS compared to unregistered and some of the lower PS values. This spatial variation is illustrated in figure 1 which shows K^{trans} maps derived from unregistered (A) and registered data sets with 1PS (B) and 100PS (C) from a representative patient. Finally, median and 90th percentile values for RMSE were significantly different from 100PS for unregistered, 0.5PS, and 1PS, but not at 5PS and 20PS suggesting no improvements to goodness of fit above 5PS.

Conclusion: Considering computation time does not significantly decrease following 5PS and that sampling lower than 5PS leads to large differences in the spatial distribution of parameter output compared to 100PS, 5PS seems to be a good balance between reducing computation time and maintaining quality of the registration.

Acknowledgement: Breast MRI coil courtesy Siemens healthcare Canada.

A Fluorine-Containing OBOC Peptide Library for the Discovery of Cancer Imaging Probes.

Murrell E 1, Luyt L 1,2,3.
1. Department of Chemistry, University of Western Ontario 2. Department of Oncology, University of Western Ontario 3. London Regional Cancer Program and Lawson Health Research Institute

The chemokine receptor CXCR4 has been implicated as a receptor of interest in prostate cancer, especially in advanced and metastatic stages.[1,2] Current peptide-based ^{18}F PET imaging agents that target CXCR4 have been based on the CXCR4-antagonist peptide T140, which was developed from the natural peptide polyphemusin II. Unfortunately, many of these imaging agents display poor pharmacokinetics and biodistribution *in vivo*.[3-5] New CXCR4-binding peptides and peptide-based imaging agents can be discovered through combinatorial methods. One-bead one-compound (OBOC) libraries are a combinatorial method of discovering new peptide-ligand interactions from millions of candidates. Although classic OBOC libraries produce simple peptides, modification of these peptides to convert them into imaging agents often decreases binding affinity. Incorporating a ^{19}F moiety into each entity in an OBOC library allows for the screening to be performed on complete imaging agents, which is important for the discovery of new peptides for molecular imaging. Fluorine-18 is a preferred radioisotope for PET imaging because of its stability, half-life and availability. We have developed an eight amino acid OBOC library containing an N-terminal functionalization with a fluoride moiety. Conveniently, the fluoride has been incorporated into the peptides through copper-free click chemistry, which will allow for quick and facile radiolabelling to produce the ^{18}F imaging agent for PET imaging. This unique combinatorial library has been screened against a U87 cell line that highly expresses CXCR4; beads that show binding to the cells are isolated and their respective peptide sequences identified by MALDI tandem mass spectrometry. The corresponding peptides can then be developed into ^{18}F cancer imaging probes for PET imaging of CXCR4-expressing prostate cancers.

(1) Chen, Q.; Zhong, T. *Drug Des Devel Ther* **2015**, *9*, 5115.
(2) Gravina, G. L.; Mancini, A.; Muzi, P.; Ventura, L.; Biordi, L.; Ricevuto, E.; Pompili, S.; Mattei, C.; Di Cesare, E.; Jannini, E. A.; Festuccia, C. *Prostate (Hoboken, NJ, U. S.)* **2015**, *75*, 1227.
(3) Yan, X.; Niu, G.; Wang, Z.; Yang, X.; Kiesewetter, D. O.; Jacobson, O.; Shen, B.; Chen, X. *Mol. Imaging Biol.* **2016**, *18*, 135.
(4) Zhang, X.-X.; Sun, Z.; Guo, J.; Wang, Z.; Wu, C.; Niu, G.; Ma, Y.; Kiesewetter, D. O.; Chen, X. *Mol Imaging Biol* **2013**, *15*, 758.
(5) Jacobson, O.; Weiss, I. D.; Kiesewetter, D. O.; Farber, J. M.; Chen, X. *J. Nucl. Med.* **2010**, *51*, 1796.

Improving Image Quality in X-Ray Images with the Apodized-Aperture Pixel (AAP) Design

Tomi Nano*, Terenz Escartin and Ian Cunningham
OICR Smarter Imaging Program, Robarts Research Institute, Western University

Introduction: In digital radiography, the risk associated with radiation exposure is a key motivator for producing images with high signal-to-noise (SNR) and low patient exposures. High SNR images have been shown to increase cancer detection rates.[1] The detective quantum efficiency (DQE) as a function of spatial-frequency quantifies x-ray detector ability to produce high SNR images using low exposures. High DQE across all image frequencies is important for detection, especially at high frequencies which pertain to fine detail. Current clinical x-ray detectors have low DQE values at high frequencies that in some cases is primarily due to noise aliasing artifacts. Noise aliasing is an imaging artifact augmenting to image noise and can reduces DQE by more than a factor of two at high frequencies.[2] The objective of this work was to develop a novel x-ray detector design, called apodized aperture pixel (AAP), which improves high-frequency DQE by eliminating noise aliasing.

Methods: The AAP detector uses an x-ray converter layer and sensor-elements of size 10-25µm to optimally synthesize typical images of pixel size 100-200µm.[3] We demonstrate a proof-of-concept comparison of conventional and AAP images qualitative detectability of high frequency content. AAP and conventional images were synthesized using Monte Carlo simulations of sinusoidal patterns at various contrast levels and frequencies. Images of star-patterns were acquired with a mammography CsI detector having 50µm elements and used to compare conventional and AAP images of 200µm pixel size.

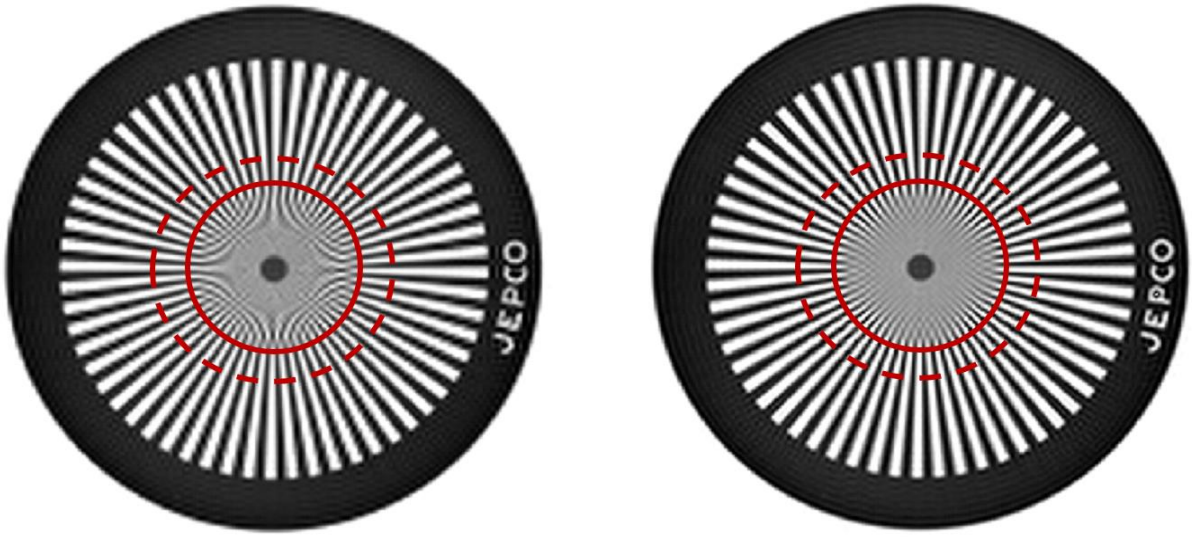

Figure 1. Conventional (left) and AAP (right) x-ray images acquired with a clinical mammography CsI detector.

Results: The AAP design is novel x-ray detector design that reduces aliasing artifacts and improves detectability of high frequencies. A demonstration of star-pattern images acquired with a CsI detector (Fig. 1) shows complete removal of aliasing artifacts (Moiré pattern) and improves visibility of high frequencies patterns close to the cut-off frequency (between the red lines in Fig. 1). Conventional images show reduced SNR with increasing frequency and decreasing contrast, while AAP images show uniform SNR with increasing frequency and contrast.

Conclusion: Image frequencies near the sampling cut-off frequency display more than double the detectability with the AAP than conventional design. A proof-of-concept implementation of the AAP approach improves image quality. The AAP approach has a role to play on detectors having substantial computational ability and where sensor elements can be manufactured smaller than what might be clinically practical.

[1] Chiarelli A. et al., "Digital compared with screen-film mammography…", Radiology, p.684-693, 2013
[2] Escartin T. et al., "Detective quantum efficiency…", Proc. of SPIE: Physics of Medical Imaging, 9783, 2016
[3] Nano T. et al., "MTF and DQE Enhancement with an AAP Design", Med. Phys. Submission Nov. 2016

Observer Study to Determine Minimal Detectable Improvement in DQE of X-Ray Detectors

Tomi Nano*, Terenz Escartin and Ian A. Cunningham
OICR Smarter Imaging Program, Robarts Research Institute, Western University

Introduction: Radiography is used for medical diagnosis of cancer and other diseases because of the high resolution and contrast in x-ray images. For a given diagnostic task, the detection accuracy for an ideal observer (that performs optimally) depends on image quality.[1] This implies that x-ray detectors capable of producing higher quality images result in better observer detectability. Due to the risk of radiation induced cancer from x-ray exposures, the lowest possible exposure must be used without compromising diagnostic accuracy. Thus, x-ray detectors should be designed to yield diagnostically useful images using low exposures. The detective quantum efficiency (DQE) quantifies a detectors ability to produce high SNR images for a given exposure. Engineering advances of detector technology and design have resulted in improved detector DQE.[2] The amount of DQE enhancement related to detectability improvements is unknown for a given observer task. The objective of this study is to determine the minimal increase in DQE that will make an observable change in image quality.

Methods: In this pilot study, we simulated Rose-phantom images that would be obtained with detectors having different DQE and measured the percentage of images correctly identified by observers that corresponds to x-ray detectors of greater DQE. Visual detectability performance was conducted using a two-alternative forced choice (2AFC) study by 10 human observers. A total of 110 images were simulated containing 7x7 disks differing in contrast and size with Poisson noise. Images are representative of DQE differences by 5% from 75% to 125% across all image spatial frequencies (separate into separate sentences). A graphic user interface was developed in C++ (GCC4.8.2, Qt5.2.1) to display images adjacently with synchronous integer zoom, window and level as shown in Fig. 1.

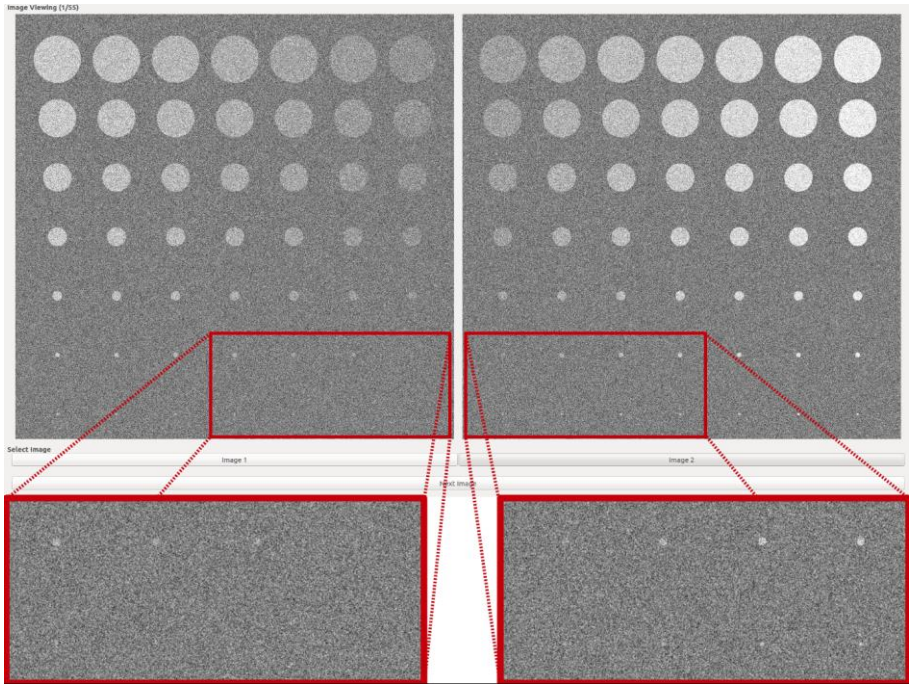

Figure 1. Two-alternative forced-choice study of detector DQE.

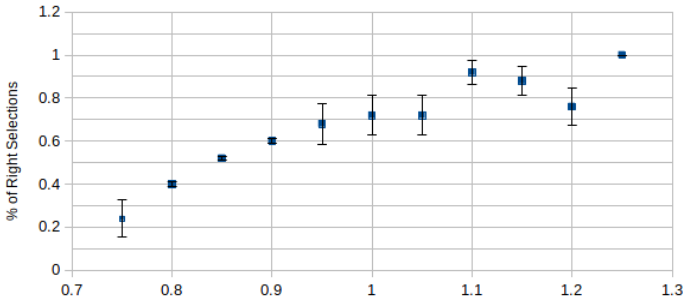

Figure 2. Visual detection of DQE differences.

Results: A DQE increase of 10%, as shown in Fig. 2, was found to improve observer visual detectability in images of disks with Poisson noise. This implies that improving DQE by 10% can result in 10% less exposure to patients without loss of detectability. A bias is present of participants selecting images displayed on the right.

Conclusions: Improvement in DQE was shown to correlate with greater observer detection of disks in simulated x-ray images. We conclude that differences in DQE by 10% or more will result in improved detection of disks in a Rose phantom and improved perception of image quality in noise-limited images.

1. Loo et al., “A comparison of physical image quality indices...”, Phys. Med. Biol, Vol.29, No.7, 837-856, 1984
2. Nano et al., “MTF and DQE Enhancement using an AAP X-Ray Detector Design”, Med. Phys., Nov. 2016

OATP1A1 as a novel clinical-field strength MRI reporter gene for cell tracking

Nivin N. Nyström[1], Hamilton AM[2], Martínez-Santiesteban FM[2], Lim H[1], Scholl TJ[1–3], Ronald JA[1,2]
[1] Department of Medical Biophysics, Western University; [2] Imaging Research Laboratories, Robarts Research Institute; [3] Ontario Institute for Cancer Research

Introduction: The ability to track cells in living organisms with sensitivity, accuracy and high spatial resolution would revolutionize the way we study disease. Reporter genes are a valuable resource as they encode detectible products, allowing for quantitative "reporting" of cells that express them. Magnetic resonance imaging (MRI), which generates high-throughput 3D information, provides a likely platform for effective cell tracking *in vivo*. However, MRI reporter genes developed to date exhibit weak sensitivities[1]. Moreover, research has largely focused on iron-based negative contrast mechanisms, which interfere with iron homeostasis and cell phenotype, thereby confounding experimental results and virtually eradicating their potential for human application[2].

Rationale: Gadolinium ethoxybenzyl diethylenetriaminepentaacetic acid (Gd-EOB-DTPA) is a clinical imaging agent capable of generating T_1-weighted MRI contrast in the liver, due to its uptake by Organic Anion-Transporting Polypeptide 1 (OATP1) proteins expressed on hepatocytes[3]. Interestingly, cells engineered to express the rat isoform (OATP1A1) had enhanced R_1 relaxation rates, allowing for their detection in mice[4]. Yet, this study was conducted using extreme parameters *e.g.* >2x the clinical Gd-EOB-DTPA dose, 9.4 Tesla (T) field strengths. We aim to assess the feasibility of OATP1A1 for research and clinical application by taking into consideration contemporary safety and accessibility limits. Specifically, we will be testing the functionality of OATP1A1 with clinical Gd-EOB-DTPA doses using a human metastatic breast cancer model at 1.5 and 3T.

Methods: MDA-MB-231 cells were engineered via lentivirus to express OATP1A1. A trypan blue assay was used to evaluate cell viability. Cells were treated with 0.25 mM Gd-EOB-DTPA for 90 minutes and washed 3× with phosphate buffered saline prior to imaging. R_1 relaxation rates of cell pellets were acquired using an Inversion Recovery Fast Spin Echo pulse sequence with TI = 50, 60, 70, 75, 80, 100, 150, 250, 350, 500, 750, 1000, 1250, 1500, 2000, 2500, 3000 ms; TR = 5000 ms; TE = 19.1 ms; and ETL = 4.

Results: No difference in cell viability was found between treated and untreated control and OATP1A1-expressing cells. Pilot *in vitro* experiments showed that, following Gd-EOB-DTPA treatment, OATP1A1-expressing cells had elevated R_1 relaxation rates (2.36 ± 0.26 Hz) relative to treated control cells (0.59 ± 0.02 Hz) at 3T (Figure 1). Further, there was no observed difference in R_1 relaxation rate between treated controls, untreated OATP1A1-expressing cells, and untreated controls.

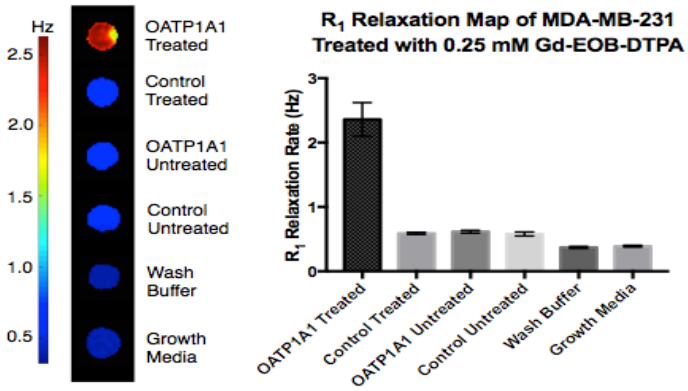

Figure 1. Spin-lattice relaxation map of OATP1A1-expressing cells and control cells, treated or untreated with 0.25 mM Gd-EOB-DTPA at 3T.

Discussion: OATP1A1 reporter gene imaging could have significant benefits over alternative MRI reporters, as well as more sensitive modalities such as positron emission tomography (PET), which has limitations in longitudinal imaging due to ionizing radiation. The development of an OATP1A1 system could shift the field of molecular imaging in a new direction, and, in the larger scheme of things, fill a vacuum of information not provided by other modalities. Our preliminary data supports further development of OATP1A1 as a novel clinical-field strength MRI reporter gene. After completing *in vitro* characterization, we hope to assess the *in vivo* sensitivity of our system in mouse models under analogous clinical parameters. Optimizing the sensitivity of reporter genes in high throughput modalities such as MRI is crucial toward improving our ability to visualize and quantify cells *in vivo*. If successful, this new technology could enable dynamic tracking of specific cell populations in their natural environments with combined high spatial resolution, sensitivity and 3D information.

References: [1] Vandsburger MH et al *NMR Biomed* 2014. [2] Pereira SM et al *Int J Mol Sci* 2015. [3] Leonhardt M et al *Drug Metab Dispos* 2010. [4] Patrick PS et al *Proc Natl Acad Sci USA* 2014.

Photoacoustic computed tomography 3D image reconstruction for detecting breast cancer

Parsa Omidi, Ivan Kosik, Muriel Brackstone, Astrid-Chamson Reig, Mamadou Diop, and Jeffrey Carson
Lawson Health Research Institute, University of Western Ontario, London, Ontario, Canada

Introduction. Photoacoustic computed tomography (PACT) is an ever growing noninvasive imaging technology, which takes advantage of high optical contrast and low acoustic scattering to capture high resolution optical images. The PACT method is described by the following sequence: short pulse high energy laser light illumination of an object, conversion of light into acoustic waves in the object, and collection of acoustic waves by a sensor array. The sensor array can be comprised of one or more scanned transducers or a stationary array of transducers. To convert the transducer measurements into PACT images, many image reconstruction algorithms have been designed by groups throughout the world. The purpose of this study was to evaluate a compressed sensing reconstruction algorithm on both a resolution phantom and *ex-vivo* tissue.

Method. The PACT system has been designed to provide 3D biomedical images and contains a tunable laser (690 - 950 nm); an arc shaped transducer array with 24 transducers, which rotates 180 degrees in 10 steps and makes a virtual hemisphere with 240 transducers; and a 50 MHz sampling rate data acquisition system. Back-projection (BP), the most common reconstruction algorithm was built on a delay-and-sum method. This method uses the fact that pressure propagating from the source reaches each detector with a different time delay. Heterogeneity of the medium with respect to speed of sound (SoS) imposes significant phase error in BP due to the assumption of uniform SoS. To compensate for this aberration, an adaptive weighting method by the name of coherence factor (CF) technique has been applied to BP. We also tested compressed sensing (CS) reconstruction algorithm, which utilizes the concept of sparsity of signals. It has been shown that for reconstruction of a signal, the Shannon sampling limitation is not mandatory if the signal is sparse. Therefore, by using CS, the reconstruction with smaller numbers of detectors could improve the images. Wavelet, curvelet, discrete Fourier transform (DCT), and total variance (TV) are some well-known transforms that can be used to sparsify signals. Each sparsification transform function can represent a specific feature of data. It has been shown that wavelet and DCT can capture homogenous texture and curvelet and TV are good at capturing edges and borders of images. For preserving all features of the image, we propose a sparsifying dictionary made out of a combination of all the mentioned sparsification transform functions.

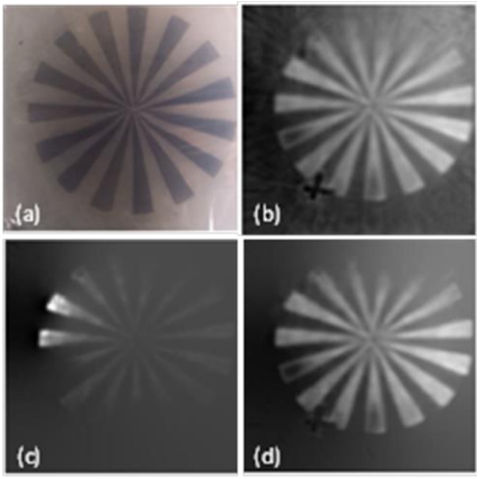

Fig.1. 2D image reconstruction algorithms for a simulated phantom made out of carbon and Agar gel: (a) photo of phantom, (b) BP, (c) BP+CF, and (d) CS (combined dictionary).

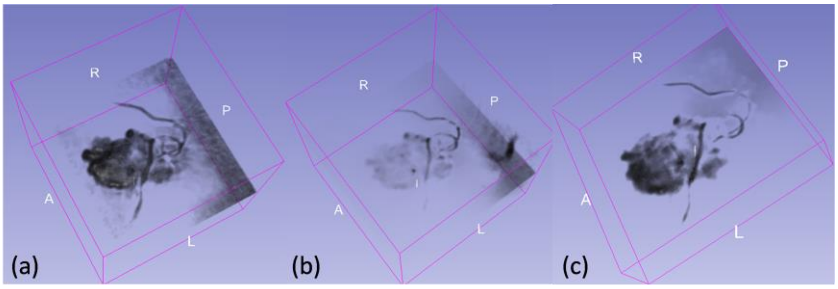

Fig. 2. 3D image reconstruction algorithms for detecting breast lumpectomy specimen: (a) BP, (b) BP+CF, and (c) CS(combined dictionary) .

Results. Fig.1 shows that even if BP has good contrast, it results in image artifacts. By applying CF some of the artifacts which belong to phase aberration have been eliminated, but at the expense of some of image detail. On the other hand CS results show that by preserving the details, it can greatly reduce image artifacts. The same algorithms have been applied to obtain 3D images of a breast lumpectomy specimen and the results show same outcomes.

Conclusion. In this work, we provide three reconstruction algorithms for detecting a 3D image of a breast cancer tumor. Based on the results, it is clear that CS with combined sparsifying method brings the best contrast with fewest image artifacts at the expense of running time (execution time in CS is 100-150 times more than BP).

Accelerated Diffusion-weighted ^{129}Xe MRI Morphometry of Emphysema

A. Ouriadov[1,2], E. Lessard[1,2], F. Guo[1,3], H. Young[1,2], A. Bhalla[1], D.G. McCormack[4] and **G. Parraga**[1,2]
[1]Robarts Research Institute, [2]Department of Medical Biophysics, [3]Graduate Program in Biomedical Engineering, [4]Division of Respirology, Department of Medicine,
The University of Western Ontario, London, Canada

Introduction: Whole-lung 3D multi-b diffusion-weighted data in a single breath-hold was shown feasible for ^{3}He lung MRI using traditional k-space sampling[1], parallel imaging[2] and compressed sensing.[3] We hypothesized that accelerated ^{129}Xe lung MRI should also permit acquisition of whole lung 3D multi-b diffusion-weighted dataset in a single 16sec breath-hold and similar to the spatial resolution of ^{3}He MRI results. Therefore, in this proof-of-concept evaluation, our objective was to evaluate ADC and morphometry estimates in a small group of never-smokers, COPD ex-smokers with emphysema and Alpha-1 Antitrypsin Deficiency (AATD) patients. The estimates were obtained for three different cases: 1) fully sampled k-space, 2) 50% undersampled k-space in the phase-encoding direction[4], (acceleration factor (AF)=2), and 3) 66% undersampled k-space (AF=3[3]).

Methods: Nine participants (four never-smokers, four COPD and one AATD patient) provided written informed consent to an ethics-board approved protocol and underwent spirometry, plethysmography, CT and ^{129}Xe MRI. Imaging was performed at 3.0T (MR750, GEHC, Waukesha WI) using whole-body gradients (5G/cm maximum) and a custom built, rigid quadrature unshielded asymmetrical RF coil.[5] In a single breath-hold (AATD case), four interleaved acquisitions (3D FGRE, VFA, TE/TR=9.0msec/10.0msec, matrix size=64x64, number of slices=7; slice thickness=30mm, and FOV=40x40cm) with and without diffusion sensitization were acquired for a given line of k-space. For all other subjects two interleaved acquisitions (2D FGRE, TE/TR=9.8msec/11.0msec, matrix size=128x128, number of slices=7; slice thickness=30mm, and FOV=40x40cm^2) with and without diffusion sensitization were acquired for a given line of k-space to ensure that RF depolarization (5^o constant flip angle was used) and T_1 relaxation effects were minimal[5]. The diffusion-sensitization gradient pulse ramp up/down time=500μs, constant time=2ms, diffusion time (Δ)=5ms, providing four b-values 0, 12.0, 20.0, and 30.0s/cm^2. Hyperpolarized ^{129}Xe (86% enriched, polarization~12-20%) was provided by a xenon polarizer system[6] (XeniSpin™, Polarean, Durham, NC). 1L of a 50/50 hyperpolarized ^{129}Xe/^{4}He gas mixture was inhaled from functional residual capacity. For COPD and never-smokers participants, a single 1L mixed dose was inhaled.[5] Two k-space masks mimicking AF=2 and AF=3 were applied to fully sampled k-space (each b-value) in order to obtain undersampled k-spaces with two different acceleration factors. The Projection-onto-Convex-Sets[4] and CS[7] were used to reconstruct diffusion-weighted images from undersampeled k-spaces with AF=2 and AF=3, respectively. ^{129}Xe mean linear intercept (L_m) maps were estimated using the stretched exponential method[3,8] $(S(b)/S_0=\int P(D)\exp(-[\mathbf{b}*D])dD$, equation provides the distribution of length scales ($L_D=[2\Delta D]^{1/2}$)) which was extended to provide the clincaly-relevant estimates such as a mean linear intercept[9] and adapted for ^{129}Xe. The morphometry maps for AF=2/AF=3 and full sampling along with two b-value (0 and 12s/cm^2) ADC, were computed on a voxel-by-voxel basis.[9]

Results: Mean ADC, and L_m estimates for the never-smokers (0.05cm^{2}s^{-1}/280μm) were significantly smaller than the corresponding mean estimates for COPD and AATD patients (0.08cm^{2}s^{-1}/600μm; all p<.001) for all three sampling methods. For never-smokers, mean differences of 1.8%/5.0% and 2.2%/5.2% were observed between fully sampled and undersampled (AF=2/AF=3) k-space ADC and L_m values, respectively. For the COPD subgroup a mean difference of 2.3%/4.6% and 4.0%/4.2% was observed between fully sampled and undersampled (AF=2/AF=3) k-space ADC and L_m values, respectively. For the AATD subject a mean difference of 5.6%/6.1% and 5.5%/6.2% observed between fully sampled and undersampled (AF=2/AF=3) k-space ADC and L_m values, respectively.

Conclusion: The results of this proof-of-concept study show that the difference in ADC and Lm_D estimates obtained from the fully sampled and undersampled k-space was similar to observed with accelerated ^{3}He multi-b diffusion-weighted MRI in healthy subjects.[3] These differences as well as L_m differences increase however, with increasing emphysema severity. Therefore, while promising, accelerated multi-b diffusion-weighted lung MRI ^{129}Xe morphometry in patients with severe emphysema requires further investigation.

References:

1. Paulin G. A. *et al*. *Physiol Rep* **3**, (2015).
2. Chang, Y. V. *et al*. *Magn Reson Med* **73**, 1609-1614, (2015).
3. Chan H. F. *et al*. *Magn Reson Med*, (2016).
4. Haacke E. M. *et al*. *J Magn Reson (1969)* **92**, 126-145, (1991).
5. Ouriadov A. *et al. Magn Reson Med* **70**, 1699-1706, (2013).
6. Cleveland Z., *et al*. *J Phys Chem. B* **113**, 12489-12499 (2009).
7. Lustig M. *et al*. *Magn Reson in Med* **58**, 1182-1195 (2007).
8. Berberan-Santos M. N. *et al*. *Chem Phys* **315**, 171-182, (2005).
9. Ouriadov A. *et al*. *ISMRM 24th Annual Meeting*, **2788** (2016).

A *Ouriadov gratefully acknowledges fellowship support from the Alpha-one Foundation (USA).*

Rapid prototyping of a lightweight bone plate for complex fracture fixation in a peregrine falcon

Adam D.M. Paish[1,3,5] (Primary Author), Tomasz Chmiel[1], Brian Salt[6], Alexander O. El-Warrak[4,5], David W. Holdsworth[1,2,3,5] (Supervisor)

Development of Novel Therapies for Bone and Joint Diseases Consortium

[1]Robarts Research Institute, [2]Department of Surgery, [3]Department of Medical Biophysics, Schulich School of Medicine and Dentistry, Bone and Joint Institute, [4]Animal Care and Veterinary Services, [5]Western University, London, Ontario, Canada, [6]Salthaven Wildlife Rehabilitation Centre, Mount Brydges, Ontario, Canada

Introduction: A two-year-old female peregrine falcon was brought to Salthaven Wildlife Rehabilitation Centre with a complex fracture of the ulna in the left wing. It was surmised that this injury was caused when the animal struck a wire during high-speed flight. Following veterinary examination, it was determined that a bone plate was required to stabilize the break enough for the animal to heal and fly again. However, the smallest available commercial plates were deemed too heavy to be safe for the bird, since it is estimated that peregrine falcons experience G-forces up to 25*g* when they hunt. We describe the development of a custom 3D metal printed bone plate for fracture fixation of the ulna in the peregrine falcon. Our objective was to create an anatomically conformal, image-based rapid prototype of low enough mass to allow the falcon to return to flight.

Methods: A radiograph, illustrating a comminuted fracture of the ulna, was provided from a local veterinary clinic. Measurements were made from this image to guide computer-aided design of a bone plate (50mm x 5.9mm) that would accommodate up to eight 2 mm diameter non-locking bone screws (Fig. 1a). Seven variations of slightly different curvature and thickness were created to allow the veterinary surgeon to select a plate-of-best-fit intraoperatively. Each bone plate was 3D printed (AM 250, Renishaw plc) using medical-grade titanium alloy (Ti6Al4V). Plates were polished using dental hand-tools to a matte finish and sterilized via autoclave before surgery. The falcon was anaesthetized using isofluorane via head cone. The component selected (0.75g, 1mm thick) by the veterinary surgeon was a version with a 10-degree curvature from end-to-end lengthwise. Four 2mm bone screws were installed, two on each side of the fracture. Micro-CT imaging (eXplore Ultra, GE Medical) was preformed post-operatively (120 kVp, 20mA, 16 seconds). A beam hardening correction was performed during image reconstruction. Collected image volumes were analyzed to assess the fit of the installed bone plate with the falcon ulna.

Results: A complication related to the anesthetic developed following installation of two screws into the bone and plate, leading to cardiac arrest. Attempts to revive the falcon were unsuccessful. In order to secure the plate for imaging, two additional screws were installed *ex vivo*. The combined mass of the screw plus plate was 1.39g. Micro-CT analysis revealed congruency of the inner curvature of the bone plate with the surface of the ulna. It was determined that the installed component would be an appropriate template for future cases of complex fracture involving high-velocity birds-of-prey.

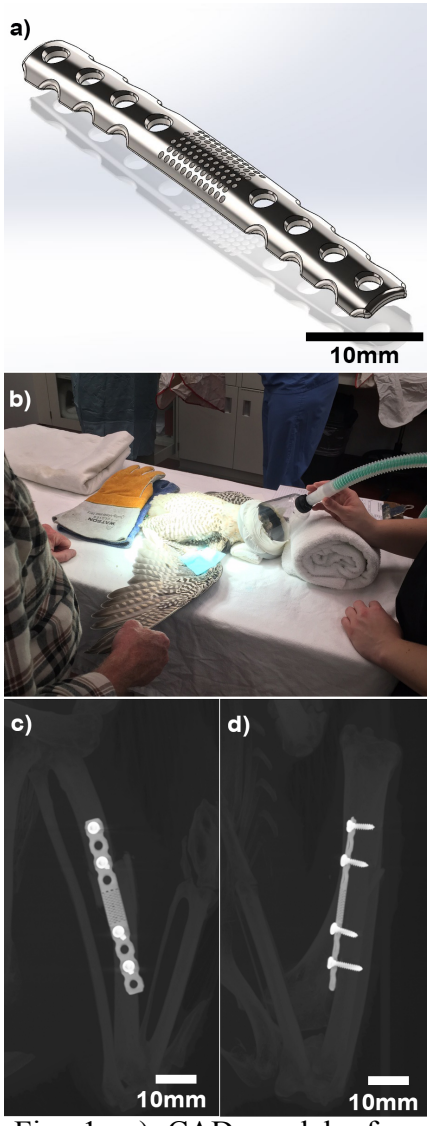

Fig. 1: a) CAD model of a custom ulnar fixation plate. b) Peregrine falcon under general anesthetic, displaying the injured wing. c) Anterior and, d) lateral maximum intensity projections reveal the installed bone plate on the left ulna.

Conclusions: We have demonstrated the rapid prototyping of a custom lightweight bone plate for fixation of a complex ulnar fracture in a peregrine falcon. Subsequent iterations of our device can be guided by analysis of the *ex vivo* micro-CT volume collected for this case. Although we were unsuccessful with the recovery of this animal, the implant we created is the first of its kind for a bird-of-prey. Because of its relatively small mass compared with commercially available components, our bone plate may offer peregrine falcons, and similar raptor species, a better chance of recovering flight following a complex fracture in the wing.

A multimodality imaging model to study concomitant tumour resistance

Katie M. Parkins, Amanda M. Hamilton, John A. Ronald, Paula J. Foster
Robarts Research Institute, The University of Western Ontario, London, Ontario, Canada

Introduction: The recurrence of cancer is believed to be related to a phenomenon referred to as dormancy; a stage in cancer progression where cancer cells survive in a quiescent state until sometime when they are triggered to become proliferative. Dormant cancer cells can present a significant therapeutic problem since they are nonproliferative and thus can evade traditional cytotoxic therapies that target only proliferative cell populations[1]. The mechanisms that influence dormancy by either activating dormant cells back into a proliferative state or maintaining cellular dormancy are poorly understood. One mechanism of interest known as concomitant tumour resistance (CTR) can be defined as the ability of the primary tumour to restrict the growth of distant metastases[2]. The aim of this work was to investigate the impact of a primary tumour on metastasis and dormancy in a mouse model of breast cancer metastasis using longitudinal noninvasive molecular imaging.

Hypothesis: The presence of a primary breast tumour can suppress the development of distant metastases by inducing tumor cell dormancy in established mouse models.

Materials and Methods: Nude mice will receive an injection of either vehicle (HBSS) or 500,000 parental MDA-MB-231 cells in the lower right mammary fat pad. Brain metastases were generated in both groups of mice using the MDA-MB-231BR cell line. MRI was used to monitor the development of primary tumors and brain metastases. 231BR cells were labeled with micron sized iron oxide particles (MPIO) to also allow for tracking of nonproliferating (dormant) cancer cells which retain MPIO and appear as signal voids in MR images of the brain. Ongoing studies are also being conducted with 231BR-FLuc cells that stably express a firefly luciferase reporter gene, allowing the use of bioluminescence imaging (BLI) to validate MRI data and provide measures of longitudinal cell viability.

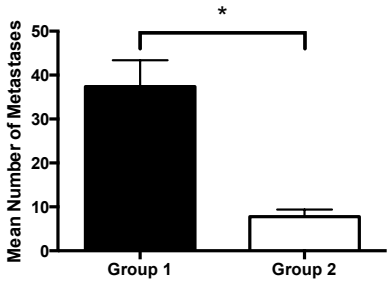

Figure 1. Fewer MRI detectable brain metastases formed in mice with a primary tumor (group 2). Data are presented as the mean and SEM. *P < .001.

Results and Discussion: In our 231/231BR model, we found that fewer brain metastases developed in mice with a primary tumour than those without; suggesting that the primary tumour can inhibit the development of brain metastases **(Figure 1)**. We also found that significantly more signal voids, which represent nonproliferative cancer cells, were seen in endpoint images of mice that had a primary tumour compared to mice that did not. This suggests that the presence of a primary tumour can induce or maintain cancer cell dormancy. In our 231BR-FLuc model, day 0 BLI provides evidence that the signal voids detectable by MRI represent live, MPIO-labeled cells in the brain **(Figure 2)**. Ongoing studies focus on the combination of BLI and cellular MRI at multiple timepoints to get direct longitudinal measures of whole-brain single cell arrest, tumour volumes, and cancer cell viability, providing a more holistic view of transplanted cancer cell fate and CTR in a mouse model.

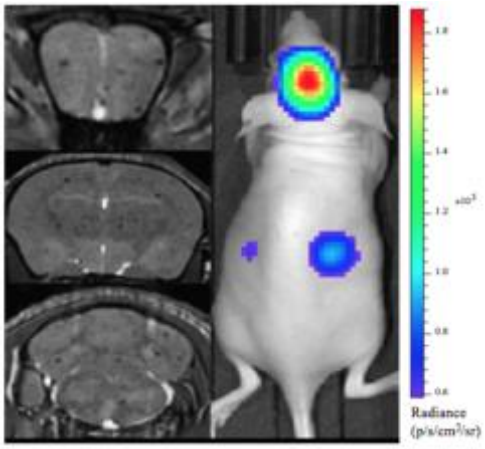

Figure 2. Bioluminescence (BLI) and MRI of a representative mouse on day 0. Whole mouse BLI shows strong signal in the brain and weaker signal in the mouse body (Right Panel). MR image slices from a 3-dimensional (3D) bSSFP image acquisition for the same mouse (Left Panel)

Conclusion: Cancer cell dormancy and recurrence are important clinical problems for breast cancer patients and their physicians. The aim of this work is to study the impact of a primary tumour on distant metastases; a possible natural regulator of dormancy and metastatic recurrence which may lead to novel therapeutic approaches to enhance dormancy or maintain dormant cancer in a nonproliferative state.

References: 1. Scully OJ, Bay BH, Yip G, Yu Y: Breast cancer metastasis. Cancer Genomics Proteomics 2012, 9(5):311-320. 2. Chiarella P, Bruzzo J, Meiss RP, Ruggiero RA. Concomitant tumor resistance: Cancer Lett. 28: 324(2): 133-41, 2012.

Ultrasound-triggered conversion of porphyrin microbubbles to nanobubbles: Extending cavitation activity beyond the vasculature

Carly Pellow[1], Christopher Acconcia[2], Maneesha Rajora[3], David Goertz[1,2,*] and Gang Zheng[1,3,4,*]
Ontario Institute for Cancer Research: Smarter Imaging Platform
*[1]Department of Medical Biophysics, University of Toronto; [2]Sunnybrook Research Institute; [3]Institute of Biomaterials and Biomedical Engineering, University of Toronto; [4]Princess Margaret Cancer Research Tower; *supervisors*

Introduction. Microbubbles (MBs) are routinely used in clinic for ultrasound vascular imaging, and have emerged in pre-clinical studies as therapeutic tools for vascular bio-effects and controlled delivery. Recently, novel porphyrin-shelled MBs extended the conventional ultrasound agent into a multimodal tool with photoacoustic and fluorescence tracking capabilities, and phototherapeutic properties[1]. When stimulated by ultrasound, these MBs increased *in situ* uptake of porphyrin nanostructures, found to contain gas[1]. In addition to photoactive porphyrin, the presence of gas in the daughter nanobubbles (NBs) opens the possibility of stimulating further bubble-mediated ultrasound imaging and therapy beyond the confines of the vasculature.

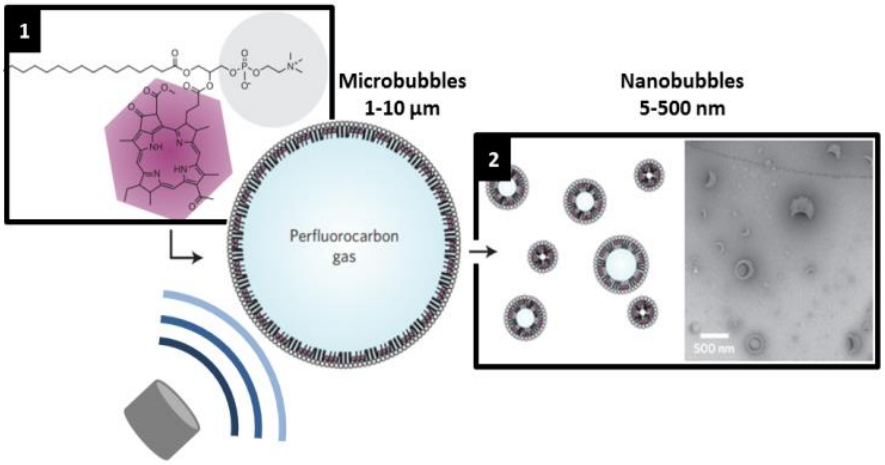

Figure 1: Ultrasound triggered conversion of porphyrin-shelled microbubbles to nanobubbles provides a platform for enhanced uptake of (1) photoactive porphyrin and (2) nanobubbles for imaging and therapy directly in the intra-tumoural space.

Methods. Bubble simulations followed the Yang-Church model[2] to compare bubble behaviour as a function of size, ultrasound parameters, and viscoelastic surroundings. A benchtop analog involved size-isolated MB (0.6-18um diameter; 10^7 MB/mL) and NB populations (<0.4um diameter; 10^7 MB/mL) flowing through a channel as a vessel mimic, or embedded in agarose gel to imitate the extravascular space. Bubbles were exposed to ultrasound (100 10 cycle bursts at 1kHz PRF, at varied pressures 0-1MPa) at 2.5MHz and 8MHz from a broadband piezocomposite 5MHz centre frequency transducer for second harmonic and subharmonic imaging sensitivity respectively. A similar setup was utilized *in vivo*, where MBs were injected intravenously into C3H mice with KHT sarcoma tumours. The tumour site was exposed to ultrasound (1min of 2.5ms pulses at 1MHz transmit and 50% duty cycle, at 150kPa) to induce MB conversion and subsequent accumulation of NBs in the intra-tumoural space, where higher pressure shorter pulses probed for the presence of NBs long after the disappearance of MBs from the vasculature.

Results. Simulations and benchtop experiments indicated higher resonant frequencies, elevated cavitation thresholds, and more sustained activity for NBs in tissue compared to their free counterparts. Despite elevated resonance frequencies and thresholds, signals consistent with the presence of NBs were detected *in vivo* at therapeutically relevant low frequencies.

Conclusions. Work to-date demonstrates differences in bubble behaviour as a function of size and surrounding environment, and implies that NBs may be detectable at therapeutically relevant low frequencies to enable bubble-mediated imaging and therapy in the intra-tumoural space. This micro-to-nano conversion provides a powerful platform to enhance delivery, prolong tumour visualization, and locally treat the lesion with multiple modalities.

References. [1] E. Huynh, *et al.* ***Nature Nanotechnology***, 10, 2015; [2] X. Yang and C. C. Church. ***J. Acoust. Soc. Am***, 118(6), 2005.

3D Lung Histology Reconstruction and Registration to *in vivo* Imaging

Sean A. K. Pentinga[12], K. Kwan[3], S. A. Mattonen[12], C. Johnson[1], D. A. Palma[124], and A. D. Ward[124]
[1]Baines Imaging Research Laboratory, London Regional Cancer Program,
Departments of [2]Medical Biophysics, [3]Pathology, [4]Oncology, The University of Western Ontario
London, Ontario, Canada
Research Supervisor: Aaron D. Ward

Introduction: The MISSILE-NSCLC study is a phase II trial measuring the integration of stereotactic ablative radiotherapy (SABR) with surgery in early non-small cell lung cancer. One of the aims is to correlate post-SABR computed tomography (CT) radiomics signatures for cancer recurrence[1] with the presence of viable tumour cells on histology. Our goal was to develop software for semi-automatic (1) 2D reconstruction of pseudo whole-mount (PWM) sections from scanned slides and (2) 3D reconstruction and registration of PWM sections to pre-surgery CT.

Methods: Patients underwent SABR 2–3 months prior to CT scanning, followed by lobectomy. The specimen was serially sectioned at 5 mm, with each section cut into blocks suitable for standard 1" × 3" slides. Sections were stained with hematoxylin and eosin and digitized at 0.5 µm/pixel using a whole-slide scanner. We developed a MATLAB-based graphical user interface that allows the operator to interactively stitch the sections into a PWM. The algorithm automatically renders non-tissue portions of the slide transparent to facilitate stitching. Using a 3D Slicer-based thin-plate spline image warping tool developed in our lab, we interactively reconstructed the PWMs in 3D and registered them to CT via correspondence of homologous intrinsic landmarks.

Results/Discussion: In this proof-of-principle study, we have executed the fusion procedure for 12 PWMs across 6 different patients. Fig. 1 shows an example PWM before and after registration to CT; arrows point to homologous blood vessels. The necrotic core of the tumour (contoured in yellow) is surrounded by dense tissue. All of these features can be seen on the CT image and the histology image. Our ongoing work includes quantitative error measurement.

Successful PWM stitching and registration to CT requires addressing several challenges. Surgical resection, slicing, and histologic processing all change the shapes of the resulting images. Resected lobes deflate, albeit not uniformly, resulting in the grossed specimens being smaller and shaped differently than the corresponding tissue on CT. As a result, for many slices, the boundaries of each section do not readily align. The histology slices are much thinner than the 3 mm CT slices, challenging perfect CT-histology slice matching.

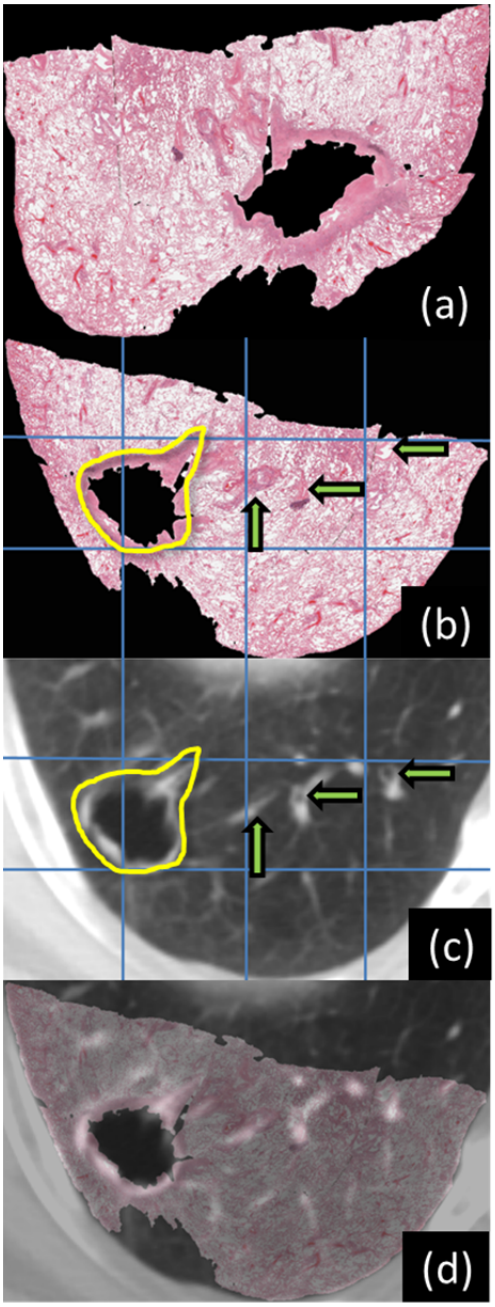

Fig 1: **(a)** Stitched PWM. **(b)** PWM warped to **(c)** corresponding CT with grid to aid in assessing correspondence. **(d)** PWM fused with CT.

Conclusion: We built a software tool to successfully stitch standard lung histology sections into PWMs and register them to pre-lobectomy CT scans, enabling the validation of CT radiomics signatures for post-SABR cancer recurrence against histologic assessments of viable tumour.

[1]Mattonen et al, Int J Radiat Oncol Biol Phys 94(5) 1121-8, 2016

Evaluation of reduced sampling schemes with 3D radial projections for ^{23}Na MRI

Paul Polak[1], Alireza Akbari[2],Michael D. Noseworthy[1,3,4]

[1] School of Biomedical Engineering, McMaster University, Hamilton; [2] Robarts Research Institute, Western University, London, ON; [3] Department of Electrical and Computer Engineering, McMaster University; [4] Imaging Research Centre, St. Joseph's Healthcare, Hamilton ON.

Introduction: In vivo ^{23}Na magnetic resonance imaging (MRI) is desirable due to sodium's essential role in cellular homeostasis, pH regulation and action potentials in neurons (1–2), but its acquisition suffers from many inherent technical challenges. Among these difficulties are the physical properties of ^{23}Na (low gyromagnetic ratio, short T_1 and T_2 relaxation times, low concentration compared to ^{1}H imaging), special hardware requirements (multi-nuclear magnet, dedicated transmit and receiver coils), non-standard pulse sequences (ultra-short or zero echo time (TE) imaging), and long acquisition times to account for low SNR (3–4). In order to overcome these problems, it is necessary to reliably evaluate ^{23}Na MRI techniques with undersampled data. We present here quantitative measures of ^{23}Na MRI at four levels of undersampling in saline phantoms.

Methods: The imaging experiments were conducted using a GE 3T MR750 (General Electric Healthcare, Milwaukee, WI), using a custom designed/built single-tune birdcage head coil (resonant frequency = 33.7 MHz). A saline reconstruction phantom constructed using 50 mL tubes and 8 different concentrations of NaCl in distilled water 2.5 g/100 mL, 1.25 g/100 mL, etc. to 0.0195 g/100 mL. The tubes were placed axially the magnet with the long axis parallel to B_0. A 3D radial projection sequence was evaluated under the context of differing acquisition window lengths (4 ms, 12 ms, 16 and 25 ms), with the amount of undersampled data points / window being 500, 1500, 2000 and 3125 respectively. The projections were designed to have a resolution of 3 x 3 mm^3. The other sequence parameters were held identical – repetition time (TR): 120 field of view: 180 mm, readout bandwidth: +/- 125 kHz, number of spokes: 11310 (divided into 6 acquisitions of 1885 spokes each), and acquisition length: 22 minutes, 42 seconds. Offline reconstruction utilized a custom MATLAB (Mathworks Inc., Natick, code and the non-uniform fast fourier transform (NUFFT) libraries from the Michigan Image Reconstruction Toolkit (University of Michigan, http://web.eecs.umich.edu/~fessler/code/index.html). NIFTI files were created from the reconstruction and resampled to an in-plane axial view of 128 x 128.

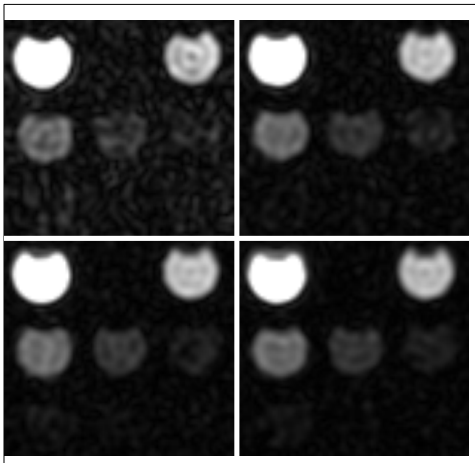

Figure 1: axial slices from the 4 acquisition windows of 4 ms (upper left), 12 ms (upper right), 16 ms (lower left) and 25 ms (lower right). Slices have been windowed identically.

Saline concentration (g / 100 mL)	SNR with acquisition window length			
	4ms	12 ms	16 ms	25 ms
2.5	36.7	80.8	86.4	116.8
1.25	17.2	38.3	42.8	57.1
0.625	8.3	20.6	24.3	28.6
0.3125	4.7	10.4	12.1	14.7
0.1562	3.5	7.1	6.7	8.5
0.0781	--	--	3.4	5.5

Table 1: Saline concentration (g / 100 mL)SNR with acquisition window length 4 ms, 12 ms, 16 ms, and 25 ms

Results: Figure 1 shows the same axial slice for all acquisitions – the images have been windowed identically. Signal to noise (SNR) measurements calculated from 5x5 regions of interest (ROIs) inside the tubes are given in Table 1.

Discussion: Not surprisingly, the best quantitative measurements were from the acquisition with most data acquired. From Figure 1, the 4 highest NaCl tube concentrations are all discernible. The 0.0781 g/100 mL tube is barely discernible with only the 16 ms and 25 ms sequences. The 4 ms sequence had the worst performance, but it is worth noting that this sequence acquired 6.25 time less data than the 25 ms sequence – although not demonstrated in this work, were this 6-fold saving in data acquisition translated into a reduced acquisition time by the same ratio, the total acquisition time would be less than 4 minutes.

Conclusions: This work demonstrates the performance and feasibility of 3D radial projection sequence of ^{23}Na MRI for four different acquisition windows. Even at the highest level of undersampling, the sequence and reconstruction still provided adequate performance for the higher concentrations of saline.

References: 1. Rose AM, Valdes R. Understanding the sodium pump and its relevance to disease. Clin Chem 1994;40:1674–1685. 2. Skou JC, Esmann M. The Na, K-ATPase. J Bioenerg Biomembr 1992;24:249–261. doi: 10.1007/BF00768846. 3. Madelin G, Lee JS, Regatte RR, Jerschow A. Sodium MRI: Methods and applications. Prog Nucl Magn Reson Spectrosc 2014;79:14–47. doi: 10.1016/j.pnmrs.2014.02.001.4. Nagel AM, Laun FB, Weber M-A, Matthies C, Semmler W, Schad LR. Sodium MRI using a density-adapted 3D radial acquisition technique. Magn Reson Med 2009;62:1565–1573. doi: 10.1002/mrm.22157.

Novel integrative framework to augment real-time MR-guided EP studies with 3D predictive modelling

-- Consortium: Image-guided device intervention for cardiovascular disease --

S Ferguson[1], M Sermesant[3], P Krahn[1,2], S Giffard-Roisin[3], S Oduneye[1,2] , L Biswas[1], N Ayache[3], G Wright[1,2], M Pop[1,2]

[1]Sunnybrook Research Institute Toronto, [2]Medical Biophysics - Univ. Toronto (Canada); [3]Inria Sophia-Antipolis (France)

Introduction: MR image-based computer models can help us understand how the peri-infarct triggers lethal arrhythmias (e.g. ventricular tachycardia, VT) [1], but require thorough pre-clinical testing prior to integration into clinical platforms. Previously, we customized 3D electrophysiology (EP) models of pig hearts with anatomy, infarct morphology and fiber directions from *ex vivo* MR images [2]. Thus, the next logical step is to develop *in vivo* models using MR methods that facilitate accurate detection of peri-infarct (i.e., VT substrate) [3] and therapeutic ablation lesions [4]. Our aim is to develop an integrative preclinical framework to augment MR-guided EP studies (e.g. infarct mapping and RF ablation) with image-based computational heart modelling.

Methods: In this work, MR-guided EP procedures were performed by inserting an Imricor catheter in the LV (left ventricle) in 5 pigs (3 with chronic infarct and 2 healthy). Another healthy pig was used for generating 2 adjacent RF ablation lesions. All pigs underwent cine MR scans; additionally, the infarcted pigs underwent *in vivo* multi-contrast late enhancement MR imaging as in [3] and the RF lesions were imaged using late Gd-enhancement as in [4], all scans at 1x1x5mm spatial resolution. We then generated volumetric meshes using CGAL libraries from stacks of segmented 2D images. We assigned different electrical conductivity values per tissue zone: normal, slow-conductive (peri-infarct and edema), and non-conductive (cores of infarct and RF lesion). Meshes integrated rule-based synthetic fibers. Finally, using our current fast numerical approaches, we simulated the propagation of depolarization wave in each 3D heart model in <1min on a 4,096(1x)MB machine, Intel® Core™ i3-2310M processor, 640 GB HD, NVIDIA® GeForce® 315M graphic adapter.

Results: We successfully built 3D LV MRI-based models for all six cases. Fig. 1a shows an infarct case, where 2D MCLE images were used to extract steady-state and T1* maps and input to a fuzzy-logic segmentation algorithm as in [3] to cluster the infarct core (black), peri-infarct (white) and healthy pixels (grey), along with a mesh (~1.5 element size). Fig 1b shows the EP mapping points (obtained under RV pacing) overlaid onto the co-registered MR image and visualized in Vurtigo [5], and a comparison between the EP map to simulations (early depolarization times in red), resulting in a small absolute error (i.e., ~14ms). Fig 2 *(top)* shows a contrast-enhanced MR image depicting the two acute RF lesions, with lesion core (no MR signal, see arrow) surrounded by edema (elevated signal intensity) and corresponding segmentation (core in red, edema in yellow), along with the 3D model output *(bottom)*. In this acute case, simulations indicate that the propagation of electrical wave is blocked by edema. However, as edema resorbs during healing, the gap between lesions' core will allow the wave to propagate through leading to VT recurrence, which can be predicted by the 3D computer modelling.

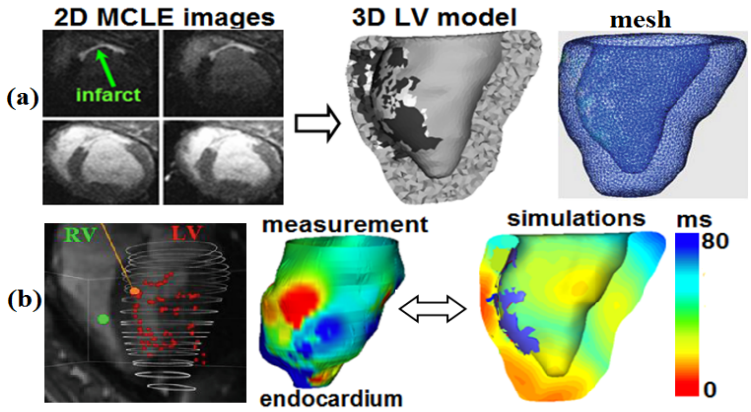

Fig 1. 3D heart model build from MCLE images of an infarcted pig heart.

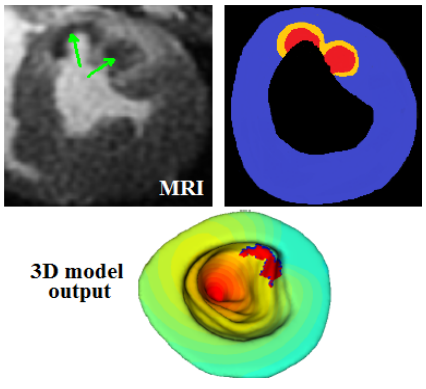

Fig 2. 3D model built from images of acute RF lesions.

Conclusion: We successfully developed a novel framework that integrates real-time MR-guided EP studies with computational modelling, allowing us to predict and visualize wave propagation in near real-time, and in 3D (compared to sparse and surfacic measurements). Such non-invasive predictions of wave propagation can be critical for the treatment planning of scar-related VT and for predictions of long-term success of RF ablation.

References: [1] Pop M et al IEEE TBME 2011; [2] Pop M *et al* Medical Image Analysis 2012; [3] Oduneye S *et al* IEEE TBME 2014; [4] Krahn P *et al* ImNO 2016, [5] www.vurtigo.ca;

MR-based computer models of chronic infarct for prediction of cardiac electro-mechanical function

Mihaela Pop[1,2], Sophie Giffard-Roisin[3], Roch Mollero[3], Robert Xu[1,2] Graham Wright[1,2], Hervé Delingette[3] Maxime Sermesant[3]
[1]Sunnybrook Research Institute Toronto, [2]Medical Biophysics - Univ. Toronto (Canada); [3]Inria-Asclepios, Nice (France)

Introduction: Chronic myocardial infarction MI (a major cause of heart failure), undergoes structural changes in tissue composition (i.e., collagen deposition in the scar) and fiber directions, affecting impulse propagation and heart contraction [1]. A key clinical diagnostic index is ejection fraction (EF), which can be predicted using electro-mechanical (e-m) simulations, as recently shown using healthy dog hearts [2]. However, such predictive models need validation in pathologic cases, as the loss of tissue anisotropy in the scar impact the simulations. The specific aim of this work is to use our preclinical pig model of chronic MI to investigate the differences in activation times and EF predicted by 3D models that integrate: a) realistic fibers from diffusion tensor (DT) images; and b) synthetic fibers generated using prior knowledge of fiber directions in healthy hearts (as in [2]).

Methods: 4 pigs underwent MI induction (approved by our REB committee). At ~5 weeks post-MI, functional MRI was performed *in vivo* on a 1.5GE MR scanner using a cine-SSFP sequence (1x1x5mm voxel) and EF was calculated from end-systolic and end-diastolic contours using clinical software (*https://www.circlecvi.com)*. The hearts were then explanted and scanned *ex vivo* using a DTI sequence (0.6x0x6x1.2mm voxel), as in [3]. Tetrahedral meshes (~230K elements, ~1.5mm element size) were built using CGAL libraries with scars segmented from DT images. Fiber directions were reconstructed using MedINRIA software (*med.inria.fr)* and integrated at each vertex in the mesh. The electrical impulse (i.e., action potential) was calculated using our previous pipeline [4], and became the "source" of active contraction, where the active-passive biomechanical behaviour was defined by the "Bestel-Clement-Sorine" mathematical model. All tissue mechanical parameters (healthy myocardium and scar) were taken from [5]. Finally, we compared the model outputs (i.e., simulated activation map and EF values) obtained using the models that integrated DTI-fibers vs synthetic fibers.

Results: The mean error in activation times predicted by models using DTI fibers vs. synthetic fibers was <5% in all hearts. Figure 1a shows an exemplary result from one heart, with the scar segmented as in [5] from DT image *(up)* and validated by histology *(bottom)*. Fig.1b-*up* shows the fibers mapped onto the 3D mesh (note the difference between DTI and synthetic fibers in the scar). Fig 1b-*bottom* shows corresponding activation maps (note: scar is not electrically conductive, early activation times are in red). The EF values predicted by models using DTI fibers were all very close to the EF calculated from *in vivo* MRI, but EF simulated using synthetic fibers overestimated those. Fig. 3 shows biomechanical simulations of the volume curves for left ventricle (LV) for the case in Figs1-2, for which we obtained EF_synthetic = 40% vs EF_DTI = 34% (and vs EF_cine =33%).

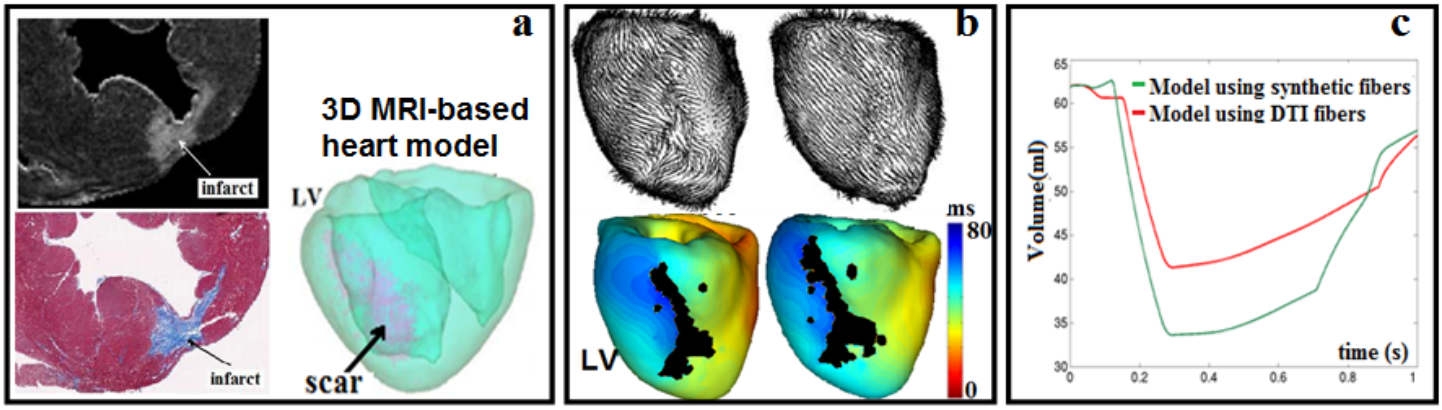

Fig 1. Results from pig with MI: (a) MR-based model; (b) DTI (left) vs synthetic (right) fibers and activation maps; and (c) predicted volume curves.

Conclusion: MRI-based computer models can non-invasively predict cardiac electro-mechanical function in pathologic cases such as chronic MI. For such models, synthetic fibers are potential surrogates of DTI fibers. The overestimated predicted EF values can be explained by the fact that 'synthetic' fibers mimic normal myocardial fiber orientations including in the scar zone, contributing to contraction. Future work will focus on developing a synthetic model of fiber directions in the scar, and improve EF predictions of mechanical models.

References: [1] Estes M; Circulation, 2011; [2] Giffard-Roisin S *et al;* LNCS (8896), 2015; [3] Pop M *et al* Phys Med Biol 2013; [4] Pop M *et al* Medical Image Analysis; 2012; [5] Alessandrini M *et al;* IEEE-TMI 2015 (e-pub).

Title: Multimodal in vivo imaging of perfusion and glycolysis in the C6 rat model of glioma

Authors: Qi Qi[1], Graeme Gillespie[6], Heeseung Lim[1], Nassir Al-Khishman[1], Robert Bartha[1,2,4], Lisa Hoffman[1,3], Timothy J. Scholl[1,4], Ting-Yim Lee[1,2,4,5], Jonathan D. Thiessen[1,5]

Departments of [1]Medical Biophysics, [2]Medical Imaging, [3]Anatomy and Cell Biology, and [4]Robarts Research Institute, The University of Western Ontario; [5]Imaging Program, Lawson Health Research Institute; [6]Department of Engineering Physics, Queen's University, Kingston, Ontario, Canada

Introduction: Tumour perfusion can deliver glucose that is utilized during tumour glycolysis and results in tumour proliferation. Tumour perfusion maps such as blood flow (BF), blood volume (BV) and permeability surface-area product (PS) can be derived by computed tomography perfusion (CTP) with Isovue as a contrast agent. Tumour glycolysis can be evaluated by positron emission tomography (PET) with fludeoxyglucose (FDG) as a contrast agent. Using MRI, different aspects of glycolysis may also be measured with either chemical exchange saturation transfer (CEST) or MR spectroscopy imaging (MRSI), using an infusion of glucose or hyperpolarized [1-^{13}C]pyruvate, respectively. In this experiment, the association between perfusion and glycolysis was investigated in vivo in the C6 rat model of glioma with CTP, FDG-PET, glucose CEST, and hyperpolarized [1-^{13}C]pyruvate MRSI.

Methods: 10^6 C6 glioma cells were implanted in the brains of Wistar rats (n=7) using stereotactic surgery. Tumours were monitored actively using CT (GE Discovery RCT) starting from Day 7 after the surgery. Isovue was injected after starting a cine CT acquisition of the brain. CTP maps were generated using signals in the carotid artery as an input function (GE CT perfusion 5). Tumour glycolysis was measured by the standard uptake value (SUV) with PET images (Siemens Inveon) acquired 60-75 minutes after a bolus of FDG (30 ± 2 MBq) between Days 11 to 13 post-surgery. CTP was measured again immediately after the PET acquisition. Glucose CEST and hyperpolarized [1-^{13}C]pyruvate MRSI measurements were acquired the following day. CEST spectra were obtained from a 9.4 T Agilent MRI using a continuous wave presaturation pulse preceding a series of fast spin-echo images. The CEST spectra were acquired prior to a 0.3 mM/kg bolus and during a constant infusion of 1.5 mM/kg/hour of glucose solution. Magnetization transfer ratio (MTR) asymmetry maps were calculated using CEST images at ±1.2 ppm and the relative change after glucose infusiosn was calculated (%CEST). Rats were transported to a GE Discovery MR750 3.0 T MRI under anesthesia and injected with 3 ml of 80 mM hyperpolarized [1-^{13}C]pyruvate. Regional maps of the ratio of lactate to pyruvate (Lac:Pyr) were acquired using MRSI following injection. The animals were euthanized immediately after the experiment.

Results: The tumour region displayed higher SUV, %CEST, Lac:Pyr, BV and PS than the contralateral normal brain region (see figure). The Pearson correlation coefficients (ρ) between tumour perfusion and glycolysis measurements for all subjects indicate that tumour perfusion measurement PS was most strongly correlated with tumour glycolysis biomarkers SUV (ρ = 0.78), Lac:Pyr (ρ = 0.78) and %CEST (ρ = -0.39), followed by BV (ρ = 0.56, 0.44 and -0.35 respectively); the tumour glycolysis measurement using %CEST was weakly correlated with SUV (ρ = -0.19).

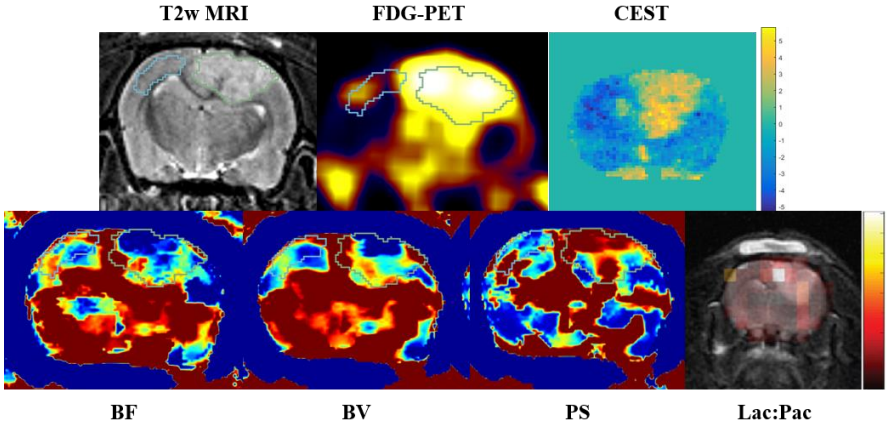

Discussion: Multimodal imaging of perfusion and glycolysis provides a more complete picture of tumour microenvironment. FDG-PET SUV, a glycolysis biomarker, was strongly correlated with the PS perfusion parameter. %CEST was weakly correlated with other tumour glycolysis measurements (SUV and Lac:Pyr).

Patterns of Porcine Acute Myocardial Infarction: Dependence on Breed and Coronary Anatomy

Xiuling Qi, MD, PhD [1], Jennifer Barry, VT, RLAT [1], Graham A. Wright, PhD [1,2,3], Nilesh R. Ghugre, PhD [1,2,3]
[1] Physical Sciences Platform, Sunnybrook Research Institute; [2] Schulich Heart Research Program, Sunnybrook Health Sciences Centre; [3] Department of Medical Biophysics, University of Toronto, Toronto, ON, Canada

Introduction: The pattern and severity of myocardial infarction (MI) is dependent on the species, coronary anatomy and the duration of the ischemia. Pig models for ischemic heart disease are popular due to the similarity in heart and coronary anatomy compared to humans. Our recent work in Yorkshire (farm) pigs has demonstrated that duration of occlusion can produce different patterns of infarction: transmural, heterogeneous or with microvascular obstruction (MVO). Yucatan mini pigs have an advantage due to slower growth rate and are ideal for chronic studies. Our objective was to compare the coronary anatomy and the subsequent infarct patterns in these two breeds of pigs using MR imaging techniques.

Methods: Our study involved a) Yorkshire pigs (N=4) with a 90 min balloon occlusion just beyond 2nd diagonal branch of the left anterior descending artery (LAD), followed by reperfusion (routine model for MI) and b) Yucatan Mini pigs (N=3) with Y1: 90 min balloon occlusion just beyond 2nd diagonal branch of LAD similar to the Yorkshire arm; Y2: 90 min balloon occlusion at 1st diagonal branch of LAD; Y3: 180 min balloon occlusion at 1st diagonal branch of LAD. Interventional procedures were guided by X-ray fluoroscopy and MRI studies were conducted on a 3T whole-body system at baseline (healthy) and day 2-3 post-MI. Cine SSFP was used to measure the cardiac function and late gadolinium enhancement was used for infarct and MVO sizes.

Results: Ejection fraction (EF), infarct size and MVO in Yorkshire (mean±SD) and Yucatan pigs (Y1-Y3) are presented in Table 1. In the Yorkshires, EF was markedly decreased ($p<0.003$) at day 2-3 post-MI in association with the presence of transmural infarction with MVO. On the other hand, the Yucatan's Y1 and Y2 with 90 min occlusions demonstrated heterogeneous infarction with no MVO. With a 180 min occlusion, Y3 presented with transmural infarction and MVO and substantial EF reduction similar to the Yorkshires. Representative X-ray angiograms and MRI are shown in Fig. 1. On X-ray angiograms, we noted that Yucatans have a long and extensive left marginal branch (M1) from left circumflex artery (LCX), which overlaps with the mid-LAD territory, possibly offering protective collateralization.

Conclusions: Level and duration of coronary occlusion can produce different ischemic injury patterns depending on the perfusion tree and collateral network. Coronary circulation in Yucatan Mini pigs was found to be more extensive than that in Yorkshires. Understanding coronary architecture is important in determining infarct patterns in animals and creating more reproducible injury patterns, which is critical when evaluating novel therapeutics for MI.

Table 1: Cardiac Function and MI Size

Pig groups – Occlusion level/duration	EF (%)	MI (%)	MVO (%)
	Baseline/ Day 2-3	Day 2-3	Day 2-3
Yorkshire: DB2/90 min	45.6±7.7/ 35.8±5.2	17.7±5	6.6±3.4
Yucatan (Y1): DB2/90 min	42.8/ 40.2	4.6	No MVO
Yucatan (Y2): DB1/90 min	51.7/ 44.1	19.8	No MVO
Yucatan (Y3): DB1/180 min	55.9/ 29.8	43.9	10.7

DB: Diagonal Branch, EF: Ejection Fraction, MI: Myocardial Infarction, MVO: Microvascular Obstruction

Fig. 1: X-ray angiograms and MR images at day 2-3 post-MI

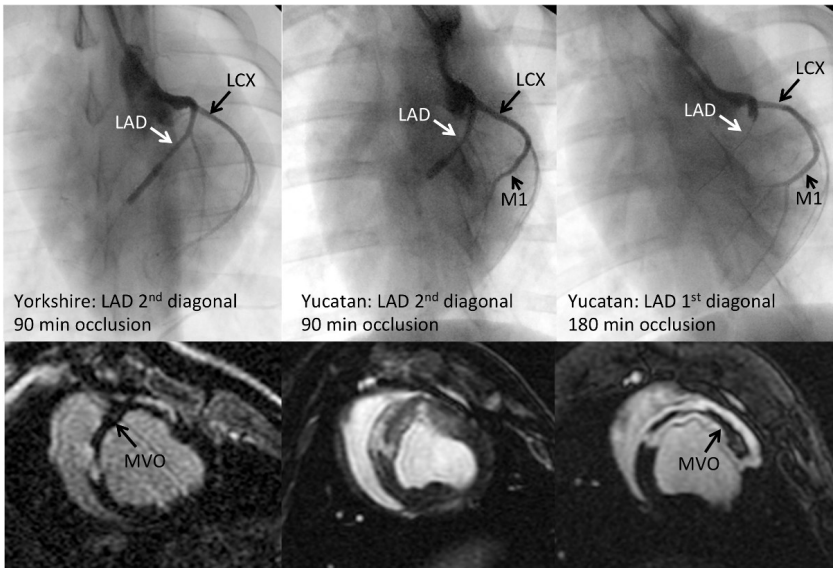

Development of a hybrid broadband NIRS/diffusion correlation spectroscopy system for real-time monitoring of cerebral perfusion and oxygenation in preterm brain injury

Ajay Rajaram[1,2], Dr. David Lee[3], Dr. Keith St. Lawrence[1,2], Dr. Mamadou Diop[1,2]

1. Department of Medical Biophysics, Western University, London, Ontario, Canada
2. Imaging Division, Lawson Health Research Institute, London, Ontario, Canada
3. Department of Pediatrics, Western University, London, Ontario, Canada

Introduction: In Canada, 8% of births occur in fewer than 37 weeks of gestation.[1] Preterm infants born with very low birth weights ($\leq$ 1500g) are at a high risk of neurodevelopmental impairment: 5-10% develop major disabilities such as cerebral palsy and 40-50% show other cognitive and behavioural deficits. The period immediately following birth is considered critical since over half of injuries, which occur in the germinal matrix and surrounding white matter, happen within the first 24 h.[3] Although numerous factors influence the occurrence of brain injury, fluctuations in cerebral blood flow (CBF) are believed to play a significant role due to the immaturity of the cerebral vascular system and complications associated with premature birth such as poor cardiac and lung function. Consequently the brain is vulnerable to periods of low CBF that can impair energy metabolism and ultimately cause tissue damage.[2] There is, therefore, a great need for an efficient neuromonitor system to alert the neonatal intensive care team to clinically significant changes in CBF and metabolism before injury occurs. Optical technologies offer cost-effective methods for neuromonitoring that are ideal for neonates since they are safe and non-invasive. Cerebral oxygen saturation (S_cO_2) can be measured by near-infrared spectroscopy (NIRS), and an emerging method referred to as diffuse Correlation Spectroscopy (DCS) can monitor CBF by tracking fluctuations in light intensity due to the movement of red blood cells through tissue. These two measures can be combined to compute the cerebral metabolic rate of oxygen consumption ($CMRO_2$) which is a key indicator of tissue viability.[3] In this study we present the development and testing of a hybrid broadband NIRS/DCS system designed to monitor CBF, S_cO_2, and $CMRO_2$ in VLBW neonates who are at high risk of brain injury.

Methods and Results: Light from a NIRS broadband light source and a DCS laser were gathered and directed towards a subject using optical fibers. A second set of fibers collected the scattered light, which propagated though the subject, and directed it to appropriate detectors for the two systems. Light from each system, however, has an influence on the opposing detector. Optical filters were implemented to separate the DCS and NIRS signals and prevent light contamination, thereby enabling a truly simultaneous acquisition. A series of optical elements, collimators, and lenses, were employed to maintain an adequate signal-to-noise ratio. Tissue phantoms and arm-occlusion tests were performed to assess the system's ability to accurately and simultaneously acquire S_cO_2 and CBF in real time.

Conclusion: This study has shown that NIRS and DCS can be combined successfully to provide a real-time measure of blood flow and metabolism. Our preliminary results indicate that this method, when applied within the developing brain, could provide clinicians with greater insight into hemodynamic events that precede brain injury. This information would enable clinicians to make adjustments to patient management to avoid brain injury, ultimately improving long-term outcome associated with VLBW infants.

References:

1. Canadian Institute for Health Information. (2012)
2. Linder, N. et al. Risk factors for intraventricular hemorrhage. *Pediatrics* (2003)
3. Verdecchia, K. et al. Quantifying the $CMRO_2$ *Journal of Biomedical Optics* (2013)

Porphyrin-lipid apoE3-lipoprotein nanoparticles as glioblastoma-targeting theranostic platforms

Maneesha A. Rajora[1,2*], Lili Ding[1], Juan Chen[1] and Gang Zheng[1,2,3]

*[1]Princess Margaret Cancer Centre, University Health Network, Toronto; [2]Institute of Biomaterials and Biomedical Engineering, University of Toronto, Toronto; [3]Department of Medical Biophysics, University of Toronto, Toronto. *Primary author and trainee. Research supervisor: Dr. Gang Zheng.*

Introduction: Glioblastoma remains a devastating cancer of the brain, with a mere 5% five-year survival rate. Two challenges associated with the development of improved glioblastoma treatment and diagnosis interventions are the blood-brain barrier (BBB), which prevents the passage of therapeutic agents from the blood stream into the brain parenchyma, and the diffuse morphology of the tumour, which challenges delineation of tumour boundaries and targeting of therapeutic interventions to cancer cells. Recently, apolipoprotein E3 (apoE3)-decorated high density lipoprotein (HDL) nanomimetics have been explored as BBB-traversing vehicles for neurological applications, including drug-delivery for glioblastoma therapy. Less explored is the added potential of exploiting the high affinity binding of apoE3 with the low density lipoprotein receptor (LDLR), which is upregulated in human glioblastoma tissue samples and cell lines. Here, we expand upon the theranostic utility of apoE3-HDL mimetics through the development of LDLR-targeted porphyrin-lipid apoE3-lipoprotein nanoparticles (PyE-LN), whereby the use of apoE3 and porphyrin moieties in unison yields a theranostic platform capable of exuding targeted multimodal glioblastoma imaging and phototherapy abilities.

Methods: Discoidal PyE-LN and cholesteryl oleate (CO)-loaded PyE-LN were formulated to represent the major morphologies of nascent HDL with physiochemical properties representative of previously explored apoE3-HDL nanoparticles. Using a lipid suspension sonication technique, particle formulations were optimized through the systematic variation of lipid, protein and CO. In vitro imaging and flow cytometry studies were conducted using LDLR-expressing U87 glioblastoma cells, and ldlA7 cells as negative controls. An orthotopic U87 mouse model was employed to assess the biodistribution and tumour-targeting abilities of radiolabeled particles in vivo.

Results: Both discoidal and CO-loaded PyE-LN formulations were tailored to maximize pyro-lipid loading, particle stability and purity while minimizing particle size. This yielded stable 30 nm particles with activateable near-infrared fluorescence. Both particles displayed LDLR-mediated uptake in U87 cells, inhibited by LDL competition and acetylation of apoE3 binding sites. This uptake was upwards of 5-fold relative to the negative control ldlA7 cell line. Tumour targeting in vivo was further observed via ex vivo brain fluorescence imaging of U87 tumour-bearing mice treated with CO-loaded PyE-LN, and particle biodistribution relative to acetylated particles.

Conclusions: Here, we present the design, optimization and evaluation of PyE-LN as a multimodal platform able to target glioblastoma cells in vitro and in vivo. This targeting ability, combined with the BBB-crossing capabilities of apoE3 and the theranostic properties of porphyrin yield a unique agent that can address challenges associated with glioblastoma therapy and imaging.

Augmented Reality Cardiac Interventions using the Microsoft HoloLens

*Adam Rankin and Terry M. Peters
Robarts Research Institute, London, Ontario, Canada; Western University, London, Ontario, Canada

INTRODUCTION: The introduction of the Microsoft HoloLens marks a significant leap forward in consumer augmented reality (AR) devices. It is a self-contained head-mounted computer that features self-referential tracking, environment tracking, and stereoscopic display capabilities. Building on the untethered nature of the device, we have started development of an AR guidance platform for minimally-invasive cardiac surgery (MICS) that uses a magnetic tracking system (MTS) and ultrasound (US) imaging. We propose that a system capable of representing real surgical elements as virtual elements to the surgeon in a natural and intuitive manner will provide MICS guidance that is safer, faster, and equally accurate.

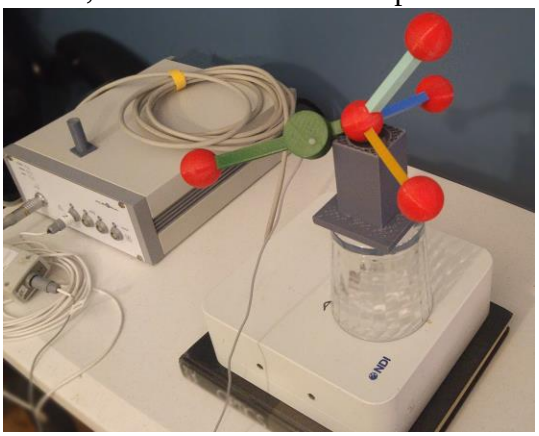

METHODS: The hardware in our system consists of the Microsoft HoloLens, an NDI Aurora MTS, a SonixTouch US system with a L14-5_38 linear probe, a Philips iE33 US system with a X7-2t TEE probe, and a calibration phantom (see Figure 1). For data capture, we are using the PLUS library [1] to send US and tracking data via Wi-Fi to the HoloLens device. We are currently developing a system that will render virtual elements in the same pose as their real world equivalent. To accomplish this, we must register the coordinate system of the HoloLens with the coordinate system of the MTS. Using images recorded by the HoloLens' integrated webcam, we automatically segment the red spheres and estimate the phantom's pose relative to the HoloLens using an iterative method based on Levenberg-Marquardt optimization as implemented in OpenCV. In parallel, we record the sphere center locations in the MTS coordinate system which have been calibrated beforehand by a series of pivot calibrations. This process is repeated, and then a landmark registration is performed to register the two coordinate systems. Additionally, the images generated by the US machines must be registered relative to their attached sensors. For 2D US from the SonixTouch, we use an N-wire calibration as described by Chen et al. [2]. For the 3D US from the iE33, we use a hand-eye calibration where a tracked spherical-tipped stylus is repeatedly identified within the US volume and the MTS. Once all devices are calibrated, virtual representations are rendered such that they overlap their real-world equivalents.

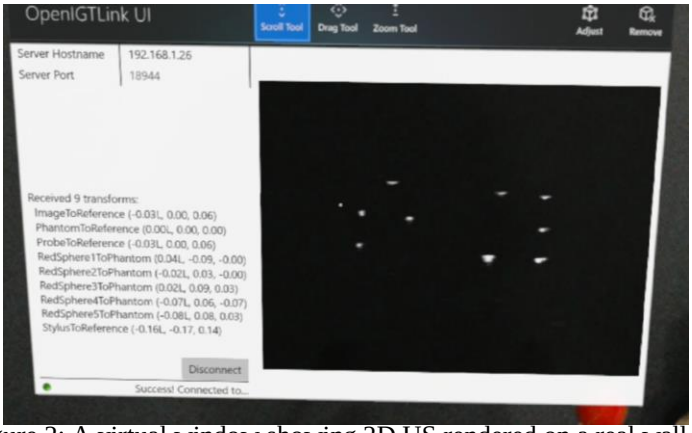

Figure 2: A virtual window showing 2D US rendered on a real wall

RESULTS: Since the system is still in development, only preliminary anecdotal evidence is available. US visualization can be seen in Figure 2, and preliminary feedback from clinicians is that the HoloLens is comfortable enough to warrant further exploration. The calibration phantom is in its third revision, as prior versions experienced issues with pose estimation accuracy. This revision appears to produce a consistent registration, but numerical analysis has not yet been performed.

1. Lasso A, Heffter T, Rankin A, Pinter C, Ungi T, Fichtinger G. PLUS: Open-Source Toolkit for Ultrasound-Guided Intervention Systems. IEEE Trans Biomed Eng. 2014 Oct;61(10):2527–37.

2. Chen TK, Thurston AD, Ellis RE, Abolmaesumi P. A Real-Time Freehand Ultrasound Calibration System with Automatic Accuracy Feedback and Control. Ultrasound Med Biol. 2009 Jan;35(1):79–93.

Application of Iterative Reconstruction Techniques to Retrospectively Gated Cardiac Micro-CT Mouse Images

B. Rathod,[1] I. Petrov,[2] S. Pollmann,[2] and M. Drangova[1,2]
[1]Department of Medical Biophysics, [2]Robarts Research Institute
University of Western Ontario, London ON, Canada

Introduction: Cardiac CT is an important clinical diagnostic tool for non-invasively assessing cardiac diseases; parallel developments [1] have also been made in micro-computed tomography to enable its use in rodent models of disease. Both cardiac and respiratory motion of the heart represent a challenge and are typically overcome by prospective or retrospective gating of the CT acquisitions. For retrospectively gated micro CT, multiple rotations of the CT scanner gantry are acquired and the projections corresponding to selected cardiac and respiratory phases are identified prior to reconstruction. To minimize motion blurring using the tightest possible cardiac and respiratory "windows" is preferred, but a trade off exists between the gating window and number of projections available for reconstruction. The commonly used filtered back projection (FBP) algorithms are limited when a small number of projections is available and result in images with streak artifacts but improvements in computing technology have made the use of iterative algorithms feasible. The objective of this study is to evaluate the application of iterative reconstruction (IR) for use in retrospectively gated cardiac micro CT.

Methods: Mouse scans from a previous study were used. Projection images were acquired at 80kVp and 50mA, for 10 complete rotations of the gantry of an eXplore Locus Ultra (GE Healthcare) scanner [1]. The ECG and respiratory signals (measured from bellows attached to the mouse) were recorded in synchrony with the projection acquisition. Retrospectively, projections corresponding to a single 12 ms cardiac phase with increasingly narrower respiratory windows were identified. The number of projections available for reconstruction were 219, 192, 103, and 67 for the selected respiratory windows. The IR algorithms were implemented in the reconstruction toolkit (RTK) [2] on a GPU-accelerated Linux computer. A two-step iterative process was implemented, where the first step used total variation and conjugate gradient reconstruction algorithms and the second step used only conjugate gradient reconstruction. The IR reconstructed images were compared to those reconstructed using the Feldkamp FBP algorithm; images were rescaled to Hounsfield units (HU). Images were compared qualitatively and analysed using MicroView software (v2.2 GE); the volume of the left ventricle was calculated using the region growing tool and the standard deviation of the intensities within a 0.6 mm^2 region of the blood pool was used to compare the effect of reducing the number of projections.

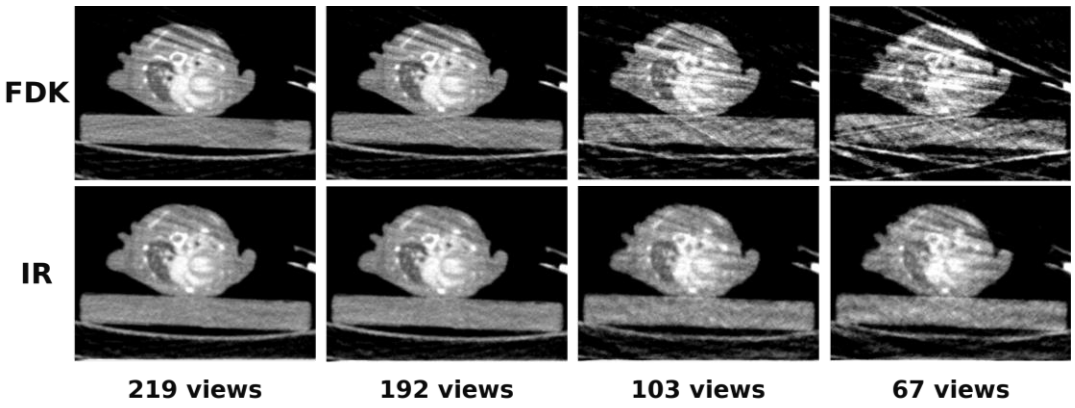

	Mean intensity ± SD			
	Views: 219	Views: 192	Views: 103	Views: 67
FBP	671 HU ± 67	629 HU ± 96	657 HU ± 158	840 HU ± 216
IR	645 HU ± 30	622 HU ± 51	645 HU ± 71	634 HU ± 76

Results and Conclusion: The image figure clearly demonstrates improved image quality with the use of the IR algorithms at fewer views. Specifically, fewer streak artifacts are present in the IR images compared to FBP – especially when the number of projections is reduced below 192. The table demonstrates the related reduction in standard deviation of the intensity values when comparing IR and FBP. The left ventricular volumes calculated from the IR images remained consistent even when the number of projections was reduced to 67 while the 67-projection FBP images were not useable. Further optimization and evaluation of the IR techniques is required but the present study demonstrates promise that improved image quality is achievable with fewer projections and can ultimately result in gated cardiac images with fewer artifacts and less motion blur.

References: [1] Drangova et al. (2007) Invest. Radiology 42 (7). [2] Rit et al. (2014) J. Phys.: Conf. Ser. 489

Quantification of myocardial blood flow with C-11-hydroxyephedrine positron emission tomography imaging

Jennifer M Renaud, Catherine Lapierre, Robert Miner, Lisa Mielniczuk, Rob SB Beanlands, Robert A deKemp

National Cardiac PET Centre, University of Ottawa Heart Institute, Ottawa ON, Canada

Introduction: Heart failure is a leading cause of death. Its progression is associated with excess activation of sympathetic nerves. C-11-hydroxyephedrine (HED) is a norepinephrine analogue used to assess cardiac sympathetic innervation with PET; however, its uptake and retention are dependent on myocardial blood flow (MBF). C-11-acetate has previously been used to assess MBF, and HED shares the same long half-life and retention properties suggesting that it may also potentially be useful for MBF quantification, which would allow for simultaneous measurement of sympathetic activity and MBF in a single scan. The objective of this study was to determine the validity of using HED as a flow tracer with PET imaging.

Methods: Fifteen heart-failure patients underwent same-day acetate and HED PET rest imaging at baseline and 1-2 months later (N=60 scans); patients were clinically stable over the baseline-followup imaging interval. Dynamic images were acquired over 20 minutes and evaluated using a one-tissue compartment model for both tracers to obtain estimates of MBF with acetate (F) using an established tracer extraction function, and the uptake rate (K1) of HED. Acetate F values were adjusted using the rate pressure product to account for hemodynamic changes between scans: $F_{Adj} = F/ RPP_{Acetate} \times RPP_{HED}$. To obtain flow estimates with HED, an extraction function E(F)=1-e-(PS(F)/F) was derived by curve fitting to the values of HED $K1/F_{Adj}$.

Results: The permeability surface-area (PS) function for HED was determined to be PS(F)=0.13+0.097×F. This function corresponds to a mean extraction fraction E=20% at MBF=1.0 mL/min/g at rest for HED. The population mean MBF value obtained using HED scans was 0.75±0.36 mL/min/g, which was not significantly different from the mean RPP-adjusted flow value obtained using acetate: 0.72±0.23 mL/min/g, and MBF the values from both tracers were reasonably well-correlated ($R^2 = 0.4$).

Conclusion: These data lend support to the use of HED PET imaging for quantification of MBF and sympathetic innervation. The measurement of MBF with HED may elucidate the dependence of this tracer's retention on flow and provide a means to separate these two physiologic parameters for improved diagnostic evaluation.

Research support: Ontario Research Fund grant.

Supporting Figure

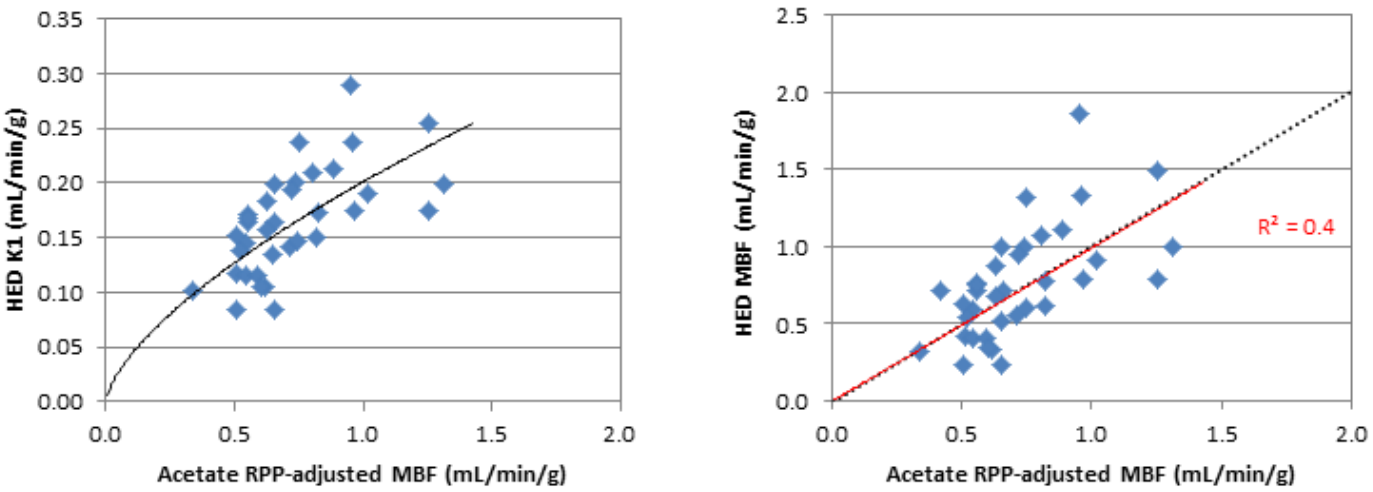

Figure. (A) K1 estimates obtained with C-11-HED vs. RPP-adjusted myocardial blood flow estimates obtained with C-11-acetate. The line of best fit represents the HED extraction function: $K1 = (1 - 0.88 \times e^{(-0.097/F)}) \times F$. (B) Flow estimates obtained with the determined HED extraction function vs. acetate RPP-adjusted flow values were well-correlated, with the line of best fit (red) close to unity (dotted).

MRI of Pluripotent Stem Cell-Derived Alveolar-Like Macrophages for Treatment of Chronic Lung Diseases

Vlora Riberdy[1,2], Michael Litvack[1], Elaine Stirrat[1], Marcus Couch[1], Martin Post[1,2], Giles Santyr[1,2]

[1]Physiology and Experimental Medicine Program, Peter Gilgan Center for Research and Learning, The Hospital for Sick Children, Toronto, Ontario, Canada. [2]Department of Medical Biophysics, University of Toronto, Toronto, ON, Canada.

Consortium – NIH Hyperpolarized 13C MRI of Placental Metabolic Abnormalities, Supervisor – Dr. Giles Santyr

Introduction: Chronic lung diseases, such as asthma, COPD and bronchopulmonary dysplasia (BPD) exact a tremendous toll on society. Collaborators have shown that innate immune cells in the lungs, called alveolar macrophages (AMs) derived from pluripotent stem cells (PSCs) can promote repair of chronic lung disease in animal models[1]. For this technique to be translated to the clinic, the PSC-AMs need to be detected and monitored non-invasively within the lungs *in vivo* during and following treatment. Magnetic resonance imaging (MRI) with superparamagnetic iron oxide nanoparticles (SPIONs) can potentially be used to confirm placement and track macrophages in the lung[2]. Combined with hyperpolarized gas MRI, SPIONs have demonstrated promise for detection of cells within the lung[3]. As a preliminary step in the detection of PSC-AMs in the lung *in vivo*, this work investigated the loading of PSC-AMs with SPIONs and subsequent effects on proton MRI signal *in vitro*.

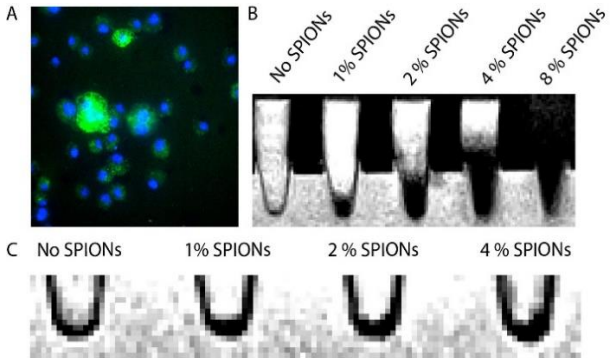

Figure 1: (A) Confocal microscopy of PSC-AMs co-incubated with green fluorescent SPIONs, indicating that 99% of PSC-AMs sequester the SPIONs. Proton MRI of aliquots containing increasing concentrations of SPIONs without (B) and with PSC-AMs (C).

Methods: PSC-AMs were produced following the method of Litvack et al[1] and loaded with varying concentrations of green fluorescence-labeled SPIONs (Molday ION EverGreen™). After four hours, confocal fluorescence microscopy was used to confirm SPION uptake by the cells. Aliquots containing 0, 1, 2, 4, and 8% SPIONs (by volume) were prepared in aqueous solution, corresponding to iron concentrations of 0, 20, 40, 80, and 160 µg Fe/mL respectively. The aliquots were imaged at 3T (Siemens, Trio) using a gradient echo (GE) sequence with TR = 500 ms, a flip angle of 10°, and varying TE times from 6 to 60 ms. The image signal to noise ratios (SNR) and transverse relaxation times (T_2^*) of the aliquots were measured. Imaging was also performed using aliquots containing PSC-AMs incubated with the same SPION concentrations as above, suspended in solution, rinsed and centrifuged into a pellet.

Results: Figure 1A shows an image of the SPION-loaded PSC-AMs obtained with confocal fluorescent microscopy, confirming the sequestration of SPIONs (green) by the PSC-AMs (blue). Figures 1B and 1C show MR images of the aliquots as function of SPION concentration with and without PSC-AMs respectively. Figure 2 shows the SNR vs. TE for the SPION samples (without PSC-AMs), revealing decreasing signal and T_2^* as concentration increases, until the signal effect becomes saturated (data not shown). The approximate T_2^* for 0, 20 and 40 µg Fe/mL are given in table 1.

Table 1- T_2^* measurements for increasing concentrations

Concentration (µg Fe/mL)	T_2^* (ms)
0	62
20	40
40	25

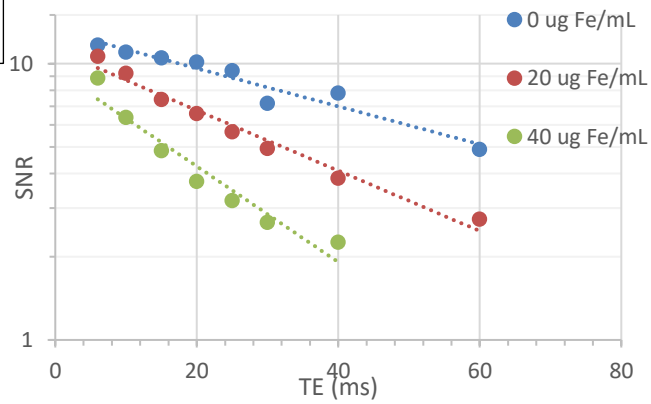

Figure 2- SNR vs. TE for varying SPION concentrations to measure T_2^*. T_2^* is the negative reciprocal of the exponential decay constant (red).

Conclusions: The presence of PSC-AMs labeled with SPIONs can be detected *in vitro* using proton MRI sequences. The next steps will be to determine the effect of SPIONs on cell viability and differentiation, as well as to determine the minimum cell concentration detection limits prior to *in vivo* studies.

References: [1] Litvack, M.L. et al. AJRCCM, 2016. [2] Faraj A. et al. BMC Med. Imaging, 2015. [3] Branca, R. T. et al. PNAS. 2010. **Acknowledgments:** The authors would like to thank the Ontario Institute for Regenerative Medicine (OIRM) for funding. Special thanks to Brandon Zanette and Andras Lindenmaier.

Open-source film dosimetry analysis application based on 3D Slicer

Alec Robinson[1], Csaba Pinter[1], Kevin Alexander[2], John L. Schreiner[3], Gabor Fichtinger[1]

[1]School of Computing; [2]Department of Physics; [3]Department of Medical Physics
Queen's University, Kingston, Canada

INTRODUCTION: High-resolution dose detectors are needed to evaluate modern radiation therapy treatments. Dosimetry using poly-diacetylene based radiochromic films such as Gafchromic™ EBT3 is the current preferred method for complex dose verification. Despite its benefits, the lack of a suitable analysis software hinders its use. Most irradiated films are analyzed with in-house Matlab scripts implemented by the medical physics staff, or commercial software that performs optimization in a black-box manner. The introduction of an open-source application carrying out film dosimetry analysis provides transparency and decreases the barriers to its use.

METHODS: SlicerRT is an open-source radiation therapy research toolkit [2], based on the 3D Slicer medical image visualization and analysis software platform for quantitative computer-assisted medicine [1]. A streamlined workflow for film dosimetry was developed as a 3D Slicer extension depending on SlicerRT. In the first step, films that were irradiated with flat doses are loaded into the application, and their dose levels entered for calibration. The light field is also captured, and entered as the flood field. The parameters of the optical density (OD) to dose function are calculated based on those images. In the second step, the DICOM-RT dose volume of the original treatment plan is loaded, along with the image of the film irradiated according to the plan, and the position of the film within the dose volume. In the third step, the OD to dose calibration function is applied to the film image, creating a volume consisting of the calculated doses in Gy. In the fourth step, the calibrated film is automatically registered to the corresponding slice from the dose volume (Fig. 1/A).

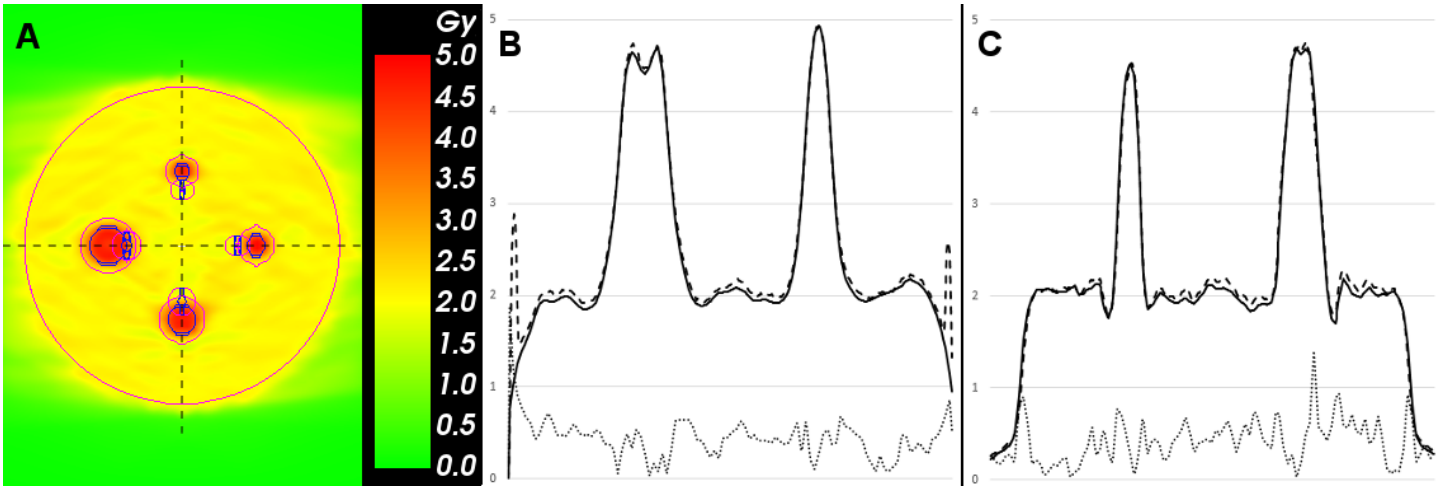

Fig. 1: A) Slice from the dose volume for the phantom brain metastases FSRT plan at the position of the film, B) Horizontal line profiles for the plan dose (solid - Gy unit), calibrated film dose (dashed - Gy unit), and the gamma values (dotted - gamma index unit), C) Vertical line profiles

RESULTS: After calibrating and registering the film measurement, the final step is to compare that measurement to the planned dose distribution using both 2D gamma comparison tools (Fig. 1/B) [3], and dose profiles (Fig. 1/C) in the application. In this work, we present a fractionated stereotactic radiation therapy (FSRT) plan as a test case, which shows good agreement between both the film and planned dose distributions.

CONCLUSIONS: A free, open-source application implementing a film dosimetry workflow was developed. This potentially encourages the more widespread adoption of 2D film-based dosimetry methods.

ACKNOWLEDGEMENTS: G. Fichtinger is supported as a Cancer Care Ontario Research Chair.

[1] Fedorov, A., Beichel, R., Kalpathy-Cramer, J., Finet, J., Fillion-Robin, J. C., Pujol, S., ... & Buatti, J. (2012). 3D Slicer as an image computing platform for the Quantitative Imaging Network. Magnetic resonance imaging, 30(9), 1323-1341. [2] C. Pinter, A. Lasso, A. Wang, D. Jaffray, and G. Fichtinger, "SlicerRT: Radiation therapy research toolkit for 3D Slicer," Medical Physics, vol. 39, no. 10, p. 6332, 2012. [3] Low, D. A., Harms, W. B., Mutic, S., & Purdy, J. A. (1998). A technique for the quantitative evaluation of dose distributions. Medical physics, 25(5), 656-661.

Intravoxel Incoherent Motion Analysis of the Guinea Pig Placenta: Preliminary Findings

CP Rockel[a], KJ Sinclair[a], LJ Friesen-Waldner[a], C van der Tuin[b], B de Vrijer[c], TRH Regnault[b,c], CA McKenzie[a,d]*.

[a]*Medical Biophysics*, [b]*Physiology & Pharmacology*, [c]*Obstetrics & Gynecology*, *Western University, London, Ontario.* *Supervisor.

Introduction: Intravoxel incoherent motion (IVIM) is a magnetic resonance imaging technique that allows calculation of fast (D*) and slow (D) diffusion rates of water molecules within a region of interest (ROI), as well as the fractional contribution of the fast component (***f***)[1]. This bi-exponential model of diffusion attributes D* to blood perfusion and D to the restricted movement of water within tissues. Previous studies have used IVIM to study placental function in both humans and murine models[2-5], as placental impairments in blood flow and nutrient supply are indicative of placental dysfunction[6]. Guinea pigs are often used in pregnancy research because their long gestational period and similar fetal development pattern compared with humans[7,8]. Therefore, the purpose of this study was to evaluate the feasibility of IVIM in a guinea pig model of placental function.

Methods: Two pregnant female guinea pigs, one carrying four pups (GP1) and the other carrying a single pup (GP2) (gestational age = 60 days), were anesthetized and scanned at 3T using a 32-channel cardiac coil (Discovery MR750, GE Healthcare, Waukesha, WI). MRI acquisition consisted of a coronal T1-weighted anatomical scan and axial diffusion-weighted volumes (20 *b*-values [0-1000 s/mm^2], TR/TE=8241/115 ms, 62 slices 2.9mm thick, 15cm FOV, 64x64 matrix, ASSET=2, scan time = 8m 6s). ROIs were drawn using 3D Slicer (4.7.0-2016-12-13, www.slicer.org) to cover each of the placental volumes while avoiding partial voluming and large blood vessels. Data was normalized based on the signal intensity of the b=0 s/mm^2 image. IVIM analysis was performed using Curve Fitting Toolbox within Matlab (2015a, The Mathworks, Natick, MA).

Results: All ROIs produced biexponential curves demonstrating excellent fit ($r^2 > 0.98$), despite the presence of motion in the placenta of GP2 (**Fig.1**). Three placentae from GP1 showed marked similarity in normalized curve fit (D* = 39.7 +/- 1.72 x10^{-3} mm^2/s, D = 1.13 +/- 0.05 x10^{-3} mm^2/s, ***f*** = 45.2 +/- 0.98%), whereas GP1-Placenta 3 and the GP2 placenta demonstrated outlying IVIM measures such as greater rate of diffusion (D = 1.58 x10^{-3} and 1.40 x10^{-3} mm^2/s, respectively) and a lower perfusion fraction (***f*** = 23.4% for both) (**Fig.1**). Upon necropsy, the fetuses associated with these two placentae were found to be growth restricted (GP1-Placenta 3) and hydrocephalic (GP2). While abnormal fetal development is not necessarily associated with abnormal placental morphology, these results suggest that future IVIM studies of placenta in a guinea pig disease model are warranted.

Conclusions: These results suggest IVIM can be implemented to study placental function within a guinea pig model of placenta. This preliminary data shows marked differences in the placentae between normal and abnormal fetuses, although more data needs to be acquired to determine if IVIM can be used to detect placental abnormalities in the guinea pig.

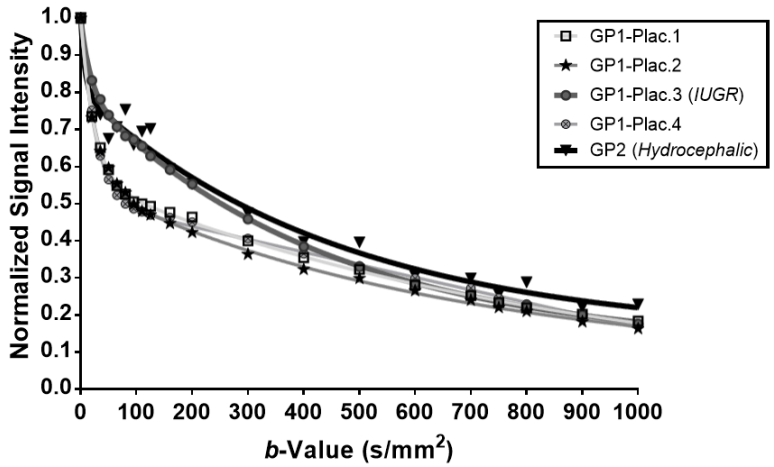

Fig 1. Raw data and fitted bi-exponential curves representing diffusion measures across 20 *b*-values in five guinea pig placentae. Placentae associated with fetal pathology display reduced perfusion fraction (***f***) and increased diffusion (**D**) relative to normal controls.

References: (1) Le Bihan *et al.* (1986). Radiol 161:401-407. **(2)** Moore *et al.* (2000). Placenta 21:726-732. **(3)** Derwig *et al.* (2013). Placenta 34:885-891. **(4)** Sohlberg et al. (2015). Ultrasound Obstet Gynecol 46:700-705. **(5)** Alison *et al.* (2013). Invest Radiol 48:17-23. **(6)** Gardosi *et al.* (2014). Public Health 128:698-702. **(7)** Carter (2007). Placenta 28:S41-S47. **(8)** Elias *et al.* (2016). Reprod Sci 23:219-227.

Towards intra-operative needle guidance in interstitial gynecologic brachytherapy using 360º 3D transvaginal ultrasound

J Rodgers[1,2], K Surry[3], D D'Souza[3], E Leung[4], A Fenster[1,2]

[1]*Biomedical Engineering Graduate Program, Western University, London, Ontario, Canada;* [2]*Robarts Research Institute, Western University, London, Ontario, Canada;* [3]*London Regional Cancer Program, London, Ontario, Canada;* [4]*Odette Cancer Centre, Toronto, Ontario, Canada*

Consortia: Ontario Institute of Cancer Research – Imaging Translation Program

Introduction. Gynecologic cancers are among the most prevalent in women worldwide, with the number of malignancies continuing to increase. Treatment may include high-dose-rate (HDR) interstitial brachytherapy, which provides a higher radiation dose to a tumour relative to the surrounding healthy tissues. The dose is delivered via needles, which are typically inserted through a perineal template stabilized by a cylinder placed into the vagina. Despite the need for precise needle placement to deliver optimal dose distributions and avoid nearby organs-at-risk, such as the bladder and rectum, there is currently no standard modality for intra-operative needle visualization. We have previously proposed three-dimensional (3D) transrectal ultrasound (TRUS) imaging for 3D visualization of the needles intra-operatively; however, this approach was limited by shadowing artefacts from the vaginal cylinder. To overcome this limitation, we have developed a 3D transvaginal ultrasound (TVUS) system to create a 360º image. We propose the use of this 360º 3D TVUS system to improve visualization and placement of needles during HDR interstitial gynecologic brachytherapy.

Methods. Using a motorized mover, the 3D TVUS system rotates a conventional 2D side-fire TRUS transducer through 360º in 24 seconds. During the image acquisition, the TRUS probe is placed inside a hollow vaginal cylinder, made with a sonolucent 2 mm thick TPX (polymethylpentene) plastic wall, maintaining the same dimensions as the clinical cylinder. During acquisition, 2D images from a clinical US machine are reconstructed into a 3D image as they are collected (real-time), allowing for visualisation of needles on all sides of the cylinder.

The geometry of the reconstructed images was validated using a phantom made up of grids of strings in 10 mm intervals, embedded in agar. The grid phantom was imaged with the 3D TVUS system and the distances between strings were measured. A second geometric phantom included an agar sphere, which was scanned twice with a 90º rotation between scans to verify volumetric accuracy and assess spatial differences based on initial probe orientation. The sphere was manually segmented three times in each image and the volume was compared to the nominal value of the mold. The surface area to volume ratio was also calculated to determine sphericity.

An agar phantom mimicking the pelvic anatomy, which included a model uterus, tumour, and vaginal canal, was created to evaluate the visualization of needles under idealised conditions. Twelve needles were imaged after insertion using 3D TVUS, which was manually, rigidly registered to an MR scan of the needle tracks to allow comparison of the needle tips and trajectories between the modalities and to the expected positions.

Results. For the grid phantom, the mean errors in each of the three image coordinate directions (x, y, z) were 0.09 mm, 0.14 mm, and 0.08 mm, respectively, which are all within 1.4% error. The measured volume for the spherical phantom had a mean error of 0.59 cm^3 (2.65%) with a mean error of 0.99% for the surface area to volume ratio. T-tests showed no significant difference ($p > 0.05$) between the results of the two images for either metric. The 3D TVUS image of the pelvic phantom is shown in Figure 1. The mean needle tip difference and mean trajectory difference between the modalities was 2.11 ± 0.73 mm and 1.07 ± 0.75 º, respectively. The mean difference in the tip positions between the 3D US and expected values was 1.84 ± 0.42 mm and the mean trajectory difference was 0.40 ± 0.35 º.

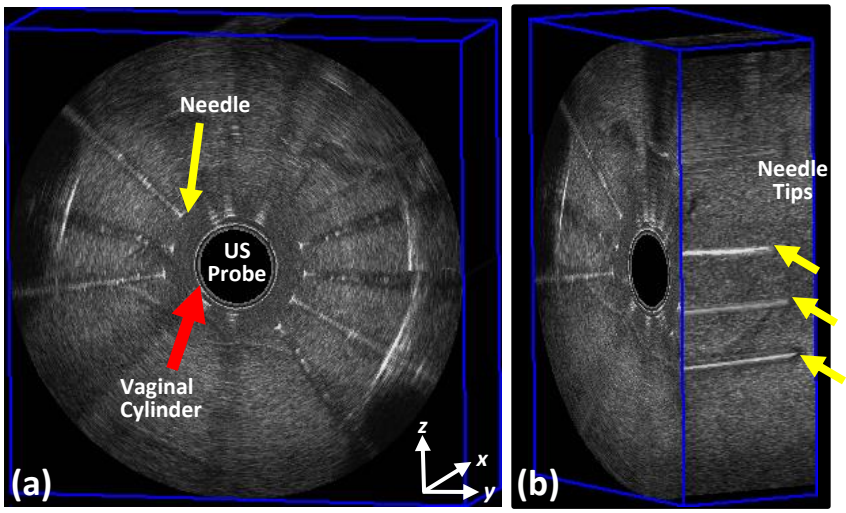

Figure 1: (a) 3D TVUS scan of the agar pelvic phantom (b) 3D TVUS scan of the agar pelvic phantom with three needles indicated.

Conclusions. Based on this initial study, a 360º 3D TVUS approach is a feasible method for visualising needles intra-operatively and a proof-of-concept patient study including 10 patients will be performed.

Does Trancranial Direct Current Stimulation Modify Glutamate: A 7 Tesla ^{1}H MR Spectroscopy Study

Kayla Ryan, Krysztof Wawrzyn, Joseph Gati, Blaine Chronik, Neil Duggal, Robert Bartha

1. Centre for Functional and Metabolic Mapping, Robarts Research Institute, University of Western Ontario, London, ON, Canada 2. Department of Medical Biophysics, University of Western Ontario, London, ON, Canada 3. Department of Physics, University of Western Ontario, London, ON, Canada

Introduction: Transcranial direct current stimulation (tDCS) is a form of non-invasive brain stimulation that has been recently studied as a way of increasing cortical activity. Literature has shown positive behavioural outcomes associated with the application of tDCS after cortical injury caused by a stroke.[1] However, the exact mechanism of action, both during and after stimulation and its associated effects on motor and cognitive faculties are largely unknown. Ultra-high magnetic field (7 Tesla) magnetic resonance spectroscopy (MRS) is a non-invasive tool that may be sensitive to tDCS induced changes in metabolite levels and could help elucidate the underlying mechanisms involved in applying tDCS to the brain. Previous research at 3T has shown decreased glutamate levels in the underlying cortex after cathodal stimulation.[2] Using ^{1}H MRS at 7T, the goal of the current study was to determine whether glutamate levels are altered in the motor cortex immediately following bihemispheric tDCS applied to the motor areas of the brain.

Methods: Ten healthy adults aged 21-40 participated in two sessions on a 7T Siemens MAGNETOM, head-only MRI. All participants had ^{1}H MRS in this single blind, sham controlled, cross-over design. Participants were randomized to receive tDCS stimulation or sham stimulation on their initial visit, and the contrary on their second visit, at least 7 days apart. tDCS consisted of 2 mA of current applied using an MR-compatible DC-STIMULATOR (NeuroConn, Germany) to bihemispheric motor areas, lasting 20 minutes (cathode on left primary motor cortex, anode on right supplementary motor area) within the scanner. ^{1}H MRS was acquired immediately following sham/stimulation from the left primary motor cortex (semi-LASER, TE/TR = 60/7500 ms, voxel size=1.6x2x1.8 cm^{3}). Temperature was monitored in real time on all subjects to ensure safety. Spectra were fitted using prior knowledge of metabolite lineshapes in the fitMAN software and normalized to creatine. Paired t-tests were performed between sham and stimulation with a significance set to $p<0.05$.

Results: tDCS was successfully applied in the 7T MRI scanner in all subjects. Average temperature change in all four probes was 0.40±0.61 ºC during the semi-LASER sequence. In this small sample, there were no significant differences in glutmate:creatine ratio when measured immediately following the sham and stimulation conditions (Figure 1).

Conclusion: The after effects of tDCS are thought to increase synaptic plasticity through modulation of the NMDA glutamate receptor.[1] To our knowledge, the current study is the first to combine ultra-high field (7T) MRI and concurrent tDCS stimulation. Although this preliminary study is underpowered, the bihemispheric montage of 2 mA of direct current stimulation for 20 minutes did not produce a measurable alteration in glutamate ratios to creatine immediately following the termination of stimulation. While previous studies have shown a change in glutamate concentration in the brain during stimulation, others have shown no significant after effects consistent with our results.

References: 1) Nitsche MA, Paulus W. Transcranial direct current stimulation – update 2011. *Restorative Neurology and Neuroscience* 2011; 29(6): 463-92 2) Stagg C, et al. Polarity-senstive modulation of cortical neurotransmitters by transcranial stimulation. *The Journal of Neuroscience* 2009;29(16):5202-5206

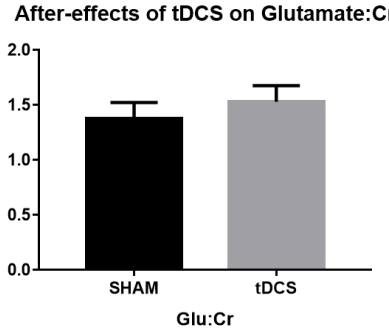

Figure 1. Average glutamate (Glu):creatine (Cr) ratio (n=10) from the left primary motor cortex immediately following 20 minutes of tDCS (gray) or sham stimulation (black). Error bars represent the standard error of the mean.

Highly Accelerated Phosphorus Metabolic Imaging using Compressed Sensing

Alejandro Santos-Diaz[1], Michael D Noseworthy[1,2]
1. School of Biomedical Engineering, McMaster University, Hamilton, ON.
2. Electrical and Computing Engineering, McMaster University, Hamilton, ON.

Introduction. Phosphorus magnetic resonance spectroscopy is a standard method to measure skeletal muscle bioenergetics. It has been widely used in the study of phosphocreatine (PCr) recovery kinetics, post-exercise [1]. However, due to the nature of this nucleus, data acquisition faces several challenges such as long acquisition time and coarse resolution. Different methods of data acquisition such as turbo spin echo (TSE) [2] and spiral trajectories [3] have been proposed for these types of dynamic experiments at low and high magnetic fields. In recent years, compressed sensing (CS) [4] has become a powerful tool to accurately reconstruct subsampled signals allowing faster acquisitions. This has been used for PCr imaging in a TSE sequence [5]. Alternatively, echo Planar Spectroscopic Imaging (EPSI) using flyback readout gradients is a technique to acquire fast spectroscopic imaging that has been used to acquire data from skeletal muscle [6]. The main objective of this study was to test the feasibility of acquiring fast ^{31}P images combining flyback-EPSI with compressed sensing.

Methods. Experiments were performed using a GE 3T MR750 (General Electric, Milwaukee, WI) with a home designed/built 3-inch surface coil tuned at 51.705 MHz . Fully sampled datasets were acquired from a homemade phantom (1L spherical phantom containing 20mM sodium phosphate at pH=7.4) using a flyback-EPSI sequence designed to achieve 1.5 cm or 2 cm spatial resolution over 18 cm or 16 cm FOV (12x12 and 8x8 voxels) and a spectral bandwidth of 454 and 476 Hz respectively (TR=1.5 s, 256 spectral points, 3 cm slice thickness). Gradient waveform design was performed using the fidepsi sequence from the GE MNS research package (GE Global Research, Munich, Germany). Pseudorandom subsampling patterns were simulated to achieve 2.4x and 2x acceleration factors. CS reconstruction was performed using the non-linear conjugate gradient algorithm. The sparsifying transform was a 1D 4-lengh Daubechies Wavelet Transform and the total variation and transform weights were empirically chosen as 0.015 and 0.005 respectively. Data was processed in MATLAB using a modified version of the SparseMRI toolbox [4]. 31P images were created as the area under the Pi peak for each voxel and interpolated to 256x256 pixels for display. SNR was measured as the intensity of the Pi signal divided by the standard deviation of the background noise.

Results. Fully sampled images were acquired in 18 and 12 seconds for the 1.5 cm and 2 cm spatial resolution respectively. After applying CS, acquisition times were 8 and 6 seconds for 2.4x and 2x acceleration. **Table 1** shows the acquisition time and SNR for all scenarios. SNR values are slightly higher for the CS reconstructions due to its denoising nature. **Figure 1** shows an example of the subsampling scheme used. **Figure 2** shows a comparison of the images for the fully sampled and compressed sensing reconstructions.

Conclusions. This preliminary study showed the feasibility of performing 31P imaging when combining flyback-EPSI with compressed sensing. Acquisition time was reduced to 8 and 6 seconds, making this sequence suitable to perform dynamic studies of High energy phosphate kinetics in skeletal muscle.

Acknowledgements. CONACYT (Mexico) scholarship (ASD). CVU:304930. NSERC Discovery grant (MDN).

References. [1] B. Chance et. al. *NMR Biomed.*, vol. 19, no. 7, 2006. [2] P. Parasoglou et. al. *Magn. Reson. Med.*, vol. 70, no. 6, 2013. [3] Valkovic et. al. *NMR Biomed.*, vol. 29, no. 12, 2016. [4] Lustig et. al. *Magn. Reson. Med.*, vol. 58, no. 6, 2007. [5] Parasoglou et. al. *Magn. Reson. Med.*, vol. 68, no. 6, 2012. [6] Santos-Diaz et. al. *Proc. Intl. Soc. Mag. Reson. Med.*, 2016.

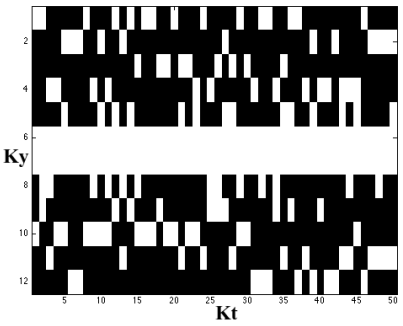

Figure 1. Pseudorandom subsampling mask with two central K-space lines fully sampled (i.e. white spaces indicate location of samples, black are absence). The same mask was applied to the fully sampled Kx dimension. Only the first 50 points of the Kt dimension are shown. Full mask size is 12x256.

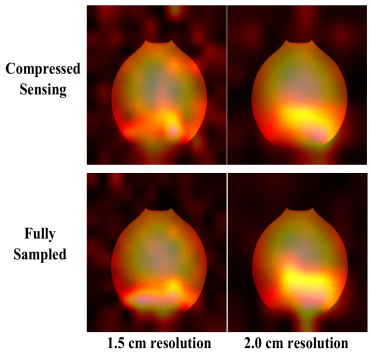

Figure 2. Example of phosphorus images created for fully sampled (bottom row) and compressed sensing (top row) reconstructions. Left column: 1.5 cm resolution. Right column: 2 cm resolution.

	Scan time (s)		SNR	
Res cm	FS	CS	FS	CS
1.5	18	8	15.1	19.5
2	12	6	17.2	24.6

Table 1. Scan time and SNR values for the fully sampled (FS) and compressed sensing (CS) reconstructions.

Reduced Brain Choline in Adolescent Hockey Players after Concussion

Amy Schranz*, BSc[1], Kathryn Y. Manning, MSc[1], Gregory A. Dekaban, PhD[1], Lisa Fischer, MD[2], Kevin Blackney, BSc[1], Christy Barreira, BSc[1], Timothy Doherty, MD, PhD[3], Douglas Fraser, MD, PhD[4], Arthur Brown, PhD[1], Ravi S. Menon, PhD[1], and Robert Bartha (Research Supervisor), PhD[1]

[1]Robarts Research Institute, The University of Western Ontario, [2]Primary Care Sport Medicine, Fowler Kennedy Sport Medicine, [3]Physical Medicine and Rehabilitation, University of Western Ontario, [4]Paediatrics Critical Care Medicine, London Health Sciences Centre, London, Ontario, Canada

Consortium Affiliation- BrainsCAN

Introduction. Concussion results from a complex pathophysiological process affecting the brain, induced by traumatic biomechanical forces [1]. Because concussion is difficult to diagnose and the prognosis post-concussion is also difficult to ascertain, athletes often return to sports when symptoms resolve but before the brain has fully healed, which increases the risk of subsequent serious brain injury. Biomarkers are urgently required to monitor the effect of concussion on the brain. In concussion, diffuse axonal injury and a secondary chemical cascade can result in mitochondrial dysfunction and altered metabolism [2] that can manifest as changes in brain metabolite levels measurable *in-vivo* by magnetic resonance spectroscopy (MRS). The occurrence of such changes within the frontal lobes can lead to executive dysfunction [2], and potentially neurodegeneration [3]. We previously found significant reduction in glutamine levels in female varsity rugby players in this region post-concussion. Recently, Stewart *et al.* [4] found that adolescent male hockey players were at the highest risk for concussion. Therefore, the purpose of this study was to measure metabolites in the prefrontal white matter of male hockey players after concussion, to determine whether glutamine levels are also affected in this cohort.

Methods. Male adolescent hockey players from the Bantam Division (ages 11-14) were enrolled in the study. Players were subdivided into two groups; those diagnosed with a single concussion (n=12) and age matched controls (n=18). Concussed athletes were evaluated 24-72 hours and 3 months post-concussion. An evaluation consisted of clinical tests (SCAT3 and ImPACT), hematology, and an MRI scan. MRI was acquired using a 3.0T Siemens (Erlangen, Germany) MRI scanner. MRS was acquired from the prefrontal white matter using single voxel point-resolved spectroscopy (PRESS: TE/TR=135/2000 ms, voxel=2x2x1.5 cm^3, 192 averages). Spectra were post-processed using in-house software to measure absolute *N*-acetyl aspartate, choline, creatine, glutamate, glutamine, and *myo*-inositol. A one-way ANOVA was used across all three groups with an alpha value of 0.05, and *P*-values were Tukey corrected.

Results and Discussion. A significant reduction in choline was observed 3 months post-concussion compared to controls (Figure 1). The choline signal reflects cell membrane turnover [5], therefore the reduction in the signal may be indicative of a reduced membrane turnover rate [6]. Consistent with the results in our previous rugby cohort, a trend in reduced glutamine was observed (Figure 2), suggesting disruptions in oxidative metabolism. No other significant metabolite changes were observed in either group.

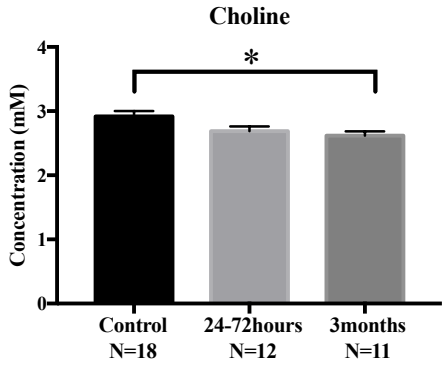

Figure 1 Mean absolute concentration of choline in the control and concussed groups (F=3.98, *P*=0.027). Standard error of the mean (SEM) is represented by vertical bars. At 3 months, levels were reduced in comparison to the control group by 10.3% (*P*=0.03)

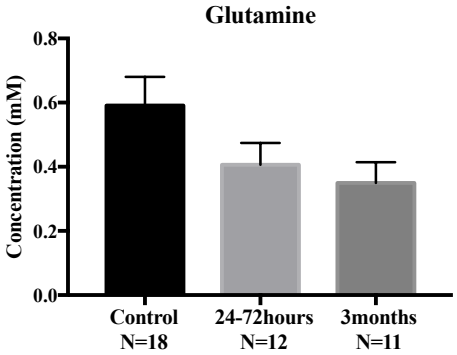

Figure 2 Mean absolute concentration of glutamine in the control and concussed groups (F=2.5, *P*=0.09). Standard error of the mean (SEM) is represented by vertical bars. In comparison to the control group, levels were reduced by 31.2% (*P*=0.25) and 40.8% (*P*=0.1) by 24-72 hours and 3 months respectively.

[1] McCrory *et al. PM R,* 1(5), 406-20, 2009. [2] Johnson *et al. Exp Neurol*, 246: 35-43, 2013. [3] McKee *et al. Acta Neuropathol*, 127(1): 29-51, 2014. [4] Stewart *et al. J Trauma Acute Care Surg,* 76(3), 736-42, 2014. [5] Maddock *et al. Curr Top Behav Neurosci,* 11, 199-251, 2012. [6] Poole *et al. Dev Neuropsychol,* 39(6), 459-73, 2014.

A Spinal Cord Phantom to Test and Standardize MEGA-PRESS γ-aminobutyric acid (GABA) Measurements

Nicholas M Simard[1], Diana Harasym[1], Aimee Nelson[2], and Michael D Noseworthy[1]

[1]School of Biomedical Engineering, McMaster University, Hamilton, ON, Canada, [2]Department of Kinesiology, McMaster University, Hamilton, ON, Canada, [3]Electrical and Computer Engineering, McMaster University, Hamilton, ON

Introduction

The goal of this feasibility study was to design and build a magnetic resonance spectroscopy (MRS) phantom of the spinal cord to test whether γ-aminobutyric acid (GABA) could be reliably measured in this region using a small voxel and a MEGA-PRESS sequence. Typically, GABA measurements are performed in the brain. Thus the current study is highly novel due to the geometry and the difficult location of the spinal cord.

Methods

A phantom was constructed using a cylindrical case of acrylic and Poly(methyl methacrylate), with dimensions of 15cm ’ diameter and 17cm ’ length. The phantom contained 7 acrylic tubes arranged in a circular arrangement (1cm apart) in the center of the phantom, each with dimensions similar to an average spinal cord (9-mm ant-post, 12-mm left-right) [1]. The tubes were filled with one of three solutions (“BRAINO[2] (General Electric Healthcare, Milwaukee, WI, USA), BRAINO+1mM GABA, and 1mM GABA). The phantom was filled with 3% agarose gel (containing 0.1% sodium azide) [3] to lower magnetic susceptibility differences that would be present between acrylic and air (Fig. 1). Imaging was performed using a GE MR750 3T MRI (General Electric Healthcare, Milwaukee, WI) and a MR Instruments 32-channel head coil. MRS acquisition was done using both PRESS (TE/TR=35/1500ms, NEX=256) and MEGA-PRESS (TE/TR=68/1500ms, NEX=256) on each tube, both with identical voxel placement for each tube. A 1x1x1cm ($1cm^3$) voxel was placed in the center of each tube. Voxel placement was crucial for the success of this study as (FWHM) linewidths above 4 Hz were rejected [4]. Spectra were analyzed using the TARQUIN software package.

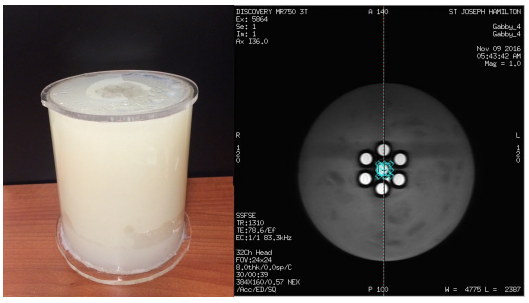

Fig. 1

Results

TARQUIN provided reliable spectra ratios based on the actual composition of each tube. TARQUIN also proved its repeatability as 5 separate data collections yielded similar spectral fit results. However, the specific pre-defined concentrations of each tube did not match the concentration amounts from the TARQUIN analysis. These conclusions apply for both PRESS and MEGA-PRESS sequences. Additionally, as expected, MEGA-PRESS demonstrated better GABA acquisition as it successfully edits GABA whereas PRESS does not (Table 1).

Metabolite	MEGA-PRESS (mM)	std. dev. (mM)
GABA	0.3704	0.4689
NAAG	0.5479	0.2566
Cr	2.4870	0.9761
Glc	0.6788	0.7734
Glx	1.3870	0.9734

Metabolite	PRESS (mM)	std. dev. (mM)
GABA	0.7167	0.9386
NAAG	0.8397	0.3140
Cr	4.2850	0.7549
Glc	0.4077	0.9724
Glx	4.0070	1.2130

Table 1 : MEGA-PRESS (left), PRESS (right)

Conclusions

Based on residual analysis, TARQUIN provided a moderately reasonable fit of parameters. Although metabolites were not adequately represented in terms of concentrations, their ratios were reasonable (within 5% error). Future work will involve embedding the tubes in bone-mimicking encasement to assess problems with magnetic susceptibility in such measures. In addition, a further step forward into designing a more robust phantom would be to introduce transverse and superior-inferior liquid flow to mimic CSF and aortic blood flow artifacts to better simulate spinal cord spectroscopy.

References

[1] Sherman J, et at (1990) AJNR 11:369-372

[2] Lattanzi R, et al (2010) NMR Biomed. Feb: 23(2): 142-151

[3] Hellerbach A, et al (2013) PlosOne 8(8): e70343

[4] Drost D, et al (2002) Med Phys Sep:29(9): 2177-97

Measurement of placental T2* in a guinea pig model of intrauterine growth restriction

KJ Sinclair[1], LJ Friesen-Waldner[1], TP Wade[2], C Vander Tuin[3], B de Vrijer[4], TRH Regnault[3,4], and CA McKenzie[1,2*]

Hyperpolarized 13C MRI of Placental Metabolic Abnormalities Consortium

[1]Medical Biophysics, [2]Robarts Research Institute, [3]Physiology and Pharmacology, [4]Obstetrics and Gynaecology, Western University, London, Ontario, Canada. *Supervisor

Introduction: Intrauterine growth restriction (IUGR) affects up to 10% of all pregnancies and is a leading cause of perinatal morbidity and mortality.[1] IUGR resulting from placental insufficiency is often associated with fetal hypoxia.[2] Oxygen supply through the placenta is the major driver for fetal growth and the ability to measure placental oxygenation can give us valuable information regarding the status of fetal development. MRI is emerging as a valuable technique to study oxygenation of tissue and blood vessels *in vivo*. In MRI experiments, the presence of deoxyhemoglobin causes more rapid signal decay than oxyhemoglobin.[3] Taking advantage of this fact, oxygenation status can be probed by examining the rate of signal decay, governed by the decay constant T2*. Thus, our objective was to use MRI to examine the placental oxygenation status in a guinea pig model of IUGR, in which an increased brain to liver volume ratio (BLVR) indicates redistribution of fetal blood flow in response to fetal hypoxia.

Methods: To induce IUGR, vessel occluders were placed bilaterally on the uterine arteries at 35 days gestation (term ~68 days, N = 4, 14 fetuses).[4] Sham surgeries were performed to produce a control group (N = 4, 18 fetuses). At ~60 days gestational age, sows were anaesthetized and scanned at 3 Tesla. A T2* mapping sequence was performed with the maternal guinea pig breathing air with an oxygen concentration of 20%. The animal was then switched to 100% oxygen and the imaging was repeated after 10 minutes. T2* maps were calculated by fitting the multi-echo images to an exponential decay function. ROIs were drawn on the T2* maps to obtain values for each placenta. T2* values were also calculated in the maternal kidneys to ensure validity of the technique.

Results: Fetuses in the surgical group were defined as IUGR if they had a BLVR >0.7. Only fetuses in mothers that responded to the inhaled oxygen concentration change based on a T2* increase in the maternal kidney were analyzed. Thus our study population consisted of 6 IUGR fetuses and 11 control fetuses. In the placentae, there was a difference in T2* change from 20% to 100% inhaled oxygen observed between control and IUGR fetuses ($P < .05$). Further, a negative correlation was observed between T2* change and BLVR (Figure 1; $r = -.53$).

Conclusions: These data suggest that fetoplacental oxygen demand in control pregnancies is sensitive to, and increases with maternal oxygenation, a response that has been curtailed in the situation of IUGR, likely due to decreased oxygen transfer capacity. Further we have demonstrated the utility of using MRI to detect changes in maternal and placental oxygenation in response to increased oxygen availability through measurement of the decay constant T2*.

References: 1. Vandenbosche and Kirchner. Am Fam Physician. 1998;58(6):1384-90. 2. Kingdom and Kaufmann. Placenta. 1997;18(8):613-21. 3. Chalouhi *et al.* Radiology. 2013;269(1):122-9. 4. Herrera *et al.* J Physiol. 2016;594.6:1553-1561.

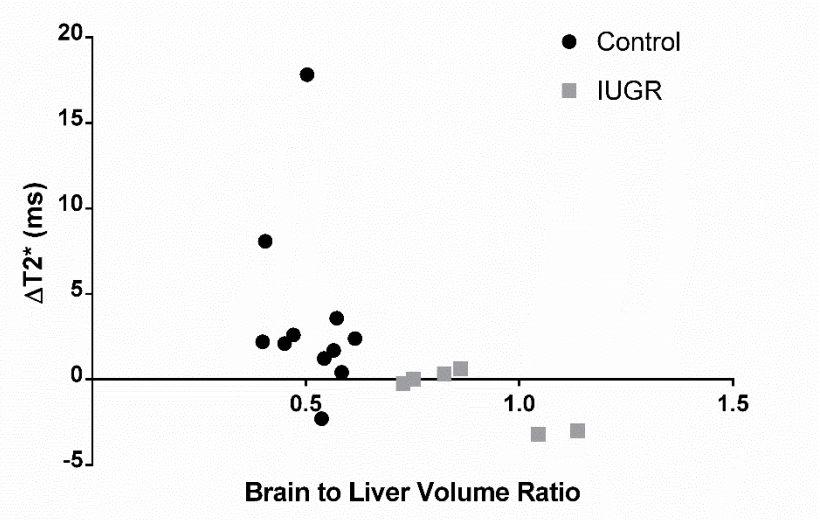

Figure 1: Change in placental T2* from 20% to 100% maternal inhaled oxygen concentration as a function of brain to liver volume ratio.

Relationship between cardiac fat and microvascular dysfunction in non-obstructive coronary artery disease

[1]Stephanie Skanes, [2]Gerald Wisenberg, [3]Ali Islam, [1,4]Ting-Yim Lee and [4]Aaron So
[1]Imaging, Robarts Research Institute; [2]Cardiology, London Health Sciences Centre, [3]Radiology, St. Joseph's Healthcare London, [4]Imaging, Lawson Health Research Institute, London, Ontario, Canada

Introduction Obesity is a traditional risk factor of coronary artery disease (CAD) but its relationship with coronary microvascular disease is not fully elucidated. Accumulation of excessive tissue fat may trigger inflammation and alter the endothelial vasoregulatory mechanism. Endothelial dysfunction may also precede the development of atherosclerotic plaques in larger coronary arteries. In this study, we investigated the correlation between cardiac fat volume (CFV) and myocardial blood flow (MBF) and blood volume (MBV) assessed by cardiac CT in CAD patients without flow-limiting epicardial coronary stenosis.

Methods We retrospectively reviewed the cardiac CT studies of 23 CAD patients performed at St Joseph's Healthcare London for the Medical Imaging Network Trial of Canada (MITNEC) B5 project. Data acquisition Each patient had coronary CT angiography (CCTA) and CT perfusion (CTP) studies at rest and during maximal vasodilatory stress. CCTA was acquired using a routine clinical protocol run on a 64-row GE CT750 HD scanner. For each CTP study, iodinated contrast was injected at 5 mL/s followed by dynamic scanning of the heart using the same scanner with a prospective ECG gated acquisition protocol: 22-25 axial scans with breath-hold at every 1-2 mid-diastoles, 140 kV tube voltage, 50 mA tube current and 350 ms gantry period. Upon the completion of rest CTP study, adenosine was administrated at 140 µg/min/kg and the CTP study was repeated at 3 minutes into adenosine infusion. Dynamic contrast-enhanced (DCE) heart images from each CTP study were corrected for beam hardening, registered with a three-dimensional non-rigid algorithm and analyzed with CT Perfusion (GE) from which MBF and MBV maps were generated using a model-based deconvolution algorithm. Data analysis Amount of cardiac fat, defined as the adipose tissue surrounding the heart within the thoracic cavity, was determined from the CCTA source images using Analyze (AnalyzeDirect Inc). Voxels with CT numbers between -190 and -30 HU were defined as fat. In each slice, the area of fat region was multiplied by the slice thickness (0.625 mm) to determine the fat volume. The fat volumes of all slices were summed to determine the total CFV. Two patients with functionally significant coronary stenosis, as assessed by catheter-based fractional flow reserve measurement (FFR, < 0.75) were excluded for analysis. The remaining patients (n=21) were divided into the younger (54-62 y.o., n=11) and older (63-74, n=10) age group. Each age group was further divided into the high (< 280 cm^3) and low fat (≥ 280 cm^3) groups. The correlation between the total CFV and myocardial hemodynamics (MBF and MBV) in each group was studied using regression analysis.

Results There was a strong inverse correlation between myocardial blood flow / blood volume and CFV in the younger age group in both rest and stress conditions. The correlation coefficients were: rest MBF (R=0.69, P=0.001), rest MBV (R=0.84, P=0.013), rest MBF*MBV (R=0.77, P=0.004), stress MBF (R=0.64, P=0.026), stress MBV (R=0.78, P=0.003), and stress MBF*MBV (R=0.81, P=0.000). By contrast, no significant correlation between myocardial parameters and CFV was observed in the older age group ($p>0.05$ for all).

Conclusion CAD patients with more fat deposited in the heart had lower MBF despite the absence of flow-limiting stenoses in the epicardial coronary arteries. The underlying mechanism is unclear but a concomitant decrease in MBV suggested endothelial dysfunction in which production of nitric oxide (vasodilator) is impaired. Furthermore, magnitude of decrease in MBF and MBV was comparable between the rest and stress conditions, indicating that myocardial blood flow and blood volume reserves (ratio of stress to rest) may not be useful for accessing coronary microvascular disease as in the case of assessing the functional significance of luminal narrowing in larger coronary arteries. The older patients could be affected by other confounding health issues and hence the correlation between cardiac fat and myocardial hemodynamics was less significant. Our results suggested that CT could detect coronary abnormality at the microvascular level prior to plaque formation in larger coronary arteries, which could facilitate early intervention to prevent disease progression.

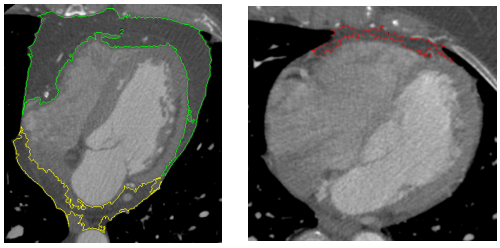

Figure 1. CCTA source images of two CAD patients without flow-limiting (obstructive) stenoses in epicardial coronary arteries. (A) The heart with a high cardiac fat volume (green and yellow regions). (B) The heart with a low cardiac fat volume (red region).

Optimizing Hyperpolarized Carbon-13 Magnetic Resonance Imaging of Fetoplacental Metabolism

Lauren Smith*, Alireza Akbari, Trevor Wade, Charles McKenzie (Research Supervisor) *Department of Medical Biophysics, Schulich School of Medicine and Dentistry, The University of Western Ontario, London, Ontario, Canada*

Introduction: Hyperpolarized carbon-13 (^{13}C) magnetic resonance imaging (MRI) allows *in vivo* real-time imaging of metabolism without using ionizing radiation[1]. These properties make it ideally suited to image fetoplacental metabolism during pregnancy to further understand the relationship between fetal growth and placental metabolism in prenatal abnormalities such as intrauterine growth restriction (IUGR) and macrosomia[2]. Hyperpolarised MRI studies are challenging because the short and irreversible T1 decay (20-40 seconds[1]) of metabolically interesting molecules like [1-^{13}C]pyruvate and its metabolic products leads to low resolution and low signal-to-noise ratio (SNR) images compared to conventional ^{1}H MRI[2]. Currently, many different techniques are being used for hyperpolarized ^{13}C MRI; however, there is no consensus on which pulse sequence parameters yield optimal SNR. The aim of this project is to optimize the SNR efficiency of a pulse sequence for fetoplacental hyperpolarized ^{13}C MRI through simulation.

Methods: Optimization of ^{13}C MRI followed two lines of inquiry: 1) use of variable flip angle (VFA) vs constant flip angle (CFA) methods; 2) use of interleaved slice selective (2D) vs volume selective (3D) acquisition[3,4]. The constant flip angle was chosen to allow 90% of the signal to decay by the last RF pulse. Bloch equation simulations were performed to determine the SNR accounting for the additional noise averaging of the slices in the 3D acquisition[5]. These simulations used parameters specific to our pregnant guinea pig model, including temporal resolution (10s per volume), TR, slice thickness, and matrix size[2].

Results: Variable flip angles allow the signal to be preserved at a constant level over the duration of the scan, compared to constant flip angles which begin with a higher relative SNR but allow the signal to deplete throughout the scan (Figure 1). This result holds when the conversion of pyruvate to lactate is considered. The 2D and 3D acquisitions result in the same SNR after taking signal averaging of 3D acquisition into account.

Conclusions: Our simulations suggest that the flip angle scheme should depend on the imaging application. CFA is preferable if high SNR images are needed only at the beginning of the scan or for one time point and VFA is advantageous when multiple images are needed throughout the entire duration of the scan. There was no difference in SNR found between 2D and 3D acquisition methods. Future work will include validating our simulation findings by MRI measurements in phantoms and in pregnant guinea pigs. Improved pulse sequences for hyperpolarised ^{13}C MRI will lead to improvements in placental imaging that may ultimately affect clinical management of at-risk pregnancies.

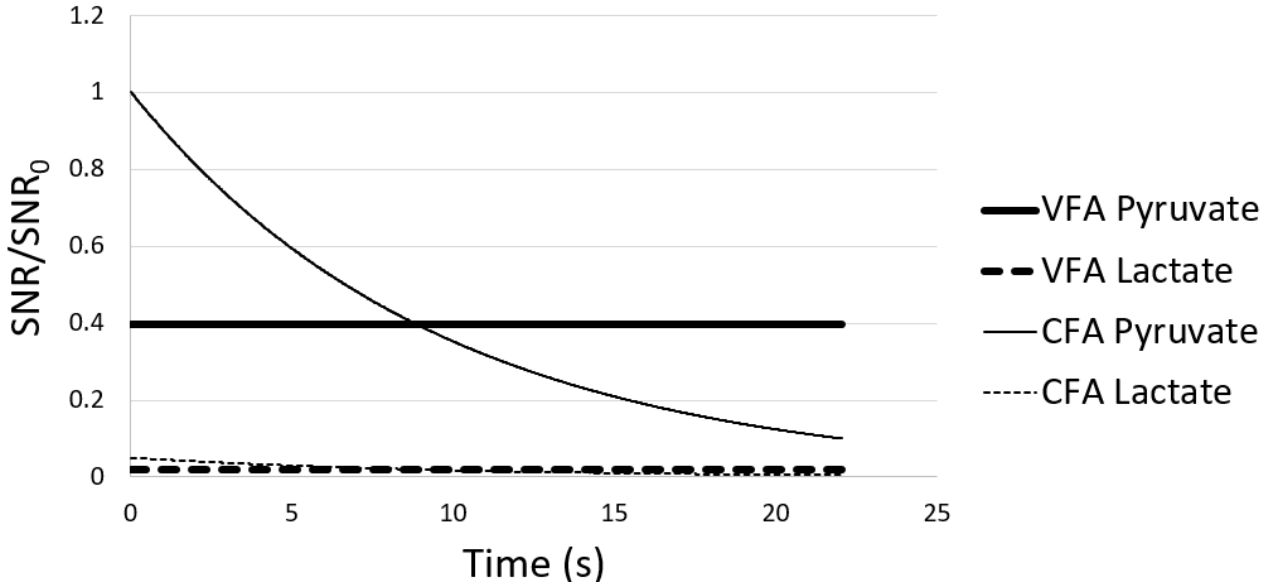

Figure 1 Plot comparing VFA to CFA for pyruvate and lactate SNR. Normalized to CFA pyruvate SNR at t=0.

References: [1] Hurd, R. E., et al. *J Magn Reson Imaging* 2012; 36(6):1314-1328. [2] Friesen-Waldner, L.J., et al. *J Magn Reson Imaging* 2015 [3] Xing, Y., et al. *J Magn Reson* 2013; 234:75-81. [4] Wild, J.M., et al. *Mag Reson Med* 2004; 52(3):673-678. [5] Zhao, L., et al. *J Magn Reson, Ser B* 1996; 113(2): 179-183.

Computer-Assisted Characterization of Malignancy and Gleason Grade of Prostate Cancer on Multi-Parametric MRI

D. Soetemans[1,2,3,8], G. S. Bauman[3,5], E. Gibson[9], M. Gaed[6], M. Moussa[6], J. A. Gomez[6], D. W. Cool[7], M. Bastian-Jordan[7,10], Z. Kassam[7], J.L. Chin[4,5], S. E. Pautler[4,5], *A. D. Ward[1,3,5,8]

[1]Baines Imaging Research Laboratory, London Regional Cancer Centre, [2]Biomedical Engineering Graduate Program, Depts. of [3]Medical Biophysics, [4]Surgery, [5]Oncology, [6]Pathology, [7]Medical Imaging, Western University, [8]Lawson Health Research Institute, London, Ontario, Canada; [9]Centre for Medical Image Computing, University College London, UK; [10]Queensland Health, Brisbane, Queensland, Australia * Research supervisor

Introduction: Prostate cancer (PCa) is one of the most prevalent cancers among men. Radiologist-identified regions from mpMRI have shown promise for detection of PCa, but substantial inter-observer variability in lesion contouring has been observed.[1] Models have been shown to significantly improve diagnostic accuracy when combining a CAD prediction with a radiologist prediction, especially among inexperienced radiologists.[2] However, many models are validated using histology obtained from biopsies that are preferentially guided toward suspicious regions identified on mpMRI; such validation sets are biased toward containing true positive lesions. We propose a computer-assisted diagnosis (CAD) system for classification of malignant vs. benign tissue and high (>3+3) vs. low tumour Gleason score for improving characterization accuracy and patient treatment selection, validated using an accurate registration system for fusion of whole-mount digitized histology to mpMRI.[3]

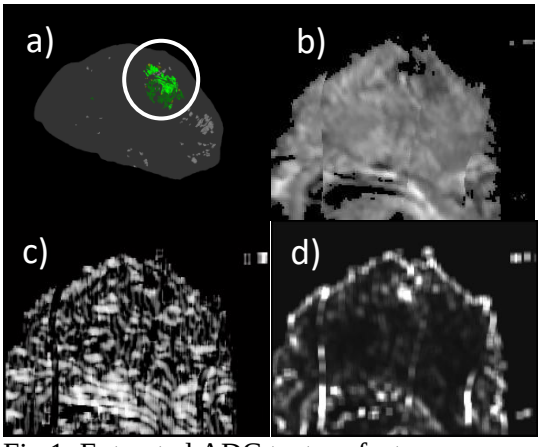

Fig 1: Extracted ADC texture features showing: a) tumour mask with dominant lesion circled, b) ADC map, c) ADC correlation texture measure and d) ADC contrast texture measure calculated using a square 2 mm window.

Methods: From a prostatectomy cohort of 22 patients who underwent T2- and diffusion-weighted MRI, 22 first and second order texture features (examples in Fig. 1) were extracted. Forward feature selection was used to select the most discriminative features. Areas under the receiver operating characteristic curve (AUC), false positive rates and false negative rates were computed during folded cross validation.

Results: Classification of cancer (n=69) vs. healthy tissue (n=44) achieved an AUC of 0.96 (0.05 FPR, 0.19 FNR). Cancer (n=69) vs. confounding radiological false positives (n=102) achieved an AUC of 0.89 (0.10 FPR, 0.29 FNR). For high (n=29) vs. low (n=49) Gleason grade an AUC of 0.60 (0.44 FPR, 0.49 FNR) was achieved, indicating a need for further refinement of this component.

Conclusions: We developed a CAD system for characterization of benign, malignant and confounding tissue on prostate mpMRI. The system is a first step toward a tool to improve radiologist characterization performance, patient treatment selection and risk stratification.

[1]M Salarian et al, SPIE Medical Imaging, 2013; [2]G Litjens et al, Eur Radiol, 2015, 25: 3187–3199;
[3]E Gibson et al, Int J Rad Oncol Biol Phys, 2016, 96, 1: 188–196

A PET/MR Approach to Non-Invasive Quantification of Cerebral Blood Flow

Tracy Ssali[1,2], Udunna Anazodo[1,2], Jonathan Thiessen[1,2], Frank S Prato[1,2], Keith St Lawrence[1,2]
[1] Lawson Health Research Institute, London Ontario, Canada,
[2] University of Western Ontario, London Ontario, Canada

Introduction: Positron emission tomography (PET) using radiolabeled water ($H_2{}^{15}O$) is the gold standard for imaging cerebral blood flow (CBF). However, quantification requires measuring the arterial input function (AIF), which is not only invasive, but an inherently noisy procedure. Arterial spin labeling (ASL) is an attractive MRI-based alternative, but its accuracy is hindered by low signal to noise and arrival time uncertainties[1,2], particularly when imaging CBF in patients with cerebrovascular disease. Considering these limitations, we propose a hybrid PET/MR approach that does not require invasive arterial sampling, but still generates quantitative CBF images. With this approach, global CBF is measured by phase-contrast MRI (PC-MRI)[3], simultaneously with $H_2{}^{15}O$-PET imaging. Global CBF is used as a reference to convert $H_2{}^{15}O$ activity data into CBF maps, thereby avoiding the need to measure the AIF. This is similar to a previously proposed PET-only technique[4], but with the important difference that global CBF is measured rather than assumed. In this study, the agreement between simultaneously measured CBF using PC-MRI and PET-only were compared in a large animal model over a range of CBF values.

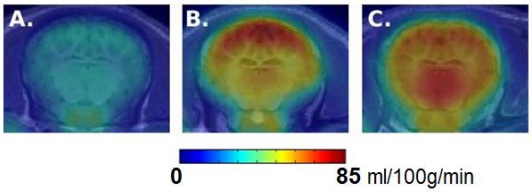

Figure 1: MR-reference PET CBF maps at (a) hypocapnia, (b) normocapnia and (c) hypercapnia.

Methods: Data were acquired in juvenile pigs (21.7 ± 2.7 kg) at baseline (n = 4), hypercapnia (n =3) and hypocapnia (n = 3). Animals were anaesthetized and PCO_2 was manipulated by adjusting the breathing rate and volume. After a rapid intravenous bolus injection of $H_2{}^{15}O$ (475±153 MBq), 5 minutes of PET list-mode data were acquired with a 3T PET/MR system (Biograph mMR Siemens). Arterial blood was sampled at 5mL/min using an MR-compatible pump (Swisstrace, Switzerland). For PC-MRI, an imaging plane orthogonal to the internal carotid and basilar arteries was identified by time-of-flight angiography. Gated PC images were acquired during PET scanning (VENC: 80 cm/s, 8 averages). Average whole brain flow was measured with PC-MRI data by contouring the feeding arteries in Argus Flow and scaling by the brain tissue weight. Raw PET data were reconstructed into 37 dynamic frames (3s x 20; 5s x 6; 15s x 6; 30s x 5) using a CT-based attenuation correction map and an ordered subset expectation maximization algorithm. These images were smoothed with a 6-mm Gaussian filter, and a non-linear optimization routine was used to fit the Kety model[5] including a blood volume term to determine CBF.

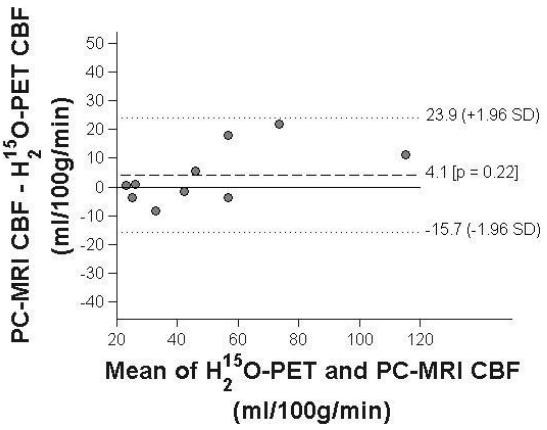

Figure 2: Bland-Altman plot comparing the difference of CBF measured with $H_2{}^{15}O$-PET and PC-MRI to their mean. The difference between measurements was not significantly different from zero, demonstrating the similarity between measurements.

Results: Mean pCO2 at hypocapnic, normocapnic and hypercapnic conditions were 25.0 ± 2.2, 37.6 ± 1.7 and 54.3 ± 4.9 mmHg. Average whole-brain CBF measured by PC-MRI and $H_2{}^{15}O$-PET are summarized in Table 1. Representative CBF images at the 3 pCO_2 conditions from the MRI-reference PET method are shown in Figure 1. Linear regression analysis was performed and a Bland-Altman was generated (Figure 2) to assess the agreement between the PET-based and PC-MRI measurements of CBF.

Table 1: Cerebral blood flow at hypo-, normo-, and hypercapnic states measured by $H_2{}^{15}O$-PET and PC-MRI.

	Hypocapnia	Normocapnia	Hypercapnia
PC-MRI	24.6 ± 1.8	46.3 ± 15.4	86.9 ± 33.0
$H_2{}^{15}O$-PET	25.3 ± 2.1	42.8 ± 4.5	77.0 ± 28.3

Conclusions: This work presents a non-invasive and quantitative method of imaging CBF by hybrid MR/PET. We believe this method could be useful for patient populations for whom it has proven challenging to obtain accurate perfusion measurements with other methods, most notably ASL, due to significant vascular disease. CBF maps shown in Figure 1 demonstrate the expected global perfusion increase and decrease in the hyper- and hypocapnic states. Linear regression showed significant positive correlation (R^2=0.92, $p<0.05$). The Bland-Altman plot demonstrated good agreement between PET and MRI measurements (NS, p=0.22). Interestingly, in the hypercapnic state, there was greater deviation between CBF measurements from PC-MRI and PET (13%). This may be attributed to limited water extraction at higher flow rates [6]. Future studies will involve comparing this reference method to ASL in CVD patients to assess its ability to quantify perfusion abnormalities.

References: [1] Heijtel, D. *et al., Neuroimage* **92,** 182–92 (2014). [2] Haga, S. *et al., J. Stroke Cerebrovasc. Dis.* **25,** 1–6 (2015). [3] Peng, S. *et al., J. Magn. Reson. Imaging*. **42**, 1126-1133 (2015). [4] Mejia, M. A. *et al., J. Nucl. Med.* **35,** 1870–7 (1994). [5] KETY, S. S. *et al., Pharmacol. Rev.* **3,** 1–41 (1951). [6] St Lawrence, K. *et al.*, J. Cereb. Blood Flow Metab. **18**, 1378–1385 (1998).

Whole time course coil combination using singular value decomposition

Olivia W. Stanley*, Ravi S. Menon (Research Supervisor), L. Martyn Klassen
Robarts Research Institute, The University of Western Ontario, London, Ontario, Canada

Introduction: Phase data is sensitive to macrovascular structure in gradient echo (GE) magnetic resonance imaging (MRI) [1]. This effect has previously been exploited to reduce downstream vascular contamination in functional MRI (fMRI) magnitude images. Despite this, conventional fMRI uses only magnitude data in the analysis. One potential reason is that in current GE-echo planar imaging (EPI) sequences, phase is reconstructed using a complex sum that incorrectly assumes coils are equally sensitive at every point in space. This leads to increased phase noise, and in the worst case, phase singularities. This is not the case in conventionally combined magnitude data where sum-of-squares combination relies on the signal itself as an estimate of each coil's sensitivity profile [2]. Using a whole time course singular value decomposition (SVD) [3] one can maximize the magnitude of the complex linear combination of the time course which maximizes the magnitude signal-to-noise ratio (SNR) of the data [4] and therefore minimizes the phase standard deviation on a voxel by voxel basis (also allowing for a spatially varying coil sensitivity profile).

Methods: Using a SVD on an m-by-n matrix (m=coils, n=time points) the left and right singular vectors were isolated from a whole EPI time course on a voxel by voxel basis. The product of the right singular vector and the primary singular value represents the signal from that voxel while the left singular value is the relative coil sensitivities. To ensure the SVD result is unique, the phase of the first point in the time series is set to zero (fMRI applications of phase are not dependent on the initial phase of a voxel). This combination is completed off-line after data collection and reconstruction.

In order to validate this method, accelerated GE-EPI scans were combined using SVD and conventional combinations. Two cases were examined: low resolution scans in a 32 channel whole head coil and high resolution scans in a 32 channel occipital-parietal coil. The low resolution scans were 2mm isotropic with a flip angle of 30^{o}, TR=1250ms, and TE=20.8ms. The high resolution scans were 0.8mm isotropic with a flip angle of 40^{o}, TR=1250ms, and TE=23.4ms. Both scans were completed with multiband factor 2 and GRAPPA factor 3 with 36 reference lines. Temporal signal-to-noise ratio (tSNR) measurements were carried out on the magnitude data after motion correction and linear detrending. The phase data was temporally unwrapped, linearly detrended, motion corrected (using the magnitude motion correction parameters), and phase standard deviation was calculated on a voxel by voxel basis. The differences in tSNR and phase standard deviation across combination methods were calculated across a tight brain mask of central slices (18 for the high resolution set, 10 for the low resolution set). These differences were checked for significance using a one sided Student's *t*-test.

Results: SVD combination was found to produce images with a higher tSNR and lower phase standard deviation with a significance value of $p<1x10^{-10}$ at both resolutions. In the low resolution case the average improvement in phase standard deviation was -0.0329±0.2312 radians (mean ± standard deviation). In the high resolution case the average difference between combinations was -0.1819±0.7284 radians. Finally, the singularity present in the low resolution data was completely resolved by using SVD combination (Figure 1).

Conclusions: This method allows for combination of phase images with spatially variant coil sensitivities ensuring that there are no singularities or excess noise in the combined phase images. This study proves SVD combination results in improved images with higher tSNR and lower phase noise from conventionally combined images. This method is currently used to collect phase data for fMRI applications in-house. This will allow for further investigation of phase applications in fMRI and other MRI applications with repeated temporal sampling.

References: [1] Menon RS. Magn Reson Med. 2002;47(1):1-9
[2] Roemer P et al. Magn Reson Med. 1990;16(2):192-225
[3] Gudbjartsson H et al. Magn Reson Med 1995;34(6): 910-914
[4] Walsh DO et al. Magn Reson Med. 2000;43(5):682-90

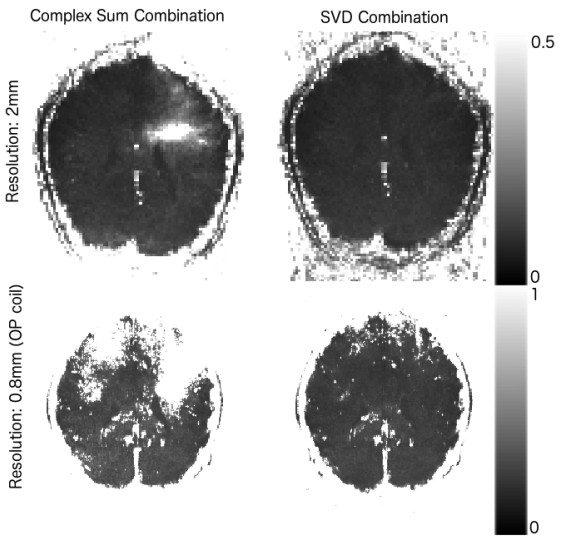

Figure 1 – Comparison of phase temporal standard deviation with different coil combination methods.

Expression of the Growth Hormone Secretagogue Receptor and Ghrelin in Human Heart Failure

Rebecca Sullivan[1], Anne Stokes[2], Derek Wu[1], Sophia Yijia Liu[1], Dov B. Kagan[1], Carlie Charlton[3], Tyler Lalonde[3], Leonard Luyt[3,5], Bob Kiaii[6], Gerald Wisenberg[4,7], and Savita Dhanvantari[1,4,7,8]

1. Pathology and Laboratory Medicine, Western University, London, Ontario, Canada; 2. Medical Sciences, University of Ottawa, Ottawa, Ontario, Canada; 3. Chemistry, Western University, London, Ontario, Canada; 4. Imaging Program, Lawson Health Research Institute, London, Ontario, Canada; 5. Department of Oncology, London Regional Cancer Program, Western University, London, Ontario, Canada; 6. Cardiac Surgery Unit, London Health Science Centre, London, Ontario, Canada; 7. Medical Biophysics, Western University, London, Ontario, Canada; 8. Metabolism and Diabetes, Lawson Health Research Institute, London, Ontario, Canada

Primary Author: Rebecca Sullivan - Graduate Student (Consortium: Heart Disease) Supervisor: Dr. Savita Dhanvantari

Introduction

The leading cause of mortality in Canada is heart disease (HD) which impacts nearly 1.6 million people with over 500,000 affected by heart failure (HF). HF is a specific condition that occurs when the heart is unable to provide enough blood flow and oxygen to organs across the body. Current prognosis for HF is poor as the current biomarkers used to detect HF are in the circulation, and not specifically in cardiac tissue. A novel biomarker of interest is the growth hormone secretagogue receptor-1a (GHS-R1a) and its ligand ghrelin. Both ghrelin and GHS-R1a are present in cardiomyocytes and may have therapeutic potential in chronic HF. Our group has developed a fluorescent analog of ghrelin, Cy5ghrelin(1-18), which incorporates the first 18 amino acids of ghrelin attached to the Cy5 fluorescent probe. We have previously shown that this analog specifically binds to GHS-R1a in cardiac tissue in situ and can be used to detect changes in GHSR-1a during cardiomyocyte differentiation. My study is focused on characterizing GHS-R1a, ghrelin and other biomarker levels in human cardiac tissue and correlating corresponding levels to the stage of HF. I expect GHS-R1a levels to correlate to the stage of HD and ultimately be used with a panel of other cardiac biomarkers to help with early diagnosis.

Materials and Methods

Samples of cardiac tissue from 2 patient cohorts have been obtained from the cardiology unit of London Health Sciences Center (LHSC) including cardiac transplant patients with samples obtained from the explanted heart and biopsies of the healthy heart at various weeks post-transplant. have used Cy5-ghrelin(1-18) and fluorescent antibodies to test for GHS-R1a and ghrelin levels respectively. Natriuretic Peptide type B (BNP) is a known cardiac biomarker of HF which we detected using fluorescent antibodies. Quantitative fluorescence microscopy was used to test for the levels of ghrelin, GHS-R1a and BNP in both patient cohorts. Images from each sample were acquired using NIS Elements Software (Nikon) and image analyses was conducted using ImageJ FIJI version 1.46 h with set parameters. Fibrosis is another biomarker of HF which measures the presence of fibrotic tissue in the heart. Masson's trichrome stain will be used and quantification will be done using ImageJ FIJI with an online script obtained from Dr. Shapiro's group at Marshall University. Levels of ghrelin, GHS-R1a, BNP and fibrosis of the explanted heart were compared to the healthy biopsies using two-tailed t-test, two-way ANOVA and Tukey's test, where significance was set at $p<0.05$. These levels will then be correlated to the clinical data for each patient (obtained from LHSC). This information will lead to the establishment of clinical parameters for classification of HF severity.

Results

We found a strong increase in GHS-R1a in end stage heart failure patients when compared to the healthy implanted heart biopsies. Ghrelin and BNP expression levels are slightly elevated in end stage heart failure patients and show the same expression level changes when comparing the severe heart failure patients and the healthy implanted heart. The levels of GHS-R1a, ghrelin and BNP are to be correlated to the clinical data and are expected to be indicative of the level of HF severity.

Conclusions

The establishment of GHS-R1a as a cardiac specific biomarker can greatly impact the diagnosis of HF and will help with individual or personalized medicine. This biomarker can be used in conjunction with a panel of biomarkers to help understand and progression of HF in patients diagnosed with HD.

Collision detection for external beam radiation therapy applications in SlicerRT

Vinith M. Suriyakumar, Renee Xu, Csaba Pinter, Gabor Fichtinger
Laboratory for Percutaneous Surgery, Queen's University, Kingston, ON, Canada

INTRODUCTION: Collision detection is important in external beam radiation therapy to help eliminate the need for dry-runs that confirm the usability of selected beam angles and prevent patient-machine collisions. Medical technology companies have developed commercial treatment planning systems (TPS) to assist radiation oncology teams with determining proper radiation doses and visualization including automated collision detection. Unfortunately, commercial TPS are expensive and proprietary restricting their use, especially in RT research. Thus, we propose the development of a collision detection module in SlicerRT, which is an open-source radiation therapy research toolkit [1] based on the 3D Slicer medical image visualization and analysis platform.

METHODS: We use an openly accessible geometric model of the Varian TrueBeam™ STx downloaded from 3D Warehouse. The model is separated into its multiple components and loaded into the SlicerRT radiation therapy research toolkit [1], which is based on the 3D Slicer medical image visualization and analysis platform. Additional treatment device models such as applicator holder and electron applicator models are created in Solid Edge™ based on visits to Kingston General Hospital where pictures of the device geometry and measurements were taken. The IEC standard specifies the set of movements and motion ranges for all RT machines. Thus, the rigid transformation matrices are developed to be in compliance with the standard's coordinate system hierarchy, which ensures the module will work will all types of RT machines. The automated collision detection applies the vtkCollisionDetectionFilter class from the vtkbioeng library [2]. Detection is performed between all the possible machine component pairs and additional treatment devices to ensure that all possible collisions could be detected.

RESULTS: The REV visualization and automated collision detection were implemented as a Room's eye View C++ module in SlicerRT. Two commonly encountered RT plans: a head and neck plan and a prostate plan were loaded into the module for testing. The module was integrated into the existing open-source TPS so that the machine was automatically transformed based on the loaded RT plan. The machine's movements were accurately modelled based on the IEC standard (Fig. 1). The automated collision detection was tested by changing the geometric parameters of machine to purposely cause collisions between machine components. The module was able to accurately indicate collisions between each pair of machine components, machine-patient collisions, and all collisions that were happening simultaneously.

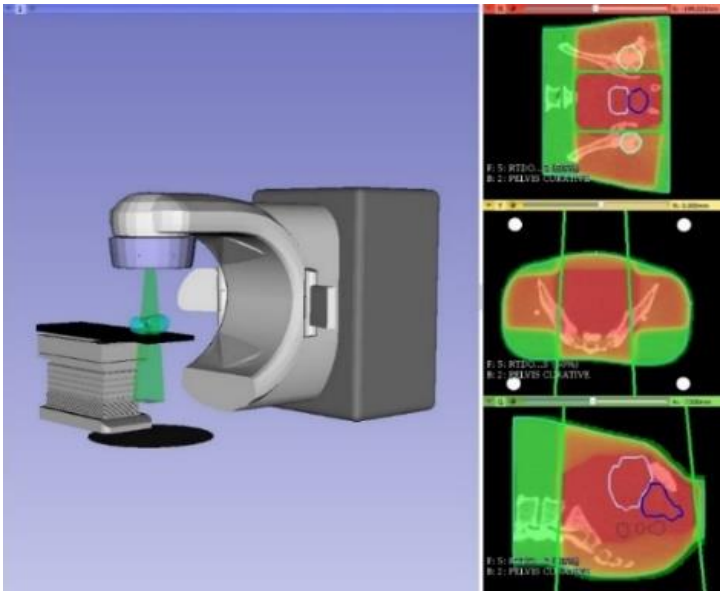

Fig. 1: Modelling of treatment machine, RT beam, and room based on geometric parameters for prostate RT plan.

CONCLUSION: A software module providing room's eye view visualization with automated collision detection was developed as a component of an open-source application in SlicerRT. The visualization and safety features provided by the open-source application will be improved due to this software module. The creation of additional treatment device models such as electron applicators position the module as being useful for certain RT research settings such as electron beam therapy.

REFERENCES:

[1] C. Pinter, A. Lasso, A. Wang, D. Jaffray, and G. Fichtinger, "SlicerRT: Radiation therapy research toolkit for 3D Slicer," Medical Physics, vol. 39, no. 10, p. 6332, 2012.
[2] vtkbioeng. http://www.bioengineering-research.com/software/vtkbioeng. (as of December 2016).

Boundary Regression Segmentation of Spinal Images

Clara Tam[a], Xiaoxu He[b,c], Shuo Li[a,b,c,*]

[a] Department of Medical Biophysics, University of Western Ontario, London, ON, Canada N6A 3K7

[b] Digital Imaging Group (DIG), London, ON, Canada N6A 4V2

[c] Department of Medical Imaging, University of Western Ontario, London, ON, Canada N6A 3K7

Introduction: Research on automated segmentation is beneficial for numerous disease diagnosis applications including but not limited to scoliosis, stenosis, and degenerative disc disease. Existing clinical practices often requires analysis and manual segmentation of multiple spinal images, which becomes laborious, tedious, and inefficient. Currently, automated segmentation is faced with large challenges due to diverse boundaries, overlapping intensity profiles, and differing structural appearances. We propose a novel automated boundary regression model to segment a combined image of the vertebrae and intervertebral disc for disease diagnosis and treatment. This regression segmentation approach formulates the segmentation task as a boundary regression problem, which leverages the advancement of machine learning in a holistic fashion.

Methods: The proposed framework consists of two processes: 1) the training process to learn the nonlinear boundary regression model $Y = F(x)$ from the training dataset; and 2) the testing process directly predicts the combined locations of the vertebrae and disc's boundary for the input image from the learnt model. The proposed model will be evaluated on cross-modality MR/CT datasets containing 412 samples (372 MR and 40 CT) of lumbar spine images collected from 103 subjects. Regression segmentation is performed using the multiple output support vector regressor (MSVR). The MSVR is a sparse kernel machine capable of modelling highly nonlinear mapping functions. MSVRs ability to predict all the boundary points in the output vector simultaneously and dependently ensures the capability of the regression segmentation to handle highly diverse boundaries.

Results: We predict that the segmentation will highly correlate to its ground truth, achieving a high dice similarity index and a low boundary distance in both MR and CT images. Contrary to conventional segmentation methods based on intensity profiles, the proposed regression segmentation model is predicted to improve accuracy, computational efficiency, and handle greater diversity.

Conclusion: The proposed boundary regression segmentation model formulates the segmentation task as a boundary regression problem. By leveraging advanced machine learning in a holistic fashion the framework will be able to accurately and efficiently segment the combined features of the vertebrae and intervertebral disc. As a result, the novel regression model is predicted to be an efficient clinical tool to aid physicians in clinical settings.

Correcting PET images for tissue transport in order to accurately quantify hypoxia in tumours

Edward Taylor[1,2], Jennifer Gottwald[1,3], Ivan Yeung[1,4], Harald Keller[1,4], Neesha C. Dhani[1,5], Michael Milosevic[1,4], David W. Hedley[1,3,5], David Jaffray[1,2,3]

1. Princess Margaret Cancer Centre, Toronto, Canada.
2. Techna Institute, University Health Network, Toronto, Ontario, Canada.
3. Department of Medical Biophysics, University of Toronto, Toronto, Ontario, Canada.
4. Department of Radiation Oncology, University of Toronto, Toronto, Ontario, Canada.
5. Division of Medical Oncology and Hematology, Princess Margaret Cancer Centre, Toronto, Canada.

Ontario Institute for Cancer Research – Imaging Translation Program

Introduction. There is indisputable clinical evidence that hypoxia in solid tumours is a major negative determinant for outcome to radiation, chemotherapy, and surgery, and yet its measurement has not yet entered routine clinical practice in part because there is not reliable way to quantify hypoxia *in vivo*. Hypoxia-sensitive positron emission tomography (PET) tracers such as fluoroazomycinarabinoside (FAZA) give a promising way of doing this. Compared to FDG, however, the binding rate of these tracers is small, meaning that tracer uptake is sensitive to the presence of hypoxia as well as the transport properties of the imaged tissue. There is a pressing need to identify these transport properties and correct for them.

Methods. Dynamic PET time-activity curves were analyzed using a compartmental model in twenty patients with pancreatic ductal adenocarcinoma. A crucial quantity—the partition coefficient—describing the ratio of tracer in tissue and blood at short times after injection was identified in this model and used to interpret dynamic and static PET uptake metrics.

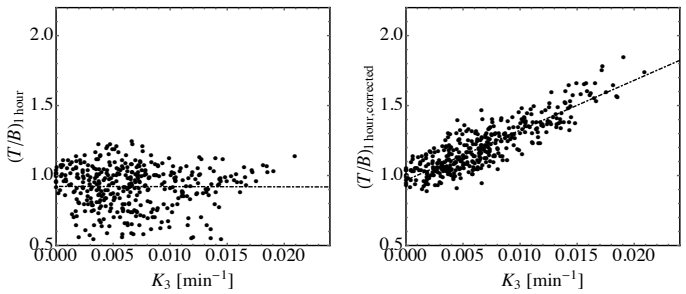

Fig. 1 Left: Tumour-to-blood uptake ratio of FAZA in the voxels of a pancreatic tumour one hour after injection versus the binding rate inferred from a compartmental model. Right: same quantity, but corrected for partitioning.

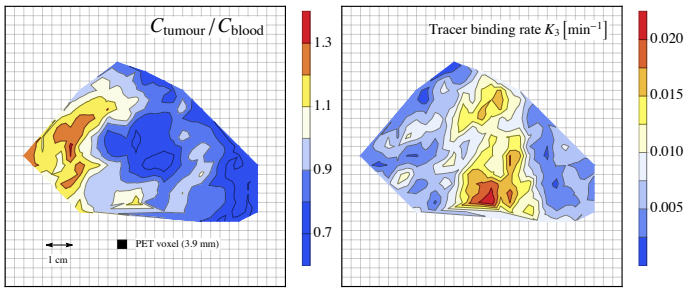

Fig. 2 Spatial distributions of tumour-to-blood uptake ratio (left) and tracer binding rate (right) in a PET scan "slice" of a tumour. Spatial concordance between the two quantities is poor.

Results. Partitioning strongly reduces the ability of static PET imaging to accurately quantify hypoxia: the tumour-to-blood uptake ratio (*T/B*) of FAZA after one hour is poorly correlated with the tracer binding rate, a direct radiobiologically-sensitive metric of hypoxia. Correcting uptake for partitioning, strong correlations were found; see Figs. 1 & 2.

Conclusions. Our results identify a key transport quantity—the partition coefficient—that confounds hypoxia quantification schemes based on static PET imaging. Correcting for partitioning, strong correlations were found between uptake and the tracer binding rate, indicating that hypoxia can be reliably quantified as long as the partition coefficient can be calculated for each imaged voxel. Although we applied compartmental models to dynamic PET data to do this, our results suggest that either short-duration dynamic PET or even static CT scans could do this.

Quantitative Dataset Similarity for Fusing Multi-Institutional Image Collections

Ryan Therrien, William Mangione, Scott Doyle
Department of Biomedical Engineering, The University at Buffalo, Buffalo, NY, USA
Department of Pathology and Anatomical Sciences, The University at Buffalo, Buffalo, NY, USA

Introduction: This project focuses on fusing digital histological image databases obtained from multiple institutions. Modern image classifiers like convolutional neural networks (CNNs) have enjoyed great success in natural image analysis. This success is dependent on vast amounts of training cases: the well-studied ImageNet database[1] contains over 14 million images described by over 20,000 phrases. Unfortunately, there is no histopathological image database of comparable size, as building such a massive collection of human-annotated data for digital pathology is a massive undertaking. To circumvent this difficulty, we aim to demonstrate a quantitative approach to compare datasets collected from multiple institutions for the purpose of dataset fusion to improve training set size.

We demonstrate our approach on digitized H&E tissue sections of colorectal cancer (CRC). Kather, et al.[2] have published a method for identifying 8 tissue classes from CRC images using support vector machines (SVMs) and texture-based features, and have provided their image data and code for download. In this study, we compare the Kather dataset (hereafter "Kather") with a set of CRC images obtained at the Erie County Medical Center ("ECMC"). This fusion allows us to extend our image database to build more robust classifiers.

Methods: We begin by extracting the top-performing texture features (as reported previously[2]) from both the "Kather" and "ECMC" image datasets. Four measures of dataset similarity are computed: (1) A Student's T-test is performed on the feature vectors in each class to establish whether the datasets are statistically significantly different. (2) Cluster plots of the features are created to visualize the differences between class structures in each dataset. (3) The variance ratio criteria (VRC), a ratio of between-cluster to within-cluster variance, is calculated to measure clustering similarity. (4) SVM classification is used to establish whether there is a difference between classifier performance.

Results: (1) The results of the t-test are given in **Figure 2**. We reject the null hypothesis, meaning that the feature vectors from the two datasets likely come from populations with different means. (2) However, the cluster plots in **Figure 3** show a similar class structure in feature space, indicating that the difference between the dataset features may not impact classifier performance. (3) The calculated VRC for "Kather" is 0.0806; for "ECMC", 0.0991. This indicates that both datasets have a similar between-cluster / within-cluster ratio, further validating the class structure similarity in feature space. (4) SVM classification results are shown in **Figure 4** for each of the 4 classes, along with the absolute difference in performance. We observe that "ECMC" achieves higher performance, commensurate with its higher VRC value.

Conclusions: Proper multi-institutional dataset fusion provides a way to build large, annotated databases of digital pathology images at a greatly reduced cost. While our statistical tests showed that there is a statistical difference between the means of the Kather and ECMC image sets feature values, the cluster analysis and classification results suggest that similar patterns in feature space allow for similar performance in SVM classification. Future work will focus on further validation of the fused datasets in additional contexts, including training deep CNN classifiers for pixel-wise tissue segmentation on high-resolution images.

[1] "Summary and Statistics." *ImageNet*. Stanford Vision Lab, Stanford University. 2016. http://image-net.org/. Last accessed: 18 Jan 2017.
[2] Kather, J. N. *et al*. Multi-class texture analysis in colorectal cancer histology. *Sci. Rep.* **6**, 27988; doi: 10.1038/srep27988 (2016).

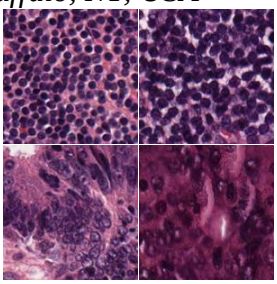

Figure 1: Lymphocytes (top row) Tumor (bottom row) ECMC(left) Kather(right)

Tumor	Stroma	Lymph	Mucin
2.6E-165	2.1E-175	2.1E-166	1.9E-55
3.9E-75	1.5E-101	1.1E-152	8.4E-07

Figure 2: P-value for null hypothesis that each sample came from a population of equal means

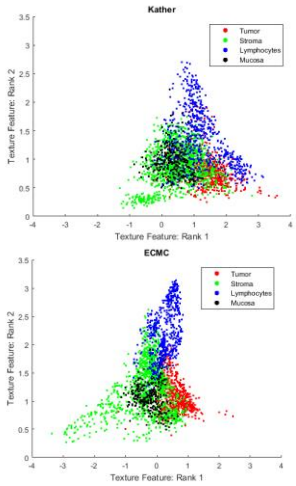

Figure 3: Scatter plots of four classes ("Tumor", "Stroma", "Lymphocytes", "Mucosa") for the Kather (left) and ECMC (right) datasets. The data shows a similar class structure, but the ECMC dataset class means shift to the negative direction of the x-axis.

tumor	stroma	lymph	mucin
0.891	0.921	0.89	0.920
0.931	0.953	0.976	0.935
0.04	0.032	0.086	0.015

Figure 4: : Accuracy in SVM classification with Kather(top) and ECMC(bottom) datasets

Method for detection of breast cancer using 3D surface scanning

Olivia Tong*, Hui Wang, Parsa Omidi, Mamadou Diop, and Jeffrey Carson
Lawson Health Research Institute, The University of Western Ontario, London, Ontario, Canada

Introduction. Many Canadian women diagnosed with breast cancer undergo chemotherapy to reduce tumor size before breast surgery. However, patients respond to chemotherapy drugs differently and monitoring treatment response is an essential component in the management of breast cancer. Currently, it requires a month or longer to determine drug effectiveness. Past research has shown that the level of blood oxygenation in the tumor area during chemotherapy increases within one day after infusion of the drug, but this phenomenon only happens in those patients that respond well to the chemotherapy drug. Our group is building a non-contact breast scanner that can non-invasively monitor blood oxygen level in the tumor during chemotherapy. The success of the project will reduce the time required to reliability determine if chemotherapy drugs are effective in individual patients from a month to as little as one day.

Methods. The focus of this work is to develop a 3D imaging system, which is a component of the non-contact scanner that captures the location and shape of the breast surface using 3D surface imaging technologies. The system is necessary for reconstructing the images acquired by other components of the non-contact scanner. Two imaging systems were built: the first imaging system used a moving camera that took images of the object from a multitude of perspectives to capture the 3D surface of the object, and the second imaging system used structural illumination methods based on three phase shifting (Figure 1) and two-dimensional gray codes (Figure 2). The images were then processed by computer algorithms that generated the 3D model of the object. As a comparison, a much slower (several minutes), but accurate 3D surface scanner was used as a standard reference to estimate the precision and accuracy of the 3D reconstruction.

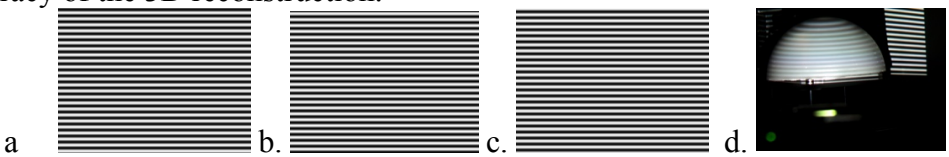

Figure 1. Patterns of three phase shifting (a-c), (d) an example of the three-phase shifting pattern on the object

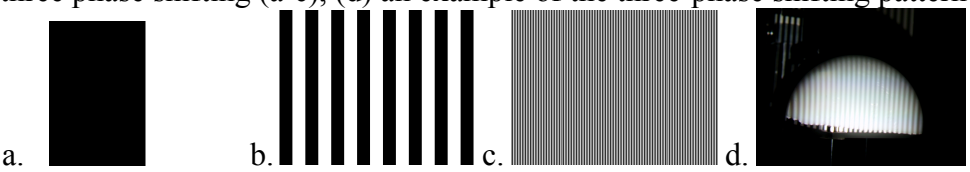

Figure 2. Patterns of gray codes (a-c), (d) an example of the gray code pattern on the object

Results. The first imaging system with a moving camera was tested and required at least nine pictures from a multitude of perspectives to reconstruct a 3D model (Figure 3a). However, our application requires a system that can capture an image in less than a second to minimize motion errors. To satisfy the requirement, a moving camera could be replaced by nine cameras. However, an imaging system with nine cameras would not be feasible for our breast scanner. For the second imaging system, both methods of structural illumination were tested and our preliminary results suggested that gray codes performed better than three-phase shifting (Figure 3b & c). The result of the standard reference is shown in Figure 3d.

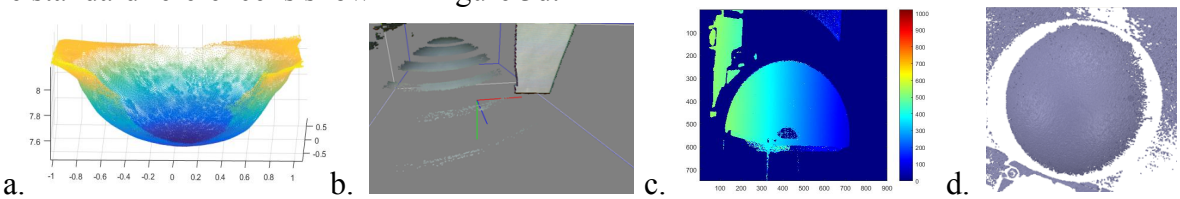

Figure 3. 3D reconstruction results from (a) the imaging system with a moving camera, (b) the imaging system using three-phase shifting, (c) the imaging system using gray code, and (d) the standard reference.

Conclusions. The two imaging systems were tested and the imaging system using structural illumination was more appropriate than the imaging system with a moving camera. More optimization work needs to be completed to improve the 3D reconstruction result.

This work supported by NSERC, CIHR, and TBCRU (OT).

Dual-Energy Micro-Computed Tomography on a Gantry-Based Micro-CT Scanner

Justin J Tse,[1,3] Vasek Pitelka,[2] Joy Dunmore-Buyze,[1,3] Maria Drangova,[1,3] and David W Holdsworth[1,3,4]
Development of Novel Therapies for Bone and Joint Diseases Consortium
[1]Robarts Research Institute, [2]Department of Physiology and Pharmacology, [3]Department of Medical Biophysics, [4]Department of Surgery
Western University, London, Ontario, Canada

Introduction: The ability to perform dual-energy micro-computed tomography (DECT) on a gantry-based micro-CT scanner would widen its capabilities; providing a larger field-of-view, higher throughput, and faster scans and the ability to perform material characterizations and segmentation. This would allow for the simultaneous study of interactions between different materials within the same sample. However, implementation of DECT on the wide range of installed gantry-based micro-CT machines around the world has been difficult due to the need for (1) minimal hardware and software modifications to the scanner; (2) customized filtration for spectral shaping; (3) customized DECT scanning protocols; (4) minimizing sample motion; (5) image co-registration; and (6) decomposition algorithms. We describe and demonstrate a combination of a novel *ex vivo* Er-based vascular perfusion contrast agent, customized filtration, DECT protocols, image co-registration, and decomposition algorithms that allow for the distinct visualization and quantification of vessels in and around bone of a rat hindlimb model.

Methods: We combined samples perfused with our novel *ex-vivo* Er-based (K-edge of 57.5 keV) vascular perfusion contrast agent with custom X-ray filtration, mounted onto a custom automated filter-switcher that fits within the bore of a gantry-based micro-CT machine and facilitates the necessary filter switches during the dual-energy scans. Dual-energy scans were done on a micro-CT scanner (Vision120, GE HealthCare). Low-energy scans were performed at 70 kVp and 50 mA, with an additional custom cylindrical Er-based [0.19 g/ml] resin (Smooth-On 321, SmoothCast) filter with a pathlength of 6 mm. High-energy scans were acquired at 90 kVp and 40 mA, with a 480 μm Cu filter. Each scan was 3 hrs, 1200 projections, 0.3° increments, 16 ms per view, and an isotropic resolution of 50 μm. Ten Teflon beads (1.58 mm) near the sample allowed for sub-voxel rigid-body fiducial registration. Decompositions were performed as previously shown by Granton *et al*., 2008.

Results: Our results demonstrate the importance of proper filtration, image co-registration, and decomposition values for ideal DECT performance. Automated acquisition of dual-energy images (Fig. 1 AB) combined with the enhanced contrast provided by our novel Er-based contrast agent (3576 ± 138 HU at low energy, 4328 ± 182 HU at high energy, Fig. 1 C), resulted in a robust and reproducible methodology for the discrete visualization of bone and perfused vasculature (Fig. 1 C) and soft tissue (not shown).

Conclusions: The successful demonstration of our combination technique (*i.e*. novel Er-based contrast agent and DECT) resulted in the decomposition of sub-voxel co-registered images into soft tissue, bone, and perfused vasculature. Apart from the obvious study of the interaction between vessels and bone in vascular/bone related diseases, this new implementation of DECT on gantry-based micro-CT scanners will open-up their capabilities for the study of soft-tissue changes in diseases related to the lung, brain, muscle, or studies that require quantitative analysis of multiple tissue components.

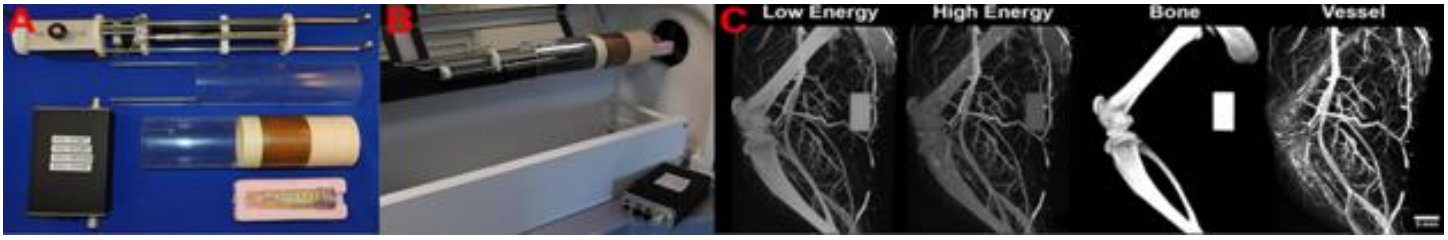

Fig. 1: (A) individual equipment pieces required for DECT; (B) DECT setup on a gantry-based micro-CT scanner; and (C) the results of DECT, resulting in automated separation into distinct volume images of Bone and Vessel.

References: **1.** Granton PV, et al. Implementation of dual- and triple-energy cone-beam micro-CT for postreconstruction material decomposition. *Med Phys* 2008;35:5030-5042.

Characterization of Bone and Soft-Tissue Structure in Developing and Aging Mice Using Micro-Computed Tomography

Joseph U. Umoh[1], P. Moon[2], K. Tyml[2], E. Tutunea-Fatan[3], R. Gros[3], M. Drangova[1,4], F. Beier[2], and D.W. Holdsworth[1,4]

Development of Novel Therapies for Bone and Joint Diseases Consortium

[1]Preclinical Imaging Research Centre, Robarts Research Institute, [2]Depts. of Physiology and Pharmacology,[3]Robarts Research Institute, [4]Depts. of Medical Biophysics and Surgery, Western University, London, ON, Canada

Introduction: Abnormal changes in bone mineral density (BMD) in human have been associated with osteoporosis. Similar changes in the tissue structure, especially in the joints, are associated with osteoarthritis. These diseases are more often linked with aging. They cause severe pain and can even hinder mobility. Studies that aim at finding therapies or implementing interventions to these diseases are ongoing[1]. Most of these studies initially start with the investigation of the BMD and tissues in small animals. The objective of this study is to characterize the BMD and tissue structure changes during the life span of a typical normal mouse.

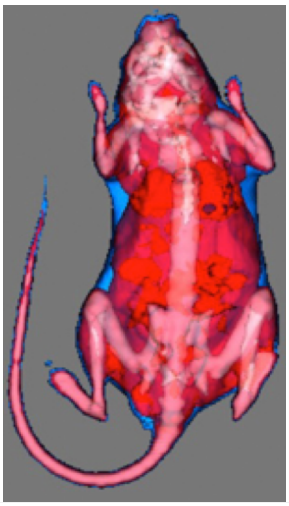

Figure 1: Micro-CT image of a mouse whole-body showing adipose (blue), lean (red), and skeletal (white) tissue.

Methods: Micro-computed tomography (micro-CT) imaging was used to acquire whole-body image data of the mice. Only wild-type male mice were used because this study focuses on describing the changes in normal mice as they age. The animals were imaged at age 0.5, 1.25, 1.5, 2, 3, 6, 8, 12, 18, 22, and 24 month. The number of mice used at those time points was 6, 8, 3, 8, 6, 5, 3, 6, 3, 7, and 10 respectively. All animals were imaged on the same micro-CT scanner (GE Locus Ultra), with the same scan protocol (x-ray tube voltage 80 kV, tube current 55 mA, 1000 projections, exposure time 16 s) and the same reconstruction parameters (154 µm 3D image voxels). Using the image data of the mice, water, and our bone-mimicking phantom (SB3), we computed BMD (expressed as mg hydroxyapatite [HA] per cm^3) and the tissue (adipose, lean, and skeletal, Fig. 1) mass as previously described[2]. Threshold grayscale values separating the adipose tissue (AT), lean tissue (LT), and skeletal tissue (ST) were -380, -30, and 190 HU respectively. Densities of AT, LT, and ST used to compute the tissue mass were 0.90, 1.05, and 1.92 g/cm^3 respectively. Density of the bone equivalent of the hydroxyapatite in the SB3 used to compute the BMD was 1.073 g/cm^3.

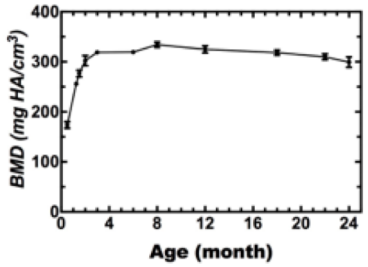

Figure 2: Plots of mean and standard deviation of mice whole-body BMD with age.

Results: BMD of the mice increases rapidly during the first three months, reaches a peak between 8 and 10 month, and gradually decreases from 12 to 24 months, so that the mean BMD (299.2 ± 10.3 mg/cm^3) at 2 years is similar to that (302.2 ± 10.2 mg/cm^3) at 2 months; and the mean BMD (318.5 ± 5.1 mg/cm^3) at 18 months is same as that (318.9 ± 3.9 mg/cm^3) at 3 months (Fig. 2). Adipose tissue mass appears to develop gradually in the first 6 months and peaks around 8 – 10 months. The skeletal tissue develops rapidly in the first 6 weeks and stays almost the same from 3 months until 2 years (Fig. 3), the final time point of our study.

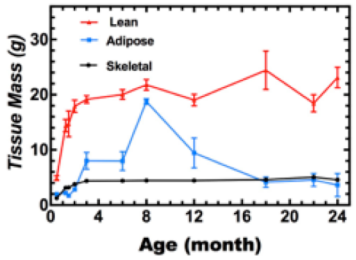

Figure 3: Plots of mean and standard deviation of mice whole-body tissue mass with age.

Conclusions: This study presents an investigation of the BMD and tissue structure through the two-year life span of typical normal mouse. The adipose tissue, followed by the BMD, appears to be more susceptible to the aging process.

References: [1] Moon *et al. J. Mol. Med* 2015; 93: 845-856. [2] Beaucage, K.L., Pollmann, S.I., Sims, S.M., Dixon, S.J., and Holdsworth, D.W. *Bone Reports* 2016; 70-80.

Registration of preoperative images for navigated brain surgery using ultrasound-accessible skull regions

Grace Underwood[1], Tamas Ungi[1], Zachary Baum[1], Andras Lasso[1], Gernot Kronreif[2], & Gabor Fichtinger[1]
[1]Laboratory for Percutaneous Surgery, Queen's University, Kingston, ON, Canada,
[2]Austrian Center for Medical Innovation and Technology, Wiener Neustadt, Austria

INTRODUCTION: Image guidance is becoming the predominant method in neurosurgery. Through real-time tracking systems, surgeons can navigate around vasculature and identify internal structures. Skull registration methods differ depending on patient orientation, and prone, facedown patient orientation presents a unique set of problems, especially with optical tracking. Optical tracking systems, are limiting as the system requires a constant line of sight [1]. Current methods of prone, facedown patient registration, result in increased registration error, inefficient workflow, or invasive procedures [2]. By utilizing tracked ultrasound, we propose a system that can access bony skull surfaces non-invasively, remove the need to collect surface points under the table, and eliminate the need to adjust the tracking camera between registration and surgical views.

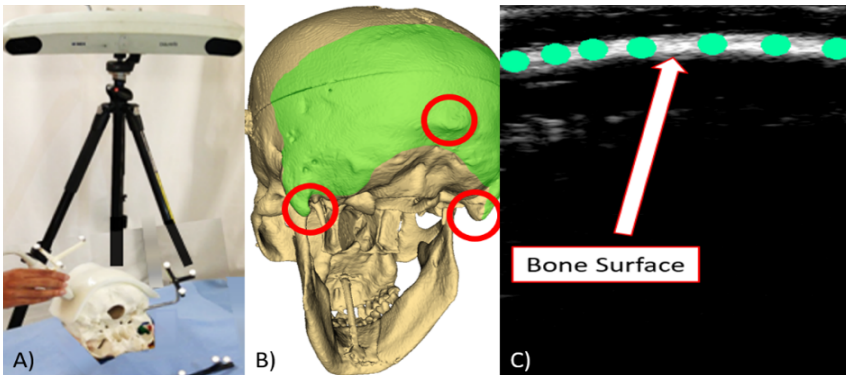

Figure 1. A) Experimental setup; B) Areas used for point collection; C) Bony surface points in ultrasound.

Trial Number	Initial registration TRE (mm)	Surface registration distance (mm)	TRE (mm)
1	2.1	0.6	1.8
2	2.4	0.5	1.6
3	2.4	0.5	1.5
4	2.4	0.7	1.5
5	3.4	0.6	1.7
Avg ± std	**2.5±0.5**	**0.6±0.1**	**1.6±0.1**

Table 1. Error metrics of registrations. TRE: Target registration error.

METHODS: The experimental setup was composed of the 3D Slicer platform, the PlusServer Toolkit, a phantom skull, a Polaris Optical Tracker, and a Telemed MicrUs ultrasound (Figure 1.A). The process proposed combines two registration methods; landmark-based and surface-based registration. The initial registration was performed using approximated anatomical landmarks around both mastoid processes, and the external occipital protuberance (Figure 1.B). A surface-based registration was then performed by selecting bony surface points in the ultrasound image (Figure 1.C), while scanning around the skull cap, the posterior base of the skull, and both mastoid processes. Using ultrasound provided more access to skull surfaces than processes utilizing a stylus. The target registration error (TRE) was measured by selecting a point within the skull and comparing the experimental registration to a ground truth registration.

RESULTS: The phantom study, exploring the feasibility of tracked ultrasound, underwent five trials (n=5), for which three different measurements were recorded. For each trial the initial registration TRE, mean surface registration distance and final TRE were recorded (Table 1). The registration method proposed had an average TRE of 1.6±0.1mm, and average surface registration distance of 0.6±0.1mm, and an average initial registration TRE of 2.5±0.5 mm.

CONCLUSION: The use of tracked ultrasound could address the problems presented in prone patient registration. Throughout all trials performed, bony surface points were collected above the table and without the need for both invasive procedures and camera adjustment. The demonstrated registration method was subject to rotational error and had minimal translational error. By exploring automated bony surface point placement and a new location for the static reference body, rotational error could be further minimized.

REFERENCES

[1] F. Kral, *et al.*, *Int J of Medical Robotics and Computer Assisted Surgery*, vol. 9, pp. 247-252, 2013.
[2] T. Ogiwara, *et al.*, *Acta Neurochir*, vol. 157, pp. 2017-2022, 2015.

Validation of radiostereometric analysis for use with reverse total shoulder arthroplasty

Madeleine Van de Kleut[1,2], Xunhua Yuan[1], George S. Athwal[4,5], Matthew G. Teeter[1,3,4,5]
[1]Robarts Research Institute, The University of Western Ontario, London, Canada
Depts. of [2]Biomedical Engineering and [3]Medical Biophysics and [4]Surgery, The University of Western Ontario, London, Canada
[5]Lawson Health Research Institute, London, Canada

Development of Novel Therapies for Bone and Joint Diseases Consortium

Introduction: Radiostereometric analysis (RSA) is a robust imaging tool for evaluating the micromotion of joint replacements [1]. It is a dual-focus x-ray technique used to determine the position and orientation of implants in 3D space to a high degree of accuracy. A calibration cage containing radio-opaque markers at known positions is placed in front of the x-ray cassettes to create a coordinate system within which implant displacements can be calculated (Figure 1). Since its approval by Heath Canada in 2003, reverse total shoulder arthroplasty (RevTSA) has grown to account for over 30% of all shoulder procedures, with its prevalence expected to increase [2]. This indicates a need for evaluation of implant fixation, as there are limited studies considering long-term survival of the joint replacement. Hip and knee implant migration within the first two years post-operatively is a predictive measure for long-term implant failure and necessity for revision. Determining whether this predictive measure is applicable to shoulder arthroplasty would greatly benefit future implant design and fixation methods. A RevTSA phantom study was therefore conducted to determine the accuracy and precision of radiostereometric analysis as a technique for evaluating implant micromotion in the shoulder.

Methods: A plastic model of the shoulder bones (Sawbones, Pacific Research Laboratories, WA, USA) was fitted with a RevTSA implant (Aequalis Ascend Flex, Tornier, MN, USA). Tantalum beads (⌀0.8 mm) were inserted in the bone surrounding the glenosphere (n = 6) and humeral stem (n = 7) at the approach angles available during surgery. A 6 degree-of-freedom translation and rotation stage (accurate to ± 0.005 mm and less than 0.02°) was used to change the pose of the phantom through fifteen known increments in translation, and twelve increments in rotation (0.02-5.00 mm and 0.1-6.0°), along each of the 6 axes. At each pose, two x-rays were taken simultaneously from different foci. Model-based RSA software (RSACore, Leiden, Netherlands) was used to locate the implant in 3D space and calculate the apparent migration at each increment (Figure 2). Apparent migration was compared to known migration, and accuracy of the system was defined as the standard deviation of the average error. Double examinations of each pose were used to determine precision, defined similarly.

Results: Accuracy was calculated as ±0.058, ±0.077, ±0.061, and ±0.068 mm for translation in the x, y, z, and resultant vectors respectively, with an associated precision of ±0.079, ±0.107, ±0.094, and ±0.148 mm. Along the rotation axes, accuracy was measured as ±0.099, ±0.130, and ±0.058 degrees in Rx, Ry, and Rz, respectively, with precisions of ±0.078, ±0.069, and ±0.066 degrees.

Conclusion: These results are comparable to, if not better than, studies validating the use of RSA for hip and knee arthroplasties (accepted as 0.05-0.50 mm) [3]. This study is the first to be performed specifically for RevTSA. A clinical trial employing RSA to detect early implant micromotion in RevTSA patients is the next step in determining the optimal standard of care for this procedure.

References: [1] Karrholm, *Acta Orthop* 1989;60:491-503. [2] Day *et al, J of Shoulder and Surg* 2015;24:766-772. [3] Valstar *et al, ISPRS J or Photogramm Remote Sens* 2002;56:376-389.

Figure 1: RSA imaging setup: two x-rays from different foci expose two radiograph cassettes; a calibration cage lies in front of the cassettes.

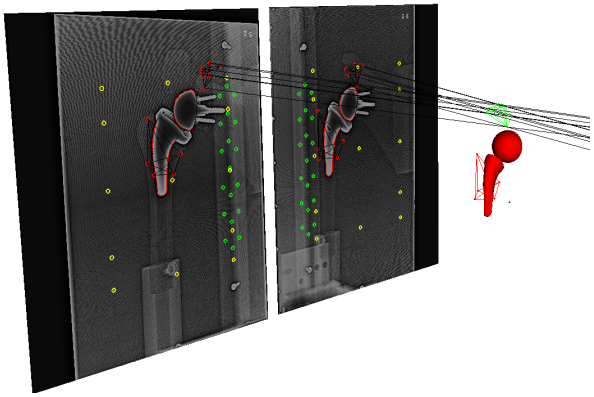

Figure 2: Location of the RevTSA implant in 3D space using a model-based RSA technique.

Image Fusion for Improved Ultrasound Mitral Valve Segmentation and Modelling

Claire Vannelli*[12], Wenyao Xia[1], John Moore[1], Terry Peters[12]

*: first author, 1: Robarts Research Institute and 2: Biomedical Engineering Program Western University, London, Canada

INTRODUCTION: With the significant increase in life expectancy over the past century, valvular heart disease has been referred to as the next cardiac epidemic and the deadliest plague facing modern medicine. Conventional open-heart cardiac surgery is often too invasive and not feasible for the aging population—a recent US study estimates the prevalence of valvular heart disease to be 2.5%, progressively increasing with age up to 13.2% at 75 years of age. Conversely, beating-heart surgery employs image-guided, minimally-invasive tools to repair and replace heart valves while minimizing procedural patient trauma. To develop these techniques, dynamic cardiac simulators are needed for testing, validation and surgical training. Patient-specific models are constructed from transesophageal echocardiography (TEE) data, used clinically to diagnose mitral valve regurgitation and disease. However, TEE images are subject to signal dropout, artefacts and low image quality which pose challenges to segmentation of valve morphology. The purpose of this study is to outline and execute a methodology for image fusion to address signal dropout and enable complete segmentation of both leaflets from patient TEE data.

METHODS: The guided filtering based fusion method follows a similar pipeline as presented by Li, *et al* (2013). An averaging filter is applied to decompose a dataset of 13 TEE short axis views into base and detail layers. To determine the weighting map, two saliency maps are constructed as complements of the estimated region of signal dropout in each image. Guided image filtering is applied to each weighting map utilizing the respective source images as a guide. Fusion by weighted averaging of the two images' base and detail layers and subsequent combination of the two fused layers yields two-scale image reconstruction. The leaflets in both the source and fused images are segmented with a continuous max-flow algorithm.

RESULTS: Pairwise fusion of two sequential slices in the TEE dataset are evaluated by visual inspection of the fused image before and after segmentation (Figure 1). As evident in Figure 1a, the anterior leaflet experiences signal dropout which results in an incomplete segmentation (Figure 1e). Upon fusion with the subsequent view in the dataset (Figure 1b), the fused image (Figure 1d) is segmented (Figure 1f) and both leaflets are clearly identified and isolated.

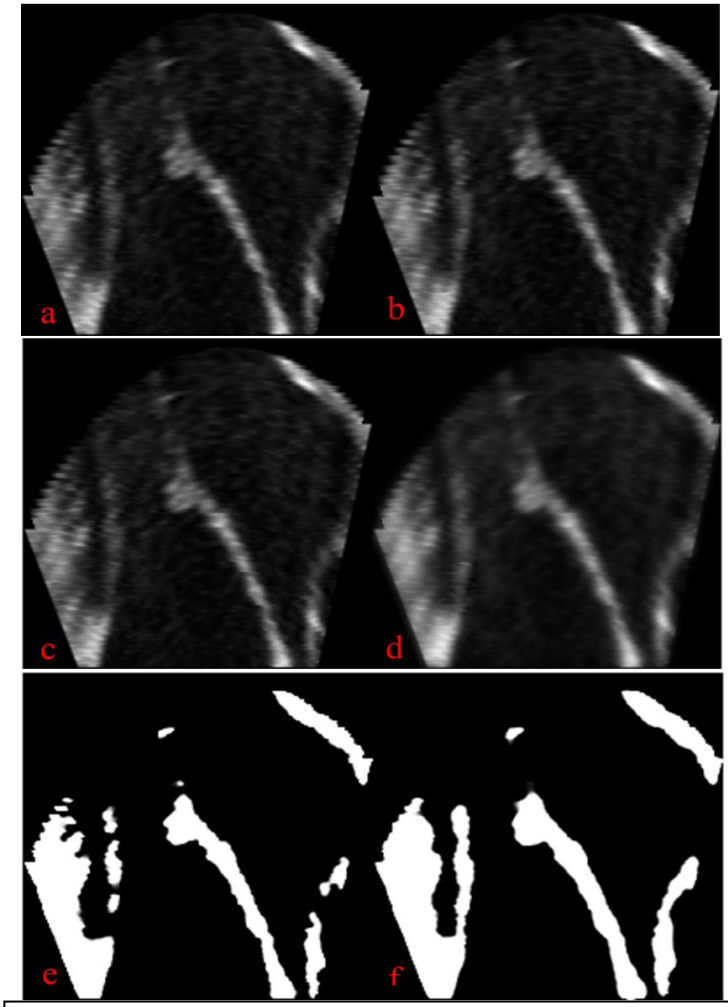

Figure 1: Short axis TEE images of the mitral valve with signal dropout before fusion (left column) compared to two fused slices (right column). a) & b) sequential views of leaflets, c) unprocessed imaging data from **a,** d) guided-filter fusion of **a** and **b**, e) segmentation of **a** f) segmentation of fused images in **d**.

CONCLUSION: The efficacy and potential for image fusion by guided filtering to improve TEE mitral valve images is made evident by these preliminary results. Future work will focus on making robust improvements to the fusion algorithm, particularly for isolating regions of signal dropout and artefacts to determine the weighting function. The improved images will be used in constructing patient-specific pre-operative models and potentially introduced into the clinical workflow for diagnoses.

Electromagnetically-generated catheter paths for breast brachytherapy

T Vaughan[1], H Brastianos[2], A Lasso[1], T Ungi[1], CB Falkson[2], G Fichtinger[1]
[1]*School of Computing, Queen's University, Kingston, Ontario*
[2]*Division of Radiation Oncology, Queen's University and Kingston General Hospital, Kingston, Ontario*
Consortium Affiliation: CANCER

INTRODUCTION: Breast conserving therapy is recommended for women with early stage breast cancer. The treatment consists of surgical removal of the tumor followed by radiation therapy. One strategy to deliver radiation therapy is multi-catheter interstitial breast brachytherapy, which involves inserting catheters through the breast then guiding radioactive sources to the tumour bed. Brachytherapy is advantageous because of its short treatment period of one week and confined area of treatment, as opposed to whole-breast irradiation which can last from three to seven weeks and exposes surrounding organs to radiation. Brachytherapy relies on accurate information about the placement of catheters to ensure appropriate radiation doses are delivered. The process of localizing catheters is usually done using CT, fluoroscopy, or ultrasound imaging, but these are difficult to interpret or they expose the patient to radiation. In this paper, we study a method for localizing catheters based on electromagnetic (EM) tracking, and evaluate it in a phantom study.

METHODS: A radiation oncology resident performed thirteen catheter insertions on two plastic phantoms (Figure) under ultrasound guidance. A small EM sensor (Figure) was fed through each of the catheters and pulled out slowly at an average rate of 5 cm per second. The PLUS toolkit [1] (www.plustoolkit.org) relayed sensor information to a navigation computer where a record of position information was kept. Least-squares polynomial curves were fit to the position information using the MarkupsToModel utility in SlicerIGT (www.slicerigt.org), a free add-on to the open-source 3D Slicer platform [2] (www.slicer.org). EM-generated catheter paths were created in this manner three times for each catheter, yielding three full sets of EM-generated paths. We evaluated these EM-generated paths against CT-generated paths, which were created by performing threshold segmentation on CT and then centerline extraction with the Vascular Modeling Toolkit (www.vmtk.org). A rigid registration was performed to align the paths and then we measured the shortest distances (error) between the EM- and CT-generated paths at uniformly-sampled points along the length of the phantom. We were evaluating the method for error lower than the 0.68 mm slice resolution of the CT scanner.

RESULTS: The mean error of EM-generated paths (Figure) was 0.38 mm, with a standard deviation of 0.13 mm. After determining that the data were normally distributed (Shapiro-Wilk test, $p < 0.001$), we performed a one-tailed one-sample t-test and determined that the error was statistically significantly lower than the slice resolution of the CT scanner ($p < 0.001$). The CT-generated path accuracy was limited by the CT resolution so we conclude that, in this study, EM-generated paths were at least as accurate as the CT-generated paths.

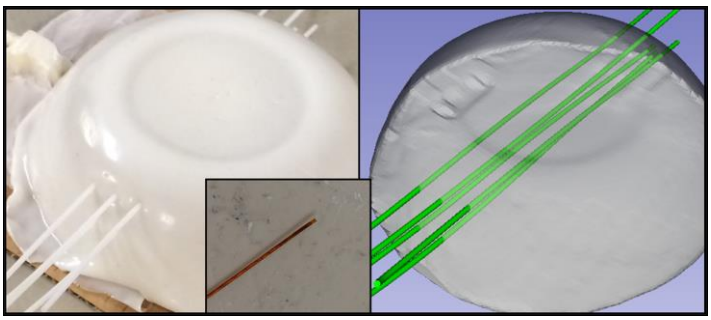

Left: Phantom. Center: EM sensor (trakSTAR model 55, NDI, Waterloo, ON). Right: EM-generated paths.

CONCLUSIONS: The EM-generated catheter paths in this study were accurate, and comparable to those generated using CT. We plan to evaluate EM-generated catheter paths further for use in clinical studies.

ACKNOWLEDGEMENTS: This work was supported in part Discovery Grants Program of the Natural Sciences and Engineering Research Council of Canada (NSERC) and the Applied Cancer Research Unit program of Cancer Care Ontario with funds provided by the Ontario Ministry of Health and Long-Term Care. Gabor Fichtinger was supported as a Cancer Care Ontario Research Chair in Cancer Imaging. Thomas Vaughan is funded by an Alexander Graham Bell Canada Graduate Scholarship (Doctoral Program).

REFERENCES: [1] Lasso *et al.* PLUS: open-source toolkit for ultrasound-guided intervention systems. IEEE TBME. 2014. 61(10):2527-37. **[2]** Pieper S, *et al.* 3D Slicer. In IEEE ISBI 2004 Apr 15 (pp. 632-635). IEEE.

Virtual views controlled by surgical tools for computer assisted interventions

T Vaughan[1], T Ungi[1], A Lasso[1], G Gauvin[2], CJ Engel[2], J Rudan[2], G Fichtinger[1]
[1]*School of Computing, Queen's University, Kingston, Ontario, Canada*
[2]*Department of Surgery, Kingston General Hospital, Kingston, Ontario, Canada*
Consortium Affiliation: CANCER

INTRODUCTION: Virtual views are commonly used in computer assisted systems to show the placement of instruments relative to target anatomy [1]. A skilled technician creates the view by aligning it with the surgeon's perspective. The surgeon and the technician typically communicate with one another and iterate on the precise placement of the view until it is satisfactory to the surgeon. This can be a lengthy process, since the operating room is a loud environment, and the technician can be confused by verbal ambiguities. Our objective was to give the surgeon direct control of the view, without complicating the procedure with additional instruments.

METHODS: In our approach, we turn a surgical instrument (*e.g.* cauterizer) into a pointing device. The virtual view is aligned with the instrument in real-time, so the surgeon can point the view wherever he or she desires and adjust it at an interactive rate. Once the view is established, the screen position of the surgical target (*e.g.* tumor) is monitored by the computer. If the surgical target moves outside the range of the screen, the virtual view will automatically pan to compensate. We are evaluating this approach in breast lumpectomies at Kingston General Hospital in Kingston, Ontario. All software was implemented in the open source SlicerIGT package (www.slicerigt.org) for the 3D Slicer platform [2] (www.slicer.org). We used the PLUS toolkit [3] (www.plustoolkit.org) to read sensor position and orientation information from our surgical instrument (cautery) and surgical target (tumor).

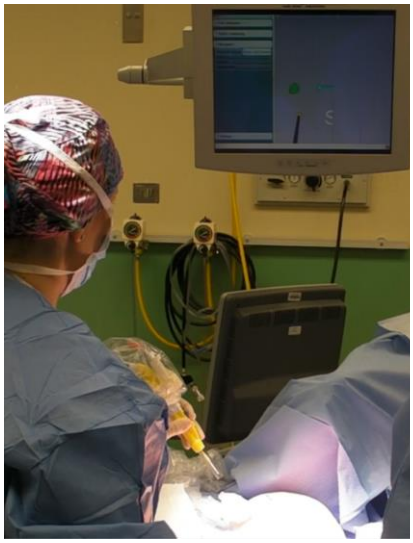
A surgeon uses a cauterizer to create a view.

RESULTS: Surgeons have used instruments to control views in 15 patient lumpectomy cases [1] so far. We later implemented the feature to monitor the screen position of the tumor and automatically pan the virtual view as necessary. This feature has been used in 12 patients so far. The regular technician for breast lumpectomies estimated that over 50 manual interactions had been eliminated per patient case.

CONCLUSIONS: We have shown that the surgeon can intuitively control virtual views in the operating room without using any extra hardware. Our approach will continue to be used in computer assisted breast lumpectomies.

ACKNOWLEDGEMENTS: This work was supported in part Discovery Grants Program of the Natural Sciences and Engineering Research Council of Canada (NSERC) and the Applied Cancer Research Unit program of Cancer Care Ontario with funds provided by the Ontario Ministry of Health and Long-Term Care. Gabor Fichtinger was supported as a Cancer Care Ontario Research Chair in Cancer Imaging. Thomas Vaughan is funded by an Alexander Graham Bell Canada Graduate Scholarship (Doctoral Program).

REFERENCES:

[**1**] Ungi *et al.* Navigated breast tumor excision using electromagnetically tracked ultrasound and surgical instruments. IEEE TBME. 2016. Available online.
[2] Pieper S, *et al.* 3D Slicer. In IEEE ISBI 2004 Apr 15 (pp. 632-635). IEEE.
[3] Lasso *et al.* PLUS: open-source toolkit for ultrasound-guided intervention systems. IEEE TBME. 2014. 61(10):2527-37.

Determining dosimetric impact of deformable image registration error in lung radiotherapy

Jason Vickress[1], Rob Barnett[1,2,3], Jerry Battista[1,2,3], Slav Yartsev[1,2,3]
Departments of [1]Medical Biophysics and [2]Oncology, Western University and
[3]London Regional Cancer Program, London Health Sciences Centre, London, Ontario

Introduction: Deformable image registration (DIR) is emerging as a tool in radiation therapy for calculating the cumulative dose distribution across multiple fractions of treatment. Unfortunately, due to the variable nature of DIR algorithms and dependence of performance on image quality, registration errors can result in dose accumulation errors. Dose accumulation errors can result in unwanted toxicities for healthy tissue and poor tumour control. In this study, landmarked images are used to characterize the DIR error throughout an image space and determine its impact on the dose distribution.

Methods: Ten thoracic 4DCT images with 300 landmarks per image study matching the 0% and 50% phases of respiration were obtained from "dir-labs" [1]. DIR was performed using commercial MIM software (version 6.5 MIM, MIM Software Inc, Cleveland, OH, USA) registering the 0% and 50% image studies. Registration error was calculated for each landmark pair as the distance between the DIR predicted position in the 50% image, and the landmark position. Dose distributions were calculated for both phases of each 4DCT study with standard IMRT plans of a 60 Gy prescription dose to 95% of the planning target volume (PTV). The range of dose uncertainty (RDU) was calculated at each landmark pair as the 5^{th} to 95^{th} percentile of the dose within a cube around the landmark in the 50% phase. The dimension of the cube was defined by a measure of DIR error which included either the actual DIR error, mean DIR error per study, constant errors of 2 or 5 mm or DIR error prediction methods inverse consistency error, transitivity error or the distance discordance metric (DDM). The RDUs were evaluated using two methods, the magnitude of dose uncertainty (MDU) and inclusion rate (IR). The MDU is the average size of the RDU in Gy and the inclusion rate is the percent of landmarks where the actual dose value lies within the RDU. DIR error prediction methods were used to calculate the RDU for every point within an image volume and produced an upper and lower bound of the dose distribution.

Results: The RDU was calculated for 300 landmark pairs on each 4DCT study for all measures of DIR error. The most representative RDU was determined using the actual DIR error with a MDU of 2.5 Gy and IR of 97%. Across all other measures of DIR error, the DDM was most predictive with a MDU of 2.47 Gy and IR of 87%, closest to the actual DIR error per study. Using the DDM the RDU was calculated at every point within a specific image study producing upper and lower bound dose distributions shown in figure 1, alongside the planned and deformed dose distributions.

Conclusions: DIR error will forever be a concern whenever highly accurate registrations are required. In our study we investigated the incorporation of registration error to determine its impact on the accumulated dose distribution presented as the RDU. Our hope is the RDU can be used with DIR to provide a practical evaluation of how the dose is accumulating during a multi-fraction treatment.

References: [1] Castillo R, Castillo E, Guerra R, et al. A framework for evaluation of deformable image registration spatial accuracy using large landmark point sets. *Phys Med Biol* 2009;54:1849-1870.

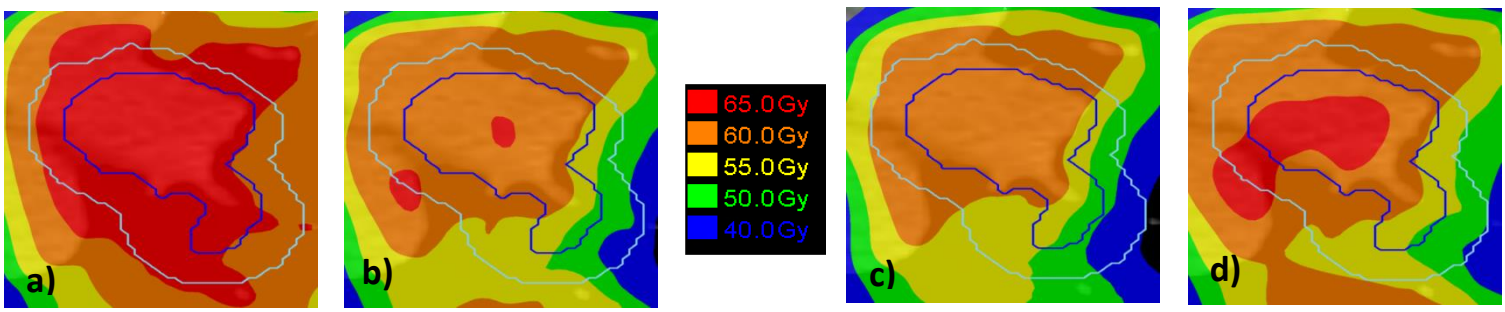

Figure 5. Distributions, of the (a) planned, (b) deformed dose, (c) lower bound, (d) upper bound of the range of dose uncertainty (RDU) calculated using DDM. Contour labels: (light blue) PTV and (dark blue) is GTV. Dose prescription was 60 Gy to 95% of the planning target volume.

Early Tumour Perfusion and Diffusion Evaluated in Multi-modal Imaging following Radiosurgery for Metastatic Brain Cancer

Xinying Wang, Brandon Driscoll, Warren Foltz, Noha Sinno, Igor Svistoun, Caroline Chung, Catherine Coolens

Radiation Medicine Program, Princess Margaret Cancer Center and University Health Network, Toronto, Ontario, Canada

Abstract

Introduction: Early change in tumour perfusion and diffusion following stereotactic radiosurgery (SRS) is a potential biomarker of response. However, efforts for quantitative model-based measures of DCE and DWI parameters have shown variable findings to-date that may reflect variability in the MR acquisition and/or analysis method. This work describes the use of a voxel-based, multi-modality GPU architecture to include various complimentary solute transport processes such as perfusion and diffusion into a common framework. This is anticipated to improve accuracy and robustness of the early imaging biomarker predictions.

Methods: Patients treated with SRS as part of REB-approved clinical trials underwent volumetric DCE-CT, DCE-MRI and DWI-MRI scans at baseline, then 7 and 20 days post-SRS. As DCE-CT is considered a good standard for tracer-kinetic validation given its signal linearity, we compared 3D pharmaco-kinetic parameter maps using a modified Tofts model (k_{trans}, v_e, V_b, AUC) from both modalities as well as the correlation between apparent diffusion coefficient ADC values from DWI-MRI and the extravascular, extracellular volume (V_e) from DCE imaging. A total of 14 tumours in 9 patients were evaluated. All imaging was co-registered to T1-Gad tumour contours and voxelwise correlations evaluated inside the GTV by Pearson correlation and Bland-Altman comparison.

Results: Voxel-wise analysis showed statistically significant correlations in K_{trans} ($P<0.001$) between DCE-CT and DCE-MRI over all imaging time points as well as excellent agreement with very little bias. Statistically significant correlations were also present between $ADC/V_{e,\ MRI}$ but a large variation was present across tumors (R^2: 0.15-0.8) and disappeared altogether when reviewing the mean ADC only hence disregarding tumor heterogeneity.

Conclusion: Utility of a common analysis platform has shown statistically higher correlations between pharmaco-kinetic parameters than has previously been reported but is highlighting the need for a better understanding of the tumor microenvironment to improve biomarker sensitivity.

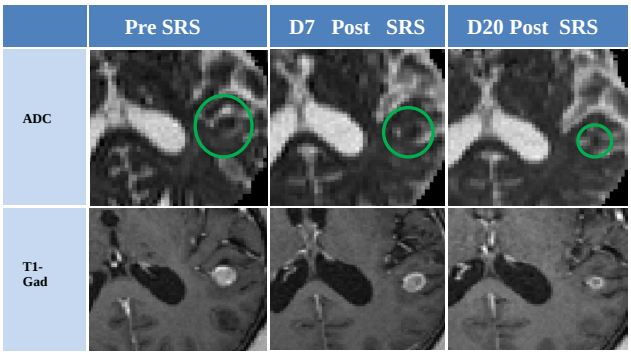

Fig.1 ADC and T1-gad Pre-Day7-Day20 post SRS for a typical tumour .

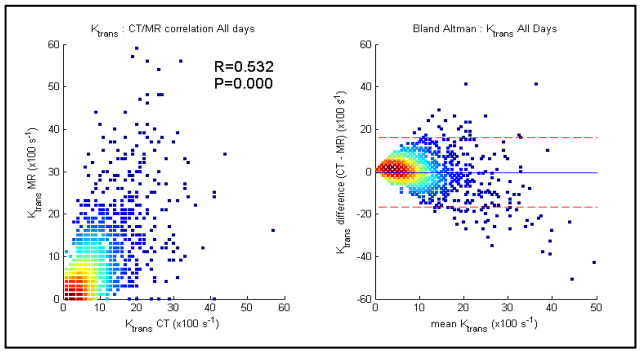

Fig.2 Correlation of CT versus MRI-based median Ktrans values

A Developing Non-contact 3D Photoacoustic Computed Tomography Scanner for Detecting Early Response to Neoadjuvant Chemotherapy in Breast Cancer Patients

Hui Wang*[1,2], Parsa Omidi[1,2], Olivia Tong[1,2], Mamadou Diop[1,2], Jeffrey Carson[1,2]
[1]The University of Western Ontario, London, Ontario, Canada
[2]Lawson Health Research Institute

Introduction: Neoadjuvant chemotherapy (NC) is often recommended in breast conserving surgery to reduce the size of the tumor before surgery [1]. Recent finding suggests that tumor blood oxygenation changes rapidly after NC. Thus, imaging methods capable of measuring tumor blood oxygenation has attracted significant interest for the purpose of detecting early chemotherapy treatment response. The purpose of this study is to build a non-contact 3D Photoacoustic Computed Tomography (PACT) scanner. The focus of this project is to develop the holographic camera (i.e., the detector of the scanner).

Methods: The holographic camera will be based on a Mach-Zehnder interferometer (Fig. 1A). The light source (laser) illuminates the surface of the object and the generated scattering lights is combined with he reference beam from the same light source. Due to the coherence, the two beams interfere and create a fringe pattern (Fig. 1B). A slight displacement of the surface of object (e.g. caused by ultrasound) will induce a shift in the fringes pattern. A high-speed camera can capture the fringes and record the shifting pattern. These shifts can be converted into surface displacements and used to reconstruct 3D image of the object as in any regular photoacoustic imaging. During the current building process, we are currently using a helium-neon laser emitting at 633nm, which will be later replaced by a pulsed laser. The laser beam is spatially filtered by a 30μm pinhole then magnified (from 1.4mm to 20mm) by a pair of biconvex lenses with diameter of 20mm and 400mm, respectively. The extended beam is divided into a reference and an object beam using a 50:50 beam splitter. Light from the object was collected by an optical lens system that also collimated the beam. A camera was placed facing the speckle pattern and record the interference patterns.

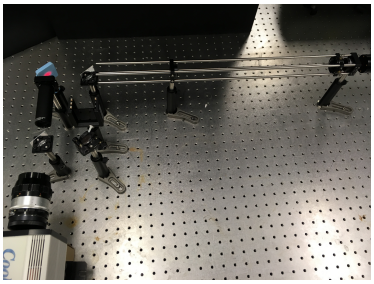

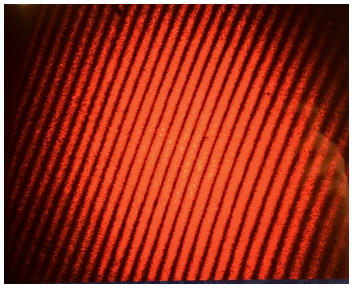

Figure 1. A: experimental setup. B: Fringe pattern generated by the interference between the reference beam and the object beam. The object was a mirror.

Results: Fig. 1B shows an interference pattern with fringes captured by the camera. By adjusting the frequency of vibration of the object, small displacements of the object' surface were generated and resulted in shifting of the fringes that could be measured by the camera.

Conclusions: The module can detect shifts in fringes pattern caused by slight displacement. The next step is to replace the idealized object (mirror) by more realistic objects such as tissue-like rubber or pork skin, to further test the system before implementing the pulsed laser and faster camera.

Reference: [1] Rebecca L. Siegel, Kimberly D. Miller and Ahmedin Jemal, *Cancer Statistics, 2015*, CA CANCER J CLIN 2015; 65:5–29.

Evaluation of a new Nonrigid-registration method using Non-local Spatio-temporal Priors on liver perfusion CT in patients with hepatic cellular carcinoma

[1]Qingguo Wang Phd, [1]Feng Su, [1]Burgers Kyle, [1,2]Ting-Yim Lee

1 Imaging, Robarts Research Institute, London, ON; 2 Imaging, Lawson Health Research Institute, London, ON

INTRODUCTION

Respiratory motion presents significant challenges for free-breathing CT perfusion which could lead to blurring of clinically definitive features such as tumors. Such blurring significantly affects detectability of tumors, accuracy of CT perfusion parameter values, and could lead to sub-optimal treatment planning. In this work, we use a new Nonrigid-registration with non-local spatio-temporal to get a stable perfusion CT data. Our aim is to evaluate the feasibility of the Nonrigid-registration method on free-breathing liver CT perfusion in comparison with standard Rigid-registration method.

METHODS

Six studies of three patients with hepatic cellular carcinoma underwent free-breathing liver CT perfusion scanning by using a 128-row CT scanner (Revolution CT, GE Healthcare, Milwaukee, WI). The original axial CT images of all studies were registered by Nonrigid-registration method using Non-local Spatio-temporal Priors (GE Healthcare, Milwaukee, WI) and standard Rigid-registration method (ANALYZE software supplied by Mayo Clinic, Rochester, MN) respectively. The CT perfusion maps (BF, BV, MTT, PS, HAF, HAP and PVP) and motion in tumor regions on images registered by Nonrigid-registration and Rigid-registration were compared.

RESULTS

The Nonrigid-registration method significantly reduced respiratory motion on whole liver region, whereas only focused tumor region can be registered well by using standard Rigid-registration in our study. All the perfusion parameters had no statistically difference between Nonrigid-registration and Rigid-registration (all *P* values > .05) (Figure 1-4).

CONCLUSION

The new Nonrigid-registration method using Non-local Spatio-temporal Priors gained better alignment on whole liver region than Rigid-registration. The Nonrigid-registration method promotes the application of free-breathing liver CT perfusion in clinical practice.

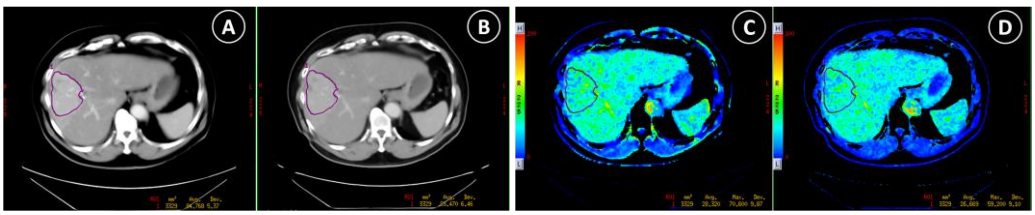

Rigid-Registration Nonrigid-Registration Rigid-Registration Nonrigid-Registration

The relationship between soft tissue balancing performed during total knee arthroplasty and postoperative tibiofemoral contact kinematics

Jared S. Webster[1,2], Dianne Bryant[3], Brent A. Lanting[2,5], Matthew G. Teeter[2,4,6,7]
[1]School of Kinesiology, Faculty of Health Sciences, Collaborative Training Program in Musculoskeletal Health Research,
[2]Bone and Joint Institute, Western University
Depts. of [3]Physical Therapy, [4]Medical Biophysics and [5]Surgery, Western University, London, Canada
[6]Robarts Research Institute, Western University, London, Canada
[7]Lawson Health Research Institute, London, Canada

Introduction: Total knee arthroplasty (TKA) is a highly successful surgical procedure designed to restore knee function and reduce pain for patients with debilitating arthritis. Despite advancements in patient care and surgical technique, nearly 20% of individuals are dissatisfied with their surgery.[1] Soft tissue balancing – an aspect of TKA surgery – serves to optimize joint kinematics and stability in flexion and extension, which cannot be accomplished through bone cuts and implant design alone.[2] The selected soft tissue balancing performed intraoperatively, whether conservative or extensive, depends on the patients' preoperative knee condition and the surgeons' professional opinion. Deviation from normal tibiofemoral kinematics has shown to increase implant component wear, which can lead to early revision surgery.[3] Previous research has shown soft tissue balancing accurately produces a mechanically balanced knee when measured intraoperatively,[4] however, little is known of the postoperative kinematic implications.

Methods: A subgroup of patients from an existing prospective cohort study who received a Triathlon Knee System (Triathlon, Stryker, Mahwah, NJ) will undergo weight-bearing biplanar radiographic imaging (radiostereometric analysis, or RSA) at least one-year postoperative. RSA images (anteroposterior and lateral directions) will be taken in 20° increments of flexion starting at 0° to their maximum attainable flexion of 100-140°. Model-based RSA software (RSACore, Leiden, Netherlands) will be used to render the 3D location of implant components. Kinematic measures of condylar liftoff, contact location, and magnitude of excursion on each condyle will be collected and analyzed (Figure 1). The extent of soft tissue balancing completed intraoperatively and clinical outcome scores will be collected and correlated to the kinematic measurements.

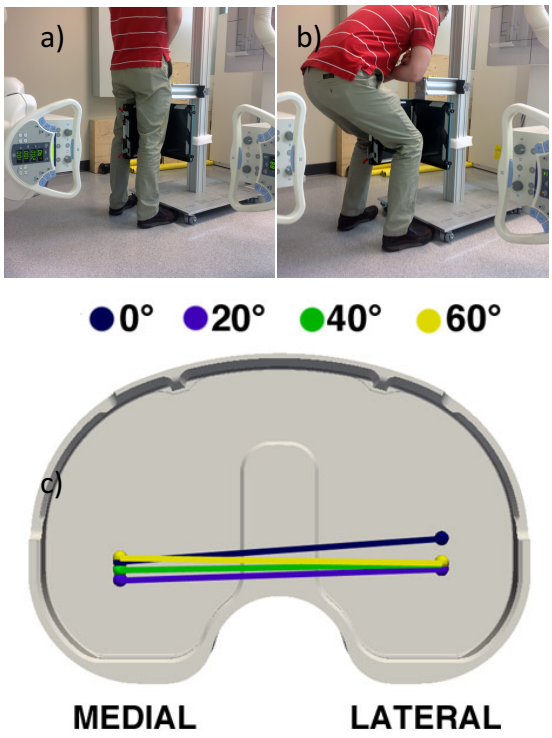

Figure 1. a) RSA trial with participant in full extension; b) RSA trial with participant in 40° flexion; and c) example depiction of the average medial and lateral condyle contact positions through 0 to 60° of flexion.

Results: Findings from this study will provide surgeons with a more complete understanding of the postoperative implications of soft tissue balancing in TKA. Correlating specific soft tissue balancing with normal or abnormal knee kinematics will allow surgeons to make more informed and personalized decisions regarding this aspect of the surgery. Ultimately we aim to further optimize the TKA procedure to prolong the lifespan of knee implants.

Conclusions: The current body of literature focused on improving patient satisfaction is limited in connecting the multiple factors associated with patient satisfaction. This research will create a previously missing link between surgical technique, knee kinematics, and patient reported outcomes to further improve upon and personalize the TKA procedure.

References: [1] Bourne, R. B., Chesworth B. M., Davis A.M., Mahomed N.N., & Charron K. D. J. Patient satisfaction after total knee arthroplasty: Who is satisfied and who is not? (2010) *Clin Orthop Relat Res*, 468, 57–63. [2] Meloni, M. C., Hoedemaeker, R. W., Violante, B., & Mazzola, C. (2014). Soft tissue balancing in total knee arthroplasty. *Joints*, 2(1), 37–40. [3] Kuster, M. S., & Stachowiak, G. W. (2002). Factors affecting polyethylene wear in total knee arthroplasty. *Orthopedics*, 25(2 Suppl), s235-42. [4] Griffin, F. M., Insall, J. N., & Scuderi, G. R. (2000). Accuracy of soft tissue balancing in total knee arthroplasty. *The Journal of arthroplasty*, *15*(8), 970-973.

Comparison of a dual-modality intravascular ultrasound and optical coherence tomography imaging catheter to each imaging modality alone using cadaveric coronary artery specimens.

Jill J. Weyers[1], Brian H. Li[2], Jonathan E. Toma[2], Natasha Alves-Kotzev[1], Wenbo Cui[1], Mark K. Harduar[3], Peter Faure[4], Anna Zavodni[5], Laura Jimenez-Juan[5], Jagdish W. Butany[4], Brian K. Courtney[2]

1 – Sunnybrook Research Institute, Department of Physical Sciences
2 – Sunnybrook Health Science Centre, Department of Cardiology
3 – Conavi Medical Inc.
4 – University Health Network, Toronto General Hospital, Department of Anatomic Pathology
5 – Sunnybrook Health Science Centre, Department of Radiology

Imaging Network Ontario Consortium: Image-Guided Device Interventions for Cardiovascular Disease

Introduction: The development of intravascular imaging devices has greatly improved our ability to visualize and diagnose the severity of atherosclerotic plaques within the coronary vasculature. Several different catheter-based modalities are currently available, but each have limitations that could potentially be overcome by using them in combination. To this end, we have built a dual-modality imaging catheter combining intravascular ultrasound (IVUS) and optical coherence tomography (OCT). IVUS imaging penetrates up to several centimeters through the vessel wall and allows differentiation of calcium from soft tissue, but it is limited by low resolution and an inability to discern soft tissue types. OCT, on the other hand, has lower tissue penetration but higher resolution, and allows discrimination of fatty vs fibrous soft tissues. These complementary pros and cons make IVUS and OCT an attractive combination. We are now testing the hypothesis that IVUS and OCT together are able to provide superior visualization of intracoronary plaque composition than either modality alone.

Methods: We have built a dual-modality imaging device that combines IVUS and OCT within a 3F intravascular catheter. The imaging transducers are aligned to simultaneously image the same point on the vessel, providing immediate registration of the two images. To test the imaging capabilities of this catheter, coronary arteries were harvested at autopsy from patients 35 years or older and transversely sliced into 3 cm segments. Each vessel segment was imaged ex-vivo using our IVUS-OCT catheter. Vessels showing interesting plaque formations were processed for histology, with sections being cut at 250 μm intervals and stained with hematoxylin and eosin. IVUS and OCT images were then extracted from pull-back video files at points corresponding to the histological sections, and all three images (IVUS, OCT, and histology) were aligned using custom Matlab scripts.

Results: Sixty vessel segments, arising from 23 vessels from 10 different hearts have been processed. The resulting images have been collected into a large database consisting of IVUS alone, OCT alone, and IVUS-OCT pairs. Images were randomized and interpreted by blinded cardiologists to determine what plaque features were visible within each image. These results were then correlated with matching histology images, which represents the gold standard for identifying plaque characteristics. The accuracy of each image set (IVUS, OCT, or IVUS-OCT paired) will be determined to see which format provides the best ability to ascertain plaque composition.

Conclusions: Our dual-modality imaging catheter generates co-registered images of IVUS and OCT. Together these two imaging modalities provide complementary information regarding plaque composition within coronary vessels.

Implementation of a parallel processing pipeline of multi-channel phase data

Timothy M Whelan,[1] Martyn L Klassen,[1] Igor Solovey,[1] Junmin Liu,[1] and Maria Drangova[1,2]
[1]Imaging Research Laboratories, Robarts Research Institute, London, ON, Canada
[2]Dept. of Medical Biophysics, Schulich School of Medicine & Dentistry, Western University, London, ON, Canada

Introduction: Evidence exists to show that phase unwrapping performed before channel combination results in fewer artifacts than when phase unwrapping occurs after channel combination (1,2). Performing pre-channel processing increases the disk storage, memory, and computation requirements by orders of magnitude. Routine research and clinical practice require reconstructed data to be available for visualization on a time scale similar to the acquisition time. We have implemented an efficient pipeline employing non-iterative phase unwrapping (3) and channel combination (1). The pipeline links the scanner to a DICOM server, where final combined images are displayed, while preserving metadata.

Methods: *The established pipeline (on the right)* begins with an algorithm in the scanner's reconstruction environment that results in complex channel images being sent, via a dedicated 1 Gb link, to a transfer node which saves the data in ISMRMRD (4) format on an off-line computing platform. A configuration file is generated from a template and the files are passed to a Gadgetron (5) instance. Phase is unwrapped using the PUROR method (3), high-pass filtered then all echoes of a single slice are collected to perform the channel combination by calculating the inter-echo variance on a pixel-by-pixel basis and using it as the weighting factor (1). The channel phase data are further processed to calculate local frequency shifts (LFS). Finally, the pipeline saves the combined channel phase and LFS images in DICOM format, preserving the relevant metadata, and transfers them to a DICOM server for viewing and analysis.

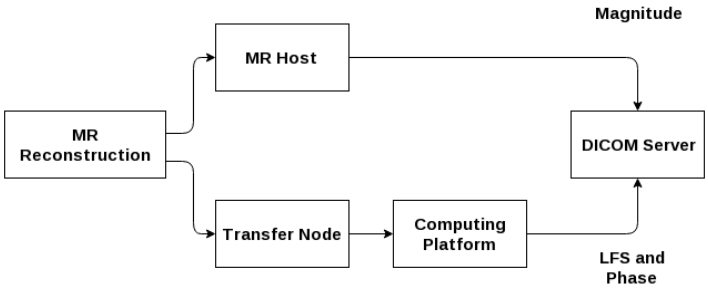

Implementation: The pipeline was implemented in C++ and parallelized using the OpenMP library. To ensure cross-platform compatibility the Gadgetron network transfer protocol was modified to transform data to network byte order for all communication.

Evaluation: The accuracy and robustness of the ISMRMRD/Gadgetron processing was compared to a verified implementation of the same algorithms in MATLAB. A range of data sets with different number of echoes and slices were evaluated. The processing times were also measured.

Results: The figure on the right is a comparison of a single LFS map calculated via the pipeline and by MATLAB. The images are nearly identical, with an average absolute difference of <1 Hz within the brain. For a 15.6 GB data set (58 channels, 96 slices, 10 echoes) the pipeline processing time was 230 s, compared to 3088 s using MATLAB. A similar time reduction was achieved with a smaller data set (3.1 GB, 14 channels, 80 slices – 52 s with the pipeline and 506 s with MATLAB).

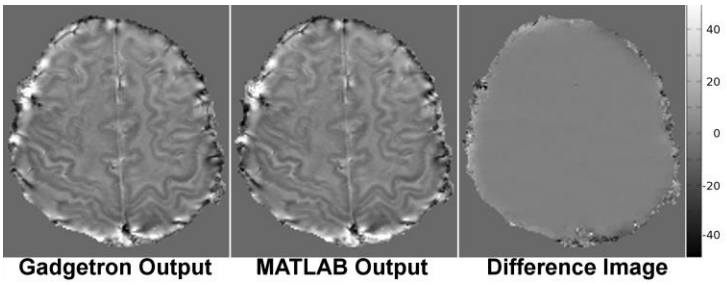

Units in Hertz

Conclusion. The implemented pipeline successfully calculates quantitative maps via channel-by-channel processing of phase data in times that are comparable to the scan time. Quantitatively, agreement with the "gold standard" MATLAB results was excellent and the calculations were achieved in a fraction of the processing time.

References. [1] Liu J, Rudko DA, Gati JS, Menon RS, Drangova M. Inter-echo variance as a weighting factor for multi-channel combination in multi-echo acquisition for local frequency shift mapping. Magn Reson Med. 73(4):1654-1661. 2015 [2] Hosseini Z, Liu J, Solovey I, Menon RS, Drangova M. Susceptibility-weighted imaging using inter-echo-variance channel combination for improved contrast at 7 tesla. J Magn Reson Imaging. 2016 (epub) [3] Liu J, Drangova M. Intervention-based multidimensional phase unwrapping using recursive orthogonal referring. Magn Reson Med. 68(4):1303-1316. 2012 [4] Inati SJ, Naegele JD, Zwart NR, et al. ISMRM Raw data format: A proposed standard for MRI raw datasets. Magn Reson Med. 2016 [5] Hansen MS, Sorensen TS. Gadgetron: an open source framework for medical image reconstruction. Magn Reson Med. 69(6):1768-1776. 2013

Assessing Health Through the Ages: Imaging and the Bioarchaeology of Tuberculosis

Renee. M Willmon[1,2]

1. Department of Anthropology, Western University
2. Laboratoire d'Anthropologie Biologique, École Pratique des Hautes Études
Research Supervisors: Dr. Andrew Nelson[1] and Dr. Olivier Dutour[2]

Introduction: Tuberculosis (TB) was one of the greatest contributors to human mortality in the past, and has recently re-emerged as a global threat to health. While the modern clinical and social impact of TB is well understood, the evolutionary origins and effects of the disease in the past are unclear. Paleopathology situates the study of human remains within their archaeological and cultural context to draw connections between the biological manifestations of disease with a broader understanding of human life. Particularly in the case of tuberculosis, a disease that manifests itself in the skeleton, paleopathology is able to contribute to our current understanding of the disease by offering significant time depth, and an understanding of the full potential effects of the condition un-hindered by pharmacologic therapy. A long-standing problem in paleopathology has been the challenge of examining hidden features within human remains. Externally recognizable changes in size, shape and texture of bone are useful to draw conclusions about life in the past, yet they represent only a small part of the data available from each specimen. Microscopic techniques are destructive, which not only significantly limits the amount of information that can be gathered from the specimen, but also poses ethical challenges when negotiating with the descendants of the individual(s) being examined, and considering the possibility for future researchers to study the specimens at hand. The objective of this research is to investigate the utility of three-dimensional imaging to improve the differential diagnosis of skeletal lesions in paleopathology, focusing specifically on lesions affecting human vertebrae that are commonly attributed to TB.

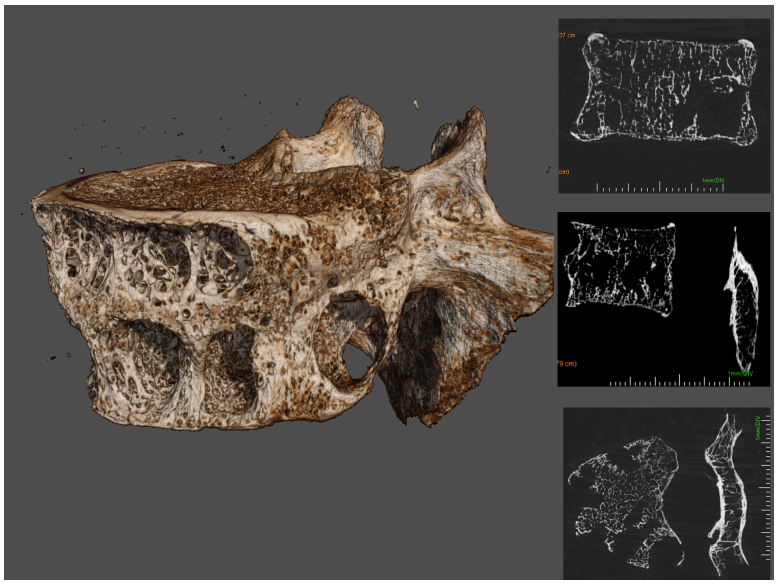

Figure 1: Micro-CT images of human thoracic vertebra affected by actinomycosis.

Methods: Computed tomography (CT) and micro-CT were used to analyze archaeologically recovered human remains in order to tailor imaging techniques for use in paleopathological studies of disease-altered bone. Eight human vertebrae affected by pathological conditions commonly considered in a macroscopic differential diagnosis of skeletal tuberculosis including brucellosis, actinomycosis and tuberculosis were scanned using a range of clinical, pre-clinical and industrial CT scanners. Qualitative methods of analysis commonly applied in bioarchaeology were adapted and incorporated with image analysis to develop guidelines on imaging in bioarchaeology, and determine the extent to which imaging can aid in the specific diagnosis of infectious disease.

Results and Conclusions: The basis of paleopathological analysis often rests on descriptive analysis. Imaging and 3D analysis contributed to the analysis of pathological alterations by offering non-destructive access to the bone's interior structures. This permitted more accurate qualitative description and quantitative analysis of lesion number, size and distribution, as well as comparison of volume ratios between affected bones. Clinical CT offered many benefits in terms of assessing and reconstruction the pathological process resulting in lesion appearance, however higher resolution achieved using micro-CT was required to detect more subtle signs of physiological progression of disease and assess trabecular variables.

Improved Glutamate Detection in the Brain at 7T Using Long Echo-Time ^{1}H-MRS

Dickson Wong, BEng, Amy Schranz, BMSc, and Robert Bartha, PhD (Research Supervisor)
Centre for Functional and Metabolic Mapping (CFMM), Robarts Research Institute, and
Department of Medical Biophysics, Western University, London, Ontario, Canada

Introduction: The J-coupled metabolite glutamate, measured in the brain by in-vivo proton magnetic resonance spectroscopy (^{1}H-MRS), is an important neurotransmitter that has been shown to be altered in neurological conditions such as Alzheimer's disease [1]. At ultra-high magnetic fields (e.g. 4T, 7T), greater signal to noise ratio and spectral dispersion leads to better separation of the glutamate and glutamine resonances, increasing quantification accuracy and precision [2,3]. However, high field ^{1}H-MRS suffers from increased chemical shift displacement error, B_1 inhomogeneity, power deposition, and shorter T_2* relaxation. The semi-LASER (localization by adiabatic selective refocusing) sequence [4,5] overcomes several of these limitations by using high-bandwidth low-amplitude adiabatic full passage (AFP) refocusing pulses that are insensitive to B_1 inhomogeneity. To detect and measure J-coupled spin systems using ^{1}H-MRS, the shortest achievable echo-time is normally used to minimize signal modulation due to J-evolution and T_2 relaxation. However, in the semi-LASER sequence, the adiabatic refocusing pulses must be made relatively long to stay within power deposition limits; typically requiring echo-times in the 38-50 ms range at 7T [6,7]. This shortest achievable echo-time is not optimal for glutamate detection. The purpose of this work was to determine the optimal echo-time for glutamate detection at 7T using semi-LASER.

Methods: The optimal echo-time for glutamate detection was estimated by time-domain simulation. Density-matrix simulations of glutamate at 7T were preformed using the PyGAMMA software library [8]. The radiofrequency pulses of a semi-LASER sequence with a 4 ms asymmetric excitation pulse, 8 ms HS4-R25 AFP refocusing pulses [5], and echo-times ranging from 37 ms to 270 ms (1 ms step-size) were simulated. T_2 effects [9, 10, 11] were also modelled. Signal energies $\left(\int |FID(t)|^2\, dt\right)$ of the simulated time-domain glutamate signals were measured as an indicator of glutamate signal strength.

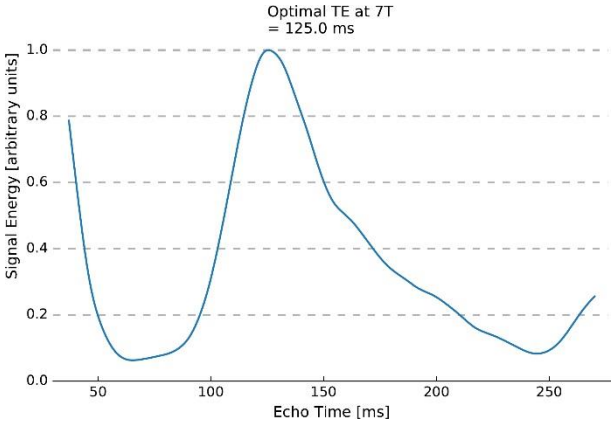

Figure 1: Energy of simulated glutamate signals at 7T as a function of echo-time.

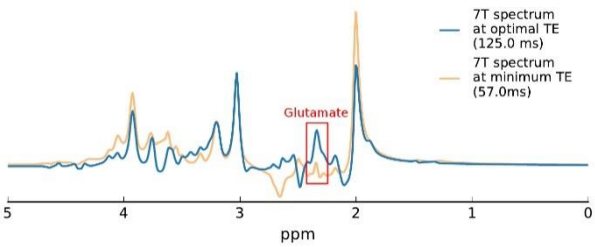

Figure 2: Comparison of simulated semi-LASER spectra at the optimal echo time (125 ms) and at the shortest achievable echo time on our 7T Siemens head-only scanner (57 ms). Note that macromolecular resonances were not included in the simulations.

Results: The optimal echo-time was found to be 125 ms (Figure 1). This echo-time produced a larger glutamate signal energy than the shortest achievable echo-time suggested in literature (35-50 ms [6,7]) and currently available on the 7T Siemens MAGNETOM head-only MRI at CFMM (57 ms). Simulated spectra (Figure 2) at 57 ms and 125 ms demonstrate a 3-fold difference in the glutamate multiplet signal at 2.3 ppm.

Conclusion: The current practice in ^{1}H-MRS is to use the shortest achievable echo-time to maximize the signal of J-coupled metabolites, including glutamate. However, this approach is sub-optimal for glutamate detection at 7T using semi-LASER, where echo-times below 40 ms are difficult to achieve. Instead, the optimal echo-time for glutamate detection is likely close to 125 ms. In-vivo measurements in multiple subjects and brain regions are needed to verify this result. Using a longer echo-time has the added benefit of reducing signals from macromolecule resonances that complicate quantification at short echo-times. Optimal glutamate detection with semi-LASER at 7T is important for the study of brain physiology and neurological conditions such as Alzheimer's disease, in which glutamate plays a major role.

[1] Rupsingh *et al.* Neurobiology of Aging 2011;32(5):802-10, [2] Bartha *et al.* Magnetic Resonance in Medicine;44(2):185-192, [3] Tkác *et al.* Magnetic Resonance in Medicine 2009;62(5), 868-879, [4] Öz *et al.* Magnetic Resonance in Medicine 2011;65(4), 901–910, [5] Garwood *et al.* Journal of Magnetic Resonance 1997;153(2), 155-177, [6] Penner *et al.* Magnetic Resonance in Medicine 2014;12(1), 4-12, [7] Scheenen *et al.* Magma 2008;27(1-2), 95-10, [8] Smith *et al.* Journal of Magnetic Resonance 1994;106(1), 75-105, [9] Marjanska *et al.* NMR in Biomedicine 2012;25(2), 332-339, [10] Andreychenko *et al.* NRM in Biomedicine 2013; 25(11), 1596-1601, [11] Kreis *et al.* Magnetic Resonance in Medicine 2005;54(4), 761-768

Assessing Reperfusion in Ischemic Stroke Patients using CT Perfusion after Successful Intra-Arterial Therapy

Consortium: Brain – Clinical Studies
Authors: Eric Wright[1] (primary author), Christopher d'Esterre[2], Enrico Fainardi[3], Ting-Yim Lee[1] (research supervisor)
[1]Department of Medical Biophysics, University of Western Ontario, London, Ontario, Canada
[2]Department of Radiology, Foothills Medical Center, University of Calgary, Calgary, Alberta, Canada
[3]Neuroradiology Unit, Azienda Ospedaliera-Universitaria Careggi, Florence, Italy

Introduction: Results from the EXTEND-IA, ESCAPE and MRCLEAN trials revealed intra-arterial therapy (IAT) is superior to IV-tPA alone for patients with large vessel occlusions. Success of recanalization is judged using the modified thrombolysis in cerebral ischemia (TICI) scale on post-treatment digital subtraction angiography (DSA) images – with scores of 2b or 3 indicating successful recanalization. However, recanalizing blocked arteries does not always lead to reperfusion of the ischemic tissue or good functional outcomes (mRS $\leq$ 2). In three major IAT clinical trials, ~17% of IAT-treated patients had TICI scores of 2b or 3 but still suffered poor clinical outcomes. It is possible that post-procedural CT Perfusion (CTP) could help identify patients who may have poor functional outcomes due to incomplete tissue reperfusion after IAT. The objective of this study is to determine the association between reperfusion and outcome in a group of IAT-treated ischemic stroke patients with post-procedural TICI scores of 2b or 3.

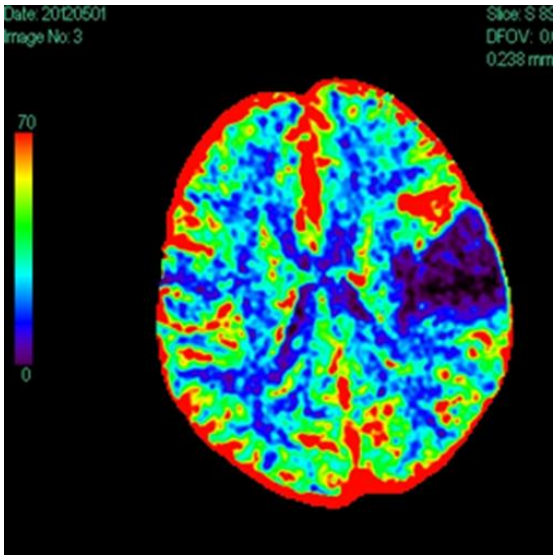

Figure 1: Cerebral blood flow map from an IAT-treated ischemic stroke patient 24hr post symptom onset showing a large volume of ischemic tissue despite successful recanalization (TICI score = 3).

Methods: Ischemic stroke patients treated with IAT received admission and 24hr follow-up CTP, post-procedural DSA, and 3-month mRS evaluation. Ischemic tissue volume was quantified on admission and 24hr CTP images using time-to-max (Tmax) thresholds from our group's prior research. The difference in ischemic tissue volume from admission to 24hr post relative to the admission volume was used to quantify reperfusion scores. The association between good functional outcome and reperfusion score was evaluated using logistic regression and ROC analysis.

Results: Approximately 30.5% of the patients in our database had poor functional outcomes despite having post-procedural TICI scores of 2b or 3. The mean reperfusion scores for patients with good (n = 8) and poor (n = 10) functional outcomes were 0.94 ± 0.02 and 0.69 ± 0.11 respectively. ROC analysis was performed to find a threshold reperfusion score for separating patients with good or poor functional outcomes. The reperfusion score threshold that corresponded to the optimal operating point of the ROC curve was 0.85, the sensitivity and specificity of this threshold were 0.70 and 0.75 respectively.

Conclusions: CTP may help identify patients who in future will report poor functional outcomes due to impaired tissue reperfusion after IAT.

Title: The Impact of Diabetes Mellitus on Global Myocardial Flow Reserve in the Presence of Epicardial Coronary Disease

Kai Yi Wu, Nicholas Timmerman, Rachel McPhedran, Rob Beanlands, Robert deKemp, Aun-Yeong Chong, ORF Heart Failure: Prevention Through Early Detection Using New Imaging Methods project, University of Ottawa Heart Institute, Ottawa, Canada

Introduction: Diabetes mellitus (DM) is associated with diffuse atherosclerosis and microvascular dysfunction which may impact measurement of flow and revascularization therapies. The impact of diabetes-related microvascular dysfunction in the presence of epicardial disease is not well known. We sought to determine if myocardial flow reserve (MFR) by ^{82}Rb positron emission tomography (PET) is reduced in patients with DM across the spectrum of coronary artery disease (CAD).

Methods: 252 consecutive patients (63.9 ± 10.6 years, 181 males, 101 DM) who had both ^{82}Rb PET and invasive coronary angiography within 6 months were included. Global MFR in the entire left ventricle (LV) was calculated using FlowQuant. To account for the effect of multiple and diffuse epicardial lesions, vessel segments were assigned SYNTAX scores multiplied by the % stenosis, and summed to generate territory-specific SYNTAX-weighted Scores (SWS). Stepwise multiple linear regression was used to evaluate the relationship between global MFR and total SWS, DM status, rate pressure product (RPP), LV ejection fraction (EF), sum stress score (SSS), ischemic ECG response, age, sex, BMI, angina status, smoking history, and the presence of hypertension, dyslipidemia, family history of CAD, and previous revascularization.

Results: Global MFR was reduced by 0.167 in patients with DM compare to non-DM with similar epicardial stenosis.

Conclusion: DM is associated with reduction in MFR independent of other risk factors and epicardial CAD, and therefore should be considered in the clinical interpretation of PET perfusion.

A combinational 3D ultrasound image segmentation approach with spatial coherency constraint for patient specific dynamic mitral valve model

Wenyao Xia[1, 2], Olivia Ginty[1], Yuanwei Xu[1], John Moore[1], Terry Peters[1, 2]

[1.] Imaging Research Laboratory, Robarts Research Institute

[2.] Medical Biophysics Graduate Program, Western University, London ON

Background:

Moderate to severe valvular disease is estimated to affect 2.5% of the general population, with mitral valve (MV) regurgitation being the most prevalent form of the disease. However, due to the complexity of mitral valve repair, almost one-third of patients develop recurrent moderate or severe mitral regurgitation (MR). Thus, in VASST lab at Robarts Research Institute, our research group is developing a patient- or pathology-specific model for pre-operative planning and training in unique, complex MV repairs.

Objective:

In order to produce an accurate and representative physical model, it is crucial to first establish a virtual model using image segmentation technique based on patient transesophageal echocardiography (TEE) data. However, due to the nature of ultrasound imaging, the obtained images are very noisy and often suffer from severe signal dropout, which affects the segmentation accuracy significantly. In this study, we propose a more robust algorithm for mitral valve segmentation on ultrasound images, which corrects for local signal dropout.

Method:

First, we combine the existing state-of-the-art approaches by using the segmentation result obtained from continuous max flow graph cut (CMF graph cut) as the initialization for the active contour method. Then, a novel spatial coherence constraint is imposed to correct possible mis-segmentation due to corrupted images and signal dropout. The spatial coherence constraint is primarily based on the number of disconnected components from the segmentation binary map. Since the spatial coherence constraint is not differentiable, a real-time solution is also proposed to find the approximated solution.

Results:

As shown in the figure below, the proposed method demonstrates superior performance over the existing segmentation algorithms. The proposed algorithm is able to detect regions affected by signal dropout and correct the segmentation results based on neighboring slides. This improves the segmentation accuracy and eliminates holes on the mitral leaflets during 3D reconstruction with no significant increase to the computational time.

Conclusion:

In this study, we proposed a robust ultrasound image segmentation for the mitral valve. The proposed method requires minimum user interaction and it is proven to be very robust when applied to low quality images with heavy signal loss. The segmented volume is then 3D reconstructed and 3D printed as a physical dynamic mitral valve phantom. The phantom's performance is compared and validated with real patient data with good resemblance.

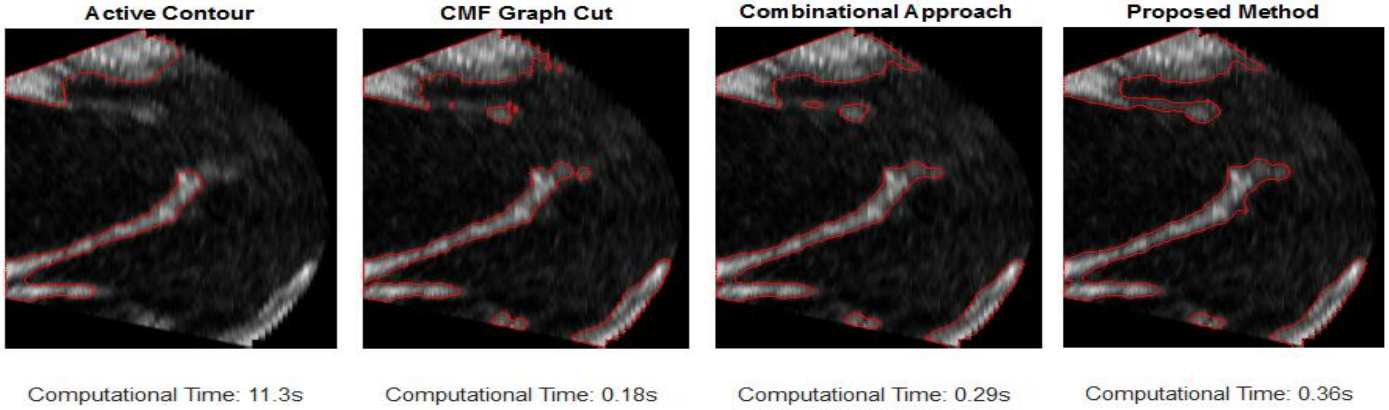

Automated vascular segmentation, reconstruction, classification and simulation on whole-slide histology

Yiwen Xu[1,2], J. G. Pickering*[2,3], D. Goldman[2], Z. Nong[3], J. S. Elkerton[1], A. D. Ward*[1,2,4]

Ontario Institute for Cancer Research - Smarter Imaging Program * Supervisors

1. Baines Imaging Research Laboratory, London Regional Cancer Program,

2. Dept. of Medical Biophysics, 3. Robarts Research Institute, 4. Dept. of Oncology, Western University

Background: Histology of the microvasculature depicts detailed characteristics relevant to tissue perfusion. One important histologic feature is the smooth muscle component of the microvessel wall, which is responsible for controlling vessel caliber. Abnormalities can cause disease and organ failure, as seen in hypertensive retinopathy, diabetic ischemia, Alzheimer's disease and improper cardiovascular development. However, assessments of smooth muscle cell content are conventionally performed on selected fields of view on 2D sections, which may lead to measurement bias. As well, microvessels are inherently 3D and include both the arterial and the venous sides. Therefore, there is a need for 3D reconstruction and separate analysis for different vessel types. We have developed a software platform for automated (1) 3D vascular reconstruction, (2) detection and segmentation of muscularized microvessels, (3) classification of vascular subtypes, and (4) simulation of function through blood flow modeling. We have applied this platform to the detection and measurement of differences between normal and regenerated vascular smooth muscle.

Methods: Vessels were immunostained for smooth muscle α-actin using 3,3'-Diaminobenzidine and the nuclei were stained with hematoxylin, assessing both normal (n = 9 mice) and post-ischemia regenerated vasculature (n = 5 at day 14, n = 4 at day 28). 2D locally adaptive segmentation [1] involved vessel detection, skeletonization, and fragment connection. 3D reconstruction was performed using our novel nucleus landmark-based registration. [2] Arterioles and venules were categorized using supervised machine learning based on texture and morphometry. [3] Simulation of blood flow for the normal and regenerated vasculature was performed at baseline and during demand based on the structural measures obtained from the above tools.

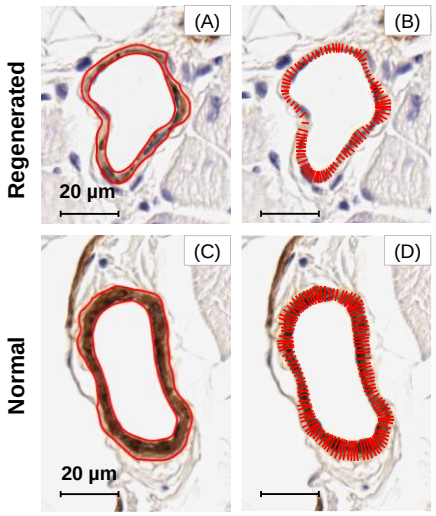

Figure 1: Contours (A, C) and thickness (B, D) of normal and regenerated vessel smooth muscle.

Results: Vessel medial area and vessel wall thickness were found to be greater in the normal vasculature as compared to the regenerated vasculature ($p < 0.001$) and a higher density of arterioles was found in the regenerated tissue ($p < 0.05$). Validation showed: a Dice coefficient of 0.88 (compared to manual segmentation) for the vascular smooth muscle segmentations (Fig. 1), a 3D reconstruction target registration error of 4 µm, and area under the receiver operator curve of 0.89 for vessel classification. We found 24% and 18% decreases in the blood flow through the network for the regenerated vasculature during increased O_2 demand as compared to the normal vasculature, respectively for 14 and 28 days post-ischemia (Fig. 2).

Conclusions: We developed an automated system to assess the arteriolar smooth muscle in the microvasculature, which allows for high throughput analysis of digital histology images and flow simulation. With microvascular measure visualization methodologies in 3D and automated segmentations, we are now capable of locating focal pathologies on a whole slide level using 3D histology reconstruction, and performing separate analyses on the arteriolar side of the microvascular tree.

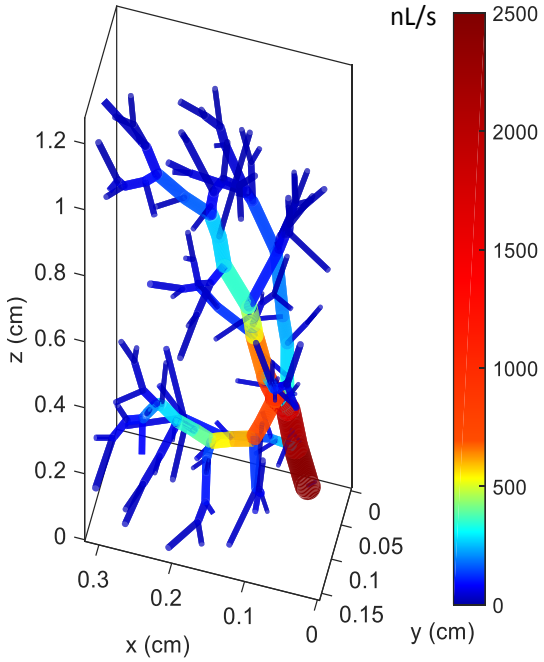

Figure 2: Simulated blood flow in the normal arteriole network modeling the demand response.

[1] Y Xu et al, Journal of Microscopy, In press.
[2] Y Xu et al, Plos One 2015.
[3] J Elkerton, Y Xu et al, Journal of Medical Imaging. In press.

Return to Program

Quantification of tumor localization needle displacement prior to tumor excision in navigated lumpectomy

Christina Yan[1], Tamas Ungi[1], Gabrielle Gauvin[2], Doris Jabs[3],
Andras Lasso[1], Jay Engel[2], John Rudan[2], Gabor Fichtinger[1]

[1]Laboratory for Percutaneous Surgery, Queen's University, Kingston, Ontario Canada
[2]Department of Surgery, Queen's University, Kingston, Ontario Canada
[3]Department of Radiology, Queen's University, Kingston, Ontario Canada

Consortium: Cancer

Introduction. Early stage breast cancer is typically treated with lumpectomy. Lumpectomy is preferred over mastectomy for cosmetic reasons. A current challenge with lumpectomy is optimizing cosmetic appearance while ensuring full tumor resection, as pre-operative imaging is not always sufficient to determine the tumor's location. Electromagnetic tracking can be used to monitor tumor position using a localization needle during surgery. The tracked needle is stabilized in the tumor with tissue locking wire hooks, which are deployed once the needle is inserted. The localization needle may displace from its initial position of insertion which provides false spatial information about the tumor position and increases the probability of an incomplete resection. In this work, we offer a quantitative investigation of the role of mechanical forces on the magnitude of needle displacement prior to tumor resection. These mechanical forces can deform the breast; deformations are strongest when ultrasound scanning motions are performed while creating a 3D tumor model for navigated lumpectomy. This can cause the tracking needle to slip out of the tissue by decompressing the stabilizing wire hooks.

Methods. Ten ultrasound scans were obtained from lumpectomy procedures, and were performed immediately before tumor resection to measure needle displacement. Needle position was approximated by the distance between the needle tip and the tumor boundary on a 2D ultrasound image, and needle displacement was defined by the change in position. Ultrasound scans were collected with a Sonix Touch (Analogic Corp., Peabody, MA, USA) ultrasound scanner, and tracking data was acquired through the Ascension 3D trakSTAR and Model 800 electromagnetic sensors (NDI, Waterloo, ON, Canada). Tumor location marked with the DuaLok hooked needle (Bard Biopsy, Tempe, Arizona, USA). The angle between the localization needle and the coronal plane was computed in an open-source software platform.

Results. A significant relationship ($p = 0.04$) was found between the needle to coronal plane angle and increased needle displacement. Needles inserted vertically, pointing towards the operating room ceiling, tended to exhibit greater needle displacement. Average needle displacement was 1.7 ±1.2 mm and maximum needle displacement was 4.5 mm.

Conclusion. Needle to coronal plane angle has been shown to affect needle displacement, and should be taken into consideration when inserting the localization needle. Results suggest that inserting the localization needle horizontally may reduce needle displacement. Future works can be directed towards investigating tools that eliminate the bulk and weight of the electromagnetic sensor clip to the tumor tracking needle, or replacing the tracking needle entirely with a flexible guidewire that has an electromagnetic sensor in the wire tip. Improving the clinical workflow and the mechanical design of the localization needle to reduce slippage during surgery are other areas for improvement.

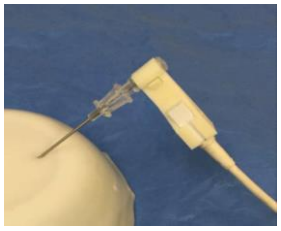

Figure 1: Electromagnetic sensor on tracking needle.

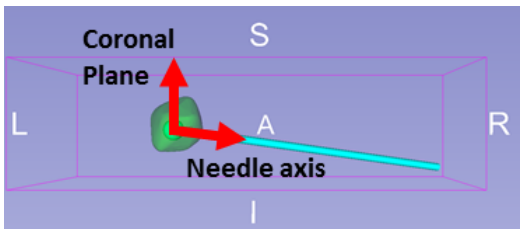

Figure 2: Needle to coronal plane angle.

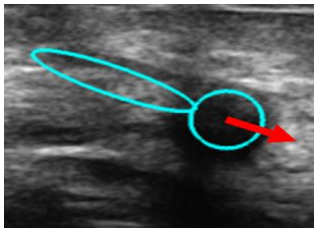

Figure 3: Distance between needle and tumor boundary.

Comparison of Dynamic ^{18}F-DCFPyL and ^{18}F-FCH PET Imaging in Patients with Prostate Cancer

Dae-Myoung (Danny) Yang*[1,4,5], Fiona Li[1,4,5], Glenn Bauman[2,5], John Valliant[7], Wenqing He[3], and Ting-Yim Lee[1,2,4,5] (Supervisor)

OICR Smarter Imaging Program Consortium

[1]Medical Biophysics, [2]Oncology, [3]Statistical and Actuarial Science, and [4]Robarts Research Institute, The University of Western Ontario, London, Ontario, Canada [5]Lawson Health Research Institute and [6]London Regional Cancer Program, London Health Sciences Centre, London, Ontario, Canada and [7]Centre for Probe Development and Commercialization, McMaster University, Hamilton, Ontario, Canada

Introduction. Currently, Positron emission tomography (PET) imaging with ^{18}F-DCFPyL has been used to localize and detect prostate cancer (PCa) nodules with high contrast to background normal prostatic tissue. In contrast many studies with ^{18}F-flourocholine (^{18}F-FCH) which previously was widely used for imaging PCa, showed that choline uptake is not always higher in tumor region. Herein we investigated whether the difference between the two tracers can be explained by their kinetic behaviour in PCa.

Methods. Patients with pathologically confirmed PCa underwent dynamic PET imaging. Seven patients with histologically confirmed PCa (mean prostate-specific antigen (PSA), 10.7 ± 7.9 ng/mL; Gleason score 3+4, proportion of prostate involved with tumour 20%) were evaluated with dynamic ^{18}F-DCFPyL PET, and another seven patients with similar characteristics (mean PSA, 7.9 ± 3.8 ng/mL, Gleason score 3+4, tumour involvement 20%) underwent dynamic ^{18}F-FCH PET. The dynamic PET imaging protocol consisted of 10 images at 10 s each, 5 at 20 s, 4 at 40 s, 4 at 60 s and 4 at 180 s (total acquisition time of 22 min). Based on prostate sextant biopsy and a standardized uptake value (SUV) map constructed from the sum of the last 4 dynamic frames (12-22 min post injection), tumour and normal tissue regions of interest (ROI) were segmented. The ROIs were evaluated semi-quantitatively using the SUV map and quantitatively using Johnson-Wilson-Lee model modified open 3-compartment model (see figure) kinetic parameters: F (Blood flow), K_1 (Influx rate), k_2 (Efflux rate constant), k_3 (Binding rate constant), k_4 (Dissociation rate constant) and K_i (Normalized net uptake rate) which describes the blood flow delivery to tissue and subsequent binding to target, which were estimated from artery (iliac or femoral) and tissue time-activity curves.

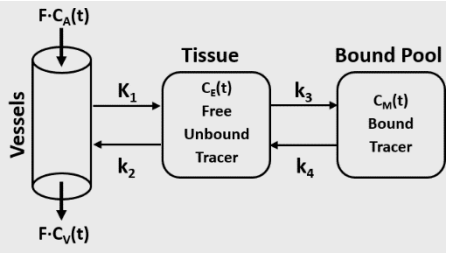

Results. Logistic regression with backward elimination showed that k_4 and K_i were the best combination amongst SUV and kinetic parameters for ^{18}F-DCFPyL to discriminate tumor from normal tissue while SUV and K1 were the best combination for ^{18}F-FCH.The normalized washout rate constant from the bound pool, as estimated by the inverse of binding potential (k_4/k_3), of ^{18}F-DCFPyL from normal tissue was greater than tumour while for ^{18}F-FCH both normal tissue and tumour had similar normalized washout rate constant. The binding rate constant (k_3) of ^{18}F-FCH was higher than ^{18}F-DCFPyL for both normal tissue and tumour.

Conclusions. Kinetic analysis of ^{18}F-DCFPyL is more sensitive than the semi-quantitative SUV for detecting and differentiating tumour from normal prostatic tissue. The ^{18}F-DCFPyL contrast between tumour and normal tissue is due to the differential normalized washout. In contrast, the lack of ^{18}F-FCH contrast between tumour and normal tissue is due to similar normalized washout. The large binding rate constant of ^{18}F-FCH vs ^{18}F-DCFPyL suggested that the former has a faster uptake rate and at time interval when binding dominates, SUV could be used to differentiate sensitively tumour from normal tissue.

Intraoperative Breast Tumour Margin Assessment: A Photoacoustic Solution

Lawrence CM Yip[1,2], Madeleine Van De Kleut[1], Ivan Kosik[1,2], Astrid Chamson-Reig[2], Jeffrey JL Carson[1,2]
[1]Western University
[2]Lawson Health Research Institute
Supervisor: Jeffrey JL Carson

INTRODUCTION

Breast cancer accounts for 25% of all cancer cases among women (Torre et al., 2015), and in many of these cases, breast conserving surgery (BCS) is recommended along with adjuvant therapy (chemotherapy or radiotherapy). In BCS, the tumour is excised with a healthy tissue margin of 2-mm to 10-mm width depending on the type of breast cancer (Azu et al., 2010). However, detection of the margin can be difficult and dependent on the skill of the surgeon. Current preoperative and intraoperative imaging techniques to guide the excision are often insufficient, and re-excision can occur up to 25% of the time, which occurs when tumour is detected in the margin (i.e. positive margin) by pathology (Park et al., 2000).

Photoacoustic imaging (PAI) is a hybrid imaging modality based on the photoacoustic effect that combines the advantages of optical imaging (excellent contrast) and ultrasound (high resolution and penetration depth) (Mallidi et al., 2011). Pulsed (safe and non-ionizing) laser light is used to irradiate tissue, which results in the generation of acoustic waves. Since the amplitude of the waves is proportional to the light absorbed, and optical absorption differs between substances, features such as size, composition and function can be determined through reconstruction of the detected signals into images. This can be particularly useful when imaging cancerous tissues; PAI can detect the increased haemoglobin and decreased oxygen concentrations that are present in tumours without the use of contrast enhancing dyes by targeting multiple wavelengths of light.

METHODS AND MATERIALS

The new imaging system was designed and built with the aid of computer-aided-design software to enable an even and dense scan pattern throughout a near-spherical surface. Custom-made sensors built by our lab were implemented for greater sensitivity and to target the desired sensor centre frequency. Imaging phantoms are being used to determine system specifications. Once complete, the system will be made portable and an initial study performed on ~5 ex vivo tumours. This will be followed by a larger study of 100 patients for statistically significant results.

RESULTS

We have built a PAI system as a potential solution to lumpectomy tumour margin assessment. Using a novel design incorporating a flexible robotic arm with 6 degrees of freedom and a custom transducer array, we will provide an intraoperative imaging solution with excellent contrast, resolution, and penetration depth. Imaging phantoms are being developed and early images show promise.

CONCLUSIONS

PAI has advantages in several areas, including great potential with differentiating healthy and cancerous tissue. As previously mentioned, PAI can be used to detect haemoglobin and oxygen concentration as well as several other functional differences. By reducing the need for re-excision, our project has the potential to not only minimize patient burden, but also alleviate the financial impact breast cancer has on our economy.

Ultra-Short Echo Time MRI Quantification of Airspace Enlargement in Bronchopulmonary Dysplasia and Alpha-1 Antitrypsin Deficiency: Parenchyma Destruction, Air trapping or Both?

Heather Young*[1,2], Dante PI Capaldi[1,2], Khadija Sheikh[1,2], David G McCormack[3], Cory M Yamashita[3], and Grace Parraga[1,2]

[1]Robarts Research Institute, [2]Department of Medical Biophysics, [3]Division of Respirology, Department of Medicine, The University of Western Ontario, London, Canada

Introduction: The onset of chronic obstructive pulmonary disease (COPD) in early adulthood is typical in patients with alpha-one antitrypsin deficiency (AATD)[1] and survivors of neonatal bronchopulmonary dysplasia (BPD).[2] There are established computed tomography (CT) radiodensity thresholds for identification of emphysema[3] (<-950 Hounsfield units (HU)) and air-trapping[4] (<-856HU). Ultra-short echo time (UTE) MRI signal-intensity (SI) is spatially and quantitatively correlated with CT density in COPD patients;[5] however, it has not yet been evaluated in young patients with obstructive lung disease stemming from AATD and BPD, where there may be different mechanisms of destruction. Thus, the objective of this work was to investigate UTE MRI SI measurements in young patients with BPD and AATD. We hypothesized that an MRI SI threshold could be determined in a small group of patients to quantify airspace-enlargement.

Methods: Subjects with a diagnosis of AATD/BPD provided written informed consent to ethics-board approved protocols and were evaluated using MRI, CT, and spirometry. Imaging was performed on a whole body 3T Discovery MR750 (General Electric Health Care [GEHC], Milwaukee, WI). UTE MRI was obtained using a 32-channel torso coil (GEHC) and 3D-cones UTE research sequence (GEHC). Eighteen coronal slices were acquired with the following parameters in breath-hold: acquisition-time=15s, TE/TR/flip-angle=0.03ms/3.5ms/5°, FOV=40×40cm, matrix=200×200, NEX=1, and slice-thickness=10mm. UTE and CT images were acquired at functional-residual-capacity (FRC)+1L as previously described.[5]

UTE SI was normalized to mean liver SI. UTE images were non-rigidly co-registered[6] with CT, which was segmented using VIDA Pulmonary Workstation (VIDA Diagnostics, Coralville, IA), as previously described[5]. CT density thresholds of -950HU and -856HU were used to identify regions suggestive of emphysema and gas-trapping, respectively, and regions with low UTE SI were identified for multiple threshold values. For each threshold, the UTE mask was compared to the CT masks using the Dice similarity coefficient (DSC) and an overlap coefficient $OC = |CTmask \cap UTEmask|/CTmask$. The leave-one-out method was used to identify an optimal normalized UTE SI threshold of 29 corresponding to the highest DSC value when compared to the -950HU mask.

Results: In this proof-of-concept demonstration, we evaluated three adults with AATD (60±7 years) and one adult survivor of BPD (27 years), with post-salbutamol FEV_1/FVC of 41±13% and 39%, respectively. Figure 1 shows CT and UTE MRI for representative AATD and BPD participants, with ≤-950HU and ≤-856HU CT masks and UTE normalized SI ≤29 mask. Compared to the -950HU mask, the mean DSC was 0.24±0.14 and mean OC was 0.60±0.18. Compared to the -856HU mask, the mean DSC was 0.62±0.13 and mean OC was 0.55±0.20.

Regions of normalized UTE SI in AATD and BPD are suggestive of airspace enlargement but it is difficult to ascertain if this is due to emphysema or gas-trapping. It should be noted that the lung volumes imaged were not the volumes previously reported to evaluate gas-trapping (full-expiration)[4] and emphysema(full-inspiration)[3]. CT/MR images were acquired at FRC+1L, so there was a slight underestimate of emphysema and overestimate of gas-trapping, altering the DSC. Further studies using UTE MRI may allow a better understanding of the mechanisms of parenchyma and airway destruction in AATD and BPD.

Conclusion: Regions of normalized UTE SI <29 may suggest airspace enlargement, and demonstrate the potential utility of UTE MRI in quantifying this without ionizing radiation in young adults with AATD and BPD.

References: (1) Kohnlein, T. & Welte, T. *Am J Med* 2008. (2) Boucherat, O. et al. *Am J Respir Crit Care Med* 2016. (3) Hayhurst, M.D., *et al. Lancet* 1984. (4) Zach, J.A., *et al. Invest Radiol* 2012. (5) Ma, W., *et al. J Magn Reson Imaging* 2016. (6) Heinrich, M.P. *et al. Medical image analysis* 2012.

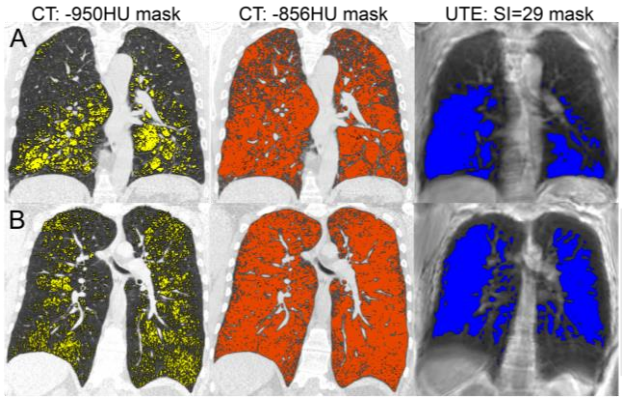

Figure 1. CT and UTE MR images for representative AATD (top row) and BPD (bottom row) subjects. On the left, the yellow mask indicates areas of CT radiodensity <-950HU, suggestive of emphysema. In the center, the orange mask indicates areas of CT radiodensity <-856HU, suggestive of gas-trapping. On the right, the blue mask on the UTE MRI indicates areas of normalized signal intensity <29. A) The UTE mask identifies areas of low radiodensity suggestive of emphysema. B) The UTE mask identifies areas of low radiodensity except near the diaphragm, where motion artifacts are present.

Ontario

OICR
Ontario Institute
for Cancer Research

NIH *Eunice Kennedy Shriver* National Institute
of Child Health and Human Development

CFREF

synaptive

Western Bone and Joint Institute